

JUNE 2022

**AJNR**

VOLUME 43 • PP 791-925

# AJNR

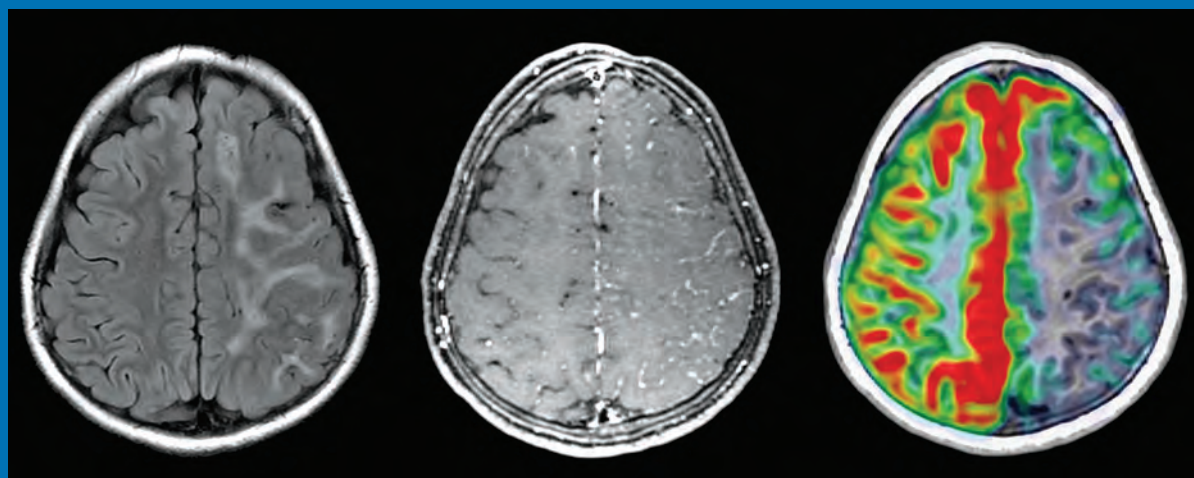
## AMERICAN JOURNAL OF NEURORADIOLOGY

JUNE 2022  
VOLUME 43  
NUMBER 6  
[WWW.AJNR.ORG](http://WWW.AJNR.ORG)

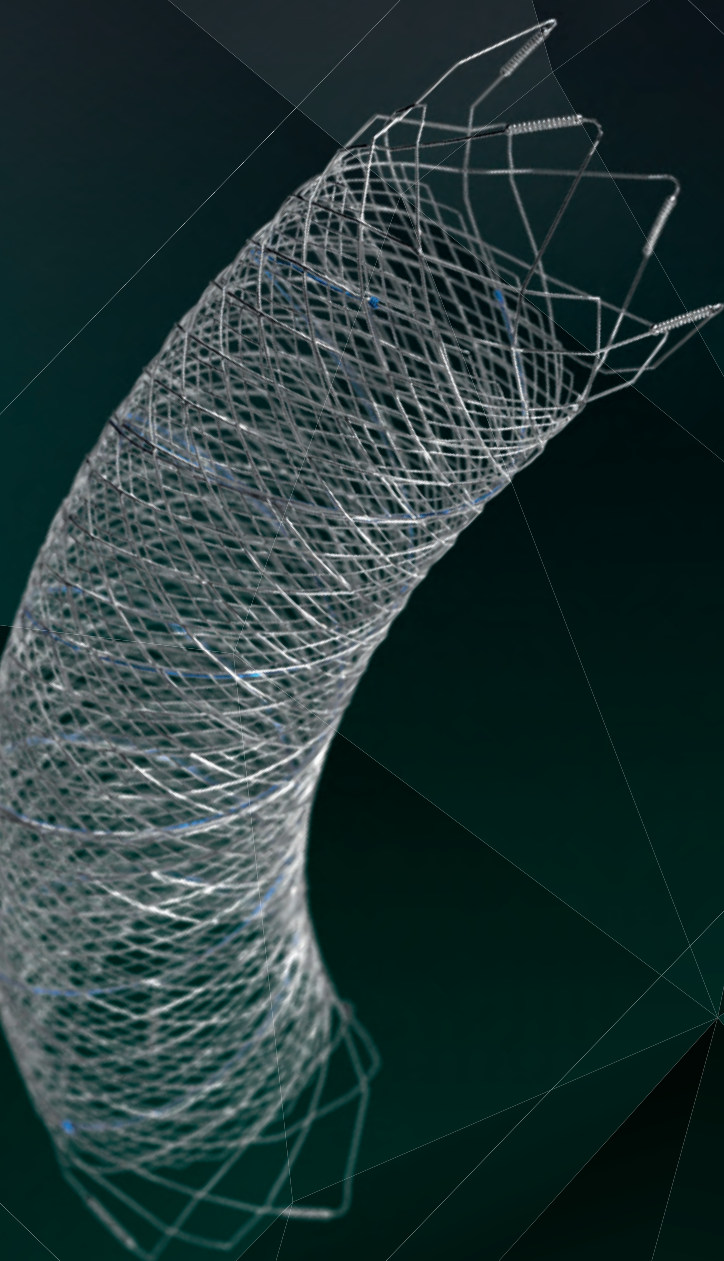
THE JOURNAL OF DIAGNOSTIC AND  
INTERVENTIONAL NEURORADIOLOGY

Brain abnormalities and epilepsy in patients with Parry-Romberg syndrome  
Intracranial aneurysms in patients with hereditary hemorrhagic telangiectasia  
Nonlesional sources of contrast enhancement in patients with multiple sclerosis

Official Journal ASNR • ASFNR • ASHNR • ASPNR • ASSR



# Introducing FRED™



## THE NEXT ADVANCEMENT IN FLOW DIVERSION TECHNOLOGY

The FRED™ X Flow Diverter features the same precise placement and immediate opening of the FRED™ Device, now with X Technology. X Technology is a covalently bonded, nanoscale surface treatment, designed to:

- » **Reduce material thrombogenicity<sup>1</sup>**
- » **Maintain natural vessel healing response<sup>2,3,4</sup>**
- » **Improve device deliverability and resheathing<sup>1</sup>**

The only FDA PMA approved portfolio with a 0.021" delivery system for smaller device sizes, and no distal lead wire.



For more information, contact your local MicroVention sales representative or visit our website. [www.microvention.com](http://www.microvention.com)



<sup>\*</sup> Data is derived from in vivo and ex vitro testing and may not be representative of clinical performance.

<sup>1</sup> Data on file

<sup>2</sup> Tanaka M et al. Design of biocompatible and biodegradable polymers based on intermediate water concept. *Polymer Journal*. 2015;47:114-121.

<sup>3</sup> Tanaka M et al. Blood compatible aspects of poly(2-methoxyethylacrylate) (PMEA) – relationship between protein adsorption and platelet adhesion on PMEA surface. *Biomaterials*. 2000;21:1471-1481.

<sup>4</sup> Schiel L et al. X Coating™: A new biopassive polymer coating. *Canadian Perfusion Canadienne*. June 2001;11(2):9.

**Indications for Use:** The FRED X System is indicated for use in the internal carotid artery from the petrous segment to the terminus for the endovascular treatment of adult patients (22 years of age or older) with wide-necked (neck width 4 mm or dome-to-neck ratio <2) saccular or fusiform intracranial aneurysms arising from a parent vessel with a diameter 2.0 mm and 5.0 mm.

**Rx Only:** Federal (United States) law restricts this device to sale by or on the order of a physician.

MICROVENTION, FRED and HEADWAY are registered trademarks of MicroVention, Inc. in the United States and other jurisdictions. Stylized X is a trademark of MicroVention, Inc. © 2022 MicroVention, Inc. MM1222 US 02/22

# WEB™ 17

Aneurysm Embolization System

# LOWER PROFILE



## NEW SIZES



## MORE ACCESS OPTIONS



#### INDICATIONS FOR USE:

The WEB Aneurysm Embolization System is intended for the endovascular embolization of ruptured and unruptured intracranial aneurysms and other neurovascular abnormalities such as arteriovenous fistulae (AVF). The WEB Aneurysm Embolization System is also intended for vascular occlusion of blood vessels within the neurovascular system to permanently obstruct blood flow to an aneurysm or other vascular malformation.

#### POTENTIAL COMPLICATIONS:

Potential complications include but are not limited to the following: hematoma at the site of entry, aneurysm rupture, emboli, vessel perforation, parent artery occlusion, hemorrhage, ischemia, vasospasm, clot formation, device migration or misplacement, premature or difficult device detachment, non-detachment, incomplete aneurysm filling, revascularization, post-embolization syndrome, and neurological deficits including stroke and death. For complete indications, potential complications, warnings, precautions, and instructions, see instructions for use (IFU provided with the device).

VIA 21, 27, 33 - The VIA Microcatheter is intended for the introduction of interventional devices (such as the WEB device/stents/flow diverters) and infusion of diagnostic agents (such as contrast media) into the neuro, peripheral, and coronary vasculature.

VIA 17, 17 Preshaped - The VIA Microcatheter is intended for the introduction of interventional devices (such as the WEB device/stents/flow diverters) and infusion of diagnostic agents (such as contrast media) into the neuro, peripheral, and coronary vasculature.

The VIA Microcatheter is contraindicated for use with liquid embolic materials, such as n-butyl 2-cyanoacrylate or ethylene vinyl alcohol & DMSO (dimethyl sulfoxide).

The device should only be used by physicians who have undergone training in all aspects of the WEB Aneurysm Embolization System procedure as prescribed by the manufacturer.

RX Only: Federal law restricts this device to sale by or on the order of a physician.

For healthcare professional intended use only.



MicroVention Worldwide  
Innovation Center

PH +1.714.247.8000

35 Enterprise  
Aliso Viejo, CA 92656 USA  
MicroVention UK Limited  
MicroVention Europe, S.A.R.L.  
MicroVention Deutschland GmbH  
Website

PH +44 (0) 191 258 6777  
PH +33 (1) 39 21 77 46  
PH +49 211 210 798-0  
microvention.com



WEB™ and VIA™ are registered trademarks  
of Sequent Medical, Inc. in the United States.

©2021 MicroVention, Inc. MM1184 WW 11/2021





TRUST EARNED

# What does seeing better with MultiHance® mean?<sup>1-4\*</sup>

**MultiHance® demonstrated significantly improved visualization and contrast enhancement of CNS lesions when compared with Gadavist® at 0.1 mmol/kg.<sup>1†</sup>**

- The 0.1 mmol/kg dose of MultiHance demonstrated consistently better lesion visualization for all readers compared to all tested MR contrast agents.<sup>1-4</sup>
- 3 blinded independent readers reported superiority for MultiHance in significantly ( $P = .0001$ ) more patients for all evaluated end points. The opinions of the 3 readers were identical for 61.9%–73.5% of the patients, resulting in values of 0.414–0.629 for inter-reader agreement.

The individuals who appear are for illustrative purposes. All persons depicted are models and not real patients.

Please see Brief Summary of Prescribing Information including Boxed Warning on adjacent page.

\*MRI imaging of the CNS in adult and pediatric patients to visualize lesions with abnormal BBB or abnormal vascularity of the brain, spine and associated tissues or to evaluate adults with known or suspected renal or aorto-ilio-femoral occlusive vascular disease.

**MultiHance® (gadobenate dimeglumine) injection, 529 mg/mL and MultiHance® Multipack™ (gadobenate dimeglumine) injection, 529 mg/mL**

## Indications and Usage:

MultiHance® (gadobenate dimeglumine) injection, 529 mg/mL is a gadolinium-based contrast agent indicated for intravenous use in:

- Magnetic resonance imaging (MRI) of the central nervous system (CNS) in adults and pediatric patients (including term neonates) to visualize lesions with abnormal blood-brain barrier or abnormal vascularity of the brain, spine, and associated tissues and
- Magnetic resonance angiography (MRA) to evaluate adults with known or suspected renal or aorto-ilio-femoral occlusive vascular disease

## IMPORTANT SAFETY INFORMATION:

### WARNING: NEPHROGENIC SYSTEMIC FIBROSIS

**Gadolinium-based contrast agents (GBCAs) increase the risk for NSF among patients with impaired elimination of the drugs. Avoid use of GBCAs in these patients unless the diagnostic information is essential and not available with non-contrasted MRI or other modalities. NSF may result in fatal or debilitating systemic fibrosis affecting the skin, muscle and internal organs.**

- The risk for NSF appears highest among patients with:
  - chronic, severe kidney disease ( $\text{GFR} < 30 \text{ mL/min/1.73m}^2$ ), or
  - acute kidney injury.
- Screen patients for acute kidney injury and other conditions that may reduce renal function. For patients at risk for chronically reduced renal function (e.g. age > 60 years, hypertension or diabetes), estimate the glomerular filtration rate (GFR) through laboratory testing.
- For patients at highest risk for NSF, do not exceed the recommended MultiHance dose and allow a sufficient period of time for elimination of the drug from the body prior to re-administration.

## CONTRAINDICATIONS

MultiHance is contraindicated in patients with known allergic or hypersensitivity reactions to gadolinium-based contrast agents.

## WARNINGS AND PRECAUTIONS

**Nephrogenic Systemic Fibrosis:** NSF has occurred in patients with impaired elimination of GBCAs. Higher than recommended dosing or repeated dosing appears to increase risk.

**Hypersensitivity Reactions:** Anaphylactic and anaphylactoid reactions have been reported, involving cardiovascular, respiratory, and/or cutaneous manifestations. Some patients experienced circulatory collapse and died. In most cases, initial symptoms occurred within minutes of MultiHance administration and resolved with prompt emergency treatment. Consider the risk for hypersensitivity reactions, especially in patients with a history of hypersensitivity reactions or a history of asthma or other allergic disorders.

**Gadolinium Retention:** Gadolinium is retained for months or years in several organs. The highest concentrations have been identified in the bone, followed by brain, skin, kidney, liver, and spleen. At equivalent doses, retention varies among the linear agents. Retention is lowest and similar among the macrocyclic GBCAs. Consequences of gadolinium retention in the brain have not been established, but they have been established in the skin and other organs in patients with impaired renal function. Minimize repetitive GBCA imaging studies, particularly closely spaced studies when possible.

**Acute Renal Failure:** In patients with renal insufficiency, acute renal failure requiring dialysis or worsening renal function have occurred with the use of GBCAs. The risk of renal failure may increase with increasing dose of the contrast agent. Screen all patients for renal dysfunction by obtaining a history and/or laboratory tests.

**Extravasation and Injection Site Reactions:** Extravasation of MultiHance may lead to injection site reactions, characterized by local pain or burning sensation, swelling, blistering, and necrosis. Exercise caution to avoid local extravasation during intravenous administration of MultiHance.

**Cardiac Arrhythmias:** Cardiac arrhythmias have been observed in patients receiving MultiHance in clinical trials. Assess patients for underlying conditions



MR Suite



LIFE FROM INSIDE

or medications that predispose to arrhythmias. The effects on QTc by MultiHance dose, other drugs, and medical conditions were not systematically studied.

**Interference with Visualization of Certain Lesions:** Certain lesions seen on non-contrast images may not be seen on contrast images. Exercise caution when interpreting contrast MR images in the absence of companion non-contrast MR images.

#### ADVERSE REACTIONS

The most commonly reported adverse reactions are nausea (1.3%) and headache (1.2%).

#### USE IN SPECIFIC POPULATIONS

**Pregnancy:** GBCAs cross the human placenta and result in fetal exposure and gadolinium retention. Use only if imaging is essential during pregnancy and cannot be delayed.

**Lactation:** There is no information on the effects of the drug on the breastfed infant or the effects of the drug on milk production. However, limited literature reports that breastfeeding after MultiHance administration to the mother would result in the infant receiving an oral dose of 0.001%-0.04% of the maternal dose.

**Pediatric Use:** MultiHance is approved for intravenous use for MRI of the CNS to visualize lesions with abnormal blood brain barrier or abnormal vascularity of the brain, spine, and associated tissues in pediatric patients from birth, including term neonates, to less than 17 years of age. Adverse reactions in pediatric patients were similar to those reported in adults. No dose adjustment according to age is necessary in pediatric patients two years of age and older. For pediatric patients, less than 2 years of age, the recommended dosage range is 0.1 to 0.2 mL/kg. The safety of MultiHance has not been established in preterm neonates.

Please see full Prescribing Information and Patient Medication Guide for additional important safety information for/regarding MultiHance (gadobenate dimeglumine) injection, 529 mg/mL at <https://www.braccoimaging.com/us-en/products/magnetic-resonance-imaging/multihance>

**You are encouraged to report negative side effects of prescription drugs to the FDA. Visit [www.fda.gov/medwatch](http://www.fda.gov/medwatch) or call 1-800-FDA-1088.**

MultiHance is manufactured for Bracco Diagnostics Inc. by BIPSO GmbH – 78224 Singen (Germany) and by Patheon Italia S.p.A., Ferentino, Italy. MultiHance is a registered trademark of Bracco International B.V. MultiHance Multipack is a trademark of Bracco International B.V. All other trademarks and registered trademarks are the property of their respective owners.

**References:** 1. Seidl Z, Vymazal J, Mechi M, et al. Does higher gadolinium concentration play a role in the morphologic assessment of brain tumors? Results of a multicenter intraindividual crossover comparison of gadobutrol versus gadobenate dimeglumine (the MERIT Study). *AJNR Am J Neuroradiol.* 2012;33(6):1050-1058. 2. Maravilla KR, Maldjian JA, Schmalfuss IM, et al. Contrast enhancement of central nervous system lesions: multicenter intraindividual crossover comparative study of two MR contrast agents. *Radiology.* 2006;240(2):389-400. 3. Rowley HA, Scialfa G, Gao PY, et al. Contrast-enhanced MR imaging of brain lesions: a large-scale intraindividual crossover comparison of gadobenate dimeglumine versus gadodiamide. *AJNR Am J Neuroradiol.* 2008;29(9):1684-1691. 4. Vaneckova M, Herman M, Smith MP, et al. The benefits of high relaxivity for brain tumor imaging: results of a multicenter intraindividual crossover comparison of gadobenate dimeglumine with gadoterate meglumine (The BENEFIT Study). *AJNR Am J Neuroradiol.* 2015 Sep;36(9):1589-1598.

Bracco Diagnostics Inc.  
259 Prospect Plains Road, Building H  
Monroe Township, NJ 08831 USA  
Phone: 609-514-2200  
Toll Free: 1-877-272-2269 (U.S. only)  
Fax: 609-514-2446

© 2022 Bracco Diagnostics Inc. All Rights Reserved. US-MH-2100018 02/22





**Rx ONLY**  
Please see full prescribing information.  
A brief summary follows.

#### WARNING: NEPHROGENIC SYSTEMIC FIBROSIS

Gadolinium-based contrast agents (GBCAs) increase the risk for NSF among patients with impaired elimination of the drugs.  
Avoid use of GBCAs in these patients unless the diagnostic information is essential and not available with non-contrast MRI or other modalities. NSF may result in fatal or debilitating systemic fibrosis affecting the skin, muscle and internal organs.

- The risk for NSF appears highest among patients with:
  - acute kidney injury.
  - chronic, severe kidney disease (GFR <30 mL/min/1.73m<sup>2</sup>), or
- Screen patients for acute kidney injury and other conditions that may reduce renal function. For patients at risk for chronically reduced renal function (e.g. age > 60 years, hypertension or diabetes), estimate the glomerular filtration rate (GFR) through laboratory testing.
- For patients at highest risk for NSF, do not exceed the recommended MultiHance dose and allow a sufficient period of time for elimination of the drug from the body prior to re-administration. [see **Warnings and Precautions (5.1)**]

#### 1 INDICATIONS AND USAGE

##### 1.1 MRI of the Central Nervous System (CNS)

MultiHance is indicated for intravenous use in magnetic resonance imaging (MRI) of the central nervous system (CNS) in adults and pediatric patients (including term neonates), to visualize lesions with abnormal blood-brain barrier or abnormal vascularity of the brain, spine, and associated tissues.

##### 1.2 MRA of Renal and Aorta-Iliofemoral Vessels

MultiHance is indicated for use in magnetic resonance angiography (MRA) to evaluate lesions with known or suspected renal or aorta-iliofemoral occlusive vascular disease.

#### 4 CONTRAINDICATIONS

MultiHance is contraindicated in patients with known allergic or hypersensitivity reactions to gadolinium-based contrast agents [see **Warnings and Precautions (5.2)**].

#### 5 WARNINGS AND PRECAUTIONS

**5.1 Nephrogenic Systemic Fibrosis (NSF)** Gadolinium-based contrast agents (GBCAs) increase the risk for nephrogenic systemic fibrosis (NSF) among patients with impaired elimination of the drugs. Avoid use of GBCAs among these patients unless the diagnostic information is essential and not available with non-contrast MRI or other modalities. The GBCA associated NSF risk appears highest for patients with chronic, severe kidney disease (GFR <30 mL/min/1.73m<sup>2</sup>) as well as patients with acute kidney injury. The risk appears lower for patients with chronic, moderate kidney disease (GFR 30-59 mL/min/1.73m<sup>2</sup>) and little, if any, for patients with chronic, mild kidney disease (GFR 60-89 mL/min/1.73m<sup>2</sup>). NSF may result in fatal or debilitating fibrosis affecting the skin, muscle and internal organs. Report any diagnosis of NSF following MultiHance administration to Bracco Diagnostics (1-800-257-5181) or FDA (1-800-FDA-1088 or [www.fda.gov/medwatch](http://www.fda.gov/medwatch)).

Screen patients for acute kidney injury and other conditions that may reduce renal function. Features of acute kidney injury consist of rapid (over hours to days) and usually reversible decrease in kidney function, commonly in the setting of surgery, severe infection, injury or drug-induced kidney toxicity. Serum creatinine levels and estimated GFR may not reliably assess renal function in the setting of acute kidney injury. For patients at risk for chronically reduced renal function (e.g., age > 60 years, diabetes mellitus or chronic hypertension), estimate the GFR through laboratory testing.

Among the factors that may increase the risk for NSF are repeated or higher than recommended doses of a GBCA and the degree of renal impairment at the time of exposure. Record the specific GBCA and the dose administered to a patient. For patients at highest risk for NSF, do not exceed the recommended MultiHance dose and allow a sufficient period of time for elimination of the drug prior to re-administration. For patients receiving hemodialysis, physicians may consider prompt initiation of hemodialysis following the administration of a GBCA in order to enhance the contrast agent's elimination. The usefulness of hemodialysis in the prevention of NSF is unknown [see **Dosage and Administration (2)** and **Clinical Pharmacology (12)**].

**5.2 Hypersensitivity Reactions** Anaphylactic and anaphylactoid reactions have been reported, involving cardiovascular, respiratory, and/or cutaneous manifestations. Some patients experienced circulatory collapse and died. In most cases, initial symptoms occurred within minutes of MultiHance administration and resolved with prompt emergency treatment. Prior to MultiHance administration, ensure the availability of personnel trained and medications to treat hypersensitivity reactions. If such a reaction occurs stop MultiHance and immediately begin appropriate therapy. Additionally, consider the risk for hypersensitivity reactions, especially in patients with a history of hypersensitivity reactions or a history of asthma or other allergic disorders. Observe patients for signs and symptoms of a hypersensitivity reaction during and for up to 2 hours after MultiHance administration.

**5.3 Gadolinium Retention** Gadolinium is retained for months or years in several organs. The highest concentrations (nanomoles per gram of tissue) have been identified in the bone, followed by other organs (e.g., brain, skin, kidney, liver, and spleen). The duration of retention also varies by tissue and is longest in bone. Linear GBCAs cause more retention than macrocyclic GBCAs. At equivalent doses, gadolinium retention varies among the linear agents with Omniscan (gadodiamide) and Optcontrast (gadoterme dimeglumine) causing greater retention than other linear agents (Eovist (gadoterate dimeglumine), Magnevist (gadopentate dimeglumine), MultiHance (gadobenate dimeglumine)). Retention is lowest and similar among the macrocyclic GBCAs (Dotarem (gadoterate dimeglumine), Gadavist (gadobutrol), ProHance (gadobutrol)).

Consequences of gadolinium retention in the brain have not been established. Pathologic and clinical consequences of GBCA administration and retention in skin and other organs have been established in patients with impaired renal function [see **Warnings and Precautions (5.1)**]. There are reports of pathologic skin changes in patients with normal renal function. Adverse events involving multiple organ systems have been reported in patients with normal renal function without an established causal link to gadolinium retention [see **Adverse Reactions (6.2)**]. While clinical consequences of gadolinium retention have not been established in patients with normal renal function, certain patients might be at higher risk. These include patients requiring multiple lifetime doses, pregnant and pediatric patients, and patients with inflammatory conditions. Consider the retention characteristics of the agent when choosing a GBCA for these patients. Minimize repetitive GBCA imaging studies, particularly closely spaced studies when possible.

**5.4 Acute Renal Failure** In patients with renal insufficiency, acute renal failure requiring dialysis or worsening renal function have occurred with the use of gadolinium-based contrast agents. The risk of renal failure may increase with increasing dose of the contrast agent. Screen all patients for renal dysfunction by obtaining a history and/or laboratory tests. Consider follow-up renal function assessments for patients with a history of renal dysfunction.

**5.5 Extravasation and Injection Site Reactions** Extravasation of MultiHance may lead to injection site reactions, characterized by local pain or burning, sensation, swelling, blistering, and necrosis. In animal experiments, local reactions including eschar and necrosis were noted even on Day 8 post perivascular injection of MultiHance. Exercise caution to avoid local extravasation during intravenous administration of MultiHance. If extravasation occurs, evaluate and treat as necessary if local reactions develop.

**5.6 Cardiac Arrhythmias** Cardiac arrhythmias have been observed in patients receiving MultiHance in clinical trials [see **Adverse Reactions (6.1)**]. Assess patients for underlying conditions or medications that predispose to arrhythmias.

A double-blind, placebo-controlled, 24-hour post dose continuous monitoring, crossover study in 47 subjects evaluated the effect of 0.2 mmol/kg MultiHance on ECG intervals, including QTc. The average changes in QTc values compared with placebo were minimal (<5 msec). QTc prolongations were noted in 20 subjects, including 11 subjects who received MultiHance vs. 11 subjects who received placebo. Prolongations ≥ 61 msec were noted in 6 subjects who received MultiHance and in 3 subjects who received placebo. None of these subjects had associated malignant arrhythmias. The effects on QTc by MultiHance dose, other drugs, and medical conditions were not systematically studied.

**5.7 Interference with Visualization of Certain Lesions** Certain lesions seen on non-contrast images may not be seen on contrast images. Exercise caution when interpreting contrast MR images in the absence of companion non-contrast MR images.

#### 6 ADVERSE REACTIONS

The following adverse reactions are discussed in greater detail in other sections of the label:
 

- Nephrogenic systemic fibrosis [see **Warnings and Precautions (5.1)**]

• Hypersensitivity reactions [see **Warnings and Precautions (5.2)**]

##### 6.1 Clinical Trials Experience

Because clinical trials are conducted under widely varying conditions, adverse reaction rates observed in the clinical trials of a drug cannot be directly compared to rates in the clinical trials of another drug and may not reflect the rates observed in practice.

**Adult** In clinical trials with MultiHance, a total of 4967 adult subjects (137 healthy volunteers and 4830 patients) received MultiHance at doses ranging from 0.005 to 0.4 mmol/kg. There were 2638 (53%) men and 2129 (43%) women with a mean age of 56.5 years (range 18 to 90 years). A total of 4403 (89%) subjects were Caucasian, 134 (3%) Black, 275 (6%) Asian, 40 (1%) Hispanic, 70 (1%) in other racial groups, and for 45 (1%) subjects, race was not reported.

The most commonly reported adverse reactions in adult subjects who received MultiHance were nausea (1.3%) and headache (1.2%). Most adverse reactions were mild to moderate in intensity. One subject experienced a serious anaphylactoid reaction with laryngeal spasm and dyspnea [see **Warnings and Precautions (5.2)**]. Serious adverse reactions consisting of convulsions, pulmonary, acute necrotizing pancreatitis, and anaphylactoid reactions were reported in 0.1% of subjects in clinical trials.

Adverse reactions that occurred in at least 0.5% of 4967 adult subjects who received MultiHance are listed below (Table 2), in decreasing order of occurrence within each system.

System	Number of subjects	Percentage
Number of subjects dosed	4967	
Number of subjects with any adverse reaction	517 (10.4%)	
Gastrointestinal Disorders		
Nausea	67 (1.3%)	
Headache	60 (1.2%)	
General Disorders and Administration Site Disorders		
Injection Site Reaction	54 (1.1%)	
Feeling Hot	49 (1.0%)	
Nervous System Disorders		
Dizziness	60 (1.2%)	
Dysgeusia	33 (0.7%)	
Paresthesia	24 (0.5%)	
Dizziness	24 (0.5%)	

The following adverse reactions occurred in less than 0.5% of the 4967 adult subjects who received MultiHance. Serious adverse reactions described above are not repeated below.

**Blood and Lymphatic System Disorders:** Basophilia, Cardiac Disorders: Atrioventricular block first degree, Eye Disorders: Eye pruritus, eye swelling, ocular hyperemia, visual disturbance, Gastrointestinal Disorders: Abdominal pain or discomfort, diarrhea, dry mouth, lip swelling, parosmia oral, tongue edema, vomiting, General Disorders and Administration Site Conditions: Chest pain or discomfort, chills, malaise, Immune System Disorders: Hypersensitivity, Investigations: Non-specific changes in laboratory tests (including hematology, blood chemistry, liver enzymes and urinalysis), blood pressure and electrocardiogram parameters (including PR, QRS and QT intervals and ST-T segment changes), Musculoskeletal and Connective Tissue Disorders: Myalgia, Nervous System Disorders: Parosmia, tremor, Respiratory, Thoracic and Mediastinal Disorders: Dyspnea, laryngospasm, nasal congestion, sneezing, wheezing, Skin and Subcutaneous Tissue Disorders: Hyperhidrosis, pruritus, rash, swelling face, urticaria.

**Pediatric** In clinical trials of MultiHance in MRI of the CNS, 217 pediatric subjects received MultiHance at a dose of 0.1 mmol/kg. A total of 112 (52%) subjects were male and the overall mean age was 6.3 years (range 4 days to 17 years). A total of 168 (79%) subjects were Caucasian, 12 (6%) Black, 12 (6%) Asian, 24 (11%) Hispanic, and 1 (<1%) in other racial groups.

Adverse reactions were reported for 14 (6.5%) of the subjects. The frequency and the nature of the adverse reactions were similar to those seen in the adult patients. The most commonly reported adverse reactions were vomiting (1.4%), pyrexia (0.9%), and hyperhidrosis (0.9%). No subject died during study participation. A serious adverse reaction of worsening of vomiting was reported for one (0.5%) patient with a brain tumor (glioma) for which a causal relationship to MultiHance could not be excluded.

**Pediatric Patients** In clinical trials of MultiHance in MRI of the CNS, 307 pediatric subjects received MultiHance at a dose of 0.1 mmol/kg. A total of 160 (52%) subjects were male and the overall mean age was 6.0 years (range, 2 days to 17 years). A total of 211 (69%) subjects were Caucasian, 24 (8%) Black, 15 (5%) Asian, 30 (13%) Hispanic, 2 (<1%) in other racial groups, and for 16 (5%), race was not reported. Adverse reactions were reported for 14 (4.6%) of the subjects. The frequency and the nature of the adverse reactions were similar to those seen in the adult patients. The most commonly reported adverse reactions were vomiting (1.0%), pyrexia (0.7%), and hyperhidrosis (0.7%). No subject died during study participation.

##### 6.2 Post-marketing Experience

The following adverse reactions have been identified during post approval use of MultiHance. Because these reactions are reported voluntarily from a population of uncertain size, it is not always possible to reliably estimate their frequency or establish a causal relationship to drug exposure.

**Immune System Disorders:** Anaphylactic, anaphylactoid and hypersensitivity reactions manifested with various degrees of severity up to anaphylactic shock, loss of consciousness and death. The reactions generally involved signs or symptoms of respiratory, cardiovascular, and/or mucocutaneous abnormalities.

**General Disorders and Administration Site Conditions:** Extravasation of MultiHance may lead to injection site reactions, characterized by local pain or burning sensation, swelling, blistering, and necrosis [see **Warnings and Precautions (5.4)**]. Adverse events with variable onset and duration have been reported after GBCA administration [see **Warnings and Precautions (5.3)**]. These include fatigue, asthenia, pain syndromes, and heterogeneous clusters of symptoms in the neurological, cutaneous, and musculoskeletal systems. Skin: Gadolinium associated plaques.

##### 7 DRUG INTERACTIONS

**7.1 Transporter-Based Drug-Drug Interactions** MultiHance and other drugs may compete for the canalicular multispecific organic anion transporter (MOAT) also referred to as MRP2 or ABCG2. Therefore, MultiHance may prolong the systemic exposure of drugs such as cisplatin, anticholinergics (e.g., donepezil, darunavir), anti-alcoholics (e.g., vincristine), methotrexate, etoposide, tamoxifen, and paliperidone. In particular, consider the potential for prolonged drug exposure in patients with decreased MOAT activity (e.g., Dublin John syndrome).

##### 8 USE IN SPECIFIC POPULATIONS

**8.1 Pregnancy Risk Summary** GBCAs cross the placenta and result in fetal exposure and gadolinium retention. The human data on the association between GBCAs and adverse fetal outcomes are limited and inconclusive [see Data]. In animal reproduction studies, gadobenate dimeglumine has been shown to be teratogenic in rabbits following repeated intravenous administration during organogenesis at doses up to 6 times the recommended human dose. There were no adverse developmental effects observed in rats with intravenous administration of gadobenate dimeglumine during organogenesis at doses up to three times the recommended human dose [see Data]. Because of the potential for gadolinium to the fetus, use MultiHance only if imaging is essential during pregnancy and cannot be delayed. The estimated background risk of major birth defects and miscarriage for the indicated population is unknown. All pregnancies have a background risk of birth defect, loss, or other adverse outcomes.

In the U.S. general population, the estimated background risk of major birth defects and miscarriage in clinically recognized pregnancies is 2 to 4% and is 15 to 20%, respectively. **Data Human Data** Contrast enhancement is visualized in the human placenta and fetal tissues after maternal GBCA administration. Cohort studies and case reports on exposure to GBCAs during pregnancy have not reported a clear association between GBCAs and adverse effects in the exposed neonates. However, a retrospective cohort study, comparing pregnant women who had a GBCA MRI to pregnant women who did not have an MRI, reported a higher occurrence of stillbirths and neonatal deaths in the group receiving GBCA MRI. Limitations of this study include a lack of comparison with non-contrast MRI and lack of information about the maternal indication for MRI. Overall, these data preclude a reliable evaluation of the potential risk of adverse fetal outcomes with the use of GBCAs in pregnancy. **Animal Data** Gadolinium Retention GBCAs administered to pregnant non-human primates (0.1 mmol/kg on gestational days 85 and 135) result in measurable gadolinium concentration in the offspring in bone, brain, skin, liver, kidney, and spleen for at least 7 months.

GBCAs administered to pregnant mice (2 mmol/kg daily on gestational days 16 through 19) result in measurable gadolinium concentration in the pups in bone, brain, kidney, liver, blood, muscle, and spleen at one month postnatal age. **Reproductive Toxicology** Gadobenate dimeglumine has been shown to be teratogenic in rabbits when administered intravenously at 2 mmol/kg/day (6 times the recommended human dose based on body surface area) during organogenesis (day 6 to 18) inducing microphthalmia/small eye and/or retinal fold in 3 fetuses from 3 separate litters. In addition, MultiHance intravenously administered at 3 mmol/kg/day (10 times the

recommended human dose based on body surface area) has been shown to increase intrauterine deaths in rabbits. There was no evidence that MultiHance induced teratogenic effects in rats at doses up to 2 mmol/kg/day (3 times the recommended human dose based on body surface area), however, rats dams exhibited no systemic toxicity at this dose. There were no adverse effects on the birth, survival, growth, development and fertility of the F1 generation at doses up to 2 mmol/kg in a rat peri- and post-natal (Segment III) study.

##### 10 OVERDOSAGE

Clinical consequences of overdose with MultiHance have not been reported. Treatment of an overdose should be directed toward support of vital functions and prompt institution of symptomatic therapy. In a Phase I clinical study doses up to 0.4 mmol/kg were administered to patients. MultiHance has been shown to be dialyzable [see **Clinical Pharmacology (12.3)**].

##### 12 CLINICAL PHARMACOLOGY

**12.1 Mechanism of Action** Gadobenate dimeglumine is a paramagnetic agent and, as such, develops a magnetic moment when placed in a magnetic field. The large magnetic moment produced by the paramagnetic agent results in a large local magnetic field, which can enhance the relaxation rates of water protons in its vicinity leading to an increase of signal intensity (brightness) of tissue.

In magnetic resonance imaging (MRI), visualization of normal and pathological tissue depends in part on variations in the radiofrequency signal intensity that occur with 1) differences in proton density, 2) differences of the spin-lattice or longitudinal relaxation times (T1), and 3) differences in the spin-spin or transverse relaxation time (T2). When placed in a magnetic field, gadobenate dimeglumine decreases the T1 and T2 relaxation time in target tissues. At recommended doses, the effect is observed with greatest sensitivity in the T1-weighted sequences.

**12.2 Pharmacokinetics** Unlike other tested paramagnetic contrast agents (See Table 3), MultiHance demonstrates weak and transient interactions with serum proteins that causes slowing in the molecular tumbling dynamics, resulting in strong increases in relaxivity in solutions containing serum proteins. The improved relaxation effect can contribute to increased contrast-to-noise ratio and lesion-to-brain ratio, which may improve visualization.

	Human plasma	
	<i>r<sub>1</sub></i>	<i>r<sub>2</sub></i>
Gadobenate	9.7 <sup>1</sup>	12.5 <sup>1</sup>
Gadopentate	4.9 <sup>1</sup>	6.3 <sup>1</sup>
Gadoterate	5.4 <sup>1</sup>	—
Gadobutrol	5.4 <sup>1</sup>	—

*r<sub>1</sub>* and *r<sub>2</sub>* relaxivities indicate the efficiency in shortening T1 and T2 relaxation times, respectively.  
<sup>1</sup> In heparinized human plasma, at 37°C.

<sup>2</sup> In citrated human plasma, at 37°C.

— Not available.

Disruption of the blood-brain barrier or abnormal vascularity allows enhancement by MultiHance of lesions such as neoplasms, abscesses, and infarcts. Uptake of MultiHance into hepatocytes has been demonstrated.

**12.3 Pharmacokinetics** Three single-dose intravenous studies were conducted in 32 healthy male subjects to assess the pharmacokinetics of gadobenate dimeglumine. The doses administered in these studies ranged from 0.005 to 0.4 mmol/kg. Upon injection, the meglumine salt is completely dissociated from the gadobenate dimeglumine complex. Staying in the molecular tumbling dynamics is based on the assay of gadobenate ion. The MRI contrast of gadobenate ion in gadobenate dimeglumine. Data for plasma concentration and area under the curve demonstrated linear dependence on the administered dose. The pharmacokinetics of gadobenate ion following intravenous administration can be best described using a two-compartment model.

**Distribution** Gadobenate ion has a rapid distribution half-life (reported as mean ± SD) of 0.084 ± 0.012 to 0.605 ± 0.072 hours. Volume of distribution of the central compartment ranged from 0.074 ± 0.097 to 0.158 ± 0.038 L/kg, and estimates of volume of distribution by area ranged from 0.170 ± 0.016 to 0.282 ± 0.079 L/kg. These latter estimates are approximately equivalent to the average volume of extracellular body water in man. *In vitro* studies showed no appreciable binding of gadobenate ion to human serum proteins.

**Elimination** Gadobenate ion is eliminated predominantly via the kidneys, with 78% to 96% of an administered dose recovered in the urine. Total plasma clearance and renal clearance estimates of gadobenate ion were similar, ranging from 0.093 ± 0.010 to 0.133 ± 0.070 L/hr/kg and 0.082 ± 0.009 to 0.104 ± 0.039 L/hr/kg, respectively. The clearance is similar to that of substances that are subject to glomerular filtration. The mean elimination half-life ranged from 1.57 ± 0.26 to 2.02 ± 0.60 hours. A small percentage of the administered dose (0.6% to 4%) is eliminated via the biliary route and recovered in feces.

**Metabolism** There was no detectable biotransformation of gadobenate ion. Dissociation of gadobenate ion *in vivo* has been shown to be minimal, with less than 1% of the free chelating agent being recovered alone in feces.

##### Pharmacokinetics in Special Populations

**Renal Impairment** A single intravenous dose of 0.2 mmol/kg of MultiHance was administered to 20 subjects with impaired renal function (6 men and 3 women with moderate renal impairment [urine creatinine clearance >30 to <60 mL/min] and 5 men and 6 women with severe renal impairment [urine creatinine clearance >10 to <30 mL/min]). Mean estimates of the elimination half-life were 6.1 ± 3.0 and 9.5 ± 3.1 hours for the moderate and severe renal impairment groups, respectively, as compared with 2.0 to 2.8 hours in healthy volunteers.

**Hemodialysis** A single intravenous dose of 0.2 mmol/kg of MultiHance was administered to 11 subjects (5 males and 6 females) with end-stage renal disease requiring hemodialysis to determine the pharmacokinetics and dialyzability of gadobenate. Approximately 72% of the dose was recovered by hemodialysis over a 4-hour period. The mean elimination half-life on dialysis was 1.21 ± 0.29 hours as compared with 4.24 ± 2.4 hours when off dialysis.

**Hepatic Impairment** A single intravenous dose of 0.1 mmol/kg of MultiHance was administered to 11 subjects (8 males and 3 females) with impaired liver function (Class B or C modified Child-Pugh Classification). Hepatic impairment had little effect on the pharmacokinetics of MultiHance with the parameters being similar to those calculated for healthy subjects.

**Gender, Age, Race** A multiple regression analysis performed using pooled data from several pharmacokinetic studies found no significant effect of sex upon the pharmacokinetics of gadobenate. Clearance appeared to decrease slightly with increasing age. Since variations due to age appeared marginal, dosage adjustment for geriatric population is not recommended. Pharmacokinetic differences due to race have not been systematically studied.

**Pediatric** A population pharmacokinetic analysis incorporated data from 25 healthy subjects (14 males and 11 females) and 15 subjects undergoing MRI imaging of the central nervous system (7 males and 8 females) between ages of 2 and 16 years. The subjects received a single intravenous dose of 0.1 mmol/kg of MultiHance. The geometric mean C<sub>max</sub> was 62.3 µg/mL (n=16) in children 2 to 5 years of age, and 64.2 µg/mL (n=24) in children older than 5 years. The geometric mean AUC<sub>0-∞</sub> was 77.9 µg·h/mL in children 2 to 5 years of age (n=16) and 82.6 µg·h/mL in children older than 5 years (n=24). The geometric mean half-life was 1.2 hours in children 2 to 5 years of age and 0.93 hours in children older than 5 years. There was no significant gender-related difference in the pharmacokinetic parameters in the pediatric patients. Over 80% of the dose was recovered in urine after 24 hours. Pharmacokinetic simulations indicate similar AUC and C<sub>max</sub> values for MultiHance in pediatric subjects less than 2 years when compared to those reported for adults; no age-based dose adjustment is necessary for this pediatric population.

##### 17 PATIENT COUNSELING INFORMATION

**17.1 Nephrogenic Systemic Fibrosis** Instruct patients to inform their physician if they:
 

- have a history of kidney and/or liver disease, or
- have recently received a GBCA.

GBCAs increase the risk for NSF among patients with impaired elimination of the drugs. To counsel patients at risk for NSF:
 

- Describe the clinical manifestations of NSF
- Describe procedures to screen for the detection of renal impairment.

Instruct the patients to contact their physician if they develop signs or symptoms of NSF following MultiHance administration, such as burning, itching, swelling, scaling, hardening and tightening of the skin; red or dark patches on the skin; stiffness in joints with trouble moving, bending or straightening the arms, hands, legs or feet; pain in the hips or ribs; or muscle weakness.

##### 17.2 Common Adverse Reactions

Inform patients that they may experience:
 

- reactions along the venous injection site, such as mild and transient burning or pain or feeling of warmth or coldness at the injection site
- side effects of feeling hot, nausea, and headache.

##### 17.3 General Precautions

Instruct patients scheduled to receive MultiHance to inform their physician if they:
 

- are pregnant or breast feeding
- have a history of renal disease, heart disease, seizure, asthma or allergic respiratory diseases
- are taking any medications
- have any allergies to any of the ingredients of MultiHance.

Rx only US Patent No. 4,916,246 Manufactured for Bracco Diagnostics Inc. Monroe Township, NJ 08831 By Patheon Italia S.p.A. - 03013 Ferentino (Italy) Revised October 2018

18-061418R

\*Multicenter double-blind randomized individual crossover study design of 123 patients with known or suspected brain tumors. Each patient received 0.1-mmol/kg doses of MultiHance and Gadavist in 2 identical MRI imaging examinations. Contrast agents were administered by IV using manual bolus injection (n=118) or a power injector (n=4). Both agents were administered at 0.1 mmol/kg of body weight, corresponding to 0.2 mL/kg for MultiHance and 0.1 mL/kg for Gadavist. The interval between the 2 MR imaging examinations was ~48 hours to avoid carryover effects but <14 days to minimize the chance of measurable disease progression or lesion evolution. All images were evaluated by 3 blinded, independent experienced radiologists who were unaffiliated with the study centers. Each reader evaluated the patient images separately and independently. Images were evaluated qualitatively for diagnostic information and scored for: 1) lesion border delineation, 2) disease extent, 3) visualization of lesion internal morphology, and 4) lesion contrast enhancement compared with surrounding normal tissue. All assessments used a 3-point scales from 1 (examination 1 superior) through 0 (examinations equal) to 1 (examination 2 superior).

Gadavist® (gadobutrol) is a registered trademark of Bayer Healthcare. Reference: Seidl Z, Vymazal J, Mechl M, et al. Does higher gadolinium concentration play a role in the morphologic assessment of brain tumors? Results of a multicenter intraindividual crossover comparison of gadobutrol versus gadobenate dimeglumine (the MERIT study). *AJNR Am J Neuroradiol*. 2012 Jun-Jul;33(6):1050-1058.

# CALL FOR AJNR EDITOR-IN-CHIEF CANDIDATES

Over the last 41 years, the editorial team of the *American Journal of Neuroradiology* (AJNR) has played a pivotal role in shaping our specialty of neuroradiology. In June 2023, Jeffrey S. Ross, MD, will complete an 8-year term as the sixth Editor-in-Chief (EIC) of the AJNR. He was preceded by a number of distinguished editors including our first AJNR EIC, Juan M. Taveras, MD (1980-1989), followed by Michael S. Huckman, MD (1990-1997), Robert M. Quencer, MD (1997-2005), Robert I. Grossman, MD (2006-2007), and Mauricio Castillo, MD (2007-2015).

We especially wish to thank Dr. Jeffrey Ross for his extraordinary dedication and exceptional contributions to the AJNR. Under his strong leadership, the AJNR remains the premier clinical neuroimaging journal with high-quality, peer-reviewed articles that serve as a beacon for achieving excellence in patient care, research, and teaching. There are an impressive 6867 subscribers across the globe: 1389 are in print and 5472 are digital.

Dr. Ross has assembled a talented international editorial board during his tenure. The AJNR issues 12 journals each year ( $\pm$  200 pages per issue)—all with peer-reviewed articles from highly respected researchers in the field. With 1700+ papers, the number of submissions to the journal was record-breaking in 2020. Over 80 COVID-19 papers have received expedited publication to date, and more than 1300 original submissions are projected for 2021. The AJNR website had an incredible 11.7 million visits in 2021. There is also a strong presence on social media and subscribers may now avail themselves of an enhanced website platform. There are 3 monthly podcasts including “Issue Highlights,” “Fellows’ Journal Club,” and “Annotated Bibliography,” which offers continuing medical education. In addition, during Dr. Ross’ tenure, the Impact Factor and h-index for the journal have steadily increased and contribute to the AJNR’s international recognition as the leading journal for all aspects of neuroimaging research, education, and best practice.

## A search for a new Editor-in-Chief will begin in early 2022.

The new Editor-in-Chief will be announced in December 2022 and will transition into the position beginning in January 2023. The actual term will begin July 1, 2023. The EIC will provide leadership and strategic vision for the journal as well as report on all editorial matters to the ASNR Board of Directors (BOD). Other responsibilities include maintaining the journal’s standard of excellence building on its reputation nationally and internationally. The EIC will be responsible for conducting, directing, and/or supervising the solicitation, evaluation, revision, and selection of all scientific and other materials to be published in the *American Journal of Neuroradiology*. The incumbent will work efficiently with the journal’s online manuscript processing system to conduct initial screening of manuscripts; make timely decisions about reviewed and revised submissions; provide constructive comments for authors as appropriate; write editorials; and meet with AJNR staff.

In addition, the EIC shall decide upon and approve of the content and design of tables of contents, letters to the editor, book reviews, advertisements, and other pages published in the AJNR as well as oversight of social media related to the journal. The EIC will also work collaboratively with the journal’s editorial board to determine the organizational structure, titles, functions, appointments, and terms of all editorial positions including reviewers, editorial advisory boards, and senior editors. The EIC may appoint senior editors who must be senior members of the ASNR. The number of senior editors shall be budgeted and approved by the ASNR BOD. Senior editors will serve at the pleasure of the EIC who shall establish the terms of service, including supervising and evaluating performance, and will exercise the right to retain or replace any senior editor as the workflow or operational demands require. The appointments of senior editors will be for a term of 1 year initially and may be extended at the discretion of the EIC.

The EIC in performing duties will observe the general Policies and Procedures established by the ASNR BOD, and will operate within the budget approved by the Board of Directors. The EIC will be consulted about, and will participate in AJNR operations including advertising, publication channels, expense management, and new or renewed contracts. The EIC will report regularly to the ASNR BOD and will attend Board of Director Meetings and other meetings as requested by the Executive Director. Each year the Editor will develop a budget along with the Managing Editor for approval by the ASNR Financial Management Committee and Board of Directors. This will be done in a manner consistent with the fiscal policies established by the Society.

## QUALIFICATIONS OF THE SUCCESSFUL CANDIDATE INCLUDE:

- MD degree; Senior Member of ASNR in North America, neuroradiology subspecialty certification
- Familiarity with AJNR and its mission
- Familiarity with ASNR and its mission

- Presently or recently engaged in a leadership role in neuroradiology with broad neuroradiology knowledge
- Excellent leadership and supervisory skills to motivate and inspire professional staff as well as interpersonal skills—impartiality, diplomacy, high ethical standards and integrity including a clear understanding of the ethical guidelines established for scholarly publishing
- Leadership needed to develop and articulate a vision and the ability to inspire people with that vision
- Demonstrated track record of academic excellence including extensive experience in both publishing in and reviewing for peer-reviewed journals
- Excellent communication and writing skills and experience in critically appraising scientific articles
- Creativity and passion about finding new ways to expand the journal content
- The ability to formulate a budget and assist leadership in oversight of journal business decisions such as selecting major vendors (e.g., printing, composition, redaction, copyediting, and other technical aspects affecting journal operations), as well as expense and revenue related decisions
- Ability to appoint a strong, diverse, and representative team of editors
- High level of organizational skills
- Editorial board or prior editorial experience preferred

The term is for 5 years renewable for an additional 3 years for a total of 8 years and subject to annual review by the ASNR Board of Directors. It is expected the EIC will devote 16-20 hours per week to these duties and a stipend will be provided.

A diverse, experienced, and knowledgeable search committee has been tasked with identifying leading candidates. The search committee consists of Tina Young Poussaint, MD, FACR, Chair, Mauricio Castillo, MD, FACR, Pina Sanelli, MD, MPH, FACR, Carolyn Meltzer, MD, FACR, Erin Simon Schwartz, MD, FACR, Joshua Nickerson, MD, Courtney Tomblinson, MD, and senior editors including Harry Cloft, MD, PhD, Christopher Filippi, MD, Thierry Huisman, MD, Peter D. Chang, MD, Lubdha Shah, MD, Gregory Zaharchuk MD, PhD, C. Douglas Phillips, MD, Yvonne Lui, MD, and Bryan Comstock. The search process will include recruiting and nominating candidates, interviewing candidates, and reviewing vision statements submitted by finalists. The appointment of the new AJNR Editor-in-Chief will be announced in December 2022.

All interested physicians are invited to provide their curriculum vitae and a vision statement to Dr. Tina Young Poussaint, tina.poussaint@childrens.harvard.edu and Karen Halm, khalm@asn.org. To ensure a broad and diverse pool of candidates, the committee welcomes nominations from the ASNR membership. The deadline for receipt of submissions is August 1, 2022.

Tina Young Poussaint, MD, FACR  
Chair, Editor-in-Chief Search Committee  
President, American Society of Neuroradiology



I am a trained neuroradiologist.  
I am a teacher.  
I am compassionate.  
I am a researcher.  
I am a leader.  
I am part of a talented community.  
I am curious.  
I am a collaborative team player.  
I am a volunteer.  
**I am ASNR.**

Don't miss out on the tools, resources and relationships you've come to rely on. Log in and renew your ASNR membership today! [www.asnr.org](http://www.asnr.org)

# In Planning for Brain Metastases Treatment, Imaging may be the Missing Link in Cost Containment<sup>1</sup>

When faced with a patient presenting with metastatic brain cancer, determining whether to use up-front stereotactic radiosurgery (SRS) vs. first treating with whole brain radiotherapy (WBRT) is a significant clinical decision.

## WBRT: The whole story on cognitive impairment

While whole brain radiotherapy (WBRT) has been the main treatment option for many years, experts agree that it often results in cognitive deterioration and a negative impact on quality of life. This mental decline has a devastating impact on patients and their families and adds ongoing costs for the healthcare systems managing these symptoms.

Using WBRT instead of SRS in some patients is estimated to decrease the total costs of brain metastasis management, though with increased toxicity.

## SRS: Fewer side effects but greater risk of missed tumors

The cost of upfront SRS is the greatest contributor to cost of brain metastasis management.<sup>1</sup> SRS is often more expensive than WBRT. What's more, multiple applications of SRS can increase the cost of treatment greatly.

Stereotactic radiosurgery (SRS) has far fewer side effects, but upfront use of SRS is expensive and can carry the risk of missed tumors, requiring repeat procedures such as salvage SRS.<sup>1</sup>

Number of lesions and lesion size are key factors to be considered when determining the treatment plan for these patients. It follows that increased diagnostic information and accuracy could be beneficial in directing the proper therapy and improving overall long-term patient outcomes and containing costs. Getting the diagnosis right the first time is crucial to ensure proper treatment begins quickly, and high cost/high stakes procedures such as SRS need precise surgical planning.

## What does optimal visualization mean for outcomes and cost?

For surgical planning with SRS, radiologists need the best visualization achievable to accurately count the number and size of the lesions. These metrics are the key predictors of the need for SRS,<sup>1</sup> WBRT, or a combination of both.

By selecting the ideal contrast agent and equipment protocols, neuroradiologists can identify the proximate numbers of metastases for upfront treatment and reduced salvage treatment occurrences.

## The role of radiology

As medical care for oncology patients continues to evolve, it will be increasingly important to assess the cost of various interventions given the often-limited life expectancy of cancer patients, the rising costs of cancer therapy, and the increasing prevalence of cancer in an aging population.

Through seeing all the tumors and tumor borders as clearly as technology allows, radiology can play a part in ensuring that proper treatment can begin quickly,

while containing costs through optimized patient care. Efforts to carefully manage treatment approaches require improvements in protocol design, contrast administration in imaging, and utilizing multimodal imaging approaches.

In this era of precision medicine, radiology departments' contribution to this improved standard of care will have significant short and long-term implications by reducing cost of care, providing a more proximate diagnosis, and ensuring optimal patient outcomes. ■



*Getting the diagnosis right the first time is crucial to ensure proper treatment begins quickly.*

**Reference: 1.** Shenker, R. F., McTyre, E. R., Taksler, D et al. Analysis of the drivers of cost of management when patients with brain metastases are treated with upfront radiosurgery. *Clin Neurol Neurosurg.* 2019 Jan;176:10-14.



For more information on MRI contrast agents, precision medicine, and reducing cost of care please visit [bracco.com](https://bracco.com)

© 2022 Bracco Diagnostics Inc.



# AJNR *go green*

***AJNR* urges American Society of Neuroradiology members to reduce their environmental footprint by voluntarily suspending their print subscription.**

The savings in paper, printing, transportation, and postage directly fund new electronic enhancements and expanded content.

The digital edition of *AJNR* presents the print version in its entirety, along with extra features including:

- Publication Preview
- Case Collection
- Podcasts
- The *AJNR* News Digest
- The *AJNR* Blog

It also reaches subscribers much faster than print. An electronic table of contents will be sent directly to your mailbox to notify you as soon as it publishes.

Readers can search, reference, and bookmark current and archived content 24 hours a day on [www.ajnr.org](http://www.ajnr.org).

ASNR members who wish to opt out of print can do so by using the *AJNR* Go Green link on the *AJNR* Website (<http://www.ajnr.org/content/subscriber-help-and-services>). Just type your name in the email form to stop print and spare our ecosystem.

# AJNR



## AMERICAN JOURNAL OF NEURORADIOLOGY

JUNE 2022  
VOLUME 43  
NUMBER 6  
WWW.AJNR.ORG


Publication Preview at [www.ajnr.org](http://www.ajnr.org) features articles released in advance of print. Visit [www.ajnrblog.org](http://www.ajnrblog.org) to comment on AJNR content and chat with colleagues and AJNR's News Digest at <http://ajnrndigest.org> to read the stories behind the latest research in neuroimaging.

791 **PERSPECTIVES** *M. Hauben*

### REVIEW ARTICLES

-  792 **Evolving Role and Translation of Radiomics and Radiogenomics in Adult and Pediatric Neuro-Oncology** *M. Ak, et al.* **ADULT BRAIN**
-  802 **The Mammillary Bodies: A Review of Causes of Injury in Infants and Children** *K.M.E. Meys, et al.* **PEDIATRICS**









### PRACTICE PERSPECTIVES

-  813 **Perfusion Scotoma: A Potential Core Underestimation in CT Perfusion in the Delayed Time Window in Patients with Acute Ischemic Stroke** *K. Abrams, et al.* **ADULT BRAIN**

### RADIOLOGY-PATHOLOGY CORRELATION

- 817 **Phosphaturic Mesenchymal Tumor** *J.C. Benson, et al.* **HEAD & NECK**

### GENERAL CONTENTS

-  823 **Investigating Brain White Matter in Football Players with and without Concussion Using a Biophysical Model from Multishell Diffusion MRI** *S. Chung, et al.* **ADULT BRAIN FUNCTIONAL**
-   829 **Microinfarcts in the Deep Gray Matter on 7T MRI: Risk Factors, MRI Correlates, and Relation to Cognitive Functioning—The SMART-MR Study** *R. Ghaznawi, et al.* **ADULT BRAIN**
-  837 **Image-Quality Assessment of 3D Intracranial Vessel Wall MRI Using DANTE or DANTE-CAIPI for Blood Suppression and Imaging Acceleration** *B. Sannanjanja, et al.* **ADULT BRAIN**
-   844 **Prevalence of Intracranial Aneurysms in Hereditary Hemorrhagic Telangiectasia: Report from a Single Reference Center** *M.S. Perez Akly, et al.* **ADULT BRAIN**
-   850 **Brain Abnormalities and Epilepsy in Patients with Parry-Romberg Syndrome** *C. De la Garza-Ramos, et al.* **ADULT BRAIN**
- 857 **Usefulness of Wave-CAIPI for Postcontrast 3D TI-SPACE in the Evaluation of Brain Metastases** *H.J. Baek, et al.* **ADULT BRAIN**

AJNR (Am J Neuroradiol ISSN 0195–6108) is a journal published monthly, owned and published by the American Society of Neuroradiology (ASNR), 820 Jorie Boulevard, Oak Brook, IL 60523. Annual dues for the ASNR include approximately 21% for a journal subscription. The journal is printed by Intellicor Communications, 330 Eden Road, Lancaster, PA 17601; Periodicals postage paid at Oak Brook, IL and additional mailing offices. Printed in the U.S.A. POSTMASTER: Please send address changes to American Journal of Neuroradiology, P.O. Box 3000, Denville, NJ 07834, U.S.A. Subscription rates: nonmember \$430 (\$505 foreign) print and online, \$320 online only; institutions \$495 (\$565 foreign) print and basic online, \$980 (\$1050 foreign) print and extended online, \$380 online only (basic), \$825 online only (extended); single copies are \$35 each (\$40 foreign). Indexed by PubMed/MEDLINE, BIOSIS Previews, Current Contents (Clinical Medicine and Life Sciences), EMBASE, Google Scholar, HighWire Press, Q-Sensei, RefSeek, Science Citation Index, SCI Expanded, ReadCube, and Semantic Scholar. Copyright © American Society of Neuroradiology.



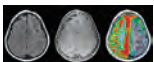
-  **864** Volumetric Measurement of Relative CBV Using TI-Perfusion-Weighted MRI with High Temporal Resolution Compared with Traditional T2\*-Perfusion-Weighted MRI in Postoperative Patients with High-Grade Gliomas *M. Seo, et al.* **ADULT BRAIN FUNCTIONAL**
-   **872** Nonlesional Sources of Contrast Enhancement on Postgadolinium “Black-Blood” 3D T1-SPACE Images in Patients with Multiple Sclerosis *L. Danieli, et al.* **ADULT BRAIN**
-   **881** Diagnostic Accuracy of High-Resolution 3D T2-SPACE in Detecting Cerebral Venous Sinus Thrombosis *A. Hakim, et al.* **ADULT BRAIN**
-   **887** Differential Subsampling with Cartesian Ordering–MRA for Classifying Residual Treated Aneurysms *P. Shahrouki, et al.* **ADULT BRAIN INTERVENTIONAL**
-   **893** ADC Level is Related to DWI Reversal in Patients Undergoing Mechanical Thrombectomy: A Retrospective Cohort Study *T. Umemura, et al.* **INTERVENTIONAL**
- 899** Clinical Significance of Prehospital Telecommunication Defined as the Critical Stroke Call Pathway in Acute Ischemic Stroke Requiring Intra-Arterial Recanalization Therapy *H. Lee, et al.* **INTERVENTIONAL**
-   **905** Diffusion-Weighted Imaging to Assess HPV-Positive versus HPV-Negative Oropharyngeal Squamous Cell Carcinoma: The Importance of b-Values *V. Lenoir, et al.* **HEAD & NECK FUNCTIONAL**
-  **913** Stroke Recurrence in Children with Vertebral Artery Dissecting Aneurysm *Z. Ritchey, et al.* **PEDIATRICS**
-   **919** Thalamus L-Sign: A Potential Biomarker of Neonatal Partial, Prolonged Hypoxic-Ischemic Brain Injury or Hypoglycemic Encephalopathy? *S.K. Misser, et al.* **PEDIATRICS**

## ONLINE FEATURES

### E14 ERRATUM

## BOOK REVIEWS *R.M. Quencer, Section Editor*

Please visit [www.ajnrblog.org](http://www.ajnrblog.org) to read and comment on Book Reviews.



Imaging of patients with Parry-Romberg Syndrome from De la Garza-Ramos, et al, in this issue.



Indicates Editor's Choices selection



Indicates Fellows' Journal Club selection



Indicates open access to non-subscribers at [www.ajnr.org](http://www.ajnr.org)



Indicates article with supplemental online data



Indicates article with supplemental online video



Evidence-Based Medicine Level 1



Evidence-Based Medicine Level 2

### EDITOR-IN-CHIEF

**Jeffrey S. Ross, MD**

Professor of Radiology, Department of Radiology,  
Mayo Clinic College of Medicine, Phoenix, AZ

### SENIOR EDITORS

**Harry J. Cloft, MD, PhD**

Professor of Radiology and Neurosurgery,  
Department of Radiology, Mayo Clinic College of  
Medicine, Rochester, MN

**Christopher G. Filippi, MD**

Professor and Alice Ettinger-Jack R. Dreyfuss  
Chair of Radiology,  
Tufts University School of Medicine,  
Radiologist-in-Chief  
Tufts University Medical Center, Boston, MA

**Thierry A.G.M. Huisman, MD, PD, FICIS, FACR**

Radiologist-in-Chief and Chair of Radiology, Texas  
Children's Hospital,  
Professor of Radiology, Pediatrics, Neurosurgery,  
and OBGYN, Baylor College of Medicine,  
Houston, TX

**Yvonne W. Lui, MD**

Associate Professor of Radiology,  
Chief of Neuroradiology,  
New York University School of Medicine,  
New York, NY

**C.D. Phillips, MD, FACR**

Professor of Radiology, Weill Cornell Medical  
College, Director of Head and Neck Imaging,  
New York-Presbyterian Hospital, New York, NY

**Lubdhra M. Shah, MD, MS**

Professor of Radiology and Director of Spine  
Imaging, University of Utah Department of  
Radiology and Imaging Sciences, Salt Lake City, UT

### STATISTICAL SENIOR EDITOR

**Bryan A. Comstock, MS**

Senior Biostatistician,  
Department of Biostatistics,  
University of Washington, Seattle, WA

### ARTIFICIAL INTELLIGENCE DEPUTY EDITOR

**Peter D. Chang, MD**

Assistant Professor-in-Residence,  
Departments of Radiological Sciences,  
Computer Sciences, and Pathology,  
Director, Center for Artificial Intelligence in  
Diagnostic Medicine (CAIDM),  
University of California, Irvine, Irvine, CA

### EDITORIAL BOARD

Ashley H. Aiken, Atlanta, GA

Lea M. Alhilali, Phoenix, AZ

Mohammed A. Almekhlafi, Calgary, Alberta,  
Canada

Joachim Berkefeld, Frankfurt, Germany

Aashim Bhatia, Pittsburgh, PA

Waleed Brinjikji, Rochester, MN

Judah Burns, New York, NY

Danielle Byrne, Dublin, Ireland

Federico Cagnazzo, Montpellier, France

J. Levi Chazen, New York, NY

James Y. Chen, San Diego, CA

Gloria C. Chiang, New York, NY

Daniel Chow, Irvine, CA

Kars C.J. Compagne, Rotterdam, The Netherlands

Arturo Consoli, Suresnes, France

Seena Dehkharghani, New York, NY

Nilesh K. Desai, Houston, TX

Yonghong Ding, Rochester, MN

Birgit Ertl-Wagner, Toronto, Ontario, Canada

Clifford J. Eskey, Hanover, NH

Massimo Filippi, Milan, Italy

Nils D. Forkert, Calgary, Alberta, Canada

Ana M. Franceschi, New York, NY

Frank Gaillard, Melbourne, Australia

Joseph J. Gemmete, Ann Arbor, Michigan

Wende N. Gibbs, Phoenix, AZ

Philipp Göltz, Erlangen, Germany

Brent Griffith, Detroit, MI

Joseph M. Hoxworth, Phoenix, Arizona

Raymond Y. Huang, Boston, MA

Gábor Janiga, Magdeburg, Germany

Christof Karmonik, Houston, TX

Timothy J. Kaufmann, Rochester, MN

Hillary R. Kelly, Boston, MA

Toshibumi Kinoshita, Akita, Japan

Alexander W. Korutz, Chicago, IL

Stephen F. Kralik, Houston, TX

Alexander Lerner, Los Angeles, CA

Yinsheng Li, Madison, WI

Franklin A. Marden, Chicago, IL

Markus A. Möhlenbruch, Heidelberg, Germany

Kambiz Nael, Los Angeles, CA

Renato Hoffmann Nunes, Sao Paulo, Brazil

Sasan Partovi, Cleveland, OH

Johannes A.R. Pfaff, Salzburg, Austria

Laurent Pierot, Reims, France

Alireza Radmanesh, New York, NY

Prashant Raghavan, Baltimore, MD

Eytan Raz, New York, NY

Paul M. Ruggieri, Cleveland, OH

Sebastian Schafer, Madison, WI

Maksim Shapiro, New York, NY

Timothy Shepherd, New York, NY

James Shin, New York, NY

Mark S. Shiroishi, Los Angeles, CA

Bruno P. Soares, Burlington, VT

Jason F. Talbott, San Francisco, CA

Ruth Thiex, Everett, Washington

Vincent Thijs, Melbourne, Victoria, Australia

Anderanik Tomasian, Los Angeles, CA

Fabio Triulzi, Milan, Italy

Anja G. van der Kolk, Utrecht, the Netherlands

Arastoo Vossough, Philadelphia, PA

Elysa Widjaja, Toronto, Ontario, Canada

Leonard Yeo, Singapore

Woong Yoon, Gwangju, South Korea

David M. Yousem, Evergreen, CO

Carlos Zamora, Chapel Hill, NC

Chengcheng Zhu, Seattle, WA

### EDITORIAL FELLOW

Vivek Yedavalli, Baltimore, MD

### SPECIAL CONSULTANTS TO THE EDITOR

#### AJNR Blog Editor

Neil Lall, Denver, CO

#### Case of the Month Editor

Nicholas Stence, Aurora, CO

#### Case of the Week Editors

Matylda Machnowska, Toronto, Ontario, Canada

Anvita Pauranik, Calgary, Alberta, Canada

Vinil Shah, San Francisco, CA

#### Classic Case Editor

Sandy Cheng-Yu Chen, Taipei, Taiwan

#### Health Care and Socioeconomics Editor

Pina C. Sanelli, New York, NY

#### Physics Editor

Greg Zaharchuk, Stanford, CA

#### Podcast Editor

Courtney Tomblinson, Nashville, TN

#### Deputy Podcast Editor

Kevin Hiatt, Winston-Salem, NC

#### Twitter Editor

Jacob Ormsby, Albuquerque, NM

### Official Journal:

American Society of Neuroradiology

American Society of Functional Neuroradiology

American Society of Head and Neck Radiology

American Society of Pediatric Neuroradiology

American Society of Spine Radiology

Founding Editor

Juan M. Taveras

Editors Emeriti

Mauricio Castillo, Robert I. Grossman,

Michael S. Huckman, Robert M. Quencer

Managing Editor

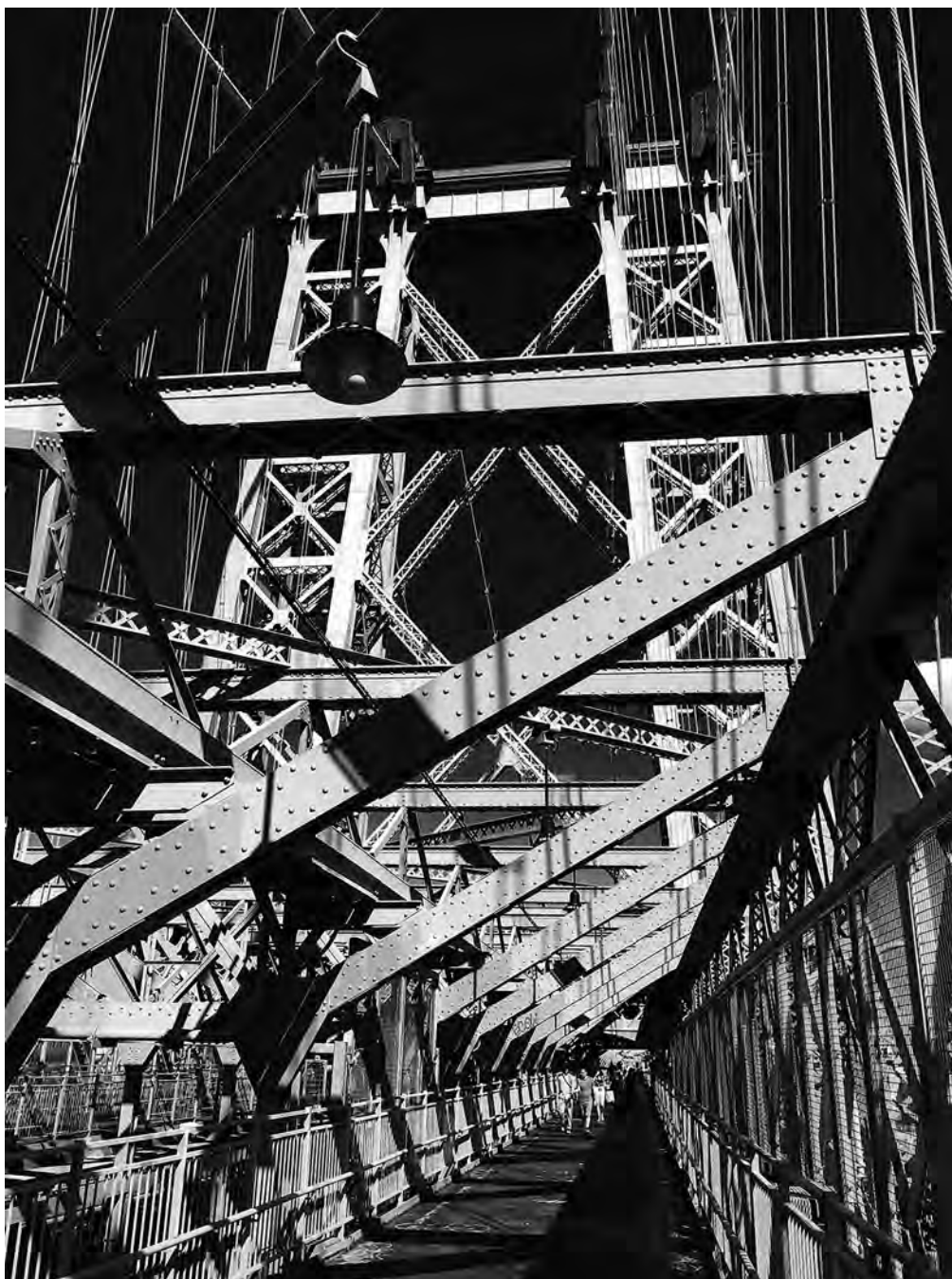
Karen Halm

Assistant Managing Editor

Laura Wilhelm

Executive Director, ASN

Mary Beth Hepp



Title: Williamsburg Bridge. The Williamsburg Bridge, opened in 1903, broke records: First all-steel suspension bridge, longest suspension bridge, heaviest load capacity, falling into most disrepair (by the 1980s). It also possibly garnered the most aesthetic knocks, such as “ugliest ever” by then New York City bridge commissioner Gustav Lindenthal, and “... it can never be made to look well,” by Henry Hornbostel, a beaux-arts trained architect commissioned by Lindenthal to beautify Leffert Lefferts Buck’s original design (many proposed improvements, such as tower finials, were never implemented). Interestingly, the Eiffel Tower generated similar vitriol when built and some postulate an influence of Eiffel on Buck, the two bridge builders having previous concurrent bridge building experience in South America. From an engineering perspective the design can boast of time and resource efficiency plus adaptability to increasing loads—an “engineer’s bridge.” Visually, its vertical lattice, deep stiffening trusses, and cantilevered side spans are heavy, skeletal, and perhaps gawky, and it can look unbalanced especially in profile. Still, the Williamsburg Bridge is a marvel and an unconventional beauty! View it from different vantage points and cross the bridge on the terrific pedestrian walkway. When you do, you know you are seeing something special.

*Manfred Hauben, MD, MPH, Pfizer Inc and NYU Langone Health, New York City*

# Evolving Role and Translation of Radiomics and Radiogenomics in Adult and Pediatric Neuro-Oncology

 M. Ak,  S.A. Toll,  K.Z. Hein,  R.R. Colen, and  S. Khatua



## ABSTRACT

**SUMMARY:** Exponential technologic advancements in imaging, high-performance computing, and artificial intelligence, in addition to increasing access to vast amounts of diverse data, have revolutionized the role of imaging in medicine. Radiomics is defined as a high-throughput feature-extraction method that unlocks microscale quantitative data hidden within standard-of-care medical imaging. Radiogenomics is defined as the linkage between imaging and genomics information. Multiple radiomics and radiogenomics studies performed on conventional and advanced neuro-oncology image modalities show that they have the potential to differentiate pseudoprogression from true progression, classify tumor subgroups, and predict recurrence, survival, and mutation status with high accuracy. In this article, we outline the technical steps involved in radiomics and radiogenomics analyses with the use of artificial intelligence methods and review current applications in adult and pediatric neuro-oncology.

**ABBREVIATIONS:** AI = artificial intelligence; AUC = area under the curve; DL = deep learning; GBM = glioblastoma; ML = machine learning; SUV = standardized uptake value

In parallel to the growing understanding of the impact of genomics and epigenomics, marked advances in clinical imaging and allied computational technologies have occurred during the past few years. These have facilitated enhanced diagnosis, molecular stratification, and targeted therapeutic clinical trials. Radiomics and radiogenomics are rapidly growing fields in imaging and, since their early inception, have been explored in the field of neuro-oncology.<sup>1</sup> Radiomics is a high-throughput computational process that unlocks microscale quantitative data hidden within conventional imaging, not otherwise visualized by the naked human eye; radiogenomics is the linkage between imaging and genomics data.<sup>2,3</sup> With use of radiomics analysis, a patient's scans are converted into mineable

quantitative data to which machine learning (ML) techniques can be applied for integrative analysis. This process has enabled the identification of quantitative imaging markers and signature models that are reflective of microscopic tumor biology, which has led to enhanced, biologically relevant classification, tumor grading, survival prediction, and treatment response in adult and pediatric brain tumors.<sup>4-8</sup> Although studies of radiomics and radiogenomics have been performed in adult brain tumors, their application and use in pediatric neuro-oncology are evolving.<sup>5,9,10</sup> Initial studies showed promising ability to distinguish posterior fossa tumors like ependymoma and pilocytic astrocytoma.<sup>9</sup> Recent studies using a combination of radiomics and ML were able to distinguish pathologic subtypes of pediatric brain tumors.<sup>10</sup> This article reviews the basics of radiomics, radiogenomics, and their clinical application; their evolving role in adult neuro-oncology; and their recent translation and application in pediatric neuro-oncology.

## Search Criteria

Details of this review article were based on a PubMed search of categories of radiomics, adult brain tumors, and pediatric neuro-oncology. The search was limited to malignant brain tumors (excluding neurologic and benign lesions of the brain).

## Technologic Methods and Computational Process

**Overview of Radiomics Workflow.** The radiomics processes can be structured into multiple phases, and they are the same in pediatric and adult patients: 1) image acquisition and data selection,


Received February 1, 2021; accepted after revision July 19.


From the Department of Radiology (M.A., R.R.C.), University of Pittsburgh, Pittsburgh, Pennsylvania; Hillman Cancer Center (M.A., R.R.C.), University of Pittsburgh Medical Center, Pittsburgh, Pennsylvania; Department of Hematology-Oncology (S.A.T.), Children's Hospital of Michigan, Detroit, Michigan; Department of Leukemia (K.Z.H.), The University of Texas MD Anderson Cancer Center, Houston, Texas; and Department of Pediatric Hematology-Oncology (S.K.), Mayo Clinic, Rochester, Minnesota.

Rivka R. Colen and Soumen Khatua are senior co-authors.

This work was funded, in part, by startup funding from The University of Pittsburgh Hillman Cancer Center (R.R.C.) and the Hillman Cancer Center's National Cancer Institute Cancer Center Support Grant No. P30CA047904 (R.R.C.).

Please address correspondence to Soumen Khatua, MD, Department of Hematology-Oncology, Mayo Clinic, 200 First Street SW, Rochester, MN 55905; e-mail: khatua.soumen@mayo.edu

 Indicates open access to non-subscribers at [www.ajnr.org](http://www.ajnr.org)

 Indicates article with online supplemental data.

<http://dx.doi.org/10.3174/ajnr.A7297>



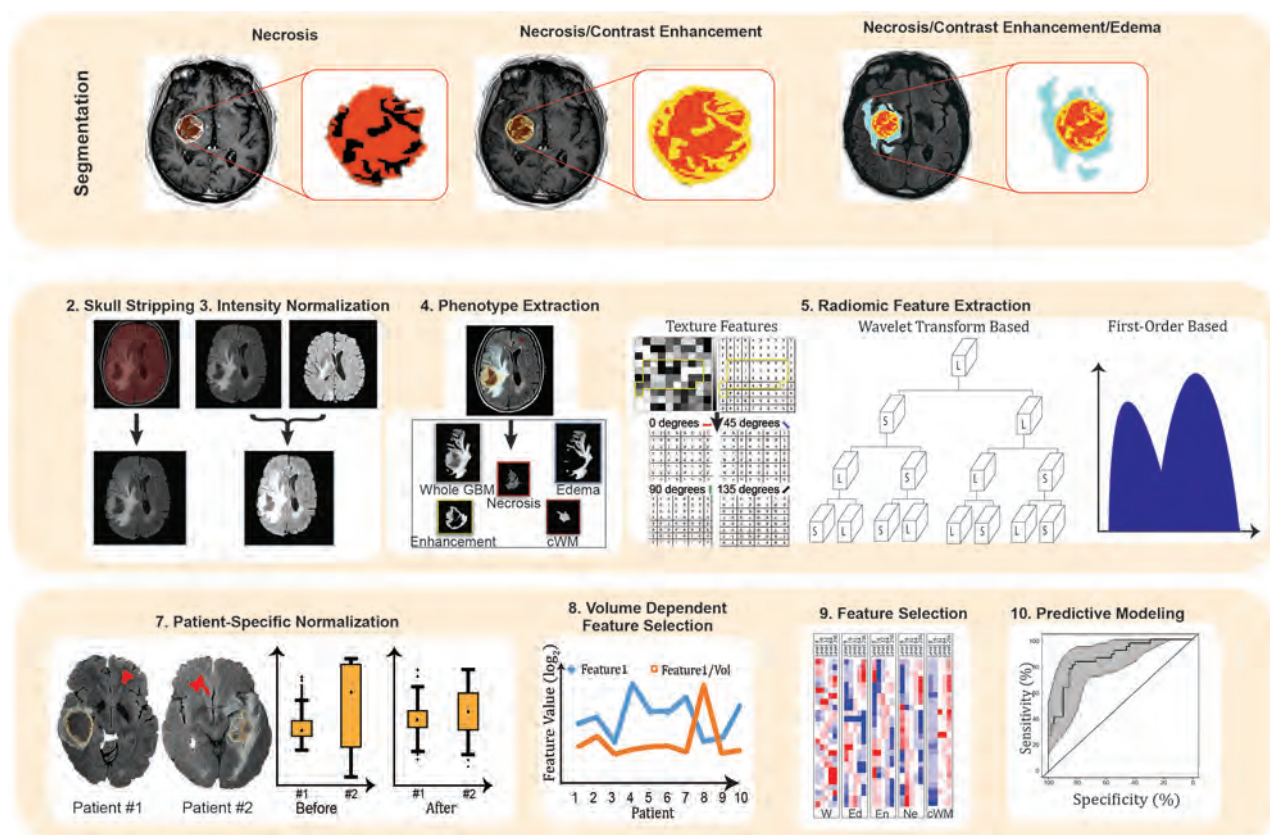


**FIG 1.** Radiomics pipeline for brain tumors. *Upper line:* Segmentation of the 3 imaging phenotypes: necrosis (*left*), enhancing tumor (*middle*), and edema/invasion (*right*). *Middle and lower lines:* Radiomics feature extraction, normalization, and volume-dependent feature generation are followed by feature selection and predictive modeling for outcomes.

2) image registration and segmentation, 3) image preprocessing, 4) radiomics feature extraction, and 5) feature selection and modeling to predict the outcomes of interest (Fig 1).

**Image Acquisition and Data Selection.** Image acquisition and data selection are considered the initial steps in the workflow. For radiomics and radiogenomics studies in neuro-oncology, MR imaging and PET are generally used.

**Image Registration and Segmentation.** Image registration refers to the spatial alignment of the various imaging sequences into the same geometric/anatomic space (Fig 2A).<sup>11</sup> Tumor segmentation refers to contour delineation of the volumes of interest (3D) or ROIs (2D) (Fig 3). Manual segmentation or semiautomated and automated segmentation with superimposed manual segmentation is the criterion standard. Complete manual segmentation is tedious and time-consuming and requires contouring of the tumor section by section; furthermore, it is prone to interobserver and intraobserver variability.<sup>12</sup> Semiautomated and automated segmentation methods have been explored in various studies to reduce manual labor and improve consistency and reproducibility to overcome these challenges.<sup>12-14</sup> Although promising, semiautomated and automated methods are not entirely accurate and typically require editing by a radiologist to ensure more precise borders.<sup>13</sup>

**Image Preprocessing.** Skull stripping: Because high-resolution structural images include a significant amount of nonbrain tissue

such as bone, skin, and eyeballs, these can affect the radiomics analysis (Fig 2B). The FSL Brain Extraction Tool (<http://fsl.fmrib.ox.ac.uk/fsl/fslwiki/BET>) and Robust Brain Extraction (<https://www.nitrc.org/projects/robex>) are the commonly used algorithms for skull stripping.<sup>15</sup> Intensity normalization: During MR imaging acquisition, the use of different scanner types and scanning parameters can result in large intensity variations. These variations can weaken the performance of subsequent radiomics analysis. It is an essential process of mapping intensities to a standard reference scale in MR imaging to account for variations between patients and longitudinal studies and to increase radiomics reproducibility. The algorithm generated by Nyúl and Udupa,<sup>16</sup> which involves the matching of histograms, is the most commonly used normalization method. Noise reduction: Noise suggests that the pixels in the image show distinct intensity values instead of actual pixel values that are achieved from the image.<sup>17</sup> Rician noise decreases the quality of MR imaging and makes quantitative feature extraction difficult.<sup>17</sup> Gaussian convolution and neighborhood filter are the most commonly used noise-reduction algorithms.<sup>17</sup> Bias field correction: The bias field signal is nonuniform low-frequency intensities that corrupt MR imaging.<sup>18</sup> The bias field is a potential confounder for radiomics analysis, and it should be corrected. The N4 bias field correction algorithm is the most commonly used approach for inhomogeneity correction.<sup>18</sup>

**Radiomics Feature Extraction.** After segmentation and preprocessing, extraction of radiomics features is then performed. Radiomics

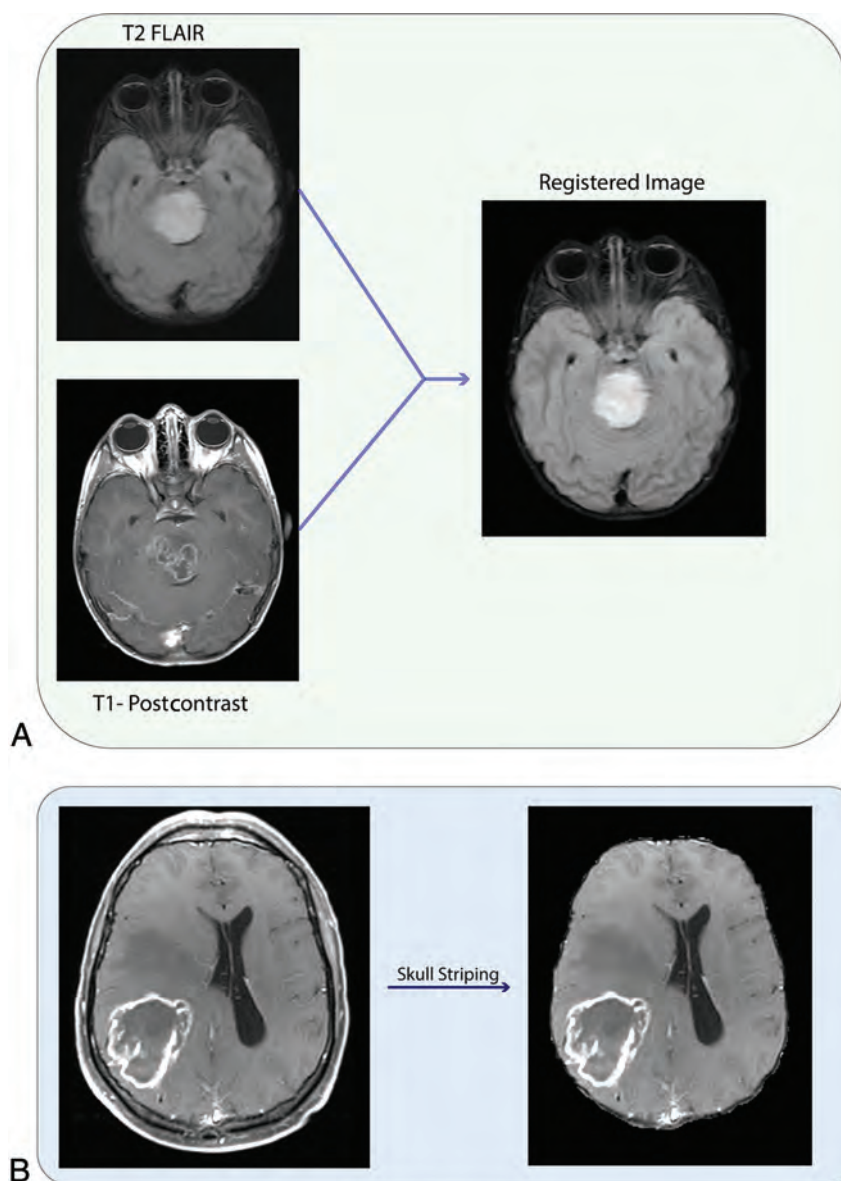


**FIG 2.** A, Registration of T1-postcontrast MR imaging and FLAIR MR imaging. B, Skull stripping.

features can be categorized as first-order, second-order, and high-order features. First-order features describe the distribution of individual voxel values without concern for spatial associations between neighboring voxels.<sup>17</sup> Second-order features calculate the statistical interrelationships between adjacent voxels. Second-order features give a measure of the spatial alignment of the voxel intensities and intralesion heterogeneity. There are multiple different ways of quantifying spatial association among pixels: Gray-level co-occurrence matrix is a most commonly used second-order statistical texture-analysis technique, which analyzes the spatial relationship among pixels and defines how frequently voxel pairs are present in different directions.<sup>17</sup> Gray-level run length matrix, another commonly used second-order feature, quantifies consequent voxels that have the same gray-level value along a fixed direction.<sup>17</sup> High-order features involve performing filters or mathematic transforms to the images before the feature-extraction process.<sup>19</sup> These features aim to detect repetitive or nonrepetitive patterns, remove noise, or highlight details. The wavelet transform-based method is a very popular approach in which the image is decomposed in multiple scales and used for texture analysis.<sup>19</sup> Laplacian transforms of the Gaussian filter identify areas of rapid intensity change (edges) in images.<sup>20,21</sup>

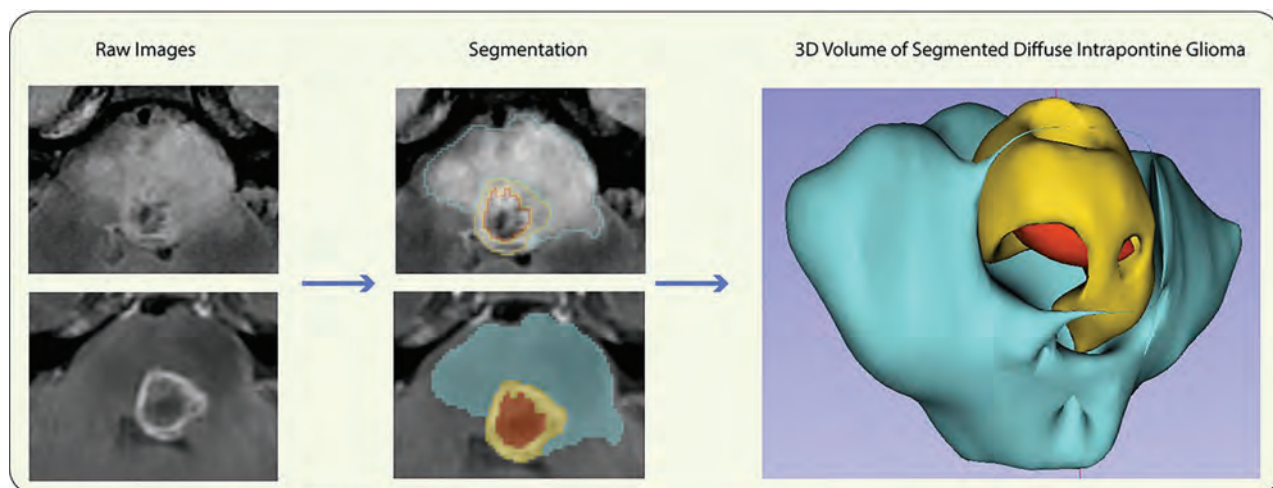


**FIG 3.** Segmentation and 3D volume extraction of a diffuse intrinsic pontine glioma.



### Artificial Intelligence Applied to Imaging: Feature Selection and Statistical Modeling

**Machine Learning.** ML is a branch of artificial intelligence (AI) in which computers are given the capability of learning like humans by feeding data and information without being explicitly programmed (Fig 4).<sup>22</sup> Fundamental to ML is that classification, regression, prediction, clustering, and association models are provided. ML methods are categorized into supervised, unsupervised, and semi-supervised learning.

**Supervised Machine Learning.** In supervised learning, a model is able to predict target clinical outcomes with the help of a labeled clinical dataset.<sup>22</sup> The supervised learning model includes 2 steps: training and testing. Model training consists of inputs paired with the corresponding outputs to train the model. During training, the algorithms search for patterns in the data that relate to outcomes. Model testing is the process of predictive performance evaluation of the trained model on the test dataset. Support vector machine,<sup>8</sup> random forests,<sup>8</sup> and eXtreme Gradient Boosting (XGBoost; <https://xgboost.ai/>)<sup>23,24</sup> are the most commonly used supervised machine learning methods in radiomics.

**Unsupervised Machine Learning.** Unsupervised learning methods can classify radiomic features into subgroups using clustering algorithms such as k-means clustering,<sup>25</sup> fuzzy clustering,<sup>26</sup> or consensus clustering.<sup>27</sup> Next, the relationships of the various features within their groups are compared. Subsequently, the

capability of various subgroups to predict clinical output can be compared; however, labeled data are not used for the initial model development. Radiomics features can also be used to provide new subclasses that may more closely align with the underlying biology of CNS tumors by using unsupervised machine learning methods.

**Deep Learning.** Deep learning (DL), also known as deep neural network, is a subfield of machine learning in AI that has multiple neural-like networks (Fig 5).<sup>28</sup> The artificial neural networks are capable of learning from data that are unstructured or unlabeled. The most significant difference between DL and conventional ML algorithms is that DL does not need any human interference such as radiomics, feature extraction, and segmentation to learn the connection between the input and the corresponding output. Some of the known deep learning algorithms are the recurrent neural network, restricted Boltzmann machine, and convolutional neural network.<sup>28</sup> The convolutional neural network is most commonly used and is popular in radiomics studies.<sup>28</sup>

**Feature Selection.** Feature selection is the process of selecting a subset of the most relevant and significant discriminatory features associated with the specific outcome. These are then used for building radiomics models. Feature selection helps in clarifying the data by revealing, in an individual, the important features and how they are related to each other and to the image itself. There are several commonly used methods for radiomics feature

selection such as Least Absolute Shrinkage and Selection Operator,<sup>8</sup> Minimum Redundancy Maximum Relevance,<sup>24,29</sup> and Generalized Linear Models with Elastic Net Penalties.<sup>30</sup>

**Modeling.** Radiomics uses prediction models for predicting outcomes, including clinical or demographic, genomic, survival, response, and resistance models.<sup>31-35</sup> AI, specifically ML and DL, provides several approaches to achieve this aim.<sup>31</sup> The support vector machine uses a hyperplane, which distinctly classifies the data points into 2 classes.<sup>31</sup> Generalizability and the possibility of

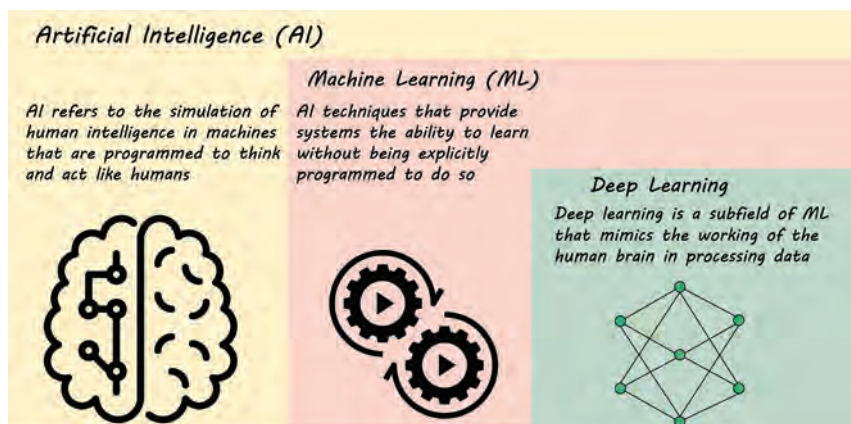


FIG 4. AI, ML, and DL.

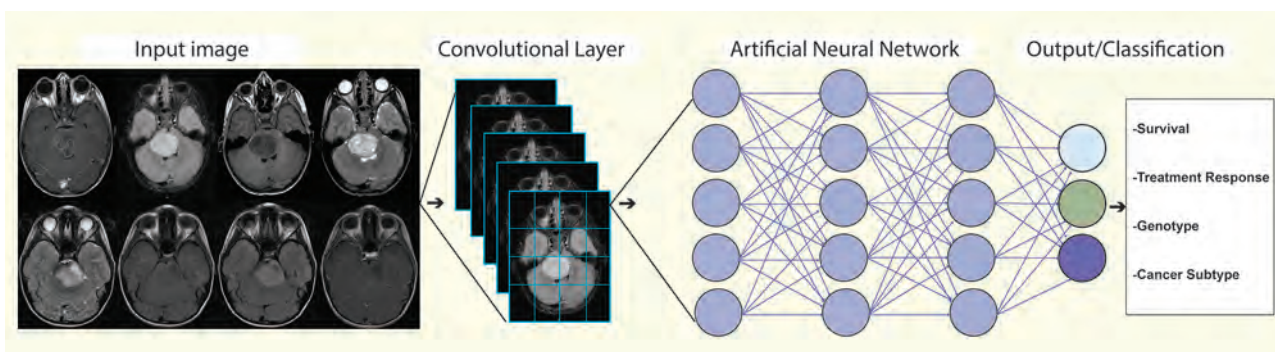


FIG 5. A deep learning-based model for predicting outcomes.

achieving probabilistic outputs are its advantages.<sup>31</sup> XGBoost is a decision tree-based ensemble algorithm that uses a gradient boosting.<sup>31,36</sup> It enables cross-validation, regularization, missing-value imputation, and flexibility.<sup>36</sup> The choice of modeling technique has been demonstrated to affect prediction performance in a radiomics study.<sup>29</sup>

**Validation.** The most effective approach for validation is the use of prospective independent external validation. In cases for which no such prospective or independent external data are available, internal validation techniques can be performed. K-fold, leave-one-out cross-validation, and hold-out are the most commonly used internal validation approaches.<sup>37</sup>

### **Clinical Applications of Radiomics in Neuro-Oncology: Adults**

Most research in radiomics was initially performed in lung cancer.<sup>38</sup> Radiogenomics, however, was initially performed in adult brain cancer, specifically glioblastoma (GBM).<sup>39</sup> Since then, numerous studies have focused on the use of radiomics and radiogenomics in various adult CNS tumors (Online Supplemental Data).<sup>4,7,40-47</sup> With increasing computing speed and the availability of computerized algorithms, large numbers of radiomics features can be extracted rapidly from MRIs and used to generate specific signature models. These have aided in noninvasively identifying histologic and molecular profiles of tumors,<sup>48,49</sup> predicting response,<sup>35</sup> differentiating pseudoprogression from true progressive disease,<sup>24</sup> and delineating oncogenic markers in the microenvironment of brain tumors.<sup>50</sup>

**Radiomics as a Diagnostic Marker.** The most recent 2016 World Health Organization classification demonstrated the importance of integrating phenotype-genotype characteristics of CNS tumors, enabling newer subclassifications of tumor groups.<sup>51</sup> This landmark article led to seminal studies<sup>44,52,53</sup> that showed that brain tumors could be directly related to a specific set of genomics, helping to preoperatively predict tumor genotype. GBM is the most common malignant brain tumor in adults, with poor survival outcome and a median survival of 15 months.<sup>54</sup> Discernment of the intratumoral genetic heterogeneity of GBMs has important implications in optimizing targeted therapy to improve survival and in understanding the mechanisms of therapeutic resistance.<sup>54,55</sup> GBMs have multiple genetically distinct clonal populations driving oncogenesis and thus have distinct therapeutic sensitivities and habitats of resistance.<sup>54</sup> Biopsy and surgery cannot capture such spatially extensive tumor heterogeneity because both comprise samples that represent a small and static molecular “snapshot” of the entire tumor, which is very heterogeneous; furthermore, these procedures are invasive.

Radiomics and radiogenomics have been shown to potentially complement biopsy by capturing regional genetic heterogeneity and by noninvasively evaluating various driver genes and prognostic markers at diagnosis.<sup>43,44,47,56-58</sup> Recent studies have shown that radiomics models can preoperatively predict *O6-methylguanine-DNA methyltransferase* (*MGMT*) methylation, epidermal growth factor (*EGFR*) amplification, and *EGFR* variant III status in GBM.<sup>48,58-60</sup> Zhang et al<sup>46</sup> demonstrated that ML algorithms generated from preoperative MR imaging and clinical features of 120 patients with grade III and IV gliomas predicted

isocitrate dehydrogenase (*IDH*) 1/2 status with accuracies of 86% and 89% in the training and validation cohorts, respectively. Similarly, Chang et al<sup>61</sup> showed the feasibility of a DL, convolutional neural network approach for the classification of genetic mutations of both low- and high-grade gliomas. They used 259 patients with either low- or high-grade gliomas to classify *IDH1* mutation, 1p/19q codeletion, and *MGMT* methylation status. Their classification demonstrated that the convolutional neural network is capable of learning significant imaging components without prior feature selection or human-directed training with high accuracy: *IDH1* mutation status, 94%; 1p/19q codeletion, 92%; and *MGMT* methylation status, 83%.

In a recent study, Hu et al<sup>50</sup> built a radiomics model to preoperatively identify 6 important driver genes (*EGFR*, *PDGFRA*, *PTEN*, *CDKN2A*, *RB1*, and *TP53*) in primary GBM. The authors evaluated 48 biopsies from the regions of enhancing and nonenhancing parenchyma of 13 patients with GBM and identified significant imaging correlations for these 6 genes. They achieved accuracies ranging from 68% to 87.5% for *PDGFRA*, *EGFR*, *CDKN2A*, *PTEN*, and *RB1* prediction models, whereas the accuracy for the *TP53* prediction model was 37%. Similarly, Zinn et al<sup>62</sup> showed that there are distinct MR imaging radiomics features associated with the *TP53-PTEN-EGFR* mutational landscape and that radiomics is approaching the complexity of whole-genome microarray expression data. Additionally, recent studies demonstrated that MR imaging-based radiomics models predicted 1p/19q codeletion status in histopathologically diagnosed gliomas.<sup>43,47</sup> The latter is a predictor of better prognosis and a durable response to therapy.<sup>63</sup> These results provide proof of concept and reaffirm that genomics-based biomarkers can be correlated and/or predicted noninvasively by radiomics, facilitating the evaluation of intratumoral genetic heterogeneity; and if prospectively validated, can be translated to the clinic as a noninvasive, cost-effective genomic test approach and advance individualized patient management.

**Tumor Type and Tumor Grading Prediction.** Noninvasive diagnosis of brain tumors is clinically challenging but necessary because various treatment strategies are needed depending on the tumor type. Conventional or advanced MR imaging techniques are often challenging in their ability to differentiate GBM from metastatic brain tumors and lymphoma. All these tumors can show enhancement on T1-weighted images with gadolinium and hyperintensity on FLAIR.<sup>64,65</sup> Although advanced MR imaging (MR spectroscopy and PWI) has shown promising results in the evaluation of brain tumors, further work is needed for a transition to the clinic as part of routine brain tumor management.<sup>64,65</sup> Radiomics-based ML techniques have demonstrated potential in differentiating GBM from metastatic brain tumors.<sup>66</sup> Another study showed that a radiomics model generated by features obtained from diffusion MR imaging yielded a better diagnostic performance than a radiomics model created by features acquired from conventional MR imaging in differentiating atypical primary CNS lymphoma, which often mimics GBM.<sup>67</sup> Similarly, Kong et al<sup>68</sup> showed that radiomics features obtained from the PET images have the potential to distinguish primary CNS lymphoma from GBM. They generated 3 groups of maps: a standardized uptake value (SUV) map,



an SUV map calibrated with the normal contralateral cortex activity, and an SUV map calibrated with the normal brain mean activity; a total of 107 radiomics features were extracted from each SUV map. Their areas under the curve (AUCs) for differentiating CNS lymphoma and GBM ranged from 0.644 to 0.999. In addition, a recently published study determined the capability of radiomics analysis to identify the primary origin of brain metastases despite neuropathologic procedures and imaging evaluations often failing to identify the primary tumor site and leading to delayed diagnosis and treatment.<sup>69</sup> However, further studies are needed to validate and reproduce these findings.

High-grade gliomas, including GBMs, are biologically elusive, due to their genetic heterogeneity and complex imaging phenotypes.<sup>54,55</sup> Previous studies have shown that radiomics can predict the pathologic behavior of gliomas, histologic/molecular subtypes/grading, and the proliferative index.<sup>49,70,71</sup> This finding could facilitate the presurgical evaluation of tumor behavior, determine the extent of surgical resection, and enable optimal clinical treatment decision-making in patients with various grades of gliomas. Histologic grade and the Ki-67 labeling index are used to help predict biologic behavior and prognosis of gliomas.<sup>72</sup> A recently published study has demonstrated that radiomics features based on T2 FLAIR images have been shown to preoperatively correlate and predict multiple immunohistochemical features of gliomas such as Ki-67, S-100, vimentin, and CD34 expression.<sup>49</sup> These insights are expected to enhance the personalized treatment of patients with gliomas.<sup>49</sup> Furthermore, radiomics-based ML techniques have shown potential in differentiating GBM from anaplastic oligodendroglioma.<sup>42</sup> Although the AUCs of the models used were >0.900, more studies in a larger cohort of patients are required to further validate these revelations.

**Risk Stratification and Prognostication of Tumors.** The 2016 World Health Organization classification considers the genomics heterogeneity of diffuse gliomas, necessitating effective risk stratification for optimizing therapy.<sup>51</sup> The invasiveness of existing methods to identify histopathologic/molecular profiles and the difficulty of replicating results demonstrated the need to identify noninvasive methods to complement and solidify the diagnostic armamentarium. Development of radiomics profiles and comprehensive analysis of radiogenomics phenotypes using multiomics molecular approaches have been successful in risk stratification and survival estimation of diffuse gliomas.<sup>6,32,33,35,41,73,74</sup> A study using MR imaging radiomics features of patients with de novo GBM determined the imaging signatures associated with poor prognosis.<sup>75</sup>

In another cohort of 82 patients with de novo GBM, analysis of 5 texture features from preoperative MR images predicted molecular subtypes and 12-month survival status (overall survival at 12 months indicating whether the patient was alive).<sup>32</sup> Another radiomics study evaluating CBV and ADC in 119 patients with newly diagnosed GBM demonstrated that radiomics-based classification allows noninvasive prediction of survival and stratification of patients with GBM with better accuracy than that determined with established conventional clinical (age and Karnofsky Performance Scale score) or radiologic risk models (Gaussian normalized relative CBV and ADC).<sup>6</sup> These methods and tools could guide planning of surgical resection, define radiation treatment margins, and optimize

the intensity of chemotherapy. The evolving and molecular profile of lower-grade gliomas, including the favorable outcome associated with *IDH1* and 1p/19q codeletion mutation status, now partially explains the heterogeneous survival outcomes; recent studies have shown that radiomics phenotyping using ML techniques can identify these genomic markers<sup>43,47</sup> and predict overall survival with better accuracy than with the use of nonimaging markers (clinical features and genomic data).<sup>41</sup> Identification of the *ATRX* mutation or loss of *ATRX* expression is a potential biomarker in gliomas and has been associated with favorable survival outcome; in a recently published article, the authors showed that radiomics could identify this genotype at diagnosis.<sup>56</sup> This could be an important addition to the noninvasive detection of pivotal biomarkers such as *IDH1* and *MGMT* in gliomas.<sup>44,46,47,58,59</sup>

**Predicting Treatment-Related Surrogate End Points.** A few studies have robustly defined the biologic heterogeneity of the peritumoral brain zone and its interaction with the microenvironment in brain tumors.<sup>55</sup> This heterogeneity contributes to therapeutic resistance and poor survival in infiltrating tumors such as GBM.<sup>55</sup> Nearly 90% of recurrences in GBM occur in the peritumoral brain zone, which is usually the nonenhancing component.<sup>55</sup> Interrogating 10 radiomics peritumoral features from the peritumoral brain zone on routine preoperative MR imaging in patients with GBM was predictive of long-term (>18 months) versus short-term (<7 months) survival.<sup>33</sup> In addition, a model generated by 6 imaging features for CD3 infiltration prediction in GBM achieved high accuracies of 97.1% and 76.5% in the training and testing sets, respectively.<sup>76</sup> The role of radiomics is being used increasingly to improve characterization and understanding of the tumor microenvironment.<sup>70,76</sup> This will have important clinical relevance in optimizing a targeted therapeutic approach.<sup>77</sup>

Bevacizumab has been widely used to treat patients with recurrent GBM; however, the data show a lack of sustained long-term efficacy.<sup>78</sup> The therapeutic responses, furthermore, vary substantially in patients.<sup>78</sup> However, quantitative imaging biomarkers that use radiomics to help identify patients who will benefit from bevacizumab treatment before initiation of therapy have been researched.<sup>35</sup>

With the use of immunotherapeutics in brain tumors, transient increases in tumor size and/or new inflammatory lesions often appear. These changes, known as pseudoprogression, typically stabilize or decrease with the continuation of treatment, and differentiating them from progressive disease is often difficult and delayed.<sup>79</sup> Conventional imaging using MR perfusion studies has been used frequently, though specificity and sensitivity remain suboptimal.<sup>80,81</sup> A multicenter study using an MR perfusion-based radiomics model was able to distinguish pseudoprogression from progressive disease with the AUC, sensitivity, and specificity of 90%, 93%, and 89%, respectively.<sup>24</sup> These studies highlight the capability of radiomics to address this important clinical distinction—an unmet need in neuroimmunotherapy.

### **Evolving Era of Radiomics in Pediatric Neuro-Oncology**

Pediatric CNS tumors have special characteristics in tissues, morphology, molecular subtype, and texture compared with their adult counterparts.<sup>82</sup> With the emerging biologic differences

between adult and pediatric brain tumors, the need for improved characterization of CNS tumors in children is imperative. Although radiomics and radiogenomics are now used in the adult clinical arena, their translation into clinical practice in pediatric neuro-oncology is still in its infancy (Online Supplemental Data). Pediatric brain tumors are the most common solid tumors in children.<sup>83</sup> Unlike adults, in whom we have seen increased use of noninvasive neuroimaging using multimodal MR imaging combining multiple sequences to enhance tissue characterization, few studies to date have been reported in pediatrics.<sup>5,9,84-87</sup> Similar noninvasive imaging studies are needed in parallel with the evolving molecular era in pediatric brain tumors, facilitating improved tumor classification (histologic and molecular), grading, survival prediction, and treatment response.

Earlier studies evaluated the role and potential of MR imaging texture analysis in capturing quantitative information of different pediatric brain tumors.<sup>88</sup> A recent multicenter study was performed within a supervised classification framework on clinical MR imaging, and a support vector machine was trained with 3D textural attributes obtained from conventional MR imaging.<sup>85</sup> The developed model was very successful in capturing transferable tumor information, and this study supported the use of 3D texture analysis on conventional MR imaging to aid in the diagnostic classification of various pediatric brain tumors. A recently published study<sup>84</sup> using a combination of radiomics and ML approaches on 3D multimodal MR imaging was able to build a radiomics model with multivariable logistic regression. These models could differentiate pediatric ependymoma and medulloblastoma (common malignant brain tumors of the posterior fossa in children) with an AUC of 0.91. Similarly, Zhou et al<sup>87</sup> demonstrated the capability of radiomics in differentiating the types of pediatric posterior fossa tumors (medulloblastoma, ependymoma, and pilocytic astrocytoma) with an accuracy of 0.85. The success of this trend needs to be evaluated further in prospective studies.

Pediatric medulloblastoma has been the most biologically interrogated malignant CNS tumor in children.<sup>89</sup> Its molecular subtypes with distinct clinical and prognostic differences now reaffirm the need to tailor therapy accordingly.<sup>89</sup> A recent study<sup>5</sup> provided proof-of-concept results for the application of radiomics and ML approaches for prediction of distinct medulloblastoma subgroups. The reproducibility of this finding would be of immense clinical significance, with noninvasive ability to diagnose and biologically subtype these neoplasms. Another research group published that model based on texture extracted from conventional MR imaging to preoperatively differentiate ependymoma and pilocytic astrocytoma and achieved high sensitivity, specificity, and AUC.<sup>9</sup> This could be an invaluable tool because often these lesions occur in the eloquent areas of the brain both at diagnosis and recurrence, precluding surgical intervention.

DNA methylation now identifies various molecular subtypes of aggressive pediatric CNS tumors, and genomics analysis was able to decipher the intrinsic tumor heterogeneity.<sup>90</sup> Noninvasive imaging that uses radiomics to correlate with these genomic aberrations would be a clinically significant addition to diagnosing these neoplasms and facilitating the design of optimal targeted therapy.

Diffuse midline gliomas in children are aggressive brain tumors with 10% overall survival at 18 months. MR imaging-based texture analysis in 32 children with diffuse midline gliomas was able to stratify patients into poor and good prognostic groups, with a median survival of 7.5 months versus 17.5 months, respectively.<sup>74</sup> Diffuse midline gliomas with more homogeneous texture on diagnostic MR imaging were associated with a worse prognosis.<sup>74</sup> These findings should be further explored and correlated with the evolving molecular subtypes, providing valuable insight into prognosis and tailored therapy for these tumors. Profiling an optimal decision tree model with the use of ADC histogram analysis and structural MR imaging findings provided the ability to differentiate 7 histopathologic subtypes of pediatric CNS tumors, with a nearly 90% accurate classification.<sup>34</sup> This decision tree model could preoperatively distinguish, with precision, 2 biologically different tumors, pilocytic astrocytomas and atypical teratoid/rhabdoid tumor, in comparison with neuroradiologists. Similar prospective studies evaluating the ability of this model to correlate with the diverse genomic aberrations would be a breakthrough in the management of targeted therapy for these tumors at diagnosis and recurrence. A major success of targeted therapy in pediatric CNS tumors has been the use of *BRAF* and *Mek* inhibitors in low-grade gliomas. Currently, a biopsy is needed to identify these molecular aberrations, often not possible due to the eloquent location of these neoplasms. A recent study showed the ability of radiomics-based prediction of *BRAF* status in pediatric low-grade gliomas before a biopsy, which could have significant implications in clinical practice.<sup>91</sup>

**Immunology.** Use of immunotherapeutic strategies, including adoptive cell therapy, vaccine therapy, and checkpoint inhibitors, in pediatric brain tumors has been rapidly evolving.<sup>92</sup> However, therapeutic efficacy is undermined by the low mutational burden seen in these tumors, precluding targeted therapy. Reviews of immunotherapy in pediatric brain tumors show some preliminary promising results, which need to be further explored. In a recently published study of natural killer cell infusion in children with recurrent medulloblastoma and ependymoma, a high radiomic performance was achieved; accuracy, sensitivity, and specificity were 100%, though it did not attain statistical significance, likely due to the low number of patients.<sup>86,92,93</sup> A few studies in adults have shown the ability of radiomics models to differentiate pseudoprogression from early tumor progression in infiltrative tumors such as GBM.<sup>24</sup> The ability to make these distinctions in pediatric neuro-oncology is important and needs to be pursued.

### Limitations

Although radiomics has shown its potential for diagnostic, prognostic, and predictive purposes in multiple neuro-oncology studies, the translation of radiomics into the clinical settings is slow because the field is facing several challenges. Most important, the repeatability, variability, and reproducibility of radiomics are still issues and often depend on the imaging sequence used, technique, size of the image, image quality, software used for feature extraction and reconstruction, as well as motion artifacts and segmentation, which can lead to greater interobserver variations in addition to the time-consuming nature of manual segmentation.

DL-based radiomics may overcome these issues because the features are extracted automatically from the huge data, and a subset of best-performing features is automatically identified. The most important pitfall of DL-based radiomics is the high association between the images and the clinical output data. Thus, in contrast to feature-based radiomics, large datasets are needed to identify the most relevant and robust features to overcome this challenge. DL-based radiomics models must validate their reliability in prospective large studies.

Another important limitation to the translation of radiomics models in clinical management is the interpretability of the radiomics features and models. Radiomics is perceived as a “black box,” ie, it is very difficult to clinically interpret the developed predictions. As an emerging technique, explainable AI is better understood, trusted, and the results are more efficiently interpreted by human-users, in contrast to the “black box” concept in ML.<sup>94</sup>

## CONCLUSIONS

In this review, we outlined the principles of radiomics analysis in a step-by-step approach and described how large amounts of imaging data can be interrogated and analyzed in patients with brain tumors. We believe that soon, with cumulative developments in AI and increasing public access to large data bases, radiomics can be expected to play an important role in clinical decision-making by answering many clinical questions of diagnostic and therapeutic relevance. However, many limitations and challenges exist, and much work needs to be done to robustly translate radiomics into the clinical arena.

## REFERENCES

1. Zhou M, Scott J, Chaudhury B, et al. **Radiomics in brain tumor: image assessment, quantitative feature descriptors, and machine-learning approaches.** *AJNR Am J Neuroradiol* 2018;39:208–16 CrossRef Medline
2. Colen RR, Rolf C, Ak M, et al. **Radiomics analysis for predicting pembrolizumab response in patients with advanced rare cancers.** *J Immunother Cancer* 2021;9:e001752 CrossRef Medline
3. Lambin P, Rios-Velazquez E, Leijenaar R, et al. **Radiomics: extracting more information from medical images using advanced feature analysis.** *Eur J Cancer* 2012;48:441–46 CrossRef Medline
4. Habib A, Jovanovich N, Hoppe M, et al. **MRI-based radiomics and radiogenomics in the management of low-grade gliomas: evaluating the evidence for a paradigm shift.** *J Clin Med* 2021;10:1411 CrossRef
5. Iv M, Zhou M, Shpanskaya K, et al. **MR imaging-based radiomic signatures of distinct molecular subgroups of medulloblastoma.** *AJNR Am J Neuroradiol* 2019;40:154–61 CrossRef Medline
6. Kickingereder P, Burth S, Wick A, et al. **Radiomic profiling of glioblastoma: identifying an imaging predictor of patient survival with improved performance over established clinical and radiologic risk models.** *Radiology* 2016;280:880–89 CrossRef Medline
7. Lin P, Peng YT, Gao RZ, et al. **Radiomic profiles in diffuse glioma reveal distinct subtypes with prognostic value.** *J Cancer Res Clin Oncol* 2020;146:1253–62 CrossRef Medline
8. Nakamoto T, Takahashi W, Haga A, et al. **Prediction of malignant glioma grades using contrast-enhanced T1-weighted and T2-weighted magnetic resonance images based on a radiomic analysis.** *Sci Rep* 2019;9:19411 CrossRef Medline
9. Li M, Wang H, Shang Z, et al. **Ependymoma and pilocytic astrocytoma: Differentiation using radiomics approach based on machine learning.** *J Clin Neurosci* 2020;78:175–80 CrossRef Medline
10. Rodriguez Gutierrez D, Awwad A, Meijer L, et al. **Metrics and textural features of MRI diffusion to improve classification of pediatric posterior fossa tumors.** *AJNR Am J Neuroradiol* 2014;35:1009–15 CrossRef Medline
11. Visser M, Petr J, Muller DMJ, et al. **Accurate MR image registration to anatomical reference space for diffuse glioma.** *Front Neurosci* 2020;14:585 CrossRef Medline
12. Akkus Z, Sedlar J, Coufalova L, et al. **Semi-automated segmentation of pre-operative low grade gliomas in magnetic resonance imaging.** *Cancer Imaging* 2015;15:12 CrossRef Medline
13. Hayes K, Buist R, Vincent TJ, et al. **Comparison of manual and semi-automated segmentation methods to evaluate hippocampus volume in APP and PS1 transgenic mice obtained via in vivo magnetic resonance imaging.** *J Neurosci Methods* 2014;221:103–11 CrossRef Medline
14. Zhao Z, Yang G, Lin Y, et al. **Automated glioma detection and segmentation using graphical models.** *PLoS One* 2018;13:e0200745 CrossRef Medline
15. Kalavathi P, Prasath VB. **Methods on skull stripping of MRI head scan images: a review.** *J Digit Imaging* 2016;29:365–79 CrossRef Medline
16. Nyúl LG, Udupa JK. **On standardizing the MR image intensity scale.** *Magn Reson Med* 1999;42:1072–81 CrossRef Medline
17. Buades A, Coll B, Morel JM. **A review of image denoising algorithms, with a new one.** *Multiscale Model Simul* 2005;4:490–530 CrossRef
18. Vovk U, Pernus F, Likar B. **A review of methods for correction of intensity inhomogeneity in MRI.** *IEEE Trans Med Imaging* 2007;26:405–21 CrossRef Medline
19. Cattell R, Chen S, Huang C. **Robustness of radiomic features in magnetic resonance imaging: review and a phantom study.** *Vis Comput Ind Biomed Art* 2019;2:19 CrossRef Medline
20. Chaurasia K, Garg PA. **Brief Review on Texture Analysis Methods.** American Society of Science and Engineering; 2013
21. Parekh V, Jacobs MA. **Radiomics: a new application from established techniques.** *Expert Rev Precis Med Drug Dev* 2016;1:207–26 CrossRef Medline
22. Deo RC. **Machine learning in medicine.** *Circulation* 2015;132:1920–30 CrossRef Medline
23. Colen RR, Ologun GO, Zinn P, et al. **Radiomic signatures to predict response to targeted therapy and immune checkpoint blockade in melanoma patients (pts) on neoadjuvant therapy.** *J Clin Oncol* 2020;38:10067 CrossRef
24. Elshafeey N, Kotrotsou A, Hassan A, et al. **Multicenter study demonstrates radiomic features derived from magnetic resonance perfusion images identify pseudoprogression in glioblastoma.** *Nat Commun* 2019;10:3170 CrossRef Medline
25. Rathore S, Akbari H, Rozycki M, et al. **Radiomic MRI signature reveals three distinct subtypes of glioblastoma with different clinical and molecular characteristics, offering prognostic value beyond IDH1.** *Sci Rep* 2018;8:5087 CrossRef Medline
26. Sompong C, Wongthanavasu S. **Brain tumor segmentation using cellular automata-based fuzzy c-means.** In: *Proceedings of the International Joint Conference on Computer Science and Software Engineering*, Khon Kaen, Thailand. July 13–15;2016:1–6 CrossRef
27. Kong DS, Kim J, Ryu G, et al. **Quantitative radiomic profiling of glioblastoma represents transcriptomic expression.** *Oncotarget* 2018;9:6336–45 CrossRef Medline
28. Parekh VS, Jacobs MA. **Deep learning and radiomics in precision medicine.** *Expert Rev Precis Med Drug Dev* 2019;4:59–72 CrossRef Medline
29. Parmar C, Grossmann P, Bussink J, et al. **Machine learning methods for quantitative radiomic biomarkers.** *Sci Rep* 2015;5:13087 CrossRef Medline



30. Sasaki T, Kinoshita M, Fujita K, et al. Radiomics and MGMT promoter methylation for prognostication of newly diagnosed glioblastoma. *Sci Rep* 2019;9:14435 CrossRef Medline
31. Sun P, Wang D, Mok VC, et al. Comparison of feature selection methods and machine learning classifiers for radiomics analysis in glioma grading. *IEEE Access* 2019;7:102010–20 CrossRef
32. Yang D, Rao G, Martinez J, et al. Evaluation of tumor-derived MRI-texture features for discrimination of molecular subtypes and prediction of 12-month survival status in glioblastoma. *Med Phys* 2015;42:6725–35 CrossRef Medline
33. Prasanna P, Patel J, Partovi S, et al. Radiomic features from the peritumoral brain parenchyma on treatment-naïve multi-parametric MR imaging predict long versus short-term survival in glioblastoma multiforme: preliminary findings. *Eur Radiol* 2017;27:4188–97 CrossRef Medline
34. Payabvash S, Aboian M, Tihan T, et al. Machine learning decision tree models for differentiation of posterior fossa tumors using diffusion histogram analysis and structural MRI findings. *Front Oncol* 2020;10:71 CrossRef Medline
35. Kickingeder P, Gotz M, Muschelli J, et al. Large-scale radiomic profiling of recurrent glioblastoma identifies an imaging predictor for stratifying anti-angiogenic treatment response. *Clin Cancer Res* 2016;22:5765–71 CrossRef Medline
36. Chen T, Guestrin C. XGBoost: a scalable tree boosting system. In: *Proceedings of the 22nd ACM SIGKDD International Conference on Knowledge Discovery and Data Mining*. Association for Computing Machinery; 2016:785–94
37. Koçak B, Durmaz EŞ, Ateş E, et al. Radiomics with artificial intelligence: a practical guide for beginners. *Diagn Interv Radiol* 2019;25:485–95 CrossRef Medline
38. Kumar V, Gu Y, Basu S, et al. Radiomics: the process and the challenges. *Magn Reson Imaging* 2012;30:1234–48 CrossRef Medline
39. Zinn PO, Majadan B, Sathyan P, et al. Radiogenomic mapping of edema/cellular invasion MRI-phenotypes in glioblastoma multiforme. *PLoS One* 2011;6:e25451 CrossRef Medline
40. Cho HH, Lee SH, Kim J, et al. Classification of the glioma grading using radiomics analysis. *PeerJ* 2018;6:e5982 CrossRef Medline
41. Choi YS, Ahn SS, Chang JH, et al. Machine learning and radiomic phenotyping of lower grade gliomas: improving survival prediction. *Eur Radiol* 2020;30:3834–42 CrossRef Medline
42. Fan Y, Chen C, Zhao F, et al. Radiomics-based machine learning technology enables better differentiation between glioblastoma and anaplastic oligodendroglioma. *Front Oncol* 2019;9:1164 CrossRef Medline
43. Han Y, Xie Z, Zang Y, et al. Non-invasive genotype prediction of chromosome 1p/19q co-deletion by development and validation of an MRI-based radiomics signature in lower-grade gliomas. *J Neurooncol* 2018;140:297–306 CrossRef Medline
44. Lohmann P, Lerche C, Bauer EK, et al. Predicting IDH genotype in gliomas using FET PET radiomics. *Sci Rep* 2018;8:13328 CrossRef Medline
45. Su C, Jiang J, Zhang S, et al. Radiomics based on multicontrast MRI can precisely differentiate among glioma subtypes and predict tumour-proliferative behaviour. *Eur Radiol* 2019;29:1986 CrossRef Medline
46. Zhang B, Chang K, Ramkissoon S, et al. Multimodal MRI features predict isocitrate dehydrogenase genotype in high-grade gliomas. *Neuro Oncol* 2017;19:109–17 CrossRef Medline
47. Zhou H, Chang K, Bai HX, et al. Machine learning reveals multimodal MRI patterns predictive of isocitrate dehydrogenase and 1p/19q status in diffuse low- and high-grade gliomas. *J Neurooncol* 2019;142:299–307 CrossRef Medline
48. Kickingeder P, Bonekamp D, Nowosielski M, et al. Radiogenomics of glioblastoma: machine learning-based classification of molecular characteristics by using multiparametric and multiregional MR imaging features. *Radiology* 2016;281:907–18 CrossRef Medline
49. Li J, Liu S, Qin Y, et al. High-order radiomics features based on T2 FLAIR MRI predict multiple glioma immunohistochemical features: a more precise and personalized gliomas management. *PLoS One* 2020;15:e0227703 CrossRef Medline
50. Hu LS, Ning S, Eschbacher JM, et al. Radiogenomics to characterize regional genetic heterogeneity in glioblastoma. *Neuro Oncol* 2017;19:128–37 CrossRef Medline
51. Colen RR, Hassan I, Elshafeey N, et al. Shedding light on the 2016 World Health Organization Classification of Tumors of the Central Nervous System in the era of radiomics and radiogenomics. *Magn Reson Imaging Clin N Am* 2016;24:741–49 CrossRef Medline
52. Gutman DA, Cooper LA, Hwang SN, et al. MR imaging predictors of molecular profile and survival: multi-institutional study of the TCGA glioblastoma data set. *Radiology* 2013;267:560–69 CrossRef Medline
53. Zinn PO, Singh SK, Kotrotsou A, et al. A co-clinical radiogenomic validation study: conserved magnetic resonance radiomic appearance of periostin expressing glioblastoma in patients and xenograft models. *Clin Cancer Res* 2018;24:6288–99 CrossRef Medline
54. Reardon DA, Wen PY. Glioma in 2014: unravelling tumour heterogeneity: implications for therapy. *Nat Rev Clin Oncol* 2015;12:69–70 CrossRef Medline
55. Lemee JM, Clavreul A, Menei P. Intratumoral heterogeneity in glioblastoma: don't forget the peritumoral brain zone. *Neuro Oncol* 2015;17:1322–32 CrossRef Medline
56. Li Y, Liu X, Qian Z, et al. Genotype prediction of ATRX mutation in lower-grade gliomas using an MRI radiomics signature. *Eur Radiol* 2018;28:2960–68 CrossRef Medline
57. Lin AL, White M, Miller-Thomas MM, et al. Molecular and histologic characteristics of pseudoprogression in diffuse gliomas. *J Neurooncol* 2016;130:529–33 CrossRef Medline
58. Xi YB, Guo F, Xu ZL, et al. Radiomics signature: a potential biomarker for the prediction of MGMT promoter methylation in glioblastoma. *J Magn Reson Imaging* 2018;47:1380–87 CrossRef Medline
59. Korfiatis P, Kline TL, Coufalova L, et al. MRI texture features as biomarkers to predict MGMT methylation status in glioblastomas. *Med Phys* 2016;43:2835–44 CrossRef Medline
60. Akbari H, Bakas S, Pisapia JM, et al. In vivo evaluation of EGFRvIII mutation in primary glioblastoma patients via complex multiparametric MRI signature. *Neuro Oncol* 2018;20:1068–79 CrossRef Medline
61. Chang P, Grinband J, Weinberg BD, et al. Deep-learning convolutional neural networks accurately classify genetic mutations in gliomas. *AJNR Am J Neuroradiol* 2018;39:1201–07 CrossRef Medline
62. Zinn PO, Singh SK, Kotrotsou A, et al. Distinct radiomic phenotypes define glioblastoma TP53-PTEN-EGFR mutational landscape. *Neurosurgery* 2017;64:203–10 CrossRef Medline
63. Kaloshi G, Benouaich-Amiel A, Diakite F, et al. Temozolomide for low-grade gliomas: predictive impact of 1p/19q loss on response and outcome. *Neurology* 2007;68:1831–36 CrossRef Medline
64. Cha S. Neuroimaging in neuro-oncology. *Neurotherapeutics* 2009;6:465–77 CrossRef Medline
65. Al-Okaili RN, Krejza J, Woo JH, et al. Intraaxial brain masses: MR imaging-based diagnostic strategy—initial experience. *Radiology* 2007;243:539–50 CrossRef Medline
66. Chen C, Ou X, Wang J, et al. Radiomics-based machine learning in differentiation between glioblastoma and metastatic brain tumors. *Front Oncol* 2019;9:806 CrossRef Medline
67. Kang D, Park JE, Kim YH, et al. Diffusion radiomics as a diagnostic model for atypical manifestation of primary central nervous system lymphoma: development and multicenter external validation. *Neuro Oncol* 2018;20:1251–61 CrossRef Medline
68. Kong Z, Jiang C, Zhu R, et al. (18)F-FDG-PET-based radiomics features to distinguish primary central nervous system lymphoma from glioblastoma. *Neuroimage Clin* 2019;23:101912 CrossRef Medline
69. Ortiz-Ramon R, Larroza A, Ruiz-Espana S, et al. Classifying brain metastases by their primary site of origin using a radiomics approach based on texture analysis: a feasibility study. *Eur Radiology* 2018;28:4514–23 CrossRef Medline



70. Sun R, Limkin EJ, Vakalopoulou M, et al. **A radiomics approach to assess tumour-infiltrating CD8 cells and response to anti-PD-1 or anti-PD-L1 immunotherapy: an imaging biomarker, retrospective multicohort study.** *Lancet Oncol* 2018;19:1180–91 CrossRef Medline
71. Tian Q, Yan LF, Zhang X, et al. **Radiomics strategy for glioma grading using texture features from multiparametric MRI.** *J Magn Reson Imaging* 2018;48:1518–28 CrossRef Medline
72. Theresia E, Malueka RG, Pranacipta S, et al. **Association between Ki-67 labeling index and histopathological grading of glioma in Indonesian population.** *Asian Pac J Cancer Prev* 2020;21:1063–68 CrossRef Medline
73. Grossmann P, Narayan V, Chang K, et al. **Quantitative imaging biomarkers for risk stratification of patients with recurrent glioblastoma treated with bevacizumab.** *Neuro Oncol* 2017;19:1688–97 CrossRef Medline
74. Szychoł E, Youssef A, Ganesan B, et al. **Predicting outcome in childhood diffuse midline gliomas using magnetic resonance imaging based texture analysis.** *J Neuroradiol* 2021;48:243–47 CrossRef Medline
75. McGarry SD, Hurrell SL, Kaczmarowski AL, et al. **Magnetic resonance imaging-based radiomic profiles predict patient prognosis in newly diagnosed glioblastoma before therapy.** *Tomography* 2016;2:223–28 CrossRef Medline
76. Narang S, Kim D, Aithala S, et al. **Tumor image-derived texture features are associated with CD3 T-cell infiltration status in glioblastoma.** *Oncotarget* 2017;8:101244–54 CrossRef Medline
77. Kotrotsou A, Zinn PO, Colen RR. **Radiomics in brain tumors: an emerging technique for characterization of tumor environment.** *Magn Reson Imaging Clin N Am* 2016;24:719–29 CrossRef Medline
78. Arevalo OD, Soto C, Rabiei P, et al. **Assessment of glioblastoma response in the era of bevacizumab: longstanding and emergent challenges in the imaging evaluation of pseudoresponse.** *Front Neurol* 2019;10:460 CrossRef Medline
79. Okada H, Weller M, Huang R, et al. **Immunotherapy response assessment in neuro-oncology: a report of the RANO working group.** *Lancet Oncol* 2015;16:e534–42 CrossRef Medline
80. Wan B, Wang S, Tu M, et al. **The diagnostic performance of perfusion MRI for differentiating glioma recurrence from pseudoprogression: a meta-analysis.** *Medicine (Baltimore)* 2017;96:e6333 CrossRef Medline
81. Huang RY, Neagu MR, Reardon DA, et al. **Pitfalls in the neuroimaging of glioblastoma in the era of antiangiogenic and immuno/targeted: detecting illusive disease, defining response.** *Front Neurol* 2015;6:33 CrossRef Medline
82. Paugh BS, Qu C, Jones C, et al. **Integrated molecular genetic profiling of pediatric high-grade gliomas reveals key differences with the adult disease.** *J Clin Oncol* 2010;28:3061–68 CrossRef Medline
83. Siegel R, Naishadham D, Jemal A. **Cancer statistics, 2013.** *CA Cancer J Clin* 2013;63:11–30 CrossRef Medline
84. Dong J, Li L, Liang S, et al. **Differentiation between ependymoma and medulloblastoma in children with radiomics approach.** *Acad Radiol* 2021;28:318–27 CrossRef Medline
85. Fetit AE, Novak J, Rodriguez D, et al. **Radiomics in paediatric neuro-oncology: a multicentre study on MRI texture analysis.** *NMR Biomed* 2018 Jan 3 [Epub ahead of print] CrossRef Medline
86. Khatua S, Cooper LJN, Sandberg DI, et al. **Phase I study of intravenous infusions of autologous ex-vivo-expanded NK cells in children with recurrent medulloblastoma and ependymoma.** *Neuro Oncol* 2020;22:1214–25 CrossRef Medline
87. Zhou H, Hu R, Tang O, et al. **Automatic machine learning to differentiate pediatric posterior fossa tumors on routine MR imaging.** *AJNR Am J Neuroradiol* 2020;41:1279–85 CrossRef Medline
88. Fetit AE, Novak J, Rodriguez D, et al. **3D texture analysis of heterogeneous MRI data for diagnostic classification of childhood brain tumours.** *Stud Health Technol Inform* 2015;213:19–22 Medline
89. Northcott PA, Robinson GW, Kratz CP, et al. **Medulloblastoma.** *Nat Rev Dis Primers* 2019;5:11 CrossRef Medline
90. Kumar R, Liu APY, Orr BA, et al. **Advances in the classification of pediatric brain tumors through DNA methylation profiling: from research tool to frontline diagnostic.** *Cancer* 2018;124:4168–80 CrossRef Medline
91. Wagner MW, Hainc N, Khalvati F, et al. **Radiomics of pediatric low-grade gliomas: toward a pretherapeutic differentiation of BRAF-mutated and BRAF-fused tumors.** *AJNR Am J Neuroradiol* 2021;42:759–65 CrossRef Medline
92. Foster JB, Madsen PJ, Hegde M, et al. **Immunotherapy for pediatric brain tumors: past and present.** *Neuro Oncol* 2019;21:1226–38 CrossRef Medline
93. Wang SS, Bandopadhyay P, Jenkins MR. **Towards immunotherapy for pediatric brain tumors.** *Trends Immunol* 2019;40:748–61 CrossRef Medline
94. Barredo Arrieta A, Díaz-Rodríguez N, Del Ser J, et al. **Explainable Artificial Intelligence (XAI): concepts, taxonomies, opportunities and challenges toward responsible AI.** *Information Fusion* 2020;58:82–115 CrossRef

# The Mammillary Bodies: A Review of Causes of Injury in Infants and Children

 K.M.E. Meys,  L.S. de Vries,  F. Groenendaal,  S.D. Vann, and  M.H. Lequin



## ABSTRACT

**SUMMARY:** Despite their small size, the mammillary bodies play an important role in supporting recollective memory. However, they have typically been overlooked when assessing neurologic conditions that present with memory impairment. While there is increasing evidence of mammillary body involvement in a wide range of neurologic disorders in adults, very little attention has been given to infants and children. Literature searches of PubMed and EMBASE were performed to identify articles that describe mammillary body pathology on brain MR imaging in children. Mammillary body pathology is present in the pediatric population in several conditions, indicated by signal change and/or atrophy on MR imaging. The main causes of mammillary body pathology are thiamine deficiency, hypoxia-ischemia, direct damage due to masses or hydrocephalus, or deafferentation resulting from pathology within the wider Papez circuit. Optimizing scanning protocols and assessing mammillary body status as a standard procedure are critical, given their role in memory processes.

**ABBREVIATIONS:** CCHS = congenital central hypoventilation syndrome; HIE = hypoxic-ischemic encephalopathy; LiTT = laser interstitial thermal therapy; MB = mammillary body; MTS = mesial temporal sclerosis; SVHD = single ventricular heart disease

The mammillary bodies (MBs) were arguably the first brain region to be implicated in memory, on the basis of the pathology observed in Korsakoff syndrome around the end of the 19th century. However, since then, they have been consistently overlooked during neuropathologic assessments, with memory impairment often being attributed to hippocampal involvement. More recent studies have re-confirmed the importance of the MBs for memory in adults.<sup>1,2</sup> Furthermore, it has been demonstrated that MB pathology is by no means restricted to Korsakoff syndrome/thiamine deficiency but can occur in numerous neurologic conditions, including strokes,<sup>3</sup> craniopharyngiomas,<sup>4</sup> colloid cysts,<sup>5,6</sup> schizophrenia,<sup>7</sup> Alzheimer disease,<sup>8</sup> multiple sclerosis,<sup>9</sup> and following acute or repetitive/prolonged hypoxia.<sup>10,11</sup>

Despite this wide-ranging involvement of the MBs in neurologic disorders in adults, far less attention has been given to the MBs in infants and children. However, several recent studies have underlined the importance of assessing the MBs in younger patients. For example, the MBs appear particularly sensitive to neonatal hypoxia-ischemia.<sup>12,13</sup> Volume loss in the MBs, the hippocampus, and fornices, is also associated with cognitive impairment, including episodic memory deficit in school-age children with a history of neonatal hypoxic-ischemic encephalopathy.<sup>14</sup> MB atrophy has also been reported following the Fontan procedure, with MB volume related to the degree of memory impairment.<sup>15</sup>

These recent studies have identified the importance of assessing the status of the MBs in infants and children, and as with adult cases of MB pathology, there is likely a wide range of conditions that can impact the MBs in younger patients. This review will identify those conditions in which MB pathology has been observed in infants and children. The focus is on human literature and includes studies that reported MB pathology on brain MR imaging in children (see the Online Supplemental Data for an overview of search terms and inclusion criteria and the list of articles identified). The conditions associated with MB pathology will be summarized below as well as implications for radiologic assessment.

## Mammillary Body Embryology, Anatomy, and Function

The MBs are a paired round structure located at the undersurface of the diencephalon. They are separated along the midline by the

Received October 18, 2021; accepted after revision November 22.


From the Department of Radiology (K.M.E.M., M.H.L.) and Neonatology (F.G., L.S.d.V.), Wilhelmina Children's Hospital, University Medical Center Utrecht and Utrecht University, Utrecht, the Netherlands; and School of Psychology (S.D.V.), Cardiff University, Cardiff, UK.

S.D. Vann and M.H. Lequin share last authorship.

S.D. Vann is supported by a Wellcome Trust Senior Research Fellowship (212273/Z/18/).

Please address correspondence to M.H. Lequin, MD, PhD, Division Imaging & Oncology, Department of Radiology & Nuclear Medicine, University Medical Center Utrecht & Princess Máxima Center for Pediatric Oncology, 3508 GA Utrecht, the Netherlands; e-mail: m.h.lequin@umcutrecht.nl

 Indicates open access to non-subscribers at [www.ajnr.org](http://www.ajnr.org)

 Indicates article with online supplemental data.

<http://dx.doi.org/10.3174/ajnr.A7463>

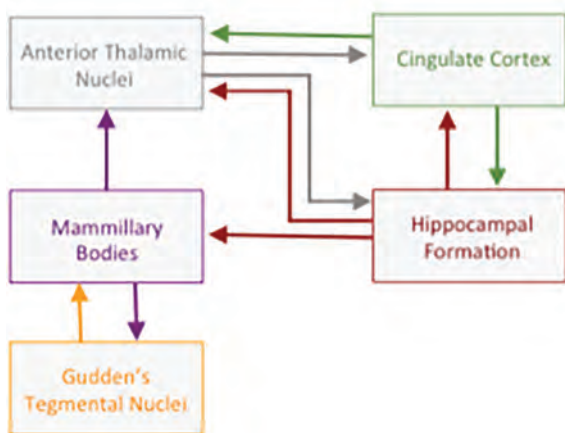


**FIG 1.** The principal connections of the mammillary bodies.

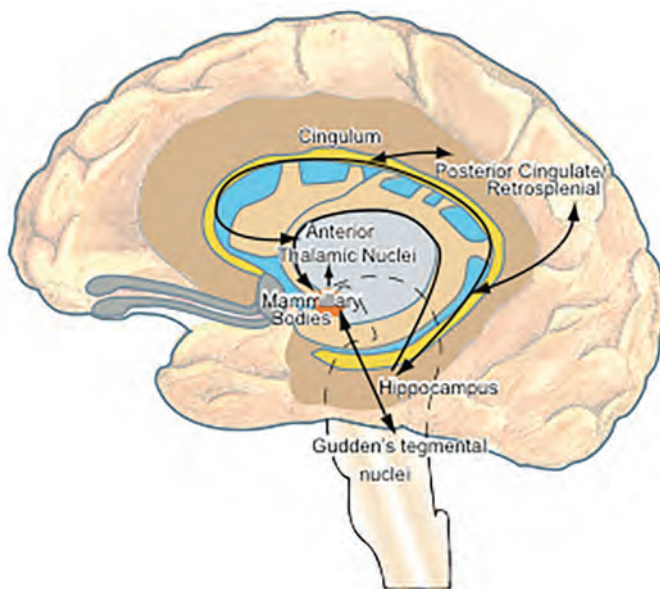
intermammillary sulcus. The MBs contain 2 gray matter structures, the medial and lateral nuclei; these are encapsulated by white matter and form the mammillothalamic and mammillotegmental tracts.

In humans, both the lateral and medial mammillary bodies are present at 10 weeks' gestation, though at this stage, the cells are undifferentiated.<sup>16</sup> By 11–14 weeks, the MBs comprise a group of homogeneous neurons; by 16 weeks' gestation, they are clearly differentiated. By 24–33 weeks, the MBs take on an appearance similar to that in adult MBs, ie, they are well-developed at the time of full-term birth.

There is some natural variation in the anatomy of the MBs in the general population.<sup>17,18</sup> In the axial plane, they can appear more circular or elliptic, and there is also variation in the depth of the intermammillary sulcus.<sup>17</sup> The MBs can also appear asymmetric without an underlying pathologic cause; for example, Tagliamonte et al<sup>17</sup> reported MB asymmetry in 13.9% of their young, healthy cohort. In most cases, this asymmetry arose from the abnormal course of the posterior cerebral artery, which resulted in dorsal displacement of the MBs. In 4 of the 78 participants, the asymmetry appeared to reflect a loss of volume of one of the MBs.

In addition to primary damage, the MBs can be affected by damage to their principal input and output (Fig 1). For example, anterograde degeneration can occur following injury to the hippocampus or fornix,<sup>19</sup> though the resultant MB atrophy is thought to reflect a loss of white matter rather than neuronal loss.<sup>20</sup> In contrast, neuronal loss in the MBs can occur as a result of retrograde degeneration following damage to the mammillothalamic tract.<sup>21</sup>

Consistent with the anatomic connectivity of the MBs with the hippocampus, fornix, and mammillothalamic tract, the MBs also form a functional network with these structures, ie, the Papez circuit (Fig 1). The MBs have an important role in integrating input from the hippocampus and the Gudden tegmental nuclei and for coordinating oscillatory activity in the hippocampus and cortex.<sup>2,22</sup> The MBs appear to be particularly important



for episodic (ie, event) memory,<sup>2,23</sup> including temporal and contextual memory.<sup>24</sup>

### **MB Pathology**

**Thiamine Deficiency.** Korsakoff syndrome, arising from thiamine (vitamin B1) deficiency, is the most common condition associated with MB pathology. Indeed, almost half of the articles identified in this literature search referred to MB abnormalities in children with thiamine deficiency. Although Korsakoff syndrome is typically associated with alcoholism in adults, many other conditions have been identified that can result in similar thiamine deficiency and resultant neuropathology in children.<sup>25,26</sup>

Thiamine deficiency may present as infantile encephalopathic beriberi (dry beriberi) or as Wernicke encephalopathy. Wernicke encephalopathy is difficult to diagnose and often goes untreated in clinical practice. This lack of detection and treatment is evidenced by the finding that Wernicke encephalopathy is first diagnosed postmortem in >80% of cases in adults<sup>27,28</sup> and >40% in children.<sup>29</sup> Because patients usually respond well to acute thiamine replacement therapy, it highlights the importance of making an early diagnosis.

Wernicke encephalopathy in children typically arises from nutritional deficiency, which can occur due to vomiting (eg, due to anorexia nervosa, hyperemesis, gastrointestinal obstruction),<sup>30–32</sup> chronic gastrointestinal disease,<sup>33</sup> and following bariatric surgery.<sup>34</sup> Wernicke encephalopathy has also been reported following acute liver failure<sup>35</sup> and pancreatitis.<sup>36</sup> The MR imaging characteristics of thiamine deficiency include symmetric T2 hyperintensities in the dorsal medial thalamus, MBs, periaqueductal gray matter, and tectal plate,<sup>26</sup> with the MBs being involved in 17%–58% of cases.<sup>37–39</sup> High-signal-intensity changes on T2-weighted images are the most frequent pathologic findings seen on MR imaging compared with low-signal-intensity changes on T1-weighted images.<sup>37</sup>

Contrast enhancement of the MBs, which is characteristic in alcohol-related Wernicke encephalopathy, occurs less frequently in



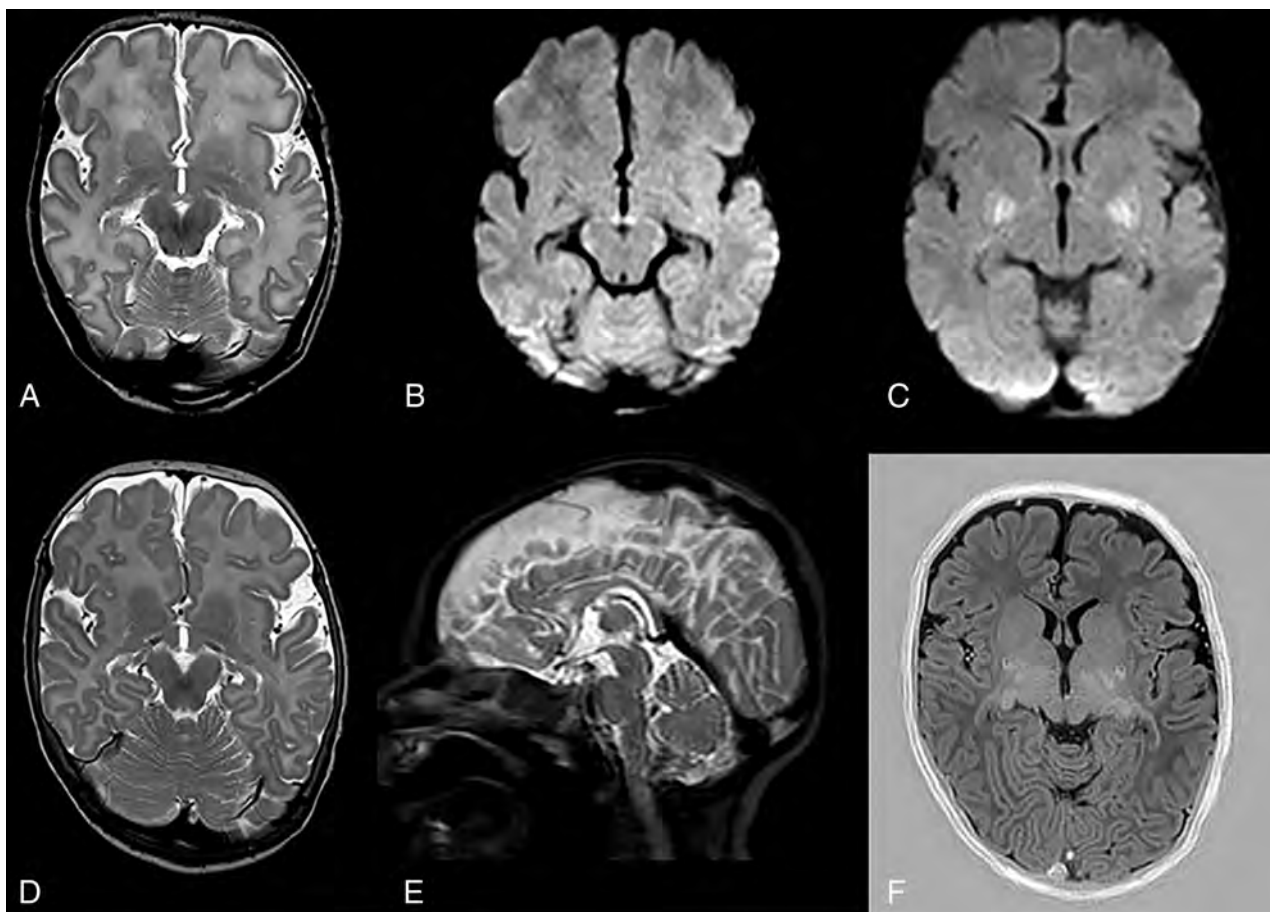


**FIG 2.** Images from a term neonate initially scanned at 6 days of age. A, A T2-weighted image with a hyperintense aspect of the MBs. B, A  $b=1000$  image shows a hyperintense aspect on the ADC map (not shown), consistent with ischemia. C, Ischemia is also seen symmetrically in the thalami and basal ganglia. Follow-up at 3 months shows atrophy of the MBs (D) with flattening on the sagittal view (E). Tissue loss and gliosis in the lentiform nucleus can also be seen (F).

Wernicke encephalopathy in nonalcoholic populations.<sup>39,40</sup> However, contrast enhancement has also been reported in children with Wernicke encephalopathy, resulting from malnutrition, for example.<sup>31,33</sup> In addition to signal changes, MB volume loss has also been reported in patients with anorexia nervosa as well as recovery of MB volume in individuals who regained weight.<sup>30</sup> Recovery of MB volume has also been reported in patients with acute liver failure following treatment with thiamine.<sup>35</sup> Furthermore, MB volume was found to correlate with blood thiamine levels.<sup>32</sup> Consistent with this observed recovery of MB volume after thiamine treatment, signal changes in Wernicke encephalopathy have also been shown to improve<sup>41</sup> or even resolve after treatment.<sup>26,38</sup> This finding suggests that the signal changes may reflect reversible vasogenic edema as opposed to acute ischemia.<sup>32</sup>

**MB Pathology in Infants with Perinatal Asphyxia.** Severe perinatal asphyxia can result in hypoxic-ischemic encephalopathy (HIE). The prevalence of HIE is approximately 1.5 per 1000 live-birth-term neonates.<sup>42</sup> The brain areas that are typically involved in HIE include the deep gray nuclei or white matter and cortex, depending on the severity and duration of the insult. Two main patterns of injury have been distinguished on MR imaging:<sup>43</sup> The

first is the basal ganglia–thalamus pattern, which is mainly associated with acute, severe perinatal asphyxia such as uterine rupture; the second is the watershed-predominant pattern of injury, which is more common after prolonged partial asphyxia. This second pattern involves the vascular watershed zones of the anterior MCA and posterior MCA. In the most severe cases, both patterns are visible—this is called a “near total” pattern of injury because on diffusion-weighted MR imaging, the cerebellum is mostly spared.

The limbic system can also be affected following HIE, with MRIs showing diffusion restriction on DWI in the hippocampal region.<sup>44,45</sup> Recent studies have also shown signal change in the MBs after perinatal asphyxia (Fig 2).<sup>12,13</sup> Molavi et al<sup>12</sup> reported a hyperintense signal change in the MBs on the T2-weighted sequences in 13.2% of neonates with HIE. In those cases with abnormal MB signal, the most common MR imaging pattern (in 41.9% of cases) was found to be abnormal signal on either T2-weighted imaging or DWI restricted to the MBs, with no other abnormalities observed. Lequin et al<sup>13</sup> performed a multicenter study looking into signal changes on both T1- and T2-weighted images as well as restricted diffusion on DWI in the MBs after HIE and therapeutic hypothermia. They observed abnormal MB signal in approximately 40% of the cooled neonates. Involvement

of the MBs was not related to the severity of encephalopathy or the severity of hypoxic-ischemic brain injury, and there was no relation to the pattern of brain injury. In both studies, the MB abnormalities were only identified retrospectively, when the MBs were specifically assessed. Thus, it is likely that many infants with MB abnormalities are currently being overlooked, with their MRI findings reported as looking normal. These results emphasize the need for optimized protocols with sufficiently thin section series (<2 mm) and for the MBs to be routinely assessed.

Annink et al<sup>14</sup> performed a retrospective observational study of neonates with HIE with follow-up at 10 years of age. Of the infants with abnormal neonatal MBs, 76% had MB atrophy at 10 years of age. MB atrophy was seen in 38% of all 10-year-old patients (50% of those who had undergone therapeutic hypothermia and 17% of those who not had hypothermia treatment). The study also showed that children with a history of HIE have long-term neurodevelopmental problems despite therapeutic hypothermia. Hippocampal volume and MB atrophy were strongly associated with neurocognitive outcome and episodic memory at 10 years of age. These findings suggest that abnormal T2 signal of the MBs in the acute phase is associated with cognitive and memory deficits later in life.

Dzieciol et al<sup>46</sup> assessed children and adolescents with developmental amnesia, which is marked by extensive bilateral damage to the hippocampus as a result of early life exposure to hypoxic-ischemic events. Developmental amnesia is characterized by impaired episodic memory with relative sparing of semantic memory.<sup>47</sup> Dzieciol et al found the MBs absent in 12 of the 18 patients with developmental amnesia. The remaining 6 patients had visible MBs, but as a group, they were significantly smaller than those in controls. Of note, all 12 patients in whom the MBs were absent experienced a hypoxic-ischemic event perinatally, whereas for the 3 patients who experienced the hypoxic-ischemic event later in life (4–15 years of age), the MBs were visible. Geva et al<sup>48</sup> also noted that the MBs were small in 10 of their 20 patients with hippocampal atrophy resulting from perinatal hypoxia-ischemia.

**Congenital Central Hypoventilation Syndrome.** Congenital central hypoventilation syndrome (CCHS) is defined as the failure of automatic control of breathing, with ventilation most severely affected during quiet sleep, when automatic neural control is predominant.<sup>49</sup> CCHS can disrupt blood pressure, glucose and temperature control, reduce the sensitivity to carbon dioxide and oxygen, as well affect intestinal motility causing malabsorption.<sup>50</sup> Patients with CCHS often show multiple cognitive impairments including learning and memory problems.<sup>51,52</sup> Initial studies on this patient group reported structural and functional changes in the hippocampus and anterior thalamus.<sup>53–55</sup> In a subsequent study, Kumar et al<sup>56</sup> found the MBs and fornix volume to be significantly reduced in patients with CCHS, suggesting that pathology within the Papez circuit, including the MBs, contributes to the memory impairment observed in this patient group.

Although only 1 study has examined the MBs in patients with CCHS, the pathology appears similar to that of other sleep-disordered breathing conditions such as obstructive sleep apnea as well as heart failure and beriberi. In addition to the chronic

hypoxia/hypoxemia present in these conditions, patients can also present with intestinal absorption abnormalities as well as low levels of thiamine and magnesium,<sup>57,58</sup> which are likely to contribute to the pathology in these patient groups.

**Congenital Heart Disease.** Single ventricular heart disease (SVHD) is considered one of the most challenging types of congenital heart disease, with an incidence of approximately 1 per 2000 live births.<sup>59</sup> Patients typically require at least 3 staged palliative operations; the Fontan procedure has the greatest impact on life expectancy. Patients with SVHD are at greater risk of brain injury and neurocognitive deficits as a direct result of the condition and comorbidities<sup>60</sup> as well as from the multiple surgical procedures.<sup>61</sup> Adolescents with SVHD exhibit brain lesions on MR imaging in approximately 60% of cases.<sup>62</sup> This finding could be due to the delayed brain maturation observed in complex heart disease, which can make the brain more vulnerable to injury.<sup>63</sup>

Cabrera-Mino et al<sup>15</sup> found reduced MB volumes in adolescents with SVHD compared with controls. Cognitive test scores were also significantly lower in the SVHD group, and performance on verbal and delayed recall memory tests correlated with MB volume, ie, poorer memory with smaller MBs. In a related study, Singh et al<sup>64</sup> investigated DTI-based diffusivity measures. Multiple brain regions including the limbic system and MBs showed changes consistent with chronic tissue injury. Given that the MRIs in this study were acquired more than a decade after the patient's last surgical procedure, the assumption was that the pathology reflected chronic changes associated with this condition, predominantly to myelin.

**Metabolic Disease.** MB abnormalities have only been reported in a few metabolic diseases. One case showed diffusion restriction in the MBs in a patient with Leigh disease arising from a mutation in the sulfide:quinone oxidoreductase enzyme.<sup>65</sup> A further case showed enhancement in the MBs in a patient with Alexander disease,<sup>66</sup> while Inui et al<sup>67</sup> found high signal intensities on T2-weighted images in the MBs of a young patient with a case of chronic infantile fucosidosis. Finally, 2 patients with biotinidase deficiency were reported showing bilateral abnormal signal intensity in the MBs and area postrema of the dorsal medulla as well as bilateral symmetric optic neuritis.<sup>68</sup>

**Epilepsy.** There is a well-documented relationship between MB abnormalities and epilepsy in adults. As will be discussed in the next section, patients with refractory mesial temporal lobe epilepsy often undergo temporal lobe surgery or laser interstitial thermal therapy (LiTT) as part of their treatment. The resultant hippocampal loss can cause anterograde degeneration in the MBs. There is some evidence that the MBs may also be implicated in epilepsy before treatment, possibly due to anterograde degeneration from the pre-existing hippocampal pathology or as a more direct effect of the epilepsy.<sup>69</sup> Indeed, a case from our own hospital demonstrates this finding of compromised MBs in a patient with epilepsy who had not undergone temporal lobe surgery or LiTT (Fig 3).

**Mesial Temporal Sclerosis.** Mesial temporal sclerosis (MTS) involves neuronal loss and gliosis of the hippocampus and is the

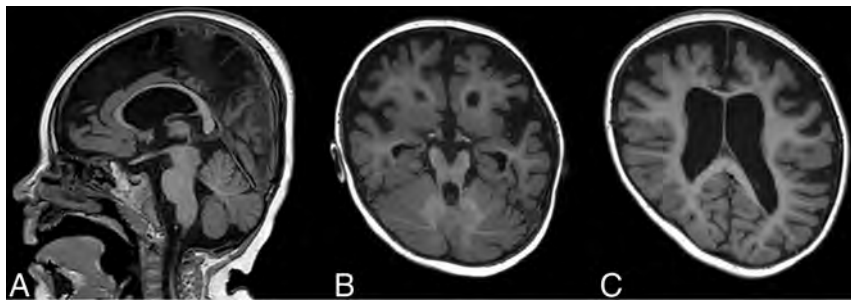


**FIG 3.** T1-weighted images show generalized atrophy of the brain with atrophy of the MBs, which are completely flattened (A and B), and ex-vacuo dilation of the ventricles (C) in a 2.5-year-old patient with severe epilepsy.

most common disease associated with mesial temporal lobe epilepsy. MB and fornix asymmetry have been repeatedly reported in MTS.<sup>18,70</sup> Ozturk et al<sup>18</sup> found asymmetry of the MBs (37.1% of cases) and fornix (34.3% of cases) when examining patients with MTS presurgery. This reported asymmetry was significantly higher than that found in a control group (6.5% for MBs and 7.9% for fornix). Kim et al<sup>71</sup> performed a similar study but observed asymmetric MBs in only 3% of patients with MTS presurgery. This discrepancy may be due to Ozturk et al using 1.5-mm slices to evaluate the MB asymmetry compared with 3-mm slices in the Kim et al study, increasing the likelihood of detecting asymmetries.

Refractory mesial temporal lobe epilepsy is the most common form of surgically treated epilepsy and is caused by MTS in ~65% of the patients undergoing surgery.<sup>72</sup> In a blinded retrospective analysis of 20 patients who underwent amygdalohippocampal LiTT, the seizure-free group showed an average 35% reduction in ipsilateral MB volume compared with 8% reduction in patients with continued seizures. This finding suggests that MB volume change could be a marker for successful ablation surgery.<sup>73</sup> In contrast, Urbach et al<sup>74</sup> did not find MB volume after amygdalo-hippocampectomy predictive of postsurgical seizure outcome in patients with unilateral MTS. Because the latter study involved twice the number of patients, there might be a selection bias in the former study; alternatively, the discrepancy could reflect differences between LiTT and amygdalo-hippocampectomy.

**Epilepsy Related to MB Pathology.** Mamourian and Brown<sup>75</sup> reported a case study of a 4.5-year-old boy who presented with staring spells and abnormal electrocardiogram activity in the right parietal region. MR imaging showed a total absence of the right MB, while the temporal lobes appeared normal. The authors raised the possibility that the seizure activity was related to the shrunken right MB. There have been other studies that have directly linked the MBs to epileptic activity rather than being indirectly affected via the hippocampus. For example, epileptiform discharges have been recorded directly from the MBs,<sup>76</sup> and a fluorodeoxyglucose PET/CT study of a 50-year-old woman found the MBs to be the focus of epileptic activity.<sup>77</sup>

Further associations between the MBs and seizures come from an adolescent with a 2-year history of complex partial seizures whose MR imaging showed encephalomalacia in the right

anteromedial thalamus, gliosis of the mamillothalamic tract, and a right-sided atrophic MB.<sup>78</sup> The mamillothalamic tract and MB pathology were thought to be the result of retrograde degeneration following a thalamic infarct. Because there was no evidence of hippocampal involvement, the partial seizures were assumed to be due to the mamillothalamic pathology.

Hypothalamic hamartomas can also be associated with epilepsy; Freeman et al<sup>79</sup> found that the common factor in a large group of patients who presented with hypothalamic hamartoma and epi-

lepsy was involvement of the MBs, suggesting that they may be the focus of the epileptic activity. Linear defects in the anterior thalamus and associated MB and fornix atrophy have also been identified in patients with chronic seizures.<sup>80</sup>

One further study reported congenital aplasia of the MBs in a young child with early infantile epileptic encephalopathy (Ohtahara syndrome), who also presented with dentato-olivary dysplasia.<sup>81</sup> The absence of the MBs, both macroscopically and microscopically, was noted at postmortem examination, leading the authors to recommend high-resolution MR imaging and detailed postmortem assessment in this patient group.<sup>81</sup>

**Masses Involving the Hypothalamic Region, Postoperative MB Abnormalities, and Other Iatrogenic Causes of MB Pathology.** The MBs can be displaced and/or compressed in numerous conditions that result in masses forming in adjacent structures, for example, hypothalamic hamartomas and suprasellar arachnoid cysts.<sup>79,82-86</sup> The MBs are an important landmark for neurosurgeons when operating on these suprasellar masses.<sup>84,87</sup> Although compression occurs, the structure of the MBs can remain intact,<sup>88</sup> and after decompression, the MBs can appear normal.<sup>84</sup>

Craniopharyngiomas are rare embryogenic malformations of the sellar/parasellar area with low-grade histologic malignancy.<sup>89</sup> Despite high survival rates, the quality of life can be affected by optic chiasm and hypothalamic pathology, resulting in visual impairment and hypothalamic obesity, respectively.<sup>90,91</sup> In a mixed population of pediatric and adult patients with craniopharyngiomas, the authors classified the MBs as “dislocated” in 34% of cases and “unrecognizable” in 19% of cases.<sup>92</sup> Involvement of the MBs was one of the main factors associated with postoperative obesity. This was in accordance with Müller et al,<sup>93</sup> who found that the extent of hypothalamic damage increased the risk of postsurgical obesity in a group of 120 children. In addition to the development of hypothalamic obesity, children with high-grade hypothalamic involvement also showed poorer performance on tests of executive function and reduced functional capabilities for daily life actions, and these cognitive impairments appear to be associated with MB involvement.<sup>94</sup>

The MBs can be directly affected by not only these masses but also the treatment protocols, including radiation therapy and chemotherapy, likely causing additional MB damage. For example, intrathecal chemotherapy for childhood acute lymphoblastic



leukemia has been shown to affect the MBs.<sup>95</sup> Ciesielski et al<sup>95</sup> found the MBs and prefrontal cortex significantly reduced in volume in the patient group with acute lymphoblastic leukemia compared with matched controls. The patient group also performed significantly worse on both visual and verbal memory tasks.

### Personal Experience

In our institution (Wilhelmina Children's Hospital), as a standard practice, we use imaging protocols that enable us to visualize the MBs in detail. Furthermore, the MBs are routinely assessed in all

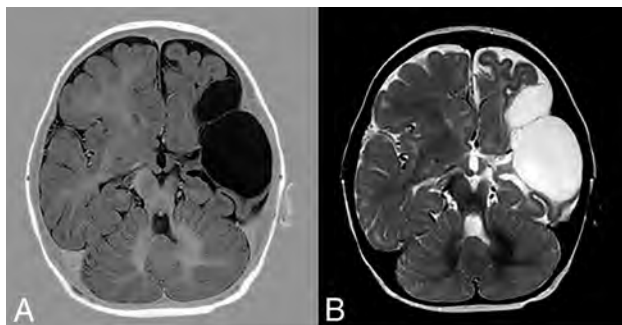


**FIG 4.** T1-weighted (A) and T2-weighted (B) images showing extensive loss of tissue due to a left-sided MCA with atrophy of the left MB. There was narrowing of the proximal MCA on MRA (not shown).

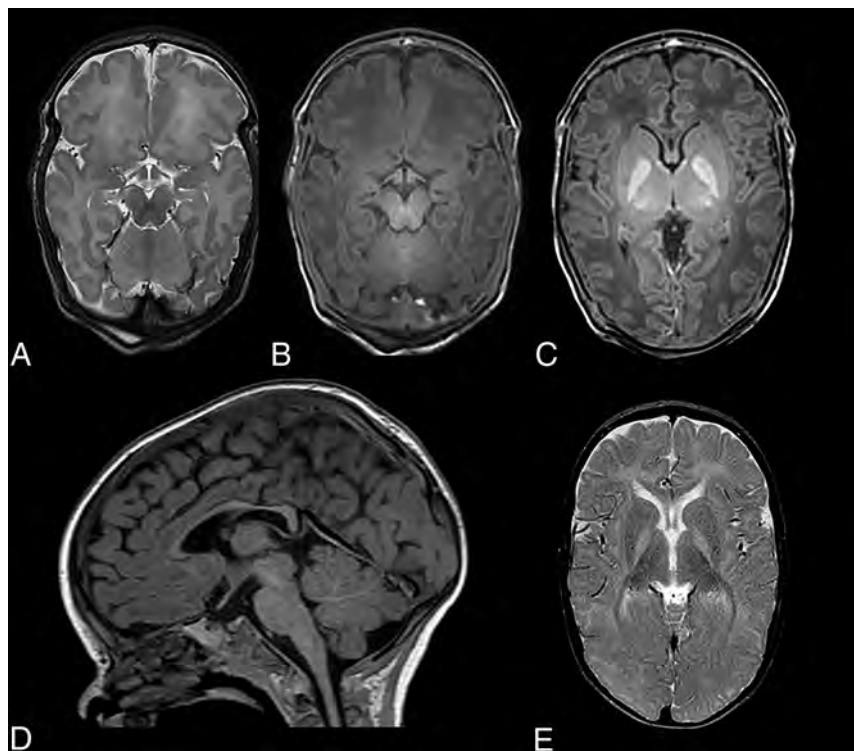


**FIG 5.** A T2-weighted image at the level of the MBs, acquired when the patient was 8 days of age, showing a hyperintense aspect of the MBs (A). A T1-weighted image (B) shows a hypointense MB signal. There is a bilateral hyperintense signal of the globus pallidus on a T1-weighted image (C), consistent with kernicterus. On follow-up after 7 months, there is atrophy with complete flattening of the MBs as seen on the sagittal T1-weighted image (D). An axial T2-weighted image shows persistent high signal of the globus pallidus bilaterally, with accompanying volume loss (E).

pediatric MRIs of the brain. This practice has resulted in MB pathology being observed in conditions that have not previously been reported in the literature. For example, when assessing the scans of neonates with an MCA infarct, we have identified several cases with damage to the MBs. One example involved a girl with hereditary spherocytosis who was severely anemic at 6 weeks and presented with right-sided hemiparesis at 2 months of age. A scan at 1 year of age showed sequelae of a large left-sided MCA infarct with little remaining basal ganglia and left-sided atrophy of the body of corpus callosum, thalamus, hippocampus, and MB (Fig 4).

Chronic bilirubin encephalopathy (kernicterus) can also cause bilateral MB abnormalities. A term neonate with an uneventful pregnancy and an uncomplicated delivery was admitted for an exchange transfusion for severe hyperbilirubinemia. The patient showed opisthotonus and convulsions/seizures. A brain MR imaging at 8 days of age showed a bilateral hypointense aspect of the MBs on T1-weighted imaging and a hyperintense T2 aspect in addition to a T1 hyperintense aspect of the globus pallidus bilaterally, consistent with kernicterus (Fig 5). At a 7-month follow-up, the MBs appeared atrophic. To our knowledge, there are no other reports of MB involvement in kernicterus.

Hydrocephalus can often affect the MBs, causing compression and making them difficult to visualize. However, it is only possible to determine whether there is long-lasting structural damage to MBs after the onset of treatment and

reduction of intracranial pressure.

The MBs are at risk from direct pressure from hydrocephalus, which can reduce blood flow to the MBs and cause local ischemia, but also from the interventional treatment procedures. A 32-week preterm neonate was born with unilateral ventricular dilation at our institution. No MB abnormalities were observed on 2-day postnatal MR imaging. Because of the suspected obstruction at the foramen of Monro, a ventricular access device was inserted. MR imaging after 2.5 months showed atrophy with an abnormal signal intensity of the left MB (Fig 6).

We have also found the MBs to be affected by group B streptococcus, the leading cause of neonatal meningitis, and herpes simplex encephalitis. One such patient was scanned at 11 weeks after group B streptococcus sepsis and possible meningitis (Fig 7). On MR imaging, the basal ganglia appeared normal, but there was minor supratentorial generalized loss of white and gray matter with subtle dilation of the lateral ventricles, and both MBs were atrophic.

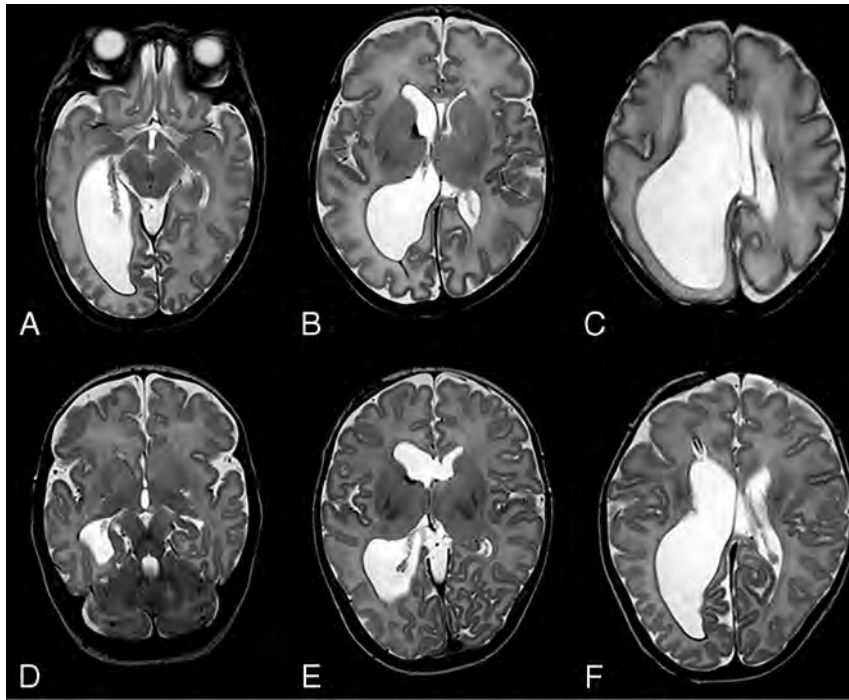


**FIG 6.** A, T2-weighted image of unilateral dilation of the right lateral ventricle with normal MBs. B, There is a suggestion of an obstruction at the foramen of Monro and increased signal intensity of the periventricular white matter due to the increased pressure. Small remains of germinal matrix hemorrhage are seen on the right. C, Intact septum. At follow-up, after insertion of a ventricular access device and a neuroendoscopic septostomy procedure, an asymmetric aspect of the MBs is found with T2 hyperintense signal in the left MB, which is also smaller than the contralateral right MB (D). Decreased ventricular dilation is also seen on E after septostomy and placement of the ventricular access device (F).

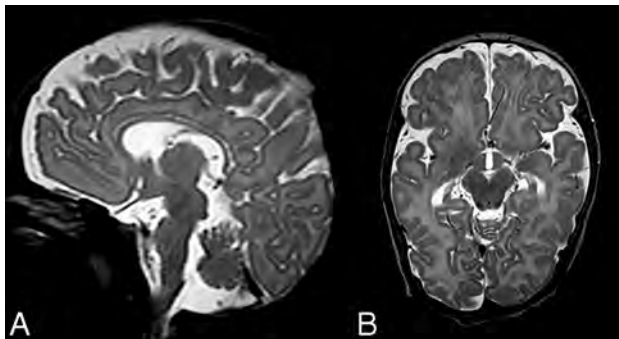


**FIG 7.** Preterm infant (gestational age of 34 + 4 weeks) scanned at 11 weeks after group B streptococcus sepsis and possible meningitis. T2-weighted images at the level of the MBs show severe atrophy with flattening of the MBs (A and B).

Finally, as previously described, metabolic disorders might also impact the MBs. From MR imaging studies, MB abnormalities have been described in Leigh disease, Alexander disease, and fucosidosis. A postmortem study, however, found necrosis and spongiosis of the MBs in a patient with methylmalonic acidemia.<sup>96</sup> Similarly, we had a patient with propionic acidemia who showed bilateral volume loss of the MBs on a 3-month follow-up scan. No MB abnormalities were seen on an initial scan at 2 weeks, but this may have been outside the window of the acute stage (Fig 8).

## DISCUSSION

While the MBs have been implicated in a wide range of neurologic conditions in adults, their involvement in neurologic conditions in infants and children is less well-documented. Thus, we have performed a review of conditions in younger patients in whom MB pathology has been reported. Perhaps unsurprisingly, given that the MBs and their connections are well-developed at birth, many of the conditions that can cause MB pathology in adults also can affect the MBs in younger individuals. While numerous diverse conditions have been associated with MB pathology across age groups, this pathology appears to typically arise from a limited number of factors: thiamine deficiency, hypoxia-ischemia direct damage due to masses or hydrocephalus, or deafferentation resulting from pathology within the wider Papez circuit.

MB pathology is most frequently associated with thiamine deficiency; indeed, MB pathology was first noted in Korsakoff syndrome at the end of the 19th century, and this provided the first link between the MBs and memory.<sup>97</sup> However, the exact mechanism by which thiamine deficiency impacts the MBs remains uncertain. It

is likely that the effects of thiamine deficiency are multifactorial, given that it can cause cell loss via various mechanisms, including mitochondrial dysfunction, glycolysis, acidosis, increased oxidative stress, excitotoxicity, and inflammation.<sup>98,99</sup> Suboptimal thiamine reserves or borderline thiamine deficiency can present in many conditions and can be exacerbated by glucose infusion,<sup>100</sup> which is often given to children on hospitalization.

There is increasing evidence that the MBs are affected by hypoxia-ischemia, particularly in neonates.<sup>12,13</sup> What is striking is that the MBs can often be the only structure to show abnormal signal, with the rest of the brain appearing normal, highlighting the sensitivity of the MBs.<sup>12,13</sup> While hypothermia treatment appears to be effective in protecting wider brain areas, the MBs do not appear to benefit from this treatment to the same extent,<sup>12</sup> as such, there is a need to identify additional treatment approaches.

Both thiamine deficiency and hypoxia can cause neural cell loss via the activation of several similar signaling pathways that result in necrosis and apoptosis. As with thiamine deficiency, hypoxia also increases mitochondrial dysfunction, excitotoxicity, oxidative stress, and acidosis.<sup>101</sup> Furthermore, both conditions disrupt the blood-brain barrier and alter levels of hypoxia-inducible factor 1 $\alpha$ .<sup>102,103</sup> Given the sensitivity of the MBs to thiamine deficiency and hypoxia, the most parsimonious conclusion is that the MBs are affected by similar underlying mechanisms in both conditions; however, as the cell loss likely occurs via multiple

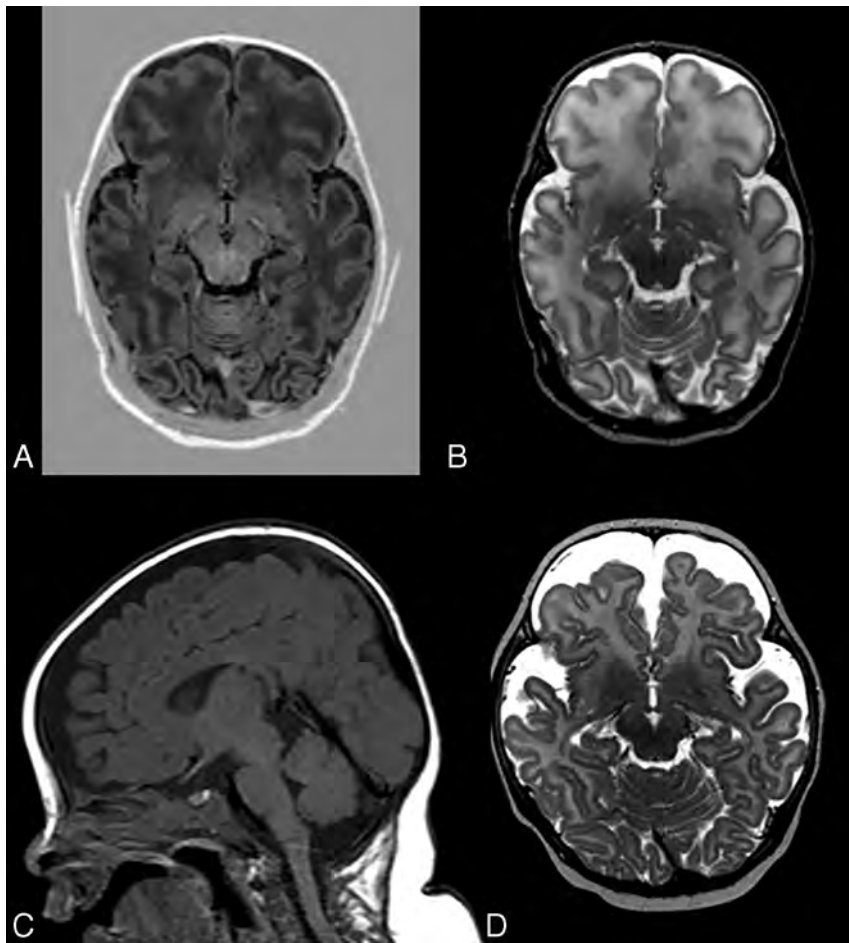


**FIG 8.** A patient with propionic acidemia. There is a normal aspect of the MBs on T1-weighted (A) and T2-weighted (B) images at 2 weeks of age. On follow-up 3 months later, volume loss is seen on the sagittal T1-weighted image (C) and axial T2-weighted image (D).

complex mechanisms, there may be selective pathways that are preferentially involved in the different conditions and even across different patients with the same condition.

A further cause of MB pathology is via direct damage, eg, due to a mass, hydrocephalus, or radiation therapy, or indirectly via anterograde or retrograde degeneration. In adults, damage to the hippocampus or fornix typically results in a loss of white matter in the MBs, with a volume reduction of up to 50%.<sup>20</sup> However, it is possible that in neonates, the MBs are more sensitive to deafferentation, and greater atrophy might be observed following damage to the hippocampus or fornix. Direct damage to the MBs should be minimized when possible, for example, when targeting masses in the vicinity of the MBs. However, there are some inconsistencies as to whether compression of the MBs can cause long-term pathology once the pressure on the MBs is removed. Therefore, further work is needed to determine those situations in which the MBs are most vulnerable to both direct and indirect damage and the time windows during which long-term pathology can be avoided.

While damage to the MBs appears to arise from similar etiologies in adults, children, and infants, it is not yet clear whether age

differentially affects the sensitivity of the MBs. There is some suggestion that neonatal brains are more resilient to some forms of damage, for example, those arising from hypoxia, because there are differing metabolic demands in cells and a different propensity to excitotoxicity.<sup>104</sup> However, the blood-brain barrier is also immature during the neonatal period,<sup>105</sup> which could exacerbate the impact of hypoxia and thiamine deficiency. Given the high rate of MB involvement in neonatal hypoxia-ischemia, it is possible that the MBs are more sensitive in this age group; however, it is difficult to directly compare with adults, given the difference in prevalence. Animal models may be required to determine whether MBs in neonates are more sensitive to hypoxia-ischemia as well as deafferentation.

The purpose of this review was to identify conditions in which MB pathology occurred rather than specifically address the functions of the MBs; indeed, most of the included studies described pathology but did not perform detailed cognitive tests. From the evidence that is available, however, it seems that little if any functional compensation occurs when MB pathology occurs earlier in life. In both children and adults, the profile of memory impairment seems remarkably similar, with episodic and recollective memory

being particularly affected. However, there are very few cognitive assessments of individuals with early-acquired MB pathology in which the damage is selective. In most cases there is co-occurring pathology in the hippocampus, making it difficult to determine the specific contribution of the MBs. This issue highlights the need to assess the extent of memory impairment in cases in which pathology is restricted to the MBs.

A limitation of this review is that many of the studies comprise case reports. Furthermore, some of the studies included mixed age groups that included not only children but also adults. In some cases, the authors did not distinguish between the pathology observed in children and adults, making it difficult to determine the relative involvement across age groups. A further complicating factor when interpreting unilateral MB pathology is that asymmetric MBs can occur in the general population, though this appears to generally reflect MB displacement rather than actual atrophy. Good-quality MRIs should help distinguish between these scenarios.

Unfortunately, the size and location of the MBs can often result in poor visualization on MRI, which is exacerbated when scan slices are not sufficiently thin. Furthermore, partial volume



effects can also affect the interpretation of MRI if imaging protocols are not optimized. Together, these are likely to have resulted in MB pathology going undetected. Given the importance of the MBs for memory, accurate identification of MB pathology is necessary to provide appropriate follow-up assessment and support for children and their families. The MBs need to be protected from damage when possible, and thiamine supplementation is an easily implemented measure for critically ill children. A better understanding of the specific pathways that are most likely to result in MB pathology is also needed so more targeted treatments can be developed.

**Disclosure forms** provided by the authors are available with the full text and PDF of this article at [www.ajnr.org](http://www.ajnr.org)

## REFERENCES

1. Tsivilis D, Vann SD, Denby C, et al. **A disproportionate role for the fornix and mammillary bodies in recall versus recognition memory.** *Nat Neurosci* 2008;11:834–42 CrossRef Medline
2. Vann SD. **Re-evaluating the role of the mammillary bodies in memory.** *Neuropsychologia* 2010;48:2316–27 CrossRef Medline
3. Male S, Zand R. **Isolated mammillary body infarct causing global amnesia: a case report.** *J Stroke Cerebrovasc Dis* 2017;26:e50–52 CrossRef Medline
4. Tanaka Y, Miyazawa Y, Akaoka F, et al. **Amnesia following damage to the mammillary bodies.** *Neurology* 1997;48:160–65 CrossRef Medline
5. Vann SD, Tsivilis D, Denby CE, et al. **Impaired recollection but spared familiarity in patients with extended hippocampal system damage revealed by 3 convergent methods.** *Proc Natl Acad Sci U S A* 2009;106:5442–47 CrossRef Medline
6. Denby CE, Vann SD, Tsivilis D, et al. **The frequency and extent of mammillary body atrophy associated with surgical removal of a colloid cyst.** *AJNR Am J Neuroradiol* 2009;30:736–43 CrossRef Medline
7. Bernstein HG, Krause S, Krell D, et al. **Strongly reduced number of parvalbumin-immunoreactive projection neurons in the mammillary bodies in schizophrenia: further evidence for limbic neuropathology.** *Ann N Y Acad Sci* 2007;1096:120–27 CrossRef Medline
8. Baloyannis SJ, Mavroudis I, Baloyannis IS, et al. **Mammillary bodies in Alzheimer's disease: a Golgi and electron microscope study.** *Am J Alzheimers Dis Other Dement* 2016;31:247–56 CrossRef Medline
9. Dineen RA, Bradshaw CM, Constantinescu CS, et al. **Extra-hippocampal subcortical limbic involvement predicts episodic recall performance in multiple sclerosis.** *PLoS One* 2012;7:e44942 CrossRef Medline
10. Johkura K, Naito M. **Wernicke's encephalopathy-like lesions in global cerebral hypoxia.** *J Clin Neurosci* 2008;15:318–19 CrossRef Medline
11. Schmidtke K. **Wernicke-Korsakoff syndrome following attempted hanging.** *Rev Neurol (Paris)* 1993;149:213–16 Medline
12. Molavi M, Vann SD, de Vries LS, et al. **Signal change in the mammillary bodies after perinatal asphyxia.** *AJNR Am J Neuroradiol* 2019;40:1829–34 CrossRef Medline
13. Lequin MH, Steggerda SJ, Severino M, et al. **Mammillary body injury in neonatal encephalopathy: a multicentre, retrospective study.** *Pediatr Res* 2021 Mar 2. [Epub ahead of print] CrossRef Medline
14. Annink KV, de Vries LS, Groenendaal F, et al. **Mammillary body atrophy and other MRI correlates of school-age outcome following neonatal hypoxic-ischemic encephalopathy.** *Sci Rep* 2021;11:5017 CrossRef Medline
15. Cabrera-Mino C, Roy B, Woo MA, et al. **Reduced brain mammillary body volumes and memory deficits in adolescents who have undergone the Fontan procedure.** *Pediatr Res* 2020;87:169–75 CrossRef Medline
16. Koutcherov Y, Mai JK, Paxinos G. **Hypothalamus of the human fetus.** *J Chem Neuroanat* 2003;26:253–70 CrossRef Medline
17. Tagliamonte M, Sestieri C, Romani GL, et al. **MRI anatomical variants of mammillary bodies.** *Brain Struct Funct* 2015;220:85–90 CrossRef Medline
18. Ozturk A, Yousem DM, Mahmood A, et al. **Prevalence of asymmetry of mamillary body and fornix size on MR imaging.** *AJNR Am J Neuroradiol* 2008;29:384–87 CrossRef Medline
19. Bachevalier J, Meunier M. **Cerebral ischemia: are the memory deficits associated with hippocampal cell loss?** *Hippocampus* 1996;6:553–60 CrossRef Medline
20. Loftus M, Knight RT, Amaral DG. **An analysis of atrophy in the medial mammillary nucleus following hippocampal and fornix lesions in humans and nonhuman primates.** *Exp Neurol* 2000;163:180–90 CrossRef Medline
21. Vann SD. **Dismantling the Papez circuit for memory in rats.** *Elife* 2013;2:e00736 CrossRef Medline
22. Dillingham CM, Milczarek MM, Perry JC, et al. **Mammillothalamic disconnection alters hippocampocortical oscillatory activity and microstructure: implications for diencephalic amnesia.** *J Neurosci* 2019;39:6696–6713 CrossRef Medline
23. Vann SD, Aggleton JP. **The mammillary bodies: two memory systems in one?** *Nat Rev Neurosci* 2004;5:35–44 CrossRef Medline
24. Dillingham CM, Milczarek MM, Perry JC, et al. **Time to put the mammillothalamic pathway into context.** *Neurosci Biobehav Rev* 2021;121:60–74 CrossRef Medline
25. Zuccoli G, Siddiqui N, Bailey A, et al. **Neuroimaging findings in pediatric Wernicke encephalopathy: a review.** *Neuroradiology* 2010;52:523–29 CrossRef Medline
26. Lallas M, Desai J. **Wernicke encephalopathy in children and adolescents.** *World J Pediatr* 2014;10:293–98 CrossRef Medline
27. Thomson AD. **Mechanisms of vitamin deficiency in chronic alcohol misusers and the development of the Wernicke-Korsakoff syndrome.** *Alcohol Alcohol Suppl* 2000;35:2–7 CrossRef Medline
28. Harper CG, Giles M, Finlay-Jones R. **Clinical signs in the Wernicke-Korsakoff complex: a retrospective analysis of 131 cases diagnosed at necropsy.** *J Neurol Neurosurg Psychiatry* 1986;49:341–45 CrossRef Medline
29. Vasconcelos MM, Silva KP, Vidal G, et al. **Early diagnosis of pediatric Wernicke's encephalopathy.** *Pediatr Neurol* 1999;20:289–94 CrossRef Medline
30. Khalsa SS, Kumar R, Patel V, et al. **Mammillary body volume abnormalities in anorexia nervosa.** *Int J Eat Disord* 2016;49:920–29 CrossRef Medline
31. Lamdhade S, Almulla A, Alroughani R. **Recurrent Wernicke's encephalopathy in a 16-year-old girl with atypical clinical and radiological features.** *J Neurol Sci* 2013;333:e627 CrossRef Medline
32. Oka M, Terae S, Kobayashi R, et al. **Diffusion-weighted MR findings in a reversible case of acute Wernicke encephalopathy.** *Acta Neurol Scand* 2001;104:178–81 CrossRef Medline
33. Sparacia G, Banco A, Lagalla R. **Reversible MRI abnormalities in an unusual paediatric presentation of Wernicke's encephalopathy.** *Pediatr Radiol* 1999;29:581–84 CrossRef Medline
34. Samanta D. **Dry beriberi preceded Wernicke encephalopathy: thiamine deficiency after laparoscopic sleeve gastrectomy.** *J Pediatr Neurosci* 2015;10:297–99 CrossRef Medline
35. Srivastava A, Yadav SK, Borkar VV, et al. **Serial evaluation of children with ALF with advanced MRI, serum proinflammatory cytokines, thiamine, and cognition assessment.** *J Pediatr Gastroenterol Nutr* 2012;55:580–86 CrossRef Medline
36. Arana-Guajardo AC, Cámara-Lemarroy CR, Rendón-Ramírez EJ, et al. **Wernicke encephalopathy presenting in a patient with severe acute pancreatitis.** *JOP* 2012;13:104–107 Medline
37. Zuccoli G, Pipitone N. **Neuroimaging findings in acute Wernicke's encephalopathy: review of the literature.** *AJR Am J Roentgenol* 2009;192:501–08 CrossRef Medline

38. Fei GQ, Zhong C, Jin L, et al. **Clinical characteristics and MR imaging features of nonalcoholic Wernicke encephalopathy.** *AJNR Am J Neuroradiol* 2008;29:164–69 CrossRef Medline
39. Zuccoli G, Gallucci M, Capellades J, et al. **Wernicke encephalopathy: MR findings at clinical presentation in twenty-six alcoholic and nonalcoholic patients.** *AJNR Am J Neuroradiol* 2007;28:1328–31 CrossRef Medline
40. Zuccoli G, Santa Cruz D, Bertolini M, et al. **MR imaging findings in 56 patients with Wernicke encephalopathy: nonalcoholics may differ from alcoholics.** *AJNR Am J Neuroradiol* 2009;30:171–76 CrossRef Medline
41. Gliebus G, Faerber EN, Valencia I, et al. **Ataxia, ophthalmoplegia, and impairment of consciousness in a 19-month-old American boy.** *Semin Pediatr Neurol* 2014;21:139–43 CrossRef Medline
42. Kurinczuk JJ, White-Koning M, Badawi N. **Epidemiology of neonatal encephalopathy and hypoxic-ischaemic encephalopathy.** *Early Hum Dev* 2010;86:329–38 CrossRef Medline
43. de Vries LS, Groenendaal F. **Patterns of neonatal hypoxic-ischaemic brain injury.** *Neuroradiology* 2010;52:555–66 CrossRef Medline
44. Alderliesten T, Nikkels PG, Benders MJ, et al. **Antemortem cranial MRI compared with postmortem histopathologic examination of the brain in term infants with neonatal encephalopathy following perinatal asphyxia.** *Arch Dis Child Fetal Neonatal Ed* 2013;98:F304–09 CrossRef Medline
45. Kasdorf E, Engel M, Heier L, et al. **Therapeutic hypothermia in neonates and selective hippocampal injury on diffusion-weighted magnetic resonance imaging.** *Pediatr Neurol* 2014;51:104–08 CrossRef Medline
46. Dzieciol AM, Bachevalier J, Saleem KS, et al. **Hippocampal and diencephalic pathology in developmental amnesia.** *Cortex* 2017;86:33–44 CrossRef Medline
47. Cooper JM, Gadian DG, Jentschke S, et al. **Neonatal hypoxia, hippocampal atrophy, and memory impairment: evidence of a causal sequence.** *Cereb Cortex* 2015;25:1469–76 CrossRef Medline
48. Geva S, Jentschke S, Argyropoulos GP, et al. **Volume reduction of caudate nucleus is associated with movement coordination deficits in patients with hippocampal atrophy due to perinatal hypoxia-ischaemia.** *Neuroimage Clin* 2020;28:102429 CrossRef Medline
49. Fleming PJ, Cade D, Bryan MH, et al. **Congenital central hypoventilation and sleep state.** *Pediatrics* 1980;66:425–28 CrossRef Medline
50. O'Brien LM, Holbrook CR, Vanderlaan M, et al. **Autonomic function in children with congenital central hypoventilation syndrome and their families.** *Chest* 2005;128:2478–84 CrossRef Medline
51. Ruof H, Hammer J, Tillmann B, et al. **Neuropsychological, behavioral, and adaptive functioning of Swiss children with congenital central hypoventilation syndrome.** *J Child Neurol* 2008;23:1254–59 CrossRef Medline
52. Vanderlaan M, Holbrook CR, Wang M, et al. **Epidemiologic survey of 196 patients with congenital central hypoventilation syndrome.** *Pediatr Pulmonol* 2004;37:217–29 CrossRef Medline
53. Macey PM, Woo MA, Macey KE, et al. **Hypoxia reveals posterior thalamic, cerebellar, midbrain, and limbic deficits in congenital central hypoventilation syndrome.** *J Appl Physiol (1985)* 2005;98:958–69 CrossRef Medline
54. Woo MA, Macey PM, Macey KE, et al. **fMRI responses to hyperoxia in congenital central hypoventilation syndrome.** *Pediatr Res* 2005;57:510–18 CrossRef Medline
55. Kumar R, Macey PM, Woo MA, et al. **Elevated mean diffusivity in widespread brain regions in congenital central hypoventilation syndrome.** *J Magn Reson Imaging* 2006;24:1252–58 CrossRef Medline
56. Kumar R, Lee K, MacEay PM, et al. **Mammillary body and fornix injury in congenital central hypoventilation syndrome.** *Pediatr Res* 2009;66:429–34 CrossRef Medline
57. Fatouleh RH, Hammam E, Lundblad LC, et al. **Functional and structural changes in the brain associated with the increase in muscle sympathetic nerve activity in obstructive sleep apnoea.** *Neuroimage Clin* 2014;6:275–83 CrossRef Medline
58. Kumar R, Woo MA, Birrer BV, et al. **Mammillary bodies and fornix fibers are injured in heart failure.** *Neurobiol Dis* 2009;33:236–42 CrossRef Medline
59. Khairy P, Fernandes SM, Mayer JE Jr, et al. **Long-term survival, modes of death, and predictors of mortality in patients with Fontan surgery.** *Circulation* 2008;117:85–92 CrossRef Medline
60. Marelli A, Miller SP, Marino BS, et al. **Brain in congenital heart disease across the lifespan: the cumulative burden of injury.** *Circulation* 2016;133:1951–62 CrossRef Medline
61. Gaynor JW, Stopp C, Wypij D, et al; International Cardiac Collaborative on Neurodevelopment (ICCON) Investigators. **Neurodevelopmental outcomes after cardiac surgery in infancy.** *Pediatrics* 2015;135:816–25 CrossRef Medline
62. Bellinger DC, Watson CG, Rivkin MJ, et al. **Neuropsychological status and structural brain imaging in adolescents with single ventricle who underwent the Fontan procedure.** *J Am Heart Assoc* 2015;4:e002302 CrossRef Medline
63. Sethi V, Tabbutt S, Dimitropoulos A, et al. **Single-ventricle anatomy predicts delayed microstructural brain development.** *Pediatr Res* 2013;73:661–67 CrossRef Medline
64. Singh S, Roy B, Pike N, et al. **Altered brain diffusion tensor imaging indices in adolescents with the Fontan palliation.** *Neuroradiology* 2019;61:811–24 CrossRef Medline
65. Friederich MW, Elias AF, Kuster A, et al. **Pathogenic variants in SQOR encoding sulfide: quinone oxidoreductase are a potentially treatable cause of Leigh disease.** *J Inher Metab Dis* 2020;43:1024–36 CrossRef Medline
66. Poloni CB, Ferey S, Haenggeli CA, et al. **Alexander disease: early presence of cerebral MRI criteria.** *Eur J Paediatr Neurol* 2009;13:556–58 CrossRef Medline
67. Inui K, Akagi M, Nishigaki T, et al. **A case of chronic infantile type of fucosidosis: clinical and magnetic resonance image findings.** *Brain Dev* 2000;22:47–49 CrossRef Medline
68. Shah S, Khan N, Lakshmanan R, et al. **Biotinidase deficiency presenting as neuromyelitis optica spectrum disorder.** *Brain Dev* 2020;42:762–66 CrossRef Medline
69. Kodama F, Ogawa T, Sugihara S, et al. **Transneuronal degeneration in patients with temporal lobe epilepsy: devaluation by MR imaging.** *Eur Radiol* 2003;13:2180–85 CrossRef Medline
70. Oikawa H, Sasaki M, Tamakawa Y, et al. **The circuit of Papez in mesial temporal sclerosis: MRI.** *Neuroradiology* 2001;43:205–10 CrossRef Medline
71. Kim JH, Tien RD, Felsberg GJ, et al. **Clinical significance of asymmetry of the fornix and mamillary body on MR in hippocampal sclerosis.** *AJNR Am J Neuroradiol* 1995;16:509–15 Medline
72. Blumcke I, Thom M, Wiestler OD. **Ammon's horn sclerosis: a maldevelopmental disorder associated with temporal lobe epilepsy.** *Brain Pathol* 2002;12:199–11 Medline
73. Grewal SS, Gupta V, Vibhute P, et al. **Mammillary body changes and seizure outcome after laser interstitial thermal therapy of the mesial temporal lobe.** *Epilepsy Res* 2018;141:19–22 CrossRef Medline
74. Urbach H, Siebenhaar G, Koenig R, et al. **Limbic system abnormalities associated with Ammon's horn sclerosis do not alter seizure outcome after amygdalohippocampectomy.** *Epilepsia* 2005;46:549–55 CrossRef Medline
75. Mamourian AC, Brown DB. **Asymmetric mamillary bodies: MR identification.** *AJNR Am J Neuroradiol* 1993;14:1332–35; discussion 1336–42 Medline
76. van Rijckevorsel K, Abu Serieh B, de Tourtchaninoff M, et al. **Deep EEG recordings of the mammillary body in epilepsy patients.** *Epilepsia* 2005;46:781–85 CrossRef Medline
77. Jha P, Agarwal KK, Sahoo MK, et al. **Mammillary body: chronic refractory epilepsy seizure focus detected by 18F-FDG PET-CT.** *Clin Nucl Med* 2016;41:419–20 CrossRef Medline
78. Assis ZA, Sevik R. **Association of transsynaptic degeneration of the Papez circuit with anterior thalamic encephalomalacia.** *JAMA Neurol* 2018;75:1437–38 CrossRef Medline

79. Freeman JL, Coleman LT, Wellard RM, et al. **MR imaging and spectroscopic study of epileptogenic hypothalamic hamartomas: analysis of 72 cases.** *AJNR Am J Neuroradiol* 2004;25:450–62 Medline
80. Tschampa HJ, Greschus S, Sassen R, et al. **Thalamus lesions in chronic and acute seizure disorders.** *Neuroradiology* 2011;53:245–54 CrossRef Medline
81. Trinka E, Rauscher C, Nagler M, et al. **A case of Ohtahara syndrome with olivary-dentate dysplasia and agenesis of mamillary bodies.** *Epilepsia* 2001;42:950–53 CrossRef Medline
82. Wang JC, Heier L, Souweidane MM. **Advances in the endoscopic management of suprasellar arachnoid cysts in children.** *J Neurosurg* 2004;100:418–26 CrossRef Medline
83. Maixner W. **Hypothalamic hamartomas—clinical, neuropathological and surgical aspects.** *Childs Nerv Syst* 2006;22:867–73 CrossRef Medline
84. Ozek MM, Urgan K. **Neuroendoscopic management of suprasellar arachnoid cysts.** *World Neurosurg* 2013;79(2 Suppl): S19e1318 CrossRef Medline
85. Perez FA, Elfers C, Yanovski JA, et al. **MRI measures of hypothalamic injury are associated with glucagon-like peptide-1 receptor agonist treatment response in people with hypothalamic obesity.** *Diabetes Obes Metab* 2021;23:1532–41 CrossRef Medline
86. Roth CL, Eslamy H, Pihoker C, et al. **Semi-quantitative analysis of hypothalamic damage on MRI predicts risk for hypothalamic obesity.** *Obesity (Silver Spring)*. 2015;23:1226–33 CrossRef Medline
87. Roth J, Bercu MM, Constantini S. **Combined open microsurgical and endoscopic resection of hypothalamic hamartomas.** *J Neurosurg Pediatr* 2013;11:491–94 CrossRef Medline
88. Leal AJ, Moreira A, Robalo C, et al. **Different electroclinical manifestations of the epilepsy associated with hamartomas connecting to the middle or posterior hypothalamus.** *Epilepsia* 2003;44:1191–95 CrossRef Medline
89. Garre ML, Cama A. **Craniopharyngioma: modern concepts in pathogenesis and treatment.** *Curr Opin Pediatr* 2007;19:471–79 CrossRef Medline
90. Roth C, Wilken B, Hanefeld F, et al. **Hyperphagia in children with craniopharyngioma is associated with hyperleptinaemia and a failure in the downregulation of appetite.** *Eur J Endocrinol* 1998;138:89–91 CrossRef Medline
91. Müller HL, Faldum A, Etavard-Gorris N, et al. **Functional capacity, obesity and hypothalamic involvement: cross-sectional study on 212 patients with childhood craniopharyngioma.** *Klin Padiatr* 2003;215:310–14 CrossRef Medline
92. Mortini P, Gagliardi F, Bailo M, et al. **Magnetic resonance imaging as predictor of functional outcome in craniopharyngiomas.** *Endocrine* 2016;51:148–62 CrossRef Medline
93. Müller HL, Gebhardt U, Teske C, et al; Study Committee of KRANIOPHARYNGEOM 2000. **Post-operative hypothalamic lesions and obesity in childhood craniopharyngioma: results of the multinational prospective trial KRANIOPHARYNGEOM 2000 after 3-year follow-up.** *Eur J Endocrinol* 2011;165:17–24 CrossRef Medline
94. Ozyurt J, Thiel CM, Lorenzen A, et al. **Neuropsychological outcome in patients with childhood craniopharyngioma and hypothalamic involvement.** *J Pediatr* 2014;164:876–81 CrossRef Medline
95. Ciesielski KT, Lesnik PG, Benzel EC, et al. **MRI morphometry of mamillary bodies, caudate nuclei, and prefrontal cortices after chemotherapy for childhood leukemia: multivariate models of early and late developing memory subsystems.** *Behav Neurosci* 1999;113:439–50 CrossRef Medline
96. Larnaout A, Mongalgi MA, Kaabachi N, et al. **Methylmalonic acidemia with bilateral globus pallidus involvement: a neuropathological study.** *J Inherit Metab Dis* 1998;21:639–44 CrossRef Medline
97. Vann SD, Nelson AJ. **The mammillary bodies and memory: more than a hippocampal relay.** *Prog Brain Res* 2015;219:163–85 CrossRef Medline
98. Martin PR, Singleton CK, Hiller-Sturmhöfel S. **The role of thiamine deficiency in alcoholic brain disease.** *Alcohol Res Health* 2003;27:134–42 Medline
99. Singleton CK, Martin PR. **Molecular mechanisms of thiamine utilization.** *Curr Mol Med* 2001;1:197–207 CrossRef Medline
100. Schabelman E, Kuo D. **Glucose before thiamine for Wernicke encephalopathy: a literature review.** *J Emerg Med* 2012;42:488–94 CrossRef Medline
101. Northington FJ, Chavez-Valdez R, Martin LJ. **Neuronal cell death in neonatal hypoxia-ischemia.** *Ann Neurol* 2011;69:743–58 CrossRef Medline
102. Wang X, Ma J, Fu Q, et al. **Role of hypoxia-inducible factor-1alpha in autophagic cell death in microglial cells induced by hypoxia.** *Mol Med Rep* 2017;15:2097–2105 CrossRef Medline
103. Zera K, Zastre J. **Stabilization of the hypoxia-inducible transcription factor-1 alpha (HIF-1alpha) in thiamine deficiency is mediated by pyruvate accumulation.** *Toxicol Appl Pharmacol* 2018;355:180–88 CrossRef Medline
104. Haddad GG, Jiang C. **O2 deprivation in the central nervous system: on mechanisms of neuronal response, differential sensitivity and injury.** *Prog Neurobiol* 1993;40:277–318 CrossRef Medline
105. Ben-Zvi A, Liebner S. **Developmental regulation of barrier- and non-barrier blood vessels in the CNS.** *J Intern Med* 2021 Mar 4 [Epub ahead of print] CrossRef Medline



# Perfusion Scotoma: A Potential Core Underestimation in CT Perfusion in the Delayed Time Window in Patients with Acute Ischemic Stroke

K. Abrams and G. Dabus



## ABSTRACT

**SUMMARY:** With the growing rise in utilization of CT perfusion for selecting patients for thrombectomy in acute ischemic stroke from large vessel occlusion, some potential pitfalls are becoming more commonly seen particularly when it comes to estimating the core infarct size on CT perfusion. Ghost infarct core has been described to account for overestimating core infarct size in the early time period (<3 hours). Herein, we describe the phenomenon of underestimating core infarct size on CT perfusion in the later time period (>6 hours), which we have termed perfusion scotoma.

As CT perfusion has grown in practice in aiding the selection of patients eligible for thrombectomy in acute ischemic stroke, some potential pitfalls are becoming more commonly seen when it is used to estimate the core infarct size. While DWI remains the criterion standard for visualizing the ischemic stroke core, most patients do not undergo MR imaging at initial presentation. Most institutions that are part of a stroke network use multimodal CT, which includes CTA and CT perfusion. This algorithm works well for most institutions due to the speed and availability of CT imaging.

Following the multiple, positive trials in 2015 for thrombectomy in large-vessel occlusion,<sup>1-3</sup> CT perfusion use started to grow exponentially, including for patients in the <6-hour time window. Soon after this growth occurred, reports of “ghost infarct core” were published.<sup>4</sup> Ghost infarct core was defined as a core infarct on perfusion (defined as CBF of <30%) that overestimated the final core infarct size. This was seen most commonly in patients presenting in the <3-hour time period. Another study noted this phenomenon in the <6-hour time period.<sup>5</sup>

Further increasing the demand for this technology were the positive results of the Clinical Mismatch in the Triage of Wake Up and Late Presenting Strokes Undergoing Neurointervention with Trevo (DAWN)<sup>6</sup> (2017) and Endovascular Therapy Following Imaging Evaluation for Ischemic Stroke 3 (DEFUSE

3)<sup>7</sup> (2018) trials, which used quantitative CT perfusion to stratify which patients would benefit from thrombectomy in the >6-hour time period. Now that the eligible time period was increased in patients last known healthy up to 24 hours (DAWN) or up to 16 hours (DEFUSE 3), widespread CT perfusion has become far more prevalent. With this increase in use, we have seen a new pitfall in estimating the core infarct volume on CT perfusion: underestimating the core infarct volume. This phenomenon was described by Copelan et al,<sup>8</sup> who looked at patients in the >6-hour time period who underwent CTA at a spoke hospital before undergoing CT perfusion (RAPID Software; <https://www.rapidsoftware.shop/>) at the hub hospital. They found that the core infarct was underestimated in this scenario and hypothesized that recent contrast administration rendered the core infarct estimation inaccurate. However, even more recently, Voleti et al<sup>9</sup> published an article correlating the ASPECTS with the CT perfusion core in large-vessel occlusion. In general, as the ASPECTS number decreases, one would expect core infarct volume to increase. The scatterplot from that article demonstrated outliers in the correlation of the core infarct volume in patients with a lower ASPECTS who also showed low core infarct volumes on perfusion. We have termed this phenomenon of a small core infarct on CT perfusion but a low ASPECTS “perfusion scotoma.”

We have seen this phenomenon in our clinical practice almost exclusively in the >6-hour time period, when ASPECTS abnormalities are apparent. These findings appear to be independent of the vendor used for CT perfusion, judging by what has appeared in the literature as well as our own clinical experience.

Figure 1 is an example of the perfusion scotoma from our clinical practice where a patient presented to one of our spoke hospitals last known healthy more than 8 hours before arrival. Only noncontrast CT of the brain was performed before transfer to our Comprehensive Stroke Center. The initial brain CT

Received February 15, 2022; accepted after revision April 7.

From the Department of Radiology (K.A.), Baptist Hospital of Miami, Miami Neuroscience Institute, Miami, Florida; and Department of Neuroendovascular Surgery (G.D.), Miami Cardiac and Vascular Institute, Miami Neuroscience Institute, Miami, Florida.

Please address correspondence to Kevin Jay Abrams, MD, FACR, Department of Radiology, Baptist Hospital of Miami, Miami Neuroscience Institute, 8900 North Kendall Dr, Coral Gables, FL 33143-3647; e-mail: drabrams@bellsouth.net

<http://dx.doi.org/10.3174/ajnr.A7524>

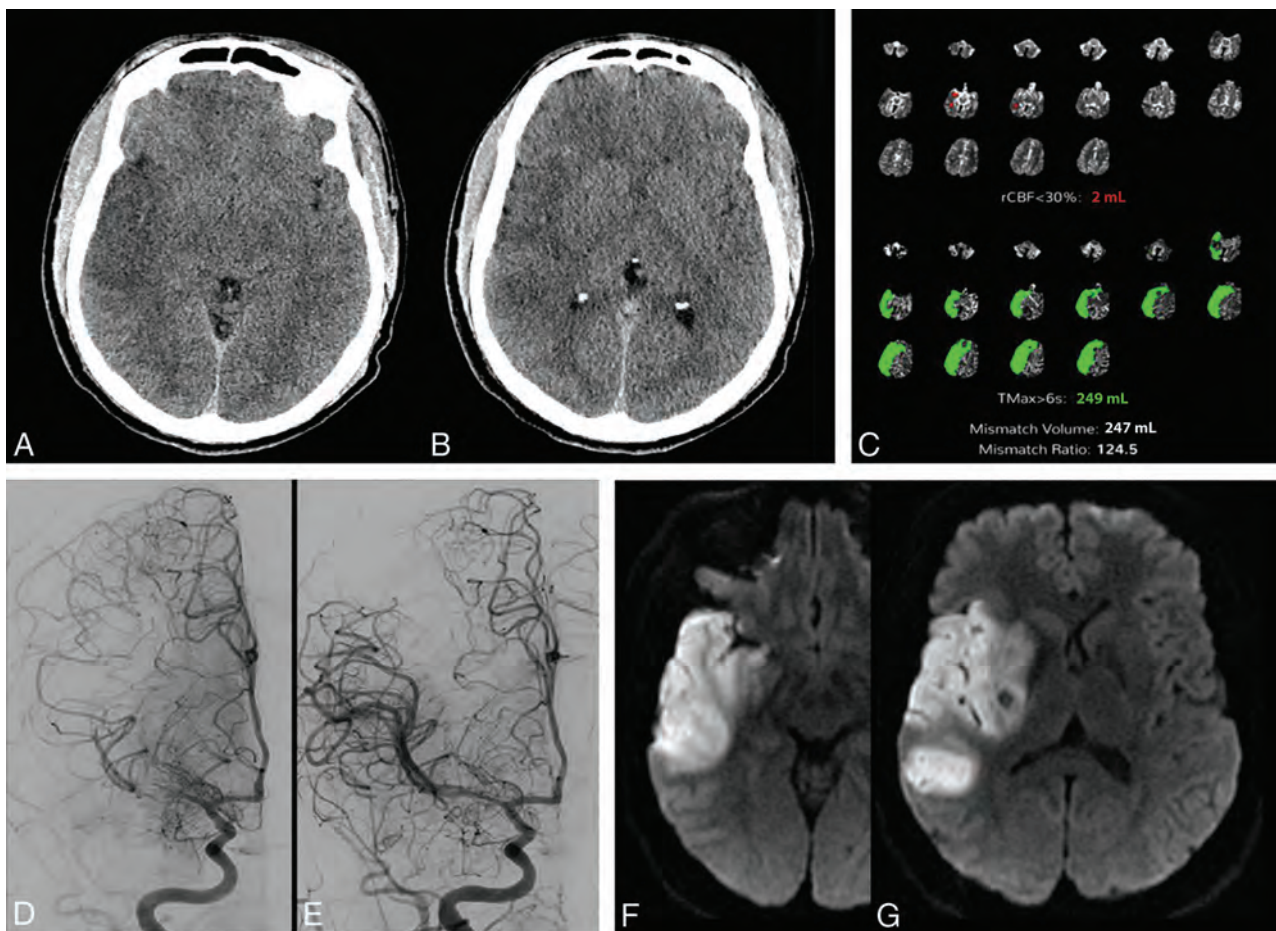


**FIG 1.** A patient presented with right MCA syndrome to an outside hospital, last known healthy >8 hours before arrival. The initial brain CT at the outside institution demonstrated acute ischemic changes in the right temporal lobe and insula with an ASPECTS of 6 (A and B). CT perfusion performed at our hospital reconstructed using both manual (Advantage Workstation; GE Healthcare, not shown) and automated (Viz.ai Intelligent Care Coordination; <https://www.viz.ai>; C) perfusion software demonstrates a large area of acute ischemia (time-to maximum, >6 seconds of 249 mL), but a minimal core infarct (CBF of <30% of 2 mL). Cerebral angiography prethrombectomy demonstrates partial recanalization of the right M1 segment with some antegrade flow (D). The patient underwent successful thrombectomy of the M1 segment (E). Follow-up MR imaging demonstrates areas of restricted diffusion corresponding to the areas of ASPECTS abnormality on the original CT scan, the “perfusion scotoma” (F and G). rCBF indicates relative CBF; Tmax, time-to-maximum.

demonstrated a hyperdense acute clot in the M1 segment of the right MCA, with early acute ischemic changes and an ASPECTS of 6. On arrival at our comprehensive stroke center, CTA and CT perfusion were performed and demonstrated an occlusive or near-occlusive clot in the M1 segment of the right MCA, with a large area of acute ischemia (time-to-maximum, >6 seconds of 249 mL), but a minimal core infarct (CBF of <30% of 2 mL). The patient underwent angiography and successful thrombectomy of a nearly totally occlusive clot of the M1 segment of the right MCA. Follow-up MR imaging demonstrated areas of restricted diffusion corresponding to the areas of ASPECTS abnormality on the original CT scan, the “perfusion scotoma.”

The likely etiology for this case and many cases of this perfusion scotoma is early reperfusion from partial recanalization as well as luxury perfusion. Although we tend to think of luxury perfusion in the 48- to 72-hour timeframe, it can also be seen within 24 hours and may contribute to this phenomenon.<sup>10</sup> We can think

of the infarcted tissue on perfusion as a continuum from reduced CBF in the <6-hour timeframe, slowly increasing with time to when it may become equivalent to normal tissue in the 6- to 24-hour timeframe and elevated in the >24-hour timeframe.

Figure 2 is an example of a patient with a subacute right superior cerebellar infarct >24 hours old but who presented with an acute left MCA syndrome. Note on the quantitative perfusion maps, not only the acute left MCA ischemia but also the absence of core infarct in the right superior cerebellar hemisphere. However, elevated CBF and CBV were noted in the cerebellar infarct on the qualitative color maps, consistent with reperfusion. The CTA also demonstrated that the right superior cerebellar artery was patent and the M2 segment of the left middle cerebral artery was occluded.

Why does the perfusion scotoma matter? When communicating the quantitative CT perfusion findings, it is imperative for the radiologist to also incorporate the ASPECTS to accurately assess the true ischemic penumbra. For example, in a

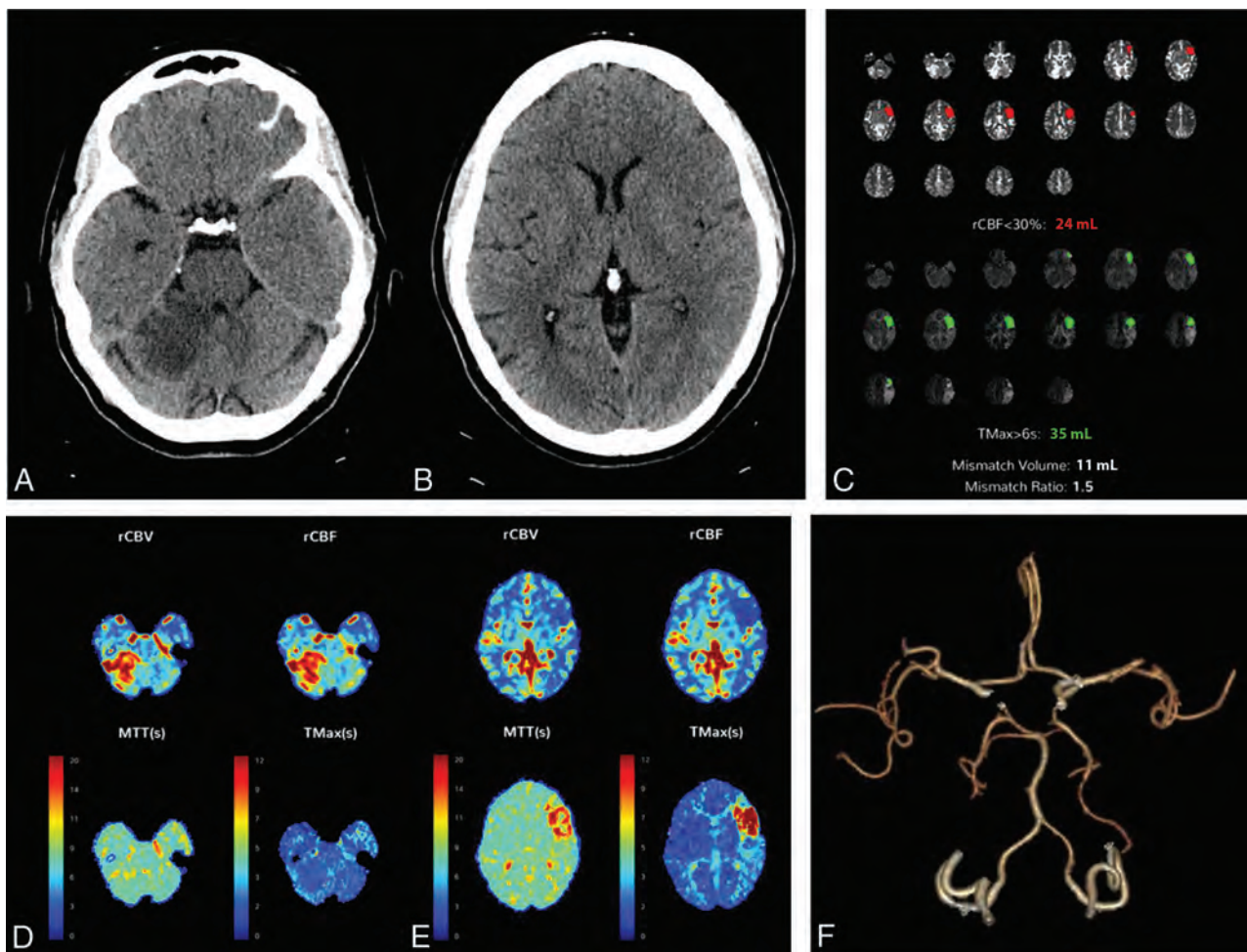


**FIG 2.** A patient presenting with an acute left MCA syndrome. CT also demonstrates an acute/subacute right superior cerebellar infarct (A and B). CT perfusion was performed and reconstructed using both manual (Advantage Workstation, not shown) and automated (C–E) perfusion software and demonstrates similar results. The quantitative perfusion maps demonstrate acute left MCA ischemia but no evidence of core infarct in the right superior cerebellar hemisphere (C). D and E, Qualitative color maps demonstrate elevated CBF and CBV in the right superior cerebellar infarct, consistent with reperfusion. CTA also demonstrates the right superior cerebellar artery to be patent and the M2 segment of the left MCA to be occluded (F). rCBF indicates relative CBF; rCBV, relative CBV; Tmax, time-to-maximum.

patient with large-vessel occlusion and a large time-to-maximum of  $>6$  seconds (eg, 150 mL) as the area of acute ischemia, the CBF of  $<30\%$  (core infarct) being very low (eg, 5 mL), with a high ASPECTS (eg,  $>6$ ), would imply that the patient is a thrombectomy candidate. However, if in that same patient, the ASPECTS is low (eg, 3 as seen in the scatterplot), this patient would, most likely, not be a thrombectomy candidate, even though the mismatch may be listed as 145 mL in this example; furthermore, thrombectomy may even be deleterious. It also allows the neurointerventionalist to give realistic expectations to the family regarding the procedure. Although we have not correlated the CT perfusion images to DWI in the early phase (our patients had MRIs at later time periods), we believe that this finding can be extrapolated, and it may represent a future area for research.

In summary, like the importance of understanding the concept of overestimating the core infarct in the  $<3$ -hour time period (ghost infarct core), physicians involved in acute

stroke care should understand the concept of underestimating the infarct core in the  $>6$ -hour time period (perfusion scotoma).

**Disclosure forms** provided by the authors are available with the full text and PDF of this article at [www.ajnr.org](http://www.ajnr.org).

## REFERENCES

- Goyal M, Demchuk AM, Menon BK, et al; ESCAPE Trial Investigators. Randomized assessment of rapid endovascular treatment of ischemic stroke. *N Engl J Med* 2015;372:1019–30 CrossRef Medline
- Saver JL, Goyal M, Bonafe A, et al; SWIFT PRIME Investigators. Stent-retriever thrombectomy after intravenous t-PA vs. t-PA alone in stroke. *N Engl J Med* 2015;372:2285–95 CrossRef Medline
- Campbell BC, Mitchell PJ, Kleinig TJ, et al; EXTEND-IA Investigators. Endovascular therapy for ischemic stroke with perfusion-imaging selection. *N Engl J Med* 2015;372:1009–18 CrossRef Medline
- Martins N, Aires A, Mendez B, et al. Ghost infarct core and admission computed tomography perfusion: redefining the role of neuroimaging in acute ischemic stroke. *Interv Neurol* 2018;7:513–21 CrossRef Medline



5. Rodrigues GM, Mohammaden MH, Haussen DC, et al. **Ghost infarct core following endovascular reperfusion: a risk for computed tomography perfusion misguided selection in stroke.** *Int J Stroke* 2021 Nov 19. [Epub ahead of print] CrossRef Medline
6. Nogueira RG, Jadhav AP, Haussen DC, et al; DAWN Trial Investigators. **Thrombectomy 6 to 24 hours after stroke with a mismatch between deficit and infarct.** *N Engl J Med* 2018;378:11–21 CrossRef Medline
7. Albers GW, Marks MP, Kemp S, et al; DEFUSE 3 Investigators. **Thrombectomy for stroke at 6 to 16 hours with selection by perfusion imaging.** *N Engl J Med* 2018;378:708–18 CrossRef Medline
8. Copelan AZ, Smith ER, Drocton GT, et al. **Recent administration of iodinated contrast renders core infarct estimation inaccurate using RAPID software.** *AJNR Am J Neuroradiol* 2020;41:2235–42 CrossRef Medline
9. Voleti S, Vidovich J, Corcoran B, et al. **Correlation of Alberta Stroke Program Early Computed Tomography Score with computed tomography perfusion core in large vessel occlusion in delayed time windows.** *Stroke* 2021;52:498–504 CrossRef Medline
10. Nagar VA, McKinney AM, Karagulle AT, et al. **Reperfusion phenomenon masking acute and subacute infarcts at dynamic perfusion CT: confirmation by fusion of CT and diffusion-weighted MR images.** *AJNR Am J Neuroradiol* 2009;193:1629–38 CrossRef Medline

# Phosphaturic Mesenchymal Tumor

J.C. Benson, J.A. Trejo-Lopez, A.M. Nassiri, K. Eschbacher, M.J. Link, C.L. Driscoll, R.D. Tiegs, J. Sfeir, and D.R. DeLone

## ABSTRACT

Phosphaturic mesenchymal tumors (PMTs) are neoplasms associated with tumor-induced osteomalacia. Patients typically present with pathologic fractures in the setting of chronic hypophosphatemic hyperphosphaturic osteomalacia, as well as gradual muscle weakness, bone pain, and difficulty walking. Because of their rarity and nonspecific symptomatology, phosphaturic mesenchymal tumors often go undiagnosed for years. Even when discovered on imaging, the tumors can be diagnostically challenging for radiologists. Phosphaturic mesenchymal tumors often tend to be small and can be located nearly anywhere in the body, and, therefore, can mimic many other tumors. This case highlights the imaging and pathologic markers of a phosphaturic mesenchymal tumor, often found in a patient with tumor-induced osteomalacia.

**ABBREVIATIONS:** FGF23 = fibroblast growth factor 23; PMT = phosphaturic mesenchymal tumor; TIO = tumor-induced osteomalacia

The patient is a 57-year-old man who presented to our institution for evaluation with a 4-year history of recurrent insufficiency fractures involving his femurs and ribs, associated with considerable disability. His initial symptom was right-hip pain that failed to resolve with conservative treatment. An MR imaging at that time showed a left subtrochanteric insufficiency fracture. Two years later, after developing pain in both thighs, the patient was diagnosed with insufficiency fractures involving the subtrochanteric regions of both proximal femurs. At the time of presentation, a review of his laboratory records revealed chronic hypophosphatemia, with serum phosphorus levels ranging between 1.7 and 2.1 mg/dL during the preceding 4 years. His serum calcium and parathyroid hormone levels have been consistently within the normal range.

Given his history and laboratory abnormalities, the diagnosis of tumor-induced osteomalacia (TIO) was entertained. Confirmatory testing (Table) demonstrated hypophosphatemia due to renal phosphate wasting, as well as elevated fibroblast growth factor 23 (FGF23).

The patient did not have skeletal deformities or a family history of bone disorders, and his bone density readings were in the osteopenia range. He then underwent a PET gallium ( $^{68}\text{Ga}$ )

DOTATATE study to examine for a mesenchymal tumor, which is the usual source of the excess FGF23 production.

## Imaging

The  $^{68}\text{Ga}$  DOTATATE examination demonstrated a focal lesion in the petrous aspect of the left temporal bone (Fig 1), considered highly suspicious for the patient's culprit lesion. Dedicated imaging of the temporal bone was therefore performed.

On MR imaging, an avidly enhancing lesion was seen along the cochlear promontory in the middle ear, extending into the anterior hypotympanum along the course of the Eustachian tube (Fig 2). Anteriorly, the mass involved the skull base, encroaching on the foramen spinosum. Posteriorly, the mass closely approximated the geniculate ganglion of the facial nerve. When read in conjunction with the  $^{68}\text{Ga}$  DOTATATE examination, this was initially thought to represent a glomus tympanicum tumor with unusual anterior growth. A glomus faciale tumor growing from the geniculate ganglion, phosphaturic mesenchymal tumor (PMT), primary neuroendocrine carcinoma, or metastasis were also considered.

On a subsequent CT, the tumoral margins were not well-demarcated because the density of the mass matched that of the fluid within the adjacent middle ear and mastoid air cells. However, the CT scans did reveal the mass to be permeative with destruction of the adjacent skull base (Fig 3). In retrospect, the patient did note a long-standing history of left-sided hearing loss and ear fullness without drainage.

Received January 3, 2022; accepted after revision March 17.

From the Departments of Radiology (J.C.B., D.R.D.), Laboratory Medicine and Pathology (J.A.T.-L., K.E.), Otorhinolaryngology (A.M.N., C.L.D.), Neurosurgery (M.J.L.), and Endocrinology (R.D.T., J.S.), Mayo Clinic, Rochester, Minnesota.

Please address correspondence to John C. Benson, MD, 200 1st St SW, Department of Radiology, Mayo Clinic, Rochester, MN 55905; e-mail: benson.john3@mayo.edu

<http://dx.doi.org/10.3174/ajnr.A7513>

#### Patient laboratory testing on presentation

Levels	Results	Reference Range
Total serum calcium	9.0	8.8–10.2 mg/dL
Albumin	4.4	3.5–5.0 g/dL
Phosphorus	1.5	2.5–4.5 mg/dL
Magnesium	2.1	1.7–2.3 mg/dL
Creatinine	0.97	0.74–1.35 mg/dL
Alkaline phosphatase	102	35–104 U/L
Parathyroid hormone	64	15–65 pg/mL
25 (hydroxyvitamin) Vitamin D	83	30–50 ng/mL
1, 25 (hydroxyvitamin) <sub>2</sub> Vitamin D	29	18–64 pg/mL
Intact <i>FGF23</i>	82	≤59 pg/mL
Tubular reabsorption of phosphate	62%	>85%

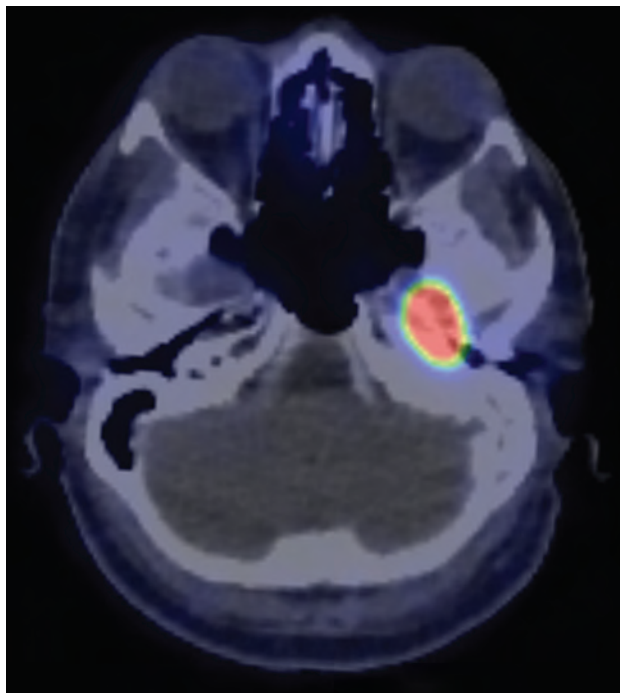


**FIG 1.** <sup>68</sup>Ga DOTATATE PET/CT demonstrates marked radiotracer uptake within the petrous aspect of the left temporal bone.

#### Operative Report

On preoperative otoscopy, the mass was easily visible within the middle ear and less intensely red than a typical paraganglioma (which is typically deep red) (Fig 4). Considering the imaging findings and clinical history, the likely diagnosis was PMT, and surgical treatment was recommended. Tumoral resection was accomplished via a left middle cranial fossa craniotomy. Intraoperatively, the tumor was noted to have eroded through the middle fossa floor just posterior and lateral to foramen spinosum. No involvement of the subtemporal dura was noted intraoperatively, though this may have been due to the dural thickening noted on imaging being reactive in nature rather than tumoral extension. It appeared to originate at the anterior aspect of the Eustachian tube and extended along the Eustachian tube inferiorly into the middle ear. The tumor was quite vascular and required piecemeal excision with frequent use of hemostatic agents and bipolar cautery during resection. Angled instruments and otologic endoscopes were used to release the inferior extent of the tumor from the middle ear. Ultimately,

gross total resection was achieved. The patient had an uneventful postoperative course without signs of CSF leak or cranial nerve deficits.

#### Pathology

Histologic examination of the tumor revealed a highly vascular neoplasm composed of predominantly spindled tumor cells with bland, ovoid nuclei with interspersed staghorn-like vessels (Fig 5). There were scattered coarse, flocculent calcifications. Neoplastic cells showed overall monotonous nuclei, with low proliferative activity and no tumor necrosis. Immunohistochemical studies revealed tumor cells to be diffusely positive for *SSTR2A*, while negative for chromogranin and synaptophysin. In addition, there was widespread expression by the tumor cells of *FGF23* mRNA by chromogenic in situ hybridization. Overall, these findings supported the final diagnosis of a morphologically benign PMT.

Histologically, PMTs are highly vascular and composed of bland, spindled-to-stellate cells in a distinctive myxoid or myxochondroid matrix with flocculent calcification.<sup>1–3</sup> *FN1-FGFR1* or *FN1-FGF1* fusions are common in PMTs (up to approximately 50%), which may activate the *FGFR1* pathway leading to increased expression of the *FGF23* gene and protein.<sup>1–3</sup> *FGF23* expression can be detected by reverse-transcription polymerase chain reaction, chromogenic in situ hybridization, or immunohistochemistry.<sup>1,2</sup>

The histologic differential diagnosis of this tumor includes solitary fibrous tumor, mesenchymal chondrosarcoma, and paraganglioma. Solitary fibrous tumors can have staghorn vessels and have a similar, bland, spindle cell appearance. However, solitary fibrous tumors lack the characteristic matrix and calcifications of PMTs and would not express *SSTR2A* or *FGF23* mRNA.<sup>2,3</sup> Mesenchymal chondrosarcomas have malignant, small, round cells; lack the characteristic calcified matrix of a PMT; and would not express *FGF23* mRNA. A highly vascular paraganglioma may, at times, be morphologically reminiscent of PMT. However, the immunophenotype of PMT (positive for *SSTR2A* and *FGF23* mRNA, negative for chromogranin and synaptophysin) excluded this possibility. Furthermore, although paragangliomas and PMTs can both exhibit high vascularity, paragangliomas lack the characteristic chondromyxoid matrix and calcifications of PMT. Unlike PMTs, paragangliomas have a characteristic nested (zellballen) architecture composed of neuroendocrine cells and are positive for neuroendocrine markers (eg, synaptophysin and chromogranin). The tumor presented here did not have the classic morphology of paraganglioma and was negative for synaptophysin and chromogranin.

#### DISCUSSION

PMTs are exceedingly rare tumors that arise primarily from bones and connective tissue. They are typically seen in middle-aged adults without an apparent sex predilection. Pediatric cases have been infrequently reported.<sup>4</sup> The median age at the time of diagnosis is 44–48 years of age.<sup>5,6</sup> Tumor locality is unpredictable; PMTs can be found in any osseous or soft-tissue location and uncommonly involve the skin.<sup>7</sup> More than half of the tumors are found within the extremities, with the femur being the most common site.<sup>8</sup> Within the head and neck, the sinonasal region is most common, followed by the mandible and maxilla. Although histologically benign, rare cases of malignant transformation and metastases have been reported.<sup>8–10</sup>



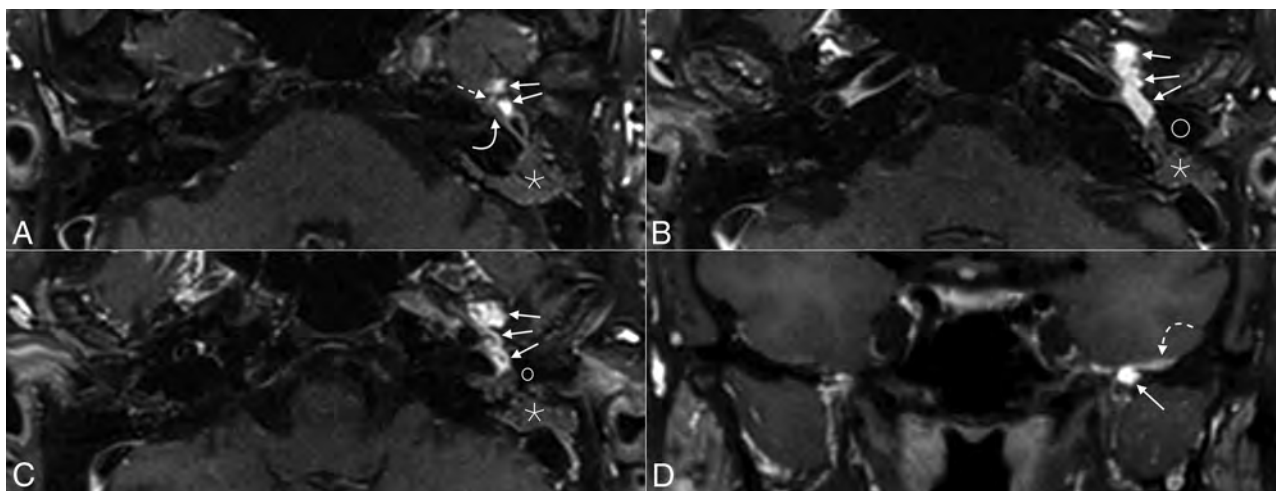


**FIG 2.** From superior to inferior, axial (A–C) MR images show an avidly enhancing mass (solid arrows) extending from the middle ear along the floor of the middle cranial fossa, with substantial intraosseous involvement. A small portion of the mass (dashed straight arrow) closely approximates the geniculate ganglion of the facial nerve (solid curved arrow) (circles in B and C denote the external auditory canal). The mastoid air cells are completely opacified (asterisks). Coronal image (D) shows the mass extending intracranially, with associated dural thickening (dashed curved arrow).

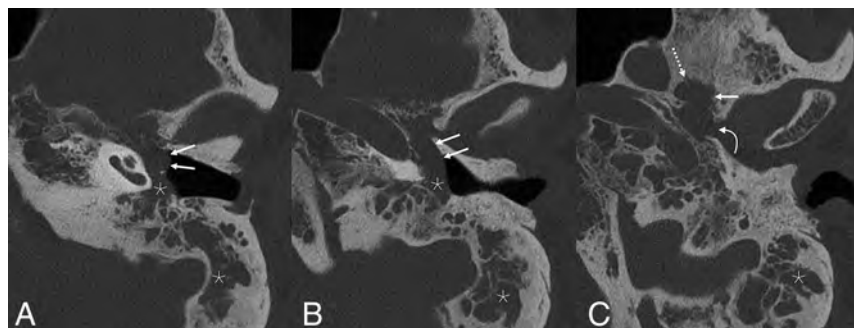


**FIG 3.** Noncontrast temporal bone CT performed 2 days after MR imaging again shows the mass (solid straight arrows) extending from the mesotympanum (A) into the anterior hypotympanum (B), which is widened. The mass is locally destructive (C), causing erosion of the skull base with involvement of the foramen spinosum (dashed straight arrow) and left temporomandibular joint (curved arrow). The margins of the mass are indistinguishable from fluid density within the middle ear and mastoid air cells (asterisks), which remained opacified.

Clinically, PMTs are associated with tumor-induced osteomalacia (TIO), also known as oncogenic osteomalacia, a paraneoplastic syndrome characterized by widespread reduction of osteoblastic activity. PMTs secrete FGF23, a peptide hormone-like regulator of phosphate levels, which decreases re-absorption of phosphate in the proximal tubules of the kidneys, causing it to be wasted within the urine. The downstream suppression of osteoblasts and mobilization of calcium and phosphate from the bones lead to widespread hypophosphatemic osteomalacia.<sup>11</sup> Patients present with bone pain, insufficiency fractures, and gradual-onset muscular weakness.<sup>12</sup>

A rare subtype of PMT has recently been identified as being nonphosphaturic.<sup>13</sup> The descriptions of these tumors are heterogeneous. Some might produce negligible amounts of FGF23 or are thought to exist in patients with a compensatory mechanism in place.<sup>3</sup> Some are thought to produce a deformed and/or inactive form of the FGF23 protein.<sup>14</sup> Other tumors may

simply have been identified in patients before symptomatic osteomalacia had developed.<sup>15</sup>

Unfortunately, the rarity of PMTs makes them notoriously under-recognized by clinicians. Many patients are symptomatic for years or decades before the tumor is diagnosed.<sup>16,17</sup> The diagnosis typically is based on a combination of clinical history, laboratory values, and imaging. Specifically, elevated serum FGF23 levels in a patient with hypophosphatemia and normal renal function is highly suggestive of a PMT. However, TIO has a known association with multiple other tumors, typically of mesenchymal origin, including solitary fibrous tumors,

giant cell tumors, chondrosarcomas, and osteosarcomas.<sup>18,19</sup> Most, but not all, of these tumors result in TIO through the secretion of FGF23; some secrete various other factors such as frizzled-related protein-4, *FGF7*, and matrix extracellular phosphoglycoprotein.<sup>20</sup>

Once the diagnosis of TIO has been established, various nuclear medicine studies can be used to search for the culprit lesion, including <sup>68</sup>Ga DOTATATE, technetium Tc99m-octreotide, and FDG PET/CT scans.<sup>21</sup> <sup>68</sup>Ga DOTATATE is now the favored technique, having been shown to have the greatest sensitivity for tumoral detection.<sup>15, 22–24</sup> This superiority of <sup>68</sup>Ga DOTATATE over other modalities is thought to be due to the higher affinity of its radiotracer to somatostatin receptors 2 and 5, which are expressed by PMTs.<sup>23</sup> Nevertheless, the sensitivity of these examinations is suboptimal. A series by El-Maouche et al<sup>23</sup> found that <sup>68</sup>Ga DOTATATE examinations found a PMT in just more than half of patients with hypophosphatemic TIO, while indium-111

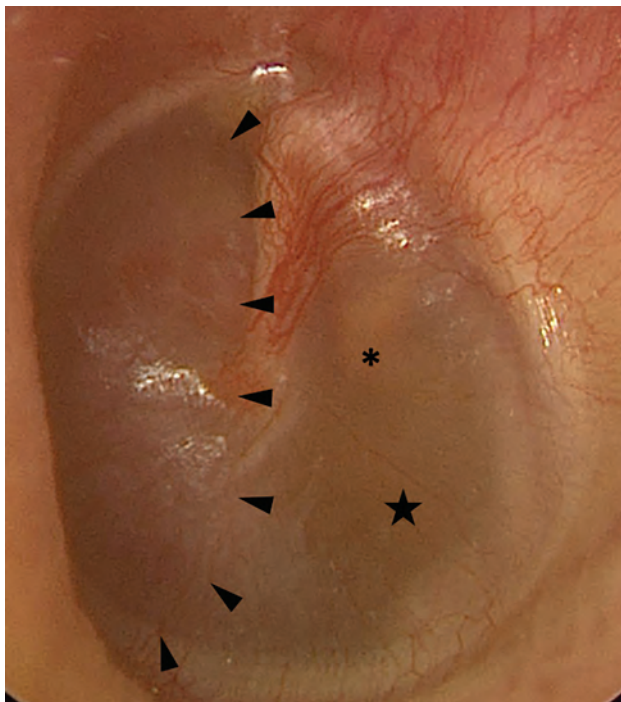


**FIG 4.** Preoperative otoscopy of the left tympanic membrane reveals a reddish mass (*arrowheads*) within the anterior mesotympanum. An amber effusion (*star*) is seen posterior to the mass, surrounding the incudostapedial joint (*asterisk*).

( $^{111}\text{In}$ ) pentetreotide (OctreoScan) SPECT/CT and [ $^{18}\text{F}$ ] FDG identified  $<50\%$ .

PMTs are not encapsulated and tend to be locally infiltrative.<sup>12</sup> On CT, intraosseous PMTs are osteolytic with a narrow zone of transition and internal matrix; soft-tissue masses are hypodense and enhance.<sup>25</sup> On MR imaging, tumors are isointense to soft tissues on T1-weighted imaging and demonstrate enhancement.<sup>26</sup> Intralesional T2 signal is variable. Most commonly, tumors are T2-hyperintense, though Broski et al<sup>22</sup> noted that PMTs characteristically have small foci of intralesional T2 hypointensity. Some may be partially cystic. Larger tumors may have intralesional flow voids.<sup>27</sup> However, most PMTs are small and slow-growing, and tumor localization is highly variable. Thus, they may present a diagnostic conundrum for radiologists, particularly when the diagnosis of TIO is unknown, or, as in this case, if the PMT mimics the appearance of a more common entity.<sup>26</sup>

The only known definitive treatment for TIO is surgical resection of the tumor. Fortunately, removal of PMTs results in complete resolution of the biochemical and physical sequelae of the paraneoplastic syndrome.<sup>7</sup> Because PMTs are often locally invasive, a wide excision is needed to successfully obtain tumor-free margins.<sup>28</sup> Although local recurrence may occur, surgical resection is considered curative in approximately 90% of cases.<sup>27,29</sup> Cryoablation has been successfully used to treat residual tumor after resection.<sup>30</sup> For patients with unresectable tumors, a fully human monoclonal antibody against FGF23, burosumab, has

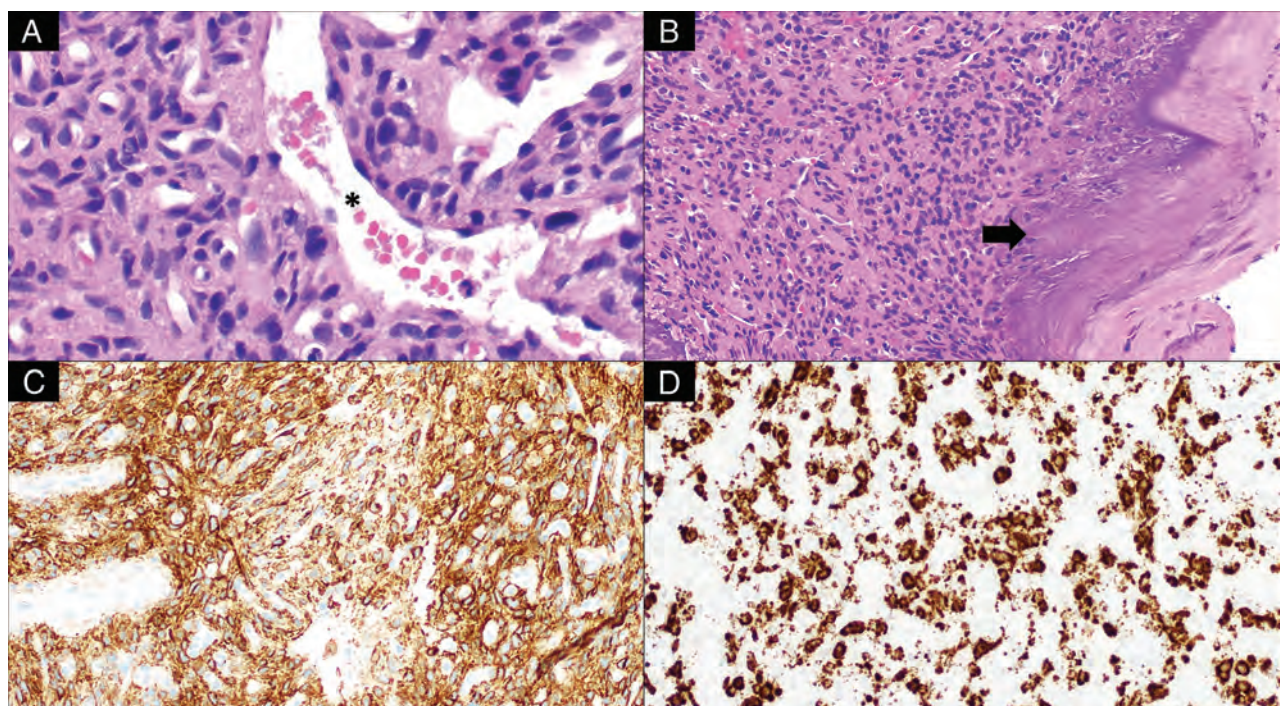


**FIG 5.** Histologic examination of this tumor reveals bland, spindled-to-stellate neoplastic cells (A, H&E, original magnification  $\times 400$ ) situated in a hyalinized matrix with a well-developed capillary network including ectatic, staghorn vessels (*asterisk*) as well as characteristic deposition of coarse calcification (B, H&E, original magnification  $\times 200$ ; *arrow*). The tumor is reactive for SSTR2A (C, immunohistochemistry, original magnification  $\times 200$ ) and shows evidence of FGF23 mRNA expression (D, chromogenic in situ hybridization, original magnification  $\times 200$ ).



been shown to provide biochemical and symptomatic improvement and was recently FDA-approved.<sup>31</sup>

Difficult cases are excellent learning opportunities, and this case is no exception. Despite the difficulty of the resection, the surgeons indicated that the available preoperative imaging was excellent, and they stated that additional imaging would not have changed the surgical approach. In retrospect, the differential considerations given in the initial radiology report could have been more precise. The case was challenging due to its location in an anatomic region that can support the growth of paragangliomas. Nevertheless, the clinical history of TIO should have served as a more convincing indicator that the tumor identified on imaging represented a PMT. Incorrectly favoring a paraganglioma over a PMT could have delayed or even prevented surgery because the purpose of the examination was to search for a lesion responsible for the patient's TIO. Fortunately, the patient ultimately underwent the best treatment course. He is expected to make a full recovery and will undergo routine surveillance imaging to monitor for recurrence.

### Case Summary

- PMTs are extremely rare entities that are associated with TIO.
- The tumors are small and can be found nearly anywhere in the body, making them a common mimic of more common malignancies.
- Surgical resection of the tumor results in resolution of a patient's osteomalacia.
- Histologically, PMTs have an unusual, hyalinized matrix that undergoes calcification with frequent expression of *FGF23* mRNA.

Disclosure forms provided by the authors are available with the full text and PDF of this article at [www.ajnr.org](http://www.ajnr.org).

### REFERENCES

- Lee J, Folpe AL. Phosphaturic mesenchymal tumor. In: Editorial Board. *WHO Classification of Tumours: Soft Tissue and Bone Tumours*. International Agency for Research on Cancer; 2020
- Bahrami A, Weiss SW, Montgomery E, et al. RT-PCR analysis for *FGF23* using paraffin sections in the diagnosis of phosphaturic mesenchymal tumors with and without known tumor-induced osteomalacia. *Am J Surg Pathol* 2009;33:1348–54 CrossRef Medline
- Folpe AL, Fanburg-Smith JC, Billings SD, et al. Most osteomalacia-associated mesenchymal tumors are a single histopathologic entity: an analysis of 32 cases and a comprehensive review of the literature. *Am J Surg Pathol* 2004;28:1–30 CrossRef Medline
- Kumar S, Shah R, Patil V, et al. Tumor-induced rickets-osteomalacia: an enigma. *J Pediatr Endocrinol Metab* 2020 July 20. [Epub ahead of print] CrossRef Medline
- Honda R, Kawabata Y, Ito S, et al. Phosphaturic mesenchymal tumor, mixed connective tissue type, non-phosphaturic variant: report of a case and review of 32 cases from the Japanese published work. *J Dermatol* 2014;41:845–49 CrossRef Medline
- Wu H, Bui MM, Zhou L, et al. Phosphaturic mesenchymal tumor with an admixture of epithelial and mesenchymal elements in the jaws: clinicopathological and immunohistochemical analysis of 22 cases with literature review. *Mod Pathol* 2019;32:189–204 CrossRef Medline
- Hodgson SF, Clarke BL, Tebben PJ, et al. Oncogenic osteomalacia: localization of underlying peripheral mesenchymal tumors with use of Tc 99m sestamibi scintigraphy. *Endocr Pract* 2006;12:35–42 CrossRef Medline
- Oyama N, Kojima-Ishii K, Toda N, et al. Malignant transformation of phosphaturic mesenchymal tumor: a case report and literature review. *Clin Pediatr Endocrinol* 2020;29:69–75 CrossRef Medline
- Morimoto T, Takenaka S, Hashimoto N, et al. Malignant phosphaturic mesenchymal tumor of the pelvis: a report of two cases. *Oncol Lett* 2014;8:67–71 CrossRef Medline
- Qiu S, Cao LL, Qiu Y, et al. Malignant phosphaturic mesenchymal tumor with pulmonary metastasis: a case report. *Medicine (Baltimore)* 2017;96:e6750 CrossRef Medline
- Ghorbani-Aghbolaghi A, Darrow MA, Wang T. Phosphaturic mesenchymal tumor (PMT): exceptionally rare disease, yet crucial not to miss. *Autops Case Rep* 2017;7:32–37 CrossRef Medline
- Pelo S, Gasparini G, Garagiola U, et al. Phosphaturic mesenchymal tumor, an unusual localization in head and neck. *J Surg Case Rep* 2018;2018:rjy091 CrossRef Medline
- Shiba E, Matsuyama A, Shibuya R, et al. Immunohistochemical and molecular detection of the expression of *FGF23* in phosphaturic mesenchymal tumors including the non-phosphaturic variant. *Diagn Pathol* 2016;11:26 CrossRef Medline
- Winters R, Bihlmeyer S, McCahill L, et al. Phosphaturic mesenchymal tumour-mixed connective tissue variant without oncogenic osteomalacia. *J Clin Pathol* 2009;62:760–61 CrossRef Medline
- Folpe AL. Phosphaturic mesenchymal tumors: a review and update. *Semin Diagn Pathol* 2019;36:260–68 CrossRef Medline
- Adnan Z, Nikomarov D, Weiler-Sagie M, et al. N. Phosphaturic mesenchymal tumors among elderly patients: a case report and review of literature. *Endocrinol Diabetes Metab Case Rep* 2019;2019:18–139 CrossRef Medline
- Drezner MK. Tumor-induced osteomalacia. *Rev Endocr Metab Disord* 2001;2:175–86 CrossRef Medline
- Cho SI, Do NY, Yu SW, et al. Nasal hemangiopericytoma causing oncogenic osteomalacia. *Clin Exp Otorhinolaryngol* 2012;5:173–76 CrossRef Medline
- Edmister KA, Sundaram M. Oncogenic osteomalacia. *Semin Musculoskelet Radiol* 2002;6:191–96 CrossRef Medline
- Jagtap VS, Sarathi V, Lila AR, et al. Tumor-induced osteomalacia: a single center experience. *Endocr Pract* 2011;17:177–84 CrossRef Medline
- Liu S, Zhou X, Song A, et al. Successful treatment of tumor-induced osteomalacia causing by phosphaturic mesenchymal tumor of the foot. *Medicine (Baltimore)* 2019;98:e16296 CrossRef Medline
- Broski SM, Folpe AL, Wenger DE. Imaging features of phosphaturic mesenchymal tumors. *Skeletal Radiol* 2019;48:119–27 CrossRef Medline
- El-Maouche D, Sadowski SM, Papadakis GZ, et al. <sup>68</sup>Ga-DOTATATE for tumor localization in tumor-induced osteomalacia. *J Clin Endocrinol Metab* 2016;101:3575–81 CrossRef Medline
- Ha S, Park S, Kim H, et al. Successful localization using <sup>68</sup>Ga-DOTATOC PET/CT of a phosphaturic mesenchymal tumor causing osteomalacia in a patient with concurrent follicular lymphoma. *Nucl Med Mol Imaging* 2018;52:462–67 CrossRef Medline
- Kawthalkar AS, Janu AK, Deshpande MS, et al. Phosphaturic mesenchymal tumors from head to toe: imaging findings and role of the radiologist in diagnosing tumor-induced osteomalacia. *Indian J Orthop* 2020;54:215–23 CrossRef Medline
- Walsh EM, Jacob J, Lucas DR, et al. Phosphaturic mesenchymal tumor of the cerebellopontine angle. *JAMA Otolaryngol Head Neck Surg* 2019;145:287–88 CrossRef Medline
- Richardson AL, Richardson OK. Phosphaturic mesenchymal tumor: case report. *Radiol Case Rep* 2019;14:1518–24 CrossRef Medline



28. Kane SV, Kakkar A, Oza N, et al. **Phosphaturic mesenchymal tumor of the nasal cavity and paranasal sinuses: a clinical curiosity presenting a diagnostic challenge.** *Auris Nasus Larynx* 2018;45:377–83 CrossRef Medline
29. Radaideh AR, Jaradat D, Abu-Kalaf MM, et al. **Resolution of severe oncogenic hypophosphatemic osteomalacia after resection of a deeply located soft-tissue tumour.** *Curr Oncol* 2009;16:87–90 CrossRef Medline
30. Horng JC, Van Eperen E, Tutton S, et al. **Persistent phosphaturic mesenchymal tumor causing tumor-induced osteomalacia treated with image-guided ablation.** *Osteoporos Int J Int* 2021;32:1895–98 CrossRef Medline
31. Brandi ML, Clunie GP, Houillier P, et al. **Challenges in the management of tumor-induced osteomalacia (TIO).** *Bone* 2021;152:116064 CrossRef Medline

# Investigating Brain White Matter in Football Players with and without Concussion Using a Biophysical Model from Multishell Diffusion MRI

S. Chung, J. Chen, T. Li, Y. Wang, and Y.W. Lui



## ABSTRACT

**BACKGROUND AND PURPOSE:** There have been growing concerns around potential risks related to sports-related concussion and contact sport exposure to repetitive head impacts in young athletes. Here we investigate WM microstructural differences between collegiate football players with and without sports-related concussion.

**MATERIALS AND METHODS:** The study included 78 collegiate athletes (24 football players with sports-related concussion, 26 football players with repetitive head impacts, and 28 non-contact-sport control athletes), available through the Federal Interagency Traumatic Brain Injury Research registry. Diffusion metrics of diffusion tensor/kurtosis imaging and WM tract integrity were calculated. Tract-Based Spatial Statistics and post hoc ROI analyses were performed to test group differences.

**RESULTS:** Significantly increased axial kurtosis in those with sports-related concussion compared with controls was observed diffusely across the whole-brain WM, and some focal areas demonstrated significantly higher mean kurtosis and extra-axonal axial diffusivity in sports-related concussion. The extent of significantly different WM regions decreased across time points and remained present primarily in the corpus callosum. Similar differences in axial kurtosis were found between the repetitive head impact and control groups. Other significant differences were seen at unrestricted return-to-play with lower radial kurtosis and intra-axonal diffusivity in those with sports-related concussion compared with the controls, mainly restricted to the posterior callosum.

**CONCLUSIONS:** This study highlights the fact that there are differences in diffusion microstructure measures that are present not only between football players with sports-related injuries and controls, but that there are also measurable differences between football players with repetitive head impacts and controls. This work reinforces previous work showing that the corpus callosum is specifically implicated in sports-related concussion and also suggests this to be true for repetitive head impacts.

**ABBREVIATIONS:** AK = axial kurtosis; AWF = axonal water fraction; CC = corpus callosum;  $D_{axon}$  = intra-axonal diffusivity;  $D_{e||}$  = extra-axonal axial diffusivity;  $D_{e\perp}$  = extra-axonal radial diffusivity; DKI = diffusional kurtosis imaging; FA = fractional anisotropy; HC = healthy controls; MD = mean diffusivity; MK = mean kurtosis; RHI = repetitive head impact; RK = radial kurtosis; SCAT3 = Sport Concussion Assessment Tool 3; SRC = sports-related concussion; TBSS = Tract-Based Spatial Statistics; WMTI = white matter tract integrity

Traumatic brain injury is a known risk factor for a host of neurodegenerative disorders,<sup>1</sup> and in recent times, there have

been growing concerns around potential risks related to sports-related concussion (SRC) and contact sport exposure to repetitive head impacts (RHIs) in our young athletes. There is mounting evidence that concussion and RHI in contact-sport athletes may predispose to long-term consequences, including serious neurologic sequelae such as chronic traumatic encephalopathy despite the lack of macroscopic brain injuries.<sup>2,3</sup> It is, thus, of increasing importance to understand the effects that SRC and RHI may have on brain tissue microstructure.

Advanced MR imaging provides one of the few windows into the human brain for detection of injury relating to concussion. In particular, investigators have used DTI to assess WM integrity in athletes with SRC, showing areas of abnormal WM fractional anisotropy (FA) and mean diffusivity (MD).<sup>4,5</sup> While DTI assumes Gaussian diffusion in biological tissue, diffusional kurtosis imaging (DKI)<sup>6</sup> has been used to detect non-Gaussian diffusion behavior as

Received January 6, 2022; accepted after revision April 4.

From the Department of Radiology (S.C., Y.W.L.), Center for Advanced Imaging Innovation and Research, and Department of Radiology (S.C., Y.W.L.), Bernard and Irene Schwartz Center for Biomedical Imaging, New York University Grossman School of Medicine, New York, New York; and Department of Electrical and Computer Engineering (J.C., T.L., Y.W.), New York University Tandon School of Engineering, Brooklyn, New York.

This work was supported by the National Institutes of Health grant Nos. NIH R01 NS119767-01A1, R01 NS039135-II, R21 NS090349, R56 NS119767, P41 EB017183; the Department of Defense, grant No. DoD PT190013; and the Leon Lowenstein Foundation.

Please address correspondence to Sohae Chung, PhD, 660 1st Ave, 4th floor, New York, NY 10016; e-mail: sohae.chung@nyulangone.org

Indicates open access to non-subscribers at www.ajnr.org

Indicates article with online supplemental data.

<http://dx.doi.org/10.3174/ajnr.A7522>

a reflective marker for microstructural heterogeneity and complexity of tissue, providing improved sensitivity to tissue microstructure. Increased kurtosis has been shown after SRC compared with matched contact-sport control athletes without SRC.<sup>7</sup> Given the inherently nonspecific nature of the empiric measures of DTI and DKI, more recent work has been done to study non-sports-related mild traumatic brain injury using compartment-specific WM models<sup>8</sup> in an attempt to describe biophysically meaningful microstructure after injury.<sup>9,10</sup> Specifically, WM tract integrity (WMTI) metrics, including axonal water fraction (AWF), intra-axonal diffusivity ( $D_{\text{axon}}$ ) along axons, and extra-axonal axial ( $D_{\text{e,||}}$ ) and extra-axonal radial ( $D_{\text{e,⊥}}$ ) diffusivities, can be derived from a straightforward, recently described standard model of multishell diffusion imaging to disentangle intra- and extra-axonal environments.<sup>8</sup> Several studies including animal validation<sup>11</sup> and in vivo human studies<sup>12–15</sup> have shown that WMTI metrics add specificity regarding underlying tissue microstructure to the empiric diffusion measures such as FA.

In this study, we hypothesized that there are subtle changes due to SRC as well as RHI exposure detectable with advanced diffusion imaging. Specifically, we sought to determine what, if any, effects there may be from SRC as well as RHI exposure encountered through routine collegiate-level contact-sport participation on brain microstructure. The data are available through the Federal Interagency Traumatic Brain Injury Research registry from the National Collegiate Athletic Association–Department of Defense Concussion Assessment, Research and Education (CARE) Consortium.<sup>16</sup>

## MATERIALS AND METHODS

### Study Population

Available data through the Federal Interagency Traumatic Brain Injury Research registry from the National Collegiate Athletic Association–Department of Defense Concussion Assessment, Research and Education (CARE) Consortium study were used in this study.<sup>16</sup> Participant school-level institutional review board approval and participant consent were obtained. Athletes with SRC within 48 hours and those without SRC during the 2016 to 2018 football seasons were studied. Inclusion criteria for this study were male football players as well as asymptomatic, non-contact-sport control athletes who had available multishell diffusion MR imaging data obtained on a 3T Magnetom Prisma scanner (Siemens). Scanner type was restricted to minimize data variability attributable to scanner hardware and software.

We studied a total of 78 collegiate athletes: 1) 24 football players within 48 hours of SRC (19.7 [SD, 1.1] years of age), 2) twenty-six football players with RHI exposure without a history of SRC during the study period (19.3 [SD, 1.2] years of age), and 3) twenty-eight non-contact-sport control athletes without RHI or a history of SRC (healthy controls [HC]; 19.7 [SD, 1.4] years of age). For all groups, symptom severity was assessed using the Sport Concussion Assessment Tool 3 (SCAT3). The non-contact-sport control group comprised asymptomatic (SCAT3<sup>17</sup> < 10)<sup>18</sup> non-contact-sport control male athletes. Non-contact-sport controls were members of the baseball ( $n = 17$ ), field event ( $n = 2$ ), and cross-country ( $n = 9$ ) teams. Longitudinal recovery trajectories for the SRC group were studied using the following 4 time points: 1) 24–48 hours after

injury, 2) asymptomatic and after passing initial clearance to begin the return-to-play protocol (asymptomatic), 3) seven days following unrestricted return-to-play, and 4) six months after injury. For comparison, the RHI and HC groups underwent MR imaging at similar time intervals matched with the subjects with SRC.

### MR Imaging Acquisition

Details of the MR imaging parameters can be found in Broglio et al.<sup>16</sup> In brief, MR images included here were all acquired on 3T Magnetom Prisma scanners. Diffusion imaging was performed with the following parameters:  $b$ -values = 1000, 2000 s/mm<sup>2</sup>, 30 diffusion directions, 8  $b=0$  images, FOV = 243 × 243 mm, matrix = 90 × 90, slices = 64, isotropic resolution = 2.7 mm, TR/TE = 7900/98 ms.

### Image Analyses

**Diffusion Image Processing.** Preprocessing steps included Marchenki-Pastur principal component analysis (MP-PCA) denoising,<sup>19</sup> Gibbs correction,<sup>20</sup> eddy current distortion, and motion correction<sup>21</sup> and outlier detection.<sup>22</sup> In-house image-processing software developed in Matlab R2019b (MathWorks) was used to generate parameter maps of DTI (FA, mean/axial/radial diffusivities), DKI (mean/axial/radial kurtosis [MK/AK/RK]), and WMTI metrics (AWF,  $D_{\text{axon}}$ ,  $D_{\text{e,||}}$ ,  $D_{\text{e,⊥}}$ ).

### Tract-Based Spatial Statistics

Tract-Based Spatial Statistics (TBSS) was used for voxelwise analyses.<sup>23</sup> Briefly, individual FA maps were affine-transformed to the FA template (Montreal Neurological Institute 152 space), and voxelwise statistics were performed on maximum FA values projected onto the WM skeleton. All parametric maps underwent unified transformations and processes. The WM skeleton was thresholded at FA = 0.2 for DTI and DKI metrics. For WMTI metrics, we restricted analysis to WM regions consisting primarily of single-fiber orientations (FA threshold = 0.4), as recommended.<sup>8</sup>

**ROI Analyses.** Post hoc subanalyses were performed in an attempt to separate the effects of SRC from RHI. Specifically, the corpus callosum (CC) was studied to understand the temporal evolution of SRC changes. ROIs of the genu, body, and splenium were generated on the basis of the ICBM-DTI-81 WM atlas labels<sup>24</sup> by nonlinearly registering each subject's FA map to the FA template.<sup>21</sup> A reversed warping procedure was performed to assign the atlas labels to each subject's space.<sup>21</sup> All ROIs were manually reviewed and edited if needed. For each ROI, the mean value was obtained only in voxels with FA ≥ 0.2 for DTI and DKI metrics and with FA ≥ 0.4 for WMTI metrics, as recommended.<sup>8</sup>

### Statistical Analyses

ANOVA was used to test group differences of SCAT3 total symptom severity scores as well as mean values within the ROIs at each time point with a Tukey post hoc pair-wise test for multiple comparisons using SPSS, Version 25 (IBM). Results were considered significant for  $P < .05$ , corrected for multiple comparisons. For TBSS, statistical tests were conducted with 5000 random permutations to identify statistically significant effects among groups.<sup>25</sup> The statistical significance level was set at  $P < .05$ , corrected for multiple comparisons by controlling the family-wise error rate with the threshold-free cluster enhancement option.<sup>26</sup>



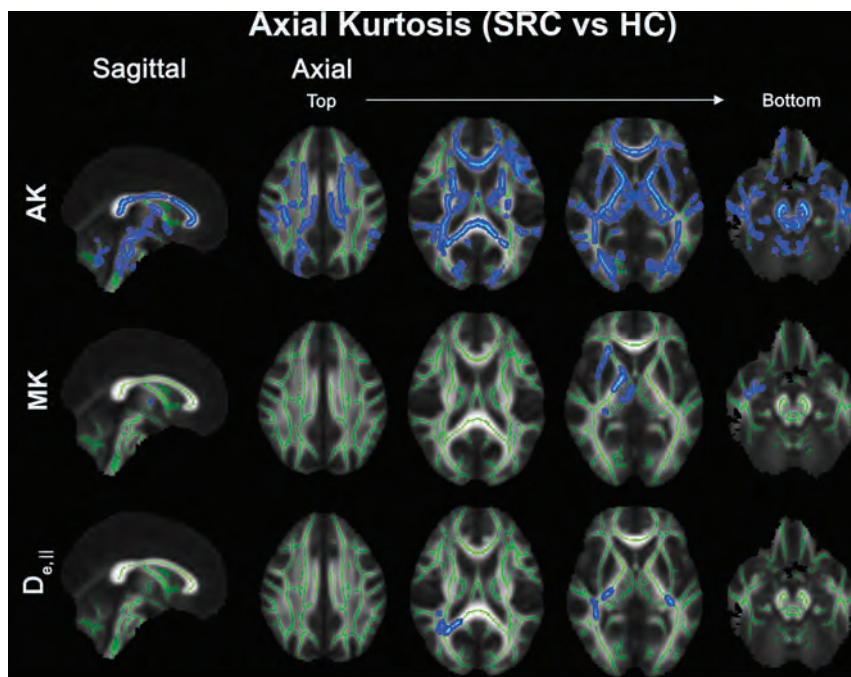


**FIG 1.** TBSS results comparing SRC and HC groups at time point 1 (24–48 hours postinjury for SRC; baseline for HC). Top, significant voxels (blue) demonstrating increased AK in the SRC group are present diffusely throughout the WM. Increased MK (middle) and  $D_{e||}$  (bottom) in the SRC group are also seen in more focal areas of middle posterior WM regions including the external capsule, posterior limb of the internal capsule, cerebral peduncle, uncinate fasciculus, inferior longitudinal fasciculus, posterior thalamic radiation, retrolenticular part of internal capsule, and splenium of the corpus callosum. The significance level was  $P < .05$ , corrected for multiple comparisons by controlling the family-wise error rate. Significant voxels were enlarged using TBSS fill (FSL command; [https://fsl.fmrib.ox.ac.uk/fsl/fslwiki/TBSS/UserGuide#Displaying\\_TBSS\\_Results](https://fsl.fmrib.ox.ac.uk/fsl/fslwiki/TBSS/UserGuide#Displaying_TBSS_Results)) for illustrative purposes and were overlapped onto the mean FA skeleton (green).

## RESULTS

The Online Supplemental Data summarize the characteristics of the study cohorts across time points. Briefly, the average time since injury was 8.1 (SD, 5.6) days to an asymptomatic state (time point 2) and 27 (SD, 12.5) days to unrestricted return-to-play (time point 3). Subjects with SRC had significantly higher SCAT3 total symptom severity scores than both the RHI and HC groups at time point 1 (Tukey test,  $P < .001$ ), but there were no significant differences at other time points. No gross intracranial abnormalities were detected. We found no significant differences between the SRC and RHI groups from both TBSS and ROI analyses.

### Football Players with SRC versus Non-Contact-Sport Healthy Controls

TBSS analysis revealed diffusely higher AK in athletes with SRC compared with the HC group at time point 1 (Fig 1). Additionally, there were some focal areas that demonstrated significantly higher MK and  $D_{e||}$  in the SRC group: namely, the middle-posterior WM regions including the external capsule, posterior limb of the internal capsule, cerebral peduncle, uncinate fasciculus, inferior longitudinal fasciculus, posterior thalamic radiation, retrolenticular part of internal capsule, and splenium of the CC. The extent of WM regions that showed significant differences in AK between the SRC

and HC groups decreased by the fourth time point (6-month follow-up) (Fig 2), though remains present, located almost entirely within the CC (Fig 2A). In addition, significantly different WM regions in MK and  $D_{e||}$  observed at time point 1 (Fig 1) were not seen at later time points. The other significant between-group differences were seen at unrestricted return-to-play (time point 3) with lower RK and  $D_{axon}$  in the SRC group compared with the HC group, mainly restricted to the posterior callosum (Online Supplemental Data). The results of the ROI analyses in the CC regions were consistent with the TBSS results, showing significantly higher AK across time points (Tukey test,  $P < .05$ ). Moreover, significantly lower RK (Tukey test,  $P = .022$ ) in the body of the CC and significantly lower  $D_{axon}$  (Tukey test,  $P = .045$ ) in the body and splenium of the CC in the SRC group were present only at time point 3 compared with the HC group, supporting the TBSS results (Online Supplemental Data).

### Nonconcussed Football Players versus Non-Contact-Sport Healthy Controls

We found widespread differences in AK between the RHI and HC groups as well as diffuse differences in MK, with higher

kurtosis measures in RHI (Fig 3). In addition, focal areas demonstrated higher  $D_{e||}$  and AWF in the RHI group compared with the HC group, including the CC, superior/anterior/posterior corona radiata, superior longitudinal fasciculus, posterior limb of the internal capsule, retrolenticular part of the internal capsule, posterior thalamic radiation, and cerebral peduncle. The ROI analysis results were also in accordance with the TBSS results, showing significantly higher MK (Tukey test,  $P = .047$ ) as well as a trend toward higher AK in the genu (Tukey test,  $P = .098$ ) and splenium (Tukey test,  $P = .053$ ). Significantly higher  $D_{e||}$  in the body of the CC (Tukey test,  $P = .016$ ) and a trend toward higher AWF in the splenium (Tukey test,  $P = .067$ ) were also observed in the RHI group compared with the HC groups.

## DISCUSSION

In this study, we demonstrate extensive and diffuse WM differences in diffusion metrics, particularly AK, not only between concussed football athletes within 48 hours of injury (SRC) and baseline non-contact-sport control subjects (HC), but also related and widespread differences between nonconcussed football athletes (RHI) and HC subjects. The findings suggest that some of the diffuse measurable microstructural changes observed in the SRC group may relate not to sports-related concussion but to a background of exposure to repeat subconcussive head impacts. Similar

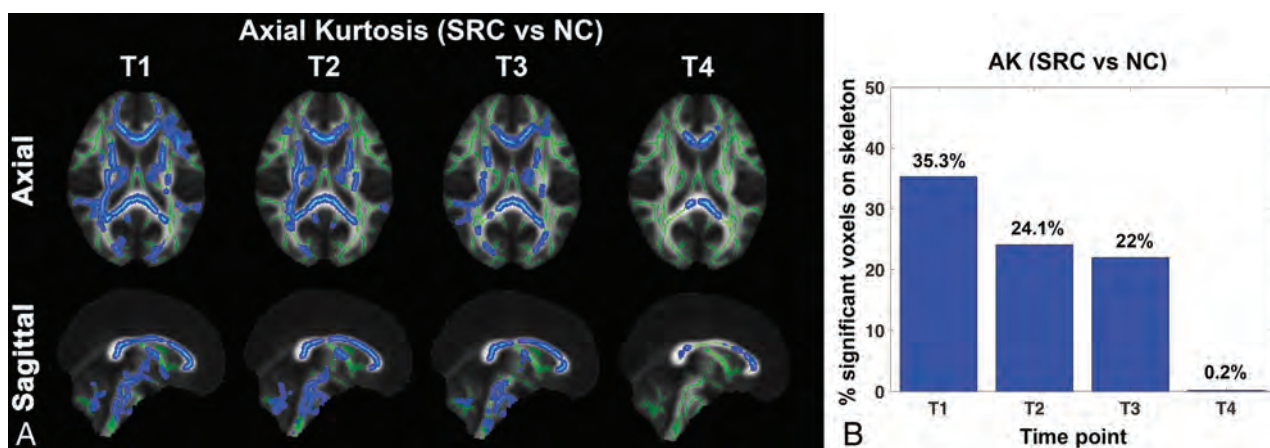


**FIG 2.** Evolution of differences in AK between the SRC and HC groups across 4 time points. A, Maps show regions along the WM skeleton that demonstrate a significant difference (blue) in AK between the SRC and HC groups across 4 time points (T1–T4). B, Corresponding bar graphs show the percentage of significantly different voxels on the skeleton across time points. The extent of significantly different WM regions decreases across time points, remaining present primarily within the corpus callosum at time point 4.

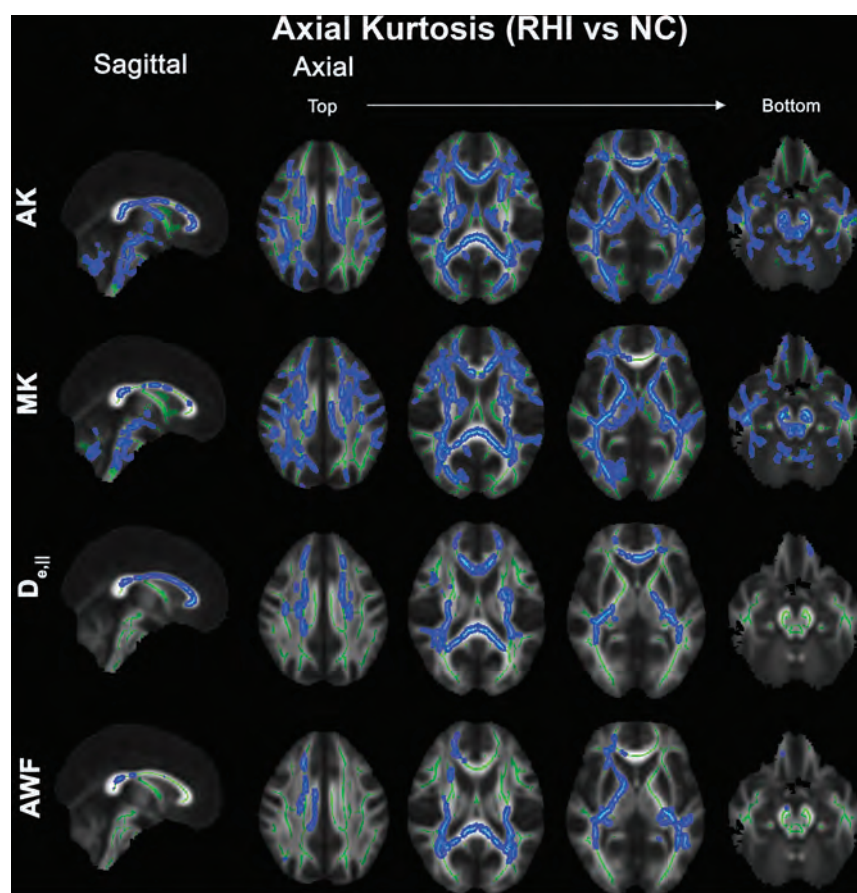


**FIG 3.** TBSS results comparing the RHI and HC groups (time point 1): Clusters of voxels (blue) demonstrating significantly higher AK and MK in the RHI group compared with the HC group are also present diffusely across the entire WM. Additionally, increased  $D_{e||}$  and AWF in the RHI group are seen in focal areas of WM regions including the corpus callosum, corona radiata, superior longitudinal fasciculus, posterior limb of the internal capsule, retrolenticular part of the internal capsule, posterior thalamic radiation, and cerebral peduncle. The significance level was  $P < .05$ , corrected for multiple comparisons by controlling the family-wise error rate.

changes of kurtosis have been reported previously in nonconcussed young football players with cumulative head impact exposure.<sup>27</sup> In addition, the affected WM regions in the SRC group compared with non-contact-sport controls decreased across time points, suggesting partial recovery of microstructural changes during the study period (Fig 2B). Most interesting, persistent higher AK in the SRC group was observed compared with the non-contact-sport controls mainly in the CC on 6-month follow-up scans (Fig 2A), suggesting longer-term persistence of microstructural changes associated with SRC. Although AK is not specific, it reflects tissue microstructural complexity along the long axis of the axon and has been previously associated with changes such as reactive astrogliosis<sup>28</sup> as well as frank axon damage.<sup>13</sup>

We observed few scattered, focal areas of higher  $D_{e||}$  in the SRC group compared with the non-contact-sport controls only at the acute stage (Fig 1); however, in the RHI group, higher  $D_{e||}$  was persistently observed across all time points compared with the non-contact-sport controls (Online Supplemental Data). Previous studies have reported  $D_{e||}$  to be sensitive to changes along the axons in the extra-axial space due to gliosis, loss of oligodendrocytes, extracellular inflammation, and vasogenic edema.<sup>15</sup>



Of note, these individuals with RHI, unlike the players with SRC who were taken out of active play, were exposed to repeat head impacts throughout the study period. Our findings of the elevated  $D_{e||}$  accompanied by the increases in AK and MK in these individuals indicate the presence of complex microstructural alterations, localizing to the extracellular space, that seem to relate to exposure to repeat head impacts. While similar findings were present at the initial time point in the SRC group, these were no longer present at later time points after a recuperation period without RHI exposure, suggesting that at least some of the white matter microstructural changes associated with RHI exposure may be reversible early on.

We also observed decreased RK and  $D_{axon}$  and increased AK in the SRC group compared with non-contact-sport controls, present only at time point 3 when the players with SRC were cleared to return to play. These observations were present mainly in the mid-posterior CC (Online Supplemental Data). Both increased AK and decreased RK have previously been reported by Zhuo et al<sup>28</sup> in a controlled compact injury rat model, similarly in the subacute stage after injury (7 days postinjury). These findings support the notion that some changes may become apparent in the subacute phase after the initial insult and that diffusion characteristics relating to the intra-axonal compartment itself are affected. Changes in  $D_{axon}$  have been attributed to a range of pathologies, including axonal disruption as well as axonal injuries such as beading, varicosity, undulation, and swelling.<sup>29–31</sup> Decreases in  $D_{axon}$  have previously been observed in the setting of ischemic brain injury<sup>13</sup> as well as in subacute civilian, non-sports-related mild traumatic brain injury.<sup>9</sup>

From biomedical modeling of torsional and stretch forces after head impact, it is known that the CC is an at-risk structure.<sup>32,33</sup> Our findings are in keeping with prior evidence that the CC is one of the most affected WM regions after SRC, and this result was also the case in our group exposed to RHI.<sup>5,9,34,35</sup> The CC is the largest transhemispheric WM structure, composed of several important anatomically and functionally distinct WM tracts. Our results reinforce the idea that WM injury, particularly affecting the CC, is mechanistically important in SRC and also suggest that this is important in RHI as well.

Our findings add to previously published results from a larger cohort from the National Collegiate Athletic Association–Department of Defense Concussion Assessment, Research and Education (CARE) Consortium study.<sup>4,5,36</sup> The current study focuses on diffusion MR imaging microstructural changes; specifically here, we study the subset of the total cohort who underwent multishell diffusion MR imaging accommodating compartment diffusion modeling as discussed in the Materials and Methods section. We also restricted our study by scanner type and sport to minimize data variability relating to these factors.<sup>37,38</sup> Moreover, the main difference between the current study and previous studies<sup>4,5,36</sup> is that we have used compartment-specific diffusion parameters to try to understand potential changes in the underlying tissue microstructure. Of note, in this restricted cohort, we found no significant differences in conventional DTI metrics such as FA or MD that were present in previous studies, possibly due to use of a smaller subset of the cohort.<sup>39</sup>

There are several limitations to this study. First, study time points were based on symptomatology and clinical status rather than a predefined follow-up interval, prohibiting parsing of the

precise temporal evolution of diffusion MR imaging changes relating to injury and/or exposure. The range in the length of the symptomatic period after injury is, however, reflective of the natural history of SRC. Second, the study includes relatively small sample sizes, which can reduce statistical power, particularly at later time points (time points 3 and 4). The smaller cohort size may have also explained why we did not see changes in FA and MD, which others have previously shown.<sup>4,5,36</sup> Finally, we used standard TBSS methods that are well-documented, but TBSS is sensitive to maximal deviations in diffusion metrics because of the use of maximum values projected onto the white matter skeleton. The benefit of such an approach is that it reduces the need for image smoothing and alleviates any residual misalignment.<sup>40</sup> In this study, we used both TBSS and post hoc ROI analyses to assess WM changes to look for consistencies between the methods.

## CONCLUSIONS

There are differences not only in concussed football athletes but also in nonconcussed football athletes compared with non-contact-sport control athletes in terms of diffusion microstructure measures. These findings reinforce previous work showing that the corpus callosum is specifically implicated in football athletes with SRC and also suggest this to be true for football athletes with RHI. Further study on the effect of RHI across time may provide insight into the temporal dynamics of injury in both SRC and athletes who may be exposed to RHI.

**Disclosure forms** provided by the authors are available with the full text and PDF of this article at [www.ajnr.org](http://www.ajnr.org).

## REFERENCES

1. Chauhan NB. **Chronic neurodegenerative consequences of traumatic brain injury.** *Restor Neurol Neurosci* 2014;32:337–65 CrossRef Medline
2. Committee on Sports-Related Concussions in Youth; Board on Children, Youth, and Families; Institute of Medicine; National Research Council. **Consequences of repetitive head impacts and multiple concussions.** In: Graham R, Rivara FP, Ford MA, et al; *Sports-Related Concussions in Youth: Improving the Science, Changing the Culture.* National Academies Press (US); 2014
3. Alisco ML, Stern RA. **The long-term consequences of repetitive head impacts: chronic traumatic encephalopathy.** *Handb Clin Neurol* 2019;167:337–55 CrossRef Medline
4. Mustafi SM, Harezlak J, Koch KM, et al. **Acute white-matter abnormalities in sports-related concussion: a diffusion tensor imaging study from the NCAA-DoD CARE Consortium.** *J Neurotrauma* 2018;35:2653–64 CrossRef Medline
5. Wu YC, Harezlak J, Elsaid NM, et al. **Longitudinal white-matter abnormalities in sports-related concussion: a diffusion MRI study.** *Neurology* 2020;95:e781–92 CrossRef Medline
6. Jensen JH, Helpert JA, Ramani A, et al. **Diffusional kurtosis imaging: the quantification of non-Gaussian water diffusion by means of magnetic resonance imaging.** *Magn Reson Med* 2005;53:1432–40 CrossRef Medline
7. Lancaster MA, Olson DV, McCrea MA, et al. **Acute white matter changes following sport-related concussion: a serial diffusion tensor and diffusion kurtosis tensor imaging study.** *Hum Brain Mapp* 2016;37:3821–34 CrossRef Medline
8. Fieremans E, Jensen JH, Helpert JA. **White matter characterization with diffusional kurtosis imaging.** *Neuroimage* 2011;58:177–88 CrossRef Medline



9. Chung S, Fieremans E, Wang X, et al. **White matter tract integrity: an indicator of axonal pathology after mild traumatic brain injury.** *J Neurotrauma* 2018;35:1015–20 CrossRef Medline
10. Grossman EJ, Kirov II, Gonen O, et al. **N-acetyl-aspartate levels correlate with intra-axonal compartment parameters from diffusion MRI.** *Neuroimage* 2015;118:334–43 CrossRef Medline
11. Jelescu IO, Zurek M, Winters KV, et al. **In vivo quantification of demyelination and recovery using compartment-specific diffusion MRI metrics validated by electron microscopy.** *Neuroimage* 2016;132:104–14 CrossRef Medline
12. Jelescu IO, Veraart J, Adisetiyo V, et al. **One diffusion acquisition and different white matter models: how does microstructure change in human early development based on WMTI and NODDI?** *Neuroimage* 2015;107:242–56 CrossRef Medline
13. Hui ES, Fieremans E, Jensen JH, et al. **Stroke assessment with diffusional kurtosis imaging.** *Stroke* 2012;43:2968–73 CrossRef Medline
14. de Kouchkovsky I, Fieremans E, Fleysher L, et al. **Quantification of normal-appearing white matter tract integrity in multiple sclerosis: a diffusion kurtosis imaging study.** *J Neurol* 2016;263:1146–55 CrossRef Medline
15. Fieremans E, Benitez A, Jensen JH, et al. **Novel white matter tract integrity metrics sensitive to Alzheimer disease progression.** *AJNR Am J Neuroradiol* 2013;34:2105–12 CrossRef Medline
16. Broglio SP, McCrea M, McAllister T, et al; CARE Consortium Investigators. **A national study on the effects of concussion in collegiate athletes and US military service academy members: the NCAA-DoD Concussion Assessment, Research and Education (CARE) Consortium structure and methods.** *Sports Med* 2017;47:1437–51 CrossRef Medline
17. Guskiewicz KM, Register-Mihalik J, McCrory P, et al. **Evidence-based approach to revising the SCAT2: introducing the SCAT3.** *Br J Sports Med* 2013;47:289–93 CrossRef Medline
18. Chen JK, Johnston KM, Collie A, et al. **A validation of the post concussion symptom scale in the assessment of complex concussion using cognitive testing and functional MRI.** *J Neurol Neurosurg Psychiatry* 2007;78:1231–38 CrossRef Medline
19. Veraart J, Fieremans E, Novikov DS. **Diffusion MRI noise mapping using random matrix theory.** *Magn Reson Med* 2016;76:1582–93 CrossRef Medline
20. Kellner E, Dhital B, Kiselev VG, et al. **Gibbs-ringing artifact removal based on local subvoxel-shifts.** *Magn Reson Med* 2016;76:1574–81 CrossRef Medline
21. Smith SM, Jenkinson M, Woolrich MW, et al. **Advances in functional and structural MR image analysis and implementation as FSL.** *Neuroimage* 2004;23(Suppl 1):S208–19 CrossRef Medline
22. Collier Q, Veraart J, Jeurissen B, et al. **Iterative reweighted linear least squares for accurate, fast, and robust estimation of diffusion magnetic resonance parameters.** *Magn Reson Med* 2015;73:2174–84 CrossRef Medline
23. Smith SM, Jenkinson M, Johansen-Berg H, et al. **Tract-based spatial statistics: voxelwise analysis of multi-subject diffusion data.** *Neuroimage* 2006;31:1487–1505 CrossRef Medline
24. Mori S, Oishi K, Jiang H, et al. **Stereotaxic white matter atlas based on diffusion tensor imaging in an ICBM template.** *Neuroimage* 2008;40:570–82 CrossRef Medline
25. Winkler AM, Ridgway GR, Webster MA, et al. **Permutation inference for the general linear model.** *Neuroimage* 2014;92:381–97 CrossRef Medline
26. Smith SM, Nichols TE. **Threshold-free cluster enhancement: addressing problems of smoothing, threshold dependence and localisation in cluster inference.** *Neuroimage* 2009;44:83–98 CrossRef Medline
27. Davenport EM, Apkarian K, Whitlow CT, et al. **Abnormalities in diffusional kurtosis metrics related to head impact exposure in a season of high school varsity football.** *J Neurotrauma* 2016;33:2133–46 CrossRef Medline
28. Zhuo J, Xu S, Proctor JL, et al. **Diffusion kurtosis as an in vivo imaging marker for reactive astrogliosis in traumatic brain injury.** *Neuroimage* 2012;59:467–77 CrossRef Medline
29. Budde MD, Frank JA. **Neurite beading is sufficient to decrease the apparent diffusion coefficient after ischemic stroke.** *Proc Natl Acad Sci U S A* 2010;107:14472–77 CrossRef Medline
30. Hill CS, Coleman MP, Menon DK. **Traumatic axonal injury: mechanisms and translational opportunities.** *Trends Neurosci* 2016;39:311–24 CrossRef Medline
31. Tang-Schomer MD, Johnson VE, Baas PW, et al. **Partial interruption of axonal transport due to microtubule breakage accounts for the formation of periodic varicosities after traumatic axonal injury.** *Exp Neurol* 2012;233:364–72 CrossRef Medline
32. McAllister TW, Ford JC, Ji S, et al. **Maximum principal strain and strain rate associated with concussion diagnosis correlates with changes in corpus callosum white matter indices.** *Ann Biomed Eng* 2012;40:127–40 CrossRef Medline
33. Patton DA, McIntosh AS, Kleiven S. **The biomechanical determinants of concussion: finite element simulations to investigate tissue-level predictors of injury during sporting impacts to the unprotected head.** *J Appl Biomech* 2015;31:264–68 CrossRef Medline
34. Lancaster MA, Meier TB, Olson DV, et al. **Chronic differences in white matter integrity following sport-related concussion as measured by diffusion MRI: 6-month follow-up.** *Hum Brain Mapp* 2018;39:4276–89 CrossRef Medline
35. Rutgers DR, Fillard P, Paradot G, et al. **Diffusion tensor imaging characteristics of the corpus callosum in mild, moderate, and severe traumatic brain injury.** *AJNR Am J Neuroradiol* 2008;29:1730–35 CrossRef Medline
36. Brett BL, Wu YC, Mustafi SM, et al. **The association between persistent white-matter abnormalities and repeat injury after sport-related concussion.** *Front Neurol* 2019;10:1345 CrossRef Medline
37. Shokouhi M, Barnes A, Suckling J, et al. **Assessment of the impact of the scanner-related factors on brain morphometry analysis with Brainvisa.** *BMC Med Imaging* 2011;11:23 CrossRef Medline
38. Selassie AW, Wilson DA, Pickelsimer EE, et al. **Incidence of sport-related traumatic brain injury and risk factors of severity: a population-based epidemiologic study.** *Ann Epidemiol* 2013;23:750–56 CrossRef Medline
39. Jelescu IO, Budde MD. **Design and validation of diffusion MRI models of white matter.** *Front Phys* 2017;28:61 CrossRef Medline
40. Bach M, Laun FB, Leemans A, et al. **Methodological considerations on tract-based spatial statistics (TBSS).** *Neuroimage* 2014;100:358–69 CrossRef Medline

# Microinfarcts in the Deep Gray Matter on 7T MRI: Risk Factors, MRI Correlates, and Relation to Cognitive Functioning—The SMART-MR Study

R. Ghaznawi, M.H.T. Zwartbol, J. de Bresser, H.J. Kuijff, K.L. Vincken, I. Rissanen, M.I. Geerlings, and J. Hendrikse, on behalf of the UCC-SMART-Study Group



## ABSTRACT

**BACKGROUND AND PURPOSE:** The clinical relevance of cortical microinfarcts has recently been established; however, studies on microinfarcts in the deep gray matter are lacking. We examined the risk factors and MR imaging correlates of microinfarcts in the deep gray matter on 7T MR imaging and their relation to cognitive functioning.

**MATERIALS AND METHODS:** Within the Second Manifestations of ARterial disease–Magnetic Resonance (SMART-MR) study, 213 patients (mean age, 68 [SD, 8] years) had a risk-factor assessment, 7T and 1.5T brain MR imaging, and a cognitive examination. Microinfarcts on 7T MR imaging were defined as lesions of <5 mm. Regression models were used to examine the age-adjusted associations among risk factors, MR imaging markers, and microinfarcts. Cognitive function was summarized as composite and domain-specific z scores.

**RESULTS:** A total of 47 microinfarcts were found in 28 patients (13%), most commonly in the thalamus. Older age, history of stroke, hypertension, and intima-media thickness were associated with microinfarcts. On 1.5T MR imaging, cerebellar infarcts (relative risk = 2.75; 95% CI, 1.4–5.33) and lacunes in the white (relative risk = 3.28; 95% CI, 3.28–6.04) and deep gray matter (relative risk = 3.06; 95% CI, 1.75–5.35) were associated with microinfarcts, and on 7T MR imaging cortical microinfarcts (relative risk = 2.33; 95% CI, 1.32–4.13). Microinfarcts were also associated with poorer global cognitive functioning (mean difference in the global z score between patients with multiple microinfarcts versus none = −0.97; 95% CI, −1.66 to −0.28,  $P = .006$ ) and across all cognitive domains.

**CONCLUSIONS:** Microinfarcts in the deep gray matter on 7T MR imaging were associated with worse cognitive functioning and risk factors and MR imaging markers of small-vessel and large-vessel disease. Our findings suggest that microinfarcts in the deep gray matter may represent a novel imaging marker of vascular brain injury.

**ABBREVIATIONS:** RR = relative risk; STRIVE = STandards for Reporting Vascular changes on nEuroimaging; WMH = white matter hyperintensity

Cerebral microinfarcts are a common neuropathologic finding in older individuals.<sup>1–3</sup> Conventionally, they are defined as

small, ischemic lesions that are not visible to the naked eye on gross pathology and can range from 100  $\mu$ m to a few millimeters.<sup>2</sup> Although small, microinfarcts often occur in large numbers, and their effect is thought to extend well beyond their lesion boundaries.<sup>2,4</sup> Associations with cognitive impairment and dementia have been reported, and microinfarcts may play an important role in silent cerebrovascular disease.<sup>4</sup>

Recently, cortical microinfarcts have been identified in vivo using 7T MR imaging.<sup>2</sup> Subsequent neuroimaging studies reported that the causes of cortical microinfarcts are heterogeneous, and their occurrence has been associated with both small-vessel and large-vessel disease, microemboli, and hypoperfusion.<sup>5–8</sup> The clinical importance of cortical microinfarcts has been demonstrated by their association with worse cognitive functioning.<sup>9</sup> In vivo data on the prevalence and risk factors of microinfarcts in the deep gray matter, however, are lacking. Moreover, it is not known to what extent microinfarcts in the deep gray matter are related to cognitive functioning. Previous histopathologic studies reported that microinfarcts as well as lacunes in the deep gray matter were associated

Received October 19, 2021; accepted after revision March 24, 2022.

From the Department of Radiology (R.G., M.H.T.Z., J.H.), Julius Center for Health Sciences and Primary Care (R.G., I.R., M.I.G.), and Image Sciences Institute (H.J.K., K.L.V.), University Medical Center Utrecht and Utrecht University, Utrecht, the Netherlands; and Department of Radiology (J.d.B.), Leiden University Medical Center, Leiden, the Netherlands.

The Netherlands Organization for Scientific Research–Medical Sciences source had no role in the design, data collection, data analyses, and data interpretation of the study or writing of the report.

Funding for this article was received as part of a grant from the Netherlands Organization for Scientific Research–Medical Sciences (project No. 904-65-095) and the European Research Council under the European Union's Horizon 2020/ERC grant agreement No. 637024 and No. 66681 (SVDs@target).

Please address correspondence to Mirjam I. Geerlings, PhD, University Medical Center Utrecht, Julius Center for Health Sciences and Primary Care, P.O. Box 85500, Stratenum 6.131, 3508 GA Utrecht, the Netherlands; e-mail: m.geerlings@umcutrecht.nl

Indicates open access to non-subscribers at [www.ajnr.org](http://www.ajnr.org)

Indicates article with online supplemental data.

<http://dx.doi.org/10.3174/ajnr.A7512>

with worse antemortem cognitive performance.<sup>10-12</sup> Identifying the risk factors and MR imaging markers associated with microinfarcts in the deep gray matter is important because these may provide clues to their underlying etiology and potential targets for intervention. Examining the association with cognitive functioning is important because it will provide evidence on whether microinfarcts in the deep gray matter are structural correlates of impaired cognitive performance.

In the current study, we examined the frequency and distribution of microinfarcts in the caudate nucleus, lentiform nucleus, and thalamus on 7T MR imaging in a large sample of older individuals with a history of arterial disease. In addition, we examined whether microinfarcts in the deep gray matter were associated with risk factors, MR imaging markers of cerebrovascular disease, and cognitive functioning.

## **MATERIALS AND METHODS**

### **Study Population**

Data were used from the Second Manifestations of ARterial disease-Magnetic Resonance (SMART-MR) study, a prospective cohort study at the University Medical Center Utrecht with the aim of investigating risk factors and consequences of brain changes on MR imaging in patients with symptomatic atherosclerotic disease.<sup>13</sup> In brief, between 2001 and 2005, thirteen hundred nine middle-aged and older adults newly referred to the University Medical Center Utrecht for treatment of symptomatic atherosclerotic disease (coronary artery disease, cerebrovascular disease, peripheral arterial disease, or abdominal aortic aneurysm) were included for baseline measurements. During a 1-day visit to our medical center, a physical examination, ultrasonography of the carotid arteries to measure the intima-media thickness (millimeters), blood and urine sampling, neuropsychological assessment, and 1.5T brain MR imaging were performed. Height and weight were measured, and the body mass index (kilograms/square meter) was calculated. Questionnaires were used for the assessment of demographics, risk factors, medical history, medication use, and cognitive and physical functioning.

Of the 1309 individuals included, 754 had follow-up measurements after an average of 4 years between January 2006 and May 2009. From November 2013, all patients alive were invited for a second follow-up, including a 7T brain MR imaging. Of the 329 individuals included between November 2013 and October 2017, two hundred thirteen had 7T MR imaging, and these patients formed the current study sample. A participation flow chart of the SMART-MR study is shown in the Online Supplemental Data.

In the present study, we used the 1.5T brain MR imaging, cognitive functioning, and vascular risk factor data obtained during follow-up. Due to logistical reasons, however, the 1.5T brain MR imaging and cognitive function measurements were obtained before the 7T brain MR imaging in 97 patients (median, 1.5 years; range, 0.6–2.7 years), whereas in 116 patients, these examinations were obtained on the same day. Also, vascular risk factor assessment was performed before the 7T brain MR imaging in 163 patients (median, 2.3 years; range, 0.6–9.4 years), whereas in 50 patients, vascular risk factors were obtained concurrently with the 7T brain MR imaging.

The SMART-MR study was approved by the medical ethics committee of the University Medical Center Utrecht according to the guidelines of the Declaration of Helsinki of 1975, and written informed consent was obtained from all patients.

### **Vascular Risk Factors**

Methods of measuring vascular risk factors are described in the Online Supplemental Data.

### **MR Imaging Protocol**

High-field imaging of the brain was performed on a whole-body 7T MR system (Philips Healthcare) with a volume transmit and 32-channel receive head coil (Nova Medical). Conventional MR imaging of the brain was performed on a 1.5T whole-body system (Gyrosan ACS-NT; Philips Healthcare). The 7T and 1.5T scan protocols are described in the Online Supplemental Data.

### **Assessment of MR Imaging Markers of Cerebrovascular Disease**

Brain infarcts (cortical, cerebellar, or brainstem), lacunes of presumed vascular origin, and white matter hyperintensity (WMH) and brain volumes were determined using 1.5T MR imaging data. Cortical microinfarcts and cerebral microbleeds were rated on 7T MR imaging data due to the enhanced conspicuity of these lesions at higher field strengths.<sup>14,15</sup> All ratings were performed blinded to patient characteristics.

Brain infarcts (cortical, cerebellar, or brainstem) and lacunes were visually rated by an experienced rater (M.H.T.Z.) with 6 years of experience in neuroradiology on the T1-weighted, T2-weighted, and FLAIR sequences of the 1.5T MR images. Lacunes were rated according to the STandards for ReportIng Vascular changes on nEuroimaging (STRIVE) criteria as round or ovoid, subcortical, fluid-filled cavities (signal similar to CSF) of 3–15 mm in diameter in the territory of 1 perforating arteriole.<sup>16</sup> Uncertain lesions were discussed during a consensus meeting (M.H.T.Z.) to reach agreement.

WMH and brain volumes were obtained using an automated segmentation program on the T1-weighted, FLAIR, and T1-weighted inversion recovery sequences of the 1.5T MR images. A probabilistic segmentation technique was performed with k-nearest neighbor classification, distinguishing gray matter, white matter, CSF, and lesions.<sup>17</sup> Brain infarcts, including lacunes and their hyperintense rim, were manually segmented. All WMH segmentations were visually checked by an investigator (R.G.) using an image-processing framework (MeVisLab 2.7.1; MeVis Medical Solutions) to ensure that brain infarcts were correctly removed from the WMH segmentations.

Periventricular WMH were defined as adjacent to or within 1 cm of the lateral ventricles, and deep WMHs were defined as located in the deep white matter tracts that may or may not have adjoined the periventricular WMH. Total brain volume was calculated by summing the volumes of gray matter, white matter, total WMH, and, if present, the volumes of brain infarcts. Total intracranial volume was calculated by summing the CSF volume and total brain volume.

Phase-contrast MR angiography was used to measure total CBF because this method has been demonstrated to be a fast,



**Table 1: Frequency of patients with microinfarcts and with infarcts of  $\geq 5$  mm in the deep gray matter on 7T MR imaging**

Microinfarct (<5 mm)	Infarct $\geq 5$ mm		
	No	Yes	Total
No	171	14	185
Yes	16	12	28
Total	187	26	213

reproducible, and noninvasive method to measure total CBF in large cohorts.<sup>18</sup> Previous studies established that phase-contrast MR angiography correlates well with arterial spin-labeling perfusion MR imaging, though estimates tend to be somewhat higher and more variable than arterial spin-labeling perfusion MR imaging.<sup>19</sup> Postprocessing of the CBF measurements was performed by 1 investigator (M.H.T.Z.). The flow through the basilar artery and the left and right internal carotid arteries was summed to calculate the total CBF (milliliters/minute). Total CBF was expressed per 100 mL of brain parenchymal volume to obtain parenchymal CBF. Cortical microinfarcts were visually rated by a rater (M.H.T.Z.) on the 3D T1-weighted, 3D T2-weighted, and 3D FLAIR sequences of the 7T MR imaging scans according to criteria previously described.<sup>2</sup> Cerebral microbleeds were rated by a rater (M.H.T.Z.) using the minimum-intensity-projection images and source images of the 7T SWI sequence. Microbleeds were labeled as lobar or deep using the Microbleed Anatomical Rating Scale.<sup>20</sup>

We considered cortical, cerebellar, and brainstem infarcts rated on 1.5T MR imaging as markers of large-vessel disease,<sup>21</sup> whereas lacunes of presumed vascular origin, WMH, and microbleeds were considered markers of small-vessel disease, consistent with the STRIVE criteria.<sup>16</sup>

### Assessment of Cognitive Functioning

All patients underwent neuropsychological assessment for memory, executive functioning, information processing speed, and working memory. The tests used to assess each of these cognitive domains are described in the Online Supplemental Data. Domain-specific  $z$  scores were calculated by converting raw test scores to standardized  $z$  scores and averaging these for each domain prior to the final  $z$  transformation. A global cognitive functioning composite  $z$  score was calculated by standardizing the averaged domain-specific  $z$  scores.

### Assessment of Microinfarcts in the Deep Gray Matter

First, all available 7T MR imaging scans were screened by an experienced neuroradiologist. All lesions hypointense on T1-weighted images, hyperintense on T2-weighted images, and either hyperintense or hypointense with a hyperintense rim on FLAIR images consistent with the imaging criteria set forth in our previous work<sup>14</sup> were rated as possible microinfarcts. The lesions were restricted to the caudate nucleus, lentiform nucleus, or thalamus and not appearing as a perivascular space, artery, vein, or microbleed on the SWI sequence. In addition, the lesion had to be detectable in the axial, coronal, and sagittal views. Uncertain lesions were discussed during a consensus meeting to reach agreement. Next, all identified possible microinfarcts were inspected by an investigator (R.G.) using MR imaging software, and the largest diameter of

each lesion was determined on the FLAIR sequence. Lesions of  $< 5$  mm in their largest diameter were accepted as microinfarcts because this value has been suggested by previous studies on cortical microinfarcts.<sup>6,22–26</sup> The presence and number of lesions of  $\geq 5$  mm in the deep gray matter were also recorded because these may act as potential confounders in the relation between microinfarcts and cognitive functioning.

### Statistical Analysis

First, vascular risk factors and MR imaging markers of cerebrovascular disease were calculated in patients with and without microinfarcts in the deep gray matter on 7T MR imaging and in the entire study sample. Second, relative risks (RRs) for the presence of microinfarcts in the deep gray matter were estimated for vascular risk factors and MR imaging markers of cerebrovascular disease using log-binomial regression, adjusted for age. For continuous variables, a relative risk of the presence of microinfarcts was estimated for a 1 SD increase. For dichotomous variables, a relative risk for microinfarcts was calculated for the presence of a vascular risk factor or MR imaging marker. Third, to examine the association between microinfarcts in the deep gray matter and cognitive functioning, ANCOVA was used to estimate age- and education level-adjusted cognitive functioning  $z$  scores for patients without microinfarcts, with a single microinfarct, and with multiple microinfarcts. Age and education level were entered as covariates because these represent the most important potential confounders in the relation between microinfarcts and cognitive functioning.

We repeated the abovementioned analyses with additional adjustment for the number of infarcts of  $\geq 5$  mm in the deep gray matter on 7T MR imaging. Statistical significance was set at a  $P < .05$ .

## RESULTS

A total of 47 deep gray matter microinfarcts (caudate nucleus,  $n = 17$ ; lentiform nucleus,  $n = 9$ ; thalamus,  $n = 21$ ) were identified in 28 patients on 7T MR imaging (range, 1–6 microinfarcts). A single microinfarct was seen in 19 patients (68%), while multiple microinfarcts were seen in 9 patients (32%). The size of the microinfarcts ranged from 2.1 to 4.8 mm (caudate nucleus, 2.1–4.7 mm; lentiform nucleus, 2.7–4.1 mm; thalamus, 2.4–4.8 mm). Of patients with microinfarcts ( $n = 28$ ), 12 patients (42%) also showed infarcts of  $\geq 5$  mm in the deep gray matter on 7T MR imaging (Table 1). Examples of deep gray matter microinfarcts are shown in Fig 1.

Twenty-six patients showed a total of 33 infarcts of  $\geq 5$  mm in the deep gray matter on 7T MR imaging, ranging from 6.7 to 15.7 mm (Table 1). Of these 33 lesions, 18 (55%) were rated as lacunes in the deep gray matter on the corresponding 1.5T MR imaging.

Baseline characteristics and MR imaging markers of patients with microinfarcts in the deep gray matter ( $n = 28$ ), in those without microinfarcts ( $n = 185$ ), and in the total study sample ( $n = 213$ ) are shown in Tables 2 and 3, respectively.

Compared with the baseline (2001–2005) characteristics of patients without a 7T brain MR imaging, patients in the study sample with a 7T brain MR imaging were younger, more often had current alcohol intake, often had less diabetes mellitus, and

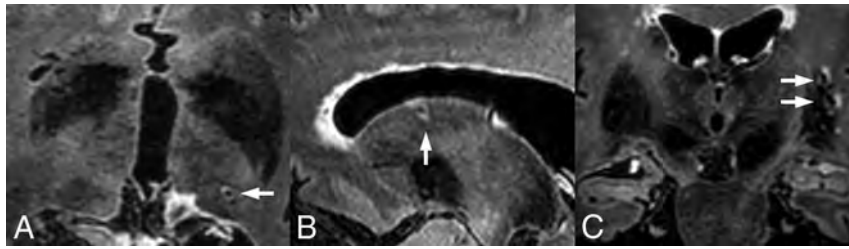


**FIG 1.** Examples of microinfarcts in the deep gray matter on 7T MR imaging. A, Microinfarct with a diameter of 2.3 mm (arrow) in the left thalamus of a 73-year-old woman on transversal 7T FLAIR. B, Microinfarct with a diameter of 2.9 mm (arrow) in the left caudate nucleus of a 64-year-old man on sagittal 7T FLAIR. C, Two microinfarcts with diameters of 3.0 and 3.2 mm (arrows) in the left putamen of a 65-year-old man on coronal 7T FLAIR. Note that the gliotic rim extends into the adjacent external capsule.

showed a slightly lower intima-media thickness and a slightly higher ankle brachial index (Online Supplemental Data).

### Vascular Risk Factors

Higher age was associated with the presence of microinfarcts in the deep gray matter (RR per year increase = 1.05; 95% CI, 1.02–1.08;  $P = .001$ ). In addition, after adjusting for age, a history of stroke (RR = 2.88; 95% CI, 1.24–6.67;  $P = .01$ ), hypertension (RR = 3.16; 95% CI, 1.30–7.65;  $P = .01$ ), and a higher intima-media thickness (RR per 1 SD increase = 1.29; 95% CI, 1.04–1.61;  $P = .02$ ) were associated with microinfarcts. The number of smoking pack years (RR per SD increase = 1.11; 95% CI, 0.87–1.42;  $P = .40$ ), carotid artery stenosis  $\geq 50\%$  (RR = 1.39; 95% CI, 0.70–2.75;  $P = .34$ ), and the presence of metabolic syndrome (RR = 1.47; 95% CI, 0.74–2.91;  $P = .27$ ) were not significantly associated with the presence of microinfarcts in the deep gray matter after adjusting for age (Table 2).

After additionally adjusting for the number of infarcts of  $\geq 5$  mm in the deep gray matter on 7T MR imaging, older age (RR per year increase = 1.04; 95% CI, 1.01–1.07;  $P = .01$ ) and hypertension (RR = 5.25; 95% CI, 1.43–19.28;  $P = .01$ ) remained associated with microinfarcts, whereas a history of stroke (RR = 2.37; 95% CI, 0.94–5.79;  $P = .07$ ) and a higher intima-media thickness (RR per 1 SD increase = 1.25; 95% CI, 0.98–1.57;  $P = .07$ ) lost statistical significance.

### MR Imaging Markers of Cerebrovascular Disease

For cerebrovascular markers on 1.5T MR imaging, cerebellar infarcts (RR = 2.18; 95% CI, 1.23–3.87;  $P = .008$ ), lacunes in the white matter (RR = 3.28; 95% CI, 1.79–6.04;  $P < .001$ ), and lacunes in the deep gray matter (RR = 3.93; 95% CI, 1.99–7.78;  $P < .001$ ) were associated with the presence of microinfarcts in the deep gray matter, after adjusting for age. For cerebrovascular markers on 7T MR imaging, cortical microinfarcts (RR = 2.33; 95% CI, 1.32–4.13;  $P = .004$ ) were associated with microinfarcts in the deep gray matter after adjusting for age. Although the RR was increased, cortical infarcts (RR = 1.64; 95% CI, 0.76–3.51;  $P = .21$ ), brainstem infarcts (RR = 3.37; 95% CI, 0.95–12.0;  $P = .07$ ), and periventricular WMH volume (RR per SD increase = 1.14; 95% CI, 0.95–1.37;  $P = .16$ ) on 1.5T MR imaging were not significantly associated with the presence of microinfarcts in the

deep gray matter after adjusting for age. Deep microbleeds (RR = 1.60; 95% CI, 0.70–3.68;  $P = .27$ ) and lobar microbleeds (RR = 1.27; 95% CI, 0.59–2.72;  $P = .54$ ) on 7T MR imaging were also not significantly associated with microinfarcts in the deep gray matter after adjusting for age (Table 3).

After additionally adjusting for the number of infarcts of  $\geq 5$  mm in the deep gray matter on 7T MR imaging, lacunes in the white matter on 1.5T MR imaging (RR = 2.76; 95% CI, 1.45–5.27;  $P = .002$ ), cerebellar infarcts on 1.5T MR imaging (RR = 2.05; 95% CI, 1.13–3.73;  $P = .02$ ), and cortical microinfarcts on 7T MR imaging (RR = 2.16; 95% CI, 1.20–3.90;  $P = .01$ ) remained associated with microinfarcts.

### Cognitive Functioning

Global cognitive functioning  $z$  scores differed significantly between patients without ( $n = 185$ ), with a single ( $n = 19$ ), and with multiple microinfarcts ( $n = 9$ ) in the deep gray matter (ANCOVA  $P = .007$ ), adjusted for age and education level. Specifically, the presence of multiple microinfarcts in the deep gray matter was associated with worse global cognitive functioning compared with the absence of microinfarcts or the presence of a single microinfarct (mean difference in  $z$  score =  $-0.92$ ; 95% CI,  $-1.53$  to  $-0.31$ ;  $P = .003$ ;  $-1.10$ ; 95% CI,  $-1.81$  to  $-0.39$ ;  $P = .002$ , respectively). This pattern was observed for each cognitive domain. The mean estimates of domain-specific  $z$  scores were lower for patients with multiple microinfarcts compared with patients with none or a single microinfarct, for memory, executive functioning, information processing speed, and working memory (Fig 2).

After additionally adjusting for the number of infarcts of  $\geq 5$  mm in the deep gray matter on 7T MR imaging, the association between microinfarcts and global cognitive functioning persisted (ANCOVA  $P = .01$ ; mean difference in  $z$  scores between patients with multiple microinfarcts versus none:  $-0.97$ ; 95% CI,  $-1.66$  to  $-0.28$ ;  $P = .006$ ; versus a single microinfarct:  $-1.13$ ; 95% CI,  $-1.88$  to  $-0.39$ ;  $P = .003$ ).

### DISCUSSION

In this cohort of patients with a history of arterial disease, microinfarcts in the deep gray matter on 7T MR imaging were detected in 13% of patients. These lesions were associated with older age, a history of stroke, hypertension, and a higher intima-media thickness. With regard to MR imaging markers, microinfarcts were associated with lacunes and cerebellar infarcts on 1.5T MR imaging and with cortical microinfarcts on 7T MR imaging. The presence of multiple microinfarcts in the deep gray matter was associated with worse global cognitive functioning independent of age, education level, and the number of infarcts of  $\geq 5$  mm.

We previously reported that small infarcts in the caudate nucleus on 7T MR imaging can be detected with excellent intrarater and interrater agreement and that the imaging characteristics of

**Table 2: Association of vascular risk factors and the presence of microinfarcts in the deep gray matter on 7T MR imaging<sup>a</sup>**

	Patients with Microinfarcts in the Deep Gray Matter (n = 28)	Patients without Microinfarcts in the Deep Gray Matter (n = 185)	All Patients (n = 213)	Microinfarct (Presence vs Absence) RR (95% CI) <sup>b</sup>
Age (yr)	70 (SD, 7)	64 (SD, 9)	64 (SD, 9)	1.05 (1.02–1.08) <sup>c,d</sup>
Sex (% men)	85.7	82.2	82.6	0.78 (0.30–2.02) <sup>e</sup>
History of stroke (%)	50.0	23.2	26.8	2.88 (1.24–6.67) <sup>d</sup>
BMI (kg/m <sup>2</sup> )	28 (SD, 4)	27 (SD, 4)	27 (SD, 4)	1.20 (0.87–1.65)
Smoking (pack-years) <sup>f</sup>	27 (0, 56)	20 (0, 47)	22 (0, 49)	1.11 (0.87–1.42)
Alcohol intake				
No or <1 U/week (%)	22.2	26.5	25.9	1 (reference)
1–10 U/week (%)	59.3	41.1	43.4	1.55 (0.67–3.61)
≥11 U/week (%)	18.5	32.4	30.7	0.65 (0.22–1.98)
Hypertension (%)	96.4	72.4	75.6	3.16 (1.30–7.65) <sup>d</sup>
Diabetes mellitus (%)	14.3	16.2	16.0	0.85 (0.32–2.21)
Carotid stenosis ≥50% (%)	17.9	7.6	8.9	1.39 (0.70–2.75)
Hypercholesterolemia (%)	77.8	86.4	85.3	1.33 (0.86–2.05)
IMT (mm)	1.0 (SD, 0.3)	0.8 (SD, 0.2)	0.9 (SD, 0.2)	1.29 (1.04–1.61) <sup>d</sup>
ABI	1.1 (SD, 0.2)	1.1 (SD, 0.1)	1.1 (SD, 0.2)	0.86 (0.67–1.11)
Homocysteine (μmol/l)	13.0 (SD, 5.2)	12.5 (SD, 4.3)	12.5 (SD, 4.4)	1.07 (0.40–2.82)
APOB (g/L)	0.8 (SD, 0.2)	0.8 (SD, 0.2)	0.8 (SD, 0.2)	0.84 (0.58–1.23)
Metabolic syndrome	60.7	51.4	52.6	1.47 (0.74–2.91)
≥1 APOE ε4 allele (%)	35.7	28.1	29.1	1.58 (0.79–3.20)

**Note:**—BMI indicates body mass index; IMT, intima-media thickness; ABI, ankle brachial index; APOB, apolipoprotein B; APOE, apolipoprotein E

<sup>a</sup> Characteristics are presented as mean (SD) or percentage. RR represents the relative risk for microinfarcts in the presence of a risk factor (in case of a dichotomous variable) or for 1 SD increase in the risk factor (in case of a continuous variable).

<sup>b</sup> Log-binomial regression with adjustment for age.

<sup>c</sup> Per year increase.

<sup>d</sup>  $P < .05$ .

<sup>e</sup> Men versus women.

<sup>f</sup> Median (10th percentile, 90th percentile). Natural log-transformed due to a non-normal distribution in the analysis.

these lesions are similar to those in the cerebral cortex.<sup>14</sup> The present study extends our previous findings and emphasizes the potential clinical importance of these lesions, which is in accordance with postmortem studies that reported associations between microinfarcts in the deep gray matter and antemortem cognitive impairment.<sup>10,12</sup> In addition, we found that most patients with microinfarcts in the deep gray matter did not show larger infarcts in the deep gray matter on 7T MR imaging and, most important, that the relationship between microinfarcts and worse global cognitive functioning was independent of infarcts of ≥5 mm. These findings suggest that microinfarcts in the deep gray matter are structural correlates of impaired cognitive functioning that are largely undetected on conventional MR imaging.<sup>1</sup>

The association between microinfarcts and worse cognitive functioning may be explained by the important role that the basal ganglia play in cognition through receiving and processing cortical information in the caudate and lentiform nuclei and sending information back to the cerebral cortex through the thalamus.<sup>27,28</sup> Damage to this neuronal network may compromise cognition.<sup>29</sup> However, we did not find differences in cognition between patients without microinfarcts and patients with a single microinfarct, suggesting that the impact of a single microinfarct on cognition may be weak, contrary to the presence of multiple lesions. A possible explanation is that the damage associated with a single microinfarct is insufficient to affect neural network integrity and therefore result in lower cognitive performance, whereas this may be the case for multiple microinfarcts. Alternatively, it may be that patients with multiple microinfarcts are also more

likely to have smaller lesions that are not discernible on 7T MR imaging.<sup>30</sup>

The associations of microinfarcts in the deep gray matter with older age, hypertension, a higher intima-media thickness, lacunes, and cerebellar infarcts suggest that small-vessel and large-vessel disease may be involved in the pathogenesis of these lesions. Support for this notion is provided by a large postmortem study in which atherosclerosis and arteriolosclerosis were associated with subcortical microinfarcts.<sup>31</sup> However, because the in vivo associations presented in this study are novel, further studies in different populations are needed to identify risk factors of microinfarcts that may pose potential targets for intervention.

Strengths of our study include the large sample size for a 7T MR imaging study and the detailed information available on vascular risk factors, MR imaging markers of cerebrovascular disease, and cognitive functioning that enabled us to examine these relationships in 1 study. A limitation of this study is that microinfarcts in the deep gray matter, cortical microinfarcts, and microbleeds were rated on 7T MR imaging data, whereas other MR imaging markers were evaluated on 1.5T MR imaging data. Several remarks have to be made with respect to this matter. First, we obtained brain volumes from 1.5T MR imaging data due to a lack of robust and validated brain-segmentation software for 7T MR imaging data. Second, CBF measurements were obtained from 1.5T MR imaging data because our standardized 7T MR imaging protocol did not contain phase-contrast sequences. Third, the greatest added value of ultra-high-field 7T MR imaging lies in its ability to visualize the smallest cerebrovascular



**Table 3: Association of MR imaging markers of cerebrovascular disease and the presence of microinfarcts in the deep gray matter on 7T MR imaging<sup>a</sup>**

	Patients with Microinfarcts in the Deep Gray Matter (n = 28)	Patients without Microinfarcts in the Deep Gray Matter (n = 185)	All Patients (n = 213)	Microinfarct (Presence vs Absence) RR (95% CI) <sup>b</sup>
Infarcts on 1.5T MR imaging (%)				
Cortical	21	11	12	1.64 (0.76–3.51)
Cerebellar	32	9	12	2.18 (1.23–3.87) <sup>c</sup>
Brainstem	7	1	2	3.37 (0.95–12.0)
Lacunes in the white matter on 1.5T MR imaging (%)	32	6	9	3.28 (1.79–6.04) <sup>c</sup>
Lacunes in the deep gray matter on 1.5T MR imaging (%)	43	8	12	3.93 (1.99–7.78) <sup>c</sup>
WMH volumes on 1.5T MR imaging (mL) <sup>d</sup>				
Total	3.3 (0.9–32.5)	2.0 (0.3–9.3)	2.0 (0.4–10.0)	1.13 (0.93–1.38) <sup>e</sup>
Periventricular	2.9 (0.7–31.7)	1.4 (0.2–8.3)	1.4 (0.3–9.0)	1.14 (0.95–1.37) <sup>e</sup>
Deep	0.2 (0.1–0.9)	0.3 (0.0–1.5)	0.2 (0.0–1.4)	0.67 (0.38–1.16) <sup>e</sup>
Total brain volume (mL)	1104.9 (SD, 116.5)	1125.3 (SD, 104.3)	1122.7 (SD, 105.9)	0.84 (0.56–2.72) <sup>f</sup>
Total intracranial volume (mL)	1449.2 (SD, 114.7)	1452.6 (SD, 126.4)	1452.16 (SD, 128.5)	1.21 (0.85–1.73)
Parenchymal CBF (mL/min per 100-mL brain volume)	50.5 (SD, 16.8)	48.2 (SD, 12.0)	48.5 (SD, 12.7)	1.13 (0.93–1.38)
Cortical microinfarcts on 7T MR imaging (%)	32	9	12	2.33 (1.32–4.13) <sup>c</sup>
Deep microbleeds on 7T MR imaging (%)	21	10	12	1.60 (0.70–3.68)
Lobar microbleeds on 7T MR imaging (%)	36	26	27	1.27 (0.59–2.72)

<sup>a</sup> Characteristics are presented as mean (SD) or percentage. RR represents the relative risk for microinfarcts in the presence of an MR imaging marker (in case of a dichotomous variable) or for 1 SD increase in the MR imaging marker (in case of a continuous variable).

<sup>b</sup> Log-binomial regression with adjustment for age.

<sup>c</sup>  $P < .05$ .

<sup>d</sup> Median (10th percentile, 90th percentile).

<sup>e</sup> Natural log-transformed due to a non-normal distribution and normalized for total intracranial volume.

<sup>f</sup> Adjusted for age and total intracranial volume.

lesions (ie, microinfarcts and microbleeds) due to the higher signal-to-noise ratio compared with conventional 1.5T MR imaging. Although it would be preferable to determine all cerebrovascular lesions on the 7T MR imaging scans for consistency, it is unlikely that 7T MR imaging yields a greater detection rate for larger lesions such as cortical infarcts.

Another limitation is the potential overlap that may occur between microinfarcts and lacunes of presumed vascular origin in the deep gray matter. According to the STRIVE criteria, lacunes of presumed vascular origin are defined as small subcortical infarcts ranging from 3 to 15 mm.<sup>16</sup> Because microinfarcts were previously defined as lesions of  $<5$  mm, it is possible that larger microinfarcts in the range of 4 mm may have been classified as lacunes on 1.5T MR imaging. The potential overlap, however, was limited because most patients with microinfarcts did not show lacunes in the deep gray matter on 1.5T MR imaging. In addition, we controlled for the effects of infarcts of  $\geq 5$  mm in the analyses.

Another possible limitation of this study is that the sample consisted of patients who completed 2 follow-up measurements, and these patients represent a slightly healthier subset. This may have led to an underestimation of the association of microinfarcts with vascular risk factors, MR imaging markers of cerebrovascular disease, and cognitive functioning. A further limitation of this study is that in some patients, the 7T brain MR imaging did not coincide with the 1.5T brain MR imaging, cognitive function measurements, and vascular risk factor assessment. Especially for the vascular risk factor assessment, the interval was quite large in some patients. Due to logistical reasons, we were not able to repeat the

measurement of vascular risk factors at the time of the brain MR imaging and cognitive assessment in these patients, possibly under- or overestimating the associations. However, in a previous analysis,<sup>32</sup> we did not see major changes in the relationship with 7T MR imaging outcomes when adjusting for the time interval between vascular risk factor assessment and 7T brain MR imaging.

## CONCLUSIONS

Our findings demonstrate that microinfarcts in the deep gray matter on 7T MR imaging are associated with worse cognitive functioning and vascular risk factors and MR imaging markers of small-vessel and large-vessel disease in patients with a history of arterial disease. These results suggest that microinfarcts in the deep gray matter may be relevant imaging markers of vascular brain injury that, together with cortical microinfarcts, could be a potential target for future prevention strategies of vascular cognitive impairment.

## ACKNOWLEDGMENTS

We gratefully acknowledge the contribution of the research nurses, R. van Petersen (data manager), B. van Dinther (study manager), and the members of the Utrecht Cardiovascular Cohort SMART study group: F.W. Asselbergs and H.M. Nathoe, Department of Cardiology; G.J. de Borst, Department of Vascular Surgery; M.L. Bots and M.I. Geerlings, Julius Center for Health Sciences and Primary Care; M.H. Emmelot, Department of Geriatrics; P.A. de Jong and T. Leiner, Department of Radiology; A.T. Lely, Department of Obstetrics/Gynaecology; N.P. van der

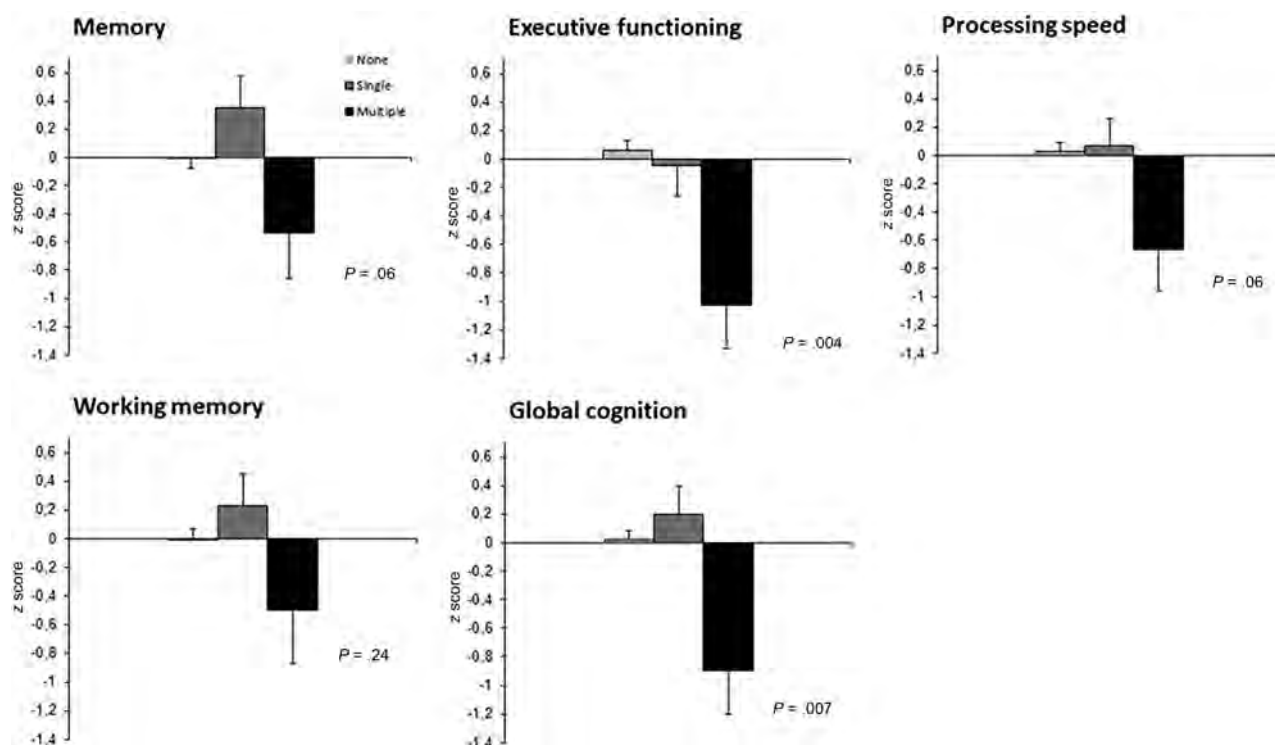


**FIG 2.** Association between microinfarcts in the deep gray matter and global and domain-specific cognitive functioning z scores. Values are mean  $\pm$  standard error z scores, adjusted for age and educational level. Memory: none,  $-0.01 \pm 0.07$ ; single,  $0.35 \pm 0.22$ ; multiple,  $-0.54 \pm 0.32$ . Executive functioning: none,  $0.05 \pm 0.07$ ; single,  $-0.05 \pm 0.21$ ; multiple,  $-1.02 \pm 0.31$ . Processing speed: none,  $0.02 \pm 0.06$ ; single,  $0.07 \pm 0.20$ ; multiple,  $-0.67 \pm 0.29$ . Working memory: none,  $-0.01 \pm 0.07$ ; single,  $0.22 \pm 0.22$ ; multiple,  $-0.50 \pm 0.37$ . Global cognition: none,  $0.02 \pm 0.06$ ; single,  $0.20 \pm 0.20$ ; multiple,  $-0.90 \pm 0.30$ .

Kaaij, Department of Cardiothoracic Surgery; L.J. Kappelle and Y. Ruigrok, Department of Neurology; M.C. Verhaar, Department of Nephrology; F.L.J. Visseren (chair) and J. Westerink, Department of Vascular Medicine, University Medical Center Utrecht and Utrecht University.

Disclosure forms provided by the authors are available with the full text and PDF of this article at [www.ajnr.org](http://www.ajnr.org).

## REFERENCES

- Smith EE, Schneider JA, Wardlaw JM, et al. Cerebral microinfarcts: the invisible lesions. *Lancet Neurol* 2012;11:272–82 CrossRef Medline
- van Veluw SJ, Shih AY, Smith EE, et al. Detection, risk factors, and functional consequences of cerebral microinfarcts. *Lancet Neurol* 2017;16:730–40 CrossRef Medline
- Brundel M, de Bresser J, van Dillen JJ, et al. Cerebral microinfarcts: a systematic review of neuropathological studies. *J Cereb Blood Flow Metab* 2012;32:425–36 CrossRef Medline
- Summers PM, Hartmann DA, Hui ES, et al. Functional deficits induced by cortical microinfarcts. *J Cereb Blood Flow Metab* 2017;37:3599–3614 CrossRef
- Wang Z, van Veluw SJ, Wong A, et al. Risk factors and cognitive relevance of cortical cerebral microinfarcts in patients with ischemic stroke or transient ischemic attack. *Stroke* 2016;47:2450–55 CrossRef Medline
- van Dalen JW, Scuric EE, van Veluw SJ, et al. Cortical microinfarcts detected in vivo on 3 Tesla MRI: clinical and radiological correlates. *Stroke* 2015;46:255–57 CrossRef Medline
- van Veluw SJ, Hilal S, Kuijff HJ, et al. Cortical microinfarcts on 3T MRI: clinical correlates in memory-clinic patients. *Alzheimers Dement* 2015;11:1500–09 CrossRef Medline
- Hilal S, Chai YL, van Veluw S, et al. Association between subclinical cardiac biomarkers and clinically manifest cardiac diseases with cortical cerebral microinfarcts. *JAMA Neurol* 2017;74:403–10 CrossRef Medline
- Hilal S, Sikking E, Shaik MA, et al. Cortical cerebral microinfarcts on 3T MRI: a novel marker of cerebrovascular disease. *Neurology* 2016;87:1583–90 CrossRef Medline
- Troncoso JC, Zonderman AB, Resnick SM, et al. Effect of infarcts on dementia in the Baltimore longitudinal study of aging. *Ann Neurol* 2008;64:168–76 CrossRef Medline
- Gold G, Kovari E, Herrmann FR, et al. Cognitive consequences of thalamic, basal ganglia, and deep white matter lacunes in brain aging and dementia. *Stroke* 2005;36:1184–88 CrossRef Medline
- White L, Petrovitch H, Hardman J, et al. Cerebrovascular pathology and dementia in autopsied Honolulu-Asia Aging Study participants. *Ann N Y Acad Sci* 2002;977:9–23 CrossRef Medline
- Geerlings MI, Appelman AP, Vincken KL, et al; SMART Study Group. Brain volumes and cerebrovascular lesions on MRI in patients with atherosclerotic disease: the SMART-MR study. *Atherosclerosis* 2010;210:130–36 CrossRef Medline
- Ghaznawi R, de Bresser J, van der Graaf Y, et al; SMART Study Group. Detection and characterization of small infarcts in the caudate nucleus on 7 Tesla MRI: the SMART-MR study. *J Cereb Blood Flow Metab* 2018;38:1609–17 CrossRef Medline
- Conijn MM, Geerlings MI, Biessels GJ, et al. Cerebral microbleeds on MR imaging: comparison between 1.5 and 7T. *AJNR Am J Neuroradiol* 2011;32:1043–49 CrossRef Medline
- Wardlaw JM, Smith EE, Biessels GJ, et al; STRIVE v1). Neuroimaging standards for research into small vessel disease and its contribution to ageing and neurodegeneration. *Lancet Neurol* 2013;12:822–38 CrossRef Medline

17. Anbeek P, Vincken KL, van Bochove GS, et al. **Probabilistic segmentation of brain tissue in MR imaging.** *Neuroimage* 2005;27:795–804 CrossRef Medline
18. Spilt A, Box FM, van der Geest RJ, et al. **Reproducibility of total cerebral blood flow measurements using phase contrast magnetic resonance imaging.** *J Magn Reson Imaging* 2002;16:1–5 CrossRef Medline
19. Dolui S, Wang Z, Wang DJJ, et al. **Comparison of non-invasive MRI measurements of cerebral blood flow in a large multisite cohort.** *J Cereb Blood Flow Metab* 2016;36:1244–56 CrossRef Medline
20. Gregoire SM, Chaudhary UJ, Brown MM, et al. **The Microbleed Anatomical Rating Scale (MARS): reliability of a tool to map brain microbleeds.** *Neurology* 2009;73:1759–66 CrossRef Medline
21. De Cocker LJ, Kloppenborg RP, van der Graaf Y, et al; SMART Study Group. **Cerebellar cortical infarct cavities: correlation with risk factors and MRI markers of cerebrovascular disease.** *Stroke* 2015;46:3154–60 CrossRef Medline
22. Takasugi J, Miwa K, Watanabe Y, et al. **Cortical cerebral microinfarcts on 3T magnetic resonance imaging in patients with carotid artery stenosis.** *Stroke* 2019;50:639–44 CrossRef Medline
23. Sagnier S, Okubo G, Catheline G, et al. **Chronic cortical cerebral microinfarcts slow down cognitive recovery after acute ischemic stroke.** *Stroke* 2019;50:1430–36 CrossRef Medline
24. Li Y, Maeda M, Ishikawa H, et al. **Cortical microinfarcts in patients with multiple lobar microbleeds on 3 T MRI.** *J Neurol* 2019;266:1887–96 CrossRef Medline
25. Fu R, Wang Y, Wang Y, et al; Chinese IntraCranial AtheroSclerosis CICAS Study Group. **The development of cortical microinfarcts is associated with intracranial atherosclerosis: data from the Chinese Intracranial Atherosclerosis Study.** *J Stroke Cerebrovasc Dis* 2015;24:2447–54 CrossRef Medline
26. van Rooden S, Goos JD, van Opstal AM, et al. **Increased number of microinfarcts in Alzheimer disease at 7-T MR imaging.** *Radiology* 2014;270:205–11 CrossRef Medline
27. Alexander GE. **Basal ganglia-thalamocortical circuits: their role in control of movements.** *J Clin Neurophysiol* 1994;11:420–31 CrossRef Medline
28. Alexander GE, Crutcher MD. **Functional architecture of basal ganglia circuits: neural substrates of parallel processing.** *Trends Neurosci* 1990;13:266–71 CrossRef Medline
29. Leh SE, Petrides M, Strafella AP. **The neural circuitry of executive functions in healthy subjects and Parkinson's disease.** *Neuropsychopharmacology* 2010;35:70–85 CrossRef Medline
30. Auriel E, Westover MB, Bianchi MT, et al. **Estimating total cerebral microinfarct burden from diffusion-weighted imaging.** *Stroke* 2015;46:2129–35 CrossRef Medline
31. Arvanitakis Z, Capuano AW, Leurgans SE, et al. **The relationship of cerebral vessel pathology to brain microinfarcts.** *Brain Pathol* 2017;27:77–85 CrossRef Medline
32. Zwartbol MHT, van der Kolk AG, Ghaznawi R, et al; SMART Study Group. **Intracranial vessel wall lesions on 7T MRI (magnetic resonance imaging).** *Stroke* 2019;50:88–94 CrossRef Medline



# Image-Quality Assessment of 3D Intracranial Vessel Wall MRI Using DANTE or DANTE-CAIPI for Blood Suppression and Imaging Acceleration

 B. Sannanjanja,  C. Zhu,  C.G. Colip,  A. Somasundaram,  M. Ibrahim,  T. Khrisat, and  M. Mossa-Basha



## ABSTRACT

**BACKGROUND AND PURPOSE:** 3D intracranial vessel wall MRI techniques are time consuming and prone to artifacts, especially flow artifacts. Our aim was to compare the image quality of accelerated and flow-suppressed 3D intracranial vessel wall MR imaging techniques relative to conventional acquisitions.

**MATERIALS AND METHODS:** Consecutive patients undergoing MR imaging had conventional postcontrast 3D T1-sampling perfection with application-optimized contrasts by using different flip angle evolution (SPACE) and either postcontrast delay alternating with nutation for tailored excitation (DANTE) flow-suppressed or DANTE-controlled aliasing in parallel imaging results in higher acceleration (CAIPI) flow-suppressed and accelerated T1-SPACE sequences performed. The sequences were evaluated using 4- or 5-point Likert scales for overall image quality, SNR, extent/severity of artifacts, motion, blood suppression, sharpness, and lesion assessment. Quantitative assessment of lumen and wall-to-lumen contrast ratios was performed.

**RESULTS:** Eighty-nine patients were included. T1-DANTE-SPACE had significantly better qualitative ratings relative to T1-SPACE for image quality, SNR, artifact impact, arterial and venous suppression, and lesion assessment ( $P < .001$  for each, respectively), with the exception of motion ( $P = .16$ ). T1-DANTE-CAIPI-SPACE had significantly better image quality, lesion assessment, arterial and venous blood suppression, less artifact impact, and less motion compared with T1-SPACE ( $P < .001$  for each, respectively). The SNR was higher with T1-SPACE compared with T1-DANTE-CAIPI-SPACE ( $P < .001$ ). T1-DANTE-CAIPI-SPACE showed significantly worse lumen ( $P = .005$ ) and wall-to-lumen contrast ratios ( $P = .001$ ) compared with T1-SPACE, without a significant difference between T1-SPACE and T1-DANTE-SPACE. T1-DANTE-CAIPI-SPACE scan time was 5:11 minutes compared with 8:08 and 8:41 minutes for conventional T1-SPACE and T1-DANTE-SPACE, respectively.

**CONCLUSIONS:** Accelerated postcontrast T1-DANTE-CAIPI-SPACE had fewer image artifacts, less motion, improved blood suppression, and a shorter scan time, but lower qualitative and quantitative SNR ratings relative to conventional T1-SPACE intracranial vessel wall MR imaging. Postcontrast T1-DANTE-SPACE had superior SNR, blood suppression, higher image quality, and fewer image artifacts, but slightly longer scan times relative to T1-SPACE.

**ABBREVIATIONS:** CAIPI = controlled aliasing in parallel imaging results in higher acceleration; DANTE = delay alternating with nutation for tailored excitation; IVW = intracranial vessel wall MR imaging; MSDE = motion-sensitized driven-equilibrium; SPACE = sampling perfection with application-optimized contrasts by using different flip angle evolution

Intracranial vessel wall MR imaging (IVW) has shown value in vasculopathy differentiation and characterization;<sup>1–6</sup> however, there is substantial technique and imaging parameter heterogeneity.<sup>3,6–14</sup> There are a number of challenges that currently exist with IVW in terms of its application and implementation. One challenge is technique-related, specifically artifactual arterial and venous wall

enhancement that can mimic pathology. Small studies have shown that artifactual enhancement on postcontrast conventional 3D variable refocusing flip angle T1-weighted techniques can mimic aneurysm wall enhancement.<sup>10,15</sup> Blood-suppression techniques can suppress such artifactual flow, including delay alternating with nutation for tailored excitation (DANTE) and motion-sensitized

Received December 27, 2021; accepted after revision April 13, 2022.

From the Department of Radiology (B.S., A.S.), Emory University, Atlanta, Georgia; Department of Radiology (C.Z., M.M.-B.), University of Washington, Seattle, Washington; Kaiser Permanente Northwest (C.G.C.), Portland, OR; Department of Radiology (M.I.), University of Kansas, Lawrence, Kansas; and Department of Surgery (T.K.), Lincoln Medical Center, New York, New York.

This work was supported by National Institutes of Health grants (NIH R01 NS092207-04, NIH R01 NS092207-04S1).

Please address correspondence to Mahmud Mossa-Basha, MD, University of Washington, Department of Radiology, 1959 NE Pacific St., Seattle, WA 98195; e-mail: mmossab@uw.edu; @mossabas

 Indicates open access to non-subscribers at [www.ajnr.org](http://www.ajnr.org)

 Indicates article with online supplemental data.

<http://dx.doi.org/10.3174/ajnr.A7531>

**Table 1: Pulse sequence acquisition parameters**

	3D T1-SPACE	DANTE-CAIPI-T1-SPACE	DANTE-T1-SPACE
TR/TE (ms)	1000/11.0	1000/11.0	1000/11.0
In-plane resolution (mm)	0.56 × 0.56	0.56 × 0.56	0.56 × 0.56
Section thickness (mm)	0.56	0.56	0.56
Flip angle	Variable	Variable	Variable
FOV (mm)	180 × 180	180 × 180	180 × 180
Parallel imaging factor	2	2	2
Averages	1	1	1
Scan time (min)	8:08	5:11	8:47
DANTE	No	Yes	Yes
CAIPI	No	Yes	No

driven equilibrium (MSDE).<sup>7,16</sup> MSDE has proved to be very valuable in carotid vessel wall MR imaging; however, this technique results in signal reduction and T2 signal decay,<sup>17</sup> which can limit its value for intracranial pathologies due to the need for high resolution for the evaluation of smaller, thinner-walled, tortuous intracranial arteries and smaller vascular pathologic lesions.<sup>3</sup>

Another challenge in IVW implementation is long scan times for conventional IVW sequences and protocols, which can add 16–20 minutes of scan time for pre- and postcontrast T1-weighted IVW sequences and much more for multicontrast protocols, which can be restrictive in clinical settings and also lead to increased motion artifacts. A number of acceleration techniques have been developed and used in IVW, including controlled aliasing in parallel imaging results in higher acceleration (CAIPI), which is a parallel imaging technique optimized for 3D acquisitions.<sup>14,18,19</sup>

To our knowledge, no prior study has compared conventional IVW with blood-suppressed or blood-suppressed and accelerated IVW in a real-world clinical cohort evaluating patients with diverse intracranial vasculopathies. In the current study, we performed quantitative and qualitative assessment of postcontrast T1-sampling perfection with application-optimized contrasts by using different flip angle evolution (SPACE; Siemens) IVW in comparison with either DANTE or DANTE-CAIPI T1-SPACE IVW, performed during the same scan as part of clinical IVW protocols, to determine which IVW technique may optimize image quality and reduce flow artifacts, while, in the case of CAIPI acquisitions, also reducing scan time.

## MATERIALS AND METHODS

### Patient Selection

This study was approved by the University of Washington institutional ethics committee, and informed consent was obtained from all study participants. Consecutive patients who underwent IVW examinations from January 2017 to April 2019 for suspected intracranial vascular disease were extracted from the institutional database. We collected demographic and clinical data: age, sex, and suspected initial and final clinical diagnoses.

### Image Acquisition

All imaging was performed on a 3T Prisma MR imaging system (Siemens) using a 64-channel neurovascular coil. The imaging protocol included precontrast and postcontrast T1-SPACE. Each patient also underwent another postcontrast T1-weighted IVW sequence, either postcontrast T1WI DANTE-CAIPI-SPACE or postcontrast T1-DANTE-SPACE. The sequence of acquisition

for postcontrast images was randomized with patients imaged with T1-SPACE followed by the other techniques and vice versa. The sequence scan parameters are listed in Table 1. Scan time was 8:08 for T1-SPACE, 5:11 for T1-DANTE-CAIPI-SPACE, and 8:41 for T1-DANTE-SPACE.

### Image Evaluation

Two board-certified neuroradiologists (M.M.-B., with 16 years, and C.G.C., with 9 years of radiology experience, respectively), blinded to the patient clinical information, independently evaluated individual postcontrast IVW sequences. All imaging studies were de-identified, and the raters were unaware of the sequence acquisition during review. Each individual postcontrast sequence was reviewed in random order on a RadiAnt DICOM viewer (<https://www.radiantviewer.com/>) with 3-plane reconstructed views, in conjunction with review of the precontrast T1-weighted sequence and the TOF-MRA. Raters evaluated overall imaging quality on the following 4-point scale: 1, optimal image quality; 2, minimally limited; 3, limited but interpretable; and 4, nondiagnostic. Image SNR was evaluated on the following 4-point scale: 1, optimal SNR; 2, mildly diminished SNR not affecting image interpretation; 3, mildly-to-moderately diminished SNR limiting image interpretation; 4, markedly diminished SNR that renders the images uninterpretable. Image artifacts were evaluated on the following 5-point scale: 1, no artifacts; 2, trace artifacts; 3, artifacts not affecting the targeted arterial anatomy; 4, artifacts mildly affecting the targeted arterial anatomy; and 5, artifacts obscuring the targeted anatomy. Arterial blood suppression was evaluated on the following 4-point scale: 1, complete blood suppression; 2, minimal central luminal flow artifacts; 3, luminal flow artifacts mimicking lesions in 1–2 segments; 4, luminal flow artifacts mimicking lesions in >2 segments. Lesion assessment for arterial wall abnormalities were evaluated on the following 4-point scale: 1, well-visualized with sharp margins; 2, minimal blurring with loss of margins but pattern and structure of involvement clear; 3, structure of involvement clear but pattern of involvement limited; 4, lesion pattern and structure involved cannot be determined.

Cases interpretable for lesion pattern (1 or 2 ratings) for both acquisitions were reviewed for patterns (eccentric, <50% circumferential wall involvement, versus concentric, ≥50% circumferential wall involvement) on each acquisition (T1-SPACE and T1-DANTE-SPACE or T1-DANTE-CAIPI-SPACE). For cases with multiple lesions, the pattern for most stenotic lesions was recorded. Consensus was reached when there was disagreement on the pattern. Venous flow suppression was evaluated on the following 4-

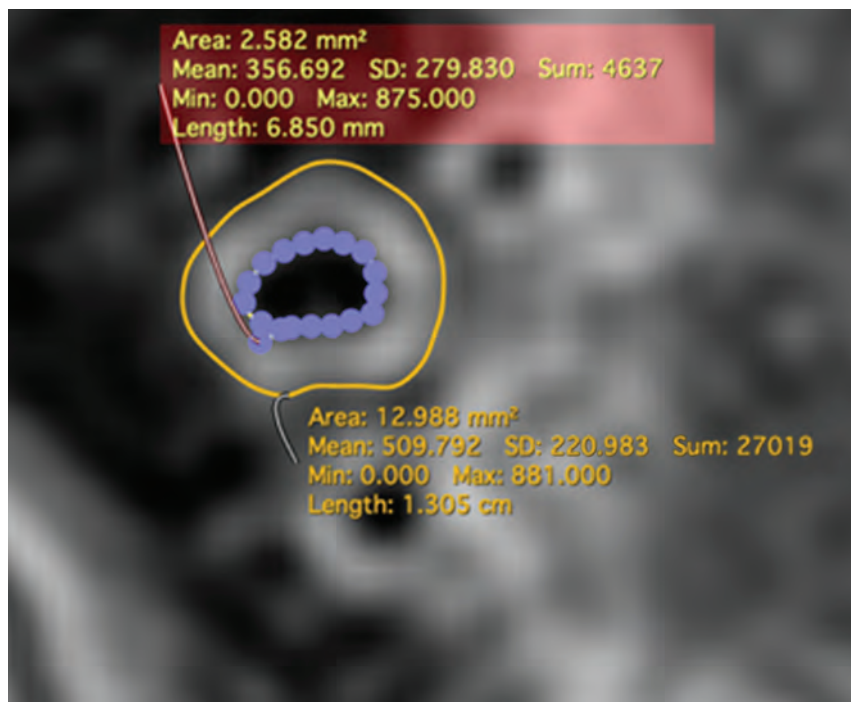


**FIG 1.** Quantitative measurement technique. Manual ROIs were drawn on representative images tracing the interface between the wall and lumen (luminal contour) and between the wall and surrounding tissues (outer wall contour). Total area of the vessel (area within the outer contour), luminal area (area within the inner contour), mean signal intensity, and SD were recorded for each patient. Sum indicates the sum of signal intensities within the selected region; Min, minimum; Max, maximum.

point scale: 1, no venous artifacts (complete suppression); 2, minimal central or peripheral nonsuppression that does not mimic a lesion; 3, central and peripheral nonsuppression that does not mimic a lesion; 4, flow nonsuppression that mimics pathology. Specific types of artifacts encountered on individual imaging acquisitions were recorded (motion, reduced SNR, arterial, and venous flow artifacts). Motion was graded on a 5-point Likert scale: 0, no motion; 1, minimal; 2, mild; 3, moderate; and 4, severe motion, based on a previously established scoring scale.<sup>20</sup> Arterial flow artifacts were documented for all acquisitions involving the following segments: vertebral arteries, petrous ICAs, cavernous ICAs, supraclinoid ICAs, M1 MCA,  $\geq$  M2 MCAs, P1 posterior cerebral artery,  $\geq$  P2 posterior cerebral arteries, A1 anterior cerebral artery,  $\geq$  A2 anterior cerebral arteries, and the basilar artery. Venous flow artifacts were recorded involving the following structures: dural venous sinuses, cortical veins, and deep veins.

In addition to qualitative imaging evaluation, quantitative evaluation was performed by a separate board-certified neuroradiologist (B.S., with 5 years of radiology experience). For each patient, manual ROIs were drawn on representative images from each postcontrast T1-SPACE, T1-DANTE-CAIPI-SPACE, and T1-DANTE-SPACE sequence (Fig 1). Measurements were performed on both diseased and normal segments, with ROI placement selected randomly between the posterior and anterior circulation for the normal-segment assessment. For those being assessed for intracranial vasculopathy (intracranial atherosclerotic disease, vasculitis, and so forth.), the measurement was taken from the lesion, while for those

undergoing IVW for aneurysm postcoiling, normal segments were selected. Two contours were generated tracing the interface between the wall and lumen (luminal contour) and between the wall and surrounding tissues (outer wall contour) using a freehand drawing tool (Horos, Lesser General Public License, Version 3.3.6; <https://horosproject.org>). The total area of the vessel (area within the outer contour), lumen area (area within the inner contour), mean signal intensity, and SD were recorded. Additional ROIs measuring 3 mm<sup>2</sup> in diameter were drawn in the normal-appearing cortical gray matter, in close proximity to the vessel being quantitatively analyzed for comparison. All measurements, labeling, and areas analyzed were saved for future reference and reproducibility assessment. Wall area was calculated as the difference in the total area of the vessel subtracted from the lumen area. The lumen contrast ratio was calculated using the following formula: Average Lumen Signal on a Single Section/Average Gray Matter Signal. The wall-to-lumen contrast ratio was determined using the following formula: Average Wall Signal on a Single Section/Average Lumen Signal. For quan-

titative measurement-reproducibility assessment, 30 randomly selected cases were analyzed using the same methodology and location by a second reviewer (A.S., with 2 years of radiology experience).

### Statistical Analysis

Analysis was performed using SPSS, Version 23.0 (IBM). Because not all the data were normally distributed as evaluated by the Kolmogorov-Smirnov test, all the data were expressed as median and interquartile range. The Wilcoxon matched-pairs signed-rank test was used to compare the measurements between different techniques. Rater values were averaged for the various sequence comparisons. A paired Student *t* test was used to compare the performance of the 2 sequences. The interobserver agreement was evaluated with the intraclass correlation coefficient, with absolute agreement and a 2-way random model. *P* < .05 was regarded as significant, and all *P* values were 2-sided.

## RESULTS

### Patient Data

A total of 96 subjects were reviewed; however, 7 early studies were excluded because T1-CAIPI-SPACE was performed without DANTE blood suppression. A total of 89 patients were included in the final analysis (55 women [61.8%]; 22–80 years of age; median age, 53 years). Of these 89 patients, 64 patients were imaged with postcontrast T1-DANTE-CAIPI-SPACE, and 25, with T1-DANTE-SPACE. The most common final clinical diagnoses were intracranial atherosclerotic disease in 33 patients and postaneurysm



**Table 2: Patient demographics**

Characteristics	Cohort
Age (age group) (median)	22–80 years, median age, 53 years
Sex (%)	
Male	34 (38.2%)
Female	55 (61.8%)
Clinical indication for IVW MR imaging	
Intracranial atherosclerotic disease	33
Aneurysm postcoiling/Pipeline stent/clipping	31
Vasculitis	11
Moyamoya disease/syndrome	3
Aneurysm	4
CADASIL	2
Radiation vasculopathy	1
Cryptogenic stroke	4

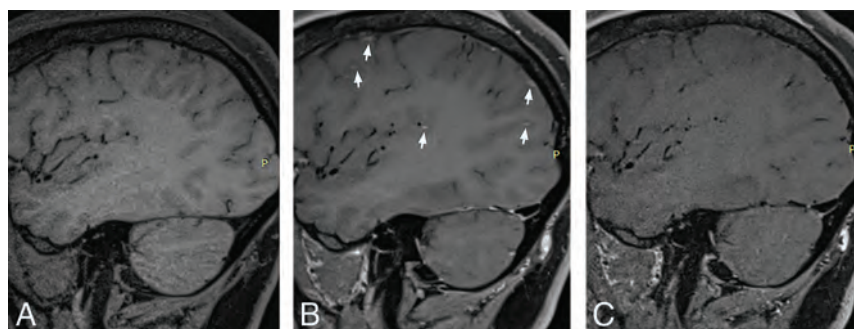


**FIG 2.** When we compare sagittal T1-SPACE precontrast (A) and sagittal T1-SPACE postcontrast (B), there are multiple focal enhancing lesions seen along the cortical surface (*small arrows*) on postcontrast IVW. On T1-DANTE-CAIPI-SPACE (C), the cortically based enhancing lesions disappear. The enhancing foci represent nonsuppression of blood signal in small cortical veins.

treatment in 31 patients. Complete patient demographic and diagnosis information is shown in Table 2.

### Qualitative Assessment

T1-DANTE-CAIPI-SPACE was rated higher than T1-SPACE for overall image quality (2, 1.5–2.5, versus 2.5, 2–3;  $P < .001$ ). T1-DANTE-CAIPI-SPACE had significantly lower SNR (2, 2–2.5, versus 1.5, 1–2,  $P < .001$ ), better arterial-suppression ratings (1.25, 1–1.5, versus 3, 2.5–3.5;  $P < .001$ ) (Online Supplemental Data), better artifact ratings (3, 2–3, versus 3.5, 3–4,  $P < .001$ ) (Online Supplemental Data), better venous blood suppression (1.5, 1.125–2 versus 3, 2–3.375;  $P < .001$ ) (Fig 2), and better lesion-assessment ratings (1.5, 1–2, versus 2, 1.5–2.5;  $P < .001$ ) compared with T1-SPACE (Online Supplemental Data). Forty-seven (73%) T1-SPACE series were adequate for lesion-pattern assessment (1 or 2); 54 (84%), on T1-DANTE-CAIPI-SPACE; and 43 (67%) were adequate on both. See Table 3 for complete T1-SPACE and T1-DANTE-CAIPI-SPACE comparison.

T1-DANTE-SPACE had significantly higher overall image quality (2, 1.5–2.5, versus 2.5, 2–3;  $P < .001$ ), higher SNR (2, 1.5–2.5, versus 2, 2–2.5;  $P < .001$ ), better artifact ratings (2.5, 2–3,

versus 3.5, 3–4;  $P < .001$ ), and improved arterial (1.5, 1–1.875, versus 3, 2.625–3.5;  $P < .001$ ) (Fig 3) and venous (2, 1.5–2, versus 3, 2–3;  $P < .001$ ) blood suppression (Fig 3) and lesion-assessment ratings (1.75, 1–2, versus 2.5, 2–3;  $P < .001$ ). Fourteen (56%) cases were adequate for lesion-pattern assessment on T1-SPACE, 22 (88%), on T1-DANTE-SPACE, and 14 (56%), on both. See Table 4 for complete T1-SPACE and T1-DANTE-SPACE comparison.

### Artifact Comparison

There was a significant difference in motion impact and scoring between T1-SPACE and T1-DANTE-CAIPI-SPACE (0, 0–0.5, versus 1, 0–2;  $P < .001$ ) (Table 3 and Online Supplemental Data). T1-SPACE and T1-DANTE-CAIPI-SPACE showed moderate or severe motion on 25% and 6.3% of comparative acquisitions, respectively. There was no significant difference in motion between T1-SPACE and T1-DANTE-SPACE ( $P = .5$ ) (Table 4 and Online Supplemental Data). T1-SPACE and T1-DANTE-SPACE each showed moderate or severe motion on 48% of comparative acquisitions.

For T1-SPACE acquisitions, the arterial segments most frequently affected by arterial flow artifacts were the V3/V4 vertebral artery segments (75.3%) (Online Supplemental Data), the petrous ICA (44.9%), M2 MCA (10.1%), and P2 of the posterior cerebral artery (4.5%). Venous flow artifacts were most frequently encountered on T1-SPACE involving the cortical veins (65.2%), dural venous sinuses (36%), and deep veins (13.5%). See the Online Supplemental Data for full details on artifacts encountered.

### Quantitative Assessment

Quantitative comparisons are listed in Tables 3 and 4. There was no significant difference between T1-SPACE and T1-DANTE-CAIPI-SPACE for lumen area or wall area comparisons. The lumen contrast ratio was significantly higher with T1-DANTE-CAIPI-SPACE (0.37, 0.27–0.48, versus 0.33, 0.26–0.43;  $P = .003$ ), possibly due to increased background noise affecting lumen measures or alterations in gray matter values; and wall-to-lumen contrast ratio was significantly lower (1.9, 1.7–2.5, versus 2.3, 1.9–2.6;  $P < .001$ ), indicating a worse wall-to-lumen signal, likely from increased background noise. There were no significant differences in the lumen area, wall area, lumen contrast ratio, or wall-to-lumen contrast ratio for the T1-SPACE and T1-DANTE-SPACE comparison.

### Agreement Analysis

Interreader agreement scores for the qualitative and quantitative assessments are listed in the Online Supplemental Data. Interreader agreement for lesion assessment (0.745) was moderate. The remaining qualitative image parameters, including image quality, SNR, artifact severity, motion, and arterial and venous blood suppression, had good-to-excellent agreement (0.771–0.938). The highest

**Table 3: SPACE versus DANTE-CAIPI-SPACE (average score of 2 reviewers)<sup>a</sup>**

	SPACE	DANTE-CAIPI-SPACE	P Value
Qualitative measurements			
Image quality	2.5 (2–3)	2 (1.5–2.5)	<.001
SNR	1.5 (1–2)	2 (2–2.5)	<.001
Artifacts	3.5 (3–4)	3 (2–3)	<.001
Art. blood suppression	3 (2.5–3.5)	1.25 (1–1.5)	<.001
Lesion	2 (1.5–2.5)	1.5 (1–2)	<.001
Ven. blood suppression	3 (2–3.375)	1.5 (1.125–2)	<.001
Motion	1 (0–2)	0 (0–0.5)	<.001
Quantitative measurement			
Lumen area (mm <sup>2</sup> )	7.9 (5.5–10.3)	7.6 (4.8–11.0)	.45
Wall area (mm <sup>2</sup> )	12.6 (9.9–16.3)	12.4 (10.1–14.6)	.04
Lumen CR	0.33 (0.26–0.43)	0.37 (0.27–0.48)	.003
Wall lumen CR	2.3 (1.9–2.6)	1.9 (1.7–2.5)	<.001

Note:—Art. indicates arterial; Ven., venous; CR, contrast ratio.

<sup>a</sup> Values are expressed as median (interquartile range).

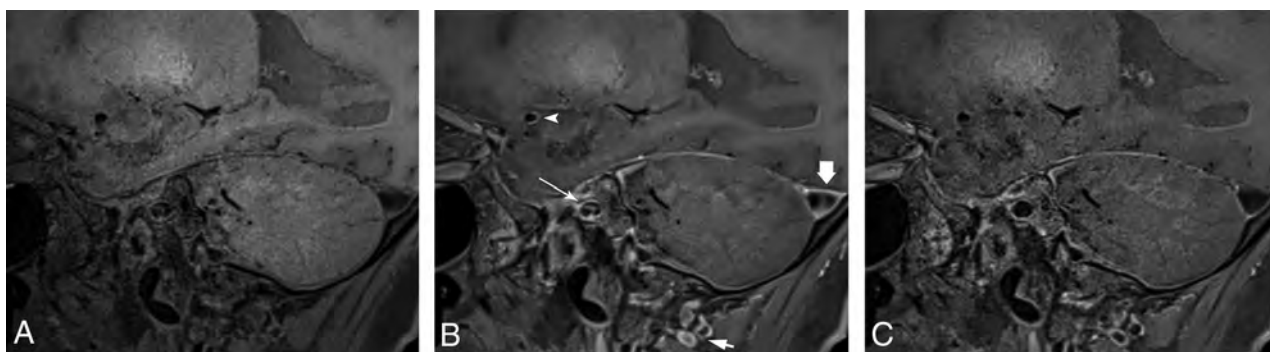


**FIG 3.** Sagittal T1-SPACE precontrast (A) shows a normal right M1 MCA segment without wall thickening. Sagittal T1-SPACE postcontrast (B) shows eccentric wall enhancement along the posterior, superior, and inferior walls of the M1 MCA (*arrowhead*) and the right V4 vertebral artery (*short arrow*) as well as nonsuppression of luminal signal in the right petrous ICA (*long arrow*) and the transverse sinus (*thick arrow*). Sagittal T1-DANTE-SPACE (C) shows the normal wall appearance of the right M1 MCA and V4 vertebral artery segments, similar to precontrast acquisition, and suppression of the venous signal.

agreement was with motion (0.938). The quantitative metrics of the lumen and wall area had excellent interreader agreement (0.969 and 0.942, respectively). The readers had good agreement for the lumen and wall-to-lumen contrast ratio (0.809 and 0.765, respectively).

In total 114 (57 SPACE, 43 DANTE-CAIPI-SPACE, and 14 DANTE-SPACE) sequences achieved sufficient lesion-pattern grades (1 or 2) to be reviewed for lesion pattern, with substantial overall interreader agreement ( $\kappa = 0.734$ ). By means of consensus assessments, SPACE and DANTE-CAIPI-SPACE showed excellent agreement for lesion pattern ( $\kappa = 0.906$ ), while SPACE and DANTE-SPACE had moderate agreement ( $\kappa = 0.512$ ); 50.9% and 48.2% of cases showed an eccentric pattern on T1-SPACE and T1-DANTE-CAIPI-SPACE/T1-DANTE-SPACE, respectively.

## DISCUSSION

The current study compares quantitative and qualitative image-quality assessments of conventional postcontrast T1-SPACE with either T1-DANTE or T1-DANTE-CAIPI-SPACE IVW. T1-DANTE-CAIPI-SPACE showed significant improvement in image quality, arterial and venous blood suppression, lesion conspicuity, and reduced artifact severity and motion, however, with lower SNR scores and quantitative metrics of SNR compared with T1-SPACE.

There was a reduction in the scan time of 37% with T1-DANTE-CAIPI-SPACE. T1-DANTE-SPACE showed significant improvements in all of the above qualitative assessments compared with T1-SPACE with the exception of motion, however, with 7% increased scan times. There were no significant quantitative metric differences between T1-SPACE and T1-DANTE-SPACE. Arterial nonsuppression artifacts on T1-SPACE most frequently affected the vertebral artery (75.3%) and petrous ICA (44.9%) segments, while venous artifacts most frequently affected the cortical veins (65.2%) and dural venous sinuses (36%). To our knowledge, no prior study has compared T1-SPACE with implementations of DANTE for blood suppression and CAIPI for imaging acceleration for IVW applications in a real-world clinical environment. These findings support the value of using DANTE for arterial and venous blood suppression in clinical IVW applications. The decision about whether to also use CAIPI for imaging acceleration depends on the clinical needs and workflow balanced against the need for higher SNR, which can be further impacted when using high-resolution imaging. While not appreciated in this evaluation, lower SNR as seen with DANTE-CAIPI may limit the image quality of IVW techniques. On the basis of the evaluations, however, the improved blood suppression and reduced motion artifacts with DANTE-CAIPI offset the SNR limitation in this study.

**Table 4: SPACE versus DANTE-SPACE (average score of 2 reviewers)<sup>a</sup>**

	SPACE	DANTE-SPACE	P Value
Qualitative measurements			
Image quality	2.5 (2–3)	2 (1.5–2.5)	<.001
SNR	2 (2–2.5)	2 (1.5–2.5)	<.001
Artifacts	3.5 (3–4)	2.5 (2–3)	<.001
Art. blood suppression	3 (2.625–3.5)	1.5 (1–1.875)	<.001
Lesion	2.5 (2–3)	1.75 (1–2)	<.001
Ven. blood suppression	3 (2–3)	2 (1.5–2)	<.001
Motion	0.5 (0–2.75)	0.75 (0–2)	.50
Quantitative measurement			
Lumen area (mm <sup>2</sup> )	5.9 (4.5–8.4)	6.8 (4.9–8.4)	.66
Wall area (mm <sup>2</sup> )	14.4 (9.9–18.2)	14.1 (10.9–20.1)	.09
Lumen CR	0.33 (0.26–0.55)	0.35 (0.26–0.53)	.22
Wall lumen CR	2.2 (1.8–2.4)	2.2 (1.9–2.6)	.46

**Note:**—Art. indicates arterial; Ven., venous; CR, contrast ratio.

<sup>a</sup> Values are expressed as median (interquartile range).

Optimal IVW requires a combination of sufficient SNR, high spatial resolution, and optimal blood suppression for vessel wall visualization and vasculopathy evaluation. Currently, T1WI fast spin-echo variable refocusing flip angle sequences are the most often used 3D IVW sequences.<sup>3</sup> These sequences use a varying flip angle sweep to maintain stable signal over the long echo-trains and have high intrinsic black-blood properties due to intravoxel dephasing among the fast-spinning protons.<sup>21</sup> 3D techniques, however, are susceptible to incomplete blood suppression, especially after intravenous gadolinium administration, which results in time-to-inversion shortening of blood.<sup>22</sup> The high-resolution requirements also result in reduced SNR, leading to increased background noise and luminal signal.<sup>23</sup> This is especially true in certain pathologies such as aneurysms, in which slow and turbulent flow within the aneurysm sac could be mistaken for aneurysm wall enhancement.<sup>10</sup> Apart from the technical requirements, longer acquisition sequence times hinder widespread clinical use, especially in critically ill, unstable, and noncooperative patients. Longer acquisition times often translate to increased patient anxiety and discomfort and the likelihood of motion-degraded images, limiting diagnostic quality.<sup>20</sup> Long IVW scan times also negatively impact imaging throughput and may not be feasible to use in busy clinical practices.

Parallel imaging is the most commonly used acceleration technique; however, it comes with a loss of SNR by a factor of the square root of the acceleration factor secondary to reduced signal averaging, and it also results in spatially varying noise amplification (g-factor).<sup>24</sup> In comparison, CAIPI acceleration modifies the appearance of aliasing artifacts during data acquisition, thereby reducing the g-factor for a certain coil geometry and a certain imaging protocol and has been shown to be superior to standard 2D generalized autocalibrating partially parallel acquisition in terms of signal loss and image quality, especially in the central imaging FOV.<sup>19</sup>

The DANTE preparation module strengthens the black-blood effect by a series of nonselective low flip-angle pulses interleaved with gradient pulses, resulting in a spoiling effect in which flowing spins cannot achieve a steady-state. In addition to providing robust arterial blood suppression, DANTE significantly improves venous blood suppression.<sup>22</sup> Our study showed similar improvements in arterial and venous blood suppression with DANTE implementation in a larger cohort and applied to the intracranial

vasculature. Cho et al<sup>7</sup> compared 3D T1-SPACE and BrainView (Philips Healthcare) with and without DANTE or MSDE in 14 healthy volunteers and found no significant difference in image-quality assessments whether DANTE was included or not. Their study, however, focused only on mid-M1 and M2 and distal basilar artery segments, while we evaluated the full intracranial and visualized extracranial vasculature with qualitative assessment. The quantitative assessment in our study, similarly, did not show any significant difference between T1-SPACE and T1-DANTE-SPACE and lower contrast ratios on T1-DANTE-CAIPI-SPACE relative to T1-SPACE. Specific segments, however, were most commonly involved with arterial flow artifacts on qualitative assessment in our study, specifically the petrous ICA and vertebral arteries, segments not evaluated by Cho et al. However, arterial flow artifacts were seen in all segments. Kalsoum et al<sup>10</sup> evaluated 22 patients with 30 intracranial aneurysms with T1-SPACE and MSDE-T1-SPACE and found that 10/30 aneurysms showed wall enhancement on T1-SPACE compared with 2/30 on MSDE-T1-SPACE ( $P < .001$ ) from artifactual enhancement on T1-SPACE secondary to flow artifacts, similar to findings in the current study. Our study, however, evaluated a different flow-suppression technique (DANTE), incorporated imaging acceleration with CAIPI, and evaluated various vasculopathies that present in a routine clinical work-up.

Our study has several limitations. First, while the sample size is sufficient for technique comparison, larger sample sizes would be needed for technique comparison for individual vasculopathies. Second, we evaluated only a limited number of blood-suppression and imaging-acceleration techniques. We did not include compressed sensing or artificial intelligence reconstruction approaches for imaging acceleration, nor did we include MSDE for blood suppression. Due to the impact on the SNR of MSDE, similar high resolution was difficult to achieve with IVW protocols for the current study. We also did not compare T1-DANTE-CAIPI-SPACE and T1-DANTE-SPACE head-to-head. These comparisons would be valuable to see in a future larger study. Future large-cohort studies are needed to validate our results and to further optimize imaging protocols. Third, while ratings were performed randomly and independently for each acquisition, an experienced rater would be able to differentiate techniques, potentially limiting absolute blinding to acquisition.



## CONCLUSIONS

Accelerated and blood-suppressed post-contrast T1-DANTE-CAIPI-SPACE had fewer image artifacts, less motion, improved blood suppression and a shorter scan time, but lower qualitative and quantitative SNR ratings relative to conventional T1-SPACE IVW. Blood-suppressed post-contrast T1-DANTE-SPACE had superior SNR, blood suppression, higher image quality and fewer image artifacts, but slightly longer scan time relative to T1-SPACE.

Disclosure forms provided by the authors are available with the full text and PDF of this article at [www.ajnr.org](http://www.ajnr.org).

## REFERENCES

1. de Havenon A, Yuan C, Tirschwell D, et al. **Nonstenotic culprit plaque: the utility of high-resolution vessel wall MRI of intracranial vessels after ischemic stroke.** *Case Rep Radiol* 2015;2015:356582 CrossRef Medline
2. Gariel F, Ben Hassen W, Boulouis G, et al. **Increased wall enhancement during follow-up as a predictor of subsequent aneurysmal growth.** *Stroke* 2020;51:1868–72 CrossRef Medline
3. Mandell DM, Mossa-Basha M, Qiao Y, et al; Vessel Wall Imaging Study Group of the American Society of Neuroradiology. **Intracranial vessel wall MRI: principles and expert consensus recommendations of the American Society of Neuroradiology.** *AJNR Am J Neuroradiol* 2017;38:218–29 CrossRef Medline
4. Mossa-Basha M, de Havenon A, Becker KJ, et al. **Added value of vessel wall magnetic resonance imaging in the differentiation of Moyamoya vasculopathies in a non-Asian cohort.** *Stroke* 2016;47:1782–88 CrossRef Medline
5. Mossa-Basha M, Shibata DK, Hallam DK, et al. **Added value of vessel wall magnetic resonance imaging for differentiation of nonocclusive intracranial vasculopathies.** *Stroke* 2017;48:3026–33 CrossRef Medline
6. Qiao Y, Anwar Z, Intrapiromkul J, et al. **Patterns and implications of intracranial arterial remodeling in stroke patients.** *Stroke* 2016;47:434–40 CrossRef Medline
7. Cho SJ, Jung SC, Suh CH, et al. **High-resolution magnetic resonance imaging of intracranial vessel walls: comparison of 3D T1-weighted turbo spin echo with or without DANTE or iMSDE.** *PLoS One* 2019;14:e0220603 CrossRef Medline
8. Dieleman N, Yang W, van der Kolk AG, et al. **Qualitative evaluation of a high-resolution 3D multi-sequence intracranial vessel wall protocol at 3 Tesla MRI.** *PLoS One* 2016;11:e0160781 CrossRef Medline
9. Hu Z, van der Kouwe A, Han F, et al. **Motion-compensated 3D turbo spin-echo for more robust MR intracranial vessel wall imaging.** *Magn Reson Med* 2021;86:637–47 CrossRef Medline
10. Kalsoum E, Chabernaud Negrier A, Tuilier T, et al. **Blood flow mimicking aneurysmal wall enhancement: a diagnostic pitfall of vessel wall MRI using the postcontrast 3D turbo spin-echo MR imaging sequence.** *AJNR Am J Neuroradiol* 2018;39:1065–67 CrossRef Medline
11. Mossa-Basha M, Huynh TJ, Hippe DS, et al. **Vessel wall MRI characteristics of endovascularly treated aneurysms: association with angiographic vasospasm.** *J Neurosurg* 2018;131:859–67 CrossRef Medline
12. Mossa-Basha M, Hwang WD, De Havenon A, et al. **Multicontrast high-resolution vessel wall magnetic resonance imaging and its value in differentiating intracranial vasculopathic processes.** *Stroke* 2015;46:1567–73 CrossRef Medline
13. Yang Q, Deng Z, Bi X, et al. **Whole-brain vessel wall MRI: Aa parameter tune-up solution to improve the scan efficiency of three-dimensional variable flip-angle turbo spin-echo.** *J Magn Reson Imaging* 2017;46:751–57 CrossRef Medline
14. Zhu C, Tian B, Chen L, et al. **Accelerated whole brain intracranial vessel wall imaging using black blood fast spin echo with compressed sensing (CS-SPACE).** *MAGMA* 2018;31:457–67 CrossRef Medline
15. Cornelissen BMW, Leemans EL, Coolen BF, et al. **Insufficient slow-flow suppression mimicking aneurysm wall enhancement in magnetic resonance vessel wall imaging: a phantom study.** *Neurosurg Focus* 2019;47:E19 CrossRef Medline
16. Wang J, Helle M, Zhou Z, et al. **Joint blood and cerebrospinal fluid suppression for intracranial vessel wall MRI.** *Magn Reson Med* 2016;75:831–38 CrossRef Medline
17. Zhu C, Graves MJ, Yuan J, et al. **Optimization of improved motion-sensitized driven-equilibrium (iMSDE) blood suppression for carotid artery wall imaging.** *J Cardiovasc Magn Reson* 2014;16:61 CrossRef
18. Balu N, Zhou Z, Hippe DS, et al. **Accelerated multi-contrast high isotropic resolution 3D intracranial vessel wall MRI using a tailored k-space undersampling and partially parallel reconstruction strategy.** *MAGMA* 2019;32:343–57 CrossRef Medline
19. Falkovskiy P, Brenner D, Feiweier T, et al. **Comparison of accelerated T1-weighted whole-brain structural-imaging protocols.** *Neuroimage* 2016;124:157–67 CrossRef Medline
20. Andre JB, Bresnahan BW, Mossa-Basha M, et al. **Toward quantifying the prevalence, severity, and cost associated with patient motion during clinical MR examinations.** *J Am Coll Radiol* 2015;12:689–95 CrossRef Medline
21. Qiao Y, Steinman DA, Qin Q, et al. **Intracranial arterial wall imaging using three-dimensional high isotropic resolution black blood MRI at 3.0 Tesla.** *J Magn Reson Imaging* 2011;34:22–30 CrossRef Medline
22. Xie Y, Yang Q, Xie G, et al. **Improved black-blood imaging using DANTE-SPACE for simultaneous carotid and intracranial vessel wall evaluation.** *Magn Reson Med* 2016;75:2286–94 CrossRef Medline
23. Kale SC, Chen XJ, Henkelman RM. **Trading off SNR and resolution in MR images.** *NMR Biomed* 2009;22:488–94 CrossRef Medline
24. Jara H, Yu BC, Caruthers SD, et al. **Voxel sensitivity function description of flow-induced signal loss in MR imaging: implications for black-blood MR angiography with turbo spin-echo sequences.** *Magn Reson Med* 1999;41:575–90 CrossRef Medline

# Prevalence of Intracranial Aneurysms in Hereditary Hemorrhagic Telangiectasia: Report from a Single Reference Center

M.S. Perez Akly, C. Vazquez, C.H. Besada, M.J. Rodriguez, M.F. Conde, A.R. Cajal, V.A. Peuchot, D. Dardik, M.M. Baccanelli, and M.M. Serra



## ABSTRACT

**BACKGROUND AND PURPOSE:** Neurologic manifestations in hereditary hemorrhagic telangiectasia include an increased incidence of brain abscesses and ischemic strokes due to paradoxical embolization in addition to a wide spectrum of symptoms and complications due to typical brain vascular malformations. Intracranial aneurysms are not part of this brain vascular malformation spectrum. The aim of this study was to determine their prevalence in patients with hereditary hemorrhagic telangiectasia.

**MATERIALS AND METHODS:** This was a single-center, retrospective study. Adult patients from the institutional Hereditary Hemorrhagic Telangiectasia registry with a definitive diagnosis of hereditary hemorrhagic telangiectasia and an available report or angiographic imaging study were included and reviewed to determine the intracranial aneurysm prevalence. In addition, the morphologic characteristics of intracranial aneurysms and possible associated risk factors were collected.

**RESULTS:** Two hundred twenty-eight patients were analyzed. Thirty-seven aneurysms in 33 patients (14.5%; 95% CI, 9.9%–19%) were found. The median diameter of intracranial aneurysms was 3.2 mm (interquartile range, 2.6–4.4 mm). No association between intracranial aneurysm and sex, age, or genetic background was noted. There were no subarachnoid hemorrhagic events due to intracranial aneurysm rupture.

**CONCLUSIONS:** Due to the high prevalence of intracranial aneurysms in adult patients with hereditary hemorrhagic telangiectasia, further studies regarding bleeding risks and monitoring should be addressed.

**ABBREVIATIONS:** *ACVRL1* = activin receptor-like kinase 1 or ALK-1; BVM = brain vascular malformation; *ENG* = endoglin; HHT = hereditary hemorrhagic telangiectasia; IA = intracranial aneurysm; IQR = 25–75 interquartile range; *MADH4* = mothers against decapentaplegic drosophila homolog 4; MMP = matrix metalloproteinase; TGF $\beta$ /BMP = Transforming Growth Factor  $\beta$ /bone morphogenetic protein

Hereditary hemorrhagic telangiectasia (HHT) is a multisystemic vascular disorder characterized by the presence of mucocutaneous telangiectasias and vascular malformations in organs including the central nervous system, liver, lungs, and the digestive tract.<sup>1</sup> It is a rare autosomal dominant disease that affects 1 in 5000–8000 people worldwide.<sup>2,3</sup> The diagnosis is based on the Curaçao criteria and/or genetic testing.<sup>3</sup> The genes affected in

HHT encode receptor proteins involved in the TGF $\beta$ /BMP signaling pathway, which plays an important role in angiogenesis and vascular remodeling.<sup>4</sup> Mutations in the *ENG* or *ACVRL1* genes are found in approximately 85% of individuals with HHT and up to 96% when the Curaçao criteria are strictly applied.<sup>5</sup> Approximately 15% of patients diagnosed with HHT do not present with any of these gene mutations, suggesting that other genes might be involved. The *MADH4* gene is mutated in patients with a combined syndrome of juvenile polyposis and HHT, representing 1%–3% of HHT cases.<sup>6</sup>

Neurologic manifestations of HHT include a higher incidence of brain abscesses and ischemic strokes due to paradoxical embolization through pulmonary arteriovenous fistulas, intracranial hemorrhages caused by BVMs, and mild or moderate psychomotor disturbances in some patients with manganese deposits in the basal ganglia.<sup>7–10</sup> The spectrum of BVMs in HHT includes classic AVMs, capillary malformations, cavernous malformations, venous angiomas/developmental venous anomalies, vein of Galen malformations, telangiectasias, enlarged capillary-sized vessels,

Received January 30, 2022; accepted after revision March 17.

From the Departments of Radiology (M.S.P.A., C.H.B., M.J.R., M.F.C.), Internal Medicine (C.V., M.M.S.), and Neurosurgery (M.M.B.), Hereditary Hemorrhagic Telangiectasia Unit (M.S.P.A., C.H.B., A.R.C., M.M.B., M.M.S.), University Institute (A.R.C., M.M.B., M.M.S.), and Internal Medicine Research Area (V.A.P.), Hospital Italiano, Buenos Aires, Argentina; A.R.G. Argentine Rendu Study Group (M.S.P.A., C.V., C.H.B., A.R.C., V.A.P., D.D., M.M.B., M.M.S.), Buenos Aires, Argentina; Translational Medicine and Biomedical Engineering Institute (A.R.C.), Buenos Aires, Argentina; and Department of Radiology (D.D.), Clínica Instituto de Diagnóstico Sociedad Anónima (INDISA), Santiago, Chile.

Please address correspondence to Manuel S. Perez Akly, MD, J.D. Peron 4190, Radiology Department, Hospital Italiano de Buenos Aires, Ciudad Autónoma de Buenos Aires, C1181ACH, Argentina; e-mail: sliman.perez@hospitalitaliano.org.ar

Indicates article with online supplemental data.

<http://dx.doi.org/10.3174/ajnr.A7505>

high-flow pial fistulas, and mixed malformations. Most classic presentations in HHT include multiple or single micro-AVMs or arteriovenous fistulas.<sup>7,10</sup> The prevalence of BVMs is around 23%,<sup>11</sup> with an estimated risk of hemorrhage that ranges from 0.27% to 0.46% annually.<sup>12</sup> Screening with MR imaging is mandatory in children and adults, but a definitive diagnosis needs conventional angiography. Once a BVM is diagnosed, the management should be discussed with an expert vascular neurosurgery team.<sup>7,10,13</sup>

Intracranial aneurysms are acquired vascular lesions with an estimated prevalence ranging from 2% to 5% in the general population.<sup>14</sup> The exact etiopathogenesis of intracranial aneurysms (IAs) still remains uncertain. It may result from congenital vascular wall defects, atheromatous disease, trauma or infectious emboli, or other systemic or local inflammatory processes.<sup>15</sup> IAs are believed to be associated with the presence of AVMs,<sup>16</sup> and IA development may be related to hemodynamic changes caused by the presence of shunting in AVMs.<sup>17</sup>

Although cases of IA have been reported in patients with HHT, the association between HHT and the existence of IA is still unclear.<sup>10</sup> The main aim of this study was to describe the prevalence of IAs and their morphologic characteristics and explore possible risk factors associated with them.

## MATERIALS AND METHODS

A descriptive/analytic cross-sectional study was designed and conducted at an HHT referral center in Buenos Aires, Argentina. Patients were eligible if they were older than 17 years of age, had definite HHT based on the presence of  $\geq 3$  Curaçao criteria (epistaxis: spontaneous and recurrent nasal bleeding; telangiectasias: multiple, at characteristic sites; visceral lesions: pulmonary, liver, gastrointestinal, cerebral, and spinal vascular malformations; family history: a first-degree relative with HHT according to these criteria) or a confirmed genetic test and had available angiographic studies (MRA, CTA, and/or cerebral angiography). The availability of these studies was defined as either images being uploaded to the hospital's medical record system or an available reliable imaging report with detailed data, in case the angiographic study was performed externally. The main outcome was to determine the prevalence of IAs within the study population. In addition, clinical and genetic factors would be analyzed to determine their possible association with an IA diagnosis. Data were obtained until December 2021 from the institutional HHT registry (ClinicalTrials.gov identifier: NCT01761981), which was started in 2012. This registry includes patients with confirmed HHT and/or who are in the process of being diagnosed. This study was approved by the local ethics review board, and each included patient consented to the use of data for research purposes. All the data analyzed in this study were properly anonymized.

### Imaging Protocol and Analysis

CTA scans were obtained with a 64-detector-row CT system (Aquilion; Toshiba) or a 320-detector-row system (Aquilion One; Toshiba), including a nonenhanced phase and a contrast-enhanced phase, with 0.5-mm-thick sections every 0.3 mm, 0.641 pitch, 300 mAs, 120 kV, and 0.5-second scan time. For the contrast-enhanced

phase, we used a 1-mL/kg dose of nonionic contrast medium (Iobitridol, Xenetix 350; Guerbet) delivered intravenously through an automatic injection pump at 4 mL/s. The DICOM data from the CT scanner were sent from a local computer to a Vitrea 2 workstation (Vital Images), where images are evaluated and 2D multiplanar reformations, 3D volume-rendering, maximum intensity projections, and minimum intensity projections were used. MRA images were obtained on 1.5T Achieva (Philips Healthcare), Magnetom Essenza (Siemens), or Magnetom Avanto (Siemens) magnets, or a 3T Ingenia (Philips Healthcare) system. The protocol included T2, FLAIR, gradient recalled-echo, DWI, and T1-weighted images in an axial plane, axial TOF volume, and contrast-enhanced T1-weighted spoiled gradient echo sagittal volume. Cerebral DSAs were performed using Integris V5000 (Phillips Healthcare), BV 300 (Phillips Healthcare), or Artis Zeego (Siemens) systems. The angiographic studies that were part of the initial clinical assessment of the included patients were retrospectively reviewed by 2 senior neuroradiologists. In case of disagreement, consensus was reached by a third neuroradiologist. The presence and number of aneurysms per patient and their imaging characteristics including geometric measurements (width, height, and neck diameter) and anatomic location were registered.

### Other Registered Variables

We registered key clinical variables: age, sex, Curaçao criteria, the presence of other vascular malformations in each enrolled patient, and the results of mutations on target genes (*ENG*, *ACVRL1*, and *MADH4*) when available. The presence of other risk factors associated with IAs in the general population such as hypertension and tobacco use were also taken into account.

### Statistical Analysis

Continuous variables are described as the mean and SD or median and interquartile range (IQR) according to distribution. Categorical variables are described as absolute frequency and percentage. The IA prevalence was determined as the proportion of patients having at least 1 IA within the total population of patients with confirmed HHT who had at least 1 suitable angiographic study available for revision. For analyzing the association between baseline clinical and genetic characteristics with the outcome, categorical data were compared using the Fisher exact test, and continuous data were compared using the Mann-Whitney test. All statistical analyses were performed using STATA, Version 14 (StataCorp). One- and 2-sided *P* values < .05 were considered statistically significant.

## RESULTS

Of the 707 patients currently enrolled in the registry, 566 had confirmed HHT. Of these, 228 (40.3%) subjects had an angiographic study and were finally included in the study. Reliable imaging reports were the only source of data in 38 (16.7%) of the included patients. Female patients represented 61.8% of the included population (Online Supplemental Data). The median age was 49.0 years (IQR, 38.4–64.1 years). Demographic characteristics are detailed in Table 1.

Thirty-seven aneurysms were identified in 33 patients (14.5%; 95% CI, 9.9%–19%), with 2 patients having 2 and another single



patient having 3 IAs. The most frequent locations of IAs were the following: 9 in the middle cerebral artery, 9 in the carotid intracavernous segment, and 8 in the ophthalmic segment of the ICA. The median diameter of IAs was 3.2 mm (IQR, 2.6–4.4 mm). Further IA characteristics are mentioned in Table 2. Angiographic images of IAs from 2 different patients are shown in Figs 1 and 2.

AVMs were found in 39 patients; within this subgroup, 7 patients also had IAs, with no statistical association between both vascular malformations. Only 2 IAs were located in the same

vascular territory as the AVM. Furthermore, among those patients who had available images for studying aneurysms outside the CNS, no association between IAs and aneurysms (mostly splanchnic) in other body segments was found. There were no differences in either age, sex, Curaçao criteria, hypertension, or tobacco use between patients with and without IAs. Genetic results were available in 81 patients (35.5%), with 39 patients having *ENG* mutations, 25 having *ACVRL1* mutations, and 10 with *MADH4* mutations. In 7 patients, genetic tests were noninformative. No statistically significant association was found between patients with and without IAs regarding the distribution of genetic results (Table 3).

**Table 1: Population characteristics**

Baseline Characteristics	n = 228
Sex (female) (No.) (%)	141 (61.8%)
Age (median) (IQR) (yr)	49.0 (38.4–64.1)
Curaçao criteria (No.) (%)	
Epistaxis	209 (91.7%)
Telangiectasias	219 (96.1%)
Arteriovenous malformations	163 (71.5%)
Family history	197 (86.4%)
Curaçao criteria (3 of 4) (No.) (%)	90 (39.5%)
Curaçao criteria (4 of 4) (No.) (%)	126 (55.3%)
CTA (No.) (%)	24 (10.5%)
MRA (No.) (%)	203 (89.0%)
Cerebral angiography (No.) (%)	36 (15.8%)
BVM (No.) (%)	60 (26.3%)
AVM (No.) (%)	39 (17.1%)
IA	33 (14.5%)

**Table 2: Intracranial aneurysm characteristics**

Characteristics	n = 37
Location (No.) (%)	
MCA	9 (24.3%)
Intracavernous carotid artery	9 (24.3%)
Ophthalmic artery	8 (21.6%)
Posterior communicating artery	3 (8.1%)
Anterior communicating artery	2 (5.4%)
Anterior cerebral artery	1 (2.7%)
Posterior cerebral artery	2 (5.4%)
Basilar artery	3 (8.1%)
Width (mm) <sup>a</sup>	3.2 (2.6–4.4)
Height (mm) <sup>a</sup>	2.3 (1.9–2.9)
Neck (mm) <sup>a</sup>	2.6 (2.0–3.8)
Aspect (mm) <sup>a</sup>	0.83 (0.6–1.3)
Size (mm) <sup>a</sup>	1.2 (1.0–1.5)

<sup>a</sup>Non-normally distributed variables are expressed in median and IQR (25th–75th percentiles).

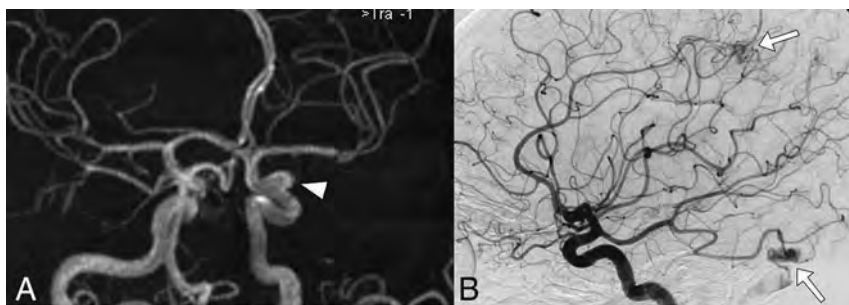


**FIG 1.** Cerebral MRA (A) and DSA (B) images of a 39-year-old female patient that meet 4 of 4 Curaçao criteria show an ophthalmic segment of a left carotid artery aneurysm (arrowhead) and AVMs in the parietal and occipital contralateral lobes (arrows).

## DISCUSSION

A high prevalence of IAs among patients with HHT was found in this study. The IA prevalence was also increased in patients with a family history of IA<sup>18</sup> and in certain inherited diseases, including autosomal dominant polycystic kidney disease and some connective tissue disorders.<sup>19</sup> A retrospective study by Kim et al<sup>20</sup> showed that the prevalence of IAs was as follows: 14% among patients with Marfan syndrome, 12% among patients with Ehlers-Danlos syndrome, 11% among patients with neurofibromatosis type 1, and 28% among patients with Loeys-Dietz syndrome. The Loeys-Dietz syndrome is associated with genetic mutations, also involving the TGF- $\beta$ /BMP pathway, especially in the SMAD2/3 proteins, a pathway that is also altered in HHT.<sup>20–22</sup> Moreover, the combined syndrome of juvenile polyposis and HHT syndrome, caused by *MADH4* mutations, is also associated with aortic root aneurysms and joint hypermobility.<sup>23,24</sup>

Numerous reports describe the presence of IAs in patients with HHT,<sup>25–33</sup> and many authors include HHT in a group of hereditary diseases that present with a higher prevalence of IAs, such as Marfan, Ehlers-Danlos, and polycystic kidney syndromes and neurofibromatosis,<sup>19,34,35</sup> but these studies do not specifically analyze the prevalence of IAs in patients with HHT in a quantitative manner. Several authors have studied the neurologic manifestations of HHT.<sup>11,36–38</sup> These researchers describe multiple kinds of BVMs and, second, mention the frequency of IAs, such as Brinjikji et al,<sup>38,39</sup> whose findings indicated that the prevalence of IAs is around 2%, similar to that of the general population. There is a specific study that looked for the prevalence of aneurysms in all locations in HHT, which reported a higher prevalence of IAs of around 4%.<sup>40</sup> The number of aneurysms in these popu-

lations might have been underestimated due to the lack of angiographic studies to evaluate many of these patients.

The prevalence of IAs in the present HHT cohort was 14.5%, whereas the reported prevalence in the general population is close to 3%–5%.<sup>18</sup> Most of the aneurysms were small, with a predilection for the anterior circulation, similar to those observed in the general population.<sup>15</sup> These findings could correlate with the vascular malformations, which these patients have in multiple

organs, even aneurysms in the splanchnic circulation. Considering that BVMs are more frequent in patients with HHT having the *ENG* mutation,<sup>41</sup> a possible link between IAs and genotypes arises, but no statistically significant association was found.

The coexistence of IA and brain AVMs in patients without HHT is estimated to be between 5% and 20%.<sup>42</sup> Although the pathogenesis of IAs in these patients is not fully understood, it is believed that it may be related to hemodynamic factors triggered by the presence of a shunt in the AVM.<sup>17</sup> AVMs and IAs were both found in 7 patients, but only 2 were in the same vascular territory as the AVM, which may be interpreted as flow-related. Even subtracting these 2 patients, the prevalence would still be high, so the increased prevalence of IAs in HHT could be explained by vascular alterations caused by mutations in genes of the *TGF $\beta$ /BMP* pathway mentioned above. There is evidence pointing to inflammation as a mechanism of aneurysm formation in patients without HHT. The process begins with a hemodynamic or inflammatory insult, with a local increase in matrix metalloproteinases (MMPs) released by macrophages and mast cells, with intimal migration and shape changes of the smooth-

muscle cells.<sup>43</sup> In HHT, a state of chronic inflammation of the vascular wall, induced by an imbalance between pro- and anti-inflammatory factors of mononuclear cells, has been widely reported. This would explain one of the possible biologic bases to suspect a higher incidence of IAs in HHT.<sup>44</sup> In addition, endoglin is involved in cell migration, proliferation, and extracellular matrix remodeling, mechanisms that involve MMPs and macrophages.<sup>44,45</sup> Furthermore, endoglin and *TGF $\beta$ /BMP* are involved in inflammation and the tissue-repair processes as well as in angiogenesis. The vascular wall of AVMs in HHT is abnormal and lacks organized mural cell layers such as pericytes and smooth-muscle cells.<sup>46</sup> Finally, drugs that inhibit MMPs such as doxycycline are proposed for the treatment of epistaxis in HHT and unruptured IAs.<sup>43,47</sup>

The present study has research limitations to be acknowledged. First, it is a retrospective study and, thus, though only patients with angiographic studies were included, not all of them were evaluated with the same angiographic imaging technique, and alternative modalities have different sensitivities and specificities to detect IAs. In addition, a small proportion of these patients had a reliable imaging report but no available image for us to re-evaluate. Along the same lines, there were missing data regarding other risk factors for aneurysm development in some patients. Patient genotypes were not available for the entire cohort, and the relationship between IAs and mutations could not be fully studied; therefore, the lack of an association found should be viewed with caution until further studies are developed. Only adult patients were enrolled, as for other BVMs, the prevalence could be similar in the pediatric population,

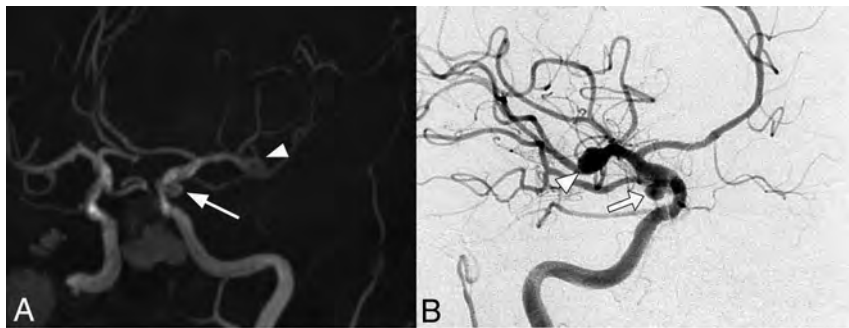


**FIG 2.** Cerebral MRA (A) and DSA (B) images of a 78-year-old female patient that meet 4 of 4 Curaçao criteria show a right MCA bifurcation aneurysm (arrowhead) and another one located in the right posterior communicating artery (arrow).

**Table 3: Bivariate analysis between baseline variables and intracranial aneurysms**

Baseline Characteristics	Intracranial Aneurysm (n = 33)	No Intracranial Aneurysm (n = 195)	P Value <sup>a</sup>
Sex (female) (No.) (%)	21 (63.6%)	120 (61.5%)	.85
Age (median) (IQR) (yr)	51.4 (43.3–69.3)	48.0 (38–63.2)	.10
Curaçao criteria (No.) (%)			
Epistaxis	33 (100%)	176 (90.3%)	.08
Telangiectasias	32 (97.0%)	187 (95.9%)	1.00
AVMs	25 (75.8%)	138 (70.8%)	.68
Family history	26 (78.8%)	171 (87.7%)	.17
BVMs (No.) (%)	13 (39.4%)	47 (24.1%)	.09
AVMs (No.) (%)	7 (21.2%)	32 (16.4%)	.46
Hypertension (n = 198) (No.) (%) <sup>b</sup>	8 (25.8%)	29 (18.0%)	.32
Tobacco use (n = 189) (No.) (%) <sup>b</sup>	11 (33.3%)	39 (25.0%)	.39
Extracranial aneurysms (No.) (%) (n = 140) <sup>b</sup>	7 (35.0%)	20 (16.7%)	.07
Genetic results (No.) (%) (n = 81) <sup>b</sup>			
<i>ENG</i>	9 (27.3%)	72 (36.9%)	
<i>ACVRL1</i>	4 (44.4%)	35 (48.6%)	
<i>MADH4</i>	3 (33.3%)	22 (30.6%)	.43
	0	10 (13.9%)	
Noninformative	2 (22.2%)	5 (6.9%)	

<sup>a</sup>Two-sided P values. Medians are analyzed with Mann-Whitney U tests, and dichotomous variables, with the Fisher exact test.

<sup>b</sup>Included patients with available data for analysis from the medical record system.

but this issue should be addressed in future studies. Finally, because this study does not have a control group and there is a lack of regional data on IA prevalence, these results have been compared with those reported in other populations.

Patients with HHT are usually evaluated for BVMs with contrast-enhanced MR imaging; however, the results found in this study may suggest adding an angiography sequence to the current screening methodology in search of IAs. The largest meta-analysis on IA rupture risk included data from 8382 patients. This study identified 6 independent risk factors for aneurysm rupture: older than 70 years of age, hypertension, previous SAH from another aneurysm, the size and site of the aneurysm, and the patient's geographic region. The subsequently developed score for prediction of aneurysm rupture risk is based on these 6 key risk factors and provides absolute estimates for a 5-year rupture risk, ranging from 0.3% to  $\geq 15\%$ .<sup>48</sup> There were no SAH events in this cohort due to IA rupture, and all patients are under close follow-up and/or have already been treated according to the usual standards of care. Although there is no prospective information about the rate of rupture of IA in patients with HHT, medical follow-up on these patients should be considered to prevent SAH with its high morbimortality rate.

## CONCLUSIONS

The present study suggests an increased prevalence of IA in HHT compared with the general population. Considering the morbimortality associated with aneurysm rupture, these findings highlight the importance of conducting larger studies in the future; including pediatric population, evaluating the etiopathogenesis of IAs associated with HHT and discussing the clinical relevance and usefulness of different detection methods, follow-up and currently available treatments.

**Disclosure forms** provided by the authors are available with the full text and PDF of this article at [www.ajnr.org](http://www.ajnr.org).

## REFERENCES

- Shovlin CL, Letarte M. Hereditary haemorrhagic telangiectasia and pulmonary arteriovenous malformations: issues in clinical management and review of pathogenic mechanisms. *Thorax* 1999;54:714–29 CrossRef Medline
- Govani PS, Shovlin CL. Hereditary haemorrhagic telangiectasia: a clinical and scientific review. *Eur J Hum Genet* 2009;17:860–71 CrossRef Medline
- Shovlin CL. Hereditary haemorrhagic telangiectasia: pathophysiology, diagnosis and treatment. *Blood Rev* 2010;24:203–19 CrossRef Medline
- Bernabeu C, Bayrak-Toydemir P, McDonald J, et al. Potential second-hits in hereditary hemorrhagic telangiectasia. *J Clin Med* 2020;9:3571 CrossRef Medline
- McDonald J, Wooderchak-Donahue W, VanSant Webb C, et al. Hereditary hemorrhagic telangiectasia: genetics and molecular diagnostics in a new era. *Front Genet* 2015;6:1 CrossRef Medline
- Abdalla SA, Letarte M. Hereditary haemorrhagic telangiectasia: current views on genetics and mechanisms of disease. *J Med Genet* 2006;43:97–110 CrossRef Medline
- Faughnan ME, Mager JJ, Hets SW, et al. Second International Guidelines for the Diagnosis and Management of Hereditary Hemorrhagic Telangiectasia. *Ann Intern Med* 2020;173:989–1001 CrossRef Medline
- Serra MM, Besada CH, Cabana Cal A, et al. Central nervous system manganese induced lesions and clinical consequences in patients

with hereditary hemorrhagic telangiectasia. *Orphanet J Rare Dis* 2017;12:92 CrossRef Medline

- Klostranec JM, Chen L, Mathur S, et al. A theory for polymicrogyria and brain arteriovenous malformations in HHT. *Neurology* 2019;92:34–42 CrossRef Medline
- Faughnan ME, Palda VA, Garcia-Tsao G, et al; HHT Foundation International Guidelines Working Group. International guidelines for the diagnosis and management of hereditary haemorrhagic telangiectasia. *J Med Genet* 2011;48:73–87 CrossRef Medline
- Fulbright RK, Chaloupka JC, Putman CM, et al. MR of hereditary hemorrhagic telangiectasia: prevalence and spectrum of cerebrovascular malformations. *AJNR Am J Neuroradiol* 1998;19:477–84 Medline
- Willemsse RB, Mager JJ, Westermann CJ, et al. Bleeding risk of cerebrovascular malformations in hereditary hemorrhagic telangiectasia. *J Neurosurg* 2000;92:779–84 CrossRef Medline
- Meybodi AT, Kim H, Nelson J, et al; Malformation Consortium HHT Investigator Group. Surgical treatment vs nonsurgical treatment for brain arteriovenous malformations in patients with hereditary hemorrhagic telangiectasia: a retrospective multicenter consortium study. *Neurosurgery* 2018;82:253 CrossRef Medline
- Amenta PS, Yadla S, Campbell PG, et al. Analysis of nonmodifiable risk factors for intracranial aneurysm rupture in a large, retrospective cohort. *Neurosurgery* 2012;70:693–701 CrossRef Medline
- Grobelyny TJ. Brain aneurysms: epidemiology, treatment options, and milestones of endovascular treatment evolution. *Dis Mon* 2011;57:647–55 CrossRef Medline
- Brown RD Jr, Wiebers DO, Forbes GS. Unruptured intracranial aneurysms and arteriovenous malformations: frequency of intracranial hemorrhage and relationship of lesions. *J Neurosurg* 1990;73:859–63 CrossRef Medline
- Rammos SK, Gardenghi B, Bortolotti C, et al. Aneurysms associated with brain arteriovenous malformations. *AJNR Am J Neuroradiol* 2016;37:1966–71 CrossRef Medline
- Vlak MH, Algra A, Brandenburg R, et al. Prevalence of unruptured intracranial aneurysms, with emphasis on sex, age, comorbidity, country, and time period: a systematic review and meta-analysis. *Lancet Neurol* 2011;10:626–36 CrossRef Medline
- Mohan D, Munteanu V, Coman T, et al. Genetic factors involves in intracranial aneurysms—actualities. *J Med Life* 2015;8:336–41 Medline
- Kim ST, Brinjikji W, Lanzino G, et al. Neurovascular manifestations of connective-tissue diseases: a review. *Interv Neuroradiol* 2016;22:624–37 CrossRef Medline
- Maleszewski JJ, Miller DV, Lu J, et al. Histopathologic findings in ascending aortas from individuals with Loeys-Dietz syndrome (LDS). *Am J Surg Pathol* 2009;33:194–201 CrossRef Medline
- Kim ST, Brinjikji W, Kallmes DF. Prevalence of intracranial aneurysms in patients with connective tissue diseases: a retrospective study. *AJNR Am J Neuroradiol* 2016;37:1422–26 CrossRef Medline
- Vorselaars VM, Diederik A, Prabhudesai V, et al. SMAD4 gene mutation increases the risk of aortic dilation in patients with hereditary haemorrhagic telangiectasia. *Int J Cardiol* 2017;245:114–18 CrossRef Medline
- Cavalli G. SMAD4 gene mutation and risk of aortic dilation: lessons from hereditary hemorrhagic telangiectasia. *Int J Cardiol* 2017;245:145–46 CrossRef Medline
- Ishii D, Takechi A, Seyama G, et al. Ruptured large basilar artery aneurysm associated with an arteriovenous malformation in hereditary hemorrhagic telangiectasia. *Neurol Med Chir (Tokyo)* 2012;52:502–05 CrossRef Medline
- Chick JF, Sheehan SE, Chauhan NR. The many faces of hereditary hemorrhagic telangiectasia: median arcuate ligament syndrome, arteriovenous malformations, and cerebral aneurysms. *Intern Emerg Med* 2012;7:385–86 CrossRef Medline
- Helmchen C, Nahser HC, Yousry T, et al. Therapy of cerebral aneurysms and arteriovenous vascular malformations in hereditary hemorrhagic telangiectasia (Rendu-Osler-Weber disease) (in German). *Nervenarzt* 1995;66:124–28 Medline



28. Roy C, Nosedá G, Arzimanoglou A, et al. **Rendu Osler disease revealed by ruptured cerebral arterial aneurysm in an infant.** *Arch Fr Pediatr* 1990;47:741–42 Medline
29. Sobel D, Norman D. **CNS manifestations of hereditary hemorrhagic telangiectasia.** *AJNR Am J Neuroradiol* 1984;5:569–73 Medline
30. Fisher M, Zito JL. **Focal cerebral ischemia distal to a cerebral aneurysm in hereditary hemorrhagic telangiectasia.** *Stroke* 1983;14:419–21 CrossRef Medline
31. Kamiyama K, Okada H, Niizuma H, et al. **A case report: Osler-Weber-Rendu disease with cerebral aneurysm, cerebral arteriovenous malformation and pulmonary arteriovenous fistula (author's transl).** *No Shinkei Geka* 1981;9:67–72 Medline
32. Román G, Fisher M, Perl DP, et al. **Neurological manifestations of hereditary hemorrhagic telangiectasia (Rendu-Osler-Weber disease): report of 2 cases and review of the literature.** *Ann Neurol* 1978;4:130–44 CrossRef Medline
33. Grollmus J, Hoff J. **Multiple aneurysms associated with Osler-Weber-Rendu disease.** *Surg Neurol* 1973;1:91–93 Medline
34. Brown RD Jr, Huston J, Hornung R, et al. **Screening for brain aneurysm in the Familial Intracranial Aneurysm study: frequency and predictors of lesion detection.** *J Neurosurg* 2008;108:1132–38 CrossRef Medline
35. Caranci F, Briganti F, Cirillo L, et al. **Epidemiology and genetics of intracranial aneurysms.** *Eur J Radiol* 2013;82:1598–605 CrossRef Medline
36. Maher CO, Piepgras DG, Brown RD Jr, et al. **Cerebrovascular manifestations in 321 cases of hereditary hemorrhagic telangiectasia.** *Stroke* 2001;32:877–82 CrossRef Medline
37. Krings T, Ozanne A, Chng SM, et al. **Neurovascular phenotypes in hereditary haemorrhagic telangiectasia patients according to age: review of 50 consecutive patients aged 1 day–60 years.** *Neuroradiology* 2005;47:711–20 CrossRef Medline
38. Brinjikji W, Iyer VN, Yamaki V, et al. **Neurovascular manifestations of hereditary hemorrhagic telangiectasia: a consecutive series of 376 patients during 15 years.** *AJNR Am J Neuroradiol* 2016;37:1479–86 CrossRef Medline
39. Woodall MN, McGettigan M, Figueroa R, et al. **Cerebral vascular malformations in hereditary hemorrhagic telangiectasia.** *J Neurosurg* 2014;120:87–92 CrossRef Medline
40. Ring NY, Latif MA, Hafezi-Nejad N, et al. **Prevalence of and factors associated with arterial aneurysms in patients with hereditary hemorrhagic telangiectasia: 17-year retrospective series of 418 patients.** *J Vasc Interv Radiol* 2021;32:1661–69 CrossRef Medline
41. Brinjikji W, Iyer VN, Wood CP, et al. **Prevalence and characteristics of brain arteriovenous malformations in hereditary hemorrhagic telangiectasia: a systematic review and meta-analysis.** *J Neurosurg* 2017;127:302–10 CrossRef Medline
42. Cagnazzo F, Brinjikji W, Lanzino G. **Arterial aneurysms associated with arteriovenous malformations of the brain: classification, incidence, risk of hemorrhage, and treatment—a systematic review.** *Acta Neurochir (Wien)* 2016;158:2095–104 CrossRef Medline
43. Chalouhi N, Hoh BL, Hasan D. **Review of cerebral aneurysm formation, growth, and rupture.** *Stroke* 2013;44:3613–22 CrossRef Medline
44. Dingenouts CK, Goumans M-J, Bakker W. **Mononuclear cells and vascular repair in HHT.** *Front Genet* 2015;6:114 CrossRef Medline
45. Aristorena M, Gallardo-Vara E, Vicen M, et al. **MMP-12, secreted by pro-inflammatory macrophages, targets endoglin in human macrophages and endothelial cells.** *Int J Mol Sci* 2019;20:3107 CrossRef Medline
46. Lebrin F, Srun S, Raymond K, et al. **Thalidomide stimulates vessel maturation and reduces epistaxis in individuals with hereditary hemorrhagic telangiectasia.** *Nat Med* 2010;16:420–48 CrossRef Medline
47. Wu V, Lee JM, Vozoris NT, et al. **Weekly epistaxis duration as an indicator of epistaxis severity in hereditary hemorrhagic telangiectasia: preliminary results from a randomized controlled trial.** *Laryngoscope Investig Otolaryngol* 2021;6:370–75 CrossRef Medline
48. Greving JP, Wermer MJH, Brown RD Jr, et al. **Development of the PHASES score for prediction of risk of rupture of intracranial aneurysms: a pooled analysis of six prospective cohort studies.** *Lancet Neurol* 2014;13:59–66 CrossRef Medline

# Brain Abnormalities and Epilepsy in Patients with Parry-Romberg Syndrome

C. De la Garza-Ramos, A. Jain, S.A. Montazeri, L. Okromelidze, R. McGeary, A.A. Bhatt, S.J.S. Sandhu, S.S. Grewal, A. Feyissa, J.I. Sirven, A.L. Ritaccio, W.O. Tatum, V. Gupta, and E.H. Middlebrooks



## ABSTRACT

**BACKGROUND AND PURPOSE:** Parry-Romberg syndrome is a rare disorder characterized by progressive hemifacial atrophy. Concomitant brain abnormalities have been reported, frequently resulting in epilepsy, but the frequency and spectrum of brain involvement are not well-established. This study aimed to characterize brain abnormalities in Parry-Romberg syndrome and their association with epilepsy.

**MATERIALS AND METHODS:** This is a single-center, retrospective review of patients with a clinical diagnosis of Parry-Romberg syndrome and brain MR imaging. The degree of unilateral hemispheric atrophy, white matter disease, microhemorrhage, and leptomeningeal enhancement was graded as none, mild, moderate, or severe. Other abnormalities were qualitatively reported. Findings were considered potentially Parry-Romberg syndrome–related when occurring asymmetrically on the side affected by Parry-Romberg syndrome.

**RESULTS:** Of 80 patients, 48 (60%) had brain abnormalities identified on MR imaging, with 26 (32%) having abnormalities localized to the side of the hemifacial atrophy. Sixteen (20%) had epilepsy. MR imaging brain abnormalities were more common in the epilepsy group (100% versus 48%,  $P < .001$ ) and were more frequently present ipsilateral to the hemifacial atrophy in patients with epilepsy (81% versus 20%,  $P < .001$ ). Asymmetric white matter disease was the predominant finding in patients with (88%) and without (23%) epilepsy. White matter disease and hemispheric atrophy had a higher frequency and severity in patients with epilepsy ( $P < .001$ ). Microhemorrhage was also more frequent in the epilepsy group ( $P = .015$ ).

**CONCLUSIONS:** Ipsilateral MR imaging brain abnormalities are common in patients with Parry-Romberg syndrome, with a higher frequency and greater severity in those with epilepsy. The most common findings in both groups are white matter disease and hemispheric atrophy, both presenting with greater severity in patients with epilepsy.

**ABBREVIATIONS:** ASM = antiseizure medication; ECDS = en coup de sabre; EEG = electroencephalogram; IQR = interquartile range; PRS = Parry-Romberg syndrome; WMD = white matter disease

Parry-Romberg syndrome (PRS) is a rare, self-limiting disorder characterized by progressive hemifacial atrophy affecting the skin and subcutaneous tissues. There is also variable involvement of underlying muscle and bone, with occasional involvement of the ipsilateral limbs or bifacial atrophy. It is difficult to differentiate PRS and en coup de sabre (ECDS), or localized scleroderma, due to overlap in the facial features present in both entities.<sup>1</sup> The pathogenesis of PRS remains poorly understood, with

many proposed theories of the etiology ranging from infection, trauma, vascular abnormalities, autonomic dysregulation, or an autoimmune process, the latter being the leading hypothesis.<sup>2,3</sup> PRS occurs more commonly in females, arising in childhood or young adulthood, with eventual stabilization of atrophic features. Once stabilized, patients often undergo reconstructive surgeries and additional treatments depending on the severity of PRS.<sup>4-9</sup>

Patients with PRS often exhibit neurologic symptoms, including headaches, seizures, and hemiplegia.<sup>3,10,11</sup> Intracranial abnormalities on neuroimaging have been previously reported, yet the timing of the development of these intracranial findings with that of the clinical features of PRS has often been inconsistent.<sup>10,12,13</sup> Because seizures are a common debilitating morbidity that affects the prognosis of PRS, further characterization of this association is needed to improve diagnosis and management. This study aimed to describe the frequency and severity of MR imaging brain abnormalities in patients with PRS and determine their association with epilepsy.

Received January 15, 2022; accepted after revision March 21.

From the Departments of Neuroradiology (C.D.I.G.-R., A.J., S.A.M., L.O., R.M., A.A.B., S.J.S.S., V.G., E.H.M.), Neurologic Surgery (S.S.G.), and Neurology (A.F., J.I.S., A.L.R., W.O.T.), Mayo Clinic, Jacksonville, Florida.

C. De la Garza-Ramos and A. Jain contributed equally to this work.

Please address correspondence to Erik H. Middlebrooks, MD, Department of Neuroradiology, Mayo Clinic Florida, 4500 San Pablo Rd, Jacksonville, FL 32224; e-mail: Middlebrooks.Erik@mayo.edu; @EMiddlebrooksMD



Indicates article with online supplemental data.

<http://dx.doi.org/10.3174/ajnr.A7517>

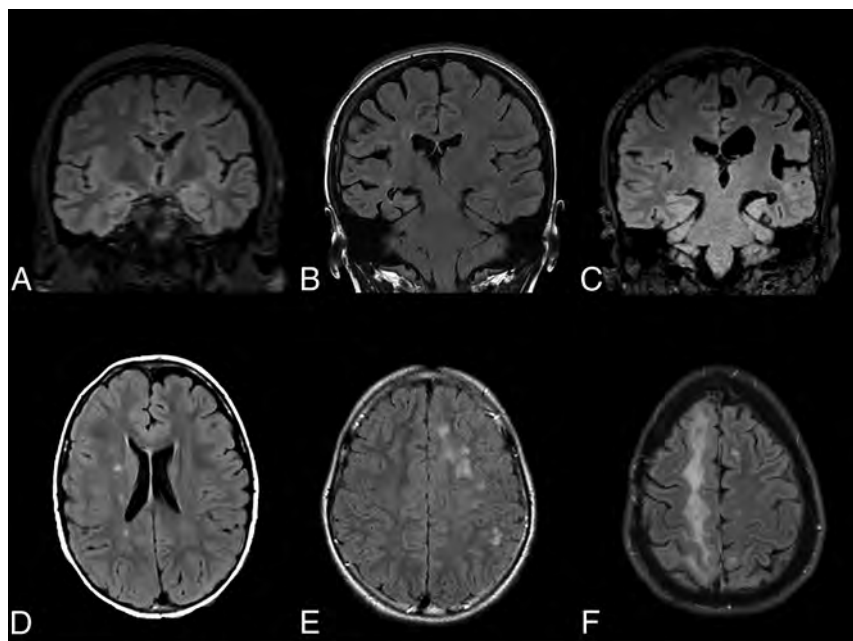


**FIG 1.** Exemplary MR imaging of atrophy and white matter disease severity. Coronal FLAIR MR imaging shows mild left hemisphere atrophy (A), moderate right hemisphere atrophy (B), and severe left hemisphere atrophy (C). Axial FLAIR MR imaging shows mild right hemisphere WMD (D), moderate left hemisphere WMD (E), and severe right hemisphere WMD (F).

## MATERIALS AND METHODS

### Patient Selection and Data Collection

This retrospective, cross-sectional study was approved by the institutional review board. A medical record review was performed to identify patients diagnosed with PRS or hemifacial atrophy from 2000 to 2020 at a multisite tertiary care center. Inclusion criteria were the following: 1) a working clinical diagnosis of PRS, and 2) available MR imaging of the brain consisting of, at minimum, standard structural imaging sequences with T1-, T2-, FLAIR, diffusion, and gradient echo/T2\*/susceptibility-weighted images obtained as part of the diagnostic evaluation. Clinical data were collected from the medical records, including patient age at the time of the PRS work-up and MR imaging, age at which hemifacial atrophy first became evident, sex, MR imaging results, clinical and neurologic manifestations, laterality of hemifacial atrophy, and the presence or absence of epilepsy. For patients with epilepsy, documented data included age of onset, seizure semiology, MR imaging, electroencephalogram (EEG), seizure/epilepsy classification, and medical or surgical management.

### Imaging Analysis

Prior MR imaging reports were reviewed, and MR imaging studies were further analyzed separately by 2 board-certified neuroradiologists for the presence of brain abnormalities. The main findings studied were hemispheric atrophy, white matter disease (WMD), microhemorrhage, and leptomeningeal enhancement. When present, atrophy, WMD, and microhemorrhage were graded as none, mild, moderate, or severe adapted from scales of global cortical atrophy<sup>14</sup> and WMD severity<sup>15</sup> established in neurodegenerative and vascular disease (Fig 1). Microhemorrhage and calcification were based on the assessment of susceptibility-weighted imaging

and/or gradient echo/multiecho gradient echo (quantitative susceptibility mapping) and verified on CT when available. Brain abnormalities were considered potentially related to PRS when occurring asymmetrically on the side ipsilateral to the hemifacial atrophy. Among patients with bilateral brain involvement of the predefined abnormalities, only conditions of patients with asymmetric hemisphere involvement on the same side as craniofacial changes were counted as likely related to PRS. The side with the highest grade (ie, moderate or severe) was reported as dominant in cases identified with bilateral brain involvement, while the hemisphere with mild involvement was not considered as the lateralized abnormality for statistical measure. The presence of additional brain abnormalities was qualitatively reported.

### Statistical Analysis

Descriptive analysis was undertaken for quantitative and qualitative variables, which are reported as median (inter-

quartile range [IQR], 25–75) and frequency (percentage), respectively. Categorical variables were compared using the  $\chi^2$  or Fischer exact test, as appropriate. Statistical analysis was performed using SPSS, Version 25.0 for Windows (IBM) with  $P < .05$  as the significance level.

## RESULTS

A total of 80 patients with a working or established clinical diagnosis of PRS and available neuroimaging with brain MR imaging were identified (Table 1). The median age at work-up was 37 years (IQR, 26–56), and most patients were female (70%). Hemifacial involvement was left-sided in 43 (54%) cases. There were 48 (60%) patients with a diagnosis of PRS and brain abnormalities on MR imaging. Of these, 46 (57%) had at least 1 of the predefined abnormalities (ie, hemispheric atrophy, WMD, leptomeningeal enhancement, or microhemorrhages), while 1 patient per cohort had additional, bilateral, intracranial findings only. Thirty-two (40%) patients had an asymmetric hemispheric predominance of brain abnormalities on MR imaging, of whom 26 (32%) patients had abnormalities localized ipsilateral to the hemifacial atrophy. Six (7%) patients had a contralateral predominance of brain abnormalities, and 15 (18%) had bilateral MR imaging brain abnormalities.

Sixteen (20%) patients with a clinical diagnosis of PRS had epilepsy, with a median age of seizure onset of 13 years (IQR, 10–16), as detailed in the Online Supplemental Data. The median number of seizures per month was 2, ranging from 1 every 3 months to 60 seizures per month. Seven (44%) reported a single semiology, while 9 (56%) had  $>1$  type of seizure during their course of illness. Most (81%) experienced seizures with motor symptomatology. Focal aware seizures were seen in 6 (37%) patients with epilepsy; focal



impaired awareness seizures, in 9 (56%); and 11 (69%) patients with epilepsy had focal-to-bilateral tonic-clonic seizures. Fourteen (87%) patients were managed with antiseizure medications (ASMs) only, with a median of 2 (range, 1–4) ASMs; 8 (50%) were controlled with a single ASM per last follow-up. Three (19%) patients were drug-resistant, with 2 (13%) receiving vagus nerve stimulation. EEG findings were abnormal in 13 (81%) patients with epilepsy. Eight (50%) had interictal epileptiform discharges on EEG, 6 (37%) arising ipsilateral to both the MR imaging brain and hemifacial findings, 1 (6%) ipsilateral to the MR imaging brain abnormalities yet contralateral to the hemifacial atrophy, and 1 (6%) patient had bilateral epileptiform discharges and bilateral

brain abnormalities. Notably, 9 (56%) patients had video EEGs, of whom, 5 (31%) had interictal epileptiform discharges which arose ipsilateral to the hemifacial atrophy in 4 (25%) of patients.

MR imaging revealed brain abnormalities in all 16 (100%) patients with epilepsy compared with 31 (48%) patients without epilepsy ( $P < .001$ ), of whom, 15 (94%) and 30 (47%), respectively, had at least 1 primary feature (ie, hemispheric atrophy, WMD, leptomeningeal enhancement, or microhemorrhages). Brain abnormalities were asymmetrically predominant in the hemisphere ipsilateral to the hemifacial atrophy in 13 (81%) patients with epilepsy compared with 13 (20%) without epilepsy ( $P < .001$ ). Two (12%) patients with epilepsy had brain abnormalities contralateral to hemifacial atrophy, and one (6%) had bilateral MR imaging brain abnormalities. Four (6%) and 14 (22%) patients without epilepsy had contralateral and bilateral brain MR imaging abnormalities, respectively.

As detailed in Table 2, the abnormalities with asymmetric involvement in the epilepsy group were hemispheric atrophy in 8 (50%) patients, WMD in 14 (87%), hemispheric microhemorrhage in 3 (18%, Fig 2), and leptomeningeal enhancement in 1 patient (6%, Fig 3). The abnormalities with asymmetric involvement in the nonepilepsy group were hemispheric atrophy in 3 (5%) patients, WMD in 15 (23%), hemispheric microhemorrhage in 3 (5%), and leptomeningeal enhancement in 1 (1%).

WMD was the most common finding in both groups. When we compared the degree of involvement between groups, the frequency and severity of WMD were higher in patients with epilepsy ( $P < .001$ ) (Table 2). Hemispheric atrophy was also present with a higher frequency and severity in patients with epilepsy ( $P < .001$ ). When present, hemispheric microhemorrhage was more severe in the epilepsy group ( $P = .015$ ).

Additional intracranial findings in the entire cohort included bilateral frontal horn heterotopia ( $n = 1$ ), bilateral supracallosal aneurysms ( $n = 1$ ), cortical and subcortical infarcts ( $n = 2$ ), and subcortical dystrophic calcification ( $n = 2$ ). Asymmetric sulcal

**Table 1: Parry-Romberg syndrome patient characteristics<sup>a</sup>**

Variables	
Total	80
Age at work-up and imaging (yr)	37 (26–56)
Age at hemifacial atrophy identification (yr)	20 (13–43)
Sex	
Male	24 (30%)
Female	56 (70%)
Laterality of hemifacial atrophy	
Right	37 (46%)
Left	43 (54%)
Bilateral	0 (0%)
Brain abnormalities on MR imaging	
Normal	32 (40%)
Abnormal	48 (60%)
Overall laterality of brain MR imaging findings	
Unilateral	34 (42%)
Bilateral	14 (17%)
Laterality of unilateral brain MR imaging findings in relation to hemifacial atrophy	
Ipsilateral	26 (35%)
Contralateral	6 (7%)
Epilepsy	
Present	16 (20%)
Absent	64 (80%)

<sup>a</sup> Data are No. (%) or median (IQR, 1–3).

**Table 2: Frequency and severity of unilateral brain abnormalities in patients with Parry-Romberg syndrome and epilepsy compared with cases without epilepsy<sup>a</sup>**

	Nonepilepsy ( $n = 64$ )	Epilepsy ( $n = 16$ )	<i>P</i> Value Categories	<i>P</i> Value Overall
Hemispheric atrophy				
None	61 (95%)	8 (50%)	$< .001$	$< .001$
Mild	1 (1.6%)	1 (6%)		
Moderate	1 (1.6%)	3 (19%)		
Severe	1 (1.6%)	4 (25%)		
WMD				
None	49 (77%)	2 (12%)	$< .001$	$< .001$
Mild	10 (15%)	7 (44%)		
Moderate	2 (3%)	4 (25%)		
Severe	3 (5%)	3 (19%)		
Hemispheric microhemorrhage				
None	61 (95%)	13 (81%)	.015	.091
Mild	3 (5%)	1 (6%)		
Moderate	0	0		
Severe	0	2 (12%)		
Leptomeningeal enhancement				
Absent	63 (98%)	15 (94%)	.362	
Present	1 (1.6%)	1 (6%)		

<sup>a</sup> Some patients had more than 1 finding.

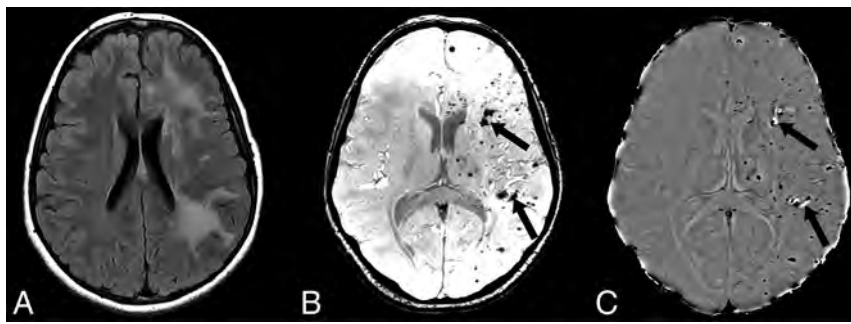


**FIG 2.** A, Axial FLAIR MR imaging in a patient with epilepsy shows severe, confluent left hemisphere white matter hyperintensity with extensive areas of punctate susceptibility artifacts throughout the left hemisphere on susceptibility-weighted imaging (B). Most of the hypointense foci on susceptibility-weighted imaging are hypointense on the matching phase image (C), consistent with prior microhemorrhages; however, few show hyperintense signal on the phase image (arrows in B and C), consistent with calcifications (confirmed by CT, not shown).

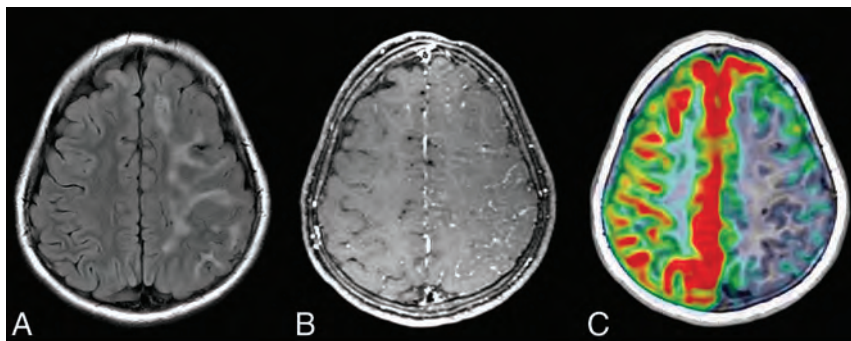


**FIG 3.** A, Axial FLAIR MR imaging in a patient with epilepsy shows severe, confluent left hemisphere white matter hyperintensity. B, Postcontrast T1-weighted MR imaging reveals leptomeningeal enhancement and sulcal effacement with decreased perfusion to the same area on arterial spin-labeling perfusion MR imaging (C).

effacement predominating in the frontoparietal region was found in 5 patients (6%, Figs 4 and 5), of whom, 3 had epilepsy. In 2 of the 3 patients, there was no change in sulcal effacement across multiple scans obtained for 17 months in 1 patient and 18 months in the second patient. Two patients with epilepsy had severe basal ganglia atrophy, located ipsilateral to the hemispheric atrophy and hemifacial atrophy. One patient per cohort was documented as having had progressive brain atrophy across the years. One patient with epilepsy and available FDG-PET showed hypometabolism in the area of sulcal effacement and WMD (Fig 4E). In another patient with epilepsy, arterial spin-labeling MR imaging showed hypoperfusion in the area of WMD and leptomeningeal enhancement (Fig 3C). <sup>1</sup>H-MR spectroscopy (Fig 6) in a patient with epilepsy revealed a reduction in Cho:Cr ratio and a reduction in NAA in the area of WMD compared with the normal contralateral hemisphere.

## DISCUSSION

PRS is clinically suspected with facial asymmetry or hemiatrophy, often in association with neurologic, ophthalmologic, and orodental manifestations. The working diagnosis is made by clinically excluding mimickers such as localized scleroderma, Barraquer-

Simons lipodystrophy, fat necrosis, contralateral hemihypertrophy, and congenital hemiatrophy. Rarely, laboratory testing or histopathology is performed to establish the diagnosis. Brain abnormalities are often seen in association with PRS, yet the frequency and severity have received limited attention. In this study, 57% of patients with a working or established clinical diagnosis of PRS and available MR imaging had at least 1 primary brain abnormality associated with PRS. The most common finding was WMD, which was observed asymmetrically in 29% of the cohort. Notably, unilateral-predominant brain abnormalities localized to the side with hemifacial atrophy were found in one-third of patients; due to the atrophic nature of the disorder, these are likely related to the pathophysiology of PRS.

Similar to our results, frequent imaging findings reported in other studies include ipsilateral white matter hyperintense signal on T2-weighted MR imaging corresponding to white matter hypoattenuation on CT, hemispheric brain atrophy, cavernous malformations/microhemorrhages, and subcortical calcifications predominantly noted in the frontal lobe.<sup>2,13,16-21</sup> We found that the primary brain findings associated with PRS were more common in patients with epilepsy compared with

those without epilepsy (94% versus 47%), as well as more commonly present on the side of craniofacial involvement in patients with epilepsy compared with those without epilepsy (81% versus 20%). When present, the degree of hemispheric atrophy, WMD, and microhemorrhage was more severe in those with epilepsy. In addition, 5 patients, including 2 without epilepsy, had remarkable asymmetric sulcal effacement located primarily in the frontoparietal region, a finding that has been rarely reported by other investigators.<sup>10,22-24</sup> Due to the low frequency of other findings, including bilateral frontal horn heterotopia, supraclinoid aneurysms, and small cortical and subcortical infarcts, it remains unclear whether these could be related to PRS.

It is often challenging to characterize the disease course, severity, and prognosis of PRS due to these overlapping features with ECDS or localized scleroderma.<sup>3</sup> Currently, the most acceptable etiology associates PRS with an underlying progressive autoimmune neurovasculitis, though other theories have been proposed.<sup>11,21,25,26</sup> Cerebral perivascular inflammation, leptomeningeal and cortical blood vessel endothelial degeneration, hyalinizing changes, and partial obliteration have been reported in PRS, possibly as a consequence of immune-mediated vascular injury and incomplete endothelial regeneration.<sup>27</sup> These changes probably account for ischemia, hemorrhages, and breakdown of the blood-brain barrier.

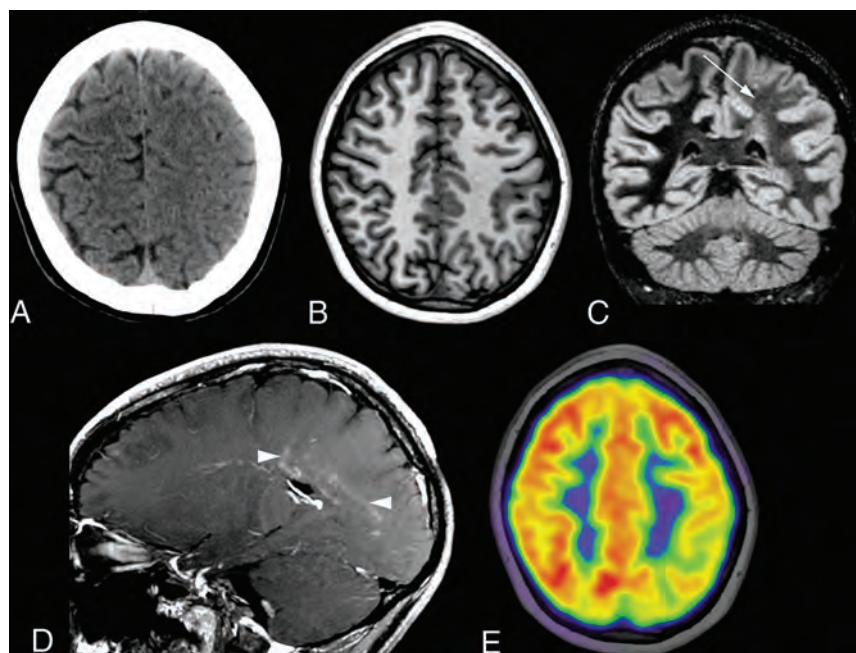


**FIG 4.** A, Initial head CT in a patient with epilepsy reveals effacement of the sulci over the left parietal high convexity. B, Subsequent T1-weighted MR imaging performed 10 months later shows improvement in sulcal effacement, but with diffuse left hemisphere white matter hyperintensity on double inversion recovery MR imaging (C, arrow). D, Sagittal postcontrast T1-weighted MR imaging shows faint periventricular and perivascular enhancement (arrowheads). E, Concomitant FDG-PET shows left parietal hypometabolism in the affected area.

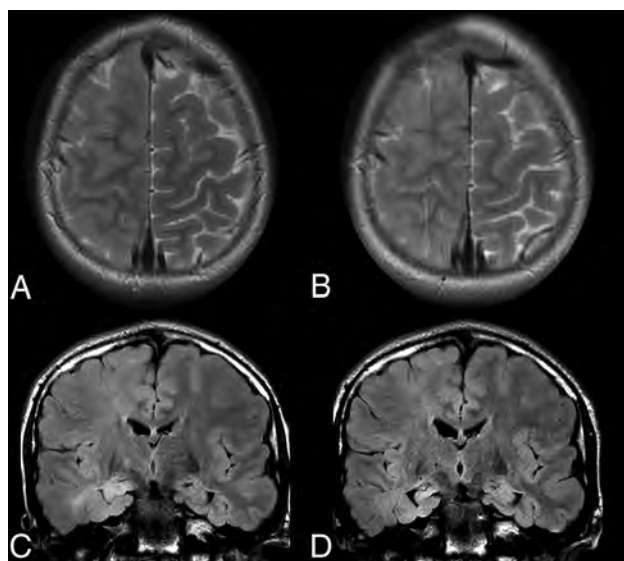


**FIG 5.** Spectrum of unilateral sulcal effacement. In 1 patient with epilepsy, axial T2-weighted MR imaging (A) shows right hemispheric sulcal effacement affecting the right frontal and parietal lobes, which remained unchanged on MR imaging performed 1 year later (B). C, Coronal FLAIR MR imaging in a second patient with epilepsy shows diffuse right hemisphere sulcal effacement with hyperintensity in the right hippocampal head, with resolution of sulcal effacement and development of right mesial temporal sclerosis on MR imaging approximately 6 months later (D).

Robust response to steroids and immune-modulating treatment in slowing the disease process also supports this etiology, in addition to histologic and laboratory evidence of inflammation.<sup>1,2</sup> Brain

abnormalities in PRS have overlap with other conditions, such as Rasmussen encephalitis, an autoimmune disorder of childhood characterized by asymmetric neuroimaging findings, epilepsy, and hemiplegia.<sup>4</sup> Characteristic craniofacial abnormalities in PRS may help differentiate the disorder from other entities.

Epilepsy can be a debilitating comorbidity in patients with PRS and further compromise quality of life, and it was found in 20% of patients in our series. A global, Internet-based survey of patients with PRS from 29 countries revealed that 11% had coexistent epilepsy,<sup>26</sup> with the highest reported epilepsy incidence of 60.5% in a pooled literature review of patients with PRS.<sup>28</sup> In a pediatric study of PRS with epilepsy, the median seizure onset was in the first decade.<sup>29</sup> In our study, the age of seizure onset was often estimated; however, most patients had onset in childhood. In our cohort, the most common type of seizure was focal-to-bilateral tonic-clonic seizures, followed by focal with impaired awareness. Most cases (81%) of epilepsy had an abnormal EEG finding, with 50% demonstrating interictal epileptiform discharges. On the basis of our observations, the severity of brain abnormalities appears to be a risk factor for development of epilepsy. However, the widespread extent of the abnormalities limits the localizing ability of MR imaging in identifying the seizure-onset zone.<sup>30</sup> Nevertheless, it appears that certain MR imaging features predispose to a higher likelihood of developing epilepsy in PRS. Similar to a recent study by Knights et al,<sup>31</sup> our cohort showed a higher frequency and severity of ipsilateral WMD in epilepsy. Their study, however, failed to show a significantly greater frequency of hemorrhagic foci in epilepsy in contradiction to our findings. Last, abnormal MR imaging findings were more frequent in patients with epilepsy in their cohort, but this was not statistically significant.<sup>31</sup> Both of these differences between studies may be related to the small number of subjects in their cohort.<sup>31</sup>

Currently, limited evidence exists regarding the role and findings of advanced brain imaging in PRS and epilepsy. Few patients in our cohort had such imaging performed, but findings were largely in agreement with prior reports.<sup>22,32</sup> Hypoperfusion of the affected brain region has been shown in several prior studies using dynamic susceptibility contrast MR imaging or SPECT,<sup>19,22,33</sup> which is in agreement with arterial spin-labeling results from 1 patient in our cohort. In 1 patient, a large region of hypometabolism was observed in the affected region on FDG-PET, which has also been previously reported.<sup>34</sup> Last, few studies have shown the findings on <sup>1</sup>H-MR spectroscopy in PRS. While findings have been mixed, most have shown a relative decrease in the Cho:Cr ratio and a decrease in NAA, similar to findings in 1 patient in our cohort.<sup>4,19,22,32</sup>

The descriptive findings in this study provide further insight into the need for brain imaging in patients with PRS and neurologic



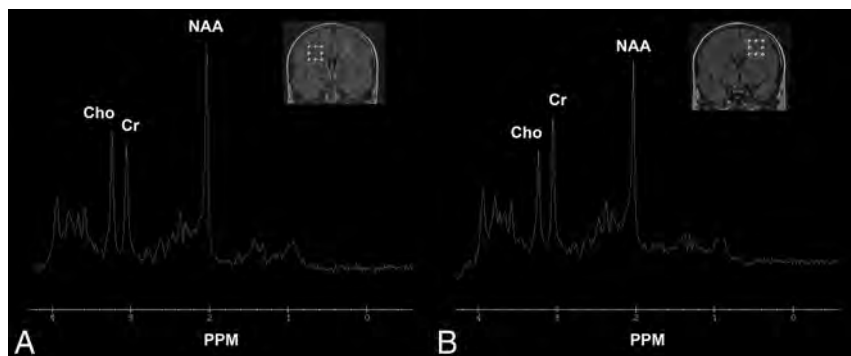


**FIG 6.** Proton MRS in a 12-year-old boy with left-sided Parry-Romberg syndrome and epilepsy shows the spectrum from the normal-appearing right hemisphere white matter (A) compared with the area of white matter FLAIR hyperintensity in the left hemisphere (B). There is a relative reduction in Cho and NAA, with a slight elevation of Cr on the abnormal side. PPM indicates parts per million.

symptoms. Recognition of the frequency and spectrum of brain abnormalities in PRS is critical because the diagnosis was delayed for years and the opportunity for timely management was missed in many of our patients. Further longitudinal studies are needed to better understand the natural history and radiographic progression to diagnose and treat patients with PRS and epilepsy more optimally. Similarly, larger prospective studies are recommended to validate the prevalence of epilepsy and the response to therapy in patients with PRS.

There are several limitations to this study. The retrospective nature leads to selection bias, with heterogeneity and gaps in clinical documentation based on chart review. Nevertheless, the number of patients is relatively large and provides additional details of the association of epilepsy with PRS. The lack of established diagnostic criteria for PRS and frequent overlap with other entities such as ECDS could have led to challenges in establishing a definitive classification of progressive hemifacial atrophy. Referral to a tertiary care center likely overestimates the true incidence of a disease state and severity of associated abnormalities and, therefore, may not be generalizable to other populations.

## CONCLUSIONS

In this study of 80 patients with a clinical diagnosis of PRS, brain abnormalities were frequently observed on MR imaging in the hemisphere ipsilateral to the hemifacial atrophy. Twenty percent of patients had focal epilepsies with most demonstrating motor signs and nearly 90% controlled by ASM. Lateralized brain abnormalities in the hemisphere ipsilateral to the hemifacial atrophy had a higher frequency and greater severity in patients with epilepsy compared with those without epilepsy. The most common MR imaging findings in both groups were WMD and hemispheric atrophy; both findings were more frequent and severe in patients with epilepsy.

**Disclosure forms** provided by the authors are available with the full text and PDF of this article at [www.ajnr.org](http://www.ajnr.org).

## REFERENCES

1. El-Kehdy J, Abbas O, Rubeiz N. **A review of Parry-Romberg syndrome.** *J Am Acad Dermatol* 2012;67:769–84 CrossRef Medline
2. Tollefson MM, Witman PM. **En coup de sabre morphea and Parry-Romberg syndrome: a retrospective review of 54 patients.** *J Am Acad Dermatol* 2007;56:257–63 CrossRef Medline
3. Tolkachjov SN, Patel NG, Tollefson MM. **Progressive hemifacial atrophy: a review.** *Orphanet J Rare Dis* 2015;10:39 CrossRef Medline
4. Longo D, Paonessa A, Specchio N, et al. **Parry-Romberg syndrome and Rasmussen encephalitis: possible association: clinical and neuroimaging features.** *J Neuroimaging* 2011;21:188–93 CrossRef Medline
5. Duymaz A, Karabekmez FE, Keskin M, et al. **Parry-Romberg syndrome: facial atrophy and its relationship with other regions of the body.** *Ann Plast Surg* 2009;63:457–61 CrossRef Medline
6. Parry CH. *Collections from the Unpublished Medical Writings of the Late Caleb Hillier Parry.* Vol 2. Underwoods; 1825
7. Mazzeo N, Fisher JG, Mayer MH, et al. **Progressive hemifacial atrophy (Parry-Romberg syndrome): case report.** *Oral Surg Oral Med Oral Pathol Oral Radiology Endod* 1995;79:30–35 CrossRef Medline
8. Moore MH, Wong KS, Proudman TW, et al. **Progressive hemifacial atrophy (Romberg's disease): skeletal involvement and treatment.** *Br J Plast Surg* 1993;46:39–44 CrossRef Medline
9. Roddi R, Riggio E, Gilbert PM, et al. **Clinical evaluation of techniques used in the surgical treatment of progressive hemifacial atrophy.** *J Craniomaxillofac Surg* 1994;22:23–32 CrossRef Medline
10. Doolittle DA, Lehman VT, Schwartz KM, et al. **CNS imaging findings associated with Parry-Romberg syndrome and en coup de sabre: correlation to dermatologic and neurologic abnormalities.** *Neuroradiology* 2015;57:21–34 CrossRef Medline
11. Wong M, Phillips CD, Hagiwara M, et al. **Parry Romberg syndrome: 7 cases and literature review.** *AJNR Am J Neuroradiol* 2015;36:1355–61 CrossRef Medline
12. Moko SB, Mistry Y, de Chalain TM. **Parry-Romberg syndrome: intracranial MRI appearances.** *J Craniomaxillofac Surg* 2003;31:321–24 CrossRef Medline
13. Chiu YE, Vora S, Kwon EK, et al. **A significant proportion of children with morphea en coup de sabre and Parry-Romberg syndrome have neuroimaging findings.** *Pediatr Dermatol* 2012;29:738–48 CrossRef Medline
14. Wahlund LO, Westman E, van Westen D, et al; Imaging Cognitive Impairment Network (ICINET). **Imaging biomarkers of dementia: recommended visual rating scales with teaching cases.** *Insights Imaging* 2017;8:79–90 CrossRef Medline
15. Fazekas F, Chawluk JB, Alavi A, et al. **MR signal abnormalities at 1.5 T in Alzheimer's dementia and normal aging.** *AJR Am J Roentgenol* 1987;149:351–56 CrossRef Medline
16. Aynaci FM, Sen Y, Erdöl H, et al. **Parry-Romberg syndrome associated with Adie's pupil and radiologic findings.** *Pediatr Neurol* 2001;25:416–18 CrossRef Medline
17. Blitstein MK, Vecchione MJ, Tung GA. **Parry-Romberg syndrome.** *Appl Radiol* 2011;40:34–36 CrossRef
18. Madasamy R, Jayanandan M, Adhavan UR, et al. **Parry Romberg syndrome: a case report and discussion.** *J Oral Maxillofac Pathol* 2012;16:406–10 CrossRef Medline
19. Okumura A, Ikuta T, Tsuji T, et al. **Parry-Romberg syndrome with a clinically silent white matter lesion.** *AJNR Am J Neuroradiol* 2006;27:1729–31 Medline
20. Sommer A, Gambichler T, Bacharach-Buhles M, et al. **Clinical and serological characteristics of progressive facial hemiatrophy: a case series of 12 patients.** *J Am Acad Dermatol* 2006;54:227–33 CrossRef Medline

21. Yano T, Sawaishi Y, Toyono M, et al. **Progressive facial hemiatrophy after epileptic seizures.** *Pediatr Neurol* 2000;23:164–66 CrossRef Medline
22. de Paula RA, Ribeiro BN, Bahia PR, et al. **Parry-Romberg syndrome: findings in advanced magnetic resonance imaging sequences: case report.** *Radiol Bras* 2014;47:186–88 CrossRef Medline
23. Cory RC, Clayman DA, Faillace WJ, et al. **Clinical and radiologic findings in progressive facial hemiatrophy (Parry-Romberg syndrome).** *AJNR Am J Neuroradiol* 1997;18:751–57 Medline
24. Fain ET, Mannion M, Pope E, et al. **Brain cavernomas associated with en coup de sabre linear scleroderma: two case reports.** *Pediatric Rheumatol Online J* 2011;9:18 CrossRef Medline
25. Pichiechio A, Uggetti C, Grazia Egitto M, et al. **Parry-Romberg syndrome with migraine and intracranial aneurysm.** *Neurology* 2002;59:606–68 CrossRef Medline
26. Stone J. **Parry-Romberg syndrome: a global survey of 205 patients using the internet.** *Neurology* 2003;61:674–76 CrossRef Medline
27. Woolfenden AR, Tong DC, Norbash AM, et al. **Progressive facial hemiatrophy: abnormality of intracranial vasculature.** *Neurology* 1998;50:1915–17 CrossRef Medline
28. Vix J, Mathis S, Lacoste M, et al. **Neurological manifestations in Parry-Romberg syndrome: 2 case reports.** *Medicine (Baltimore)* 2015;94:e1147 CrossRef Medline
29. Rocha R, Kaliakatsos M. **Epilepsy in paediatric patients with Parry-Romberg syndrome: a review of the literature.** *Seizure* 2020;76:89–95 CrossRef Medline
30. Careta MF, da Costa Leite C, Cresta F, et al. **Prospective study to evaluate the clinical and radiological outcome of patients with scleroderma of the face.** *Autoimmun Rev* 2013;12:1064–69 CrossRef Medline
31. Knights H, Minas E, Khan F, et al. **Magnetic resonance imaging findings in children with Parry-Romberg syndrome and en coup de sabre.** *Pediatr Rheumatol Online J* 2021;19:42 CrossRef Medline
32. Rigamonti P, Squarza S, Politi M, et al. **Parry-Romberg syndrome: conventional and advanced MRI follow-up in a boy.** *Neuroradiol J* 2017;30:445–47 CrossRef Medline
33. DeFelipe J, Segura T, Arellano JI, et al. **Neuropathological findings in a patient with epilepsy and the Parry-Romberg syndrome.** *Epilepsia* 2001;42:1198–203 CrossRef Medline
34. Uhrhan K, Rabenstein M, Kobe C, et al. **Brain glucose metabolism in Parry-Romberg syndrome.** *Clin Nucl Med* 2017;42:e251–52 CrossRef Medline

# Usefulness of Wave-CAIPI for Postcontrast 3D T1-SPACE in the Evaluation of Brain Metastases

H.J. Baek, Y.J. Heo, D. Kim, S.Y. Yun, J.W. Baek, H.W. Jeong, H.J. Choo, J.Y. Lee, and S.-I. Oh

## ABSTRACT

**BACKGROUND AND PURPOSE:** High-resolution postcontrast 3D T1WI is a widely used sequence for evaluating brain metastasis, despite the long scan time. This study aimed to compare highly accelerated postcontrast 3D T1-weighted sampling perfection with application-optimized contrasts by using different flip angle evolution by using wave-controlled aliasing in parallel imaging (wave-TI-SPACE) with the commonly used standard high-resolution postcontrast 3D T1-SPACE for the evaluation of brain metastases.

**MATERIALS AND METHODS:** Among the 387 patients who underwent postcontrast wave-TI-SPACE and standard SPACE, 56 patients with suspected brain metastases were retrospectively included. Two neuroradiologists assessed the number of enhancing lesions according to lesion size, contrast-to-noise ratio<sub>lesion/parenchyma</sub>, contrast-to-noise ratio<sub>white matter/gray matter</sub>, contrast ratio<sub>lesion/parenchyma</sub>, and overall image quality for the 2 different sequences.

**RESULTS:** Although there was no significant difference in the evaluation of larger enhancing lesions (>5 mm) between the 2 different sequences ( $P = .66$  for observer 1,  $P = .26$  for observer 2), wave-TI-SPACE showed a significantly lower number of smaller enhancing lesions (<5 mm) than standard SPACE (1.61 [SD, 0.29] versus 2.84 [SD, 0.47] for observer 1; 1.41 [SD, 0.19] versus 2.68 [SD, 0.43] for observer 2). Furthermore, mean contrast-to-noise ratio<sub>lesion/parenchyma</sub> and overall image quality of wave-TI-SPACE were significantly lower than those in standard SPACE.

**CONCLUSIONS:** Postcontrast wave-TI-SPACE showed comparable diagnostic performance for larger enhancing lesions (>5 mm) and marked scan time reduction compared with standard SPACE. However, postcontrast wave-TI-SPACE showed underestimation of smaller enhancing lesions (<5 mm) and lower image quality than standard SPACE. Therefore, postcontrast wave-TI-SPACE should be interpreted carefully in the evaluation of brain metastasis.

**ABBREVIATIONS:** CNR = contrast-to-noise ratio; CR = contrast ratio; DANTE = delay alternating with nutation for tailored excitation; SPACE = sampling perfection with application-optimized contrasts by using different flip angle evolution; wave-CAIPI = wave-controlled aliasing in parallel imaging

Early detection of brain metastasis is important for the treatment decisions of patients. Stereotactic radiosurgery delivers highly focused radiation to small metastatic lesions with minimal damage to adjacent normal brain tissue, thereby improving the safety of the patients and the outcome. Currently, high-resolution postcontrast 3D T1WI is widely used for evaluating brain metastasis due to its higher sensitivity for detecting small enhancing

lesions than postcontrast 2D T1WI. However, the long scan time (5~10 minutes) of high-resolution postcontrast 3D T1WI is a major drawback<sup>1-3</sup> for patients with cancer who could not tolerate the scan time due to poor their general conditions.<sup>4</sup> Long scan times may contribute to increased motion artifacts and the patient's anxiety.<sup>5</sup>

Recently, accelerated 3D acquisition techniques have been developed to reduce the scan time of high-resolution 3D T1WI sequences while preserving image quality.<sup>6-8</sup> There are several studies<sup>6-8</sup> that have used accelerated 3D acquisition techniques, such as 3D-FLASH pulse sequence, multishot 3D EPI, and compressed sensing. They showed comparable diagnostic performance for the detection of enhancing intracranial lesions and sufficient image quality compared with standard 3D T1WI. Wave-controlled aliasing in parallel imaging (Wave-CAIPI; Siemens) is an advanced parallel imaging technique that combines a corkscrew gradient trajectory with CAIPI shifts in the ky

Received February 3, 2022; accepted after revision March 24.

From the Department of Radiology (H.J.B.), Gyeongsang National University School of Medicine and Gyeongsang National University Changwon Hospital, Changwon, Republic of Korea; Department of Radiology (H.J.B.), Institute of Health Sciences, Gyeongsang National University School of Medicine, Jinju, Republic of Korea; and Departments of Radiology (Y.J.H., D.K., S.Y.Y., J.W.B., H.W.J., H.J.C.), Internal Medicine (J.Y.L.), and Neurology (S.-I.O.), Inje University Busan Paik Hospital, Busan, Republic of Korea.

Please address correspondence to Young Jin Heo, MD, Department of Radiology, Inje University Busan Paik Hospital, Bokji-ro 75, Busanjin-Gu, Busan 47392, Republic of Korea; e-mail: youngjin726@hanmail.net

<https://dx.doi.org/10.3174/ajnr.A7520>



and *kz* directions to efficiently encode the *k*-space and evenly spread the voxel aliasing in all dimensions. This feature takes better advantage of the 3D coil-sensitivity information to provide highly accelerated parallel imaging with negligible artifacts and SNR penalties.<sup>9</sup>

There have been several comparative studies<sup>9-15</sup> between Wave-CAIPI and standard MR images. However, there was only 1 study<sup>10</sup> applying postcontrast wave-T1-sampling perfection with application-optimized contrasts by using different flip angle evolution (SPACE; Siemens) to the evaluation of brain metastasis. This study reported noninferiority and equivalent diagnostic performance of postcontrast wave-T1-SPACE compared with standard postcontrast 3D T1-SPACE for visualization of enhancing lesions. However, the authors did not perform quantitative comparison between the 2 sequences and included only a small number of brain metastases. To the best of our knowledge, no previous studies have evaluated the diagnostic performance of subcentimeter enhancing metastases using postcontrast wave-T1-SPACE. Therefore, we evaluated the diagnostic performance according to the lesion size and overall image quality of postcontrast wave-T1-SPACE and compared it with the commonly used standard high-resolution postcontrast 3D T1-SPACE sequence for the evaluation of brain metastases. We hypothesized that wave-T1-SPACE shows comparable diagnostic performance and sufficient image quality for the evaluation of brain metastasis compared with standard SPACE, according to the results of a previous study.<sup>9</sup>

## MATERIALS AND METHODS

### Patients

**Patient Population.** This study was approved by the institutional review board of Inje University Busan Paik Hospital, and the need for informed consent was waived due to the retrospective nature of our study. Between August 2020 and July 2021, three hundred eighty-seven patients with histologically confirmed primary tumors (lung cancer, 45; breast cancer, 4; colorectal cancer, 2; renal cell carcinoma, 2; esophageal cancer, 1; hepatocellular carcinoma, 1; malignant melanoma, 1) underwent a brain MR imaging for the work-up or follow-up of brain metastasis. They underwent postcontrast 3D T1WI performed using standard SPACE with the delay alternating with nutation for tailored excitation (DANTE) sequences and wave-T1-SPACE in the same imaging session for the evaluation of brain metastases. Two experienced neuroradiologists with 21 and 6 years of experience in neuroimaging determined the brain metastases, according to the following criteria: 1) newly occurring enhancing lesions or morphologic change of the existing lesions on follow-up MR imaging after treatment; 2) not an artifact or normal enhancing structure (such as vascular structure); and 3) a brain parenchymal enhancing lesion. Determination of brain metastases was made by consensus on the basis of previous and follow-up MR imaging. Patients without enhancing lesions ( $n = 298$ ), patients who had enhancing lesions but did not undergo follow-up MR imaging ( $n = 24$ ), patients with suspected leptomeningeal metastasis ( $n = 8$ ), or patients who presented with severe motion artifacts ( $n = 1$ ) were

**Table 1: Parameters of postcontrast wave-T1-SPACE and standard SPACE**

	Wave-T1-SPACE	Standard SPACE
FOV (mm)	230 × 230	230 × 230
Matrix size	256 × 256	256 × 256
Section thickness (mm)	0.9	0.9
TR/TE (ms)	700/12	700/28
Flip angle	T1 variable	T1 variable
Echo-train length	60	60
Acceleration factor	4 (phase: 2; section: 2)	2 (phase: 2)
No. of slices	200	192
Scan time	2 min 2 seconds	3 min 55 seconds

excluded. Finally, 56 patients with a mean age of 64.7 years (age range, 45–88 years; 35 men and 21 women) were included. A total of 207 enhancing lesions were considered as brain metastases.

### Imaging Acquisition

All studies were performed using a 3T MR imaging scanner (Magnetom Skyra; Siemens) with a 64-channel head coil. In addition to the postcontrast SPACE with DANTE and wave-T1-SPACE with fat suppression, standard imaging sequence with axial FLAIR, T2-weighted, T1-weighted, and gradient-echo sequences were obtained. A dose of 0.2 mL/kg body weight of gadoterate meglumine (Dotarem; Guerbet) was injected by a power injector (Spectris Solaris EP MR injector system; Medrad), followed by a saline flush of 10 mL. The 2 different postcontrast 3D SPACE sequences were obtained in a consistent order with standard SPACE followed by wave-T1-SPACE. The detailed technical parameters of the postcontrast 3D T1WI are described in Table 1.

### Image Analysis

Two neuroradiologists with 7 and 3 years of experience independently evaluated both MR images for the presence of brain metastases in each patient. Two observers reviewed all images using a PACS and were blinded to the clinical diagnosis. However, the observers were not blinded to the type of sequences due to the distinctive characteristics of the MR images. Both observers were instructed to report every enhancing lesion in the brain parenchyma except for artifacts or normal anatomic structures. The metastatic lesions were classified according to the maximal diameter of the enhancing lesions: large ( $>5$  mm) and small ( $\leq 5$  mm). Each MR image was reviewed at 2 different time points at least 4 weeks apart, to avoid recall bias.

For quantitative analysis, the contrast ratio (CR) and contrast-to-noise ratio (CNR) of lesions to normal parenchyma ( $CNR_{\text{lesion/parenchyma}}$ ) and CNR of white matter to gray matter ( $CNR_{\text{white matter/gray matter}}$ ) for wave-T1-SPACE and standard SPACE were estimated. We selected homogeneous, solid enhancing lesions of  $>5$  mm in the largest diameter for the evaluation of  $CNR_{\text{lesion/parenchyma}}$  and  $CR_{\text{lesion/parenchyma}}$ , but we excluded the cystic portion or necrosis due to difficulty in drawing the ROI. The CR and CNR were calculated using the following formula, according to previous studies:<sup>2,16,17</sup>

**Table 2: Comparison of lesion detectability according to the types of MR images and enhancing lesion size**

	Wave-T1-SPACE	Standard SPACE	P <sup>a</sup>
No. of enhancing lesions (<5 mm) (mean)			
Observer 1	1.61 (SD, 0.29)	2.84 (SD, 0.47)	<.001
Observer 2	1.41 (SD, 0.19)	2.68 (SD, 0.43)	<.001
Interobserver agreement <sup>b</sup>	0.72 (0.59–0.84)	0.81 (0.74–0.88)	<.001
No. of enhancing lesions (>5 mm) (mean)			
Observer 1	1.34 (SD, 0.28)	1.32 (SD, 0.27)	.66
Observer 2	1.29 (SD, 0.27)	1.29 (SD, 0.27)	.26
Interobserver agreement <sup>b</sup>	0.95 (0.91–1.00)	1.00 (0.99–1.00)	<.001

<sup>a</sup> P values derived from the Wilcoxon signed-rank test.

<sup>b</sup> Values were calculated using  $\kappa$  statistics and numbers in parentheses are 95% CIs.

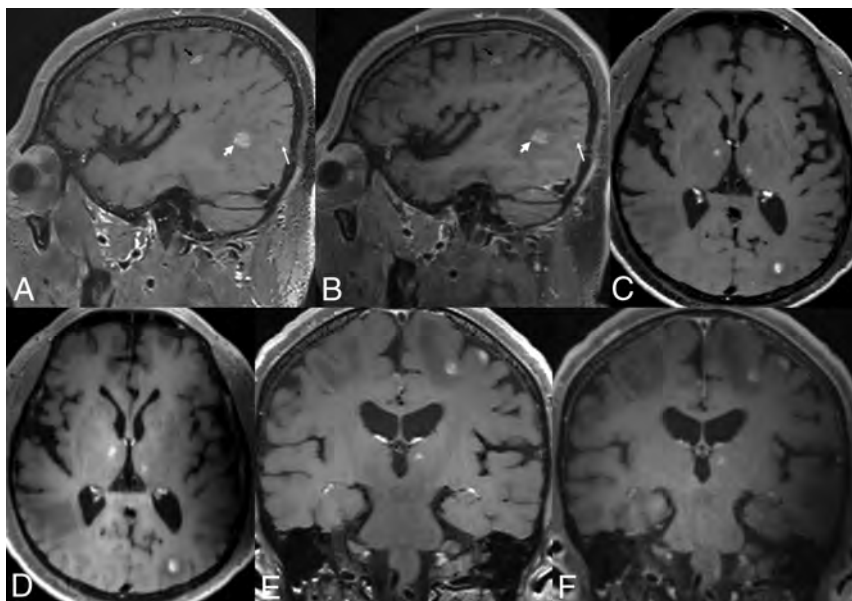


**FIG 1.** Brain MR imaging of a 62-year-old male patient with lung cancer. Postcontrast standard SPACE images (A, C, and E) show multiple variable-sized, enhancing lesions in both cerebral hemispheres. Multiple enhancing lesions are also well-visualized on postcontrast wave-T1-SPACE (B, D, and F), though more noise was present than in standard SPACE.

$$CR_{\text{lesion/parenchyma}} = [(SI_{\text{lesion}} - SI_{\text{parenchyma}}) / SI_{\text{parenchyma}}] \times 100$$

$$CNR_{\text{lesion/parenchyma}} = (SI_{\text{lesion}} - SI_{\text{parenchyma}}) / SD_{\text{parenchyma}}$$

$$CNR_{\text{white matter/gray matter}} = (SI_{\text{white matter}} - SI_{\text{gray matter}}) / SD_{\text{white matter}}$$

SI is the mean signal intensity of the ROI, and SD is the standard deviation of the noise. One neuroradiologist (with 7 years of experience) tried to draw ROIs in the center of the enhancing lesion, and ROIs of each sequence were placed visually in a side-by-side comparison, trying to draw an identical size and location. ROIs for the SI and SD of the parenchyma were placed in the adjacent parenchyma, including both white matter and gray matter because of inhomogeneous noise distribution in parallel imaging.<sup>18</sup> The corpus callosum and the head of caudate nucleus were selected for the ROIs of white matter and gray matter. Every ROI of normal parenchyma (white and gray matter) measured 23.41 mm<sup>2</sup>, but the areas of the ROIs of enhancing lesions were variable, depending on lesion size (from 9.83 to 32.01 mm<sup>2</sup>).

For qualitative analysis, we visually analyzed the overall diagnostic image quality for the different enhanced 3D T1WI sequences using a 5-point Likert scale: 5 = excellent image quality, 4 = slight blurring but not compromising the image assessment, 3 = moderate blurring that slightly compromised the evaluation, 2 = severe blurring resulting in a major limitation in evaluation, 1 = nondiagnostic image quality.<sup>1</sup>

### Statistical Analysis

All statistical analyses were performed using statistical software packages (SPSS; Version 26.0, IBM; and MedCalc, Version 19.8; MedCalc Software). All data obtained from the qualitative and quantitative analyses are reported as the means. The Kolmogorov-Smirnov test was used to test the distribution of variables.  $CNR_{WM/GM}$ ,  $CNR_{\text{lesion/parenchyma}}$ , and  $CR_{\text{lesion/parenchyma}}$  had a normal distribution; the paired *t* test was used for the analyses. The Wilcoxon signed-rank

test was used to compare the difference in the number of enhancing lesions and overall diagnostic image quality scores between the 2 different sequences. Interobserver agreement between the 2 readers was calculated by weighted  $\kappa$  statistics; 0–0.20, 0.21–0.40, 0.41–0.60, 0.61–0.80, and 0.81–1.00 were interpreted as slight, fair, moderate, substantial, and almost perfect agreement, respectively, on the basis of the method of Landis and Koch.<sup>19</sup> Statistical significance was set at *P* < .05.

### RESULTS

For the mean number of enhancing lesions of <5 mm, standard SPACE showed a significantly higher number of contrast-enhancing lesions than wave-T1-SPACE for both observers (2.84 [SD, 0.47] versus 1.61 [SD, 0.29] for observer 1, and 2.68 [SD, 0.43] versus 1.41 [SD, 0.19] for observer 2) (*P* < .001 for both observers) (Table 2 and Figs 1 and 2). Sixty-nine enhancing lesions were missed by observer 1, and 71 were missed by observer 2, using wave-T1-SPACE (Fig 3). Standard SPACE showed almost perfect agreement (weighted  $\kappa$ , 0.81; 95% CI, 0.74–0.88) and wave-T1-SPACE showed substantial agreement (weighted  $\kappa$ ,

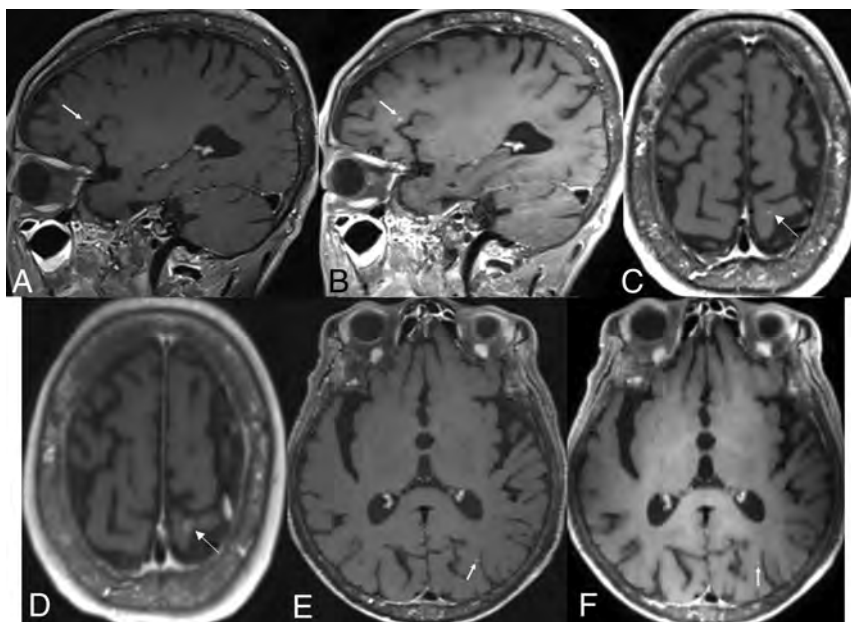


**FIG 2.** Brain MR imaging of a 68-year-old male patient with lung cancer. Postcontrast standard SPACE (A, C, and E) shows multiple tiny enhancing lesions in both cerebral hemispheres. Although these tiny enhancing lesions are also visible on postcontrast wave-T1-SPACE (B, D, and F), they are somewhat less pronounced (arrows).

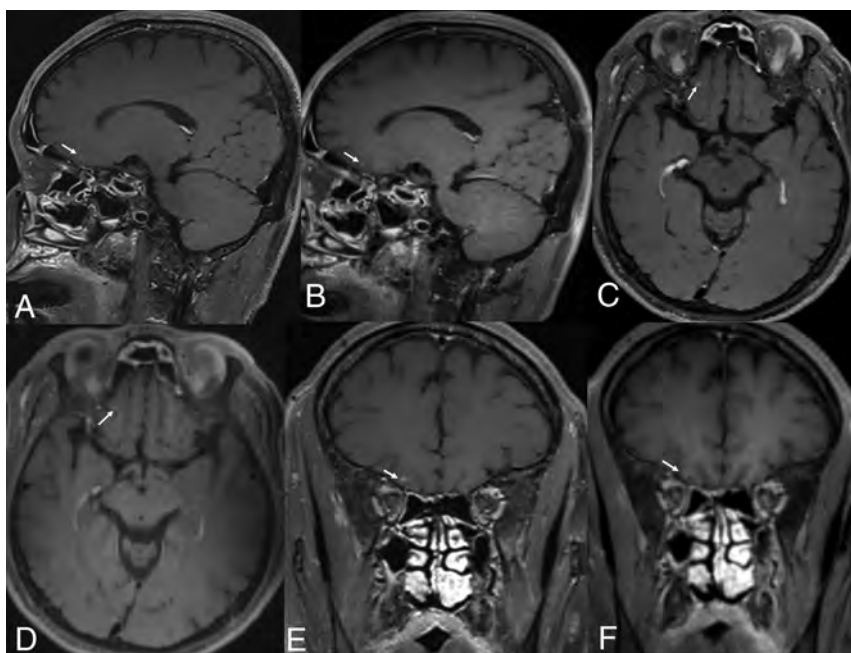


**FIG 3.** Brain MR imaging of a 54-year-old male patient with lung cancer. Postcontrast standard SPACE (A, C, and E) shows a tiny enhancing lesion (arrows) in the right frontal lobe, but it is almost invisible on postcontrast wave-T1-SPACE (B, D, and F).

0.72; 95% CI, 0.59–0.84) between the 2 observers. However, there was no significant difference between standard SPACE and wave-T1-SPACE for the mean number of enhancing lesions of  $>5$  mm ( $P = .66$  for observer 1, and  $P = .26$  for observer 2) (Fig 4). Only 1 enhancing lesion was missed by observer 1, and none of the enhancing lesions were missed by observer 2 using wave-T1-

SPACE. Both MR images showed almost perfect agreement between the 2 observers (weighted  $\kappa$ , 0.95; 95% CI, 0.91–1.00 for wave-T1-SPACE and 1.00; 95% CI, 0.99–1.00 for standard SPACE) for the measurement of the number of enhancing lesions of  $>5$  mm.

A total of 21 patients with homogeneous and solid, enhancing lesions larger than 5 mm in size were evaluated for measurement of  $CNR_{\text{lesion/parenchyma}}$  and  $CR_{\text{lesion/parenchyma}}$  (Table 3). The mean  $CNR_{\text{lesion/parenchyma}}$  and  $CR_{\text{lesion/parenchyma}}$  of standard SPACE (53.74 [SD, 8.15], 99.75 [SD, 10.88], respectively) were significantly higher than those of wave-T1-SPACE (23.03 [SD, 3.63], 63.42 [SD, 8.68], respectively) ( $P < .0001$ ). However, the mean  $CNR_{\text{white matter/gray matter}}$  of standard SPACE ( $-0.99$  [SD, 0.40]) was significantly lower than wave-T1-SPACE (2.86 [SD, 0.47]) ( $P < .0001$ ).

Although the mean scores of overall diagnostic image quality were significantly lower with wave-T1-SPACE (4.27 [SD, 0.49]) than with standard SPACE (4.98 [SD, 0.13]) ( $P < .0001$ ), wave-T1-SPACE showed sufficient image quality with an average image-quality assessment rating of more than grade IV (Table 3).

## DISCUSSION

In this study, the number of measured, smaller enhancing lesions ( $<5$  mm in maximal diameter) and  $CNR_{\text{lesion/parenchyma}}$  of postcontrast wave-T1-SPACE was significantly lower than that of postcontrast standard SPACE. However, there was no significant difference in the evaluation of larger enhancing lesions ( $>5$  mm in maximal diameter) between the 2 types of post-contrast SPACE sequences, and scan-time reduction was achieved using wave-controlled aliasing in parallel imaging (wave-CAIPI) compared with standard SPACE (2 minutes 2 seconds versus 3 minutes 55 seconds). Furthermore, 98.2% (55/56) of wave-T1-SPACE showed excellent image quality or slight blurring that did not compromise image quality, though the

image quality of wave-T1-SPACE was significantly lower than that of standard SPACE.

Wave-T1-SPACE has been reported as not susceptible to imaging blurring and geometric distortion caused by the inhomogeneity of the main magnetic field.<sup>20,21</sup> It has proved to be a promising, accelerated MR imaging technique that was noninferior to standard



MR images for the evaluation of pathology, artifacts, and overall diagnostic quality with decreasing scan time and motion artifacts.<sup>12,13</sup> Goncalves Filho et al<sup>15</sup> reported that postcontrast wave-T1-SPACE further emphasizes the advantage of the SPACE sequence and causes the enhancing lesions to stand out more by decreasing the background signal intensity and removing signal from vascular flow-related artifacts. They showed noninferior visualization and diagnostic quality of postcontrast wave-T1-SPACE compared with standard SPACE for the evaluation of parenchymal and meningeal enhancing lesions without loss of clinically important information.

However, our study showed that postcontrast wave-T1-SPACE showed lower image quality and inferior visualization for smaller enhancing lesions than postcontrast standard SPACE. Although Goncalves Filho et al<sup>15</sup> reported that postcontrast wave-T1-SPACE was noninferior to standard SPACE for visualization of enhancing pathology, both observers preferred more

cases of standard SPACE over wave-T1-SPACE for diagnostic quality and less background noise and motion artifacts. Postcontrast standard SPACE was also preferred over wave-T1-SPACE for the background noise and motion artifacts in another study by these authors.<sup>10</sup> These results were consistent with ours; however, they did not perform a quantitative comparison between the 2 types of postcontrast SPACE, and they did not evaluate the diagnostic performance for the subcentimeter enhancing lesions, unlike our study.

Recently developed other types of accelerated 3D acquisition techniques<sup>6-8</sup> have also shown lower image quality than standard postcontrast 3D T1WI. Postcontrast 3D-FLASH showed more reduced susceptibility and motion artifacts than standard MPAGE.<sup>7</sup> However, it showed inferior conspicuity of very small or mildly enhancing lesions than standard MPAGE due to a lower SNR.<sup>7</sup> Postcontrast ultrafast 3D-EPI also showed lower image quality than standard MPAGE. In addition, it

had pseudolesions due to susceptibility artifacts and inevitable geometric distortion of the EPI-derived sequence, though it can achieve post-contrast 3D T1WI with 30 seconds.<sup>8</sup> Therefore, it is thought that there is a trade-off problem between scanning time and image quality in accelerated 3D acquisition techniques including wave-T1-SPACE.

Postcontrast 3D T1WI using wave-CAIPI has more noise than standard SPACE, and this result was consistent with those of previous studies.<sup>11,12,15</sup> In previous studies,<sup>11,12,15</sup> increased noise did not affect the diagnostic performance, and similarly, in our study, it did not affect the detection of larger enhancing lesions. The authors explained the cause of more noise being the interactions between the wave-CAIPI approach and motion/flow-related artifacts, free induction decay-related artifacts, other 3D spin-echo related artifacts, or imperfections of the wave-CAIPI acquisition

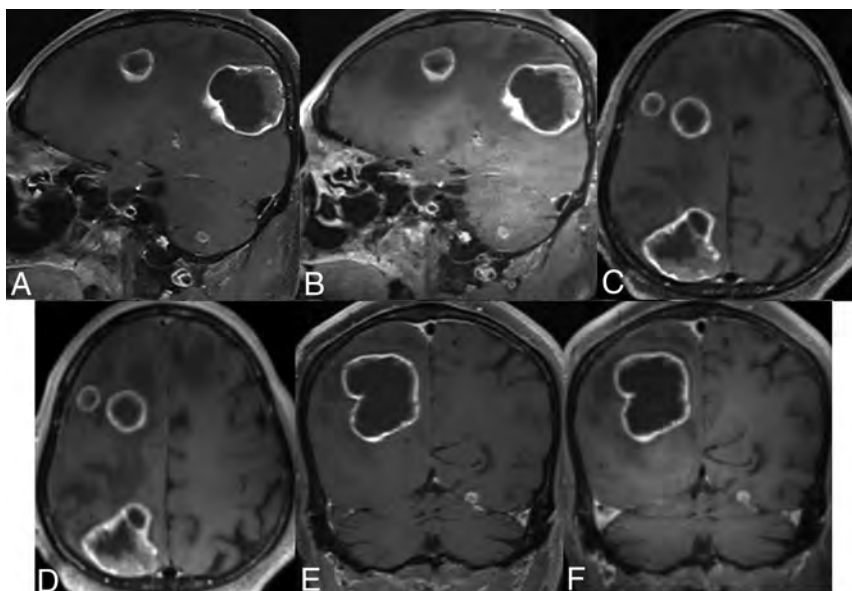


**FIG 4.** Brain MR imaging of a 77-year-old male patient with colorectal cancer. Postcontrast standard (A, C, and E) and wave-T1-SPACE (B, D, and F) show multiple large-sized, enhancing masses in both cerebral hemispheres, and there was no significant difference in the visualization of enhancing lesions, though more noise was observed in postcontrast wave-T1-SPACE.

**Table 3: CNR<sub>lesion/parenchyma</sub>, CNR<sub>white matter/gray matter</sub>, and CR<sub>lesion/parenchyma</sub> and image quality of postcontrast wave-T1-SPACE and standard SPACE**

	Wave-T1-SPACE	Standard SPACE	P Value <sup>a</sup>
CNR (n = 21) (mean)			
Lesion/parenchyma	23.03 (SD, 3.63)	53.74 (SD, 8.15)	<.001
White matter/gray matter	2.86 (SD, 0.47)	-0.99 (SD, 0.40)	<.001
CR, lesion/parenchyma (n = 21)	63.42 (SD, 8.68)	99.75 (SD, 10.88)	<.001
Overall image quality (mean)	4.27 (SD, 0.49)	4.98 (SD, 0.13)	<.001
Grade V	16 (28.6) <sup>b</sup>	55 (98.2) <sup>b</sup>	
Grade IV	39 (69.6) <sup>b</sup>	1 (0.18) <sup>b</sup>	
Grade III	1 (1.78) <sup>b</sup>	0 (0) <sup>b</sup>	
Grade II	0 (0) <sup>b</sup>	0 (0) <sup>b</sup>	
Grade I	0 (0) <sup>b</sup>	0 (0) <sup>b</sup>	

<sup>a</sup> P values derived from the Wilcoxon signed-rank test.

<sup>b</sup> Data are number of patients, and data in parentheses are percentages.

and reconstruction process.<sup>15</sup> Further evaluation of the accurate causes of noise and technical development of wave-CAIPI images in the future will improve diagnostic quality of wave-T1-SPACE.<sup>11</sup>

Our study has several limitations. First, there was an inevitable selection bias due to the single-center and retrospective nature of the study. Second, we could not randomize the order of the wave-T1-SPACE and standard SPACE because of the retrospective nature of the study. Thus, the timing bias between contrast injection and image acquisition might affect the difference between the 2 MR images. Further randomized studies on the order of image acquisition with a large number of patients are needed to further validate the results. Third, complete blindness of the sequence type was impossible due to the distinctive characteristics of each MR image. Fourth, pathologic confirmation of all metastatic lesions was not possible because patients with brain metastases usually do not undergo surgical intervention. Last, we did not apply the recommended time delay for obtaining enhanced T1WI in brain tumor imaging.<sup>3,22</sup> Ellingson et al<sup>3</sup> and Kaufmann et al<sup>22</sup> suggested 4 and 8 minutes after contrast injection, respectively, but it was difficult to apply the recommended protocol in clinical practice due to the limited number of MR imaging resources.

## CONCLUSIONS

Postcontrast wave-T1-SPACE could markedly decrease the scan time of postcontrast SPACE T1WI (2 minutes 2 seconds versus 3 minutes 55 seconds), and there was no significant difference in the evaluation of larger-sized enhancing lesions (>5 mm in maximal diameter). Furthermore, 98.2% of wave-T1-SPACE images showed excellent image quality or slight blurring without compromising image assessment. However, postcontrast wave-T1-SPACE showed underestimation of smaller enhancing lesions (<5 mm in maximal diameter) and more noise than standard postcontrast 3D SPACE. Therefore, it is necessary to recognize these limitations, and postcontrast wave-T1-SPACE should be interpreted with caution in clinical practice.

## ACKNOWLEDGMENTS

The authors thank Kang Soo Kim and In Seong Kim (Siemens, South Korea) for applying and optimizing the wave-CAIPI and DANTE.

Disclosure forms provided by the authors are available with the full text and PDF of this article at [www.ajnr.org](http://www.ajnr.org).

## REFERENCES

- Likert R. A technique for the measurement of attitudes. *Arch Psychol* 1932
- Kim D, Heo Y, Jeong H, et al. Usefulness of the delay alternating with nutation for tailored excitation pulse with T1-weighted sampling perfection with application-optimized contrasts using different flip angle evolution in the detection of cerebral metastases: comparison with MP-RAGE imaging. *AJNR Am J Neuroradiol* 2019;40:1469–75 CrossRef Medline
- Ellingson BM, Bendszus M, Boxerman J, et al. Jumpstarting Brain Tumor Drug Development Coalition Imaging Standardization Steering Committee. Consensus recommendations for a standardized Brain Tumor Imaging Protocol in clinical trials. *Neuro Oncol* 2015;17:1188–98 CrossRef Medline
- Fagundes J, Longo M, Huang S, et al. Diagnostic performance of a 10-minute gadolinium-enhanced brain MRI protocol compared with the standard clinical protocol for detection of intracranial enhancing lesions. *AJNR Am J Neuroradiol* 2017;38:1689–94 CrossRef Medline
- Munn Z, Pearson A, Jordan Z, et al. Patient anxiety and satisfaction in a magnetic resonance imaging department: initial results from an action research study. *J Med Imaging Radiat Sci* 2015;46:23–29 CrossRef Medline
- Vranic J, Cross N, Wang Y, et al. Compressed sensing-sensitivity encoding (CS-SENSE) accelerated brain imaging: reduced scan time without reduced image quality. *AJNR Am J Neuroradiol* 2019;40:92–98 CrossRef Medline
- Patel SH, Batchala PP, Schallert K, et al. 3D fast low-angle shot (FLASH) technique for 3T contrast-enhanced brain MRI in the inpatient and emergency setting: comparison with 3D magnetization-prepared rapid gradient echo (MPRAGE) technique. *Neuroradiology* 2021;63:897–904 CrossRef Medline
- Ryu K, Baek H, Skare S, et al. Clinical feasibility of ultrafast contrast-enhanced T1-weighted 3D-EPI for evaluating intracranial enhancing lesions in oncology patients: comparison with standard 3D MPRAGE sequence. *AJNR Am J Neuroradiol* 2022;43:195–201 CrossRef Medline
- Bilgic B, Gagoski BA, Cauley SF, et al. Wave-CAIPI for highly accelerated 3D imaging. *Magn Reson Med* 2015;73:2152–62 CrossRef Medline
- Goncalves Filho AL, Conklin J, Longo MF, et al. Accelerated post-contrast Wave-CAIPI T1 SPACE achieves equivalent diagnostic performance compared with standard T1 SPACE for the detection of brain metastases in clinical 3T MRI. *Front Neurol* 2020;11:587327 CrossRef Medline
- Longo M, Conklin J, Cauley S, et al. Evaluation of ultrafast wave-CAIPI MPRAGE for visual grading and automated measurement of brain tissue volume. *AJNR Am J Neuroradiol* 2020;41:1388–96 CrossRef Medline
- Ngamsombat C, Gonçalves Filho A, Longo M, et al. Evaluation of ultrafast wave-controlled aliasing in parallel imaging 3D-FLAIR in the visualization and volumetric estimation of cerebral white matter lesions. *AJNR Am J Neuroradiol* 2021;42:1584–90 CrossRef Medline
- Conklin J, Longo M, Cauley S, et al. Validation of highly accelerated wave-CAIPI SWI compared with conventional SWI and T2\*-weighted gradient recalled-echo for routine clinical brain MRI at 3T. *AJNR Am J Neuroradiol* 2019;40:2073–80 CrossRef Medline
- Yim Y, Chung MS, Kim SY, et al. Wave-controlled aliasing in parallel imaging magnetization-prepared gradient echo (wave-CAIPI MPRAGE) accelerates speed for pediatric brain MRI with comparable diagnostic performance. *Scientific Reports* 2021;11:13296 CrossRef Medline
- Goncalves Filho AL, Longo MG, Conklin J, et al. MRI highly accelerated Wave-CAIPI T1-SPACE versus standard T1-SPACE to detect brain gadolinium-enhancing lesions at 3T. *J Neuroimaging* 2021;31:893–901 CrossRef Medline
- Kammer N, Coppenrath E, Treitl K, et al. Comparison of contrast-enhanced modified T1-weighted 3D TSE black-blood and 3D MP-RAGE sequences for the detection of cerebral metastases and brain tumours. *Eur Radiol* 2016;26:1818–25 CrossRef Medline
- Kato Y, Higano S, Tamura H, et al. Usefulness of contrast-enhanced T1-weighted sampling perfection with application-optimized contrasts by using different flip angle evolutions in detection of small brain metastasis at 3T MR imaging:

- comparison with magnetization-prepared rapid acquisition of gradient echo imaging.** *AJNR Am J Neuroradiol* 2009;30:923–29 CrossRef Medline
18. Rand S, Maravilla KR, Schmiedl U. **Lesion enhancement in radio-frequency spoiled gradient-echo imaging: theory, experimental evaluation, and clinical implications.** *AJNR Am J Neuroradiol* 1994;15:27–35 Medline
  19. Landis JR, Koch GG. **The measurement of observer agreement for categorical data.** *biometrics* 1977;33:159–74 CrossRef Medline
  20. Polak D, Cauley S, Bilgic B, et al. **Ultrafast multi-contrast high-resolution 3D brain MRI: a technical description of Wave-CAIPI.** *MAGNETOM Flash* 2020;76:21–27
  21. Gagoski BA, Bilgic B, Eichner C, et al. **RARE/turbo spin echo imaging with simultaneous multislice Wave-CAIPI.** *Magn Reson Med* 2015;73:929–38 CrossRef Medline
  22. Kaufmann TJ, Smits M, Boxerman J, et al. **Consensus recommendations for a standardized brain tumor imaging protocol for clinical trials in brain metastases.** *Neuro Oncol* 2020;22:757–72 CrossRef Medline



# Volumetric Measurement of Relative CBV Using T1-Perfusion-Weighted MRI with High Temporal Resolution Compared with Traditional T2\*-Perfusion-Weighted MRI in Postoperative Patients with High-Grade Gliomas

 M. Seo,  K.-J. Ahn,  Y. Choi,  N.-Y. Shin,  J. Jang, and  B.-S. Kim



## ABSTRACT

**BACKGROUND AND PURPOSE:** T1-PWI with high temporal resolution may provide a reliable relative CBV value as a valid alternative to T2\*-PWI under increased susceptibility. The purpose of this study was to assess the technical and clinical performance of T1-relative CBV in patients with postoperative high-grade gliomas.

**MATERIALS AND METHODS:** Forty-five MRIs of 34 patients with proved high-grade gliomas were included. In all MRIs, T1- and T2\*-PWIs were both acquired and processed semiautomatically to generate relative CBV maps using a released commercial software. Lesion masks were overlaid on the relative CBV maps, followed by a histogram of the whole VOI. The intraclass correlation coefficient and Bland-Altman plots were used for quantitative and qualitative comparisons. Signal loss from both methods was compared using the Wilcoxon signed-rank test of zero voxel percentage. The MRIs were divided into a progression group ( $n = 20$ ) and a nonprogression group ( $n = 14$ ) for receiver operating characteristic curve analysis.

**RESULTS:** Fair intertechnique consistency was observed between the 90th percentiles of the T1- and T2\*-relative CBV values (intraclass correlation coefficient = 0.558,  $P < .001$ ). T2\*-PWI revealed a significantly higher percentage of near-zero voxels than T1-PWI (17.7% versus 3.1%,  $P < .001$ ). There was no statistically significant difference between the area under the curve of T1- and T2\*-relative CBV (0.811 versus 0.793,  $P = .835$ ). T1-relative CBV showed 100% sensitivity and 57.1% specificity for the detection of progressive lesions.

**CONCLUSIONS:** T1-relative CBV demonstrated exquisite diagnostic performance for detecting progressive lesions in postoperative patients with high-grade gliomas, suggesting the potential role of T1-PWI as a valid alternative to the traditional T2\*-PWI.

**ABBREVIATIONS:** AUC = area under the curve; CE = contrast-enhanced; ICC = intraclass correlation coefficient; rCBV = relative CBV; ROC = receiver operating characteristic; SSE = substantial susceptibility effects; T1-rCBV = T1-PWI-derived relative CBV; T2\*-rCBV = T2\*-PWI-derived relative CBV

Perfusion MR imaging is a well-established method used to evaluate the degree of angiogenesis in brain tumors, especially gliomas.<sup>1,2</sup> Among the various parameters measured in perfusion MR imaging, relative CBV (rCBV) plays a key role in glioma grading,<sup>3,4</sup> discriminating pseudoprogression and progression of posttreatment glioblastoma,<sup>5-8</sup> and predicting future progression.<sup>9</sup>

T2\*-PWI, also known as dynamic susceptibility contrast, is the most commonly used technique for the calculation of rCBV.<sup>10</sup> On the basis of T2\*-weighted EPI, T2\*-PWI provides exponential

signal change and high temporal resolution (<3 seconds per phase) without greatly sacrificing spatial resolution. With frequent sampling of the signal intensity, T2\*-PWI can be used to draw precise concentration curves for both tissue perfusion and arterial input function, assuring proper deconvolution of parameters. However, because of its high sensitivity to magnetic susceptibility, it is limited by image degradation near the sources of field heterogeneity, such as metallic surgical materials, air-containing anatomic structures, blood products, or calcifications. Some studies reported suboptimal evaluation in postoperative imaging with T2\*-PWI due to the increased prevalence of the aforementioned conditions.<sup>11-13</sup>

T1-PWI, also known as dynamic contrast enhancement, is another technique based on linear signal change related to T1 shortening of the tissue and is characterized by increased resilience to the susceptibility induced by postsurgical changes. Several attempts were made to calculate CBV by using this method at the advent of perfusion MR imaging.<sup>14,15</sup> Owing to the relatively low temporal

Received October 13, 2021; accepted after revision April 8, 2022.

From the Department of Radiology, Seoul St. Mary's Hospital, College of Medicine, Catholic University of Korea, Seoul, Republic of Korea.

Please address correspondence to Kook-Jin Ahn, MD, PhD, Department of Radiology, Seoul St. Mary's Hospital, College of Medicine, Catholic University of Korea, 222 Banpo-daero, Seocho-gu, Seoul, 06591, Republic of Korea; e-mail: ahn-kj@catholic.ac.kr

 Indicates article with online supplemental data.

<http://dx.doi.org/10.3174/ajnr.A7527>

resolution of many T1-PWI acquisition techniques, however, arterial input functions may be insufficient, leading to unreliable perfusion metrics, especially when scanning the whole brain with source images of acceptable quality. Narrow coverage and thick-section imaging may increase the temporal resolution, though some tumor information may be missed.

With the recent widespread application of MR imaging acceleration techniques, several studies have assessed the clinical utility of T1-PWI-derived rCBV.<sup>13,16-22</sup> However, few studies have focused on its usefulness for postoperative imaging, the most typical susceptibility-prone situation.<sup>13,17</sup> Only 2 studies provided histogram analysis,<sup>19,22</sup> while others used maximal rCBV values within the radiologist-drawn ROI. Most of the studies used their own in-house software due to the lack of an optimized commercial program, which provides established theoretic accuracy but is difficult for other investigators to reproduce. In the current study, we conducted a postoperative volumetric analysis of T1-PWI-derived rCBV (T1-rCBV) using readily available software, achieving a temporal resolution of 2.2 seconds with whole-brain coverage, and ensuring image quality.

Therefore, the purpose of this study was to assess the technical and clinical performance of T1-rCBV, scanned and measured with a high-temporal-resolution protocol in postoperative patients with high-grade gliomas using commercially released software as a valid alternative to the traditional T2\*-PWI.

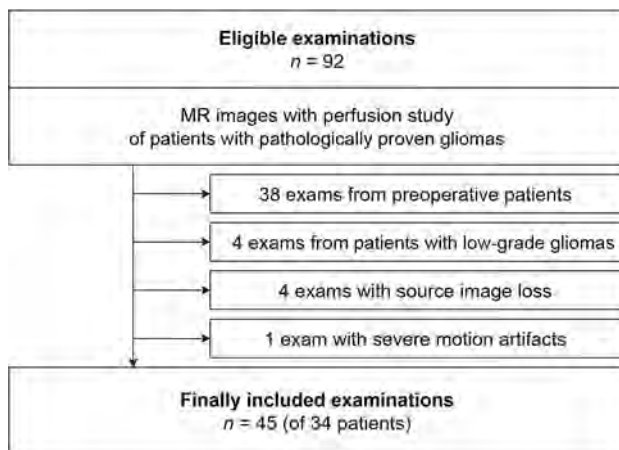


**FIG 1.** A flow chart outlining the selection of patients and examinations is shown.

## MATERIALS AND METHODS

### Study Population

This retrospective study was approved by our institutional review board. Informed consent of enrolled patients was waived due to its retrospective nature.

In our PACS, we identified MR imaging studies, including perfusion scans, performed in patients with pathologically proved high-grade gliomas from April 2018 to January 2021. Among 92 MR imaging examinations, 45 examinations of 34 patients were finally included in the study. Figure 1 shows the flow chart for patient selection.

### Image Acquisition

All MR images were acquired on a 3T scanner (Ingenia; Philips Healthcare). Routine precontrast sequences included sagittal and axial T1WI, coronal and axial T2WI, axial T2 FLAIR images, axial T2\*WI, and axial DWI.

T2\*-PWI requires contrast agent preload to avoid the T1 shinnethrough effect.<sup>13,23</sup> Therefore, T1-PWI scans with a time resolution of 2.2 seconds were obtained previously, assisted by sensitivity encoding and accelerated by factors  $R = 2.2$  and  $1.2$  for phase and partition encoding directions ( $y$  and  $z$  directions), respectively. For both perfusion imaging techniques,  $0.1$  mmol/kg of gadobutrol (Gadovist; Bayer Schering Pharma) was administered intravenously with an injection rate of  $3$  mL/s, injecting  $4$  mL first during the preceding T1-PWI scan, followed by  $6$  mL for the T2\*-PWI scan. Following the perfusion study, 3D contrast-enhanced (CE)-T1WI was acquired with a 3-plane MPR.

The parameters used for key sequences are summarized in Table 1.

### Image Postprocessing

All image-processing steps were performed using the commercial software nordicICE (Version 4.1.3; NordicNeuroLab). First, all images were coregistered on the reference image, CE-T1WI. Lesion masks were produced on CE-T1WI using a semiautomatic segmentation tool with the seed-growing method. Visual assessment was used to avoid large vessels and internal content of the surgical cavity, such as fluid, hemorrhage, or necrosis.

For T1-PWI analysis, we used the perfusion analysis module of nordicICE, which was originally more commonly used in T2\*-PWI analysis. Signal conversion into a concentration curve was based on  $1/T1$  acquired by spoiled gradient-echo images, rather than  $R2^*$  change versus time. A fixed baseline T1 time ( $1400$  ms) was used during the conversion, referring to recent studies.<sup>24,25</sup> We

**Table 1: Parameters of key MR imaging sequences**

	T1-PWI	T2*-PWI	T2WI	T2 FLAIR	3D CE-T1WI
Sequence	3D T1-FFE	3D T2-FFE	TSE	TSE	3D TSE
TR/TE (ms)	4.2/2.3	1800/30	3000/80	9000/100	550/30
Flip angle	8°	40°	90°	90°	90°
FOV (mm <sup>2</sup> )	220 × 220	210 × 210	230 × 230	230 × 230	240 × 240
Matrix	137 × 137	128 × 128	404 × 382	308 × 290	240 × 240
Section thickness (mm)	5	5	5	5	1
Slices	30	25	26	26	200
Time resolution (sec)	2.2	1.8			
Phases	150	50			
Note					Black-blood, Dixon fat suppression

**Note:**—FFE indicates fast-field echo.

also performed motion correction, leakage correction, and model-independent deconvolution by standard singular value decomposition. Pixels for arterial input functions were semiautomatically searched in the circle of Willis, and the peak shapes of all arterial input functions were visually assessed. The high temporal resolution of the T1-PWI scan facilitated the easy selection of appropriate arterial input functions. The WM mask was automatically generated by the software to obtain normalized rCBV values. An identical procedure was performed for the analysis of T2\*-PWI source images, except for the signal conversion step.

Lesion masks, representing the VOIs, were overlaid on T1- and T2\*-PWI-derived rCBV (T2\*-rCBV) maps for histogram analysis of the whole enhancing lesion. Basic statistics of T1- and T2\*-rCBV values were recorded for each MR imaging examination, including the mean, median, SD, and 90th percentile.

### Statistical Analysis

For each lesion, susceptibility effects and visualization grades were qualitatively evaluated on the basis of a consensus of 2 neuroradiologists (one with >20 years of experience and another with 5 years of experience). A linear T2\*WI dark lesion along the surgical margin with <5-mm thickness was regarded as marginal hemorrhage. Hemorrhage measuring >5 mm with apparently defective visualization of the VOI was regarded as considerable hemorrhage. The visualization grade was assessed for all lesions on T1- and T2\*-PWI. The grade was defined by visually estimating the fraction of signal loss within the VOI: grade 3 = <20% signal loss, grade 2 = 20%–50% signal loss, grade 1 = 50%–80% signal loss, and grade 0 = >80% signal loss. The results of visualization grading of the 2 methods were compared using the Pearson  $\chi^2$  test.

For comparison of T1- and T2\*-PWI, the intraclass correlation coefficient (ICC), and the Pearson correlation coefficient *R* were calculated for the 90th percentile and the mean values of the rCBV histogram. On the basis of the 95% confidence interval of the ICC estimate, values were interpreted as follows: ICC < 0.50 = poor, 0.5–0.74 = moderate, 0.75–0.89 = good, >0.90 = excellent.<sup>26</sup> Bland-Altman plots were constructed for qualitative assessment of the correlation between T1- and T2\*-rCBVs.

Cumulative and noncumulative histograms of rCBV in all VOIs were plotted for visual comparison of rCBV distribution. The number of voxels with an absolute zero value was counted in a voxelwise manner from T1- and T2\*-PWI, and the percentage of voxels containing zero-valued rCBV within the whole VOI was calculated in each tumor. The Wilcoxon signed-rank test was performed to quantitatively compare the zero voxel percentages of T1- and T2\*-PWI.

Receiver operating characteristic (ROC) curve analysis was used to evaluate the clinical performance, discriminating progression and nonprogression in postoperative examinations. The examination was assigned to a progression group if it included a pathologically confirmed tumor in the reoperation within 3 months or if it revealed a clearly measurable lesion according to Response Assessment in Neuro-Oncology criteria with additional radiologic or clinical evidence of progression within 3 months (clinical progression meant death or obvious deterioration). If the lesion of interest was surgically confirmed to contain <5% viable tumor cells within 3 months or if the lesion was radiologically not measurable

and frank local progression was not observed for the next 6 months, the examination was assigned to a nonprogression group. The areas under the curve (AUCs) calculated from ROC curves of T1- and T2\*-rCBV were compared with each other via the DeLong test.

Additional subgroup ROC curve analysis was performed. One subgroup included examinations with substantial susceptibility effects (SSE, defined as grades 0–1; ie, <50% visualization on T2\*-PWI), and another subgroup included examinations without SSE (grades 2–3; ie, >50% visualization on T2\*-PWI). ROC curves were drawn, and AUC values were calculated in each subgroup.

All statistical analyses were performed using an open-source statistical language (R Studio, Version 1.4.1106; <http://rstudio.org/download/desktop>). A *P* value  $\leq .05$  was interpreted as statistically significant.

### RESULTS

The overall characteristics of the 45 examinations of 34 patients are shown in the Online Supplemental Data. All patients were at least once surgically diagnosed with high-grade glioma before or during the study period. Among them, 24 patients were eventually diagnosed with grade 4 lesions, and another 10 patients eventually exhibited grade 3 lesions. During the study period, 8 patients had undergone multiple perfusion MRIs.

Among 45 examinations, 15 examinations (33.3%) were conducted within 6 months of the operation. In 9 examinations, the VOI was located at the skull base area, with mild or considerable susceptibility effects by location. More than 90% of the cases showed marginal or considerable hemorrhage because all examinations were postoperative MRIs. Only 13 lesions were fully visible (28.9%, grade 3) on T2\*-PWI, while another 32 lesions were suboptimal (71.1%, grades 0–II). Nine T2\*-PWIs were difficult to interpret due to SSE, meaning that half or more of the VOI was shaded by signal loss (20%, grades 0–I). One sample case of grade 1 visualization is presented in Fig 2, and 2 more illustrative sample cases are presented in the Online Supplemental Data. On the other hand, only 4 lesions were suboptimally visualized (8.9%, grades 0–II), while other lesions were fully evaluated on T1-PWI (91.1%, grade 3). The Pearson  $\chi^2$  test revealed significant differences in the visualization grade between the 2 methods (*P* < .001).

The scatterplot of T2\*-rCBV versus T1-rCBV is presented in Fig 3. For both the 90th percentile and the mean of the whole lesion, rCBV measurement showed fair intertechnique consistency (ICC = 0.558 and 0.566, respectively, both *P* < .001). Additionally, Pearson correlation analysis revealed a significant positive correlation of the 90th percentile and mean values (*R* = 0.614 and 0.663, respectively, both *P* < .001) between the 2 methods. In 39 examinations, the 90th percentiles of rCBV were within the limits of agreement on the Bland-Altman plot (Fig 4), displaying 4 upper and 2 lower outliers.

T1- and T2\*-rCBV values of all lesions of interest were drawn as a cumulative histogram (Fig 5), with the T2\*-rCBV curves more frequently showing a higher initial cumulative fraction of near-zero voxels than the T1-rCBV curves. Noncumulative histograms of both methods can be found in the Online Supplemental Data. The mean percentages of zero-valued voxels within VOIs were 3.1% and 17.7% in T1- and T2\*-PWI, respectively, demonstrating a significant difference (*P* < .001).



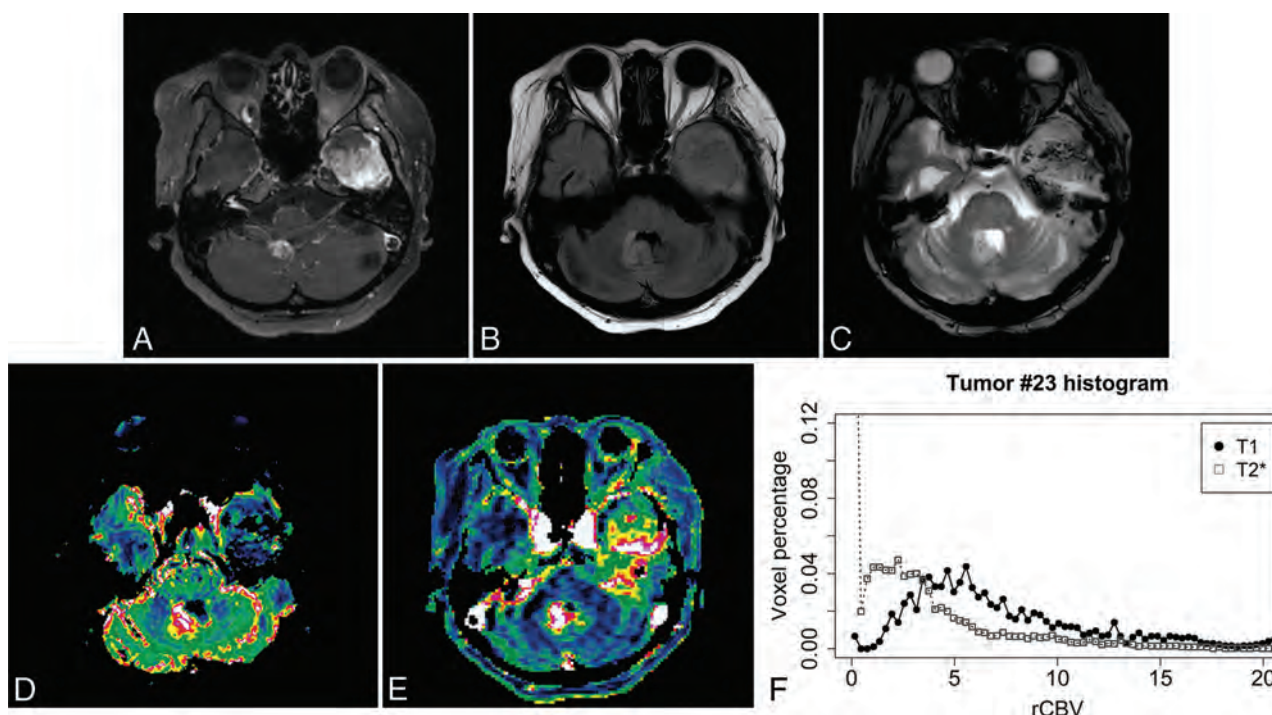


**FIG 2.** A 53-year-old woman with primary glioblastoma located in the left thalamus. On the follow-up image 10 months after the operation (7 months after the last radiation therapy), new enhancing lesions are noticed in the left temporal lobe base and fourth ventricle (A and B). Owing to its location and considerable amount of internal hemorrhage (C), signal loss shades the portions of the left temporal lobe lesion, resulting in grade 1 visualization on T2\*-PWI (D, rCBV 90th percentile, 8.18). Grade 3 visualization is achieved on T1-PWI (E, rCBV 90th percentile, 23.92). Susceptibility-induced signal loss of the T2\*-PWI is also well-noticed on the histogram, with the leftmost peak of near-zero voxels (F). The patient died in 1 month and was assigned to the progression group on ROC curve analysis.

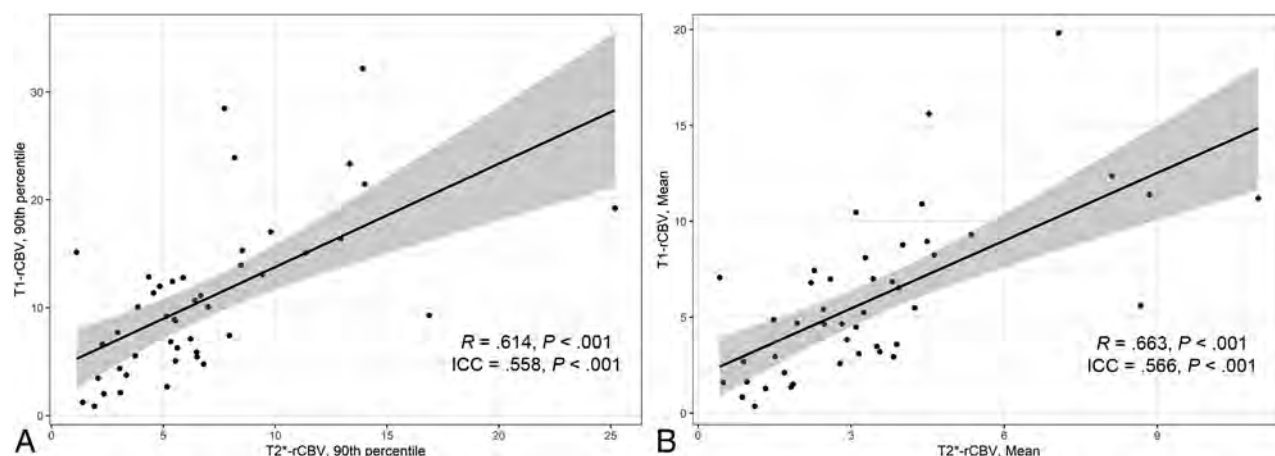


**FIG 3.** Scatterplots of rCBV values derived from T1- and T2\*-PWI. A, Ninetieth percentile of the whole lesion rCBV values, with fair consistency (ICC = 0.558) and a positive correlation ( $R = 0.614$ ). B, Mean of the whole-lesion rCBV values, with fair consistency (ICC = 0.566) and a positive correlation ( $R = 0.663$ ).

The 90th percentiles of T1- and T2\*-rCBV values were both significantly higher in the progression group than in the nonprogression group (Table 2). Boxplots comparing T1- and T2\*-rCBV between the progression and nonprogression groups are provided in the Online Supplemental Data. The AUCs of the 90th percentiles of T1- and T2\*-rCBV were 0.811 and 0.793, respectively, on the ROC curve presented in Fig 6, with no significant difference ( $P = .835$ ). At the cutoff value of 4.930, T1-rCBV was used to detect all eventually progressed tumors, with

100% sensitivity and 57.1% specificity. The optimal cutoff value of T2\*-rCBV was 4.453, with 90.0% sensitivity and 64.3% specificity.

According to the subgroup ROC analysis, as shown in the Online Supplemental Data, the AUC of T2\*-rCBV was lower than that of T1-rCBV (0.500 versus 0.750,  $P = .117$ ) in the subgroup with SSE. In the subgroup without SSE, on the other hand, the AUC of T2\*-rCBV was slightly higher than that of T1-rCBV (0.875 versus 0.824,  $P = .597$ ).

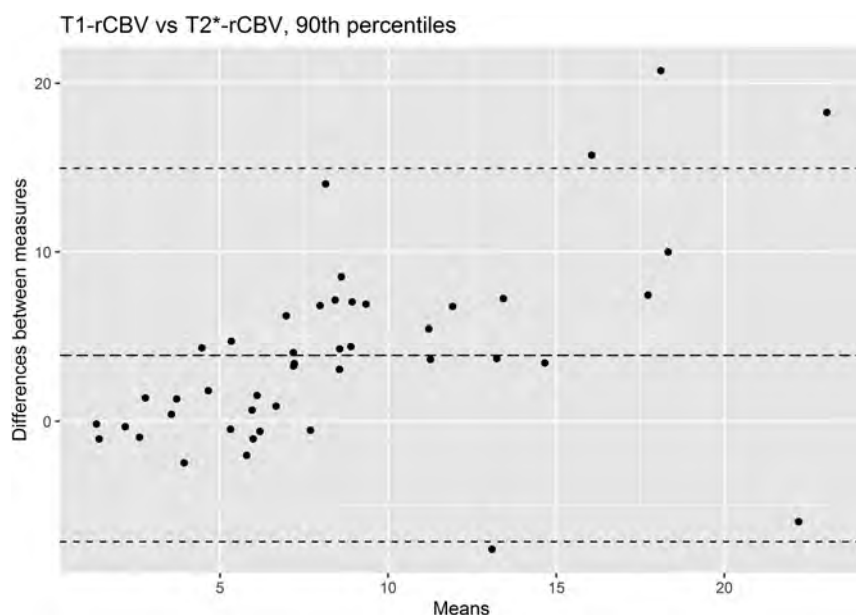


**FIG 4.** A Bland-Altman plot representing the 90th percentile of rCBV values derived from T1- and T2\*-PWI. The upper and lower dashed lines represent the 1.96 and -1.96 limits of agreement, respectively (95% confidence interval not indicated).

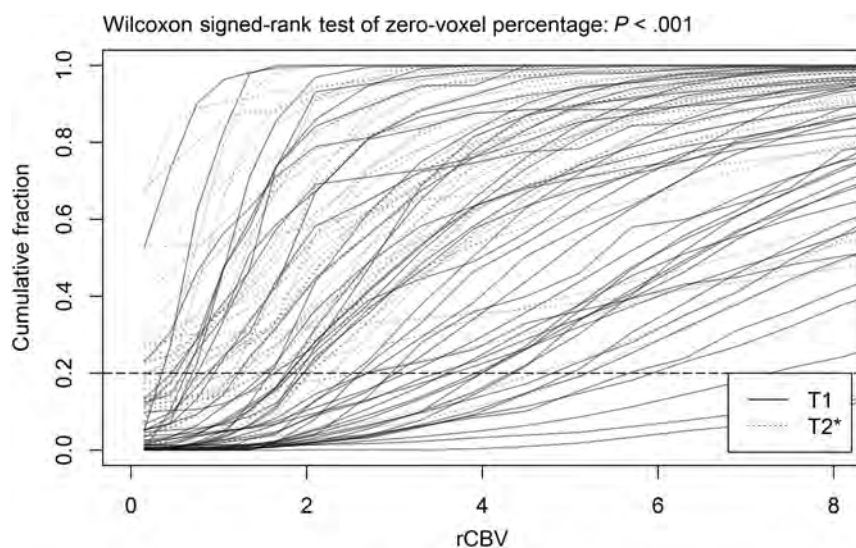


**FIG 5.** Cumulative histogram of T1- and T2\*-rCBV values in all included examinations. With T2\*-rCBV measurement, the leftmost beginning point of the cumulative fraction is  $>0.2$  (horizontal dashed line) in 17 lesions (37.8%), implying that in each entire VOI of those lesions, more than one-fifth of the voxels contained rCBV values of  $<0.3$  (the first bin of histogram). With T1-PWI-based rCBV measurements, in contrast, only 2 lesions (4.4%) show an initial cumulative fraction above 0.2.

## DISCUSSION

In the current study, rCBV values were independently calculated using T1- and T2\*-PWI in patients with postoperative high-grade gliomas, showing a positive correlation and fair consistency. The ICC was slightly lower than the previously reported values (0.56 versus 0.74).<sup>13</sup> T1- and T2\*-rCBV revealed a fine diagnostic performance in discriminating eventually progressed tumors from nonprogressive lesions (AUC = 0.811 and 0.793, respectively). The difference between AUCs was more pronounced in the subgroup with SSE (0.500 versus 0.750), though without statistical significance

( $P = .117$ ). All results are covered by the range of previously reported AUC values (0.739–0.938) in the studies differentiating progression from pseudoprogression with the use of rCBV based on conventional T2\*-PWI,<sup>5–7</sup> except the T2\*-rCBV results in examinations with SSE.

Most of the few previous studies involving T1-PWI validated its clinical significance based on glioma grading<sup>13,18–22</sup> and reported calculated AUC values of 0.72–0.99.<sup>13,19,21</sup> Only 1 study by Saini et al<sup>13</sup> performed a statistical comparison of its diagnostic performance with T2\*-rCBV in discriminating grade 3 and grade 4 gliomas, with no significant difference in AUC values (0.723 versus 0.767). In our results, T1- and T2\*-rCBV similarly showed sufficient diagnostic performance in differentiating progressive from nonprogressive lesions. In another report by Larsen et al,<sup>17</sup> evaluating the clinical usefulness of T1-PWI in discriminating tumor recurrence from radiation necrosis, rCBV was able to accurately detect all 3 regressing lesions of 14 classified lesions, strongly consistent with FDG-PET. Our T1-PWI also demonstrated 100% sensitivity in detecting recurrent lesions with acceptable specificity (57.1%). Additional Kaplan-Meier survival curves and genomic subclass analyses are provided in the Online Supplemental Data, also showing consistency with the well-known results of previous studies.<sup>9,27–29</sup>

In the Bland-Altman plot comparing the 90th percentiles of the rCBV of both methods, 4 upper and 2 lower outliers were present, as previously suggested in Fig 4. VOIs of 2 upper and 2 lower outliers were located at the skull base and were disturbed by partial signal loss. One upper outlier with a pituitary stalk lesion (Online Supplemental Data) demonstrated a lower T2\*-rCBV than the calculated cutoff value, being a

false-negative case, while appropriately detected by T1-PWI. Another upper outlier was limited not only by its location but also due to considerable internal hemorrhage (Fig 2), with underestimation of T2\*-rCBV due to a large area of signal loss. Marginal hemorrhage was also combined in the skull base lesions of the 2 lower outliers. Although rare, calcification was another source of T2\*-PWI degradation, as shown in the Online Supplemental Data.

Several studies documented the rate of uninterpretable T2\*-PWI owing to susceptibility-induced signal loss and geometric

**Table 2: Summary of T1- and T2\*-rCBV values distinguishing the progression group (n = 20) from the nonprogression group (n = 14)**

Values	P Group (mean)	NP Group (mean)	P Value <sup>a</sup>	AUC	Cutoff <sup>b</sup>	Sensitivity	Specificity	P Value versus T1-rCBV <sup>c</sup>
T1-rCBV, 90th percentile	13.0 (SD, 6.9)	6.6 (SD, 6.1)	.008	0.811	4.930	100.0%	57.1%	
T2*-rCBV, 90th percentile	7.9 (SD, 4.0)	4.3 (SD, 3.1)	.009	0.793	4.453	90.0%	64.3%	.835

**Note:**—P Group indicates progression group; NP Group, nonprogression group.

<sup>a</sup>Independent t test.

<sup>b</sup>Youden index.

<sup>c</sup>DeLong test.

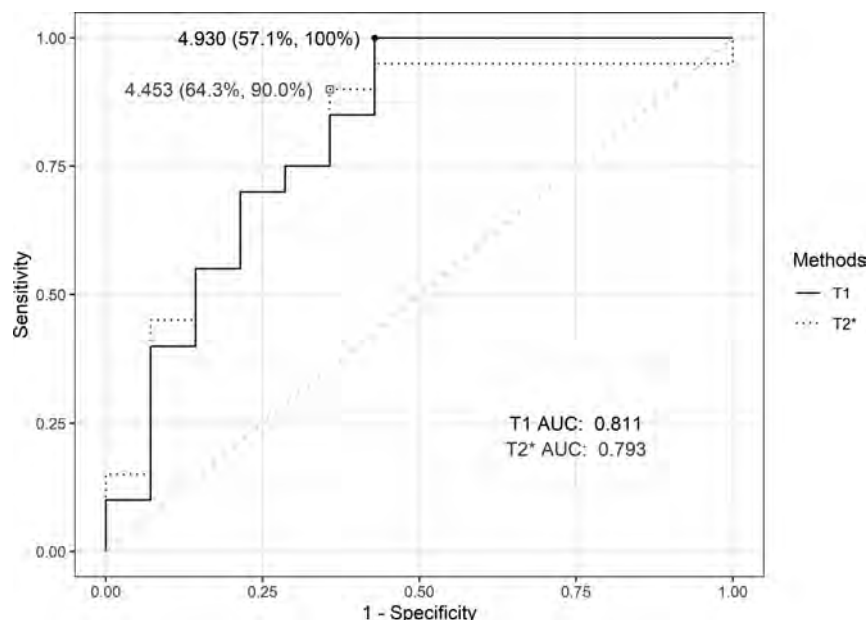


**FIG 6.** The ROC curves of T1- and T2\*-rCBV using 90th percentile values. The AUC values of T1- and T2\*-rCBV revealed no significant difference ( $P = .835$ ).

distortion.<sup>11,12,30,31</sup> A lower percentage of image degradation was seen in patients with preoperative gliomas (4.3%)<sup>31</sup> than in postoperative populations (7.0%–10.9%).<sup>11,12,30</sup> Compared with their results, our study demonstrated a slightly higher rate of SSE (20.0%, visualization grades 0–I on T2\*-PWI). In the study by Saini et al<sup>13</sup> involving a mixed population of preoperative and postoperative patients (43 and 6 patients, respectively), the rate of suboptimal T2\*-PWI (visualization grades 0–II) was lower than in our patients (32.7% versus 71.1%). No previous studies were found, however, regarding the statistical comparison of signal loss between T1- and T2\*-PWI. In our study, voxelwise analysis showed that postoperative T2\*-PWI contained a significantly higher prevalence of signal loss than T1-PWI (17.7% versus 3.1%, respectively). In particular, T1-PWI showed a higher AUC value than T2\*-PWI in the examinations with SSE (0.750 versus 0.500), though no significant difference was observed, possibly due to the small number of subgroups (3 examinations with progressed lesions, 4 examinations with non-progressed lesions).

Only 2 previous studies directly compared the rCBV values obtained from T1- and T2\*-based perfusion MR imaging in patients

with gliomas.<sup>13,19</sup> In both studies, T1-rCBV values tended to be slightly lower than in conventional T2\*-rCBV, contrary to our results. Saini et al<sup>13</sup> also compared the consistency of T1- and T2\*-rCBV measurements, reporting a higher ICC (0.74) between the 2 methods than in our result (0.56). Because both studies included more preoperative patients and used hotspot measurements of rCBV, avoiding areas with signal loss, histograms of T2\*-rCBV values in our study might have been more affected by susceptibility effects, resulting in different T1- and T2\*-rCBV relationships under postoperative circumstances than in those 2 previous reports. Although T2\*-rCBV is a reasonable reference value obtained using the established method, because of its apparent partial inaccuracy due to susceptibility effects, other modalities may be considered the criterion standard for comparison. As previously mentioned, Larsen et al<sup>17</sup>

used FDG-PET to compare the clinical performance of T1-rCBV in surgically treated patients. Some recent articles compared amino acid PET with T2\*-rCBV in posttreatment patients with gliomas to differentiate progression from treatment-related changes,<sup>32,33</sup> and T1-rCBV may also be compared with amino acid PET in further studies. Likewise, arterial spin-labeling and amide proton transfer techniques are other candidates for clinical validation of T1-rCBV, in the same manner as in previous reports.<sup>34,35</sup> Further investigations comparing T1-PWI with CT perfusion studies may yield data with higher reliability regarding its technical performance in postoperative cases.

The dynamic contrast-enhancement permeability analysis based on the extended Tofts model has also provided useful information in patients with gliomas. A meta-analysis by Liang et al<sup>36</sup> demonstrated that volume transfer constant ( $k^{trans}$ ) and volume of extravascular extracellular space ( $V_e$ ) were reliable parameters for glioma grading, while some studies also suggested the usefulness of  $k^{trans}$  and volume of blood plasma ( $V_p$ ) in the differentiation of recurrence from treatment changes.<sup>6,37</sup> With the high temporal resolution protocol suggested in our study, both traditional permeability



imaging and the T1-PWI-derived rCBV map can be acquired in a single scan, thereby allowing simultaneous analysis of permeability and hemodynamic properties of the tumor.

Our study has several limitations. This study was conducted retrospectively with a relatively small number of patients. The non-randomized patient assignment may have caused selection bias. Second, nordicICE enabled normalization of rCBV via automated WM segmentation without allowing manual selection of normal WM. Because the released perfusion analysis tool was optimized to T2\*-weighted source images, WM masks produced by T1-PWI source images were suboptimal in some patients and carried a risk of error in the rCBV calculation. Additionally, Sahoo et al<sup>21</sup> reported a slightly lower diagnostic accuracy of T1-rCBV calculated by the automated method compared with manual selection by the expert. Further software optimization is needed to provide appropriate CBV normalization.

Another technical limitation was the presence of aliasing artifacts with the use of parallel imaging in some source images of T1-PWI, caused by bright subcutaneous fat, which can be diminished by fat suppression or the low in-plane sensitivity encoding factor but requires a longer acquisition time. Parameter optimization regarding the trade-off of spatial and temporal resolution is important and may be further compensated for by using advanced artifact-free acceleration techniques in the future.

## CONCLUSIONS

Relative CBV acquired from T1-based perfusion MR imaging with high temporal resolution showed a fine clinical performance in patients with postoperative high-grade gliomas, suggesting its potential role as a valid alternative to the traditional T2\*-PWI. The relative clinical usefulness of T1-PWI compared with T2\*-PWI might be more pronounced in examinations with SSE. Technically, T1- and T2\*-PWI were fairly consistent in terms of calculated rCBV values. The prevalence of signal loss was significantly higher in T2\*-PWI than in T1-PWI, which might have affected the consistency between the 2 methods. We suggest further validation of the T1-PWI in future studies for widespread application in susceptibility-prone situations.

**Disclosure forms** provided by the authors are available with the full text and PDF of this article at [www.ajnr.org](http://www.ajnr.org).

## REFERENCES

1. Cha S, Johnson G, Wadghiri YZ, et al. **Dynamic, contrast-enhanced perfusion MRI in mouse gliomas: correlation with histopathology.** *Magn Reson Med* 2003;49:848–55 CrossRef Medline
2. Provenzale JM, Mukundan S, Barboriak DP. **Diffusion-weighted and perfusion MR imaging for brain tumor characterization and assessment of treatment response.** *Radiology* 2006;239:632–49 CrossRef Medline
3. Aronen HJ, Gazit IE, Louis DN, et al. **Cerebral blood volume maps of gliomas: comparison with tumor grade and histologic findings.** *Radiology* 1994;191:41–51 CrossRef Medline
4. Law M, Yang S, Babb JS, et al. **Comparison of cerebral blood volume and vascular permeability from dynamic susceptibility contrast-enhanced perfusion MR imaging with glioma grade.** *AJNR Am J Neuroradiol* 2004;25:746–55 Medline
5. Young RJ, Gupta A, Shah AD, et al. **MRI perfusion in determining pseudoprogression in patients with glioblastoma.** *Clin Imaging* 2013;37:41–49 CrossRef Medline
6. Shin KE, Ahn KJ, Choi HS, et al. **DCE and DSC MR perfusion imaging in the differentiation of recurrent tumour from treatment-related changes in patients with glioma.** *Clin Radiol* 2014;69:e264–72 CrossRef Medline
7. Prager AJ, Martinez N, Beal K, et al. **Diffusion and perfusion MRI to differentiate treatment-related changes including pseudoprogression from recurrent tumors in high-grade gliomas with histopathologic evidence.** *AJNR Am J Neuroradiol* 2015;36:877–85 CrossRef Medline
8. Wan B, Wang S, Tu M, et al. **The diagnostic performance of perfusion MRI for differentiating glioma recurrence from pseudoprogression: a meta-analysis.** *Medicine (Baltimore)*. 2017;96:e6333 CrossRef Medline
9. Law M, Young RJ, Babb JS, et al. **Gliomas: Predicting time to progression or survival with cerebral blood volume measurements at dynamic susceptibility-weighted contrast-enhanced perfusion MR imaging.** *Radiology* 2008;247:490–98 CrossRef Medline
10. Jahng GH, Li KL, Ostergaard L, et al. **Perfusion magnetic resonance imaging: a comprehensive update on principles and techniques.** *Korean J Radiol* 2014;15:554–77 CrossRef Medline
11. Heo YJ, Kim HS, Park JE, et al. **Uninterpretable dynamic susceptibility contrast-enhanced perfusion MR images in patients with post-treatment glioblastomas: cross-validation of alternative imaging options.** *PLoS One* 2015;10:e0136380 CrossRef Medline
12. Hu LS, Baxter LC, Smith KA, et al. **Relative cerebral blood volume values to differentiate high-grade glioma recurrence from post-treatment radiation effect: direct correlation between image-guided tissue histopathology and localized dynamic susceptibility-weighted contrast-enhanced perfusion.** *AJNR Am J Neuroradiol* 2009;30:552–58 CrossRef Medline
13. Saini J, Gupta RK, Kumar M, et al. **Comparative evaluation of cerebral gliomas using rCBV measurements during sequential acquisition of T1-perfusion and T2-perfusion MRI.** *PLoS One* 2019;14:e0215400 CrossRef Medline
14. Dean BL, Lee C, Kirsch JE, et al. **Cerebral hemodynamics and cerebral blood volume: MR assessment using gadolinium contrast agents and T1-weighted turbo-FLASH imaging.** *AJNR Am J Neuroradiol* 1992;13:39–48 Medline
15. Hackländer T, Reichenbach JR, Hofer M, et al. **Measurement of cerebral blood volume via the relaxing effect of low-dose gadopentetate dimeglumine during bolus transit.** *AJNR Am J Neuroradiol* 1996;17:821–30 Medline
16. Sourbron S, Ingrisch M, Siefert A, et al. **Quantification of cerebral blood flow, cerebral blood volume, and blood-brain-barrier leakage with DCE-MRI.** *Magn Reson Med* 2009;62:205–17 CrossRef Medline
17. Larsen VA, Simonsen HJ, Law I, et al. **Evaluation of dynamic contrast-enhanced T1-weighted perfusion MRI in the differentiation of tumor recurrence from radiation necrosis.** *Neuroradiology* 2013;55:361–69 CrossRef Medline
18. Roy B, Gupta RK, Maudsley AA, et al. **Utility of multiparametric 3-T MRI for glioma characterization.** *Neuroradiology* 2013;55:603–13 CrossRef Medline
19. Falk A, Fahlström M, Rostrup E, et al. **Discrimination between glioma grades II and III in suspected low-grade gliomas using dynamic contrast-enhanced and dynamic susceptibility contrast perfusion MR imaging: a histogram analysis approach.** *Neuroradiology* 2014;56:1031–38 CrossRef Medline
20. Gupta PK, Saini J, Sahoo P, et al. **Role of dynamic contrast-enhanced perfusion magnetic resonance imaging in grading of pediatric brain tumors on 3T.** *Pediatr Neurosurg* 2017;52:298–305 CrossRef Medline
21. Sahoo P, Gupta RK, Gupta PK, et al. **Diagnostic accuracy of automatic normalization of CBV in glioma grading using T1-weighted DCE-MRI.** *Magn Reson Imaging* 2017;44:32–37 CrossRef Medline
22. Sengupta A, Ramanikhan AK, Gupta RK, et al. **Glioma grading using a machine-learning framework based on optimized features obtained from T1 perfusion MRI and volumes of tumor components.** *J Magn Reson Imaging* 2019;50:1295–306 CrossRef Medline

23. Conte GM, Castellano A, Altabella L, et al. **Reproducibility of dynamic contrast-enhanced MRI and dynamic susceptibility contrast MRI in the study of brain gliomas: a comparison of data obtained using different commercial software.** *Radiol Med* 2017;122:294–302 CrossRef Medline
24. Conte GM, Altabella L, Castellano A, et al. **Comparison of T1 mapping and fixed T1 method for dynamic contrast-enhanced MRI perfusion in brain gliomas.** *Eur Radiol* 2019;29:3467–79 CrossRef Medline
25. Tietze A, Mouridsen K, Mikkelsen IK. **The impact of reliable prebolus T1 measurements or a fixed T1 value in the assessment of glioma patients with dynamic contrast enhancing MRI.** *Neuroradiology* 2015;57:561–72 CrossRef Medline
26. Koo TK, Li MY. **A guideline of selecting and reporting intraclass correlation coefficients for reliability research.** *J Chiropr Med* 2016;15:155–63 CrossRef Medline
27. Gahramanov S, Muldoon LL, Varallyay CG, et al. **Pseudoprogression of glioblastoma after chemo- and radiation therapy: diagnosis by using dynamic susceptibility-weighted contrast-enhanced perfusion MR imaging with ferumoxylol versus gadoteridol and correlation with survival.** *Radiology* 2013;266:842–52 CrossRef Medline
28. Álvarez-Torres M del M, Fuster-García E, Juan-Albarracín J, et al. **Local detection of microvessels in IDH-wildtype glioblastoma using relative cerebral blood volume: an imaging marker useful for astrocytoma grade 4 classification.** *BMC Cancer* 2022;22:40 CrossRef Medline
29. Wang K, Li Y, Cheng H, et al. **Perfusion CT detects alterations in local cerebral flow of glioma related to IDH, MGMT and TERT status.** *BMC Neurol* 2021;21:460 CrossRef Medline
30. Mangla R, Singh G, Ziegelitz D, et al. **Changes in relative cerebral blood volume 1 month after radiation-temozolomide therapy can help predict overall survival in patients with glioblastoma.** *Radiology* 2010;256:575–84 CrossRef Medline
31. Nguyen TB, Cron GO, Perdrizet K, et al. **Comparison of the diagnostic accuracy of DSC- and dynamic contrast-enhanced MRI in the preoperative grading of astrocytomas.** *AJNR Am J Neuroradiol* 2015;36:2017–22 CrossRef Medline
32. Paprottka KJ, Kleiner S, Preibisch C, et al. **Fully automated analysis combining [18F]-FET-PET and multiparametric MRI including DSC perfusion and APTw imaging: a promising tool for objective evaluation of glioma progression.** *Eur J Nucl Med Mol Imaging* 2021;48:4445–55 CrossRef Medline
33. Steidl E, Langen KJ, Hmeidani SA, et al. **Sequential implementation of DSC-MR perfusion and dynamic [18F]FET PET allows efficient differentiation of glioma progression from treatment-related changes.** *Eur J Nucl Med Mol Imaging* 2021;48:1956–65 CrossRef Medline
34. Choi YJ, Kim HS, Jahng GH, et al. **Pseudoprogression in patients with glioblastoma: Added value of arterial spin labeling to dynamic susceptibility contrast perfusion MR imaging.** *Acta Radiol* 2013;54:448–54 CrossRef Medline
35. Park YW, Ahn SS, Kim EH, et al. **Differentiation of recurrent diffuse glioma from treatment-induced change using amide proton transfer imaging: incremental value to diffusion and perfusion parameters.** *Neuroradiology* 2021;63:363–72 CrossRef Medline
36. Liang J, Liu D, Gao P, et al. **Diagnostic values of DCE-MRI and DSC-MRI for differentiation between high-grade and low-grade gliomas: a comprehensive meta-analysis.** *Acad Radiol* 2018;25:338–48 CrossRef Medline
37. Thomas AA, Arevalo-Perez J, Kaley T, et al. **Dynamic contrast enhanced T1 MRI perfusion differentiates pseudoprogression from recurrent glioblastoma.** *J Neurooncol* 2015;125:183–90 CrossRef Medline

# Nonlesional Sources of Contrast Enhancement on Postgadolinium “Black-Blood” 3D T1-SPACE Images in Patients with Multiple Sclerosis

 L. Danieli,  L. Roccatagliata,  D. Distefano,  E. Prodi,  G.C. Riccitelli,  A. Diociani,  L. Carmisciano,  A. Cianfoni,  T. Bartalena,  A. Kaelin-Lang,  C. Gobbi,  C. Zecca, and  E. Pravata



## ABSTRACT

**BACKGROUND AND PURPOSE:** We hypothesized that 3D T1-TSE “black-blood” images may carry an increased risk of contrast-enhancing lesion misdiagnosis in patients with MS because of the misinterpretation of intraparenchymal vein enhancement. Thus, the occurrence of true-positive and false-positive findings was compared between standard MPRAGE and volumetric interpolated brain examination techniques.

**MATERIALS AND METHODS:** Sampling perfection with application-optimized contrasts by using different flip-angle evolution (SPACE) images obtained from 232 patients with MS, clinically isolated syndrome, or radiologically isolated syndrome were compared with standard MPRAGE and volumetric interpolated brain examination images. The intraparenchymal vein contrast-to-noise ratio was estimated at the level of the thalami. Contrast-enhancing lesions were blindly detected by 2 expert readers and 1 beginner reader. True- and false-positives were determined by senior readers’ consensus. True-positive and false-positive frequency differences and patient-level diagnosis probability were tested with the McNemar test and OR. The contrast-to-noise ratio and morphology were compared using the Mann-Whitney *U* and  $\chi^2$  tests.

**RESULTS:** The intraparenchymal vein contrast-to-noise ratio was higher in SPACE than in MPRAGE and volumetric interpolated brain examination images ( $P < .001$ , both). There were 66 true-positives and 74 false-positives overall. SPACE detected more true-positive and false-positive results ( $P$  range  $< .001$ – $.07$ ) but did not increase the patient’s true-positive likelihood (OR = 1.129,  $P = .478$ – $1$ ). However, the false-positive likelihood was increased (OR = 3.03–3.55,  $P = .008$ – $.027$ ). Venous-origin false-positives ( $n = 59$ ) with contrast-to-noise ratio and morphology features similar to small-sized ( $\leq 14 \text{ mm}^3$ ,  $P = .544$ ) true-positives occurred more frequently in SPACE images ( $P < .001$ ).

**CONCLUSIONS:** Small intraparenchymal veins may confound the diagnosis of enhancing lesions on postgadolinium black-blood SPACE images.

**ABBREVIATIONS:** BR = beginner reader; CEL = contrast-enhancing lesion; CNR = contrast-to-noise ratio; ER = experienced reader; FP = false positive; iV = intraparenchymal vein; Lw-FDR = lesion-wise false discovery rate; SPACE = sampling perfection with application-optimized contrasts by using different flip-angle evolution; TP = true positive; vFP = venous-origin FP; VIBE = volumetric interpolated brain examination

**M**S is a chronic inflammatory, degenerative disease of the central nervous system typically affecting young people

Received August 21, 2021; accepted after revision April 8, 2022.

From the Departments of Neuroradiology (L.D., D.D., E. Prodi, A.C., E. Pravata) and Neurology (G.C.R., A.K.-L., C.G., C.Z.), Neurocenter of Southern Switzerland, Ente Ospedaliero Cantonale, Lugano, Switzerland; Dipartimento di Scienze della Salute (L.R., A.D.) and Department of Health Sciences, Section of Biostatistics (L.C.), Università degli Studi di Genova, Genoa, Italy; Faculty of Biomedical Sciences (G.C.R., A.C., A.K.-L., C.G., C.Z., E. Pravata), Università della Svizzera Italiana, Lugano, Switzerland; Department of Neuroradiology (A.C.), Inselspital of Bern, University of Bern, Bern, Switzerland; and Department of Radiology (T.B.), Poliambulatorio Zappi Bartalena, Imola, Italy.

C. Zecca and E. Pravata contributed equally to this work.

This study received a grant from the Advisory Board of Research of Ente Ospedaliero Cantonale, Bellinzona, Switzerland.

Please address correspondence to Emanuele Pravata, MD, Neurocenter of Southern Switzerland, Neuroradiology, EOC, Via Tesserete 46, 6900, Lugano, Switzerland; e-mail: emanuele.pravata@eoc.ch

 Indicates article with online supplemental data.

<http://dx.doi.org/10.3174/ajnr.A7529>

and often impairing their quality of life.<sup>1</sup> To balance the efficacy and adverse event risk, pharmacologic treatment should be tailored according to disease activity.<sup>2</sup> Evidence of disease activity on MR imaging may prompt treatment re-challenge because new lesions are linked to an increased risk of a future relapse.<sup>3</sup> Crucially, it was shown that the occurrence of just 1 contrast-enhancing lesion (CEL) carries an increased risk of relapse and subsequent disability.<sup>4–6</sup>

Previous studies demonstrated that 3D T1-weighted TSE images provide superior sensitivity to enhancing MS lesions (CELs) in the brain and minimize vessel enhancement confounders due to the 3D-TSE “black-blood” characteristics related to the intravoxel spin-dephasing mechanism.<sup>7–9</sup> Furthermore, 3D-TSE T1 yielded significantly improved conspicuity in the evaluation of brain metastases<sup>10</sup> and meningeal abnormalities.<sup>11</sup> However, cases of CEL misdiagnosis linked to misinterpretation of the enhancement of normal intraparenchymal veins (iVs) were also reported



with this technique.<sup>8,12</sup> Indeed, experience from routine clinical imaging shows that signal from slow-flowing blood may not be suppressed on 3D-T1-TSE images and enhancing iVs may be found within T2-visible lesions (Online Supplemental Data). Recent studies indicate that developmental venous anomalies, representing relatively common sources of intraparenchymal venous enhancement,<sup>13</sup> may be more frequently visualized in patients with MS.<sup>14</sup> iVs and CEL can be as small as a few voxels.<sup>15,16</sup> Thus, they represent a risk for misdiagnosis in the clinical imaging routine and are an acknowledged challenge for automated CEL detection tools.<sup>15-19</sup>

Our working hypothesis was that 3D-T1-TSE black-blood images may carry an increased risk of CEL misdiagnosis because of misinterpretation of iVs. Thus, the occurrence of true-positive (TP) and false-positive (FP) findings was compared between the 3D-T1-TSE black-blood and the MPRAGE and volumetric interpolated brain examination (VIBE) standard techniques. Information about the size, enhancement, and morphologic features of both TPs and FPs was extracted.

## MATERIALS AND METHODS

### Participants

This study was approved by the Ethics Committee of Canton Ticino. Written informed consent was obtained from all participants. Between April 2015 and May 2017, we enrolled 246 consecutive adult patients undergoing brain MR imaging at the Ospedale Regionale di Lugano (Lugano, Switzerland) for MS, clinically isolated syndrome,<sup>20</sup> or radiologically isolated syndrome.<sup>21</sup> Patients' neurologic statuses (according to the Expanded Disability Status Scale), attacks, disease duration, and disease-modifying treatments were assessed within 4 weeks of MR imaging. Exclusion criteria were the following: other known inflammatory and/or neoplastic diseases potentially causing CEL occurrence; impossibility of receiving paramagnetic contrast agent due to allergy and/or the patient's refusal; pregnancy; and incomplete MR imaging examination.

### Data Acquisition

Participants were examined using three 3T Magnetom Skyra (Siemens) scanners with the same 20-channel head coil model and software version. An optimized protocol aimed at minimizing potential biases from the different sequence geometry parameters, scan duration, and time gap between the first and last acquired image after contrast injection was used (Online Supplemental Data).<sup>22</sup> The sampling perfection with application-optimized contrasts by using different flip-angle evolution (SPACE) is a 3D-TSE T1-weighted MR imaging technique providing vessel signal suppression (black-blood) characteristics related to the intravoxel dephasing mechanism.<sup>7</sup> The MPRAGE and VIBE are 3D fast gradient-echo T1-weighted commonly used MR imaging sequences without blood-signal-suppression image characteristics. One-millimeter SPACE, MPRAGE, and VIBE sequences were consecutively performed in a randomized order, the first scan being started 5 minutes after contrast injection of a constant dose of 0.1 mL/Kg of gadobutrol. Sagittal 1-mm 3D FLAIR and axial 3-mm dual-echo (T2/proton-density weighted) images were acquired before contrast administration and used during the reference consensus

determination (see below) to colocalize T2-visible lesions. All patients received at least 1 follow-up MR imaging examination, including, in doubtful cases, additional SWI to help distinguish venous-enhancement sources.<sup>23</sup>

### Image Analysis

**Image Quality.** Image degradation due to artifacts was rated by an experienced neuroradiologist (E. Pravata, with 15 years of experience) using a previously used 3-point scale:<sup>12,24</sup> 0 = no relevant artifacts; 1 = mild artifacts not preventing analysis; 2 = artifacts preventing analysis. Cases with grade 2 artifacts were excluded from analysis.

**Vein Quantitative Conspicuity.** To obtain reproducible estimations of the conspicuity of iV enhancement, we calculated the contrast-to-noise ratio (CNR) at the level of the superior thalamic iV in all patients according to the procedure described in the Online Supplemental Data.

**Reference Consensus.** TPs were determined by 2 senior readers, 1 neuroradiologist (E. Pravata), and 1 neurologist (C.G., with 20 years of experience in MS neuroimaging), both having all examination sequences available, including multiplanar and MIP reconstructions of postgadolinium images, as well as follow-up examinations. As previously proposed,<sup>16</sup> a CEL was defined as contrast-enhancement area of at least 3 contiguous voxels showing typical T2, proton-density, and/or T2-FLAIR hyperintensity.<sup>25</sup> Absence of proton-density/T2-FLAIR signal hyperintensity, persistent (>3 months) enhancement on follow-up,<sup>26</sup> spontaneous unenhanced T1-weighted hyperintensity, and/or "atypical" enhancement patterns<sup>25</sup> were considered as unrelated findings of MS disease. CEL morphology was classified as nodular, tubular, and ring/open-ring. Images were reviewed on a PACS PC workstation running syngo via (Siemens).

**Blind CEL Detection.** Two different experienced readers (ER 1 and ER 2) (E. Prodi and D.D., with 11 and 9 years of experience, respectively), and 1 beginner reader (BR) (A.D., with 1 year of experience) reviewed independently all SPACE, MPRAGE, and VIBE images. They were asked to mark CELs according to the above-specified 3-voxel size criterion. Images were presented in a randomized order using the same PC setting described above.

**FP Determination and Classification.** In a separate session, the 2 senior readers again reviewed all images including follow-up examinations and determined the FP findings under consensus according to the readers' blinded annotations. Morphology was categorized using the same TP classification. FP location was assessed as periventricular, corticojuxtacortical, or infratentorial according to the Magnetic Resonance Imaging in Multiple Sclerosis consensus guidelines.<sup>9,27</sup> Each FP was assigned to 1 of the following categories: venous (vFP, including intraparenchymal vein, developmental venous anomalies, capillary angioma); spontaneous T1-hyperintensity (spontaneously hyperintense FP, including cavernous malformation, bleeding, paramagnetic material); and other/undetermined FP. Finally, CNR and volume values were estimated (L.D.) applying the procedure for iVs.

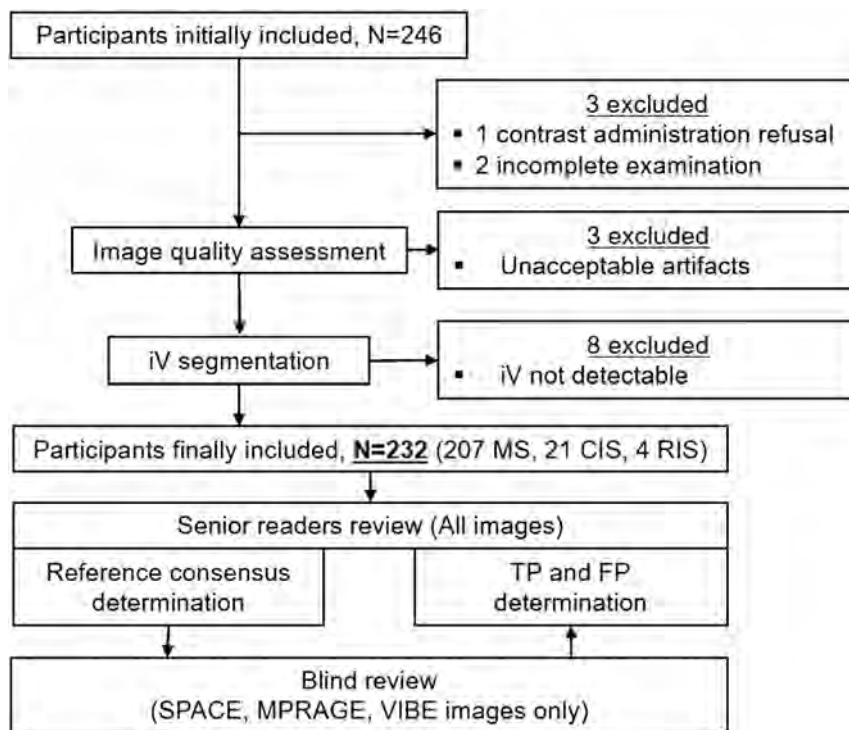


**FIG 1.** Flow chart shows the included and excluded participants and the TP and FP determination procedure including blinded readers' and senior readers' image review. CIS indicates clinically isolated syndrome; RIS, radiologically isolated syndrome.

### Statistical Analysis

Sequence-acquisition order and TP and FP spatial distribution and morphology differences were tested using the  $\chi^2$  test. The Wilcoxon signed-rank test was used to compare image-quality grading. Interrater agreement was reported with the Cohen  $\kappa$ , with values between 0.21 and 0.4 interpreted as fair; 0.41–0.6, as moderate; 0.61–0.8, as good; and 0.81–1.00, as excellent agreement. TP/FP frequency differences between sequences and readers were assessed using the McNemar test. The lesion-wise false discovery rate (Lw-FDR) was calculated adapting a previously proposed approach:<sup>17</sup>  $Lw-FDR_{sequence} = FP_{sequence} / (TP_{sequence} + FP_{sequence})$ .

To assess the effect of volume on CNR differences, we categorized vFP and TP into small ( $\leq 14 \text{ mm}^3$ ) and large ( $> 14 \text{ mm}^3$ ) by performing a median split of their volume value distribution. Differences in the frequency of morphology types, volume, and CNR, were assessed with Pearson  $\chi^2$  and Mann-Whitney  $U$  tests, respectively.

By using a logistic regression model, we estimated the likelihood of the sequence to produce FPs compared with the others using ORs and their 95% confidence intervals as effect measures. The same approach was used separately for TPs. CNR and volume differences were assessed using the Mann-Whitney  $U$  test as appropriate based on data distribution. Correlations between CNR and volume were tested using the Spearman  $\rho$ . We applied the Bonferroni method to account for multiple comparisons whenever a single hypothesis was tested multiple times due to subgroup analyses, specifically when

comparing each rater's heterogeneity in the TP or FP rate among SPACE, MPRAGE, and VIBE sequences, expressed as head-to-head comparisons, and assessing the association between the TP or FP rate and image characteristics among patients, grouped according to vFP and TP volume (higher or lower than the sample median).  $P$  values  $< .05$  were considered significant. SPSS software, Version 20.0.0 (IBM) was used for analyses.

### RESULTS

Images of 3 patients were excluded from analysis, one because of incomplete scan examination (1 scan was interrupted by the patient, 1 scan was interrupted due to patient's motion shortly after initiation) and one due to contrast refusal (Fig 1). Image quality was acceptable (grade 0 or 1 artifacts) in 99.6% (SPACE), 99.2% (MPRAGE), and 98.7% (VIBE) of cases. The overall artifact grading was comparable between SPACE and MPRAGE ( $P = .705$ ) scans, but worse in VIBE ( $P = .022$ ) compared with the SPACE scan because of a higher frequency of grade 1

artifacts (29.7% versus 8.5%, respectively). Unacceptable artifacts (grade 2) were found in scans of 3 patients (VIBE: 3 patients, MPRAGE: 2 patients; SPACE: 2 patients), and they were excluded. iVs could be identified and segmented in at least 1 sequence and 1 hemisphere in 232 (96.7%) patients; the remaining 8 were excluded from further analysis (Fig 1).

Demographics, clinical characteristics, and disease-modifying treatments of the evaluable patients are listed in Table 1. Proportions of patients on moderate, high, and very high disease-modifying treatment<sup>28</sup> were 60.9%, 4.3%, and 17.4% respectively, while 17.4% were untreated.

Sequence-acquisition order after contrast administration was not significantly different among the sequences ( $P = .454$ ). The mean iV CNR differed significantly among sequences ( $P < .001$ ), being higher for SPACE (4.49 [SD, 1.61]) compared with MPRAGE (2.11 [SD, 1.09],  $P < .001$ ) and VIBE (2.28 [SD, 0.99],  $P < .001$ ).

### TP Enhancement Sources

Senior readers identified 66 CELs in 21 (9.1%) of the 232 patients. Of these, 38 (57.6%) were periventricular; 21 (31.8%), corticojuxtacortical; and 7 (10.6%), infratentorial.

The results of the readers' blinded review are reported in Table 2. The agreement between the 2 ERs was good ( $\kappa = 0.67$ , 0.72, and 0.78 for SPACE, MPRAGE, and VIBE, respectively). TPs occurred more frequently with SPACE acquisitions, except for ER 1 with MPRAGE, but this difference did not reach statistical significance ( $P = .070$ ). The BR's reading performance for all sequences ( $P$  range .008–.039) was poorer than that of the ERs,

**Table 1: Included patients' main demographics, clinical characteristics, and DMT**

Demographics	
No. of evaluable patients	232
Relapsing-emitting MS	177 (76.3%)
Secondary-progressive MS	20 (8.6%)
Primary-progressive MS	10 (4.3%)
CIS (%)	21 (9.1%)
RIS (%)	4 (1.7%)
Age (mean) (yr)	46 (SD, 12.65)
Sex (men/women)	81:151
EDSS <sup>a</sup> (median) (interquartile range)	2.5/2
Disease duration <sup>a</sup> (median) (interquartile range)	11/11
DMT efficacy <sup>b</sup>	
Moderate <sup>c</sup>	126 (60.9%)
High <sup>d</sup>	9 (4.3%)
Very high <sup>e</sup>	36 (17.4%)
No DMT	36 (17.4%)

**Note:**—CIS indicates clinically isolated syndrome; RIS, radiologically isolated syndrome; EDSS, Expanded Disability Status Scale; DMT, disease-modifying treatment.

<sup>a</sup> Patients with relapsing-remitting, secondary-progressive, or primary-progressive MS only.

<sup>b</sup> According to Dobson et al.<sup>28</sup>

<sup>c</sup> Includes dimethyl fumarate, glatiramer acetate, interferon- $\beta$  1- $\alpha$ , interferon- $\beta$ -1b, and teriflunomide.

<sup>d</sup> Includes fingolimod, siponimod, and ozanimod.

<sup>e</sup> Includes alemtuzumab, cladribine, mitoxantrone, natalizumab, and ocrelizumab.

**Table 2: Frequency of TP and FP sources of enhancement for each SPACE, MPRAGE, VIBE sequence, and blind readers**

	SPACE	MPRAGE	VIBE	P <sup>a</sup> (SPACE vs MPRAGE)	P <sup>a</sup> (SPACE vs VIBE)
TP enhancement sources (No. of patients)					
ER 1	50 (19)	44 (16)	42 (15)	.070	.042 <sup>b</sup>
ER 2	53 (15)	42 (15)	41 (15)	.026 <sup>b</sup>	.008 <sup>b</sup>
BR	42 (14)	34 (13)	36 (12)	.006 <sup>b</sup>	.016 <sup>b</sup>
FP enhancement sources (No. of patients)					
ER 1	22 (20)	8 (6)	8 (7)	.004 <sup>b</sup>	.008 <sup>b</sup>
ER 2	24 (23)	7 (7)	9 (8)	.004 <sup>b</sup>	.006 <sup>b</sup>
BR	31 (28)	6 (6)	11 (11)	<.001 <sup>b</sup>	.006 <sup>b</sup>

<sup>a</sup> McNemar test.

<sup>b</sup> Statistically significant results.

suggesting an effect of the reader's experience on CEL-detection sensitivity. Furthermore, similar to the ERs, the BR was able to detect significantly more TPs in scans acquired with SPACE compared with MPRAGE and VIBE ( $P$  range = .008–.016).

### FP Enhancement Sources

Considering all readers' blinded reviews and sequences, 126 FPs were reported on SPACE, VIBE, and MPRAGE images of 46 patients. Of these, 52 FPs were recorded as the same findings by  $\geq 2$  readers, leading to 74 univocal FP findings in all sequences. FP spatial distribution differed compared with TP, being relatively more frequent in the infratentorial (41.8%) and less frequent in the periventricular (26.2%) compartment ( $P$  = .048). Both ERs misdiagnosed FP more frequently in SPACE (Lw-FDR = 0.31 for both) than in MPRAGE (Lw-FDR = 0.15 and 0.14), and VIBE (Lw-FDR = 0.16 and 0.18) ( $P$  range = .004–.008) (Table 2). Contrary to TP detection, the BR's performance was not significantly different from that of the ERs for all sequences ( $P$  range =

.15–1), suggesting no advantage of the reader's experience to discriminate FP. However, similar to the ERs, the BR reported significantly more FPs on SPACE (Lw-FDR = 0.42) than MPRAGE (Lw-FDR = 0.16,  $P$  < .001) and VIBE (Lw-FDR = 0.27,  $P$  = .006) scans.

### Patient-Level Diagnostic Accuracy

The average diagnostic sensitivity was 76% for SPACE (specifically 90% for ER 1, 71% for ER 2, and 67% for the BR), 67% for MPRAGE (specifically 76% for ER 1, 71% for ER 2, and 62% for the BR), and 66% for VIBE (specifically 71% for ER 1, 71% for ER 2, and 57% for the BR); while specificity was 89% for SPACE (specifically 91% for ER 1, 89% for ER 2, and 87% for the BR), 97% for MPRAGE (specifically 97% for ER 1, 97% for ER 2, and 97% for the BR), and 96% for VIBE (specifically 97% for ER 1, 96% for ER 2, and 95% for the BR). The Online Supplemental Data present the summary confusion matrix for each sequence and all raters averaged.

The patient's likelihood of being diagnosed with at least 1 CEL was moderately, but not statistically, significantly higher when using the SPACE rather than MPRAGE (OR = 1.2 and 1, respectively) or VIBE (OR = 1.29 and 1, respectively) ( $P$  range = .478–1) techniques. However, the FP misdiagnosis likelihood was significantly higher for the SPACE technique than for MPRAGE (OR = 3.55 and 3.53,

respectively) and VIBE (OR = 3.03 and 3.08, respectively) ( $P$  range = .008–.015). Similar results were obtained by the BR (Table 3).

### FP Categories

Of the 74 univocal FPs, most were vFPs ( $n$  = 59, 79.7%) and only 8 (10.8%) were spontaneously hyperintense FPs and 7 (9.5%) were other/undetermined FPs. Significantly more vFPs were encountered on SPACE ( $n$  = 38, 64.4% of cases) compared with VIBE ( $n$  = 10, 16.9%) and MPRAGE ( $n$  = 11, 18.6%) ( $P$  < .001, both). Exemplary cases of vFP are given in Figs 2 and 3 and in the Online Supplemental Data, and cases of spontaneously hyperintense FPs and other/undetermined FPs are presented in the Online Supplemental Data.

### vFP Features on SPACE Images

Table 4 illustrates the contrast-enhancement volume, CNR, and morphology features of vFP compared with TP. Overall, vFPs were smaller ( $P$  = .027) and had lower CNR values ( $P$  = .003) than TPs



**Table 3: Patient-wise diagnostic accuracy results by OR analysis<sup>a</sup>**

	SPACE vs MPRAGE	SPACE vs VIBE	P (SPACE vs MPRAGE)	P (SPACE vs VIBE)
Chance of detecting more patients with TP				
ER 1	1.20 (0.6–2.4)	1.29 (0.6–2.6)	.598	.478
ER 2	1.00 (0.48–2.09)	1.00 (0.48–2.09)	1.000	1.000
BR	1.08 (0.5–2.4)	1.18 (0.53–2.6)	.686	.687
Chance of detecting more patients with FP				
ER 1	3.55 (1.4–9.1)	3.03 (1.25–7.3)	.015 <sup>b</sup>	.027 <sup>b</sup>
ER 2	3.53 (1.5–8.4)	3.08 (1.3–7.1)	.008 <sup>b</sup>	.015 <sup>b</sup>
BR	5.17 (2.1–12.7)	2.76 (1.3–5.7)	<.001 <sup>b</sup>	.012 <sup>b</sup>

<sup>a</sup> OR and 95% CI are provided for SPACE versus MPRAGE and SPACE versus VIBE comparisons and for each reader.

<sup>b</sup> Statistically significant results.

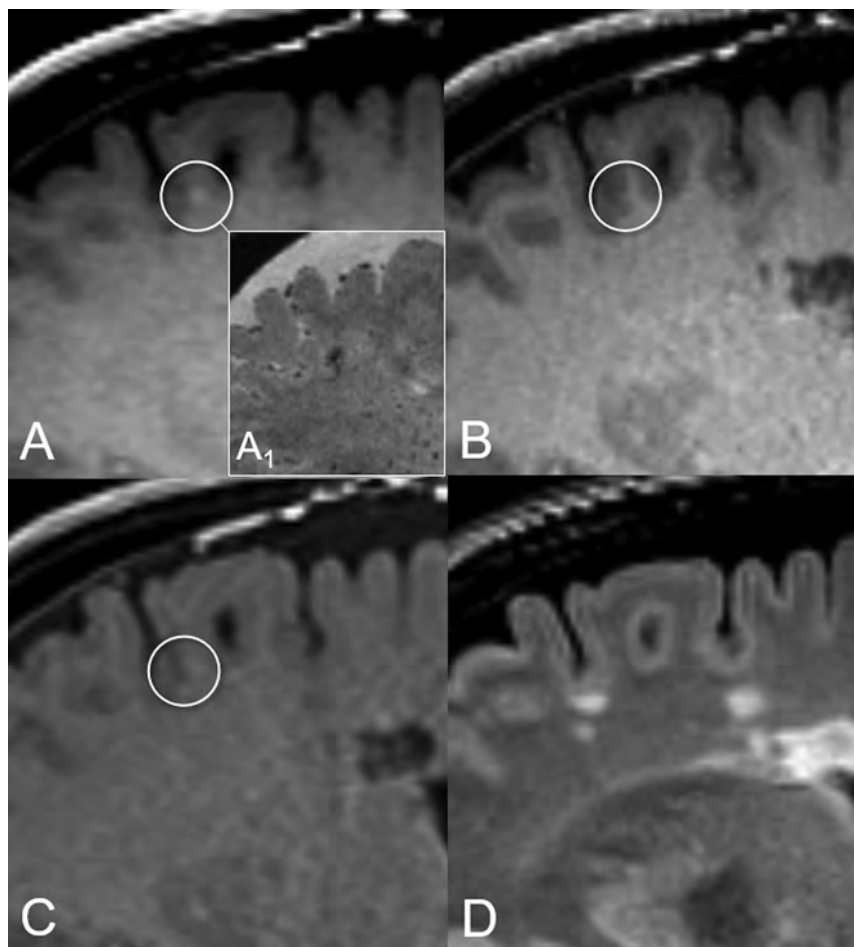


**FIG 2.** Illustrative case of nodular vFP enhancement. A tiny juxtacortical enhancement source on SPACE (circle in A), corresponding to a triangle-shaped hypointensity on the high-resolution susceptibility-weighted image (A1), is not detected on MPRAGE and VIBE images (circles in B and C, respectively). The corresponding FLAIR T2-weighted image (D) shows no evidence of demyelinating lesions at this level. This vFP was reported by ER 1 and the BR.

(Table 4). Higher CNR values were associated with larger volumes in TPs ( $\rho = 0.644$ ,  $P < .001$ ), but not in vFPs ( $\rho = 0.096$ ,  $P = .568$ ) (Fig 4).

While the CNR was significantly lower in vFP<sub>large</sub> than in TP<sub>large</sub> ( $P = .01$ ), it was similar between vFP<sub>small</sub> and TP<sub>small</sub> ( $P = .544$ ) (Fig 4).

The most frequent morphology was the “nodular” in both vFPs (68.4%) and TPs (78.8%). The “ring/open ring” presentation was found in 28.1% and 21.2%, and the “tubular,” in 10.5% and 0% of vFPs and TPs, respectively. Morphology category distribution was

significantly different between vFP<sub>large</sub> and TP<sub>large</sub> only ( $P = .036$ ), with less frequent nodular and more frequent ring/open ring presentations found in vFP<sub>large</sub>.

## DISCUSSION

This study corroborates previous evidence from the literature demonstrating the superiority of black-blood 3D-T1-TSE with respect to standard 3D T1 gradient recalled-echo images in the detection of enhancing MS lesions.<sup>8,9</sup> This finding is in line with the results obtained with enhancing brain tumors.<sup>22,29,30</sup> SPACE is a 3D-T1-TSE MR imaging technique providing inherent black-blood characteristics related to the intravoxel dephasing mechanism, resulting in suppression of confounding high signal coming from high-flow and relatively larger vessels.<sup>7</sup> Despite such characteristics, we show that in fact, small iVs may not be suppressed when using the 3D-T1-TSE SPACE technique, potentially mimicking CEL and leading to misdiagnosis of active inflammation. These findings are particularly relevant for both radiologists and neurologists involved in MS imaging and additionally for the design of automated CEL-detection software tools. Indeed, the classification of enhancement sources into a lesional or nonlesional origin relies on the colocalization of a typical hyperintensity on the corresponding T2, proton-density, and/or

T2 FLAIR-weighted sequences. Whereas contrast enhancement in active demyelinating lesions is caused by the development of blood-brain barrier permeability, which follows the pathophysiologic MS-related inflammation cascade,<sup>31</sup> venous enhancement derives from shortening of the blood T1-relaxation time after gadolinium injection. Because iVs may sit within a T2-visible lesion (Online Supplemental Data), these might mimic active and/or re-activating inflammation. It was previously acknowledged<sup>16,17</sup> that relying on T2-visible lesion correlation alone may be challenging due to

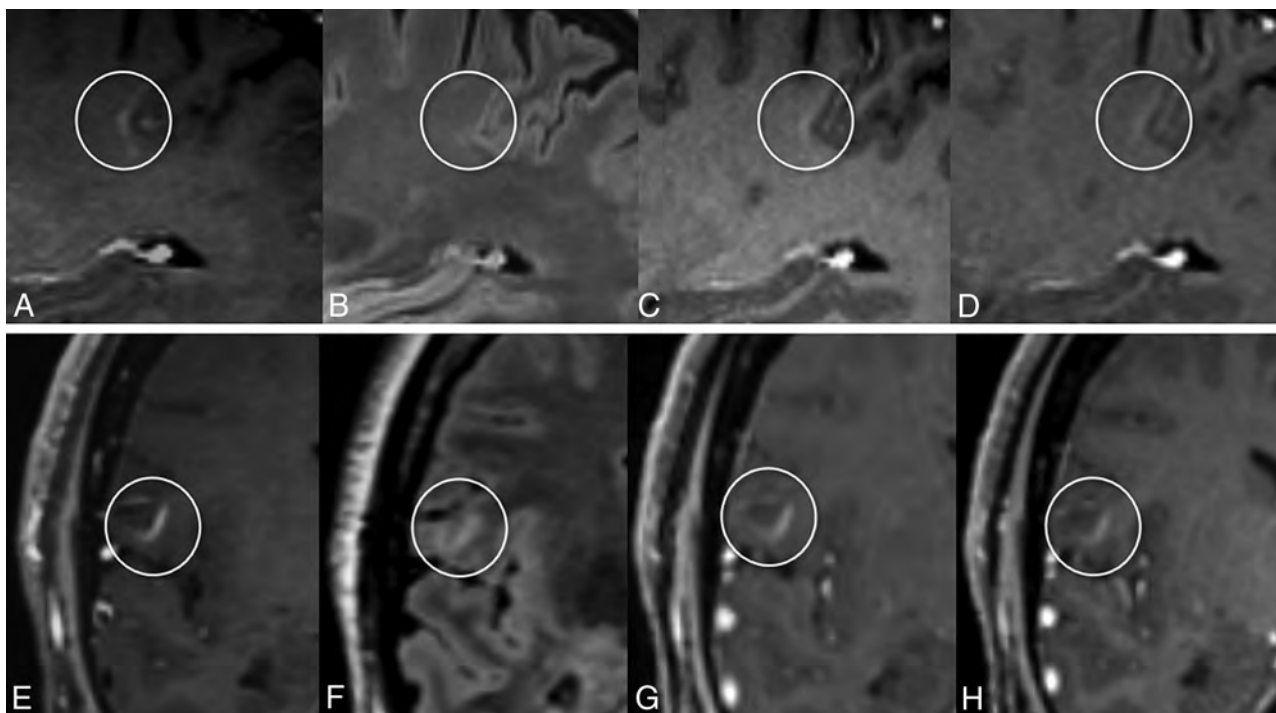


**FIG 3.** The upper panel shows an open-ring vFP enhancement consistent with a developmental venous anomaly and mimicking a TP enhancing juxtacortical CEL on SPACE images. Characteristic arcuate enhancement on SPACE image with subtle margins (*circles*) in the juxtacortical white matter (A), associated with faint hyperintensity on FLAIR T2 image (B), is barely visible on MPRAGE (C) and VIBE (D) images. This vFP was reported by the BR only. TP CELs with morphology similar to that of A on SPACE image (E) exhibits characteristic T2-FLAIR hyperintensity (F). In this case, CEL enhancement is clearly detected on MPRAGE (G) and VIBE (H) images as well.

**Table 4: Quantitative characteristics of vFP and TP contrast-enhancement sources on SPACE images<sup>a</sup>**

	vFP	TP	<i>P</i>	vFP <sub>small</sub>	TP <sub>small</sub>	<i>P</i>	vFP <sub>large</sub>	TP <sub>large</sub>	<i>P</i>
No.	38	66		28	29		10	37	
Volume (mm <sup>3</sup> )									
Median	11.5	16	.027 <sup>b,d</sup>	7.5	9	.981 <sup>b</sup>	34	49	.730 <sup>b</sup>
Range	3–84	3–565		3–14	3–14		30–84	15–565	
CNR									
Median	7.73	11.18	.003 <sup>b,d</sup>	7.66	8.38	.544 <sup>b</sup>	7.85	15.87	.015 <sup>b,d</sup>
Range	1.67–22.67	2.18–44.06		1.67–22.37	2.18–20.28		3.92–22.67	5.67–44.06	
Morphology (No.) (%)									
Nodular	26 (68.4%)	52 (78.8%)	.078 <sup>c</sup>	22 (78.6%)	26 (89.7%)	.292 <sup>c</sup>	4 (40%)	26 (70.3%)	.036 <sup>c,d</sup>
Tubular	4 (10.5%)	0 (0%)		2 (7.1%)	0 (0%)		2 (20%)	0 (0%)	
Ring/open-ring	8 (28.1%)	14 (21.2%)		4 (14.3%)	3 (10.3%)		4 (40%)	11 (29.7%)	

<sup>a</sup> Large and small TPs and vFPs are categorized according to the median of their volume-distribution frequency (14 mm<sup>3</sup>).

<sup>b</sup> Mann-Whitney *U* test.

<sup>c</sup> Pearson  $\chi^2$ .

<sup>d</sup> Statistically significant results.

segmentation and colocalization errors, particularly when dealing with small lesions. In addition, developmental venous anomalies, representing potential sources of nonlesional contrast enhancement in up to 9.6% of the adult population,<sup>13</sup> may also exhibit some T2-FLAIR signal hyperintensity,<sup>14,32</sup> thus potentially mimicking inflammation-related edema and/or demyelination.

### Impact of the Reader's Experience

Two relevant findings emerged from the performance of readers with different levels of experience. First, SPACE images facilitated both TP detection and FP misdiagnosis in a similar manner between

ERs and BRs. Second, even though the BR performance was expectedly lower than the ERs' performance in terms of TP detection, it was remarkably similar for FP misdiagnosis. Taken together, these results indicate a strong effect of the sequence choice for the assessment of TPs and FPs, being relatively independent of the level of the reader's experience.

### Impact on MRI Estimation of Disease Activity

Even though SPACE sequences detected significantly more CELs, the superiority did not lead to a statistically significant advantage in terms of diagnosis probability at the patient level. More

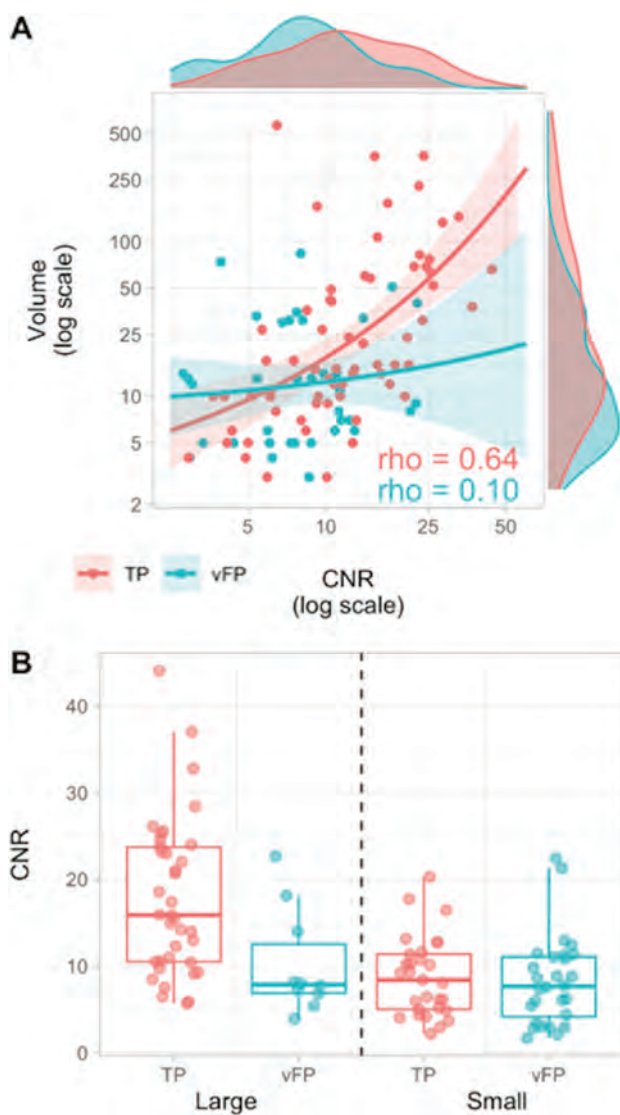


**FIG 4** A, Relationships between CNR and volume variables in TP (red) and vFP (cyan) findings. Higher CNR and larger volume values are more frequently represented in TP than in vFP (marginal density plots). The variables are significantly correlated in TP ( $\rho = 0.644$ ,  $P < .001$ ), but not in vFP ( $\rho = 0.096$ ,  $P = .568$ ). B, Boxplots represent CNR value-distribution differences between TP and vFP after median split categorization into small ( $\leq 14 \text{ mm}^3$ ) and large ( $> 14 \text{ mm}^3$ ). CNR values are lower in vFP compared with TP in the large category only, but similar in the small category.

specifically, the probability of diagnosing 1 patient with at least 1 CEL was only slightly higher but not statistically significant compared with MPRAGE and VIBE. This intriguing finding might be explained, at least in part, by the relatively low prevalence of patients with at least 1 CEL in our cohort (9.1%), providing insufficient statistical power to test small sensitivity differences. Most important, however, this finding is in line with other recent studies reporting a relatively low incidence of patients with active lesions.<sup>33-35</sup> This is likely representative of the disease-activity features encountered in the current MS population and reflects the availability of increasingly effective drugs to suppress inflammation. Different MR imaging activity thresholds were suggested as a cutoff to define a patient as a nonresponder to a given treatment, but in several previous

studies, even a single CEL was found to correlate with subsequent clinical worsening.<sup>4-6</sup> Crucially, misclassification of nonlesional enhancement as an MS CEL might lead to unnecessary change of treatment, with highly effective disease-modifying treatment being generally associated with a higher risk of adverse events.

#### Quantitative vFP Features

Because CEL detection and segmentation can be time-consuming and subject to intra- and interrater variability, there is a growing interest in obtaining robust automated detection and/or segmentation tools, especially for processing large amounts of data in clinical trials.<sup>15-19</sup> Various strategies were proposed to minimize errors on the basis of prior T2-visible lesion segmentation,<sup>18</sup> adaptive local segmentation size,<sup>18</sup> shape and anatomic location,<sup>19</sup> conditional random field framework,<sup>16</sup> and deep learning<sup>17</sup> techniques. Despite the effort, misdiagnosis risk remains an acknowledged limitation, mainly due to the small size of both CELs and vFPs, leading to T2-lesion mislocalization and misregistration, unless conservative limitations in terms of detectable lesion size<sup>17</sup> and/or dedicated pulse sequences<sup>15</sup> are used. Here, we provided descriptions of the size, enhancement conspicuity, and morphology features of iV enhancement sources virtually indistinguishable from active demyelinating lesions when using SPACE images alone. In our cohort, small ( $\leq 14 \text{ mm}^3$ ) vFPs could not be distinguished from CELs on the basis of the overlapping enhancement and morphology features. Indeed, the CNR (reflecting the enhancement conspicuity with respect to the background parenchyma) was similar and the nodular morphology was the most frequent one in vFP<sub>small</sub> and TP<sub>small</sub>. Thus, the vFP and TP features presented in this work provide previously undescribed knowledge about inherent limitations to the categorization of lesional and nonlesional sources of enhancement in patients with MS. On the basis of the groundwork laid in the present study, future investigations may test the benefit of multicontrast data set training (including SPACE, MPRAGE, and/or VIBE images, together with T2-FLAIR weighting) on the diagnostic accuracy of computer-assisted and neural network CEL-detection tools.

#### Limitations

SPACE black-blood intrinsic characteristics may be further explored using optimized techniques,<sup>7,9,36</sup> potentially leading to an improved vFP suppression not assessed in the present study. Furthermore, we did not assess the variability of different magnetic field strengths and other black-blood techniques from different MR imaging vendors. Therefore, our results cannot be generalized to other settings. Readers could not have been completely blinded to the sequence type because they might have easily recognized each typical image appearance.<sup>22,37</sup> The vFP number misdiagnosed in MPRAGE and VIBE scans was too low and prevented descriptive and comparative analyses for these techniques. Finally, we have not tested whether patients with specific T2-lesion-burden profiles may be more prone to have vFP findings. This issue deserves future computer-assisted investigations, possibly using lesion feature-extraction approaches.

#### CONCLUSIONS

Postgadolinium black-blood 3D-T1-TSE SPACE images provide superior sensitivity for the detection of active MS lesions compared



with MPRAGE and VIBE scans. However, small venous enhancement sources may be indistinguishable on SPACE images alone, due to the overlapping enhancement and morphology features.

## ACKNOWLEDGMENTS

The Authors thank Liliane Petrini for her help with manuscript editing.

Disclosure forms provided by the authors are available with the full text and PDF of this article at [www.ajnr.org](http://www.ajnr.org).

## REFERENCES

- Thompson AJ, Baranzini SE, Geurts J, et al. **Multiple sclerosis.** *Lancet* 2018;391:1622–36 CrossRef Medline
- Lublin FD, Reingold SC, Cohen JA, et al. **Defining the clinical course of multiple sclerosis: the 2013 revisions.** *Neurology* 2014;83:278–86 CrossRef Medline
- Río J, Rovira À, Tintoré M, et al. **Disability progression markers over 6-12 years in interferon- $\beta$ -treated multiple sclerosis patients.** *Mult Scler* 2018;24:322–30 CrossRef Medline
- Gasparini C, Prosperini L, Tintoré M, et al; the MAGNIMS Study Group. **Unraveling treatment response in multiple sclerosis: a clinical and MRI challenge.** *Neurology* 2019;92:180–92 CrossRef Medline
- Bermel RA, You X, Foulds P, et al. **Predictors of long-term outcome in multiple sclerosis patients treated with interferon  $\beta$ .** *Ann Neurol* 2013;73:95–103 CrossRef Medline
- Prosperini L, Mancinelli C, Haggia S, et al. **Minimal evidence of disease activity (MEDA) in relapsing-remitting multiple sclerosis.** *J Neurol Neurosurg Psychiatry* 2020;91:271–77 CrossRef Medline
- Mandell DM, Mossa-Basha M, Qiao Y, et al; Vessel Wall Imaging Study Group of the American Society of Neuroradiology. **Intracranial vessel wall MRI: principles and expert consensus recommendations of the American Society of Neuroradiology.** *AJNR Am J Neuroradiol* 2017;38:218–29 CrossRef Medline
- Thaler C, Schneider T, Sedlacik J, et al. **T1w dark blood imaging improves detection of contrast enhancing lesions in multiple sclerosis.** *PLoS One* 2017;12:e0183099 CrossRef Medline
- Sommer NN, Saam T, Copenrath E, et al. **Multiple sclerosis: improved detection of active cerebral lesions with 3-dimensional T1 black-blood magnetic resonance imaging compared with conventional 3-dimensional T1 GRE imaging.** *Invest Radiol* 2018;53:13–19 CrossRef Medline
- Kato Y, Higano S, Tamura H, et al. **Usefulness of contrast-enhanced T1-weighted sampling perfection with application-optimized contrasts by using different flip angle evolutions in detection of small brain metastasis at 3T MR imaging: comparison with magnetization-prepared rapid acquisition.** *AJNR Am J Neuroradiol* 2009;30:923–29 CrossRef Medline
- Jeevanandham B, Kalyanpur T, Gupta P, et al. **Comparison of post-contrast 3D-T1-MPRAGE, 3D-T1-SPACE and 3D-T2-FLAIR MR images in evaluation of meningeal abnormalities at 3-T MRI.** *Br J Radiol* 2017;90:20160834 CrossRef Medline
- Hodel J, Outteryck O, Ryo E, et al. **Accuracy of postcontrast 3D turbo spin-echo MR sequence for the detection of enhanced inflammatory lesions in patients with multiple sclerosis.** *AJNR Am J Neuroradiol* 2014;35:519–23 CrossRef Medline
- Brinjikji W, El-Rida El-Masri A, Wald JT, et al. **Prevalence of developmental venous anomalies increases with age.** *Stroke* 2017;48:1997–99 CrossRef Medline
- Grazzini I, Calchetti B, Cuneo GL. **Developmental venous anomalies in patients with multiple sclerosis: is that a coincidence or an ancillary finding?** *Neurol Sci* 2021;42:2453–60 CrossRef Medline
- Bedell BJ, Narayana PA. **Volumetric analysis of white matter, gray matter, and CSF using fractional volume analysis.** *Magn Reson Med* 1998;39:961–69 CrossRef Medline
- Karimaghloo Z, Shah M, Francis SJ, et al. **Automatic detection of gadolinium-enhancing multiple sclerosis lesions in brain MRI using conditional random fields.** *IEEE Trans Med Imaging* 2012;31:1181–94 CrossRef Medline
- Coronado I, Gabr RE, Narayana PA. **Deep learning segmentation of gadolinium-enhancing lesions in multiple sclerosis.** *Mult Scler* 2021;27:519–27 CrossRef Medline
- He R, Narayana PA. **Automatic delineation of Gd enhancements on magnetic resonance images in multiple sclerosis.** *Med Phys* 2002;29:1536–46 CrossRef Medline
- Goldberg-Zimring D, Achiron A, Miron S, et al. **Automated detection and characterization of multiple sclerosis lesions in brain MR images.** *Magn Reson Imaging* 1998;16:311–18 CrossRef Medline
- Polman CH, Reingold SC, Banwell B, et al. **Diagnostic criteria for multiple sclerosis: 2010 revisions to the McDonald criteria.** *Ann Neurol* 2011;69:292–302 CrossRef Medline
- Granberg T, Martola J, Kristoffersen-Wiberg M, et al. **Radiologically isolated syndrome-incidental magnetic resonance imaging findings suggestive of multiple sclerosis, a systematic review.** *Mult Scler* 2013;19:271–80 CrossRef Medline
- Danieli L, Riccitelli GC, Distefano D, et al. **Brain tumor-enhancement visualization and morphometric assessment: a comparison of MPRAGE, SPACE, and VIBE MRI techniques.** *AJNR Am J Neuroradiol* 2019;40:1140–48 CrossRef Medline
- El-Koussy M, Schroth G, Gralla J, et al. **Susceptibility-weighted MR imaging for diagnosis of capillary telangiectasia of the brain.** *AJNR Am J Neuroradiol* 2012;33:715–20 CrossRef Medline
- Pravatà E, Roccatagliata L, Sormani MP, et al. **Dedicated 3D-T2-STIR-ZOOMit imaging improves demyelinating lesion detection in the anterior visual pathways of patients with multiple sclerosis.** *AJNR Am J Neuroradiol* 2021;42:1061–68 CrossRef Medline
- Geraldes R, Ciccarelli O, Barkhof F, et al; MAGNIMS study group. **The current role of MRI in differentiating multiple sclerosis from its imaging mimics.** *Nat Rev Neurol* 2018;14:199–213 CrossRef Medline
- Filippi M, Preziosa P, Banwell BL, et al. **Assessment of lesions on magnetic resonance imaging in multiple sclerosis: practical guidelines.** *Brain* 2019;142:1858–75 CrossRef Medline
- Filippi M, Rocca MA, Ciccarelli O, et al. **MRI criteria for the diagnosis of multiple sclerosis: MAGNIMS consensus guidelines.** *Lancet Neurol* 2016;15:292–303 CrossRef Medline
- Dobson R, Giovannoni G. **Multiple sclerosis: a review.** *Eur J Neurol* 2019;26:27–40 CrossRef Medline
- Kaufmann TJ, Smits M, Boxerman J, et al. **Consensus recommendations for a standardized brain tumor imaging protocol for clinical trials in brain metastases.** *Neuro Oncol* 2020;22:757–72 CrossRef Medline
- Goncalves Filho AL, Conklin J, Longo MG, et al. **Accelerated post-contrast wave-CAIPI T1 SPACE achieves equivalent diagnostic performance compared with standard T1 SPACE for the detection of brain metastases in clinical 3T MRI.** *Front Neurol* 2020;11:587327 CrossRef Medline
- Filippi M, Rocca MA, Barkhof F, et al; Attendees of the Correlation between pathological and MRI findings in MS workshop. **Association between pathological and MRI findings in multiple sclerosis.** *Lancet Neurol* 2012;11:349–60 CrossRef Medline
- Santucci GM, Leach JL, Ying J, et al. **Brain parenchymal signal abnormalities associated with developmental venous anomalies: detailed MR imaging assessment.** *AJNR Am J Neuroradiol* 2008;29:1317–23 CrossRef Medline
- Tsantes E, Curti E, Ganazzoli C, et al. **The contribution of enhancing lesions in monitoring multiple sclerosis treatment: is gadolinium always necessary?** *J Neurol* 2020;267:2642–47 CrossRef Medline
- Sadigh G, Saindane AM, Waldman AD, et al. **Comparison of unenhanced and gadolinium-enhanced imaging in multiple sclerosis: is contrast needed for routine follow-up MRI?** *AJNR Am J Neuroradiol* 2019;40:1476–80 CrossRef Medline

35. Mattay RR, Davtayan K, Bilello M, et al. **Do all patients with multiple sclerosis benefit from the use of contrast on serial follow-up MR imaging? A retrospective analysis.** *AJNR Am J Neuroradiol* 2018;39:2001–06 CrossRef Medline
36. Xie Y, Yang Q, Xie G, et al. **Improved black-blood imaging using DANTE-SPACE for simultaneous carotid and intracranial vessel wall evaluation.** *Magn Reson Med* 2016;75:2286–94 CrossRef Medline
37. Kammer NN, Coppenrath E, Treitl KM, et al. **Comparison of contrast-enhanced modified T1-weighted 3D TSE black-blood and 3D MP-RAGE sequences for the detection of cerebral metastases and brain tumours.** *Eur Radiol* 2016;26:1818–25 CrossRef Medline

# Diagnostic Accuracy of High-Resolution 3D T2-SPACE in Detecting Cerebral Venous Sinus Thrombosis

 A. Hakim,  C. Kurmann,  K. Pospieszny,  T.R. Meinel,  M.A. Shahin,  M.R. Heldner,  R. Umarova,  S. Jung,  M. Arnold, and  M. El-Koussy



## ABSTRACT

**BACKGROUND AND PURPOSE:** Assessment of cerebral venous sinus thrombosis on MR imaging can be challenging. The aim of this study was to evaluate the diagnostic accuracy of high-resolution 3D T2 sampling perfection with application-optimized contrasts by using different flip angle evolution (SPACE) in patients with cerebral venous sinus thrombosis and to compare its performance with contrast-enhanced 3D T1-MPRAGE.

**MATERIALS AND METHODS:** We performed a blinded retrospective analysis of T2-SPACE and contrast-enhanced MPRAGE sequences from patients with cerebral venous sinus thrombosis and a control group. The results were compared with a reference standard, which was based on all available sequences and clinical history. Subanalyses were performed according to the venous segment involved and the clinical stage of the thrombus.

**RESULTS:** Sixty-three MR imaging examinations from 35 patients with cerebral venous sinus thrombosis and 51 examinations from 40 control subjects were included. The accuracy, sensitivity, and specificity calculated from the initial MR imaging examination for each patient were 100% each for T2-SPACE and 95%, 91%, and 98%, respectively, for contrast-enhanced MPRAGE. The interrater reliability was high for both sequences. In the subanalysis, the accuracy for each venous segment involved and if subdivided according to the clinical stage of thrombus was  $\geq 95\%$  and  $\geq 85\%$  for T2-SPACE and contrast-enhanced MPRAGE, respectively.

**CONCLUSIONS:** Both T2-SPACE and contrast-enhanced MPRAGE offer high accuracy for the detection and exclusion of cerebral venous sinus thrombosis; however, T2-SPACE showed a better overall performance and thus could be a useful tool if included in a multiparametric MR imaging protocol for the diagnosis of cerebral venous sinus thrombosis, especially in scenarios where gadolinium administration is contraindicated.

**ABBREVIATIONS:** CE = contrast-enhanced; CVST = cerebral venous sinus thrombosis; SPACE = sampling perfection with application-optimized contrasts using different flip angle evolution

Cerebral venous sinus thrombosis (CVST) is an infrequently occurring but potentially life-threatening condition.<sup>1</sup> Around 0.5% of acute strokes are caused by CVST.<sup>2</sup> However, excluding CVST is one of the most frequent reasons for referral to the neuro-radiology department. CVST has also recently been reported in patients with coronavirus disease 2019 (COVID-19)<sup>3</sup> and after


COVID-19 vaccination in the setting of thrombosis and thrombocytopenia syndrome.<sup>4</sup> Both CT and MR imaging can be used for the diagnosis, but in many centers and in certain circumstances, such as in younger patients and pregnant women, MR imaging has become the method of choice.<sup>5</sup> A combination of MR imaging sequences is usually used to verify the diagnosis.<sup>6</sup> This combination aims to visualize the thrombus, detect absent flow in the segments involved, and identify the concomitant changes in the brain parenchyma.<sup>5</sup>

Absent flow is assessed using phase-contrast or TOF MR venography, but these flow-sensitive sequences are subject to multiple pitfalls.<sup>7</sup> Contrast-enhanced (CE) sequences, such as venous angiography<sup>8</sup> or CE-MPRAGE have provided better results;<sup>9</sup> therefore, a contrast agent is usually introduced to exclude venous thrombosis. However, administration of a contrast agent is not always appropriate, for example during pregnancy<sup>10</sup> or in patients with allergic reactions<sup>11</sup> and impaired renal function.<sup>11</sup> Furthermore,

Received November 5, 2021; accepted after revision April 12, 2022.

From the University Institute of Diagnostic and Interventional Neuroradiology (A.H., C.K., K.P., M.E.) and Department of Neurology (T.R.M., M.R.H., R.U., S.J., M.A.), Bern University Hospital, Inselspital, University of Bern, Bern, Switzerland; and Department of Radiodiagnosis (M.A.S.), Faculty of Medicine, Cairo University Hospitals, Cairo, Egypt.

Please address correspondence to Arsany Hakim, MD, Institute of Diagnostic and Interventional Neuroradiology, Bern University Hospital, Inselspital, Freiburgstr 10, CH 3010, Bern, Switzerland; e-mail: arsan\_y\_hakim@yahoo.com; @ScanNeuroradBE

 Indicates open access to non-subscribers at [www.ajnr.org](http://www.ajnr.org)

 Indicates article with online supplemental data.

<http://dx.doi.org/10.3174/ajnr.A7530>



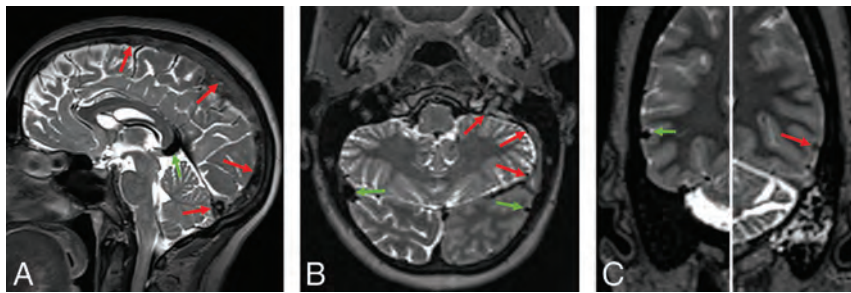


**FIG 1.** T2-SPACE obtained from different patients. The normal segments (green arrows) show a homogeneous physiologic flow void. In the thrombosed segments (red arrows, A), superior sagittal sinus and torcular; left sigmoid sinus and jugular vein (B); and the left vein of Labbé (C), the flow void is absent and the signal is mostly inhomogeneous. According to the stage of the thrombus, expansion of the sinus may be seen (superior sagittal sinus in A).

patients may refuse the administration of contrast, following the widespread discussions regarding gadolinium deposition in the brain.<sup>12</sup> In such cases, there is uncertainty in the diagnosis or exclusion of CVST. Therefore, non-contrast-dependent sequences with a higher sensitivity for the detection of CVST are required.

The conventional T2 spin-echo sequence depicts signal changes within the thrombotic material,<sup>5</sup> with absence of the physiologic flow void. However, due to the hypointense signal in thrombi at certain stages, which mimic a flow void,<sup>8,13</sup> as well as the complex blood flow in the venous sinuses, radiologists cannot solely rely on this sequence.<sup>5</sup> Another drawback is the limitation of visualization of small venous structures in 2D sequences due to the partial volume effect. However, the data obtained on the utility of the conventional T2 sequences is based on older techniques.<sup>13-17</sup>

In recent years, MR imaging manufacturers have developed an optimized single-slab 3D FSE sequence that has a clinically acceptable acquisition time.<sup>18,19</sup> This technique provides a high-resolution 3D volume with millimeter section thickness with adequate SNR and optimized tissue contrast,<sup>18</sup> without a limitation in the specific absorption rate.<sup>18,20</sup> One such sequence is the so-called 3D T2 sampling perfection with application-optimized contrasts by using different flip angle evolution (SPACE) sequence. We hypothesized that this sequence would have high accuracy in the detection of CVST. Thus, we aimed to evaluate the performance of T2-SPACE in comparison with one of the widely used CE gradient-echo sequences, namely 3D CE-MPRAGE.<sup>9,21</sup>

## MATERIALS AND METHODS

### Patients

This retrospective study was approved by the Bern University Hospital medical ethics committee. A search was performed in the PACS of our tertiary hospital as well as the local stroke registry for 2 groups of participants: 1) patients with a final diagnosis of CVST, and 2) a control group of subjects who underwent MR imaging but were negative for CVST. The inclusion criterion for both groups was the presence of both T2-SPACE and CE-MPRAGE in the same scanning protocol. Absence of one or both of these sequences was the exclusion criterion. To avoid bias during imaging interpretation due to the possibility of the presence of parenchymal lesions (eg, venous edema) in patients with CVST, the presence of parenchymal lesions in the control group was not an

exclusion criterion. The first available MR imaging, the “baseline-MR imaging” containing both sequences was considered for the primary analysis. Further follow-up MRIs from the same patient, with both sequences acquired during each examination, were also considered for further subanalysis regarding the clinical stage of the thrombus.

### MR Imaging Protocol

Patients were examined on either 1.5T or 3T scanners (Magnetom Avanto, Aera, Skyra, Prisma, or Vida; Siemens). The scanning parameters are shown in the Online Supplemental Data. The

MR imaging protocol also included other sequences that varied according to the clinical indication.

### Index Test: Imaging Interpretation

Images from patients with CVST and the control group were anonymized and randomized. Two readers, blinded to the clinical information and final diagnosis, reviewed the images independently. Reader 1 was a board-certified neuroradiologist with >14 years of experience, and reader 2 was a neuroradiology resident with 1 year of experience in vascular neuroradiology. The rating began with T2-SPACE for all patients, while raters were blinded to the other sequences. On T2-SPACE, the diagnosis of thrombosis was defined by the absence of the physiologic flow void with an inhomogeneous signal in the venous segment involved (Fig 1). The images were analyzed in the multiplanar reconstruction tool to evaluate each segment in multiple projections. Studies from the same patient were rated during different sessions. Rating of CE-MPRAGE began a month after finishing the rating of the T2-SPACE analyses. The readers assessed the following venous segments: superior sagittal sinus, torcular Herophili, transverse sinus, sigmoid sinus, jugular vein, straight sinus, vein of Galen, internal cerebral veins, vein of Labbé, and cortical veins including the vein of Trolard and reported their final impression regarding the presence or absence of CVST. Disagreement between the 2 readers was resolved by a third senior reader with 25 years of experience in neuroradiology.

### Reference Standard

Reader 1 and the senior reader established the reference standard, which was the final diagnosis and location of CVST based on the evaluation of all available MR imaging sequences (T2-SPACE, T1, FLAIR, DWI, SWI, TOF, or phase-contrast venography; 3D CE-MPRAGE; and CE venous angiography) from each examination. A valid reference standard included at least T2-SPACE, 3D CE-MPRAGE, and  $\geq 1$  venous angiography sequence (TOF, phase-contrast, and/or CE venous angiography). In only 3 examinations was venous angiography not performed on the examination; however, in these 3 cases, it was performed within 2 days. All MR imaging examinations and clinical data were taken into consideration during the evaluation of each venous segment. To avoid misinterpretation of the segment involved due to evolution

**Table 1: Characteristics of patients included in the analysis**

	Control	CVST
No. of patients	41	35
Male/female ratio	14:27	14:21
Age (median) (interquartile range) (yr)	38.5 (27–56)	43.5 (34–61)
No. of MR imaging examinations	51	63
1.5T/3T	34:17	37:26

of the thrombus, the reference standard was performed for each MR imaging examination included in the study.

### Clinical Data

Clinical data from the group of patients with CVST were obtained from the Swiss Stroke Registry. Data included symptom onset, which was used to estimate the clinical stage of the thrombus according to the interval between symptom onset and imaging as follows: acute = 0–5 days; subacute = 6–15 days; chronic, >15 days, or late chronic, >1 year.<sup>5</sup>

### Statistical Analysis

The results obtained from each sequence (T2-SPACE and CE-MPRAGE) based on the baseline MR imaging were compared with the reference standard to obtain the sensitivity, specificity, accuracy, and the positive and negative predictive values. Interrater reliability was calculated using the Cohen  $\kappa$  coefficient. All available examinations (ie, the baseline MR imaging as well as follow-ups) were included to perform 2 different subanalyses according to the clinical stage and the location of the thrombus.

## RESULTS

From May 2016 to September 2019, thirty-five patients with CVST fulfilled the inclusion criteria and 20 patients were initially examined on a 1.5T and 15 on a 3T scanner. In total, 16/35 patients (45.7%) showed parenchymal lesions (vasogenic edema, cytotoxic edema, and/or hemorrhage). A total of 63 examinations from the patients with CVST were included in the subanalysis. Table 1 and the Online Supplemental Data summarize the patient characteristics.

The clinical stage of thrombus was identified as acute ( $n = 16$ ), subacute ( $n = 13$ ), chronic ( $n = 23$ ), and late chronic ( $n = 10$ ). In 1 examination, the stage was uncertain. The Online Supplemental Data summarize the stage and location of the thrombi. Very few examinations revealed thrombosis of the vein of Galen and internal cerebral veins. These were excluded from the subanalysis.

Fifty-one MRIs obtained from 41 individuals without CVST (control group) were included. Around half of these examinations were performed to exclude CVST. Thirty-two studies revealed no parenchymal lesions, while the other 19 examinations revealed other parenchymal lesions such as perifocal edema due to hemorrhage or other pathologies. In total, 114 examinations obtained from 76 patients were included.

### T2-SPACE

Based on the baseline MR imaging, the final diagnosis of CVST was accurately identified in all study participants (ie, 35 patients with CVST and all 41 controls) on T2-SPACE (Fig 1, Table 2,

**Table 2: Results of T2-SPACE and CE-MPRAGE based on the first available MR imaging examinations<sup>a</sup>**

	T2-SPACE	CE-MPRAGE
Sensitivity	1 (0.9–1)	0.91 (0.8–1)
Specificity	1 (0.9–1)	0.98 (0.9–1)
Accuracy	1 (0.9–1)	0.95 (0.9–1)
Positive predictive value	1 (0.9–1)	0.97 (0.8–1)
Negative predictive value	1 (0.9–1)	0.93 (0.8–1)

<sup>a</sup> Data in parentheses are 95% confidence intervals.

and the Online Supplemental Data), with the Cohen  $\kappa = 0.92$  (Online Supplemental Data).

In the subanalysis, the venous segment involved was correctly identified in >95% of cases for each segment (Online Supplemental Data). The negative predictive value was >90% for all segments.

In the subanalysis regarding the clinical stage (Fig 2), the final diagnosis of the acute and subacute stages was correct in 100% of cases (Online Supplemental Data). In the chronic and late chronic stages, the accuracy reached 99% and 97%, respectively. The interrater reliability was better in the acute ( $\kappa = 0.81$ ) and chronic stages ( $\kappa = 0.82$ ) than in the subacute ( $\kappa = 0.79$ ) and late chronic ( $\kappa = 0.67$ ) stages (Online Supplemental Data). The Online Supplemental Data provide examples showing false-positive and false-negative results of T2-SPACE.

### CE-MPRAGE

In the final diagnosis based on the initial MR imaging, CE-MPRAGE correctly identified 32/35 patients with CVST and 40/41 controls. The accuracy, sensitivity, and specificity were 95%, 91%, and 98%, respectively, with the Cohen  $\kappa = 0.87$  (Table 2 and Online Supplemental Data). The performance of 3T was better than that of the 1.5T scanner (accuracy, 100% versus 91%) (Online Supplemental Data).

Subanalysis showed the correct diagnosis in  $\geq 85\%$  for each segment (Online Supplemental Data). The lowest accuracy was 85% in the torcular. The specificity was at the lowest in the sigmoid sinus, reaching 95%; this was higher than the lowest sensitivity, which dropped to <50% for the cortical veins.

In the subanalysis regarding the clinical stage of the thrombus (Fig 2), the accuracy in the acute phase was 97% (Online Supplemental Data), while in the subacute and chronic phases, the accuracy was 92%. In the late chronic stage, the accuracy was 85%. The interrater reliability was better in the acute ( $\kappa = 0.93$ ) and chronic ( $\kappa = 0.9$ ) stages than in the subacute ( $\kappa = 0.8$ ) and late chronic ( $\kappa = 0.74$ ) stages (Online Supplemental Data).

## DISCUSSION

The main findings of this study are that T2-SPACE has a slightly higher sensitivity and specificity than CE-MPRAGE in the diagnosis of CVST. The interrater agreement was slightly better for CE-MPRAGE than for T2-SPACE. For T2-SPACE, agreement ranged from moderate (in the subacute and late chronic phases) to strong (in the acute and chronic phases). The accuracy of T2-SPACE was >95% in a subanalysis of all venous vascular segments, and it exceeded 95% accuracy for each of the different clinical stages of thrombus. The results also highlight the disadvantages of relying solely on contrast-based sequences for



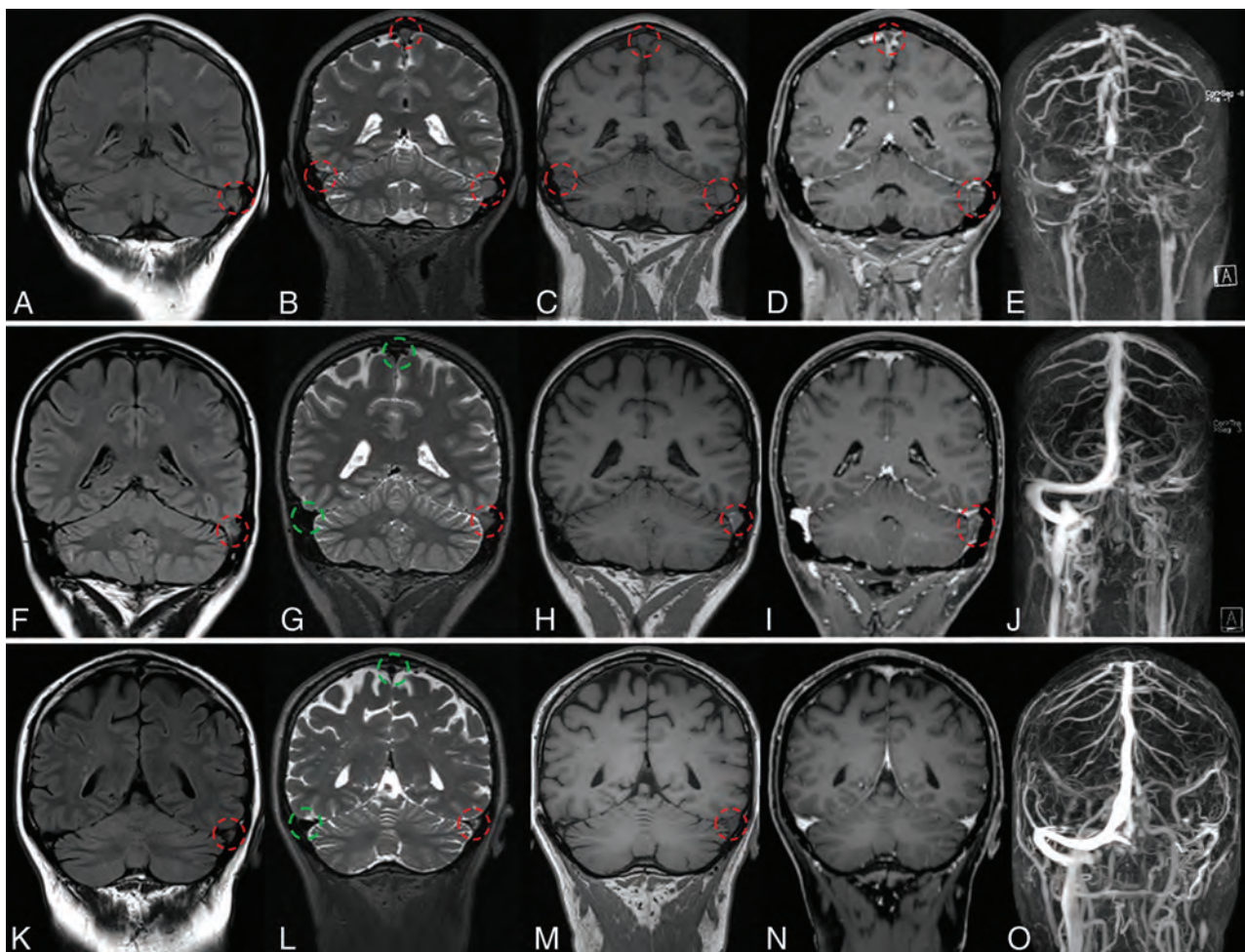


**FIG 2.** Coronal MR imaging from 3 different patients showing 3 phases of CVST. From left to right, FLAIR (A, F, K), T2-SPACE (B, G, L), T1-SPACE (C, H, M), CE-T1-MPRAGE (D, I, N), and MIP of CE MRA (E, J, O). Thrombosed and patent veins are marked with red and green circles, respectively. The latter exhibit a physiologic flow void, clearly visible on SPACE images. Upper row, A–E, Acute CVST in a 45-year-old woman with headache and vomiting. MR imaging, performed on the day of symptom onset shows extensive thrombosis (red circles) of the transverse and sigmoid sinuses, jugular vein, torcular Herophili, and superior sagittal sinus. The flow void is absent on the T1 and T2 sequences. There are filling defects on CE-MPRAGE. The extension of the thrombosis is seen on the CE-MRA. Middle row, F–J, Subacute CVST in a 30-year-old woman who presented initially with headache. A follow-up MR imaging 13 days after the initial presentation shows thrombosis with an absent flow void on SPACE of the left transverse/sigmoid sinus and jugular vein. Lower row, K–O, Chronic CVST in a 63-year-old male patient who initially presented with headache. A follow-up MR imaging after 200 days shows a thrombus in the left transverse sinus. The flow void is absent on T2 and T1, but CVST is not detectable on CE-MPRAGE.

excluding CVST and emphasize the potential value of adding T2-SPACE to CVST protocols.

Exclusion of CVST is one of the common reasons for referrals to the radiology department during pregnancy and the postpartum period.<sup>22</sup> However, during pregnancy and lactation, gadolinium-based contrast agents should be used with caution and only if the diagnosis cannot be made without them.<sup>10,11,23</sup> Administration of contrast is also not desired in patients with renal impairment<sup>11</sup> and in patients who refuse gadolinium due to increasing evidence of its deposition in the brain.<sup>12</sup> Therefore, finding an MR imaging protocol that reduces the need for gadolinium is of utmost importance. The addition of the T2-SPACE to the routine CVST protocol can increase the sensitivity and specificity of the MR imaging, especially in the above-mentioned situations.<sup>24,25</sup>

T2-SPACE is an isotropic 3D FSE technique characterized by very long echo-train lengths, ultrashort echo spacing, and reduced

flip angles.<sup>26</sup> It has a high sampling efficiency and a high turbo factor due to use of nonselective short refocusing pulse trains with variable flip angles. One of the advantages of this sequence is that it combines the properties of spin-echo with the advantage of speedy acquisition by reading multiple lines in phase-encoding following each excitation pulse.<sup>18</sup> T2 spin-echo-based sequences are important because they provide optimal image contrast<sup>27</sup> and are resistant to magnetic field inhomogeneities.<sup>28,29</sup> There is intrinsic blood suppression,<sup>18,28</sup> allowing the reduction of flow artifacts. Therefore, T2-SPACE is not only valuable for evaluating brain parenchyma but also for the assessment of the vessel lumen. One of its important advantages is the delineation of the outer wall of the vein or sinus, which enables the differentiation between lumen narrowing due to a thrombus or a hypoplastic sinus (Online Supplemental Data), thus avoiding one of the pitfalls in angiographic imaging. Furthermore, expansion of the vein lumen by a clot in T2-SPACE is useful in



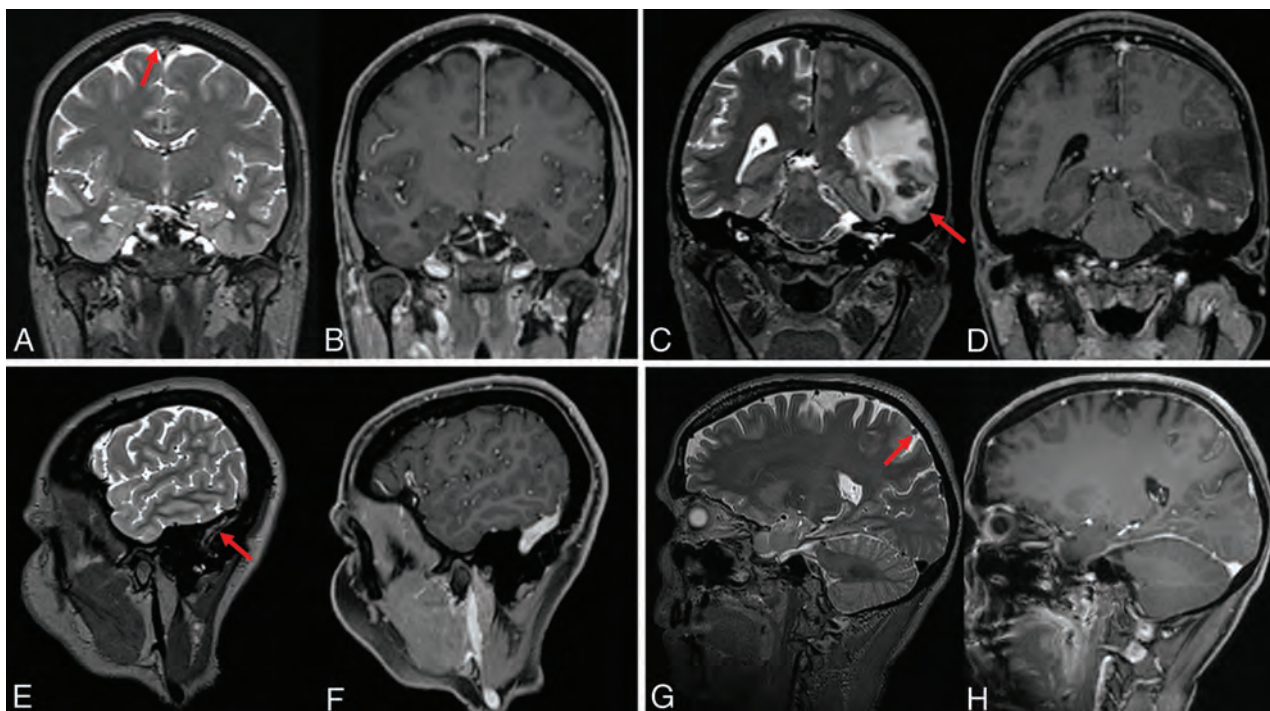


**FIG 3.** Examples from 4 different patients showing a thrombus (red arrows) on the T2-SPACE in the superior sagittal sinus (A), the vein of Labbé (C), the sigmoid sinus (E), and the cortical vein (G). CVST was missed on the CE T1-MPRAGE (B, D, F, and H).

interpretation (Fig 1A and Fig 2B). The 3D and isotropic imaging allow retrospective postprocessing, even of small veins, in different projections so that the acquisition of one 3D sequence replaces multiple conventional 2D T2 series.<sup>18</sup> Another advantage over 2D T2 is the coverage of the jugular vein (which is usually not covered in conventional axial 2D T2). Filling defects in TOF or phase-contrast venography due to arachnoid granulations are correctly classified in T2-SPACE (Online Supplemental Data). Moreover, as in the case of dark-blood sequences,<sup>30</sup> T2-SPACE offers advantages when evaluating vascular segments adjacent to tumors, allowing reliable assessment of sinus invasion (Online Supplemental Data).

Disadvantages of T2-SPACE include motion artifacts, as is the case with any 3D sequences. Collateralization and recanalization could be difficult to evaluate (Online Supplemental Data). Collateralization is usually assessed on an angiographic sequence with background suppression.<sup>31</sup> Recanalization is also usually assessed using an angiographic sequence<sup>31,32</sup> and could be difficult to evaluate using solely T2-SPACE due to the possibility of inhomogeneous signal of the thrombus. However, using T2-SPACE in a multiparametric approach (signal intensity, signal void, and filling defects on MR venography) could help in detecting recanalization and in assessing the thrombus load score.<sup>33</sup> In our study, we did not perform longitudinal comparisons to calculate the thrombus load score due to the relative inhomogeneity of data regarding the clinical stage of thrombosis, but this could be of interest for future studies.

A thrombus demonstrates signal evolution with time. The detection of an acute or chronic thrombus with an iso- or hypointense signal on conventional T1 and T2 imaging could be troublesome; thus, conventional angiography is usually required.<sup>8</sup> However, in our patient sample, the accuracy of the T2-SPACE in the final diagnosis was very high for thrombi at all clinical stages.

We suggest that the signal changes in T2-SPACE are probably related not only to the signal of the thrombus but also to flow alterations. Furthermore, a thrombus at certain stages may be missed in contrast-based sequences when the thrombus signal is hyperintense on T1 or due to enhancement of the thrombus (Fig 3). In general, subacute thrombus with the presence of methemoglobin is well-depicted on precontrast T1 and also on SWI due to the presence of blooming artifacts.<sup>7,34</sup> Diffusion restriction can be identified, especially in the subacute clots.<sup>5</sup> Here, multiparametric imaging plays a very important role because it increases the sensitivity and specificity. A protocol to exclude sinus thrombosis without the need for contrast administration should be based on multiparametric MR imaging, using FLAIR, T1, DWI, SWI, phase-contrast venography, and adding T2-SPACE instead of conventional 2D T2. This choice will increase the accuracy and reduce the number of cases in which contrast is needed because the high negative predictive value of T2-SPACE makes it suitable for thrombus exclusion when combined with other sequences.

### Strengths and Limitations

In this study, we included T2-SPACE and CE-MPRAGE from the same patient sample, enabling a fair comparison between the 2 isotropic sequences with the same rater experience. The inclusion of the control group with parenchymal lesions also allowed an unbiased comparison because the presence of edema or hemorrhage in the CVST group could influence the diagnosis.

The study has the limitations typical of a single-center retrospective analysis. The sample size was relatively small, given that CVST is an uncommon condition, and the size was further reduced by the inclusion criterion that the same MR imaging examination should include both T2-SPACE and CE-MPRAGE. Including multiple

MRIs from the same patient is also a substantial limitation; however, the main aim here was to allow subanalysis according to the stage of thrombus. Clinical data (ie, time from initial symptoms) were used to define the clinical stage of the thrombus, which could be challenging in patients with nonspecific symptoms. Another limitation was the lack of patients with involvement of the cavernous sinus or cerebellar veins as well as the small number of cases with involvement of the vein of Galen and internal cerebral veins, meaning that the accuracy of these subgroups cannot be calculated. This study had aimed to assess the sensitivity and specificity of T2-SPACE as a potential sequence to be used in pregnancy. However, no pregnant patients were included in the study; in our institution, pregnant patients do not usually receive contrast agents and thus did not fulfill the inclusion criteria.

## CONCLUSIONS

T2-SPACE has a high accuracy in the detection and exclusion of CVST at all clinical stages of thrombus and should be added to the routine CVST MR imaging protocol, especially if a contrast injection is contraindicated or undesirable.

Disclosure forms provided by the authors are available with the full text and PDF of this article at [www.ajnr.org](http://www.ajnr.org).

## REFERENCES

- Bonneville F. **Imaging of cerebral venous thrombosis.** *Diagn Interv Imaging* 2014;95:1145–50 CrossRef Medline
- Boussier MG, Ferro JM. **Cerebral venous thrombosis: an update.** *Lancet Neurol* 2007;6:162–70 CrossRef Medline
- Al-Mufti F, Amuluru K, Sahni R, et al. **Cerebral venous thrombosis in COVID-19: a New York Metropolitan Cohort Study.** *AJNR Am J Neuroradiol* 2021;42:1196–1200 CrossRef Medline
- Sánchez van Kammen M, Aguiar de Sousa D, Poli S, et al; Cerebral Venous Sinus Thrombosis with Thrombocytopenia Syndrome Study Group. **Characteristics and outcomes of patients with cerebral venous sinus thrombosis in SARS-CoV-2 vaccine-induced immune thrombotic thrombocytopenia.** *JAMA Neurol* 2021;78:1314 CrossRef Medline
- Linn J, Brückmann H. **Cerebral venous and dural sinus thrombosis: state-of-the-art imaging.** *Clin Neuroradiol* 2010;20:25–37 CrossRef Medline
- Patel D, Machnowska M, Symons S, et al. **Diagnostic performance of routine brain MRI sequences for dural venous sinus thrombosis.** *AJNR Am J Neuroradiol* 2016;37:2026–32 CrossRef Medline
- Dmytriw AA, Song JS, Yu E, et al. **Cerebral venous thrombosis: state of the art diagnosis and management.** *Neuroradiology* 2018;60:669–85 CrossRef Medline
- Leach JL, Fortuna RB, Jones BV, et al. **Imaging of cerebral venous thrombosis: current techniques, spectrum of findings, and diagnostic pitfalls.** *Radiographics* 2006;26(Suppl 1):S19–41 CrossRef Medline
- Sari S, Verim S, Hamcan S, et al. **MRI diagnosis of dural sinus-cortical venous thrombosis: immediate post-contrast 3D GRE T1-weighted imaging versus unenhanced MR venography and conventional MR sequences.** *Clin Neurol Neurosurg* 2015;134:44–54 CrossRef Medline
- Ray JG, Vermeulen MJ, Bharatha A, et al. **Association between MRI exposure during pregnancy and fetal and childhood outcomes.** *JAMA* 2016;316:952–61 CrossRef Medline
- Thomsen H, Morcos SK; European Society of Urogenital Radiology. **USUR guidelines on contrast agents.** *Abdom Imaging* 2006;31:131–40 CrossRef Medline
- Kanda T, Ishii K, Kawaguchi H, et al. **High signal intensity in the dentate nucleus and globus pallidus on unenhanced T1-weighted MR images: relationship with increasing cumulative dose of a gadolinium-based contrast material.** *Radiology* 2014;270:834–41 CrossRef Medline
- Hinman JM, Provenzale JM. **Hypointense thrombus on T2-weighted MR imaging: a potential pitfall in the diagnosis of dural sinus thrombosis.** *Eur J Radiol* 2002;41:147–52 CrossRef Medline
- Bianchi D, Maeder P, Bogousslavsky J, et al. **Diagnosis of cerebral venous thrombosis with routine magnetic resonance: an update.** *Eur Neurol* 1998;40:179–90 CrossRef Medline
- Vogl TJ, Bergman C, Villringer A, et al. **Dural sinus thrombosis: value of venous MR angiography for diagnosis and follow-up.** *AJR Am J Roentgenol* 1994;162:1191–98 CrossRef Medline
- Isensee C, Reul J, Thron A. **Magnetic resonance imaging of thrombosed dural sinuses.** *Stroke* 1994;25:29–34 CrossRef Medline
- Dormont D, Anxionnat R, Evrard S, et al. **MRI in cerebral venous thrombosis [in French].** *J Neuroradiol* 1994;21:81–99 Medline
- Mugler JP 3rd. **Optimized three-dimensional fast-spin-echo MRI.** *J Magn Reson Imaging* 2014;39:745–67 CrossRef Medline
- Mugler JP, Bao S, Mulkern RV, et al. **Optimized single-slab three-dimensional spin-echo MR imaging of the brain.** *Radiology* 2000;216:891–99 CrossRef Medline
- Mugler JP, Wald LL, Brookeman JR. **T2-weighted 3D spin-echo train imaging of the brain at 3 Tesla: reduced power deposition using low flip-angle refocusing RF pulses.** In: *Proceedings of the 9th Annual Meeting of International Society for Magnetic Resonance in Medicine*, Glasgow, Scotland. April 21–27, 2001
- Saindane AM, Mitchell BC, Kang J, et al. **Performance of spin-echo and gradient-echo T1-weighted sequences for evaluation of dural venous sinus thrombosis and stenosis.** *AJR Am J Roentgenol* 2013;201:162–69 CrossRef Medline
- Hacein-Bey L, Varelas PN, Ulmer JL, et al. **Imaging of cerebrovascular disease in pregnancy and the puerperium.** *AJR Am J Roentgenol* 2016;206:26–38 CrossRef Medline
- American College of Radiology. **ACR Manual on Contrast Media.** 2021. <https://www.acr.org/Clinical-Resources/Contrast-Manual>. Accessed July 29, 2021
- Hand JW, Li Y, Thomas EL, et al. **Prediction of specific absorption rate in mother and fetus associated with MRI examinations during pregnancy.** *Magn Reson Med* 2006;55:883–93 CrossRef Medline
- Barrera CA, Francavilla ML, Serai SD, et al. **Specific absorption rate and specific energy dose: comparison of 1.5-T versus 3.0-T fetal MRI.** *Radiology* 2020;295:664–74 CrossRef Medline
- Lichy MP, Horger W, Mugler JP, et al. **T2-weighted 3D MR imaging of the Torso—First Clinical Experiences with SPACE.** *CLINICAL SPACE*. 2005;1. [https://cdn0.scrvt.com/39b415fb07de4d9656c7b516d8e2d907/180000000081895/b135e0f62913/T2-weighted\\_3D\\_MR\\_Imaging\\_of\\_the\\_Torso\\_Page\\_58-60\\_1800000000081895.pdf](https://cdn0.scrvt.com/39b415fb07de4d9656c7b516d8e2d907/180000000081895/b135e0f62913/T2-weighted_3D_MR_Imaging_of_the_Torso_Page_58-60_1800000000081895.pdf). Accessed April 28, 2020
- Bitar R, Leung G, Perng R, et al. **MR pulse sequences: what every radiologist wants to know but is afraid to ask.** *Radiographics* 2006;26:513–37 CrossRef Medline
- Mihai G, Winner MW, Raman SV, et al. **Assessment of carotid stenosis using three-dimensional T2-weighted dark blood imaging: initial experience.** *J Magn Reson Imaging* 2012;35:449–55 CrossRef Medline
- Morelli JN, Runge VM, Ai F, et al. **An image-based approach to understanding the physics of MR artifacts.** *Radiographics* 2011;31:849–66 CrossRef Medline
- Wang D, Lu Y, Yin B, et al. **3D fast spin-echo T1 black-blood imaging for the preoperative detection of venous sinus invasion by meningioma.** *Clin Neuroradiol* 2019;29:65–73 CrossRef Medline
- Qureshi AI, Qureshi Z, Center SR. **A classification scheme for assessing recanalization and collateral formation following cerebral venous thrombosis.** *J Vasc Interv Neurol* 2010;3:1–2 Medline
- Ferro JM, Bendszus M, Jansen O, et al; RE-SPECT CVT Study Group. **Recanalization after cerebral venous thrombosis: a randomized controlled trial of the safety and efficacy of dabigatran etexilate versus dose-adjusted warfarin in patients with cerebral venous and dural sinus thrombosis.** *Int J Stroke* 2022;17:189–97 CrossRef Medline
- Aguiar de Sousa D, Lucas Neto L, Arauz A, et al. **Early recanalization in patients with cerebral venous thrombosis treated with anticoagulation.** *Stroke* 2020;51:1174–81 CrossRef Medline
- Ghoneim A, Straiton J, Pollard C, et al. **Imaging of cerebral venous thrombosis.** *Clin Radiol* 2020;75:254–64 CrossRef Medline

# Differential Subsampling with Cartesian Ordering–MRA for Classifying Residual Treated Aneurysms

P. Shahrouki, R. Gupta, P. Belani, A. Chien, A.H. Doshi, R. De Leacy, J.T. Fifi, J. Mocco, and K. Nael



## ABSTRACT

**BACKGROUND AND PURPOSE:** Differential Subsampling with Cartesian Ordering (DISCO), an ultrafast high-spatial-resolution head MRA, has been introduced. We aimed to determine the diagnostic performance of DISCO-MRA in grading residual aneurysm in comparison with TOF-MRA in patients with treated intracranial aneurysms.

**MATERIALS AND METHODS:** Patients with endovascular treatment and having undergone DISCO-MRA, TOF-MRA, and DSA were included for review. The voxel size and acquisition time were  $0.75 \times 0.75 \times 1 \text{ mm}^3/6$  seconds for DISCO-MRA and  $0.6 \times 0.6 \times 1 \text{ mm}^3/6$  minutes for TOF-MRA. Residual aneurysms were determined using the Modified Raymond-Roy Classification on TOF-MRA and DISCO-MRA by 2 neuroradiologists independently and were compared against DSA as the reference standard. Statistical analysis was performed using the  $\kappa$  statistic and the  $\chi^2$  test.

**RESULTS:** Sixty-eight treated intracranial aneurysms were included. The intermodality agreement was  $\kappa = 0.82$  (95% CI, 0.67–0.97) between DISCO and DSA and 0.44 (95% CI, 0.28–0.61) between TOF and DSA. Modified Raymond-Roy Classification scores matched DSA scores in 60/68 cases (88%;  $\chi^2 = 144.4$ ,  $P < .001$  for DISCO and 46/68 cases (68%;  $\chi^2 = 65.0$ ,  $P < .001$ ) for TOF. The diagnostic accuracy for the detection of aneurysm remnants was higher for DISCO (0.96; 95% CI, 0.88–0.99) than for TOF (0.79; 95% CI, 0.68–0.88).

**CONCLUSIONS:** In patients with endovascularly treated intracranial aneurysms, DISCO-MRA provides superior diagnostic performance in comparison with TOF-MRA in delineating residual aneurysms in a fraction of the time.

**ABBREVIATIONS:** ARC = Autocalibrating Reconstruction for Cartesian; CE = contrast-enhanced; DISCO = Differential Subsampling with Cartesian Ordering; EVT = endovascular treatment; IA = intracranial aneurysm; IQR = interquartile range; MRRC = Modified Raymond-Roy Classification; NPV = negative predictive value; PPV = positive predictive value

Endovascular treatment (EVT) is considered the primary strategy for intracranial aneurysms (IAs) in most cases in many institutions, with lower morbidity and mortality compared with microsurgical clipping for most aneurysms.<sup>1,2</sup>

However, subtotal occlusion or recanalization has been raised as a limitation of EVT, with reports of up to 20% of patients demonstrating deterioration in occlusion status on follow-up imaging.<sup>3–5</sup>

Therefore, noninvasive imaging such as CTA or MRA is commonly used in the serial follow-up of these patients, and while there is no universally accepted strategy, the frequency and type of imaging used should be balanced against patient safety and cost.<sup>6</sup>

For institutions that use MRA for follow-up of patients with treated aneurysms, both TOF-MRA and contrast-enhanced MRA (CE-MRA) can be used, each with some benefits and drawbacks. During the past 2 decades, there has been an increasing evolution of CE-MRA techniques, with improved diagnostic performance, which was achieved, at least partly, via the introduction of fast imaging tools such as Generalized Autocalibrating Partially Parallel Acquisition or Autocalibrating Reconstruction for Cartesian (ARC) imaging and a variety of  $k$ -space undersampling schemes.<sup>7–11</sup>

An ultrafast, high-spatiotemporal-resolution CE-MRA, using Differential Subsampling with Cartesian Ordering (DISCO) has been introduced for the depiction of IAs.<sup>12</sup> In this study, we aimed to assess the diagnostic accuracy of DISCO-MRA in treated aneurysms and to classify aneurysm occlusion in a comparative analysis with TOF-MRA, with DSA as the reference standard.

Received September 11, 2021; accepted after revision April 14, 2022.

From the Department of Radiological Sciences (P.S., A.C., K.N.), University of California Los Angeles, Los Angeles, California; and Departments of Radiology (R.G., P.B., A.H.D., K.N.) and Neurosurgery (R.D.L., J.T.F., J.M.), Icahn School of Medicine at the Mount Sinai Hospital, New York, New York.

This work was supported by the National Institutes of Health (NIH R01HL152270) for Aichi Chien.

Please address correspondence to Kambiz Nael, MD, Department of Radiological Sciences, University of California Los Angeles, 757 Westwood Plaza, Suite 1621, Los Angeles, CA 90095–7532; e-mail: kambiznael@gmail.com; @KambizNael

Indicates open access to non-subscribers at [www.ajnr.org](http://www.ajnr.org)

Indicates article with online supplemental data.

<http://dx.doi.org/10.3174/ajnr.A7532>



## MATERIALS AND METHODS

### Patients

This retrospective review of prospectively collected data was approved by the Mount Sinai Hospital Institutional Review Board. Patients with IAs who presented between January 2016 and January 2019 were reviewed and included if they had an aneurysm treated by EVT and had follow-up DSA and MRA after treatment.

### Image Acquisition

CE-MRA and TOF-MRA were concurrently performed in all patients on a 3T MR imaging system (Discovery MR750; GE Healthcare) using an 8-channel head coil for signal reception.

For CE-MRA, a single-echo 3D radiofrequency-spoiled gradient-echo sequence was used with the following parameters: TR/TE = 3.7/1.4 ms; flip angle = 12°; matrix = 320 × 256 mm<sup>2</sup>; FOV = 240 × 192 mm<sup>2</sup>; 160 slices × 1.0 mm thick. The DISCO *k*-space segmentation scheme using pseudorandom variable-density *k*-space segmentation and a view-sharing reconstruction was applied,<sup>12</sup> in addition to ARC with an acceleration factor of 2 in both phase-encoding and section-encoding directions. With these settings, a 3D volume with voxel sizes of 0.75 × 0.75 × 1 mm<sup>3</sup> was obtained covering the entire head in a 6-second acquisition. A timing bolus was used to determine the contrast transit time to the intracranial carotid bifurcation during a 30-second image acquisition. A total of 0.05 mmol/kg of gadolinium was injected at 1.5 mL/s to perform CE-MRA.

Multislab TOF-MRA was performed with 6 axial slabs of 32 slices per slab, each 1 mm thick with the following parameters: TR/TE = 20/5.7 ms; flip angle = 20°; matrix = 320 × 296 mm<sup>2</sup>; FOV = 180 × 180 mm<sup>2</sup>; and ARC × 2 (phase-encoding), resulting in the acquisition of 3D voxel sizes of 0.6 × 0.6 × 1 mm<sup>3</sup> during a 6-minute acquisition time.

DSA was performed via transfemoral access and by selective catheterization of the ICA and/or the vertebral artery as appropriate and according to the aneurysm location. Images were obtained in the anteroposterior and lateral projections and in 2 oblique projections (−45° and +45°) for each catheterization. We used the following parameters: matrix = 1024 × 1024 mm; FOV = 17 cm, resulting in spatial resolution of 0.15 × 0.15 mm. The injected volume of contrast medium ranged between 3 and 5 mL per injection. Additional 3D rotational projections were obtained for challenging cases and based on the interventionist's judgment at the time of the procedure in 17 patients (25%).

### Image Analysis

The aneurysm occlusion status was evaluated using the Modified Raymond-Roy Classification (MRRC): class I = complete obliteration; II = residual neck; IIIa = contrast opacification within the coil interstices of a residual aneurysm; or IIIb = contrast opacification outside the coil interstices along the residual aneurysm wall.<sup>13</sup>

Image analysis was performed independently by 2 board-certified neuroradiologists (K.N. and P.B. with 10 and 6 years of experience, respectively) who were blinded to DSA results. DISCO-MRAs and TOF-MRAs were analyzed in different reviewing sessions, and the studies were introduced in a random order to minimize recall bias. All-source MRA data were available and reviewed on a commercially available 3D workstation (Vitre software, Version 7.14; Vital

**Table 1: Patient and aneurysm characteristics**

Characteristics	
Female (No.) (%)	59 (86)
Age (mean) (yr)	59.4 (SD, 11.4)
Aneurysm location	
Internal carotid artery (No.) (%)	28 (41)
Anterior cerebral artery (No.) (%)	3 (4)
Anterior communicating artery (No.) (%)	8 (12)
Middle cerebral artery (No.) (%)	4 (6)
Posterior communicating artery (No.) (%)	17 (25)
Posterior circulation <sup>a</sup> (No.) (%)	8 (12)
Endovascular treatment	
Stent only (No.) (%)	6 (9)
Coil only (No.) (%)	34 (50)
Stent-assisted coil (No.) (%)	28 (41)

<sup>a</sup> Includes aneurysms involving the posterior cerebral artery (*n* = 1), vertebral artery (*n* = 3), and basilar artery (*n* = 4).

Images) with 3D multiplanar reformations available. Disagreements in the grading of residual aneurysms were resolved by a consensus read, which was, in turn, used for comparative analysis against DSA. The aneurysm occlusion class on DSA was extracted from our aneurysm data registry, which is prospectively collected and updated as patients undergo treatment.

### Statistical Analysis

Continuous data were presented as means with SDs or median with interquartile range (IQR), and categorical data were presented as absolute values with percentages.  $\kappa$  statistic and 95% confidence intervals were calculated to determine both the interobserver and intermodality agreement. The  $\chi^2$  test was used to determine differences in MRRC matches between DISCO-MRA and TOF-MRA. The sensitivity, specificity, positive predictive value (PPV), negative predictive value (NPV), and accuracy of DISCO and TOF-MRA for the detection of aneurysm remnants were determined. Statistical analysis was performed on SPSS software (Version 27.0; IBM). A *P* value < .05 was considered statistically significant.

## RESULTS

Sixty-eight treated IAs in 68 patients (59 women; mean age, 59.4 [SD, 11.4] years) were included for analysis (Table 1). Aneurysm locations included the anterior circulation (60/68, 88%) and posterior circulation (8/68, 12%; Table 1). The median time between the MRA and DSA was 99 days (IQR = 29–186 days), with DSA performed before MRA in most cases (47/68, 69%). The median time between endovascular treatment to the first follow-up examination (MRA or DSA) was 598 days (IQR, 567–622 days).

The interobserver agreement for the MRRC of aneurysms was near-identical for DISCO-MRA and TOF-MRA ( $\kappa$  = 0.61; 95% CI, 0.45–0.77 for DISCO-MRA and  $\kappa$  = 0.63; 95% CI, 0.44–0.81 for TOF-MRA). The intermodality agreement for the MRRC was higher between DISCO and DSA ( $\kappa$  = 0.82; 95% CI, 0.67–0.97) than between TOF and DSA ( $\kappa$  = 0.44; 95% CI, 0.28–0.61).

Analysis of the MRRC revealed a higher number of class matches between the DISCO and DSA evaluations (60/68, 88%;  $\chi^2$  = 144.4, *P* < .001) compared with TOF and DSA (46/68, 68%;  $\chi^2$  = 65.0, *P* < .001) (Table 2).

Among 33 completely occluded treated aneurysms (MRRC I), 32 (97%) were correctly identified by both DISCO and TOF-MRA.

**Table 2: MRRC class matches between DSA and DISCO-MRA and TOF-MRA<sup>a</sup>**

DSA	DISCO-MRA					TOF-MRA				
	I	II	IIIa	IIIb	Total	I	II	IIIa	IIIb	Total
I	32	1	0	0	33 (49)	32	1	0	0	33 (49)
II	2	15	3	0	20 (29)	11	9	0	0	20 (29)
IIIa	0	2	6	0	8 (12)	1	4	3	0	8 (12)
IIIb	0	0	0	7	7 (10)	1	4	0	2	7 (10)
Total	34 (50)	18 (26)	9 (13)	7 (10)	68 (100)	45 (66)	18 (26)	3 (4)	2 (3)	68 (100)

<sup>a</sup> Data are presented as counts with percentages in parenthesis.

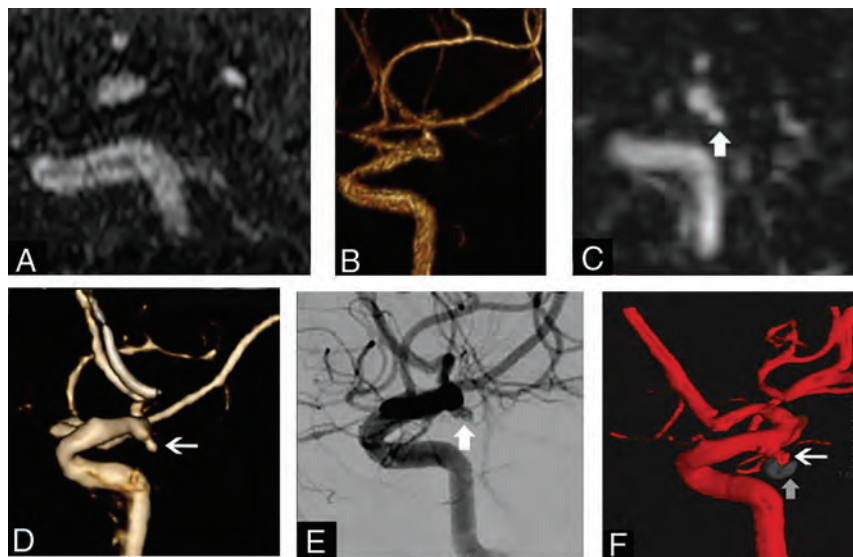


**FIG 1.** A 56-year-old woman status post coil embolization of a posterior communicating artery aneurysm. Sagittal multiplanar reformats and volume-rendered images from TOF-MRA (A and B) and DISCO-MRA (C and D) in addition to sagittal projection and 3D from DSA (white arrows in E and F) are shown. There is a recanalized aneurysm measuring approximately 5 mm (MRRC IIIB) seen on the DSA images (E and F). Note the location of the embolization coil mass (vertical arrow on F). The recanalized aneurysm is visualized with a similar size and conspicuity on DISCO-MRA (arrows on C and D), while it is not clearly seen on TOF-MRA (A and B).

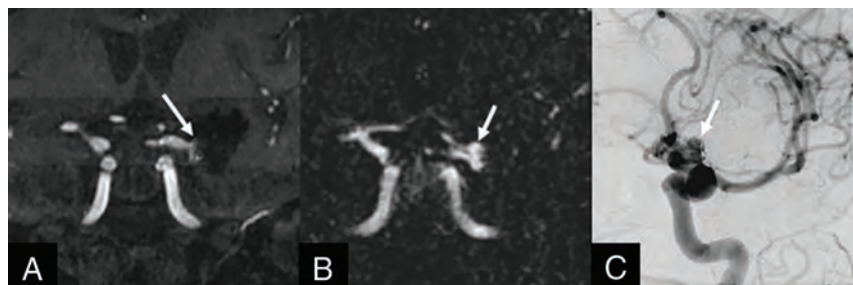


**FIG 2.** A 70-year-old woman status post endovascular treatment of a left ICA bifurcation aneurysm. Coronal multiplanar reformats from TOF-MRA (A) and DISCO-MRA (B) and coronal-oblique DSA (C) are shown. There is a 6-mm residual neck (MRRC II) at the base of the coil embolization mass on DSA (arrow in C), which is also noted with a similar size and conspicuity on DISCO-MRA (arrow in B). The residual aneurysm neck is less conspicuous on TOF-MRA (arrow in A), where it was scored as MRRC I by 1 observer.

However, class matches for recanalized IAS (MRRC II–IV) against DSA were 28/35 (80%) for DISCO-MRA and 14/35 (40%) for TOF-MRA (Table 2). In particular, among patients with higher grade remnants (MRRC IIIa/IIIb,  $n = 15$ ), 13 (86%) remnants were correctly identified on DISCO-MRA, while only 5 (33%) were identified

on TOF-MRA. Examples of aneurysm recanalization seen on TOF-MRA and DISCO-MRA in comparison with DSA are shown in Figs 1 and 2.

The diagnostic accuracy of DISCO-MRA was higher than that of TOF-MRA for the detection of aneurysm remnants (MRRC II–IIIb; Online Supplemental Data). The specificity and PPV were comparable between the modalities (equal low false-positive counts), with the sensitivity and NPV of DISCO-MRA being higher than that of TOF-MRA (Online Supplemental Data).

In a subgroup analysis comparing aneurysms that were treated with stents versus no stents, similar results were identified, with the specificity and PPV being comparable, while the sensitivity and NPV were substantially higher in DISCO-MRA versus TOF-MRA (Online Supplemental Data). Figure 3 shows an example of an aneurysm treated by a stent; the higher grade of the aneurysm remnant was correctly identified by DISCO-MRA.

The sensitivity and NPV in patients treated with stents were 100% and 100%, respectively, for DISCO-MRA in comparison with 63% and 74% for TOF-MRA. In the stented subgroup, a total of 13 aneurysm remnants were misclassified by TOF-MRA versus 3 by DISCO-MRA. The breakdown of aneurysm-remnant misclassification in this group for TOF-MRA versus DISCO-MRA was the following: grade I (1 versus 1), grade II (5 versus 0), grade IIIa (4 versus 2), and grade IIIb (3 versus 0).

In the absence of stent placement, the sensitivity and NPV were 89% and 88% for DISCO in comparison with 63% and 68% for TOF-MRA (Online Supplemental Data). In the nonstented subgroup, a total of 9 aneurysm remnants were misclassified by TOF-MRA versus 5 misclassified by DISCO-MRA. The breakdown of aneurysm-remnant misclassification in this group for TOF-MRA versus DISCO-MRA was the following: grade II (6 versus 5), grade IIIa (1 versus 0), and grade IIIb (2 versus 0).

## DISCUSSION

Results showed that in patients with IAs treated by EVT, ultrafast, high-spatial-resolution CE-MRA achieved by DISCO outperformed TOF-MRA compared with the conventional standard for the evaluation of residual aneurysms. DISCO-MRA had higher

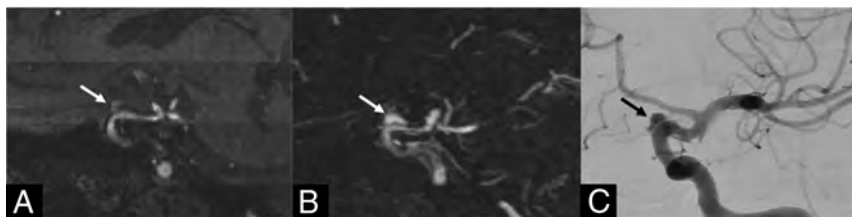


**FIG 3.** A 67-year-old woman with an aneurysm of the left supraclinoid ICA, treated with a Pipeline Embolization Device (Medtronic) stent. Sagittal oblique multiplanar reformats from TOF-MRA (A) and DISCO-MRA (B) and sagittal-oblique DSA (C) are shown. There is a 4-mm residual aneurysm (MRRC IIIb) projecting superior to the stent on DSA (arrow in C), which is also noted with similar size and conspicuity on DISCO-MRA (arrow in B). The residual aneurysm is less conspicuous on TOF-MRA (arrow in A), where it was scored as MRRC I by one observer and II by the other.

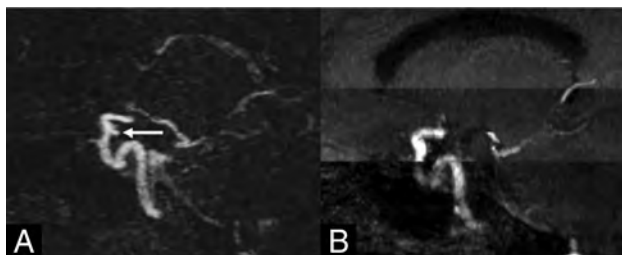


**FIG 4.** A 57-year-old woman with an aneurysm of the right supraclinoid ICA, treated with coil embolization. Sagittal oblique multiplanar reformats from DISCO-MRA (A) and TOF-MRA (B) are shown. There is a 3-mm posteriorly projecting residual aneurysm at the base of coil embolization noted on DISCO-MRA (arrow in A), which was acquired during a 6-second acquisition time. Note that the residual aneurysm is not well-evaluated on the concurrent motion-degraded TOF-MRA, which was obtained during an approximately 6-minute acquisition time.

accuracy and agreement with DSA than TOF-MRA and was performed in a fraction of the time.

The specificity and PPV were similar between DISCO and TOF-MRA (>90%), and the sensitivity and NPV were markedly lower for TOF-MRA for the detection of aneurysm remnants. When there was no remnant (MRRC I), both DISCO and TOF-MRA correctly identified the MRRC in most cases (97% for both). We showed that the difference in class matches was most pronounced for the higher classes, particularly class III. The MRRC highlights the importance of differentiating between class IIIa and IIIb because the latter has a higher risk of incomplete occlusion, recanalization, and possibly rupture.<sup>13,14</sup> Therefore, underestimating class III aneurysms, as was more common with TOF-MRA in our study (10 for TOF-MRA compared with 2 for DISCO-MRA) could prove to be a critical limitation of TOF-MRA in long-term follow-up of patients with treated intracranial aneurysms. The reason for this underestimation is likely related to the sensitivity of TOF-MRA to turbulent or slow flow, a common finding in patients after EVT.<sup>15</sup> Conversely, CE-MRA is substantially faster than TOF-MRA and avoids flow-related artifacts by using intravascular contrast. However, although our study showed that both DISCO-MRA and TOF-MRA had very few cases in which the MRRC was overestimated, there were a few more overestimated with DISCO-MRA (4/68) than with TOF-MRA (1/68). This finding

may be explained by differences in spatial resolution and slightly larger voxel sizes of DISCO-MRA in comparison with TOF-MRA, with a potential for volume averaging.

In terms of diagnostic performance, our results are concordant with the results of prior studies, showing slightly higher performance of CE-MRA compared with TOF-MRA in identifying residual aneurysms.<sup>16-18</sup> However, our study reports a disproportionately lower sensitivity of TOF-MRA compared with prior reports mainly due to a high false-negative count.

This finding is consistent with those of prior reports,<sup>19-21</sup> with the higher false-negative rate in TOF-MRA attributed to flow-related disturbance in the presence of flow-diverting stents or slow flow associated with coil embolization, despite residual/recanalized aneurysms. Our subanalysis revealed a higher proportion of aneurysm-remnant misclassification via TOF-MRA in patients treated with stents (13 versus 3 by DISCO-MRA) in comparison with 9 versus 5 in patients treated without stents.

The superior accuracy of DISCO-MRA compared with TOF-MRA, paired with its shorter acquisition time, makes it an attractive alternative for routine follow-up of endovascularly treated IAs. Shorter acquisition times can facilitate the examination of patients with claustrophobia, decrease the likelihood of a motion artifact-degraded study (Fig 4), and improve throughput. In comparison with conventional CE-MRA techniques, DISCO-MRA provides substantially faster acquisition time over a large FOV (whole-head coverage) without compromising image quality, which has traditionally been a concern with ultrafast MR imaging protocols.<sup>22</sup> One clear limitation of DISCO-MRA is the requirement for the administration of gadolinium-based contrast, with a small risk of an allergic reaction or other unwanted adverse effects, especially given recent concerns for tissue deposition.<sup>23</sup> However, the superior diagnostic performance in identifying higher class residuals may outweigh this risk. One way to mitigate the concerns about long-term and repetitive use of gadolinium injection would be to adopt a hybrid protocol of performing CE-MRA for the first 2 years, when the risk of recanalization is highest, and then switching to TOF-MRA or alternative follow-up examinations. Newer noncontrast MRA techniques have also been developed such as Silent MRA<sup>24-26</sup> and pointwise encoding time reduction with radial acquisition MRA,<sup>27</sup> with promising results in the detection of residual aneurysms.

Also, although contrast administration can increase the cost compared with non-contrast-enhanced studies (TOF-MRA) on an individual level,<sup>6</sup> the ultrafast protocol used allows streamlined workflow, potentially decreasing the long-term cost to an institution.

Our study has several limitations. Our sample size is relatively small. The retrospective nature introduces unknown bias. The inherent difference in spatial resolution between DISCO-MRA and TOF-MRA can limit reliable comparisons. 3D DSA was only performed in a selected group of challenging cases ( $n=17$ ), while 2D DSA, as a less ideal reference, was used in the remainder of



patients. The time differences (median: 99 days) between MRA examinations and DSA as the criterion standard were another limitation. It is plausible that aneurysm-occlusion grading has undergone some interval change, introducing variability in comparative analysis between DSA and MRA. However, this potential interval change in aneurysm residuals should have a modest effect in comparisons between TOF- and DISCO-MRA because they were obtained at the same time.

Another limitation is that MRRC was originally presented as a classification system for treated IAs assessed by DSA, and to the authors' knowledge, only 1 study has validated its use in MRA to date.<sup>28</sup> However, our study did not aim to prove the prognostic value of MRA, only to strictly prove the anatomic accuracy of DISCO-MRA compared with TOF-MRA, which aligns with the original intent of the unmodified Raymond-Roy occlusion classification to anatomically classify treated aneurysms.<sup>29</sup> Future studies should look at the prognostic value of the MRRC evaluated by MRA, including using the DISCO scheme in a larger sample size.

## CONCLUSIONS

3T DISCO-MRA outperforms TOF-MRA with respect to accuracy and speed, with increased concordance to conventional DSA for the evaluation and grading of residual IAs after EVT. This technique may be of value in the follow-up evaluation of treated IAs.

**Disclosure forms** provided by the authors are available with the full text and PDF of this article at [www.ajnr.org](http://www.ajnr.org).

## REFERENCES

- Molyneux A, Kerr R, Stratton I, et al; International Subarachnoid Aneurysm Trial (ISAT) Collaborative Group. **International Subarachnoid Aneurysm Trial (ISAT) of neurosurgical clipping versus endovascular coiling in 2143 patients with ruptured intracranial aneurysms: a randomised trial.** *Lancet* 2002;360:1267–74 CrossRef Medline
- Naggara ON, White PM, Guilbert F, et al. **Endovascular treatment of intracranial unruptured aneurysms: systematic review and meta-analysis of the literature on safety and efficacy.** *Radiology* 2010;256:887–97 CrossRef Medline
- De Leacy RA, Fargen KM, Mascitelli JR, et al. **Wide-neck bifurcation aneurysms of the middle cerebral artery and basilar apex treated by endovascular techniques: a multicentre, core lab adjudicated study evaluating safety and durability of occlusion (BRANCH).** *J Neurointerv Surg* 2019;11:31–36 CrossRef Medline
- Ferns SP, Sprengers ME, van Rooij WJ, et al. **Coiling of intracranial aneurysms: a systematic review on initial occlusion and reopening and retreatment rates.** *Stroke* 2009;40:e523–29 CrossRef Medline
- Molyneux AJ, Birks J, Clarke A, et al. **The durability of endovascular coiling versus neurosurgical clipping of ruptured cerebral aneurysms: 18-year follow-up of the UK cohort of the International Subarachnoid Aneurysm Trial (ISAT).** *Lancet* 2015;385:691–97 CrossRef Medline
- Soize S, Gawlitza M, Raoult H, et al. **Imaging follow-up of intracranial aneurysms treated by endovascular means: why, when, and how?** *Stroke* 2016;47:1407–12 CrossRef Medline
- Korosec FR, Frayne R, Grist TM, et al. **Time-resolved contrast-enhanced 3D MR angiography.** *Magn Reson Med* 1996;36:345–51 CrossRef Medline
- Lim RP, Shapiro M, Wang EY, et al. **3D time-resolved MR angiography (MRA) of the carotid arteries with time-resolved imaging with stochastic trajectories: comparison with 3D contrast-enhanced bolus-chase MRA and 3D time-of-flight MRA.** *AJNR Am J Neuroradiol* 2008;29:1847–54 CrossRef
- Madhuranthakam AJ, Hu HH, Barger AV, et al. **Undersampled elliptical centric view-order for improved spatial resolution in contrast-enhanced MR angiography.** *Magn Reson Med* 2006;55:50–58 CrossRef
- Stalder AF, Schmidt M, Quick HH, et al. **Highly undersampled contrast-enhanced MRA with iterative reconstruction: integration in a clinical setting.** *Magn Reson Med* 2015;74:1652–60 CrossRef Medline
- Griswold MA, Jakob PM, Heidemann RM, et al. **Generalized autocalibrating partially parallel acquisitions (GRAPPA).** *Magn Reson Med* 2002;47:1202–10 CrossRef Medline
- Nael K, Drummond J, Costa AB, et al. **Differential Subsampling with Cartesian Ordering for ultrafast high-resolution MRA in the assessment of intracranial aneurysms.** *J Neuroimaging* 2020;30:40–44 CrossRef Medline
- Mascitelli JR, Moyle H, Oermann EK, et al. **An update to the Raymond-Roy occlusion classification of intracranial aneurysms treated with coil embolization.** *J NeuroInterv Surg* 2015;7:496–502 CrossRef Medline
- Stapleton CJ, Torok CM, Rabinov JD, et al. **Validation of the Modified Raymond-Roy classification for intracranial aneurysms treated with coil embolization.** *J NeuroInterv Surg* 2016;8:927–33 CrossRef Medline
- Deuschmann HA, Augustin M, Simbrunner J, et al. **Diagnostic accuracy of 3D time-of-flight MR angiography compared with digital subtraction angiography for follow-up of coiled intracranial aneurysms: influence of aneurysm size.** *AJNR Am J Neuroradiol* 2007;28:628–34 Medline
- Ahmed SU, Mocco J, Zhang X, et al. **MRA versus DSA for the follow-up imaging of intracranial aneurysms treated using endovascular techniques: a meta-analysis.** *J Neurointerv Surg* 2019;11:1009–14 CrossRef Medline
- Anzalone N, Scmazzone F, Cirillo M, et al. **Follow-up of coiled cerebral aneurysms at 3T: comparison of 3D time-of-flight MR angiography and contrast-enhanced MR angiography.** *AJNR Am J Neuroradiol* 2008;29:1530–36 CrossRef Medline
- van Amerongen MJ, Boogaarts HD, de Vries J, et al. **MRA versus DSA for follow-up of coiled intracranial aneurysms: a meta-analysis.** *AJNR Am J Neuroradiol* 2014;35:1655–61 CrossRef Medline
- Attali J, Benaissa A, Soize S, et al. **Follow-up of intracranial aneurysms treated by flow diverter: comparison of three-dimensional time-of-flight MR angiography (3D-TOF-MRA) and contrast-enhanced MR angiography (CE-MRA) sequences with digital subtraction angiography as the gold standard.** *J Neurointerv Surg* 2016;8:81–86 CrossRef Medline
- Binyamin TR, Dahlin BC, Waldau B. **Comparison of 3D TOF MR angiographic accuracy in predicting Raymond grade of flow-diverted versus coiled intracranial aneurysms.** *J Clin Neurosci* 2017;42:182–85 CrossRef Medline
- Boddu SR, Tong FC, Dehkharghani S, et al. **Contrast-enhanced time-resolved MRA for follow-up of intracranial aneurysms treated with the Pipeline embolization device.** *AJNR Am J Neuroradiol* 2014;35:2112–18 CrossRef Medline
- Tsao J. **Ultrafast imaging: principles, pitfalls, solutions, and applications.** *J Magn Reson Imaging* 2010;32:252–66 CrossRef Medline
- Mathur M, Jones JR, Weinreb JC. **Gadolinium deposition and nephrogenic systemic fibrosis: a radiologist's primer.** *Radiographics* 2020;40:153–62 CrossRef Medline
- Ryu KH, Baek HJ, Moon JI, et al. **Usefulness of noncontrast-enhanced silent magnetic resonance angiography (MRA) for treated intracranial aneurysm follow-up in comparison with time-of-flight MRA.** *Neurosurgery* 2020;87:220–28 CrossRef Medline
- Oishi H, Fujii T, Suzuki M, et al. **Usefulness of silent MR angiography for intracranial aneurysms treated with a flow-diverter device.** *AJNR Am J Neuroradiol* 2019;40:808–13 CrossRef Medline
- Takano N, Suzuki M, Irie R, et al. **Non-contrast-enhanced silent scan MR angiography of intracranial anterior circulation**

- aneurysms treated with a low-profile visualized intraluminal support device. *AJNR Am J Neuroradiol* 2017;38:1610–16 CrossRef
27. Heo YJ, Jeong HW, Baek JW, et al. Pointwise encoding time reduction with radial acquisition with subtraction-based MRA during the follow-up of stent-assisted coil embolization of anterior circulation aneurysms. *AJNR Am J Neuroradiol* 2019;40:815–19 CrossRef Medline
28. Patzig M, Forbrig R, Gruber M, et al. The clinical value of ceMRA versus DSA for follow-up of intracranial aneurysms treated by coil embolization: an assessment of occlusion classifications and impact on treatment decisions. *Eur Radiol* 2021;31:4104–13 CrossRef Medline
29. Raymond J, Guilbert F, Weill A, et al. Long-term angiographic recurrences after selective endovascular treatment of aneurysms with detachable coils. *Stroke* 2003;34:1398–403 CrossRef

# ADC Level is Related to DWI Reversal in Patients Undergoing Mechanical Thrombectomy: A Retrospective Cohort Study

T. Umemura, T. Hatano, T. Ogura, T. Miyata, Y. Agawa, H. Nakajima, R. Tomoyose, H. Sakamoto, Y. Tsujimoto, Y. Nakazawa, T. Wakabayashi, T. Hashimoto, R. Fujiki, W. Shiraishi, and I. Nagata



## ABSTRACT

**BACKGROUND AND PURPOSE:** In patients with ischemic stroke, DWI lesions can occasionally be reversed by reperfusion therapy. This study aimed to ascertain the relationship between ADC levels and DWI reversal in patients with acute ischemic stroke who underwent recanalization treatment.

**MATERIALS AND METHODS:** We conducted a retrospective cohort study in patients with acute ischemic stroke who underwent endovascular mechanical thrombectomy with successful recanalization between April 2017 and March 2021. DWI reversal was assessed through follow-up MR imaging approximately 24 hours after treatment.

**RESULTS:** In total, 118 patients were included. DWI reversal was confirmed in 42 patients. The ADC level in patients with reversal was significantly higher than that in patients without reversal. Eighty-three percent of patients with DWI reversal areas had mean ADC levels of  $\geq 520 \times 10^{-6} \text{ mm}^2/\text{s}$ , and 71% of patients without DWI reversal areas had mean ADC levels of  $< 520 \times 10^{-6} \text{ mm}^2/\text{s}$ . The mean ADC threshold was  $520 \times 10^{-6} \text{ mm}^2/\text{s}$  with a sensitivity and specificity of 71% and 83%, respectively. In multivariate analysis, the mean ADC level (OR, 1.023; 95% CI, 1.013–1.033;  $P < .0001$ ) was independently associated with DWI reversal. Patients with DWI reversal areas had earlier neurologic improvement (NIHSS at 7 days) than patients without reversal areas ( $P < .0001$ ).

**CONCLUSIONS:** In acute ischemic stroke, the ADC value is independently associated with DWI reversal. Lesions with a mean ADC of  $\geq 520 \times 10^{-6} \text{ mm}^2/\text{s}$  are salvageable by mechanical thrombectomy, and DWI reversal areas regain neurologic function. The ADC value is easily assessed and is a useful tool to predict viable lesions.

**ABBREVIATIONS:** IQR = interquartile range; MT = mechanical thrombectomy

In acute ischemic stroke, DWI lesions are considered markers of irreversible ischemia but can occasionally be reversed. Defining the irreversible infarct core is crucial in assessing the risks and benefits of mechanical thrombectomy (MT) in acute ischemic stroke. Various MR imaging methods for selecting patients with ischemic salvageable regions for reperfusion therapies have been reported.<sup>1–3</sup> In these reports, DWI lesions were considered the infarct core; however, there have also been several studies on DWI lesion reversal through reperfusion therapy.<sup>4–6</sup>

The ADC is a measure of the diffusivity of water molecules in tissues. In ischemic tissues, cytotoxic edema leads to a reduction

in the ADC. Severe reduction of the ADC is associated with metabolic energy failure, which subsequently results in an infarct core.<sup>7,8</sup> Given the DWI lesion reversal, mild ADC reduction could be reversed to normal ADC levels with early reperfusion.<sup>6,9</sup> Such findings suggest that mild ADC reduction before metabolic energy failure is still reversible by reperfusion therapy.

We hypothesized that an ADC threshold that preserves the viability by reperfusion therapy exists in DWI lesions, explaining the concept of DWI reversal and neurologic improvement. Thus, in this study, we aimed to investigate the association between the ADC level and DWI reversal in patients with acute ischemia due to large-vessel occlusion recanalized by endovascular MT.

## MATERIALS AND METHODS


### Study Design and Patient Selection

This was a retrospective cohort study of patients with acute ischemic stroke who underwent endovascular MT between April 2017 and March 2021. The study protocol was approved by the institutional review board of our hospital. The requirement for written

Received November 17, 2021; accepted after revision March 17, 2022.

From the Departments of Neurosurgery (T.U., T.H., T.O., T.M., Y.A., H.N., R.T., H.S., Y.T., Y.N., T.W., I.N.) and Neurology (T.H., R.F., W.S.), Stroke Center, Kokura Memorial Hospital, Kitakyushu City, Japan.

Please address correspondence to Takeru Umemura, MD, PhD, Department of Neurosurgery, Kokura Memorial Hospital, 3-2-1 Asano, Kokurakita-ku, Kitakyushu City, Fukuoka 802-8555, Japan; e-mail: takeru.u115@gmail.com

 Indicates article with online supplemental data.

<http://dx.doi.org/10.3174/ajnr.A7510>



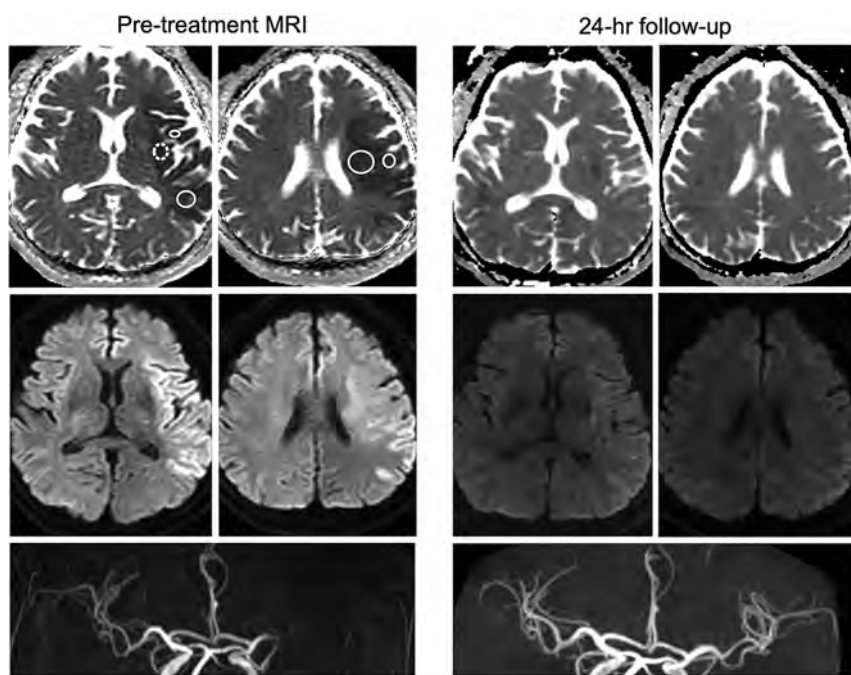


**FIG 1.** Lesions with DWI reversal assessed by MR imaging DWI/ADC, DWI, ADC, and MRA images show a subtotal reversal of the left frontal ischemic lesion 24 hours after MT for MI occlusion. The ADC values (mean, maximum, minimum) with reversal are measured in the ROIs (white circled area with a continuous line) in the pretreatment MR imaging, and each parameter is averaged. The ADC values (mean, maximum, minimum) without reversal are measured in the ROI (white circled area with a dotted line) at the pretreatment MR imaging. The ADC values of lesions with DWI reversal (mean, maximum, minimum) are  $525 \times 10^{-6} \text{ mm}^2/\text{s}$ ,  $748 \times 10^{-6} \text{ mm}^2/\text{s}$ , and  $368 \times 10^{-6} \text{ mm}^2/\text{s}$ , respectively. The ADC values of lesions without DWI reversal (mean, maximum, minimum) are  $434 \times 10^{-6} \text{ mm}^2/\text{s}$ ,  $560 \times 10^{-6} \text{ mm}^2/\text{s}$ , and  $311 \times 10^{-6} \text{ mm}^2/\text{s}$ , respectively.

informed consent was waived due to the retrospective nature of the study. This study was conducted in accordance with the principles of the Declaration of Helsinki.

Patients diagnosed with acute cerebral infarction were treated with intravenous tPA (0.6 mg/kg) within 4.5 hours of stroke onset and/or MT within 24 hours of onset. Follow-up MR imaging was performed 23–27 hours after MT to evaluate the status of the DWI lesion and recanalized artery.

The inclusion criteria were as follows: 1) diagnosis of symptomatic ischemic stroke; 2) anterior circulation occlusion (ICA, M1, M2, M3); 3) initial and follow-up MR imaging performed; and 4) successful recanalization by MT. The occlusion location was selected on the basis of the most proximal occluded segment on MRA. The degree of vessel occlusion at presentation and after treatment was defined using the modified TICI classification.<sup>10</sup> In this study, successful recanalization was defined as TICI  $\geq 2b$ . Stroke onset time was defined as the onset of symptoms or when a patient was last seen well if the onset was unknown. Recanalization time was defined as the time when the occluded artery reached TICI  $\geq 2b$ . Patients whose conditions worsened due to other health problems or who lacked follow-up MR imaging data because of severe stroke or intracranial hemorrhage were excluded.

We collected the following information from medical records: age, sex, prestroke mRS score, initial NIHSS score, risk factors (hypertension, diabetes mellitus, hyperlipidemia, current

smoking status, prior strokes), stroke subtype, occluded artery, emergency treatment (MT or tPA + MT), ASPECTS-DWI,<sup>11</sup> stroke onset to imaging time, imaging to recanalization time, stroke onset to recanalization time, FLAIR lesions, and ADC values (mean, maximum, and minimum) in DWI lesions. The study end point was the mRS score 3 months after stroke.

### MR Imaging Protocol

Initial and follow-up MR imaging was performed with a 3T scanner (Ingenia 3T CX; Philips Healthcare). The MR imaging protocol included DWI/ADC, T2\*, FLAIR, and intracranial MRA. ADC maps were created for all patients. DWI was performed with single-shot spin-echo diffusion EPI with the following parameters: 220-mm FOV, twenty-seven 4-mm axial sections with a 1.0-mm gap, and a b-value of  $1000 \text{ s/mm}^2$  along 3 orthogonal directions.

### Measurement of ADC and DWI Volume

DWI reversal was evaluated by comparing the initial and 23- to 27-hour posttreatment MR images and was defined as regional ADC normalization at the follow-up.<sup>6</sup> The DWI lesion volume was represented as 11 minus the ASPECTS-DWI<sup>11</sup> score at the initial and follow-up MR imaging. DWI reversal volume was calculated by subtracting the follow-up DWI scores from the initial scores. In cases with DWI reversal, the mean, maximum, and minimum ADC values in the reversal area were measured on the initial MR image. These parameters were obtained from 6- to 10-mm circular ROIs placed in them, excluding the cortex and CSF, in each of 11 areas of DWI lesions using the ASPECTS-DWI method, and the average was calculated (Fig 1). Cases without a reversal area were similarly evaluated (Online Supplemental Data). The ADC values of DWI lesions with reversal were similarly evaluated (Fig 1) and compared with the ADC values without reversal in the same cases.

Image analysis was performed by 2 neurologists (T.U. and T.M.) with at least 10 years of experience in assessing acute ischemic stroke with MR imaging. Both readers were blinded to all clinical and patient information. DWI reversal was determined by consensus, and interrater agreement was evaluated ( $\kappa = 0.92$ ).

### Statistical Analysis

Statistical analyses were performed using GraphPad Prism, Version 7 (GraphPad Software). Categorical variables are expressed as frequencies and percentages, whereas continuous variables are expressed as means (SD) or medians (interquartile range [IQR]).

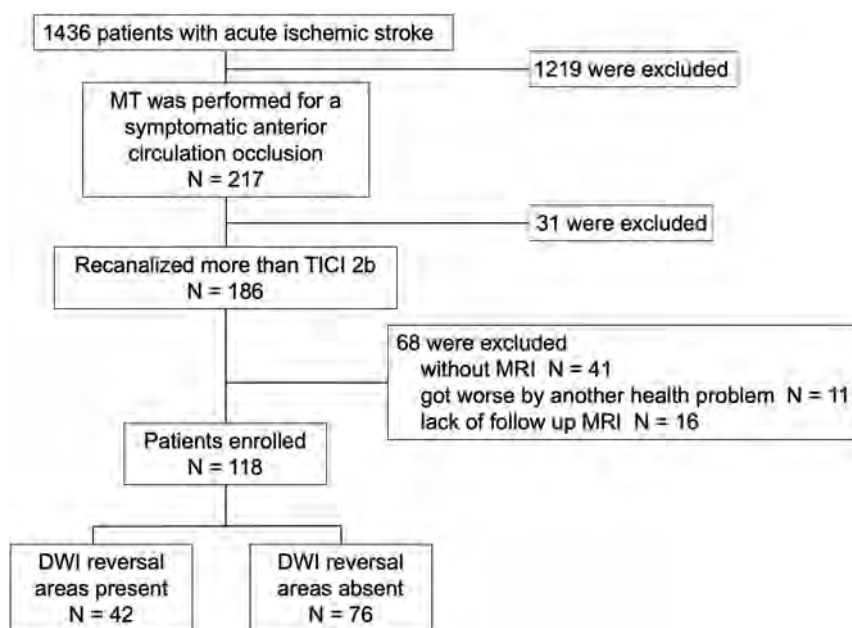


**FIG 2.** Flowchart of the study process.

Baseline characteristics were compared between groups on the basis of the presence or absence of DWI reversal using the  $\chi^2$  test for categoric variables or the Mann-Whitney  $U$  test for continuous variables. Logistic regression analysis was performed using JMP (SAS). The level of statistical significance was set at  $P < .05$ .

## RESULTS

The study included 1436 consecutive patients admitted to our hospital with acute ischemic stroke between April 2017 and March 2021. Among them, MT was performed on 217 patients with symptomatic anterior large-vessel occlusion, and recanalization (TICI  $\geq 2b$ ) was achieved in 186 (86%) patients. Of these 186 patients, those who did not undergo MR imaging due to a cardiac pacemaker or other reasons ( $n = 41$ ), those whose conditions worsened due to other health problems ( $n = 11$ ), and those who did not undergo follow-up MR imaging because of severe stroke conditions or intracranial hemorrhage ( $n = 16$ ) were excluded. After excluding these 68 patients, 118 patients were finally enrolled (Fig 2).

The baseline, clinical, and imaging characteristics, and outcomes of the patients are shown in the Online Supplemental Data. On the basis of the Stop Stroke Study of the Trial of Org 10172 on Acute Stroke Treatment classification<sup>12</sup> and the embolic stroke of undetermined source criteria,<sup>13</sup> stroke subtypes were classified as cardioembolic stroke ( $n = 89$ ), large-artery atherosclerosis ( $n = 15$ ), embolic stroke of undetermined source ( $n = 12$ ), and others ( $n = 2$ ). The “others” classification included cases of ICA dissection. The occluded arteries included the ICA, M1, M2, and M3, and the number of patients with one of these arteries occluded was 27, 62, 28, and 1, respectively. On admission, 58 patients received tPA. The median ASPECTS-DWI was 8 (IQR, 7–9). The median stroke onset to imaging time was 119 minutes (IQR, 60–178 minutes), the imaging to recanalization

time was 59 minutes (IQR, 40–82 minutes), and the stroke onset to recanalization time was 190 minutes (IQR, 112–270 minutes). In the initial MR image, the mean, maximum, and minimum median ADC levels were 515 (IQR, 459–578)  $\times 10^{-6}$  mm<sup>2</sup>/s, 693 (IQR, 581–759)  $\times 10^{-6}$  mm<sup>2</sup>/s, and 387 (IQR, 313–440)  $\times 10^{-6}$  mm<sup>2</sup>/s, respectively. The second MR imaging was performed 23–27 hours after treatment. DWI reversal areas were observed in 42 (36%) of the 118 patients. Representative findings of DWI reversal assessed by MR imaging DWI/ADC are shown in Fig 1 and the Online Supplemental Data. All 118 patients had a DWI/FLAIR mismatch. All 42 patients with DWI reversal did not have FLAIR high intensity in DWI reversal areas at the second MR imaging, and 76 patients without DWI reversal had FLAIR high intensity in all initial DWI lesions at the second

MR imaging. The median baseline, follow-up, and DWI reversal 11 minus ASPECTS-DWI scores were 3 (IQR, 2–5), 3 (IQR, 1–5), and 0 (IQR, 0–1), respectively. The recanalization states were classified as TICI 2b ( $n = 59$ ) or TICI 3 ( $n = 59$ ).

Regarding outcomes, 15 (13%) patients had parenchymal hemorrhage at the follow-up MR imaging. The median NIHSS score at 7 days was 4 (IQR, 2–12), and the median mRS at 3 months was 2 (IQR, 1–4).

There were no significant differences in vascular risk factors, stroke subtypes, occluded arteries, imaging to recanalization time, tPA treatment, ASPECTS-DWI, baseline 11 minus ASPECTS-DWI score, and recanalization state between the groups with and without DWI reversal areas. Patients with DWI reversal areas had significantly shorter times from onset to imaging and onset to recanalization than patients without DWI reversal areas ( $P = .049$ , .01). Additionally, patients with DWI reversal areas had significantly higher mean, maximum, and minimum ADC levels than those without DWI reversal areas (median: 575 [IQR, 539–621] versus 478 [IQR, 434–534],  $P < .0001$ ; 747 [IQR, 695–798] versus 641 [IQR, 562–726],  $P < .0001$ ; and 441 [IQR, 392–517] versus 346 [IQR, 294–411],  $P < .0001$ ). Notably, 83% (35 of 42) of patients with DWI reversal areas had mean ADC values of  $\geq 520 \times 10^{-6}$  mm<sup>2</sup>/s, and 71% (54 of 76) without DWI reversal areas had mean ADC values of  $< 520 \times 10^{-6}$  mm<sup>2</sup>/s (Fig 3). Seventy-four percent (31 of 42) of patients with DWI reversal areas had maximum ADC values of  $\geq 700 \times 10^{-6}$  mm<sup>2</sup>/s, and 66% (50 of 76) of those without DWI reversal areas had ADC values of  $< 700 \times 10^{-6}$  mm<sup>2</sup>/s. Seventy-four percent (31 of 42) of patients with DWI reversal areas had minimum ADC values of  $\geq 400 \times 10^{-6}$  mm<sup>2</sup>/s, and 68% (52 of 76) of those without DWI reversal areas had mean ADC values of  $< 400 \times 10^{-6}$  mm<sup>2</sup>/s. To ascertain the threshold that had reversibility by MT, we performed a receiver operating characteristic analysis using the ADC values of

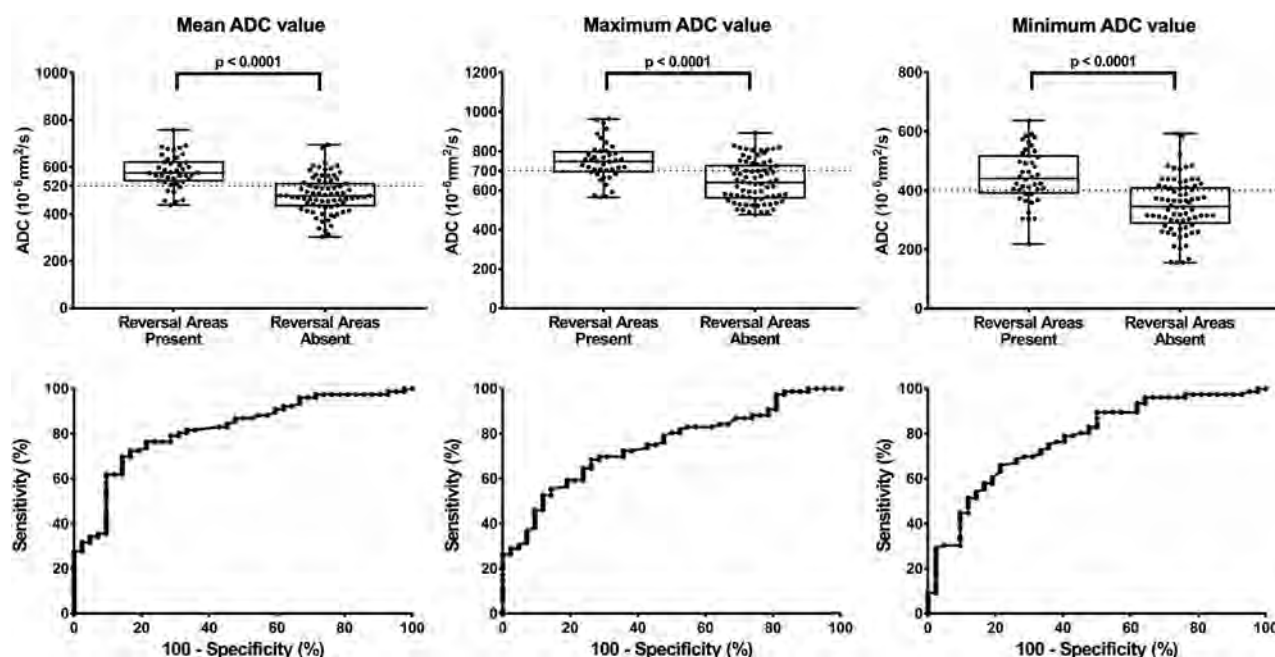


**FIG 3.** The ADC values of the initial DWI lesion (mean, maximum, minimum) according to the presence or absence of DWI reversal areas. Eighty-three percent (35 of 42) of patients with DWI reversal areas had mean ADC values of  $\geq 520 \times 10^{-6} \text{ mm}^2/\text{s}$ , and 71% (54 of 76) of patients without DWI reversal areas had ADC values of  $< 520 \times 10^{-6} \text{ mm}^2/\text{s}$ . Seventy-four percent (31 of 42) of patients with DWI reversal areas had maximum ADC values of  $\geq 700 \times 10^{-6} \text{ mm}^2/\text{s}$ , and 66% (50 of 76) of patients without DWI reversal areas had ADC values of  $< 700 \times 10^{-6} \text{ mm}^2/\text{s}$ . Seventy-four percent (31 of 42) of patients with DWI reversal areas had minimum ADC values of  $\geq 400 \times 10^{-6} \text{ mm}^2/\text{s}$ , and 68% (52 of 76) of patients without DWI reversal areas had ADC values of  $< 400 \times 10^{-6} \text{ mm}^2/\text{s}$ . The ADC values (mean, maximum, minimum) were significantly higher in patients with DWI reversal areas than in those without DWI reversal areas ( $P < .0001$ ). The receiver operating characteristic curve for the collected data of this study (mean, maximum, minimum) shows that the ADC reflects areas that could be reversed by reperfusion therapy. The areas under the curves (mean, maximum, minimum) are 0.82, 0.75, and 0.78, respectively. The optimal mean, maximum, and minimum ADC thresholds for discriminating reversibility from DWI lesions are  $520 \times 10^{-6} \text{ mm}^2/\text{s}$ ,  $700 \times 10^{-6} \text{ mm}^2/\text{s}$ , and  $400 \times 10^{-6} \text{ mm}^2/\text{s}$  with sensitivities of 71%, 68%, and 68% and specificities of 83%, 74%, and 74%, respectively.

reversal and nonreversal areas (Fig 3). The optimal mean, maximum, and minimum ADC thresholds for discriminating reversibility from DWI lesions were  $520 \times 10^{-6} \text{ mm}^2/\text{s}$ ,  $700 \times 10^{-6} \text{ mm}^2/\text{s}$ , and  $400 \times 10^{-6} \text{ mm}^2/\text{s}$  with sensitivities of 71%, 68%, and 68% and specificities of 83%, 74%, and 74%, respectively. The areas under the curve were 0.82, 0.75, and 0.78, respectively (Fig 3).

Patients with DWI reversal areas had significantly lower rates of parenchymal hemorrhage than patients without reversal areas ( $P = .002$ ). The NIHSS score at 7 days and the mRS score at 3 months were significantly lower in patients with DWI reversal than in patients without reversal ( $P < .0001$ ,  $P = .0009$ ). Good functional outcome (mRS scores  $\leq 0-2$ ) after 3 months favored patients with DWI reversal areas ( $P = .011$ ). The mRS distribution calculated at 3 months in patients with and without DWI reversal areas is shown in Fig 4.

In 42 cases with DWI reversal, 22 cases had DWI lesions with and without DWI reversal. In these cases, the ADC values between DWI lesions with and without DWI reversal were compared in the same patients. There was no significant difference between mean and maximum ADC values, excluding minimum ADC values (Online Supplemental Data).

To identify factors associated with DWI reversal, we performed logistic regression analysis for factors (age, sex, initial NIHSS, ASPECTS-DWI, onset to image time, image to recanalization time, mean ADC, and recanalization state). In the multivariate analysis, mean ADC values (OR, 1.023; 95% CI, 1.013–

1.033;  $P < .0001$ ) were associated with DWI reversal (Online Supplemental Data). To identify factors associated with good functional outcomes (mRS 0–2), we performed logistic regression analysis for certain factors (age, sex, initial NIHSS score, ASPECTS-DWI, onset to image time, image to recanalization time, mean ADC, recanalization state, DWI reversal, and parenchymal hemorrhage). In the multivariate analysis, sex (men) (OR, 3.065; 95% CI, 1.081–8.690;  $P = .035$ ), higher ASPECTS-DWI scores (OR, 2.527; 95% CI, 1.666–3.832;  $P < .0001$ ), and recanalization states (TICI 3) (OR, 2.952; 95% CI, 1.074–8.113;  $P = .036$ ) were associated with good functional outcomes (Online Supplemental Data).

## DISCUSSION

This study suggests that the ADC value is independently associated with DWI reversal by reperfusion treatment and that DWI reversal results in early neurologic improvement (NIHSS score at 7 days) and a good prognosis (mRS at 3 months). In previous reports, the reversibility of DWI lesions by reperfusion therapy was unclear. Campbell et al<sup>14</sup> reported that diffusion restriction could indicate irreversible ischemic damage, and Purushotham et al<sup>15</sup> reported that the infarct core region showed an ADC of  $\leq 620 \times 10^{-6} \text{ mm}^2/\text{s}$ . In contrast, permanent DWI lesion reversal is well-established in animal studies using a temporary artery occlusion model.<sup>4,16</sup> In patients treated within 4.5 hours of symptom onset, DWI reversal has often been confirmed and



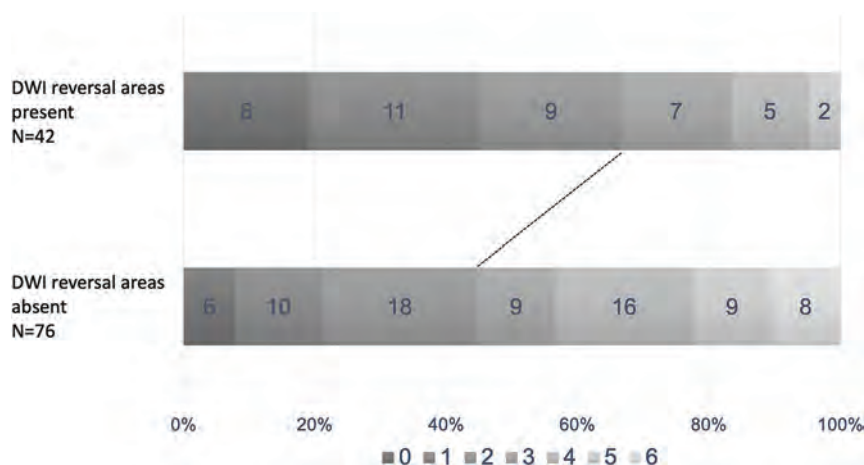


**FIG 4.** mRS score 3 months after treatment. The rate of functional independence (mRS = 0–2) was significantly higher in patients with DWI reversal than in patients without DWI reversal ( $P = .011$ ).

resulted in early neurologic improvement.<sup>5</sup> The current study also supports the reversibility of DWI lesions by reperfusion therapy.

The reported prevalence of patients with DWI reversal varies widely among studies, ranging from 7% to 85%.<sup>14,17</sup> In our study, 42/118 (36%) patients were found to have DWI reversal areas. Discrepancies in the rates of occurrence are likely explained by differences in the operational definition of DWI reversal, particularly in the timing of both acute and follow-up imaging. Our DWI reversal definition was based on follow-up MR imaging performed 23–27 hours after treatment, reflecting the treatment response. Accordingly, 24-hour DWI lesion volumes predict functional outcomes and late FLAIR of infarct volumes.<sup>14</sup> Therefore, our study confirmed that angiographic recanalization (TICI  $\geq$  2b) and consequent DWI reversal are possible. Recently, Yoo et al<sup>18</sup> reported DWI reversal after endovascular treatment in 15.5% of patients with stroke. However, in our study, the rate of DWI reversal was 36%. Two observations can explain this difference. First, the onset-to-recanalization time in the study of Yoo et al (mean DWI reversal: 369 [SD, 212], mean DWI increase: 417 [SD, 232]) was much longer than that in our study. Second, they included patients with TICI 1 or TICI 2a. Meanwhile, our study included only successful recanalization (>TICI 2b). These factors resulted in the high rate of DWI reversal.

Concerning the ADC threshold, Shinoda et al<sup>9</sup> reported that a high relative ADC ratio, indicating the ratio of the ADC values of the affected territory to the ADC values of the contralateral normal brain regions, could result in DWI reversal, with an average relative ADC ratio of 0.890 (SD, 0.045) in reversible DWI lesions and 0.640 (SD, 0.041) in final infarct DWI lesions. Under these circumstances, a mean ADC of  $\geq 520 \times 10^{-6} \text{ mm}^2/\text{s}$  is suitable because the normal ADC level on the contralateral side was  $650\text{--}750 \times 10^{-6} \text{ mm}^2/\text{s}$ . In addition, our study considered maximum and minimum ADC values. Among these parameters, the mean ADC value (ADC threshold:  $520 \times 10^{-6} \text{ mm}^2/\text{s}$ ) had the highest sensitivity and specificity (Fig 3). No significant differences were observed in the mean and maximum ADC values between lesions

with and without reversal in the same cases (Online Supplemental Data). This finding might suggest that the degree of ADC decrease is the same in every DWI lesion. Multivariate analysis showed that the mean ADC value is independently associated with DWI reversal ( $P < .0001$ , Online Supplemental Data). The literature review suggests that early treatment and complete recanalization are associated with DWI reversal.<sup>5,18</sup> However, the ADC value was not included. Therefore, we believe that the mean ADC value is the most important factor to predict DWI reversal, and placement of ROIs might be possible anywhere in DWI lesions.

Thomalla et al<sup>19</sup> reported that in patients with acute stroke with an unknown time of onset, tPA treatment

was effective for patients with a DWI/FLAIR mismatch. This phenomenon also partially reflects DWI reversal. In our study, all patients had DWI/FLAIR mismatch at the initial MR imaging. The ADC value is more accurate and sensitive for reflecting DWI reversal.

According to the literature, it is unknown whether DWI reversal areas retrieve neuronal function.<sup>6,20,21</sup> In our study, the NIHSS score at 7 days in patients with DWI reversal was significantly lower than that in patients without DWI reversal ( $P < .0001$ ), and there were no significant differences in the initial NIHSS and ASPECTS-DWI scores between patients with and without DWI reversal. These results suggest that patients with DWI lesions with reversal regain neurologic function.

Regarding outcomes, the mRS at 3 months was significantly lower in patients with DWI reversal than in those without DWI reversal ( $P = .0009$ ). This result suggests that patients with DWI reversal tend to improve. However, the factors associated with good functional outcomes (mRS, 0–2) were sex (men), a high ASPECTS-DWI score, and complete recanalization in logistic regression analysis ( $P = .035$ ,  $P < .001$ ,  $P = .036$ , respectively). Patients with a high ASPECTS-DWI score might have smaller infarct cores, and successful recanalization in such patients could cause complete improvement. Yoo et al<sup>18</sup> also reported complete recanalization as an important factor for a good functional outcome. In a previous report,<sup>22</sup> female sex and older age were predictive of cardiogenic embolism, and patients with high NIHSS scores have a poor prognosis in old age. These circumstances could result in male patients having a good functional outcome.

In this study, successful recanalization was an inclusion criterion. Moreover, we established this criterion to confirm recanalization at the DWI lesion and predict the effectiveness of this qualitative diagnosis. We believe that this new perspective could help ascertain the effectiveness of MT in cases with a low ASPECTS. Cases with low ASPECTS-DWI with mild ADC reduction improve with MT. In contrast, MT should not be performed in cases with low ASPECTS with severe ADC reduction. In our study, the rate of parenchymal hemorrhage of cases

without DWI reversal was significantly higher than that of those with DWI reversal (Online Supplemental Data). Furthermore, 16 of the patients excluded due to lack of MR imaging with severe stroke or intracranial hemorrhage had severe ADC reduction at the initial MR imaging (mean of the median ADC values:  $447 \text{ (IQR, } 385\text{--}465) \times 10^{-6} \text{ mm}^2/\text{s}$ ). A recent article suggested that cases with a low ASPECTS could achieve good functional outcomes,<sup>23</sup> and this might result from these patients having mild ADC reduction. Therefore, the ADC value is needed to decide on MT for cases with a low ASPECTS-DWI.

Therefore, we believe that DWI lesions are not infarct core. ADC mild reduction, especially a mean ADC of  $\geq 520 \times 10^{-6} \text{ mm}^2/\text{s}$ , is still viable and salvageable by MT. DWI reversal lesions could retrieve neurologic function. Because the ADC value is easily obtained, it could be a good predictor of the efficacy of reperfusion treatment.

This study had some limitations. First, the ADC values were obtained from circular ROIs that were placed manually on ADC maps. Therefore, they do not reflect all lesions with DWI reversal. Second, patients who did not undergo follow-up MR imaging because of severe stroke conditions or intracranial hemorrhage ( $n=16$ ) were excluded, and the ADC values of these patients decreased severely. Therefore, the prognosis of patients without DWI reversal might not be completely reflected. Third, the study sample was small. Last, this was a retrospective cohort study, and a prospective study is, therefore, necessary to confirm these results.

## CONCLUSIONS

The ADC value is independently associated with DWI reversal. In the acute ischemic stage, DWI lesions with mild ADC reduction, especially those with a mean ADC value of  $\geq 520 \times 10^{-6} \text{ mm}^2/\text{s}$ , could be salvageable by MT, and patients with DWI reversal have early neurologic improvement (NIHSS score at 7 days). The ADC value is easily assessed and is a useful tool to predict viable lesions.

## ACKNOWLEDGMENTS

We gratefully acknowledge the work of past and present members of our department.

**Disclosure forms** provided by the authors are available with the full text and PDF of this article at [www.ajnr.org](http://www.ajnr.org).

## REFERENCES

- Donnan GA, Davis SM. **Breaking the 3 h barrier for treatment of acute ischaemic stroke.** *Lancet Neurol* 2008;7:981–82 CrossRef Medline
- Dávalos A, Blanco M, Pedraza S, et al. **The clinical-DWI mismatch: a new diagnostic approach to the brain tissue at risk of infarction.** *Neurology* 2004;62:2187–92 CrossRef Medline
- Lansberg MG, Thijs VN, Bammer R, et al. **The MRA-DWI mismatch identifies patients with stroke who are likely to benefit from reperfusion.** *Stroke* 2008;39:2491–96 CrossRef Medline
- Li F, Han SS, Tatlisumak T, et al. **Reversal of acute apparent diffusion coefficient abnormalities and delayed neuronal death following transient focal cerebral ischemia in rats.** *Ann Neurol* 1999;46:333–42 CrossRef Medline
- Labeyrie MA, Turc G, Hess A, et al. **Diffusion lesion reversal after thrombolysis: a MR correlate of early neurological improvement.** *Stroke* 2012;43:2986–91 CrossRef Medline
- Fiehler J, Knudsen K, Kucinski T, et al. **Predictors of apparent diffusion coefficient normalization in stroke patients.** *Stroke* 2004;35:514–19 CrossRef Medline
- Hoehn-Berlage M, Norris DG, Kohno K, et al. **Evolution of regional changes in apparent diffusion coefficient during focal ischemia of rat brain: the relationship of quantitative diffusion NMR imaging to the reduction in cerebral blood flow and metabolic disturbances.** *J Cereb Blood Flow Metab* 1995;15:1002–11 CrossRef Medline
- Lin W, Lee JM, Lee YZ, et al. **Temporal relationship between apparent diffusion coefficient and absolute measurements of cerebral blood flow in acute stroke patients.** *Stroke* 2003;34:64–70 CrossRef Medline
- Shinoda N, Hori S, Mikami K, et al. **Utility of relative ADC ratio in patient selection for endovascular revascularization of large vessel occlusion.** *J Neuroradiol* 2017;44:185–91 CrossRef Medline
- Zaidat OO, Yoo AJ, Khatri P, et al; STIR Thrombolysis in Cerebral Infarction (TICI) Task Force. **Recommendations on angiographic revascularization grading standards for acute ischemic stroke: a consensus statement.** *Stroke* 2013;44:2650–63 CrossRef Medline
- Hirai T, Sasaki M, Maeda M, et al. **Diffusion-weighted imaging in ischemic stroke: effect of display method on observers' diagnostic performance.** *Acad Radiol* 2009;16:305–12 CrossRef Medline
- Ay H, Furie KL, Singhal A, et al. **An evidence-based causative classification system for acute ischemic stroke.** *Ann Neurol* 2005;58:688–97 CrossRef Medline
- Hart RG, Diener HC, Coutts SB, et al; Cryptogenic Stroke/ESUS International Working Group. **Embolic strokes of undetermined source: the case for a new clinical construct.** *Lancet Neurol* 2014;13:429–38 CrossRef Medline
- Campbell BC, Purushotham A, Christensen S, et al; EPITHET-DEFUSE Investigators. **The infarct core is well represented by the acute diffusion lesion: sustained reversal is infrequent.** *J Cereb Blood Flow Metab* 2012;32:50–56 CrossRef Medline
- Purushotham A, Campbell BC, Straka M, et al. **Apparent diffusion coefficient threshold for delineation of ischemic core.** *Int J Stroke* 2015;10:348–53 CrossRef Medline
- Meng X, Fisher M, Shen Q, et al. **Characterizing the diffusion/perfusion mismatch in experimental focal cerebral ischemia.** *Ann Neurol* 2004;55:207–12 CrossRef Medline
- Kidwell CS, Saver JL, Mattiello J, et al. **Thrombolytic reversal of acute human cerebral ischemic injury shown by diffusion/perfusion magnetic resonance imaging.** *Ann Neurol* 2000;47:462–69 CrossRef Medline
- Yoo J, Choi JW, Lee SJ, et al. **Ischemic diffusion lesion reversal after endovascular treatment.** *Stroke* 2019;50:1504–09 CrossRef Medline
- Thomalla G, Cheng B, Ebinger M, et al. **DWI-FLAIR mismatch for the identification of patients with acute ischaemic stroke within 4.5h of symptom onset (PRE-FLAIR): a multicentre observational study.** *Lancet Neurol* 2011;10:978–86 CrossRef Medline
- DeLaPaz RL, Shibata D, Steinberg GK, et al. **Acute cerebral ischemia in rabbits: correlation between MR and histopathology.** *AJNR Am J Neuroradiol* 1991;12:89–95 Medline
- Li F, Silva MD, Sotak CH, et al. **Temporal evolution of ischemic injury evaluated with diffusion-, perfusion-, and T2-weighted MRI.** *Neurology* 2000;54:689–96 CrossRef Medline
- Umemura T, Hachisuka K, Miyachi H, et al. **Clinical outcomes of cerebral infarction in nonagenarians compared among four age groups.** *Neurol Sci* 2020;41:2471–76 CrossRef Medline
- Diestro JD, Dmytriw AA, Broocks G, et al. **Endovascular thrombectomy for low ASPECTS large vessel occlusion ischemic stroke: a systematic review and meta-analysis.** *Can J Neurol Sci* 2020;47:612–19 CrossRef Medline

# Clinical Significance of Prehospital Telecommunication Defined as the Critical Stroke Call Pathway in Acute Ischemic Stroke Requiring Intra-Arterial Recanalization Therapy

H. Lee, S.H. Kim, J.W. Baek, and S.-C. Jin

## ABSTRACT

**BACKGROUND AND PURPOSE:** To reduce the door-to-puncture time, which is a prognostic factor for the clinical outcome after intra-arterial recanalization therapy, we established a prehospital telecommunication strategy between neurointerventionalists and emergency medical technicians, namely, the critical stroke call pathway. We retrospectively evaluated the clinical significance of the critical stroke call pathway by comparing the door-to-puncture time and clinical outcome of the critical stroke call pathway with those of the routine stroke pathway.

**MATERIALS AND METHODS:** From January 2018 to June 2020, one hundred seventy-one patients with anterior circulation occlusion who underwent arterial recanalization therapy via the emergency department were included in this study. Patients were divided into the critical stroke call pathway group ( $n = 75$ , 43.9%) and the routine stroke pathway group ( $n = 96$ , 56.1%).

**RESULTS:** The critical stroke call pathway group exhibited a shorter door-to-puncture time than the routine stroke pathway group (median, 87 minutes; interquartile range, 63–107 minutes;  $P < .001$ ). On multivariable analysis, a good clinical outcome (3-month mRS, 0–2) was independently associated with a shorter door-to-puncture time (adjusted OR, 0.998; adjusted 95% CI, 0.996–1.000;  $P = .027$ ). In patients with an NIHSS score on admission of  $\leq 11$ , an excellent clinical outcome (3-month mRS, 0–1) was more frequently achieved in the critical stroke call pathway group than in the routine stroke pathway group (22/33, 66.7%, versus 21/48, 43.8%;  $P = .042$ ).

**CONCLUSIONS:** In our study, compared with the routine stroke pathway, the critical stroke call pathway remarkably reduced the door-to-puncture time for arterial recanalization therapy, with better clinical outcomes, especially in patients with a relatively good clinical status.

**ABBREVIATIONS:** CSCP = critical stroke call pathway; EMT = emergency medical technician; IAT = intra-arterial recanalization therapy; IQR = interquartile range; RSP = routine stroke pathway

Intra-arterial recanalization therapy (IAT) has been considered the standard treatment option for acute ischemic stroke caused by large cerebral artery occlusion.<sup>1–5</sup> The time from symptom onset to reperfusion is known to be the strongest predictor of clinical outcomes in patients with acute ischemic stroke. The door-to-puncture time is a modifiable factor that can be shortened in the steps from symptom onset to reperfusion.<sup>6–8</sup>

Recently, the acute ischemic stroke pathway has focused on the communication of a patient's neurologic status between emergency medical technicians (EMTs) and physicians before arrival at the hospital to reduce the door-to-puncture time.<sup>9,10</sup>

Communication between EMTs and emergency physicians can help deliver patients with suspected stroke to IAT-capable hospitals by sharing real-time information about emergency department status and IAT availability. However, several steps remain after a patient with suspected stroke arrives at an IAT-capable hospital, and these steps require time for a patient with suspected stroke to receive reperfusion therapy.

In our hospital, the routine stroke pathway (RSP) proceeds as follows: 1) the emergency physician first calls a resident of the neurology department after brain CT of the patient with suspected stroke shows no intracranial hemorrhage; 2) the resident of the neurology department examines the neurologic status of the patient with suspected stroke, performs further imaging studies,

Received December 15, 2021; accepted after revision March 21, 2022.

From the Department of Neurosurgery (H.L.), Dongnam Institute of Radiological & Medical Sciences, Busan, Republic of Korea; Department of Neurosurgery (S.-C.J.), Inje University Haeundae Paik Hospital, Busan, Republic of Korea; Department of Neurosurgery (S.H.K.), Samsung Changwon Hospital Sungkyunkwan University School of Medicine, Changwon, Republic of Korea; and Department of Radiology (J.W.B.), Inje University Busan Paik Hospital, Busan, Republic of Korea.

Please address correspondence to Sung-Chul Jin, MD, Department of Neurosurgery, Inje University Haeundae Paik Hospital, 875, Haeundae-gu, Busan, Republic of Korea, 48108; e-mail: kusmal@outlook.kr

<https://dx.doi.org/10.3174/ajnr.A7516>



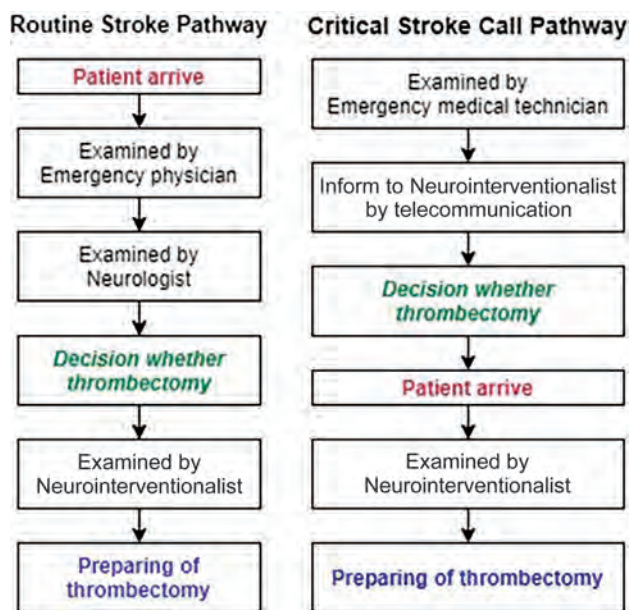


**FIG 1.** Flow diagrams of the RSP and the CSCP.

and calls a neurologist on duty; 3) the neurologist decides whether to perform IAT and calls a neurointerventionalist; and 4) the neurointerventionalist calls a neurointervention team, including the radiologic technicians and nurses on duty, and prepares the IAT.

To reduce the time these steps take, we established a telecommunication hotline defined as the critical stroke call pathway (CSCP) between EMTs and neurointerventionalists (Fig 1). EMTs responding to calls from patients or patients' guardians examine the neurologic status of the patients, and communicate with the interventional neurosurgeons via telephone before the ambulance arrives at the hospital. The interventionalist on call, emergency medical doctors, and neurosurgical residents on duty are on standby for the arrival of the patient and EMTs. After a patient with suspected stroke arrives at the hospital, the neurointerventionalist on call examines the patient's neurologic status and prepares for the possibility of performing IAT with the neurointervention team.

If the plain brain CT of the patient with suspected large cerebral artery occlusion shows a high density related to parenchymal hemorrhage, the attending neurointerventionalist calls the on-duty neurosurgeons who decide the treatment technique according to the patient's neurologic status and brain images. If the image work-up of the patient shows acute cerebral infarction without large-vessel occlusion, antiplatelet medication loading, including aspirin or clopidogrel (Plavix), is administered to the patient. If the image work-up of the patient reveals no lesion, the neurointerventionalist calls the emergency doctors and medical doctors on duty who then manage the patient who presented with a medical condition that mimicked large-vessel occlusion.

This protocol used in our hospital shortened the door-to-puncture time using CT-based decision-making by neurointerventionalists and arrival of the neurointervention team before completion of the image work-up. We hypothesized that the CSCP would reduce the door-to-puncture time for IAT. We also hypothesized that the CSCP would improve clinical outcomes after IAT for patients with acute ischemic stroke.

In this study, we compared the door-to-puncture time and the clinical outcome between the CSCP group and RSP group. We also evaluated factors associated with the clinical outcome in patients who underwent IAT for acute ischemic stroke.

## MATERIALS AND METHODS

### Study Cohort

From January 2018 to June 2020, two hundred twenty-four patients with large cerebral artery occlusion were treated with IAT via the emergency department in our hospital. Of the 224 patients, 44 patients with posterior circulation occlusions were excluded to ensure study population homogeneity. Nine patients were additionally excluded owing to previous disability ( $n = 2$ ) and loss to follow-up ( $n = 7$ ). Therefore, 171 consecutive patients were included in this study.

Because the CSCP is a voluntary system without legal obligation, we could not intentionally select the patients who required IAT and did not know who was included in the CSCP and RSP groups. Patients were divided into 2 groups based on their route to the emergency department. The CSCP group was defined as patients delivered to the emergency department with prehospital telecommunication, and the RSP group was defined as patients delivered to the emergency department without prehospital telecommunication.

### Imaging Work-up and Endovascular Treatment

It is not possible to selectively report patients with large-vessel occlusion before vascular imaging. Thus, we evaluated plain brain CT images of the patients with suspected large-vessel occlusion. If there was an absence of high density in these images, we directly called the neurointervention team on call during the evaluation of additional CT neck angiography and CT perfusion in the CSCP group to reduce the door-to-puncture time.

In both the CSCP and RSP groups, patients with suspected stroke were evaluated using CT-based imaging studies, including CT perfusion and CT angiography. If it was difficult to decide whether to perform IAT on the basis of these imaging studies, diffusion-weighted imaging was additionally considered. IAT was generally performed using a hybrid method of combined stent retrieval and catheter aspiration, which we have reported previously.<sup>11</sup> When in situ stenosis was observed during IAT, rescue treatments, such as balloon angioplasty or stent placement, were performed.

### Data

Patient data were collected from medical records as baseline characteristics, the times of treatment stage, and clinical and radiologic outcomes. The medical records and imaging data were reviewed with the approval of the institutional review board (2020-12-016). Baseline characteristics included age, sex, and medical history, such as diabetes mellitus, hypertension, dyslipidemia, atrial fibrillation, coronary artery occlusive disease, occlusion location, and the NIHSS score on admission. The patient's NIHSS score on admission was assessed by experienced neurointerventionalists (the authors). The times of the treatment were divided into 3 stages: 1) the time from symptom onset to hospital arrival, 2) the door-to-puncture time, and 3) the procedure time.

**Table 1: Comparison of baseline characteristics, time of treatment stage, and clinical and radiologic outcomes between CSCP and RSP**

Characteristic	Patients		P Value
	CSCP (n = 75)	RSP (n = 96)	
Age (median) (IQR) (yr)	74 (65–80)	75 (63–81)	.932 <sup>a</sup>
Male (No.) (%)	36 (48.0)	50 (48.3)	.596 <sup>b</sup>
Diabetes mellitus (No.) (%)	18 (24.0)	22 (22.9)	.868 <sup>b</sup>
Hypertension (No.) (%)	39 (52.0)	54 (56.3)	.580 <sup>b</sup>
Dyslipidemia (No.) (%)	8 (10.7)	15 (15.6)	.346 <sup>b</sup>
Atrial fibrillation (No.) (%)	24 (32.0)	24 (25.0)	.312 <sup>b</sup>
CAOD (No.) (%)	11 (10.5)	13 (13.5)	.834 <sup>b</sup>
Occlusion location (right) (No.) (%)	35 (46.7)	49 (51.0)	.570 <sup>b</sup>
Initial NIHSS score (median) (IQR)	14 (8–18)	12 (8–15)	.049 <sup>a</sup>
Time of treatment stage			
Symptom onset to hospital arrival (median) (IQR) (min)	171 (55–544)	92 (42–258)	.082 <sup>a</sup>
Door to puncture (median) (IQR) (min)	87 (63–107)	142 (106–177)	<.001 <sup>a</sup>
Symptom onset to puncture (median) (IQR) (min)	268 (145–665)	254 (184–490)	.466 <sup>a</sup>
Procedure time (median) (IQR) (min)	65 (49–86)	59 (40–85)	.200 <sup>a</sup>
Radiologic and clinical outcome (No.) (%)			
Successful recanalization (TICI 2b, 3)	64 (85.3)	79 (82.3)	.594 <sup>b</sup>
Good clinical outcome (3-m mRS 0–2)	44 (58.7)	59 (61.5)	.711 <sup>b</sup>
Excellent clinical outcome (3-m mRS 0–1)	32 (42.7)	35 (36.5)	.409 <sup>b</sup>

**Note:**—CAOD indicates coronary artery occlusive disease; 3-m mRS, 3-month mRS.

<sup>a</sup> P value obtained using the Mann-Whitney *U* test.

<sup>b</sup> P value obtained using the Pearson  $\chi^2$  test.

The door-to-puncture time was defined as the time from hospital arrival to groin puncture. The procedure time was defined as the time from groin puncture to recanalization.

The radiologic outcome was assessed by the TICI grade immediately following cerebral angiography. Successful recanalization was defined as a TICI grade of 2b or 3.

The clinical outcome was assessed by the mRS score at 3 months after IAT. The mRS score was estimated by a neurointerventionalist or stroke neurologist during a routinely scheduled clinical visit. A good clinical outcome was defined as a 3-month mRS score of  $\leq 2$ , and an excellent clinical outcome was defined as a 3-month mRS score of 0 or 1. A 3-month mRS score of  $\geq 3$  was defined as a poor clinical outcome.

### Statistical Analysis

Baseline characteristics and time of treatment stage were compared between the CSCP and RSP groups and between patients with good clinical outcomes and those with poor clinical outcomes. Univariate analysis was performed using the Mann-Whitney *U* test for continuous variables and the Pearson  $\chi^2$  test for categorical variables. Radiologic and clinical outcomes were compared between the CSCP and RSP groups and between the good and poor clinical outcome groups using the Pearson  $\chi^2$  test. Furthermore, we investigated the variables that were independently associated with good clinical outcomes through a multivariable logistic regression model. Clinically important variables (age, sex, and time of treatment stage) as well as variables with  $P < .20$  in the univariate analysis, suggesting their association with good clinical outcomes, were entered into the model. A stepwise method was used for backward elimination.

The area under the receiver operating characteristic curve was calculated to estimate the optimal threshold of the initial NIHSS score for a good clinical outcome.

Statistical analysis and creation of figures were performed using SPSS, Version 25 (IBM) and Excel (Microsoft). All reported *P* values  $< .05$  were considered statistically significant.

### RESULTS

Of the 171 patients, 86 (50.3%) were men, and the median patient age was 75 years (interquartile range [IQR], 64–80 years). The occlusion locations were as follows: internal carotid artery ( $n = 47$ ), M1 ( $n = 86$ ), M2 ( $n = 32$ ), and anterior cerebral artery ( $n = 6$ ).

Successful recanalization was achieved in 143 patients (83.6%), and good clinical outcomes were achieved in 103 patients (60.2%). The mortality rate was 5.8% ( $n = 10$ ). Nine patients had other medical problems such as stomach cancer ( $n = 1$ ), septic shock ( $n = 3$ ), and heart failure ( $n = 5$ ). One patient died from progression of a cerebral infarction with unsuccessful recanalization.

Table 1 shows the comparison between the CSCP and RSP groups. Baseline characteristics except the NIHSS score on admission did not differ significantly between the 2 groups. The NIHSS score on admission was significantly higher in the CSCP group than in the RSP group (median, 14; IQR, 8–18, versus median, 12; IQR, 8–15;  $P = .049$ ). The CSCP group had a longer time from symptom onset to hospital arrival than the RSP group (median, 171 minutes; IQR, 55–544 minutes, versus median, 92 minutes; IQR, 42–258 minutes); however, the difference was not statistically significant ( $P = .082$ ). Notably, the door-to-puncture time was significantly shorter in the CSCP group than in the RSP group (median, 87 minutes; IQR, 63–107 minutes, versus median, 142 minutes; IQR, 106–177 minutes;  $P < .001$ ). The radiologic and clinical outcomes were not significantly different between the 2 groups.

A comparison of patients with good clinical outcomes and patients with poor clinical outcomes is shown in Table 2. Patients with poor clinical outcomes were significantly older than those with good clinical outcomes (median, 78 years; IQR, 66–83 years, versus median, 73 years; IQR, 62–78 years;  $P = .007$ ). The initial NIHSS score was significantly higher in patients with poor clinical outcomes than in patients with good clinical outcomes (median, 14; IQR, 12–18, versus median, 10; IQR, 7–14;  $P < .001$ ).

**Table 2: Comparison of baseline characteristics, time of treatment stage, and clinical and radiologic outcomes between the good clinical outcome group and the poor clinical outcome group**

Characteristic	Patients		P Value
	Good Clinical Outcome (n = 103)	Poor Clinical Outcome (n = 68)	
Age (median) (IQR) (yr)	73 (62–78)	78 (66–83)	.007 <sup>a</sup>
Male (No.) (%)	55 (53.4)	31 (45.6)	.317 <sup>b</sup>
Diabetes mellitus (No.) (%)	23 (22.3)	17 (25.0)	.686 <sup>b</sup>
Hypertension (No.) (%)	59 (57.3)	34 (50.0)	.349 <sup>b</sup>
Dyslipidemia (No.) (%)	14 (13.6)	9 (13.2)	.947 <sup>b</sup>
Atrial fibrillation (No.) (%)	33 (32.0)	15 (22.1)	.155 <sup>b</sup>
CAOD (No.) (%)	18 (17.5)	6 (8.8)	.111 <sup>b</sup>
Occlusion location (right) (No.) (%)	47 (45.6)	37 (54.4)	.261 <sup>b</sup>
Initial NIHSS score (median) (IQR)	10 (7–14)	14 (12–18)	<.001 <sup>a</sup>
Time of treatment stage			
Symptom onset to hospital arrival (median) (IQR) (min)	120 (46–330)	122 (46–433)	.891 <sup>a</sup>
Door to puncture (median) (IQR) (min)	108 (83–147)	109 (83–157)	.595 <sup>a</sup>
Symptom onset to puncture (median) (IQR) (min)	255 (160–515)	254 (171–643)	.612 <sup>a</sup>
Procedure time (median) (IQR) (min)	60 (44–85)	65 (44–86)	.925 <sup>a</sup>
Successful recanalization	91 (88.3)	52 (76.5)	.040 <sup>b</sup>

Note:—CAOD indicates coronary artery occlusive disease.

<sup>a</sup> P value obtained using the Mann-Whitney U test.

<sup>b</sup> P value obtained using the Pearson  $\chi^2$  test.

**Table 3: Multivariable logistic regression analysis of good clinical outcome**

	Adjusted OR	Adjusted 95% CI	P Value
Door-to-puncture time	0.998	0.996–1.000	.027
Initial NIHSS score	0.790	0.722–0.865	<.001
Successful recanalization	4.102	1.501–11.211	.006
Occlusion location (right: 1 or left: 2)	2.687	1.215–5.939	.015
Atrial fibrillation	2.602	1.139–5.941	.023

Successful recanalization was more frequently achieved in patients with good clinical outcomes than in patients with poor clinical outcomes (91/103, 88.3%, versus 52/68, 76.5%),  $P = .040$ .

Multivariable logistic regression analysis, which included age, sex, atrial fibrillation, coronary artery occlusive disease, initial NIHSS score, occlusion location (right), time of treatment stage, and successful recanalization, showed that good clinical outcome was independently associated with the door-to-puncture time, initial NIHSS score, successful recanalization, occlusion location (right), and atrial fibrillation (Table 3). Additionally, in the patients with an initial NIHSS score of  $\leq 11$ , multivariable logistic regression analysis showed that a good clinical outcome was independently associated with successful recanalization (adjusted OR, 2.74; 95% CI, 0.087–0.555;  $P = .008$ ) and the initial NIHSS score (adjusted OR,  $-2.072$ ; 95% CI,  $-0.077$  to  $-0.001$ ;  $P = .042$ ).

A receiver operating characteristic curve model was constructed between the NIHSS score and good clinical outcome. The area under the receiver operating characteristic curve was 0.719 (95% CI, 0.641–0.796;  $P < .001$ ). The maximal Youden index J was 0.40 with 76.5% sensitivity and 63.1% specificity (Fig 2), and the optimal threshold of the NIHSS score was 11.5. In the patients with an initial NIHSS score of  $\leq 11$ , if recanalization was successful, the patient may have a good clinical outcome. However, in patients with an initial NIHSS score of  $> 12$ , if recanalization was successful, the patient was not expected to have a good clinical outcome based on the analysis of our data. Accordingly, we

investigated the patients with an initial NIHSS score of  $\leq 11$  to evaluate the difference in good or excellent clinical outcomes between the CSCP and RSP groups. In the patients with an initial NIHSS score of  $\leq 11$  who underwent IAT ( $n = 81$ ), the good clinical outcome of the CSCP group ( $n = 29/33$ , 87.9%) was not significantly different from that of the RSP group ( $n = 36/48$ , 75.0%) ( $P = .153$ ). However, the excellent clinical outcome of the CSCP group ( $n = 22/33$ , 66.7%) was significantly different from that of the RSP group ( $n = 21/48$ , 43.8%) ( $P = .042$ ) (Fig 3).

## DISCUSSION

Recently, the successful recanalization rate has been reported to reach 90% after IAT for patients with acute ischemic stroke using aspiration alone, stent retriever alone, or a combination of these 2 methods.<sup>1,2,4,12–14</sup> It seems difficult to develop a new game changer for IAT devices to improve successful recanalization. Therefore, we focused on reducing the door-to-puncture time for IAT to improve clinical outcomes.

A door-to-puncture time within 90 minutes was recently considered an ideal time goal, and many doctors and stroke centers are trying to reach this goal. Our results showed that the median door-to-puncture time of the CSCP group was 87 minutes, which is in line with this time goal. The reduction in the door-to-puncture time in the CSCP group can be explained by reductions in the time required for each step from patient arrival and triage to



notification between doctors and preparation for the procedure by the neurointervention team.

In our study, in contrast to our expectations, the CSCP group did not achieve significantly better clinical outcomes than the RSP group (58.7% versus 61.5%,  $P = .711$ ), despite the difference in the door-to-puncture time. This finding can be partially explained by the difference in the initial NIHSS scores between the CSCP and RSP groups (median, 14; IQR, 8–18, versus median, 12; IQR, 8–15;  $P = .049$ ). The CSCP group had more severe ischemic injuries than the RSP group at admission, which might have affected the clinical outcomes. Because the patients with a poor neurologic status were not permitted to be delivered to adjacent hospitals for thrombectomy, the EMTs who delivered the patients unavoidably called the neurointerventionalists on call at our hospital, and more patients with an initially poor neurologic status were probably included in the CSCP group. Our multivariable logistic regression analysis also showed that the NIHSS score on admission had a lower OR than the door-to-puncture time (0.790 versus 0.998). This can also explain the clinical outcomes, which were not significantly different between the CSCP and RSP

groups, despite the difference in the door-to-puncture times between the 2 groups.

In the patients with an NIHSS score of  $\leq 11$  ( $n = 81$ ), the good clinical outcome of the CSCP group ( $n = 29/33$ , 87.9%) was not significantly different from that of the RSP group ( $n = 36/48$ , 75.0%) ( $P = .153$ ). However, the excellent clinical outcome of the CSCP group ( $n = 22/33$ , 66.7%) was different from that of the RSP group ( $n = 21/48$ , 43.8%) ( $P = .042$ ). This result suggested that the CSCP group will have a greater possibility of an excellent clinical outcome, especially for patients with NIHSS scores of  $\leq 11$ .

Our results also showed that the CSCP group had a significantly shorter door-to-puncture time than the RSP group, and a shorter door-to-puncture time was an independent prognostic factor for a good clinical outcome despite the low adjusted OR (0.998). However, the door-to-puncture time based on our results is not a statistically significant cardinal factor for a good clinical outcome. This is probably because the CSCP group had a longer time from symptom onset to hospital arrival than the RSP group (median 171 minutes; IQR, 55–544 minutes, versus median, 92 minutes; IQR, 42–258 minutes). Conclusively, there was no significant difference between the CSCP group (median, 254.5 minutes; IQR, 184.5–485.0 minutes) and the RSP group (median, 254.5 minutes; IQR, 184.5–485.5 minutes) from symptom onset to femoral puncture time ( $P = .913$ ). Accordingly, the clinical significance of the door-to-puncture time is probably low, unlike our expectation. Nevertheless, our study suggests that pre-hospital telecommunication between EMTs and neurointerventionalists has clinical significance for good clinical outcomes in patients with acute ischemic stroke.

The limitation of our study is the retrospective design without randomization between the CSCP and RSP groups. However, the selection bias may be low because all patients who underwent IAT during the study period were included. In addition, we tried to treat patients with acute ischemic stroke as quickly as possible, regardless of their route to the emergency department and whether they were in the CSCP or RSP group, reducing the likelihood of selection bias. Additionally, we have not used IV tPA in the patients with large-vessel occlusion within 4.5 hours of symptom onset. Because, there was no beneficial gain of IV tPA administration in patients with large-vessel occlusion treated with thrombectomy, on the basis of our results. Therefore, there was no direct clinical comparison of bridge therapy with IV tPA between the 2 groups. Another limitation of our study is that it was a single-center study with a small sample size. Further studies with large sample sizes are necessary to confirm these preliminary results. Nevertheless, our study could be meaningful because it suggests the clinical significance of prehospital telecommunication between EMTs and neurointerventionalists in improving clinical outcomes as well as reducing the door-to-puncture time.

## CONCLUSIONS

Compared with the RSP, the CSCP significantly reduced the door-to-puncture

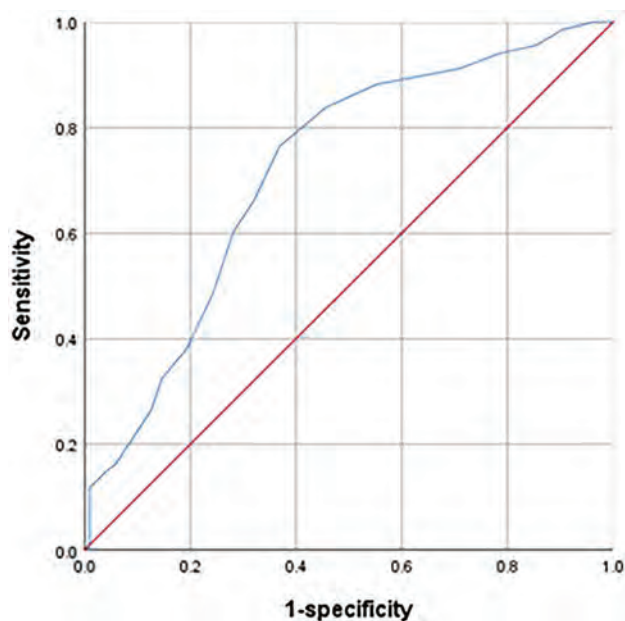


**FIG 2.** Receiver operating characteristic curve of the initial NIHSS score for prediction of a good clinical outcome (mRS = 0–2) at 90 days. The area under the curve of the NIHSS score was 0.714.

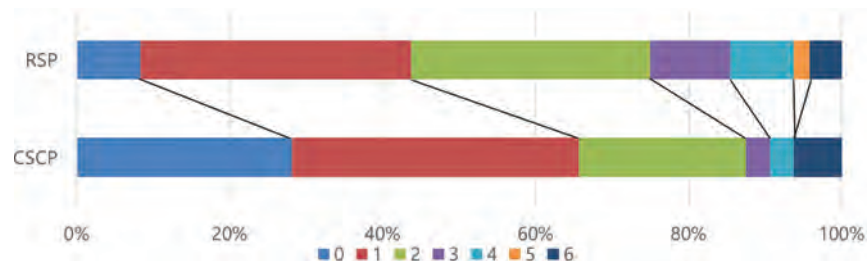


**FIG 3.** Graph comparing the 90-day mRS scores of the CSCP group and RSP group in the low NIHSS score ( $\leq 11$  points) group.

time for IAT, with better clinical outcomes, especially in patients with a relatively good neurologic status. Our study suggests the clinical significance of prehospital telecommunication in the treatment of patients with acute ischemic stroke. Further studies with large sample sizes are necessary to confirm these preliminary results.

## ACKNOWLEDGMENT

The authors wish to thank Busan Metropolitan Fire Headquarters, Gijang 119 Safety Center, and Haeundae 119 Safety Center. In particular, they wish to acknowledge the help of Kim JeongHwan and Lee Minho with the Haeundae 119 Safety Center in establishing and fine-tuning the CSCP.

**Disclosure forms** provided by the authors are available with the full text and PDF of this article at [www.ajnr.org](http://www.ajnr.org).

## REFERENCES

- Campbell BC, Mitchell PJ, Kleinig TJ, et al. **Endovascular therapy for ischemic stroke with perfusion-imaging selection.** *N Engl J Med* 2015;372:1009–18 CrossRef Medline
- Berkhemer OA, Fransen PS, Beumer D, et al; MR CLEAN Investigators. **A randomized trial of intraarterial treatment for acute ischemic stroke.** *N Engl J Med* 2015;372:11–20 CrossRef Medline
- Goyal M, Demchuk AM, Menon BK, et al. **Randomized assessment of rapid endovascular treatment of ischemic stroke.** *N Engl J Med* 2015;372:1019–30 CrossRef Medline
- Saver JL, Goyal M, Bonafe A, et al. **Stent-retriever thrombectomy after intravenous t-PA vs. t-PA alone in stroke.** *N Engl J Med* 2015;372:2285–95 CrossRef Medline
- Jovin TG, Chamorro A, Cobo E, et al; REVASCAT Trial Investigators. **Thrombectomy within 8 hours after symptom onset in ischemic stroke.** *N Engl J Med* 2015;372:2296–2306 CrossRef Medline
- Jahan R, Saver JL, Schwamm LH, et al. **Association between time to treatment with endovascular reperfusion therapy and outcomes in patients with acute ischemic stroke treated in clinical practice.** *JAMA* 2019;322:252–63 CrossRef Medline
- Fassbender K, Grotta JC, Walter S, et al. **Mobile stroke units for pre-hospital thrombolysis, triage, and beyond: benefits and challenges.** *Lancet Neurol* 2017;16:227–37 CrossRef Medline
- Fassbender K, Walter S, Grunwald IQ, et al. **Prehospital stroke management in the thrombectomy era.** *Lancet Neurol* 2020;19:601–10 CrossRef Medline
- Itrat A, Taqui A, Cerejo R, et al; Cleveland Pre-Hospital Acute Stroke Treatment Group. **Telemedicine in prehospital stroke evaluation and thrombolysis: taking stroke treatment to the doorstep.** *JAMA Neurol* 2016;73:162–68 CrossRef Medline
- Czap AL, Singh N, Bowry R, et al. **Mobile stroke unit computed tomography angiography substantially shortens door-to-puncture time.** *Stroke* 2020;51:1613–15 CrossRef Medline
- Kim SH, Lee H, Kim SB, et al. **Hybrid mechanical thrombectomy for acute ischemic stroke using an intermediate aspiration catheter and Trevo stent simultaneously.** *J Clin Neurosci* 2020;76:9–14 CrossRef Medline
- Humphries W, Hoit D, Doss VT, et al. **Distal aspiration with retrievable stent assisted thrombectomy for the treatment of acute ischemic stroke.** *J Neurointerv Surg* 2015;7:90–94 CrossRef Medline
- Jindal G, Serulle Y, Miller T, et al. **Stent retrieval thrombectomy in acute stroke is facilitated by the concurrent use of intracranial aspiration catheters.** *J Neurointerv Surg* 2017;9:944–47 CrossRef Medline
- Hopf-Jensen S, Preiß M, Marques L, et al. **Impact and effectiveness of dual aspiration technique in stent-assisted mechanical thrombectomy: recent improvements in acute stroke management.** *Cardiovasc Intervent Radiol* 2016;39:1620–28 CrossRef Medline

# Diffusion-Weighted Imaging to Assess HPV-Positive versus HPV-Negative Oropharyngeal Squamous Cell Carcinoma: The Importance of b-Values

V. Lenoir, B.M.A. Delattre, Y. M'Rad, C. De Vito, T. de Perrot, and M. Becker



## ABSTRACT

**BACKGROUND AND PURPOSE:** Controversy exists as to whether ADC histograms are capable to distinguish human papillomavirus-positive (HPV+) from human papillomavirus-negative (HPV-) oropharyngeal squamous cell carcinoma. We investigated how the choice of b-values influences the capability of ADC histograms to distinguish between the two tumor types.

**MATERIALS AND METHODS:** Thirty-four consecutive patients with histologically proved primary oropharyngeal squamous cell carcinoma (11 HPV+ and 23 HPV-) underwent 3T MR imaging with a single-shot EPI DWI sequence with 6 b-values (0, 50, 100, 500, 750, 1000 s/mm<sup>2</sup>). Monoexponentially calculated perfusion-sensitive (including  $b=0$  s/mm<sup>2</sup>) and perfusion-insensitive/true diffusion ADC maps (with  $b \geq 100$  s/mm<sup>2</sup> as the lowest b-value) were generated using Matlab. The choice of b-values included 2 b-values (ADC<sub>b0-1000</sub>, ADC<sub>b100-1000</sub>, ADC<sub>b500-1000</sub>, ADC<sub>b750-1000</sub>) and 3-6 b-values (ADC<sub>b0-750-1000</sub>, ADC<sub>b0-500-750-1000</sub>, ADC<sub>b0-50-100-1000</sub>, ADC<sub>b0-50-100-750-1000</sub>, ADC<sub>b0-50-100-500-750-1000</sub>). Readers blinded to the HPV- status contoured all tumors. ROIs were then copied onto ADC maps, and their histograms were compared.

**RESULTS:** ADC histogram metrics in HPV+ and HPV- oropharyngeal squamous cell carcinoma changed significantly depending on the b-values. The mean ADC was lower, and skewness was higher in HPV+ than in HPV- oropharyngeal squamous cell carcinoma only for ADC<sub>b0-1000</sub>, ADC<sub>b0-750-1000</sub>, and ADC<sub>b0-500-750-1000</sub> ( $P < .05$ ), allowing distinction between the 2 tumor types. Kurtosis was significantly higher in HPV+ versus HPV- oropharyngeal squamous cell carcinoma for all b-value combinations except 2 perfusion-insensitive maps (ADC<sub>b500-1000</sub> and ADC<sub>b750-1000</sub>). Among all b-value combinations, kurtosis on ADC<sub>b0-1000</sub> had the highest diagnostic performance to distinguish HPV+ from HPV- oropharyngeal squamous cell carcinoma (area under the curve = 0.893; sensitivity = 100%, specificity = 82.6%). Acquiring multiple b-values for ADC calculation did not improve the distinction between HPV+ and HPV- oropharyngeal squamous cell carcinoma.

**CONCLUSIONS:** The choice of b-values significantly affects ADC histogram metrics in oropharyngeal squamous cell carcinoma. Distinguishing HPV+ from HPV- oropharyngeal squamous cell carcinoma is best possible on the ADC<sub>b0-1000</sub> map.

**ABBREVIATIONS:** AJCC = American Joint Committee on Cancer; AUC = area under the curve; HNSCC = head and neck squamous cell carcinoma; HPV+ = human papillomavirus positive; HPV- = human papillomavirus negative; OPSCC = oropharyngeal squamous cell carcinoma

Infection with human papillomavirus (HPV) is a well-documented risk factor for oropharyngeal squamous cell carcinoma (OPSCC).<sup>1</sup>

Received November 30, 2021; accepted after revision March 26, 2022.

From the Divisions of Radiology (V.L., B.M.A.D., Y.M., T.d.P., M.B.) and Clinical Pathology (C.D.V.), Diagnostic Department, Geneva University Hospitals, University of Geneva, Geneva, Switzerland.

This study was part of a clinical research project supported by the Swiss National Science Foundation under grant SNSF No 320030\_173091/1.

Please address correspondence to Minerva Becker, MD, Division of Radiology, Diagnostic Department, Geneva University Hospitals, University of Geneva, Rue Gabrielle-Perret-Gentil 4, 1211 Geneva 14, Switzerland; e-mail: Minerva.Becker@hcuge.ch

Indicates open access to non-subscribers at www.ajnr.org

Indicates article with online supplemental data.

<http://dx.doi.org/10.3174/ajnr.A7521>

The literature suggests that HPV-positive (HPV+) OPSCC is a distinct tumor entity with an improved response to radiation therapy and a better outcome in comparison with HPV-negative (HPV-) OPSCC.<sup>2,3</sup> As a result, the latest editions of the American Joint Committee on Cancer (AJCC) and the *TNM Classification of Malignant Tumors* staging manuals use different OPSCC staging criteria depending on HPV status.<sup>4,5</sup> The HPV status is established by p16 immunohistochemistry complemented by polymerase chain reaction to detect HPV DNA or by in situ hybridization for virus DNA and oncoprotein E6/E7 messenger RNA.<sup>6</sup>

Several studies have shown that HPV+ OPSCC differs from HPV- OPSCC in terms of not only pathogenesis and prognosis but also histopathologic characteristics and microstructural heterogeneity.<sup>7,8</sup> DWI allows quantification of the Brownian motion of



**Table 1: Choice of b-values for each calculated ADC map**

No. of b-Values	Used b-Values						Monoexponential Model
2	0					1000	ADC <sub>b0-1000</sub>
4	0	50	100			1000	ADC <sub>b0-50-100-1000</sub>
5	0	50	100		750	1000	ADC <sub>b0-50-100-750-1000</sub>
6	0	50	100	500	750	1000	ADC <sub>b0-50-100-500-750-1000</sub>
3	0				750	1000	ADC <sub>b0-750-1000</sub>
4	0			500	750	1000	ADC <sub>b0-500-750-1000</sub>
2			100			1000	ADC <sub>b100-1000</sub>
2				500		1000	ADC <sub>b500-1000</sub>
2					750	1000	ADC <sub>b750-1000</sub>

water molecules in vivo, and ADC values, expressed in square millimeter per second, are inversely correlated with cellular density. ADC metrics could, therefore, serve as imaging biomarkers in head and neck squamous cell carcinoma (HNSCC), with the advantage of being able to evaluate the entire tumor noninvasively in vivo, thus avoiding the inconsistency inherent to invasive tissue sampling.

Some investigators found that HPV+ OPSCCs have lower mean ADC values than HPV- OPSCCs, most likely because of differences in the cellular microenvironment.<sup>8-11</sup> However, these observations have not been confirmed by others.<sup>12,13</sup> ADC metrics are influenced by DWI acquisition protocols, choice of b-values, scanner characteristics that may vary among vendors, and lesion segmentation techniques that are operator-dependent.<sup>11,14,15</sup> When ADC values are calculated with a monoexponential decay model including  $b=0$  as the lowest b-value, molecular diffusion is influenced by tissue perfusion effects. Although these tend to increase ADC values, they can be corrected for using either higher b-values or multiple b-values.<sup>16</sup> From a practical point of view, monoexponential ADC calculation using 2 b-values reduces the acquisition time in clinical routine as opposed to the acquisition of multiple b-values.

The effect of perfusion on ADC maps used as cancer biomarkers is not completely clear and may vary from one tumor to another. Not surprising, the choice of the right number and type of b-values for the assessment of HNSCC is still somewhat controversial, and varies among 2,<sup>8-10</sup> 3,<sup>12,13</sup> or 6 b-values.<sup>17,18</sup> It has been recommended that for monoexponentially calculated ADCs with 2 b-values, the lowest b-value should be in the range of 100–150 s/mm<sup>2</sup> and the highest b-value should be between 500 and 1000 s/mm to obtain a “perfusion-insensitive” and thus a “true diffusion” ADC estimation.<sup>14</sup> However, some studies evaluating ADC characteristics of HPV+ and HPV- OPSCC are based on ADCs calculated monoexponentially with 2 b-values only, namely 0 s/mm<sup>2</sup> and 1000 s/mm<sup>2</sup>. To the best of our knowledge, it is not yet clear whether in patients imaged for HNSCC, ADC maps calculated with several b-values (“multi-b ADC maps”) allow a better distinction between HPV+ and HPV- OPSCC than maps calculated only with 2 b-values and whether the perfusion effect on the ADC calculation, which occurs with  $b=0$ , has a role in this context.

The purpose of the current study was to investigate how the choice of b-values influences the ability of ADC histogram metrics to differentiate HPV+ from HPV- OPSCC and which combination of b-values performs best for distinguishing between the 2 tumor types. We, therefore, compared histograms of ADC maps obtained with 2 b-values, multiple b-values, and different combinations thereof and correlated the results with the HPV- status.

## MATERIALS AND METHODS

### Patient Inclusion Criteria

This retrospective study was approved by the Institutional Ethics and Research Committee and was performed according to the guidelines of the Helsinki II declaration. Informed consent was waived. The inclusion criteria for patients in this study were 3-fold: 1) consecutive adult patients imaged in our institution for histologically proved primary OPSCC, 2) HPV status determined by p16 immunohistochemistry (nuclear and cytoplasmic staining of  $\geq 70\%$  of neoplastic cells required for HPV- positivity)<sup>19</sup> and polymerase chain reaction for HPV DNA, and 3) MR imaging examinations obtained on the same scanner with a 6 b-value DWI sequence allowing retrospective calculation of ADC maps with different b-value combinations. During 24 months, 49 consecutive patients with OPSCC underwent MR imaging with the above-mentioned DWI sequence. Fifteen patients were excluded from the study because of previous radiation therapy ( $n=11$ ), lack of documentation of the HPV- status ( $n=2$ ), tumor size too small for segmentation ( $n=1$ ), or dental hardware artifacts impairing DWI quality ( $n=1$ ). Therefore, 34 patients with primary OPSCC fulfilled the inclusion criteria.

### MR Imaging Protocol

Images in all patients were obtained on a 3T Ingenuity TF PET/MR imaging (Philips Healthcare) system with a routine imaging protocol, which included morphologic sequences covering the area between the skull base and the thoracic inlet (axial T1 and T2, coronal T2 STIR, axial and coronal T1 after IV injection of a gadolinium-based contrast agent) and 2 single-shot EPI DWI sequences with 6 b-values (0, 50, 100, 500, 750, 1000s/mm<sup>2</sup>), each DWI sequence covering 12 cm in the craniocaudal direction, ie, a first sequence covering the suprahoid neck followed by a second sequence covering the infrahyoid neck. The EPI DWI sequences had the following parameters: FOV = 230 × 254 mm<sup>2</sup>, acquired resolution = 2 × 2 × 3 mm<sup>3</sup>, reconstructed resolution = 1.3 × 1.3 × 3 mm<sup>3</sup>, TE/TI/TR = 73/230/6859 ms, sensitivity encoding acceleration factor = 2, slices = 40, total acquisition time = 4 minutes 7 seconds. Because we were interested in the DWI characteristics of primary OPSCC, only the sequences covering the primary tumors were used for analysis.

### Generation of ADC Maps with Different b-Values

Reconstruction of ADC maps with different b-value combinations using the monoexponential decay model was performed with an in-house-developed Matlab software program (Matlab

**Table 2: Patient and tumor characteristics**

	HPV– OPSCC (n = 23)	HPV+ OPSCC (n = 11)	P Value
Average age (range) (yr)	62 (50–82)	62 (48–85)	.986 <sup>a</sup>
Sex			
Women	7 (7/23, 30%)	6 (6/11, 55%)	.329 <sup>b</sup>
Men	16 (16/23, 70%)	5 (5/11, 45%)	
Tumor location			
Oropharynx	23 (23/23, 100%)	11 (11/11, 100%)	.944 <sup>c</sup>
T classification according to AJCC 2018 <sup>4,5</sup>			
T1	3 (3/23, 13%)	0 (0/11, 0%)	
T2	3 (3/23, 13%)	2 (2/11, 18%)	
T3	5 (5/23, 22%)	2 (2/11, 18%)	
T4	12 (12/23, 52%)	7 (7/11, 64%)	.138 <sup>c</sup>
N classification according to AJCC 2018 <sup>4,5</sup>			
N0	5 (5/23, 22%)	0 (0/11, 0%)	
N1	3 (3/23, 13%)	5 (5/11, 45%)	
N2	15 (15/23, 65%)	6 (6/11, 55%)	
N3	0 (0/23, 0%)	0 (0/11, 0%)	.630 <sup>c</sup>
M classification according to AJCC 2018 <sup>4,5</sup>			
M0	22 (22/23, 96%)	11 (11/11, 100%)	
M1	1 (1/23, 4%)	0 (0/11, 0%)	.140 <sup>b</sup>
Tumor keratinization at histopathology			
Present	14 (14/23, 61%)	7 (7/11, 64%)	
Absent	9 (9/23, 39%)	4 (4/11, 36%)	
Mean proliferation index, MIB-1 (range) (%)	55 (15–90)	69 (50–90)	.126 <sup>d</sup>

<sup>a</sup> T test.<sup>b</sup> Pearson  $\chi^2$  test.<sup>c</sup> Fisher exact test.<sup>d</sup> Mann-Whitney-Wilcoxon test.

release 2009b 32 bit; MathWorks). When only 2 b-values were considered for monoexponential ADC calculation (4 combinations in this study), we used the following formula:  $ADC = (\ln SI_{b1} - \ln SI_{b2}) / (b2 - b1)$ , where b1 and b2 were the 2 b-values used. When using multiple b-values (5 combinations in this study), multi-b ADC ( $ADC_{multiple-b}$ ) was calculated by fitting the linearized version of the monoexponential decay model to the data on the basis of the following formula:  $SI_b / SI_0 = \exp(-b \times ADC_{multiple-b})$ , where  $SI_b$  is the signal intensity in the pixel measured for each b-value and  $SI_0$  is the signal intensity in the pixel without diffusion-weighted sensitization ( $b=0$ ). This type of ADC calculation was chosen because it corresponds to the least-squares exponential fitting model used widely for multiple b values and as provided in clinical routine by all MR imaging vendors. Calculations using the biexponential or the stretched exponential model were not considered on the basis of the current recommendations<sup>20</sup> and because the monoexponentially calculated ADC has been shown to be the most reliable diffusion parameter in different tumor types.<sup>21,22</sup> Table 1 shows the choice and combination of b-values for each calculated ADC map.

### Tumor Segmentation

The OsiriX MD, Version 11, software (Pixmeo) was used for ROI placement. Freehand ROIs were drawn by 2 subspecialty board-certified head and neck radiologists (with >10 years' experience) on the basis of side-by-side visualization of axial T2, contrast-enhanced T1,  $b=1000$ , and ADC images. The ADC maps used for segmentation were the ADC maps generated automatically by the MR imaging scanner (6 b-values) and used in clinical routine. Both radiologists were blinded to the HPV status and clinical data. The freehand ROIs encompassed the largest cross-sectional tumor areas on 2 consecutive axial slices without excluding necrotic

portions.<sup>8,10</sup> Tumor areas for ROI placement were selected on the basis of the agreement of both readers, and ROI boundaries were drawn in consensus. The reasons for contouring the largest cross-sectional tumor areas on 2 consecutive slices were as follows: First, other studies evaluating ADC values in HPV+ and HPV– OPSCC also used the same approach;<sup>8,10</sup> second, because whole-tumor segmentation is time-consuming and because we aimed to use a method that would be feasible during clinical routine, this choice appeared as a good compromise between contouring only 1 largest cross-sectional area (with potentially too few pixels for analysis) and whole-tumor segmentation.

### Quantitative and Semiquantitative (Visual) Analysis

The same ROIs were then copied on all ADC maps (Online Supplemental Data), and a csv file containing all pixel information from the ROIs was then exported from OsiriX to Matlab. ADC histogram parameters resulting from the combined voxel data from both ROIs into 1 large histogram were analyzed for each ADC map separately (ie, for each investigated b-value combination). The evaluated parameters included the following: mean ADC, skewness, and excess kurtosis. Comparison between histogram parameters in HPV– and HPV+ OPSCCs was done for all combinations of b-values. Receiver operating characteristic curves and areas under the curve (AUCs) were calculated to assess the diagnostic performance for distinguishing HPV+ from HPV– OPSCC. In addition, to avoid overly optimistic estimates of AUCs resulting from analysis of the full data set, we used a leave-one-out cross-validation approach with linear discriminant analysis as a model. The linear discriminant analysis score function was estimated on the training set after leaving 1 observation out. The process was repeated for all observations, and each of the left-out observations was predicted

**Table 3: Comparison of ADC histograms in HPV+ versus HPV– OPSCC for each b-value combination<sup>a</sup>**

	HPV– OPSCC	HPV+ OPSCC	P Value <sup>b</sup>
<b>ADC Mean<sup>c</sup></b>			
ADC <sub>b0–1000</sub>	1117 (SD, 151)	977 (SD, 183)	.038
ADC <sub>b0–50–100–1000</sub>	1029 (SD, 176)	924 (SD, 185)	.164
ADC <sub>b0–50–100–750–1000</sub>	1051 (SD, 168)	925 (SD, 176)	.077
ADC <sub>b0–50–100–500–750–1000</sub>	1061 (SD, 167)	935 (SD, 176)	.084
ADC <sub>b0–750–1000</sub>	1141 (SD, 156)	983 (SD, 177)	.017
ADC <sub>b0–500–750–1000</sub>	1127 (SD, 156)	970 (SD, 177)	.017
ADC <sub>b100–1000</sub>	947 (SD, 245)	875 (SD, 206)	.214
ADC <sub>b500–1000</sub>	838 (SD, 255)	758 (SD, 287)	.176
ADC <sub>b750–1000</sub>	900 (SD, 360)	942 (SD, 340)	.942
<b>Skewness</b>			
ADC <sub>b0–1000</sub>	0.156 (SD, 0.453)	0.486 (SD, 0.444)	.031
ADC <sub>b0–50–100–1000</sub>	0.266 (SD, 0.442)	0.393 (SD, 0.48)	.258
ADC <sub>b0–50–100–750–1000</sub>	0.331 (SD, 0.526)	0.363 (SD, 0.609)	.445
ADC <sub>b0–50–100–500–750–1000</sub>	0.31 (SD, 0.542)	0.363 (SD, 0.649)	.383
ADC <sub>b0–750–1000</sub>	0.177 (SD, 0.518)	0.506 (SD, 0.483)	.046
ADC <sub>b0–500–750–1000</sub>	0.2 (SD, 0.496)	0.499 (SD, 0.458)	.034
ADC <sub>b100–1000</sub>	0.136 (SD, 0.427)	0.069 (SD, 0.486)	.468
ADC <sub>b500–1000</sub>	0.229 (SD, 0.431)	0.103 (SD, 0.47)	.537
ADC <sub>b750–1000</sub>	0.672 (SD, 0.739)	0.435 (SD, 0.383)	.214
<b>Excess kurtosis</b>			
ADC <sub>b0–1000</sub>	0.12 (SD, 0.71)	1.22 (SD, 0.45)	< .001
ADC <sub>b0–50–100–1000</sub>	0.34 (SD, 0.81)	1.36 (SD, 0.69)	< .001
ADC <sub>b0–50–100–750–1000</sub>	0.57 (SD, 1.25)	1.64 (SD, 1.15)	.008
ADC <sub>b0–50–100–500–750–1000</sub>	0.55 (SD, 1.25)	1.74 (SD, 1.23)	.007
ADC <sub>b0–750–1000</sub>	0.21 (SD, 0.81)	1.22 (SD, 0.58)	.002
ADC <sub>b0–500–750–1000</sub>	0.2 (SD, 0.84)	1.19 (SD, 0.53)	.002
ADC <sub>b100–1000</sub>	0.51 (SD, 1.2)	1.22 (SD, 1.09)	.019
ADC <sub>b500–1000</sub>	0.19 (SD, 0.84)	0.7 (SD, 1.1)	.188
ADC <sub>b750–1000</sub>	0.76 (SD, 2.18)	0.3 (SD, 1.09)	.942

<sup>a</sup> Data are means.<sup>b</sup> Mann-Whitney-Wilcoxon test.<sup>c</sup> Units in  $\times 10^{-6} \text{mm}^2/\text{s}$ .

across this estimated score function. By means of the linear relation between the linear discriminant analysis scores and the original observations, the optimal threshold was calculated to determine the sensitivity, specificity, and accuracy for each ADC map.

Furthermore, to visually evaluate differences between tumors on the studied ADC maps, we generated a customized color map (Online Supplemental Data). This customized map aimed to facilitate visual (semiquantitative) assessment of possible differences between ADC pixel values and their distribution. Visual assessment of tumor ROIs on the color-coded ADC maps was done by the same 2 radiologists without knowledge of the HPV– status, and discrepancies between the scores were solved by consensus. A 5-point Likert scale (1 = definitely HPV–, 2 = probably HPV–, 3 = indeterminate, 4 = probably HPV+, 5 = definitely HPV+) was used. Criteria for visual ROI scoring included perceived tumor heterogeneity and ADC values, both presumed lower in HPV+ OPSCCs.

Statistical analysis was performed with R (Version 3.3.2; RStudio: Integrated Development for R; <https://www.rstudio.com/products/rstudio/download/>). Differences between the 2 tumor groups (HPV+ and HPV– OPSCC) were assessed with a significance level set at  $P < .05$ .

## RESULTS

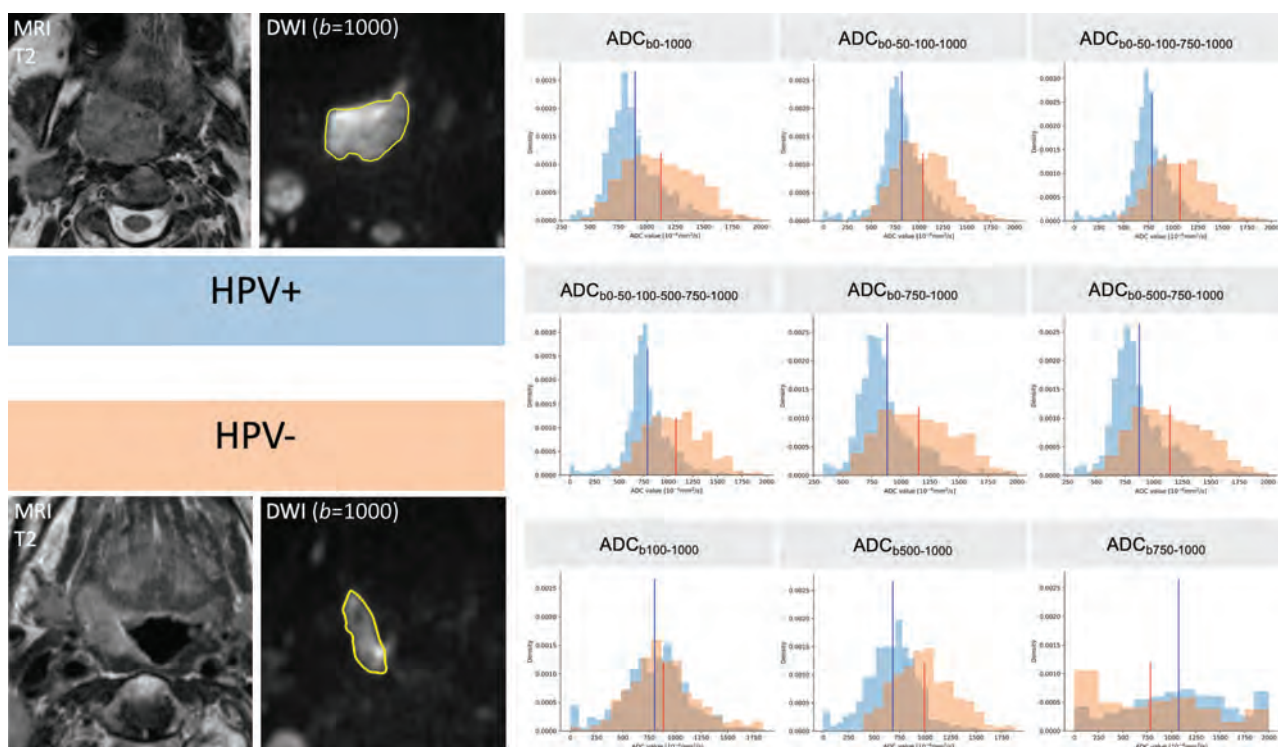
Among the 34 patients included in this study, 23 patients had HPV– OPSCC and 11 patients had HPV+ OPSCC. Patient and tumor characteristics are shown in Table 2.

Table 3 summarizes the results of pair-wise comparisons between ADC histogram parameters of HPV+ versus HPV– OPSCC for all investigated ADC maps on the basis of the ROIs drawn in consensus by the 2 readers. A significantly lower mean ADC was found in HPV+ OPSCC versus HPV– OPSCC only for 3 b-value combinations (ADC<sub>b0–1000</sub>, ADC<sub>b0–750–1000</sub>, and ADC<sub>b0–500–750–1000</sub>), however, not for the other 6 combinations. Likewise, ADC skewness was significantly higher in HPV+ OPSCC than in HPV– OPSCC for the same b-value combinations, however, not for all other combinations. ADC excess kurtosis was significantly higher in HPV+ OPSCC than in HPV– OPSCC for all b-value combinations excepting 2 pure diffusion ADC maps (ADC<sub>b500–1000</sub> and ADC<sub>b750–1000</sub>). The results of pair-wise comparisons are equally illustrated as boxplots in the Online Supplemental Data.

Depending on the choice of b-values, ADC histogram shapes showed significant changes for the same tumor ROI. While HPV+ and HPV– OPSCC could be distinguished from one another on the basis of their different histogram shapes on ADC maps calculated with  $b=0$ , this was not the case for the perfusion-insensitive ADC<sub>b100–1000</sub>, ADC<sub>b500–1000</sub>, and ADC<sub>b750–1000</sub> maps due to overlapping metrics (Fig 1).

Receiver operating curve analyses to discriminate between HPV+ and HPV– OPSCC were performed for all parametric ADC maps. Table 4 illustrates the AUCs for the ADC maps with statistically significant differences between HPV+ and HPV– OPSCC for





**FIG 1.** ADC histogram changes caused by b-value choice illustrated in 2 different patients with OPSCC. T2 and corresponding  $b=1000$  images with tumor ROIs (in yellow) are shown on the left side of the figure. The histograms in blue were obtained from the pixel values of the HPV+ OPSCC ROI, and the histograms in orange, from the pixel values of the HPV- OPSCC ROI. ADC mean values are indicated in blue for the HPV+ OPSCC and in red for the HPV- OPSCC, respectively. On ADC maps with  $b=0$ , HPV+ OPSCC histograms have lower ADC mean values, a slender peak (leptokurtic shape), and a right skew, whereas HPV- OPSCC histograms have higher ADC mean values, lower kurtosis (flatter shape), and a more symmetric shape (Gaussian distribution). On ADC maps with  $b=0$ , the histograms of the 2 tumors can be easily distinguished one from another. This is hardly possible on perfusion-insensitive ADC maps ( $ADC_{b100-1000}$ ,  $ADC_{b500-1000}$ ,  $ADC_{b750-1000}$ ) due to overlapping metrics.

all 3 evaluated metrics, ie, ADC mean, skewness, and kurtosis (Table 3), as well as for the  $ADC_{b100-1000}$  recommended in the literature.<sup>14</sup> Pair-wise comparisons showed that the highest diagnostic performance to distinguish HPV+ from HPV- OPSCC was achieved with excess kurtosis on a mixed perfusion-diffusion map, ie, the  $ADC_{b0-1000}$  map (AUC = 0.893; sensitivity = 100%, specificity = 82.6%, threshold = 0.641). The AUC of excess kurtosis on the  $ADC_{b0-1000}$  map was superior to the AUC of excess kurtosis on the other ADC maps ( $P < .05$ ). However, for ADC mean and skewness, the respective AUCs on  $ADC_{b0-1000}$ ,  $ADC_{b0-750-1000}$ , and  $ADC_{b0-500-750-1000}$  were similar ( $P < .05$ ). In contrast, ADC mean and skewness on  $ADC_{b100-1000}$  could not distinguish HPV+ from HPV- OPSCC ( $P < .05$ ).

The Online Supplemental Data show the same data as in Table 4 but with AUCs calculated with leave-one-out cross-validation and linear discriminant analysis as a model. Results were similar for all maps, albeit with slightly different thresholds.

By means of the customized color map for all tumors, discrepant scores regarding the distinction between HPV+ and HPV- OPSCC were present in 10% of readings (31 of 306 ADC maps). These discrepant readings were solved by consensus. On the basis of a consensus reading, a clearly visible difference between HPV+ and HPV- OPSCCs was found on most ADC maps in terms of heterogeneity and ADC mean values; however, this difference disappeared on the perfusion-insensitive pure diffusion ADC maps calculated

with  $b \geq 500$  (Fig 2). The AUC for visually distinguishing HPV+ from HPV- OPSCC (semiquantitative assessment by the 2 readers in consensus using a 5-point Likert score) was highest for  $ADC_{b0-1000}$  (AUC = 0.723) and  $ADC_{b0-50-100-1000}$  (AUC = 0.715) and lowest for  $ADC_{b500-1000}$  (AUC = 0.649) and  $ADC_{b750-1000}$  (AUC = 0.514), respectively.

## DISCUSSION

HPV+ OPSCC is a distinct tumor entity with a better treatment response in comparison with HPV- OPSCC.<sup>2,3</sup> Several authors have pointed out that noninvasive analysis of tissue-specific parameters with DWI may have implications in the context of personalized treatment and follow-up concepts. Previous studies have indicated that quantitative analysis of textural ADC features may be a useful in vivo biomarker for the assessment of OPSCC, allowing a more comprehensive analysis of tumor tissue than localized biopsy.<sup>8,10</sup> Our study focused specifically on OPSCC because from a clinical point of view, it appears important to investigate tumors from specific sites separately because their characteristics may vary and treatment may differ from one site to another. From a radiologic point of view, there is an interest in optimizing the performance of DWI sequences to better understand differences between HPV+ and HPV- OPSCC at pretreatment imaging and during follow-up while reducing time-consuming MR imaging protocols to the necessary minimum.

**Table 4: Diagnostic performance of ADC maps capable of distinguishing HPV+ from HPV- OPSCC on the basis of ADC mean, skewness, and kurtosis<sup>a</sup>**

Feature	AUC	P Value	TP	FP	TN	FN	Sensitivity	Specificity	Accuracy	Optimal Threshold
ADC <sub>b0-1000</sub>										
ADC mean	0.723	.019	8	7	16	3	0.727	0.695	0.706	1062.429 <sup>b</sup>
ADC skewness	0.731	.016	8	6	17	3	0.727	0.739	0.735	0.349
ADC kurtosis <sup>c</sup>	0.893	<.001	11	4	19	0	1.000	0.826	0.882	0.640
ADC <sub>b0-750-1000</sub>										
ADC mean	0.755	.009	8	7	16	3	0.727	0.695	0.706	1088.702 <sup>b</sup>
ADC skewness	0.715	.023	8	5	18	3	0.727	0.783	0.765	0.500
ADC kurtosis <sup>c</sup>	0.826	.001	10	5	18	1	0.909	0.783	0.823	0.651
ADC <sub>b0-500-750-1000</sub>										
ADC mean	0.755	.009	8	5	18	3	0.727	0.783	0.765	1034.222 <sup>b</sup>
ADC skewness	0.727	.009	8	4	19	3	0.727	0.826	0.794	0.525
ADC kurtosis <sup>c</sup>	0.826	.001	10	5	18	1	0.909	0.783	0.823	0.620
ADC <sub>b100-1000</sub>										
ADC mean	0.636	.105	8	8	15	3	0.727	0.652	0.676	958.089 <sup>b</sup>
ADC skewness	0.581	.231	7	9	14	4	0.636	0.609	0.618	0.133
ADC kurtosis <sup>c</sup>	0.751	.010	9	7	16	2	0.818	0.696	0.735	0.484

**Note:**—TP indicates true-positive; FP, false-positive; TN, true-negative; FN, false-negative.

<sup>a</sup>For comparison, the diagnostic performance of the perfusion-insensitive map recommended in the literature<sup>14</sup> is equally shown. *P* values to distinguish HPV+ from HPV- OPSCC were calculated with the Mann-Whitney-Wilcoxon test. Sensitivity, specificity, and accuracy were calculated using the optimal threshold (Youden index from receiver operating curve analysis).

<sup>b</sup>ADC mean thresholds in  $\times 10^{-6} \text{mm}^2/\text{s}$ .

<sup>c</sup>Excess kurtosis.

The results published in the literature vary concerning the ability of ADC values to distinguish HPV+ OPSCC from HPV- OPSCC. Some authors have demonstrated significant differences between mean ADC values in HPV+ versus HPV- OPSCC,<sup>8-10</sup> and a recent meta-analysis based on 5 studies concluded that mean ADC values are lower in HPV+ OPSCC than in HPV- OPSCC.<sup>11</sup> Other authors, however, could not confirm the usefulness of ADC quantification in the context of OPSCC.<sup>12,13</sup>

The results of our study indicate that the choice of b-values is extremely important in DWI sequences because some b-value combinations fail to successfully distinguish HPV+ from HPV- OPSCCs, whereas other combinations have a high diagnostic performance in this respect. In particular, using only b-values of  $\geq 100$  for ADC calculation appears to be ineffective regarding this specific question. ADC values calculated with high b-values only are perfusion-insensitive, whereas ADC values calculated with  $b=0$  and  $b=1000$  reflect mixed perfusion-diffusion phenomena. It, therefore, appears that the perfusion component of ADC calculation may actually play a more important role in distinguishing HPV+ from HPV- OPSCC than previously thought. Leaving out  $b=0$  values from ADC calculation leads to significant changes in histogram metrics and, as a consequence, the ADC histograms in HPV+ and HPV- OPSCCs tend to overlap, thereby hindering distinction between the 2 tumor types (Fig 1). This finding may explain the conflicting results of previous studies because only EPI DWI protocols with  $b=0$  reported differences in mean ADC values between HPV+ OPSCC and HPV- OPSCC, whereas those without  $b=0$  did not. This perfusion-related effect is most pronounced on mean ADC and skewness, whereas excess kurtosis appears to be a more robust feature because it retains statistical significance on most ADC maps, including the ADC<sub>b100-1000</sub> map (Table 3).

So far, only very few authors have reported a higher ADC excess kurtosis in HPV+ OPSCC compared with HPV- OPSCC.<sup>8,10</sup> Our study confirms this observation. This higher excess kurtosis

observed on most ADC maps can be explained by the fact that HPV+ OPSCCs tend to be more homogeneous tumors; therefore, the number of pixels with the same ADC value in a tumor ROI is higher than in the ROI of a more heterogeneous tumor with variable cellularity and variable amounts of keratinization and/or necrosis, such as HPV- OPSCCs.<sup>8</sup> In addition, it appears that the ADC<sub>b0-1000</sub>, ADC<sub>b0-750-1000</sub>, and ADC<sub>b0-500-750-1000</sub> maps are the most robust to distinguish HPV+ from HPV- OPSCC as on these 3 maps, all studied parameters (mean, skewness, kurtosis) revealed significant differences between the 2 tumor types. Furthermore, when using a customized color scale to distinguish HPV+ from HPV- OPSCC, differences in ADC values and ROI heterogeneity were particularly well visualized on ADC maps with  $b=0$ , whereas both tumor types showed similar features on the perfusion-insensitive ADC maps calculated with  $b \geq 500$  (Fig 2). Finally, our study showed equally that by means of a classic monoexponential model, the acquisition of  $b=0$  and  $b=1000$  was sufficient for distinguishing HPV+ from HPV- OPSCC. Therefore, acquiring multiple b-values did not offer advantages in comparison with ADC<sub>b0-1000</sub>. This result has practical implications because it allows decreasing DWI acquisition times in clinical routine. The time invested in acquiring multiple b-values could thus be used for other sequences or to improve spatial DWI resolution.

Our study has several limitations, and some elements inherent in all methodologies of texture analysis may limit the reproducibility of our observations. First, technical parameters of MR imaging equipment may differ from one vendor to another, making direct comparisons difficult. Second, segmentation is an operator-dependent process and may lead to different definitions of ROIs. Third, the sample size in this study is small. Finally, the focus on OPSCC enhances clinical specificity, but it also limits data generalization to HNSCC arising from other sites. The data of the present study, which focused on primary OPSCC, showed that tumor heterogeneity as reflected by ADC maps can be influenced by the choice of b-

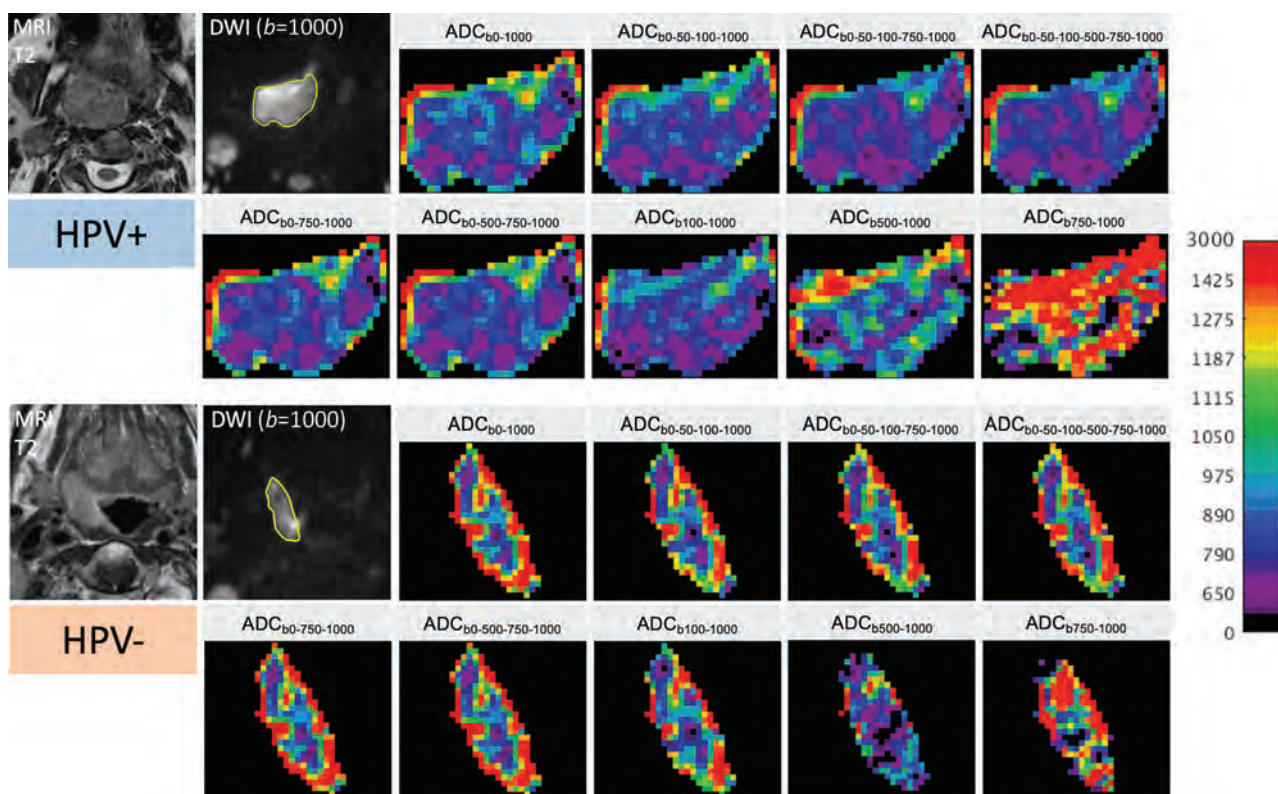


**FIG 2.** Color-coded maps in 2 different patients with OPSCC (same patients as in Fig 1) illustrating changes in ADC pixel values and distribution caused by the choice of b-values. T2 images and corresponding  $b=1000$  images with tumor ROIs (in yellow) are shown on the left. The upper 2 rows on the right show the color-coded ADC maps of the HPV+ OPSCC, while the lower 2 rows show the respective maps of the HPV- OPSCC. For all images, the same color map with the same quantitative scale ( $0\text{--}3000 \times 10^{-6} \text{mm}^2/\text{s}$ ) was used to display the original gray levels. Note the clearly visible difference between HPV+ versus HPV- OPSCC on the ADC maps with  $b=0$ , with HPV+ OPSCC having lower ADCs and less ROI heterogeneity than HPV- OPSCC. This difference disappears on maps calculated with higher b-values only, and the distinction between the 2 tumor types is visually hardly possible on maps calculated with  $b \geq 500$ . The 2 readers correctly identified the HPV+ and the HPV- OPSCC on the first 7 ADC maps; they failed, however, to correctly distinguish between the 2 tumor types on the last 2 ADC maps.

values on EPI DWI sequences. Therefore, further work is needed to determine which microstructural tissue properties are precisely responsible for the observed differences. Future studies may also determine the place of the most appropriate b-value choice in ADC quantification for the follow-up of OPSCC.

## CONCLUSIONS

Our study based on a small population of patients with OPSCC showed that ADC mean, skewness, and kurtosis derived from perfusion-sensitive ADC maps calculated with  $b=0$  and  $b=1000$  can distinguish HPV+ from HPV- OPSCC, whereas mean and skewness from ADC maps calculated with only  $b \geq 100$  values (perfusion-insensitive maps) cannot. The acquisition of multiple b-values did not improve differentiation of HPV+ from HPV- OPSCC.

Disclosure forms provided by the authors are available with the full text and PDF of this article at [www.ajnr.org](http://www.ajnr.org).

## REFERENCES

- Chaturvedi AK, Engels EA, Pfeiffer RM, et al. Human papillomavirus and rising oropharyngeal cancer incidence in the United States. *J Clin Oncol* 2011;29:4294–4301 CrossRef Medline
- Ang KK, Harris J, Wheeler R, et al. Human papillomavirus and survival of patients with oropharyngeal cancer. *N Engl J Med* 2010;363:24–35 CrossRef Medline
- Kaplan AW, Galloway TJ, Bhayani MK, et al. Effect of HPV status on survival of oropharynx cancer with distant metastasis. *Otolaryngol Head Neck Surg* 2020;163:372–74 CrossRef Medline
- Glastonbury CM, Mukherji SK, O'Sullivan B, et al. Setting the stage for 2018: how the changes in the American Joint Committee on Cancer/Union for International Cancer Control Cancer Staging Manual Eighth Edition impact radiologists. *AJNR Am J Neuroradiol* 2017;38:2231–37 CrossRef Medline
- Brierley DE, Gospodarowicz MK, Wittekind C. *TNM Classification of Malignant Tumors*. 8th ed. Wiley-Blackwell; 2017
- Thomas J, Primeaux T. Is p16 immunohistochemistry a more cost-effective method for identification of human papilloma virus-associated head and neck squamous cell carcinoma? *Ann Diagn Pathol* 2012;16:91–99 CrossRef Medline
- Westra WH. The pathology of HPV-related head and neck cancer: implications for the diagnostic pathologist. *Semin Diagn Pathol* 2015;32:42–53 CrossRef Medline
- de Perrot T, Lenoir V, Domingo AM, et al. Apparent diffusion coefficient histograms of human papillomavirus-positive and human papillomavirus-negative head and neck squamous cell carcinoma: assessment of tumor heterogeneity and comparison with histopathology. *AJNR Am J Neuroradiol* 2017;38:2153–60 CrossRef Medline



9. Nakahira M, Saito N, Yamaguchi H, et al. **Use of quantitative diffusion-weighted magnetic resonance imaging to predict human papilloma virus status in patients with oropharyngeal squamous cell carcinoma.** *Eur Arch Otorhinolaryngol* 2014;271:1219–25 CrossRef Medline
10. Ravanelli M, Grammatica A, Tononcelli E, et al. **Correlation between human papillomavirus status and quantitative MR imaging parameters including diffusion-weighted imaging and texture features in oropharyngeal carcinoma.** *AJNR Am J Neuroradiol* 2018;39:1878–83 CrossRef Medline
11. Payabvash S, Chan A, Jabejdar Maralani P, et al. **Quantitative diffusion magnetic resonance imaging for prediction of human papillomavirus status in head and neck squamous-cell carcinoma: a systematic review and meta-analysis.** *Neuroradiol J* 2019;32:232–40 CrossRef Medline
12. Schouten CS, de Graaf P, Bloemena E, et al. **Quantitative diffusion-weighted MRI parameters and human papillomavirus status in oropharyngeal squamous cell carcinoma.** *AJNR Am J Neuroradiol* 2015;36:763–67 CrossRef Medline
13. Wong KH, Panek R, Welsh L, et al. **The predictive value of early assessment after 1 cycle of induction chemotherapy with 18F-FDG PET/CT and diffusion-weighted MRI for response to radical chemoradiotherapy in head and neck squamous cell carcinoma.** *J Nucl Med* 2016;57:1843–50 CrossRef Medline
14. Padhani AR, Liu G, Koh DM, et al. **Diffusion-weighted magnetic resonance imaging as a cancer biomarker: consensus and recommendations.** *Neoplasia* 2009;11:102–25 CrossRef Medline
15. Kolff-Gart AS, Pouwels PJ, Noij DP, et al. **Diffusion-weighted imaging of the head and neck in healthy subjects: reproducibility of ADC values in different MRI systems and repeat sessions.** *AJNR Am J Neuroradiol* 2015;36:384–90 CrossRef Medline
16. Bihan DL. **What can we see with IVIM MRI?** *Neuroimage* 2019;187:156–67 CrossRef Medline
17. Becker M, Varoquaux AD, Combescure C, et al. **Local recurrence of squamous cell carcinoma of the head and neck after radio(chemo)therapy: diagnostic performance of FDG-PET/MRI with diffusion-weighted sequences.** *Eur Radiol* 2018;28:651–63 CrossRef Medline
18. Vandecaveye V, De Keyser F, Vander Poorten V, et al. **Head and neck squamous cell carcinoma: value of diffusion-weighted MR imaging for nodal staging.** *Radiology* 2009;251:134–46 CrossRef Medline
19. Bishop JA, Lewis JS Jr, Rocco JW, et al. **HPV-related squamous cell carcinoma of the head and neck: an update on testing in routine pathology practice.** *Semin Diagn Pathol* 2015;32:344–51 CrossRef Medline
20. Barnes A, Alonzi R, Blackledge M, et al. **UK quantitative WB-DWI technical workgroup: consensus meeting recommendations on optimisation, quality control, processing and analysis of quantitative whole-body diffusion-weighted imaging for cancer.** *Br J Radiol* 2018;91:20170577 CrossRef Medline
21. Feng Z, Min X, Margolis DJ, et al. **Evaluation of different mathematical models and different b-value ranges of diffusion-weighted imaging in peripheral zone prostate cancer detection using b-value up to 4500 s/mm<sup>2</sup>.** *PLoS One* 2017;12:e0172127 CrossRef Medline
22. Zhang J, Suo S, Liu G, et al. **Comparison of monoexponential, biexponential, stretched-exponential, and kurtosis models of diffusion-weighted imaging in differentiation of renal solid masses.** *Korean J Radiol* 2019;20:791–800 CrossRef Medline

# Stroke Recurrence in Children with Vertebral Artery Dissecting Aneurysm

 Z. Ritchey,  T.J. Bernard,  L.Z. Fenton,  J.A. Maloney,  D.M. Mirsky,  I. Neuberger,  I. Sriram,  J. Seinfeld, and  N.V. Stence



## ABSTRACT

**BACKGROUND AND PURPOSE:** Pediatric vertebral artery dissecting aneurysm is a subtype of vertebral artery dissection that can be challenging to diagnose and may be associated with stroke recurrence. This study examines the presenting features, clinical outcomes, and recurrence risk in a cohort of children with vertebral artery dissection, comparing those with aneurysms with those without.

**MATERIALS AND METHODS:** The medical records of children evaluated for vertebral artery dissection were retrospectively reviewed for neurologic presentation, treatment, stroke recurrence, and angiographic appearance of dissection. Cohort patients were categorized into 2 groups based on the presence or absence of a vertebral artery dissecting aneurysm and compared via the Fisher exact test, Student *t* test, and log-rank analyses. *P* < .05 was deemed statistically significant.

**RESULTS:** Thirty-two patients met the inclusion criteria, including 13 with vertebral artery dissecting aneurysms. Five cases of vertebral artery dissecting aneurysm were missed on the initial evaluation and diagnosed retrospectively. All patients received antiplatelet or anticoagulation therapy at the time of diagnosis. Children in the vertebral artery dissecting aneurysm group were more likely to present with stroke (*P* = .059), present at a younger age (*P* < .001), and have recurrent stroke (*P* < .001) compared with the group of children with vertebral artery dissection without an aneurysm. After surgery, no patients with vertebral artery dissecting aneurysm experienced recurrent stroke (*P* = .02).

**CONCLUSIONS:** Vertebral artery dissecting aneurysm is often missed on the initial diagnostic evaluation of children presenting with stroke. In children with vertebral artery dissection, the presence of an aneurysm is associated with stroke presentation at a younger age and stroke recurrence.

**ABBREVIATIONS:** PCAIS = posterior circulation arterial ischemic stroke; RVAC = rotational vertebral artery compression; VAD = vertebral artery dissection; VADA = vertebral artery dissecting aneurysm

In children who present with posterior circulation arterial ischemic stroke (PCAIS), vertebral artery dissecting aneurysms

(VADAs) are a rare and often challenging-to-diagnose subtype of vertebral artery dissection (VAD) that can be detected on angiography. These types of aneurysms are also sometimes referred to as pseudoaneurysms or dissecting pseudoaneurysms, but for clarity in this article and to avoid confusion with the more common colloquial use of the term pseudoaneurysm for post-arterial access lesions, the term VADA will be used. Literature regarding VAD with aneurysm formation is sparse, especially in children.<sup>1-5</sup> The few published cases of pediatric VADA are often grouped together with cases of carotid artery dissection, making it difficult to determine how the study findings relate to this specific patient population. Preceding trauma is a common risk factor for children with VAD or VADA, similar to adults,<sup>4</sup> though a traumatic history is not always elicited. Associations between pediatric VAD and congenital cervical anomalies, eg, odontoid anatomic variants and Klippel-Feil syndrome, have also been reported.<sup>5</sup>

Moreover, several studies have described patients with VAD in the V3 region associated with occlusion of the artery during head-turning, which is sometimes termed rotational vertebral

Received January 17, 2022; accepted after revision March 21.

From the Department of Radiology (Z.R.), Section of Child Neurology (T.J.B.), Department of Pediatrics, Hemophilia and Thrombosis Center (T.J.B.), Department of Pediatrics (I.S.), and Department of Neurosurgery (J.S.), University of Colorado School of Medicine and Children's Hospital Colorado, Aurora, Colorado; and Department of Radiology (L.Z.F., J.A.M., D.M.M., I.N., N.V.S.), Children's Hospital Colorado, University of Colorado Denver, Anschutz Medical Campus, Aurora, Colorado.

This study was supported, in part, by the American Stroke Association/Bugher Foundation Stroke Collaborative Research Center (grant No.14BFSC17540000). This project was also supported, in part, by the Health Resources and Services Administration of the US Department of Health and Human Services under grant number, 2H30MC24049, Mountain States Hemophilia Network.

This information or content and conclusions are those of the authors and should not be construed as the official position or policy of nor should any endorsements be inferred by the Health Resources and Services Administration, US Department of Health and Human Services, or the US Government.

Please address correspondence to Nicholas V. Stence, MD, Department of Radiology, Children's Hospital Colorado, University of Colorado Denver, Anschutz Medical Campus, 13123 E 16th Ave, Aurora, CO 80045; e-mail: nicholas.stence@childrenscolorado.org

 Indicates open access to non-subscribers at [www.ajnr.org](http://www.ajnr.org)

<http://dx.doi.org/10.3174/ajnr.A7518>

artery compression (RVAC) or pediatric bowhunter syndrome. These studies note a high recurrence risk, presumably secondary to chronic recurrent trauma from dynamic compression of the injured portion of the vertebral artery.<sup>6,7</sup> These articles also described the presumed pathophysiology of pediatric bowhunter syndrome, the male predominance in this condition, and the lack of recurrent stroke after surgical interventions, such as endovascular occlusion of the vertebral artery, decompression of the vertebral artery canal, and/or C1–C2 fusion. However, no previous study has compared the clinical course and outcomes in patients with VAD on the basis of the presence or absence of VADA. In our experience, patients with VAD with imaging findings of VADA experience a more malignant clinical course. Thus, the purpose of this study was to report the presenting features, clinical outcomes, and recurrence risk in a cohort of children with VAD, comparing those with VADA with those without.

## MATERIALS AND METHODS

This single-center, Health Insurance Portability and Accountability Act–compliant retrospective study was approved by the Children’s Hospital of Colorado institutional review board. The medical records of children (younger than 18 years of age at symptom onset) evaluated for PCAIS between 2000 and 2020 were reviewed for inclusion criteria: 1) neurologic deficit suspicious for PCAIS at presentation, and 2) VAD confirmed on angiography. Identification of patients included in our study was facilitated by a PACS keyword search using different combinations of the terms “vertebral,” “vertebral artery,” “dissection,” and “aneurysm.” In addition, most patients in our study were already indexed in pre-existing stroke research databases maintained by the authors. Initial diagnostic evaluation at the time of presentation involved a combination of head and neck CT, MR imaging, CTA, MRA, and cerebral angiography studies. Head-turning angiography, which was not routinely performed at this center in the early part of the 20-year study period, was also performed in later selected cases. Follow-up imaging, typically MR imaging/MRA, was routinely performed in patients followed at our institution 3 months after presentation and at 1-year intervals thereafter, and sometimes more frequently following stroke recurrence or change in therapy.

A board-certified pediatric neuroradiologist with 14 years of experience evaluated each case for the presence of cervical VAD and associated features, including the presence of intraluminal thrombus, luminal irregularity, stenosis, occlusion, dissecting aneurysm, and cervical spine abnormalities. Dissecting aneurysms specifically were defined as either fusiform or saccular focal enlargement of a vertebral artery segment. In cases in which an infarct was definitively visualized on initial imaging, a pediatric neuroradiologist and a pediatric neurologist independently confirmed the diagnosis of PCAIS in each patient and classified the causes of stroke using the Childhood AIS Standardized Classification and Diagnostic Evaluation criteria, which is in essence a consensus classification system for childhood arterial ischemic stroke established by the International Pediatric Stroke Study consortium.<sup>8</sup> Cases with any diagnostic uncertainty or with imaging that was thought to be nondiagnostic were excluded. Demographic and clinical information, including age at presentation, sex, race, ethnicity, presenting signs and symptoms, neurologic symptoms at follow-up, and treatment was recorded via chart review. When applicable, testing for thrombophilia and connective

tissue disorders was also documented. Children diagnosed with VAD were separated into 2 comparison groups based on the presence (VADA) or absence (non-VADA) of dissecting aneurysm.

Data analyses were performed by the Fisher exact test and the 2-tailed Student *t* test using GraphPad software (<http://www.graphpad.com/quickcalcs>). In addition, the Kaplan-Meier (log-rank) test was used to compare pre- and postsurgery stroke recurrence in the patients who underwent surgical treatment.  $P < .05$  was deemed statistically significant. The data sets generated during the current study are available from the corresponding author on request.

## RESULTS

### Patients and Presentation

Thirty-two patients met the inclusion criteria, including 13 with VADA. Five cases of VADA were diagnosed on retrospective review because the aneurysm was not described in the initial angiography report. Most of the cohort was male, with a greater male prevalence in the VADA group (Table). If one compared the average age at presentation, patients in the VADA group tended to be younger (4.7 years of age) than those in the non-VADA group (11.8 years of age,  $P < .001$ ).

Common presenting signs and symptoms, similar in incidence between both VADA and non-VADA groups, included headache, hemiparesis, altered mental status, vision change, dysarthria, ataxia, emesis, and seizure. Preceding trauma, eg, trampoline fall, sports injury, or motor vehicle collision, was commonly reported at presentation and not statistically different between groups (7/13 in the VADA group, 10/19 in the non-VADA group,  $P = 1.00$ ).

### Imaging

The initial diagnosis was made on CTA in 16 patients and on MRA in the other 16. Bilateral injuries were seen in 4 total cases, 3 of which were in the VADA group. There were 2 cases with congenital cervical spine anomalies. One patient in the non-VADA group had an anomalous bone spur identified at the C2 level, and the other in the VADA group had an os odontoideum. An additional 5 patients, all in the non-VADA group, presented after traumatic fractures of the cervical spine, and the vertebral artery abnormalities began at the level of fracture in these cases.

In the non-VADA group, the injury most often consisted of a tapered stenosis in the V2 or V3 segments leading to complete or near-complete occlusion of the more upstream segments of the vertebral artery, including the V4 segments. In contrast to injuries in the non-VADA group, VADA occurred almost exclusively in the proximal V3 segment, just after the vertebral artery exit from the transverse foramen. Common imaging features of VADA are summarized in Fig 1. Acutely in these patients with a VADA, the areas of intraluminal narrowing and/or irregularity were seen in combination with focally dilated arterial segments. Intraluminal thrombus was commonly identified in the dilated arterial segments in the setting of acute infarction. Often, a focal outpouching was seen projecting from the proximal V3 segment either anteriorly on axial images or superiorly on coronal images. In contrast to patients without VADA, the vertebral artery lumen in most (12/13) patients with VADA was not completely occluded either at or downstream from the aneurysmally dilated V3 segment. Typically, after



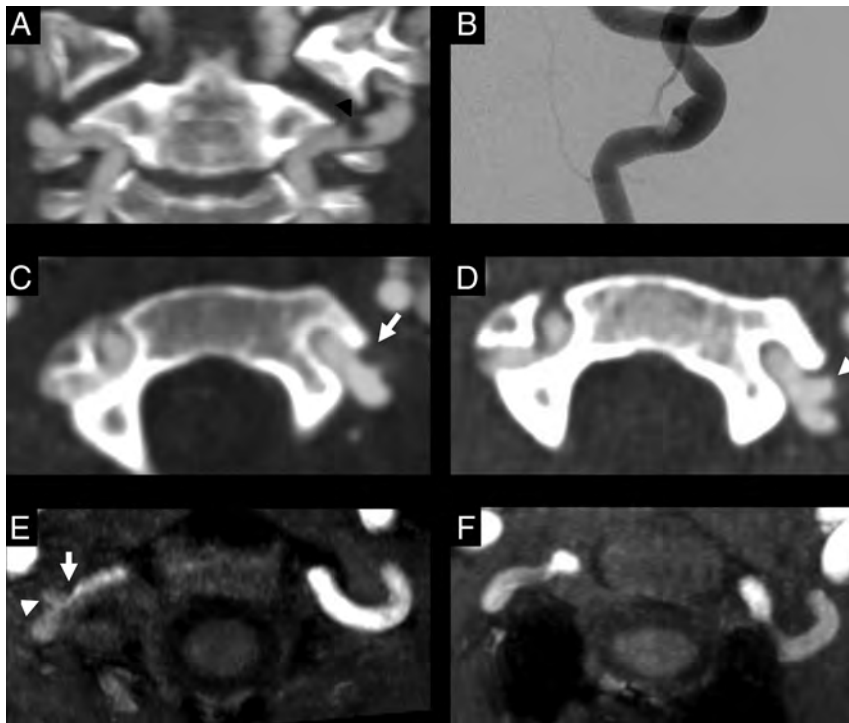


**FIG 1.** Imaging features of VADA. A 6-year-old boy with recurrent posterior circulation infarctions. Coronal CTA (A) and an anterior-posterior image from conventional angiography (B) demonstrate a focal filling defect in a fusiform dilation of the proximal left V3 segment (black arrowhead). C and D, A 7-year-old boy with recurrent posterior circulation infarctions. Axial CTA (C) from presentation shows a focally dilated proximal left V3 segment with a small filling defect (white arrow). Axial CTA (D) after several months of anticoagulation shows that the filling defect has resolved, leaving a saccular outpouching of the same proximal V3 segment (white arrowhead) that was best seen in the axial plane. E and F, Another 7-year-old boy with recurrent posterior infarctions. Axial MRA (E) at presentation shows the focal filling defect in the proximal right V3 segment (white arrow) with focal dilation downstream (white arrowhead). Flow-related enhancement in the entire right vertebral artery was decreased. Axial MRA (F) several months after cervical fusion shows that the filling defect has resolved and the focal dilation is no longer apparent.

anticoagulation or antiplatelet therapy, follow-up imaging showed that the intraluminal thrombus resolved and the areas of outpouching remodeled into more normal-appearing segments.

Thirteen of the 19 patients (68%) in the non-VADA group presented with PCAIS (the other 6 were diagnosed with TIA), while all 13 patients with VADA presented with stroke as confirmed by initial imaging ( $P = .059$ ). There were no cases of recurrent stroke in the non-VADA group (0/19), while the incidence of recurrent stroke was found to be statistically significant in the VADA group (9/13,  $P < .001$ ). Stroke recurrence over time for all patients in the VADA group is presented in a Kaplan-Meier curve in Fig 3).

### Treatment

All 32 patients in the non-VADA and VADA groups received antiplatelet or anticoagulation therapy at the time of diagnosis with either aspirin or unfractionated heparin. Initial treatment with anticoagulation or antiplatelet therapy was relatively homogeneous between the VADA and non-VADA groups. Beginning in 2021, hard cervical collars were used for cervical spine stabilization in patients with VADA per another institution's recommendations,<sup>7</sup>

with no stroke recurrence for the 2 patients in whom they were used. Five patients, all in the VADA group, had definitive surgical treatment following a stroke recurrence after initiation of medical therapy, with 2 of these patients undergoing cervical fusion and 2 undergoing endovascular vertebral artery occlusion (Fig 2). The fifth patient was treated with vertebral artery decompression, as originally described by Fox et al.<sup>6</sup> Pre- and postsurgery stroke recurrence was statistically significant in these 5 patients with VADA ( $P = .02$ ) because none of them had subsequent stroke after surgical intervention.

No patients in the cohort died during their initial hospitalization. All were discharged home in stable condition. Patients in the VADA group were followed for an average of 1914 days following presentation, while the group of patients without VADA were followed for an average of 899 days. At last clinical follow-up, persistent neurologic deficits were common in both the VADA and the non-VADA groups.

### DISCUSSION

To our knowledge, this is the first study to describe the unique differences in long-term outcome between children with VAD involving aneurysms (VADA group) and those without aneurysms (non-VADA group). Despite the rarity of pediatric VADA in the literature,

approximately 41% of our cohort demonstrated VAD with associated aneurysms.

We also believe that this is the first article to clearly describe the high recurrence risk (69%) in pediatric patients with VADA, irrespective of RVAC. Recurrent stroke in these patients tends to occur within the first 6–12 months, as demonstrated by these data. Thus, early treatment of patients with VADA with measures to prevent recurrent injury of the aneurysm is likely warranted, possibly even without an initial trial of medical management. Short-term treatment regimens can consist of antithrombotic therapy and cervical spine stabilization with a hard collar to prevent recurrent injury, as suggested by Braga et al.<sup>7</sup> Indeed, medical management failures in our patients with VADA all occurred while they were treated with a soft collar or no collar. We began using hard collars in 2021 as an additional precaution per the recommendations of Braga et al, and we have observed no stroke recurrences in the 2 patients stabilized in this way.

It remains unclear whether patients with VADA without stroke recurrence, or even with a single recurrent event, benefit from surgical therapy, especially since recurrent events after 1

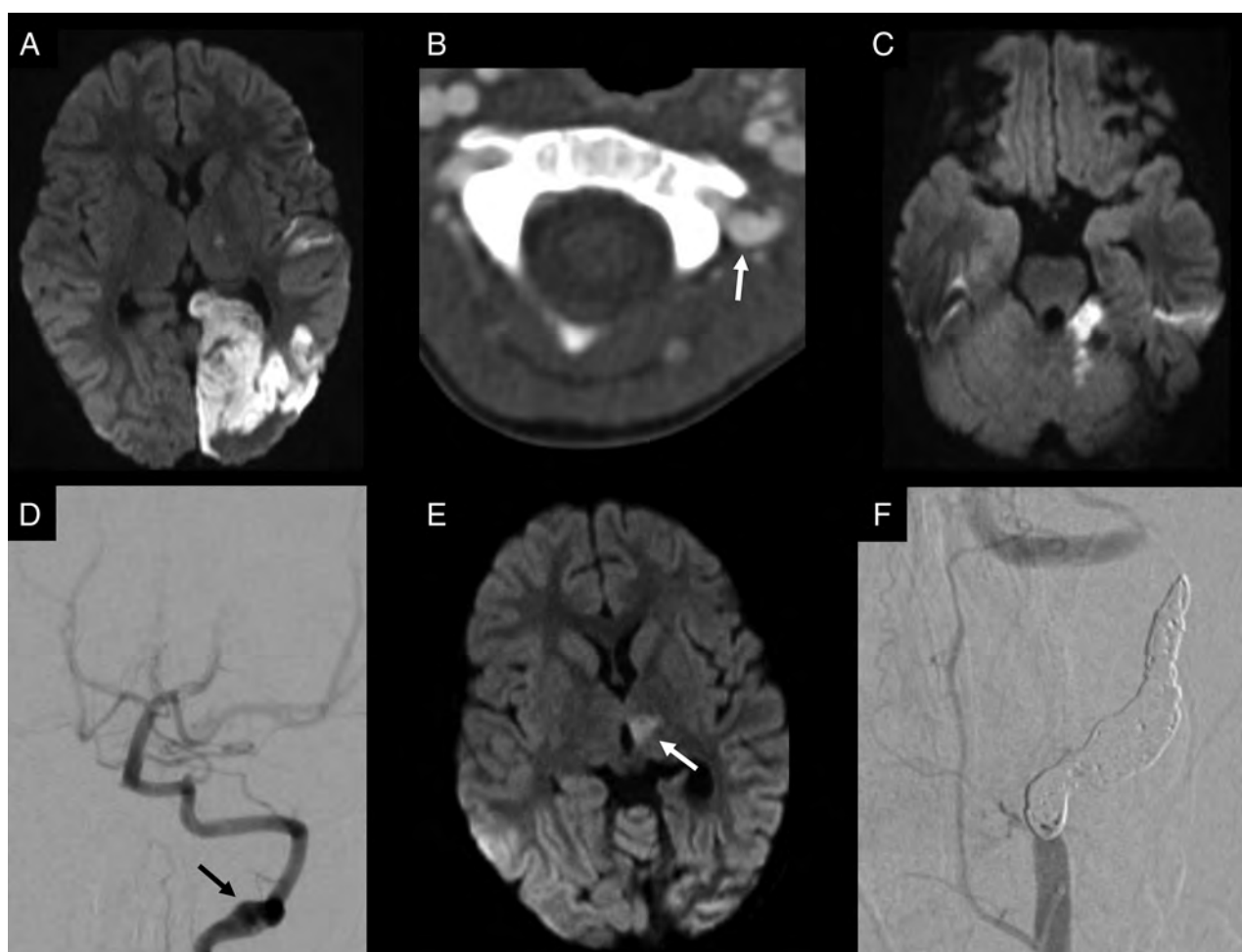


**FIG 2.** A 3-year-old boy initially presenting with syncope. *A*, Axial DWI demonstrates multiple areas of diffusion restriction in the posterior circulation. Abnormalities were bilateral and of differing signal intensity on ADC maps, implying different ages (not shown). *B*, Axial CTA image from the same day as image *A* shows focal dilation of the left V3 proximal segment (*white arrow*). This abnormality was not diagnosed at the time of imaging. *C*, Repeat DWI 3 weeks after initial presentation following new neurologic symptoms while on aspirin demonstrates a new area of restricted diffusion in the left superior cerebellum. *D*, Conventional angiography, performed 2 days after image *C*, demonstrates the focal area of left proximal V3 segment dilation and irregularity (*black arrow*). This abnormality was only present on a single series due to a misalignment of the lateral camera of the biplane, and it was not diagnosed at the time of the procedure. *E*, Axial DWI obtained 8 weeks after initial presentation following another acute neurologic deterioration while on anticoagulation demonstrates a new area of diffusion restriction in the left thalamus (*white arrow*). *F*, Catheter angiogram demonstrates complete coil occlusion of the abnormal vertebral artery segment. No recurrent symptoms or new areas of infarction occurred following this procedure.

year with or without surgical intervention appear to be rare. None of our 13 patients with VADA had recurrent stroke >12 months after their first event. The high rate of recurrent stroke events in this series of patients with VADA suggests that aggressive therapy such as surgical intervention is reasonable and, if not undertaken, should be highly considered with recurrent stroke events.

Five patients in our VADA group who had stroke recurrence underwent surgical intervention, and none had further events. This result is consistent with prior reports of favorable outcomes in children with VAD who had definitive surgical treatment following failed medical management.<sup>9,10</sup> Currently there is a lack of consensus on which surgical treatment is most appropriate, though at our institution vessel-sparing procedures, ie, cervical decompression or fusion, are typically favored over endovascular

coiling, given the lifetime risk of compromise to the contralateral vessel. Generally, we recommend decompression in unilateral cases and fusion in cases of bilateral disease or with findings of cervical spine instability. The alternative of endovascular coiling may be considered when decompression is not feasible, particularly in cases with rapid stroke recurrence and negative findings of RVAC on rotational angiography. However, given the paucity of reported pediatric VADA cases treated by surgery, further multicenter investigation is necessary to determine the efficacy and durability of these techniques.

VADA is commonly acknowledged to be a difficult diagnosis that is sometimes missed on the initial imaging evaluation of children who present with PCAIS or strokelike symptoms. This occurred in 3 of our patients seen between 2000 and 2010.<sup>11</sup> Missed or delayed diagnosis of VADA can lead to inappropriate

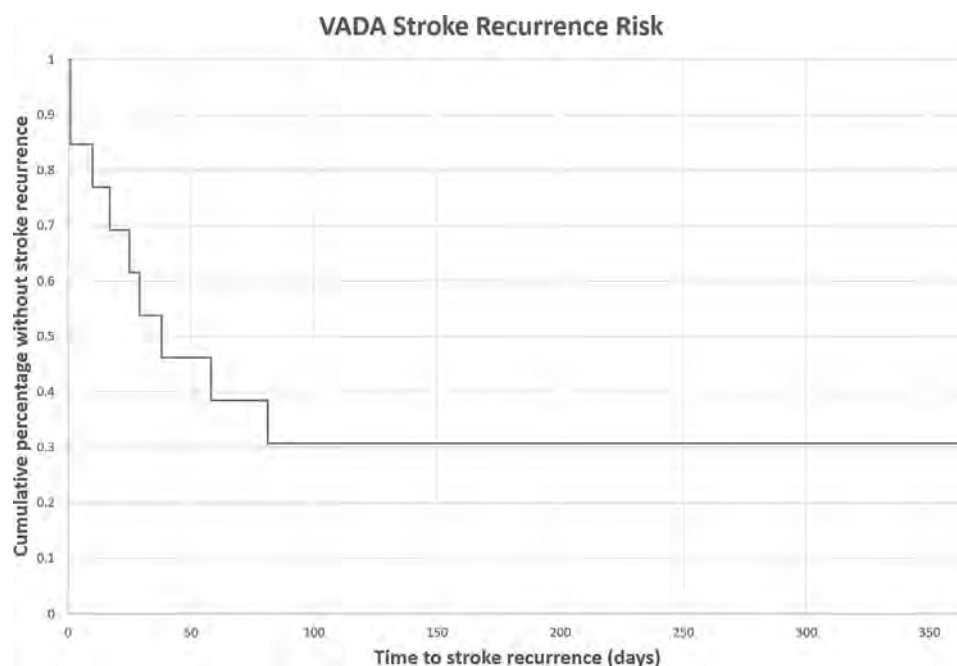


**FIG 3.** Stroke recurrence in the VADA group.

#### Comparison of clinical characteristics at presentation

	Cohort	VADA	Non-VADA	P Value
Age (yr)	8.9	4.7	11.8	<.001
Sex (No.)				.45
Male	21	10	11	
Female	11	3	8	
Initial diagnosis				.059
Stroke	26	13	13	
TIA	6	0	6	
Signs and symptoms (No.)				
Headache	13	5	8	
Hemiparesis	13	6	7	
Altered mental status	10	4	6	
Vision change	7	4	3	
Ataxia	5	4	1	
Emesis	5	2	3	
Dysarthria	5	1	4	
Seizure	4	2	2	
Nausea	3	1	2	
Numbness	2	0	2	
Abdominal pain	1	1	0	
Vertigo	1	1	0	

treatment and possibly poor outcomes. Antithrombotic and/or antiplatelet therapy was initiated in all patients in our cohort. Unfortunately, even when appropriate therapy was initiated soon after diagnosis, many of our patients with VADA experienced recurrent stroke.

The reason that the presence of a dissecting aneurysm in VAD increases the risk of stroke recurrence in children remains unclear. Possibly the aneurysm causes slow or turbulent blood flow in the vertebral artery that, with time, leads to thrombus formation and embolic stroke. Furthermore, patients with VAD with RVAC, ie,

pediatric bowhunter syndrome, may be predisposed to developing VADA. In RVAC, neck rotation causes episodic vertebral artery compression, sometimes in association with a cervical bony abnormality, that can predispose to recurrent vertebral artery injuries and thromboembolism. Although the association between RVAC and pediatric vertebral artery dissection is well documented,<sup>10,12</sup> VADA without RVAC is also seen, and treatment in these cases is uncertain. Currently most institutions do not routinely perform angiography with provocative maneuvers to definitively diagnose RVAC, so the true incidence of pediatric RVAC may be underreported. It is now our practice to perform conventional angiography with head rotation in most of our patients with VADA. In the VADA group of our cohort, only 3 patients, all males, presented with a history and imaging findings consistent with RVAC on rotational angiography.

The limitations of this study include its small sample size, retrospective design, and lack of uniform follow-up. Improvements in neuroimaging quality and increased diagnostic awareness that occurred during the 20-year study period could have impacted the incidence of diagnoses of PCAIS, VAD, and VADA. In addition, there may have been a selection bias toward enrolling patients with more severe symptoms because our cohort was recruited in a tertiary care setting.

## CONCLUSIONS

In our cohort of children with VAD, those with VADA were likely to present with recurrent stroke within 12 months of the initial event. VADA was often missed on the initial diagnostic work-up of children presenting with PCAIS or strokelike symptoms. Clinicians and radiologists evaluating children with PCAIS should carefully assess the presence of VADA and be aware of its influence



on stroke recurrence, even when appropriate therapy is initiated at diagnosis. Neck stabilization during the acute phase with a hard collar is likely warranted, and consideration of surgical treatment should be pursued in cases of failed medical management and possibly as first-line therapy in those with RVAC.

Disclosure forms provided by the authors are available with the full text and PDF of this article at [www.ajnr.org](http://www.ajnr.org).

## REFERENCES

1. Uohara MY, Beslow LA, Billingshurst L, et al. **Incidence of recurrence in posterior circulation childhood arterial ischemic stroke.** *JAMA Neurol* 2017;74:316–23 CrossRef Medline
2. Nash M, Rafay MF. **Craniocervical arterial dissection in children: pathophysiology and management.** *Pediatr Neurol* 2019;95:9–18 CrossRef Medline
3. McCrea N, Saunders D, Bagkeris E, et al. **Diagnosis of vertebral artery dissection in childhood posterior circulation arterial ischemic stroke.** *Dev Med Child Neurol* 2016;58:63–69 CrossRef Medline
4. Mortazavi MM, Verma K, Tubbs RS, et al. **Pediatric traumatic carotid, vertebral and cerebral artery dissections: a review.** *Childs Nerv Syst* 2011;27:2045–56 CrossRef Medline
5. Tan MA, Armstrong D, MacGregor DL, et al. **Late complications of vertebral artery dissection in children: pseudoaneurysm, thrombosis, and recurrent stroke.** *J Child Neurol* 2009;24:354–60 CrossRef Medline
6. Fox CK, Fullerton HJ, Hetts SW, et al. **Single-center series of boys with recurrent strokes and rotational vertebral arteriopathy.** *Neurology* 2020;95:e1830–34 CrossRef Medline
7. Braga BP, Sillero R, Pereira RM, et al. **Dynamic compression in vertebral artery dissection in children: apropos of a new protocol.** *Childs Nerv Syst* 2021;37:1285–93 CrossRef Medline
8. Bernard TJ, Manco-Johnson MJ, Lo W, et al. **Towards a consensus-based classification of childhood arterial ischemic stroke.** *Stroke* 2012;43:371–77 CrossRef Medline
9. Sedney CL, Rosen CL. **Cervical abnormalities causing vertebral artery dissection in children.** *J Neurosurg Pediatr* 2011;7:272–75 CrossRef Medline
10. Rollins N, Braga B, Hogge A, et al. **Dynamic arterial compression in pediatric vertebral arterial dissection.** *Stroke* 2017;48:1070–73 CrossRef Medline
11. Stence NV, Fenton LZ, Goldenberg NA, et al. **Craniocervical arterial dissection in children: diagnosis and treatment.** *Curr Treat Options Neurol* 2011;13:636–48 CrossRef Medline
12. Caton MT, Narsinh K, Baker A, et al. **Asymptomatic rotational vertebral artery compression in a child due to head positioning for cranial surgery: illustrative case.** *Neurosurg: Case Lessons* 2021;1 CrossRef

# Thalamus L-Sign: A Potential Biomarker of Neonatal Partial, Prolonged Hypoxic-Ischemic Brain Injury or Hypoglycemic Encephalopathy?

S.K. Misser, J.W. Lotz, R. van Toorn, N. Mchunu, M. Archary, and A.J. Barkovich



## ABSTRACT

**BACKGROUND AND PURPOSE:** Considerable overlap exists in the MR imaging features of hypoglycemic injury and hypoxic-ischemic brain injury, with similar predilections for the occipital and parietal lobes. In partial, prolonged hypoxia-ischemia, there is cortical destruction at the interarterial watershed zones, and in concomitant hypoglycemia and hypoxia-ischemia, an exaggerated final common pathway injury occurs. We interrogated secondary white matter tract-based thalamic injury as a tool to separate pure injuries in each group.

**MATERIALS AND METHODS:** A retrospective observational study of the MRIs of 320 children with a history of hypoxia-ischemia and/or hypoglycemia was undertaken with 3 major subgroups: 1) watershed-type hypoxic-ischemic injury, 2) neonatal hypoglycemia, and 3) both perinatal hypoxia-ischemia and proved hypoglycemia. Cerebral and thalamic injuries were assessed, particularly hyperintensity of the posterolateral margin of the thalami. A modified Poisson regression model was used to assess factors associated with such thalamic injury.

**RESULTS:** Parieto-occipital injuries occurred commonly in patients with hypoglycemia and/or hypoxia-ischemia. Eighty-five of 99 (86%) patients with partial, prolonged hypoxia-ischemia exhibited the thalamus L-sign. This sign was also observed in patients who had both hypoglycemia and hypoxia-ischemia, predominantly attributable to the latter. Notably, the risk of a thalamus L-sign injury was 2.79 times higher when both the parietal and occipital lobes were injured compared with when they were not involved (95% CI, 1.25–6.23;  $P = .012$ ). The thalamus L-sign was not depicted in patients with pure hypoglycemia.

**CONCLUSIONS:** We propose the thalamus L-sign as a biomarker of partial, prolonged hypoxia-ischemia, which is exaggerated in combined hypoglycemic/hypoxic-ischemic injury.

**ABBREVIATIONS:** HGI = hypoglycemic injury; HIBI = hypoxic-ischemic brain injury

The MR imaging features of hypoglycemic injury (HGI) and hypoxic-ischemic brain injury (HIBI) are well-documented.

Received December 24, 2021; accepted after revision March 21, 2022.

From the Departments of Radiology (S.K.M.) and Pediatrics (M.A.), Faculty of Health Sciences, University of KwaZulu-Natal, Nelson R Mandela School of Medicine, Durban, South Africa; Lake Smit and Partners Inc (S.K.M.), Durban, South Africa; Departments of Radiodiagnosis (J.W.L.) and Paediatrics and Child Health (R.v.T.), Faculty of Medicine and Health Sciences, Stellenbosch University, Cape Town, South Africa; Biostatistics Research Unit (N.M.), South African Medical Research Council, Durban, South Africa; School of Mathematics, Statistics and Computer Sciences, (N.M.), University of KwaZulu-Natal, Pietermaritzburg, South Africa; Centre for the AIDS Programme of Research in South Africa (N.M.), Urban, South Africa; and School of Medicine (A.J.B.), University of California, San Francisco, San Francisco, California.

Please address correspondence to Shalendra Kumar Misser, MD, Department of Radiology, University of KwaZulu-Natal, Faculty of Health Sciences, Nelson R Mandela School of Medicine, Durban, South Africa, Lake Smit and Partners Inc, Suite 301-327, The Atrium, Overport City, Durban, South Africa; e-mail: shalendra.misser@lakesmit.co.za

Indicates open access to non-subscribers at [www.ajnr.org](http://www.ajnr.org)

Indicates article with online supplemental data.

<http://dx.doi.org/10.3174/ajnr.A7511>

In pure HGI, without HIBI, some authors have demonstrated a posterior-predominant pattern of cerebral injury with a predilection for the occipital and parietal lobes.<sup>1–4</sup> Other studies have noted that the pattern of HGI may be more widespread and not always limited to the parieto-occipital areas.<sup>5</sup> In the partial, prolonged type of HIBI, destruction of the cortex typically involves the interarterial anterior, posterior, and peri-Sylvian watershed zones and the contiguous white matter.<sup>6–10</sup> HIBI-associated thalamic injury has been less frequently described, and in this study, we attempted to investigate thalamic involvement in children with documented partial, prolonged HIBI, neonatal hypoglycemia, or combined hypoxic-ischemic and hypoglycemic injuries.

## MATERIALS AND METHODS

MR imaging studies performed on 320 term neonates with suspected HIBI and/or HGI were analyzed for specific anatomic patterns of injury. The retrospective, multicenter nature of the study

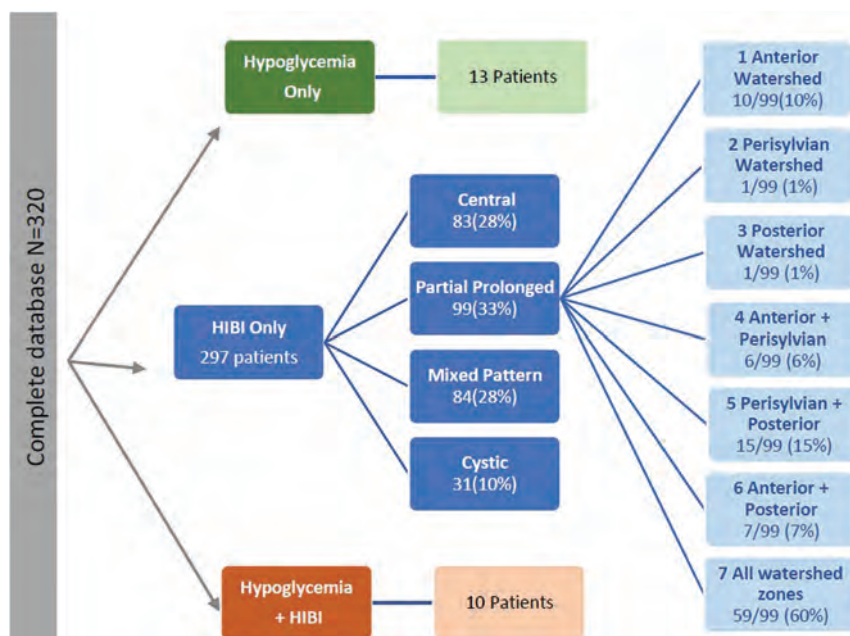


**FIG 1.** Derivation of the 3 major study groups, the subgroups of HIBI, and the subtypes of watershed patterns of injury in patients who had partial, prolonged HIBI.

and the various clinical setups did not allow time standardization of imaging; all imaging occurred after the acute phase of injury. Imaging studies were conducted on 1.5T MR imaging scanners (Siemens). The sequences performed in all patients included sagittal T1-weighted volumetric: 1-mm-slice GE (TR/TE = 1900/2.95 ms), coronal volumetric inversion recovery: 1.1-mm-slice spin-echo (TR/TE = 4000/363 ms), axial T2-weighted, axial FLAIR, axial diffusion-weighted/ADC, coronal inversion recovery through the temporal lobes, axial susceptibility-weighted and coronal T2-weighted sequences were obtained in all patients. Ethics approval was obtained from University of KwaZulu-Natal (BREC00001036/2020).

After anonymization, images were reviewed by 2 radiologists (S.K.M. and J.W.L. with 15 and 30 years of experience in neuroradiology respectively), who were blinded to all patient data. Brain MR imaging findings were divided by consensus into 3 major study subgroups (Fig 1). The HIBI subgroup was categorized into 4 patterns; additionally, the partial prolonged HIBI group was further subdivided into 7 (Fig 1) watershed injury pattern subtypes. We noted 3 categories of thalamic involvement: posterolateral/pulvinar, atypical, and no thalamic injury. In particular, the first category referred to those patients with an injured pulvinar and the lateral margin of the thalamus abutting the posterior limb of the internal capsule. In patients with a documented central (basal ganglia–thalamus) pattern or mixed-type HIBI (with partial, prolonged, and central patterns), there is often ventral thalamic injury, usually of the ventral posterior lateral nuclei.<sup>6,9</sup> In addition, assessment of the posterolateral aspect of the thalami is difficult in patients who have had multilobar cystic encephalomalacia with severe or total brain injury. Patients with these 3 patterns (central, mixed, and cystic encephalomalacia) of HIBI were excluded, as well as those with incomplete clinical information and poor-quality images.

A separate cohort of 13 patients (uppermost in Fig 1) with documented neonatal hypoglycemia was evaluated for thalamic and cerebral injuries, to assess pulvinar and cortical, especially parieto-occipital, injury. Each of these 13 patients had a similar set of MR imaging sequences (as above). These studies were independently reviewed by S.K.M. and J.L.

Blood glucose levels were documented in all neonates who had symptomatic hypoglycemia. Neonatal hypoglycemia was defined by a recorded plasma glucose value of <1.8 mmol/L during the first 2 hours of life or <2.6 mmol/L thereafter.<sup>11</sup> Hypoxic-ischemic encephalopathy was excluded on the basis of the absence of fetal distress, normal findings on blood gas analysis, reassuring Apgar scores at 1 and 5 minutes, and the absence of multiorgan hypoxia.

The third group of 10 patients (lowermost in Fig 1) included those in whom both perinatal hypoxic-ischemic encephalopathy and hypoglycemia were documented. Particular attention was paid to identification of injury to the watershed

zones and pulvinar involvement in these patients. The Apgar scores together with documented perinatal hypoxia-ischemia and blood gas analyses confirmed HIE, and there was also recorded hypoglycemia in all these children, either after birth or in the first 2 days of life as per the criteria outlined above.

### Statistical Analysis

Categoric variables of the key features of each partial, prolonged HIBI subtype and thalamic injury location were expressed as frequencies and percentages and compared using either the  $\chi^2$  test or the Fisher exact test if there were <5 observations in any cell. A modified Poisson regression model was used to assess factors associated with pulvinar thalamic injury versus nil and atypical subtypes combined. A 2-tailed  $P < .05$  indicated statistical significance. All statistical analyses were conducted using SAS, Version 9.4 (SAS Institute).

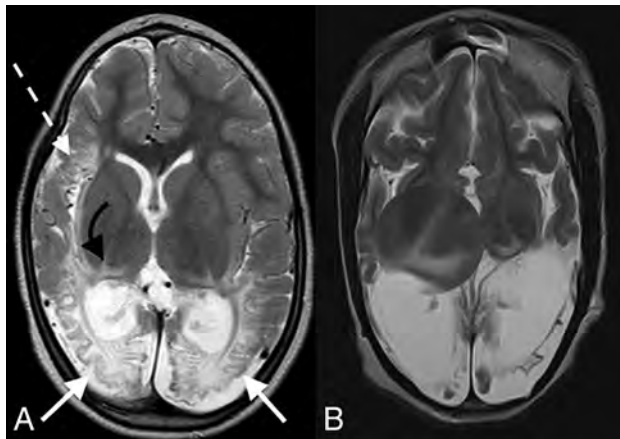
### RESULTS

The group of 99 term neonates with HIBI demonstrating partial, prolonged patterns of injury were imaged in the chronic phase of injury, with the average age at the time of imaging being 6 years. This sample ( $n = 99$ ) included 41 female patients and 58 male patients and were categorized into 7 subtypes, as shown in Fig 1. Table 1 highlights the prevalence, type, and severity of thalamic injury in children with each subtype of partial, prolonged HIBI in relation to the cortical injuries located in the frontal, parietal, occipital, peri-Sylvian, and hindbrain regions. There was a high degree of correlation of the MR imaging features between both readers with no major discrepant findings. Lobar involvement was shown to be high across all 4 cerebral lobes in descending order: occipital (91.9%), parietal (89.9%), frontal (88.9%), and temporal lobes



**Table 1: Key features of the 7 subtypes of partial prolonged/watershed HIBI**

Lobe/Structure	Features	Subtype 1	Subtype 2	Subtype 3	Subtype 4	Subtype 5	Subtype 6	Subtype 7	Overall
		Anterior (n = 10)	Peri-Sylvian (n = 1)	Posterior (n = 1)	Anterior + Peri-Sylvian (n = 6)	Peri-Sylvian + Posterior (n = 15)	Anterior + Posterior (n = 7)	All 3 Zones (n = 59)	(n = 99)
Thalamic injury location (No.) (%)	Nil			1 (16.7)		3 (30.0)			4 (4.0)
	Atypical Thalamus L-sign	1 (100.0)	1 (100.0)	2 (33.3) 3 (50.0)	15 (100.0)	7 (70.0)	1 (14.3) 6 (85.7)	59 (100.0)	10 (10.1) 85 (85.9)
Thalamus score (No.) (%)	Not/less involved	1 (100.0)	1 (100.0)	6 (100.0)	14 (93.9)	10 (100.0)	6 (85.7)	53 (89.8)	91 (91.9)
	Markedly destroyed				1 (6.7)		1 (14.3)	6 (10.2)	8 (8.1)
Parietal (No.) (%)	Not involved			3 (50.0)		6 (60.0)	1 (14.3)		10 (10.1)
	Involved	1 (100.0)	1 (100.0)	3 (50.0)	15 (100.0)	4 (40.0)	6 (85.7)	59 (100.0)	89 (89.9)
Occipital (No.) (%)	Not involved	1 (100.0)				7 (70.0)			8 (8.1)
	Involved		1 (100.0)	6 (100.0)	15 (100.0)	3 (30.0)	7 (100.0)	59 (100.0)	91 (91.9)
Frontal (No.) (%)	Not involved		1 (100.0)		8 (53.3)	1 (10.0)		1 (1.7)	11 (11.1)
	Involved	1 (100.0)		6 (100.0)	7 (46.7)	9 (90.0)	7 (100.0)	58 (98.3)	88 (88.9)
Temporal (No.) (%)	Not involved				3 (20.0)	6 (60.0)	3 (42.9)	3 (5.1)	15 (15.2)
	Involved	1 (100.0)	1 (100.0)	6 (100.0)	12 (80.0)	4 (40.0)	4 (57.1)	56 (94.9)	84 (84.8)
Cerebellum (No.) (%)	Not involved		1 (100.0)	4 (66.7)	10 (66.7)	7 (70.0)	5 (71.4)	40 (67.8)	67 (67.7)
	Involved	1 (100.0)		2 (33.3)	5 (33.3)	3 (30.0)	2 (28.6)	19 (32.2)	32 (32.3)
Brainstem (No.) (%)	Not involved	1 (100.0)	1 (100.0)	6 (100.0)	14 (93.3)	10 (100.0)	7 (100.0)	49 (83.1)	88 (88.9)
	Involved				1 (6.7)			10 (16.9)	11 (11.1)

**FIG 2.** Axial T2-weighted images in a child with partial, prolonged HIBI demonstrating interarterial injuries at the peri-Sylvian (*dashed white arrow*) and posterior parieto-occipital (*solid white arrows*) watershed regions. Note the thalamus L-sign (*curved arrows* in A and highlighted by the loupe in a second patient in B).

(84.8%) (Table 1). In the subgroup of patients who demonstrated all 3 watershed zone injuries (9/99), we found injury to the posterolateral margin of the thalamus (adjacent to the posterior limb of internal capsule) and posterior thalamic (pulvinar and lateral geniculate) nuclei on both sides, shown in Fig 2, which we term the “thalamus L-sign.” Overall, the thalamus L-sign was present in 86% (85/99) of patients with prolonged, partial HIBI. Furthermore, subtype 7 with involvement of all 3 watershed zones was the most prevalent HIBI subtype among the 85 (69.4%) patients demonstrating the thalamus L-sign injury.

None of the patients ( $n = 10$ ) with isolated anterior watershed injury had a thalamus L-sign. In some cases, signal abnormalities were evident in the anterior thalamus, usually medially and ventrally, but these never included the ventral posterior lateral nucleus. All patients (61/99) in subtypes 2, 3, and 7 showed a bilateral thalamus L-sign. When the anterior and peri-Sylvian watershed zones were involved together (in subtype 4), we noted that half of those patients had a positive thalamus L-sign, but in each of these, the sign was identified unilaterally, only on the side where the peri-Sylvian cortex was destroyed. One patient in subtype 5 had a faint unilateral posterior thalamic hyperintensity on the side where the watershed cortex destruction was more pronounced, but this was not categorized as a thalamus L-sign. The rest of the patients in subtype 5 all demonstrated a bilateral thalamus L-sign. One patient of subtype 6 did not demonstrate the sign; however, the anterior watershed zone was severely destroyed in this instance, with only minimal posterior watershed involvement. This patient’s pattern of injury simulates that of subtype 1.

A key correlation is the concomitant injury at the posterolateral thalamus and the lobes involved in the watershed zones of the cerebrum. There were statistically significant differences between the thalamus L-sign injury versus the other types of injuries combined; in particular, injuries involving the parietal, occipital, and temporal lobes were significantly more prevalent in the thalamus L-sign injury compared with other thalamic injuries (nil and atypical) (Table 2). Critically, the risk of experiencing a thalamus L-sign-type injury was 7.38 times higher when an occipital lobe injury was identified compared with when it was not involved (95% CI, 1.18–46.23), and this finding was statistically significant ( $P = .033$ ). Similarly, the risk of experiencing a thalamus L-sign injury was 3.07 times higher when a parietal injury was present compared

**Table 2: Key features involved in thalamus L-sign injury compared with other thalamic injuries (nil and atypical)**

Lobe/Structure	Features	Thalamus L-Sign (n = 85)	Other (n = 14)	Overall (n = 99)	P Value
Thalamus score (No.) (%)	Not/less involved	77 (90.6)	14 (100.0)	91 (91.9)	<.001
	Markedly destroyed	8 (9.4)			
Parietal (No.) (%)	Not involved	3 (3.5)	7 (50.0)	10 (10.1)	<.001
	Involved	82 (96.5)	7 (50.0)	89 (89.9)	
Occipital (No.) (%)	Not involved	1 (1.2)	7 (50.0)	8 (8.1)	<.001
	Involved	84 (98.8)	7 (50.0)	91 (91.9)	
Frontal (No.) (%)	Not involved	10 (11.8)	1 (7.1)	11 (11.1)	1.000
	Involved	75 (88.2)	13 (92.9)	88 (88.9)	
Temporal (No.) (%)	Not involved	9 (10.6)	6 (42.9)	15 (15.2)	.007
	Involved	76 (89.4)	8 (57.1)	84 (84.8)	
Cerebellum (No.) (%)	Not involved	57 (67.1)	10 (71.4)	67 (67.7)	1.000
	Involved	28 (32.9)	4 (28.6)	32 (32.3)	
Brainstem (No.) (%)	Not involved	74 (87.1)	14 (100.0)	88 (88.9)	.355
	Involved	11 (12.9)		11 (11.1)	

**Table 3: Factors associated with the thalamic L-sign injury**

Lobe/Structure	RR	95% CI	P Value
Parietal	3.07	1.19–7.93	.020
Occipital	7.38	1.18–46.23	.033
Frontal	0.94	0.76–1.15	.539
Temporal	1.51	0.99–2.29	.055
Cerebellum	1.03	0.87–1.21	.738
Brainstem	1.19	1.09–1.30	<.001
Parietal + occipital	2.79	1.25–6.23	.012

Note:—RR indicates relative risk.

with when it was not involved (95% CI, 1.19–7.93), and this finding was statistically significant ( $P = .020$ ). Notably, the risk of experiencing a thalamus L-sign injury was 2.79 times higher when both parietal and occipital injuries were involved compared with when they were not involved (95% CI, 1.25–6.23), and this finding was also statistically significant ( $P = .012$ ) (Table 3).

The risk of experiencing a thalamus L-sign injury was 1.19 times higher when a brainstem injury was present compared with when it was not involved (95% CI, 1.09–1.30), and this finding was statistically significant ( $P < .001$ ). The risk of experiencing a thalamus L-sign injury was also higher when the frontal lobe, temporal lobe, and cerebellar injuries were all present compared with when they were not involved; however, this finding was not statistically significant at a 5% level of significance (Table 3).

The second major group of patients studied included those with isolated hypoglycemic injury. This cohort comprised 13 term-gestation neonates with 9 males and 4 females. We noted that in all of these patients with confirmed pure HGI (without any documented hypoxic-ischemic injury), there was cerebral injury identified with gray and white matter involvement (as shown in Fig 3 and the Online Supplemental Data), which included collation of axial T2-weighted and FLAIR images (at the level of the thalamus) for 10 selected patients in this subgroup. In all these patients, we found cortical injuries, particularly involving the posterior watershed zones of the parietal and occipital lobes. The encephalomalacia seen in these brain areas on the chronic-phase imaging studies performed was largely indistinguishable from that seen in children who had HIBI. We did not identify anterior watershed cortical territory involvement in any of these 13 patients. Of critical importance, the posterior thalami were never injured in any of these 13 children with HGI. This is a key distinguishing feature from those children who had posterior

watershed HIBI, in whom we consistently identified the thalamus L-sign.

In the third group of 10 patients who sustained both HGI and HIBI, the thalamus L-sign was also observed in all patients on MR imaging studies acquired at the average age of 5 years. The axial T2-weighted images of these patients are compiled in the Online Supplemental Data. The blood glucose levels, Apgar scores at 1 and 5 minutes, as well as other clinical parameters of hypoxic-ischemic encephalopathy were documented in each child. When concomitant injury was incurred, there was an exaggerated final common pathway injury through the dorsal aspect of the thalami, which manifested as an L-shaped hyperintensity involving the pulvinar and lateral margin of the thalamus superimposed on features of watershed territory ischemic injury. This pattern of injury (common to all patients in this subgroup) is shown in 2 such examples in Fig 4. The degree of thalamic signal hyperintensity and volume loss was marked in all of these patients.

## DISCUSSION

In partial, prolonged HIBI,<sup>6,8–10</sup> especially affecting the posterior and peri-Sylvian watershed zones, we have repeatedly shown involvement of the posterior and lateral aspects of the thalamus, which we believe to be a highly sensitive biomarker. This thalamus L-sign described here is consistently identified in children who have a perinatal, partial, prolonged pattern of HIBI. Additionally, we note that in our study, the thalamus L-sign was not observed in patients who had isolated, pure HGI without HIBI. We, therefore, propose the thalamus L-sign as a possible biomarker for HIBI of the partial, prolonged subtype, particularly when the posterior watershed territories have been involved. Furthermore, in patients who have endured combined hypoglycemia and hypoxia-ischemia, the phenomenon is exaggerated, likely due to the compounded lack of usable substrates for brain metabolism.<sup>12</sup>

The thalamus is a central hub serving to interconnect several brain structures to each other and to the cerebellum, spinal cord, and peripheral nervous system.<sup>13</sup> Injuries to the thalamus provide an indirect indication of tract-based injuries to other parts of the brain, and by analyzing the involved substrates, we can infer a pattern of injury that can be assigned to a particular pathophysiologic process.<sup>14</sup> Thalamic involvement in the HIBI of the central subtype injury pattern is well-documented<sup>15,16</sup> and typically

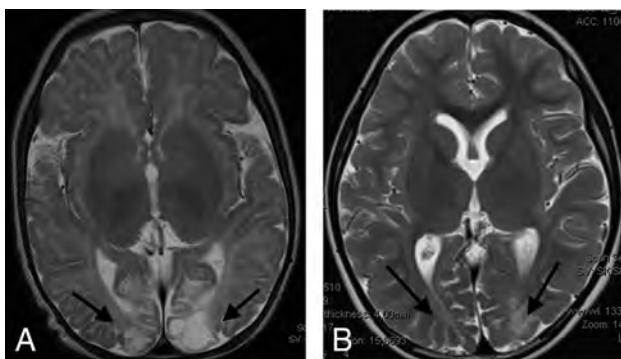


**FIG 3.** Axial T2-weighted images in 2 children with proved neonatal hypoglycemia. There is bilateral occipital lobe encephalomalacia (arrows) related to hypoglycemic brain injury. Note the absence of any thalamic injury.

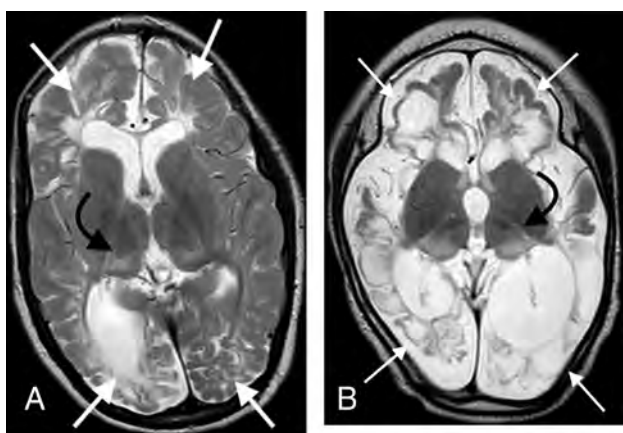


**FIG 4.** Combined hypoxic-ischemic and hypoglycemic brain injury in 2 children with documented neonatal encephalopathy. Note the exaggerated signal abnormality and thalamic volume loss (black arrows). There are multiple watershed areas (white arrows) demonstrating encephalomalacia change.

demonstrates sparing of the pulvinar and lateral margin of the thalami.

The pulvinar or hockey stick sign has been linked to other disorders, including Fabry disease,<sup>17</sup> a variant-type Creutzfeldt-Jakob disease,<sup>18</sup> status epilepticus,<sup>19</sup> and Wernicke encephalopathy.<sup>20</sup> In contrast, in the cases described here, we found an inverted configuration to the hockey stick, with a characteristically repeated L-shape due to involvement of the posterior and lateral substrates of the thalamus rather than the paramedian nuclei. The thalamic nuclei involved, shown in Figs 2, 4, and 5, probably include the thalamic reticular nucleus (abutting the posterior limb of internal capsule), the pulvinar nucleus, and the lateral geniculate nucleus. Typically, these structures when contiguously involved lead to an L-shaped signal abnormality in the thalami. We postulated that these anatomic structures collaborate as a functional unit enabling the dorsal and ventral stream pathways that operate via multiple transthalamic connections.<sup>21</sup> The dorsal stream pathway is responsible for recognition of objects in space and proposing or guiding subsequent actions.<sup>22</sup> This stream begins with the visual (occipital) cortex identification of objects in the visual field, followed by spatial awareness

of the object through parietal lobe connections. The ventral stream pathway also begins with visual cortex input, which passes through the lateral geniculate nuclei (especially the parvocellular layer) and from there onward to the temporal lobe (for limbic and memory connections) or to the parietal lobe via the dorsal stream (for accurate object location and motion initiation).<sup>23</sup>

Jang et al<sup>24</sup> performed a tract-based DTI analysis of the ascending reticular activating system in 14 children with HIBI. They demonstrated lower reticular activating system involvement in patients with impaired arousal. We believe that the posterolateral thalamic margin that we see in children with partial, prolonged HIBI includes, in part, involvement of the thalamic extension of the reticular activating system, which is located in this portion of the thalamus. Some of the hyperintensity may well be due to Wallerian degeneration change adjacent to the posterior limb of internal capsule secondary to the white matter involvement in the parietal, occipital, and peri-Sylvian regions, which pass through these corticospinal long tracts.<sup>9</sup>

We have found that all those with HIBI who demonstrated posterior watershed involvement either on its own or with peri-Sylvian watershed zone involvement also had a high correlation with a positive thalamus L-sign. In fact, all 59 patients (100%) who had partial, prolonged HIBI, all with watershed zone involvement, showed the thalamus L-sign.

In contrast, all those individuals with isolated anterior watershed involvement did not demonstrate the thalamus L-sign. When the anterior watershed was associated with other watershed territory involvement, we noted that the thalamus L-sign was often present, probably consequent to the more posterior cerebral injury. The posterior watershed territories supply axons that contribute to the projection fibers that traverse the centrum ovale, forceps major, and optic radiation. These white matter tracts and neural networks feed into the lateral geniculate nuclei and the pulvinar of the thalami. We found the risk of experiencing a thalamus L-sign injury to be 2.79 times higher when the parietal and occipital injuries were involved compared with when they were not involved (95% CI, 1.25–6.23), and this finding was statistically significant ( $P = .012$ ) (Table 3). We speculate that the involvement of these thalamic nuclei may well reflect Wallerian degeneration along these tracts.

The patterns of brain injury seen in partial, prolonged HIBI have been found to be very similar to those of HGI, and there is considerable overlap in the injuries in these 2 entities.<sup>5,25</sup> Most studies involve heterogeneous groups of children with concomitant or sequential hypoxic-ischemic and hypoglycemic brain injuries having been sustained. Wong et al<sup>5</sup> demonstrated that specific imaging findings could be identified for both hypoglycemia and hypoxia-ischemia in term infants with neonatal encephalopathy. They showed an 82% positive predictive value for the radiologic diagnosis of hypoglycemic brain injury with selective posterior white matter and pulvinar edema the most predictive of clinical hypoglycemia. In contrast, none of the patients with hypoglycemia in our study demonstrated any signal abnormalities in the pulvinar or posterolateral thalami. We suspect that the changes described by Wong et al<sup>5</sup> correspond to the third group in our study, in which a final common pathway injury was found. This suggestion is based on a listed limitation by the authors in that they were unable to separate HIBI from HGI in their cohort studied, and the described



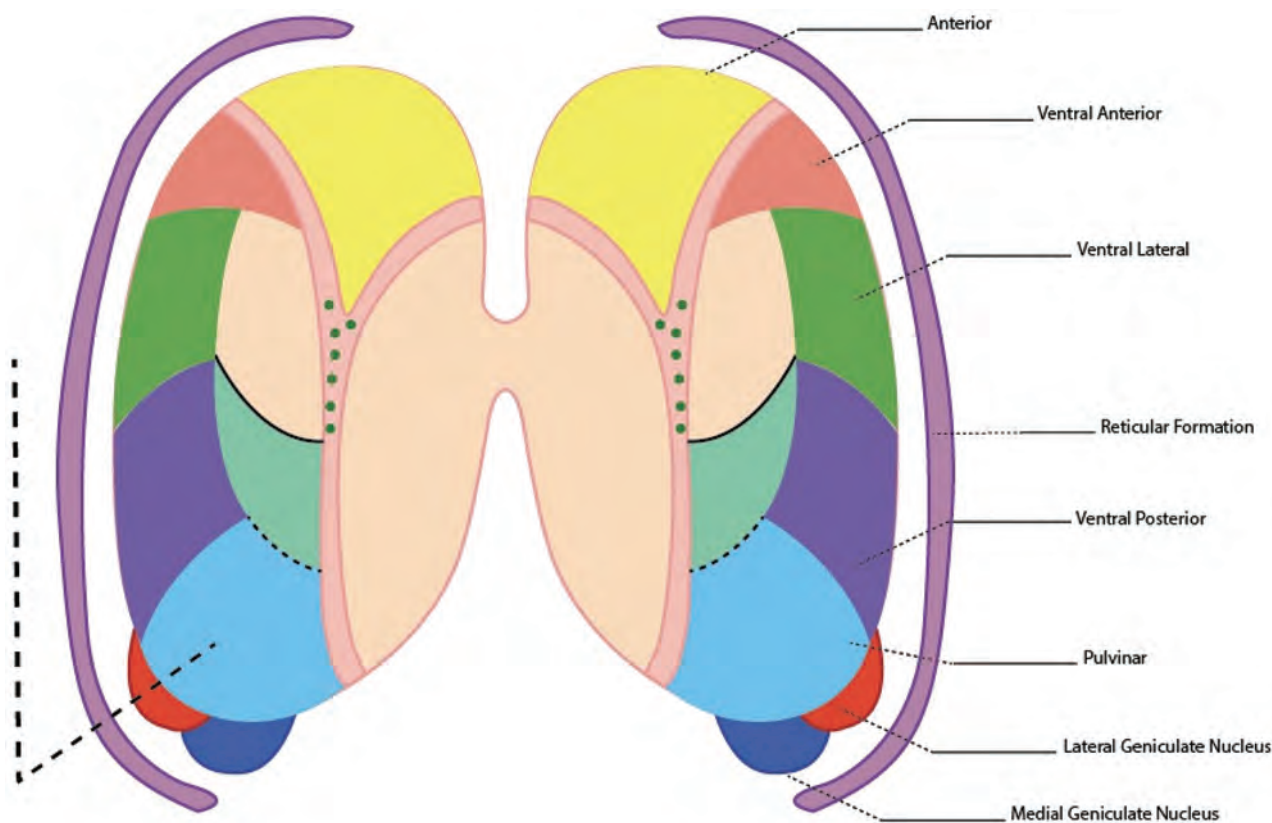


**FIG 5.** The key thalamic nuclei identified as components of the thalamus L-sign (dotted line) include the pulvinar, the lateral geniculate nucleus, and the reticular formation nuclei. Illustration by Neil Northey.

posterior thalamic injuries in that study were more likely representative of the mixed, final common pathway.

Tam et al<sup>25</sup> showed an increased risk of injury to the corticospinal tracts in children who had perinatal hypoglycemia. Using multivariate logistic regression analysis to adjust for biomarkers of HIBI, the authors described an association between corticospinal tract injury and neonatal hypoglycemia. These patients, however, were not children with isolated hypoglycemia; many probably had HIBI, and the degree of corticospinal tract and other substrate injuries may largely be due to hypoxia-ischemia. An important conclusion raised by the same authors was the need for specific biomarkers to separate HIBI from HGI, something this study attempts to prove using the thalamus L-sign. Another limitation of that study<sup>25</sup> was the variability in the timing of blood glucose measurement revealing hypoglycemia. This is a universal occurrence (which we also noted) with the timing of blood glucose monitoring and not a standardized practice. The variability in neonatal glucose levels warrants investigation, with a view to further establishing norms for the timing of the measurement thereof. In our study, we were fortunate in that all the patients that we identified with hypoglycemia had documented blood glucose levels either in the immediate neonatal period or in the first days of life.

This recommendation was echoed in the study by Basu et al,<sup>26</sup> in which patients were referred to a central hospital from outlying hospitals and early glycemic measurements were not obtained in

all patients. However, a strength noted in their study was the correlation between hypoglycemia and the predominant watershed pattern of brain injury, resonating the findings of previous studies.<sup>1</sup> It has been shown that the combination of hypoglycemia and hypoxia-ischemia is associated with worse perinatal and long-term outcomes, including mortality.<sup>27,28</sup> The upshot of anaerobic metabolism on a fetus that had hypoxia-ischemia is inefficient energy production and the glucose that is available is rapidly used, with attendant hypoglycemia and inadvertent lower energy output (1 glucose molecule yields 2 adenosine triphosphate molecules versus a 1:38 ratio in aerobic conditions).<sup>29</sup> The difficulty has always been to separate the 2 entities.<sup>12</sup> We have shown that by using this thalamus-L sign described here, we were able to possibly distinguish HIBI from pure HGI.

A limitation of our study was the retrospective evaluation of patients who were born some years earlier, with a lack of standardized recording of clinical information and timing of the MR imaging studies. Lack of complete medical records and blood test results (blood gas and glucose levels) was an exclusion criterion. All patients included here had available medical records. The possibility of having included other patients (if records were available) would have increased the subgroup numbers. It would possibly also improve the validity of the study with larger groups, and such prospective studies with timeous blood gas and glucose analyses would be encouraged.

## CONCLUSIONS

The vicious interplay between hypoxia and hypoglycemia and their attendant secondary inflammatory cascades leads to a combined final common pathway injury, especially in patients whose mother had prolonged labor. The thalamus L-sign, we propose, is an indication of a partial, prolonged type of HIBI and occurs in patients who have endured additional HGI. In the patients presented here, who had documented, isolated, pure HGI without HIBI, the thalamus L-sign was not observed. We, therefore, introduce this sign as a possible biomarker for HIBI of the partial prolonged subtype, particularly when the posterior watershed territories have been involved. This phenomenon is exaggerated in patients with combined HGI and HIBI due to the compounded lack of usable substrates for brain metabolism.<sup>12</sup> Future prospective studies, preferably with the MR imaging scans performed around the time of suspected perinatal injury, with clinical correlation of obstetric events (such as prolonged obstructive labor, uterine hyperstimulation, and other key factors) would serve to validate our study findings in the acute setting.

Disclosure forms provided by the authors are available with the full text and PDF of this article at [www.ajnr.org](http://www.ajnr.org).

## REFERENCES

1. Barkovich AJ, Ali FA, Rowley HA, et al. **Imaging patterns of neonatal hypoglycemia.** *AJNR Am J Neuroradiol* 1998;19:523 CrossRef Medline
2. Spar JA, Lewine JD, Orrison WW. **Neonatal hypoglycemia: CT and MR findings.** *AJNR Am J Neuroradiol* 1994;15:1477 Medline
3. Alkalay AL, Flores-Sarnat L, Sarnat HB, et al. **Brain imaging findings in neonatal hypoglycemia: case report and review of 23 cases.** *Clin Pediatr (Phila)* 2005;44:783–90 CrossRef Medline
4. Burns CM, Rutherford MA, Boardman JP, et al. **Patterns of cerebral injury and neurodevelopmental outcomes after symptomatic neonatal hypoglycemia.** *Pediatrics* 2008;122:65–74 CrossRef Medline
5. Wong DS, Poskitt KJ, Chau V, et al. **Brain injury patterns in hypoglycemia in neonatal encephalopathy.** *AJNR Am J Neuroradiol* 2013;34:1456–61 CrossRef Medline
6. de Vries LS, Groenendaal F. **Patterns of neonatal hypoxic-ischaemic brain injury.** *Neuroradiology* 2010;52:555–66 CrossRef Medline
7. Ghei SK, Zan E, Nathan JE, et al. **MR imaging of hypoxic-ischaemic injury in term neonates: pearls and pitfalls.** *Radiographics* 2014;34:1047–61 CrossRef Medline
8. Huang BY, Castillo M. **Hypoxic-ischemic brain injury: imaging findings from birth to adulthood.** *Radiographics* 2008;28:417–39 CrossRef Medline
9. Misser SK, Barkovich AJ, Lotz JW, et al. **A pictorial review of the pathophysiology and classification of the magnetic resonance imaging patterns of perinatal term hypoxic ischemic brain injury: what the radiologist needs to know.** *SA J Radiol* 2020;24:1915 CrossRef Medline
10. Chacko A, Andronikou S, Mian A, et al. **Cortical ischaemic patterns in term partial-prolonged hypoxic-ischaemic injury: the inter-arterial watershed demonstrated through atrophy, ulegyria and signal change on delayed MRI scans in children with cerebral palsy.** *Insights Imaging* 2020;11:53 CrossRef Medline
11. Narvey MR, Marks SD. **The screening and management of newborns at risk for low blood glucose.** *Paediatr Child Health* 2019;24:536–44 CrossRef Medline
12. Basu P, Som S, Choudhuri N, et al. **Contribution of the blood glucose level in perinatal asphyxia.** *Eur J Pediatr* 2009;168:833–38 CrossRef Medline
13. Hwang K, Bertolero MA, Liu WB, et al. **The human thalamus is an integrative hub for functional brain networks.** *J Neurosci* 2017;37:5594–5607 CrossRef Medline
14. Squarcina L, Bertoldo A, Ham TE, et al. **A robust method for investigating thalamic white matter tracts after traumatic brain injury.** *Neuroimage* 2012;63:779–88 CrossRef Medline
15. Van Cauter S, Severino M, Ammendola R, et al. **Bilateral lesions of the basal ganglia and thalami (central grey matter)-pictorial review.** *Neuroradiology* 2020;62:1565–605 CrossRef Medline
16. Sie LT, van der Knaap MS, Oosting J, et al. **MR patterns of hypoxic-ischemic brain damage after prenatal, perinatal or postnatal asphyxia.** *Neuropediatrics* 2000;31:128–36 CrossRef Medline
17. Lidove O, Klein I, Lelièvre JD, et al. **Imaging features of Fabry disease.** *AJR Am J Roentgenol* 2006;186:1184–91 CrossRef Medline
18. Macfarlane RG, Wroe SJ, Collinge J, et al. **Neuroimaging findings in human prion disease.** *J Neurol Neurosurg Psychiatry* 2007;78:664–70 CrossRef Medline
19. Katramados AM, Burdette D, Patel SC, et al. **Periictal diffusion abnormalities of the thalamus in partial status epilepticus.** *Epilepsia* 2009;50:265–75 CrossRef Medline
20. Zuccoli G, Santa Cruz D, Bertolini M, et al. **MR imaging findings in 56 patients with Wernicke encephalopathy: nonalcoholics may differ from alcoholics.** *AJNR Am J Neuroradiol* 2009;30:171–76 CrossRef Medline
21. Sheth BR, Young R. **Two visual pathways in primates based on sampling of space: exploitation and exploration of visual information.** *Front Integr Neurosci* 2016;10:37 CrossRef Medline
22. Laycock R, Cross AJ, Lourenco T, et al. **Dorsal stream involvement in recognition of objects with transient onset but not with ramped onset.** *Behav Brain Funct* 2011;7:34 CrossRef Medline
23. Kaas JH, Lyon DC. **Pulvinar contributions to the dorsal and ventral streams of visual processing in primates.** *Brain Res Rev* 2007;55:285–96 CrossRef Medline
24. Jang SH, Kim SH, Lim HW, et al. **Injury of the lower ascending reticular activating system in patients with hypoxic-ischemic brain injury: diffusion tensor imaging study.** *Neuroradiology* 2014;56:965–70 CrossRef Medline
25. Tam EW, Haeusslein LA, Bonifacio SL, et al. **Hypoglycemia is associated with increased risk for brain injury and adverse neurodevelopmental outcome in neonates at risk for encephalopathy.** *J Pediatr* 2012;161:88–93 CrossRef Medline
26. Basu SK, Ottolini K, Govindan V, et al. **Early glycemic profile is associated with brain injury patterns on magnetic resonance imaging in hypoxic ischemic encephalopathy.** *J Pediatr* 2018;203:137–43 CrossRef Medline
27. Vannucci RC, Vannucci SJ. **Cerebral carbohydrate metabolism during hypoglycemia and anoxia in newborn rats.** *Ann Neurol* 1978;4:73–79 CrossRef Medline
28. Bathla G, Policeni B, Agarwal A. **Neuroimaging in patients with abnormal blood glucose levels.** *AJNR Am J Neuroradiol* 2014;35:833–40 CrossRef Medline
29. Singh M. **Care of the baby in the labor room.** In: Singh M, ed. *Care of the Newborn*. 6th ed. Sagar Publications; 2004:107

In the article “Prediction of Wound Failure in Patients with Head and Neck Cancer Treated with Free Flap Reconstruction: Utility of CT Perfusion and MR Perfusion in the Early Postoperative Period” (Y. Ota, A.G. Moore, M.E. Spector, et al, *AJNR Am J Neuroradiol* 2022;43:585–91; 10.3174/ajnr.A7458, 35361578), Dr Andreea Gabriela Moore, who is listed as the second author, should be recognized as a co-first author due to her contribution.

The authors regret this error.

<http://dx.doi.org/10.3174/ajnr.A7506>